Universidade de Aveiro Departamento de Física
2017

André Antunes de Carvalho Albuquerque

Processamento Ótico de Sinal para Sistemas de Comunicações Óticas

All-Optical Signal Processing for Optical Communication Systems

André Antunes de Carvalho Albuquerque

Processamento Ótico de Sinal para Sistemas de Comunicações Óticas

All-Optical Signal Processing for Optical Communication Systems

Tese apresentada à Universidade de Aveiro para cumprimento dos requesitos necessários à obtenção do grau de Doutor em Engenharia Física, realizada sob a orientação científica de Rogério Nunes Nogueira, Investigador Principal no Instituto de Telecomunicações, Universidade de Aveiro e co-orientação científica de Miguel Vidal Drummond, Investigador no Instituto de Telecomunicações, Universidade de Aveiro.

Apoio financeiro da Fundação para a Ciência e a Tecnologia através da bolsa de investigação SFRH/BD/79482/2011 e POPH/FSE.

FCT
Fundação para a Ciência e a Tecnologia
MINISTÉRIO DA EDUCAÇÃO E CIÊNCIA

POPH
QUALIFICAR É CRESCER.

QREN
QUADRO DE REFERÊNCIA ESTRATÉGICO NACIONAL
PORTUGAL 2007.2013

GOVERNO DA REPÚBLICA PORTUGUESA

UNIÃO EUROPEIA
Fundo Social Europeu

o júri / the jury

presidente / president

Doutor Fernando Manuel dos Santos Ramos
Professor Catedrático, Departamento de Comunicação e Arte da Universidade de Aveiro

vogais / examiners committee

Doutora Camille-Sophie Brès
Assistant Professor, Institute of Electrical Engineering, École Polytechnique Fédérale de Lausanne (EPFL), Lausanne.

Doutor Adolfo da Visitação Tregeira Cartaxo
Professor Catedrático, Departamento de Ciências e Tecnologias da Informação, ISCTE - Instituto Universitário de Lisboa.

Doutor João Lemos Pinto
Professor Catedrático, Departamento de Física da Universidade de Aveiro.

Doutor Rogério Nunes Nogueira
Investigador Principal, Instituto de Telecomunicações, Aveiro.

Doutor Orlando José Reis Frazão
Professor Auxiliar Convidado, Departamento de Física e Astronomia, Faculdade de Ciências da Universidade do Porto.

É em lágrimas que te escrevo. Infelizmente a tua alegria e boa disposição já não preenche as nossas vidas. Resta-nos a tua memória.

Aprendi contigo muitas coisas, preparaste-me para a vida, e com o teu exemplo aprendi a ser um homem. Sei que tinhas um orgulho imenso em mim e os teus olhos brilhavam sempre que regressava a casa aos fins de semana. Também eu tenho muito orgulho em ti, e sei bem tudo o que passaste para que nunca me faltasse nada. Sentimos muito a tua falta.

Recordo perfeitamente o quanto ansiavas pelo dia em que terminasse o meu doutoramento. Porém, a vida pode ser bastante cruel, e foi já na recta final que partiste. De todas as pessoas, sei que tu eras quem mais desejava este dia. Também sei que estiveste e estás a meu lado a dar-me força e coragem.

Por tudo o que foste, por tudo o que fizeste, dedico-te a ti esta tese.

Muito obrigado por tudo Pai.
Continuas e continuarás para sempre nos nossos corações.

agradecimentos / acknowledgments

Over the last four and a half years I have been extraordinarily privileged to work with very talented, generous and wonderful people, to whom I express my sincere gratitude.

First and foremost I would like to acknowledge my supervisors, Dr. Rogério Nogueira and Dr. Miguel Drummond for accepting me as a Ph.D. student and for their attention and advice. Without their support and guidance I would not be able to finish my Ph.D. Dr. Rogério Nogueira is a very resourceful and experienced advisor, who had the incredible ability of quickly finding solutions and alternatives for the problems I faced during my Ph.D. He has always cared about my academic studies, as well as my professional career. I cannot thank Dr. Rogério enough for all that he has done for me. Dr. Miguel Drummond has not only been an excellent and supporting advisor, but he has also been a good friend. I admire his creativity and his ability to make me laugh, even in the most disappointing and darkest moments. Dr. Miguel Drummond is also a role model of dedication and hard work.

I would like to express my gratitude to Dr. Naoya Wada for letting me stay at the National Institute of Information and Communications Technology as a trainee student and to Dr. Benjamin Puttnam, who supervised my work therein. I learned from Dr. Benjamin Puttnam how to properly conduct experiments and address the main problems found in the lab. He is also a very good friend and companion. I miss our badminton and football games.

All the members of the Photonic Network System Laboratory were very kind and often stopped their work to help me. In particular, I would like to thank Dr. Ruben Luis, Dr. Jose Mendinueta, Dr. Satoshi Shinada and Dr. Guo-Wei Lu for helping me with my experiments.

I am very grateful to Dr. Rui Morais for teaching me the fundamentals of optical networks and helping me revising my thesis. His kindness and positive attitude are very inspiring.

My dear friends Álvaro Almeida, Ana Rita Araújo, Daniel Gonçalves, Fábio Pereira, João Araújo, Magda Sousa, Saul Sales, Telmo Almeida, Tiago Veiga and Vanessa Duarte played an important role during my Ph.D., and I am very thankful for the incredible and funny moments we had together.

Getting a Ph.D. often comes with sacrifices on your personal life and Ana Nascimento has been very supportive and understanding. We shared this journey together, side by side.

Last, but not the least, I would like to thank to my parents, who I also dedicate this thesis, for their sacrifices and encouragement. They consider that education should be the foundation of any society and I absolutely agree with them.

Muito obrigado!
André Albuquerque

Palavras Chave

Comunicações óticas, processamento ótico de sinal, ótica não-linear, guias de onda em niobato de lítio com inversão periódica dos domínios ferroelétricos, fibras fortemente não-lineares, conversão de comprimento de onda, amplificação sensível à fase, regeneração de fase.

Resumo

O processamento ótico de sinal é uma alternativa possível para melhorar o desempenho e eficiência de sistemas de comunicações óticas, mas o seu estágio atual de desenvolvimento é ainda insuficiente para aplicações em sistemas reais. De forma a inverter esta situação, novas estratégias e possibilidades para processamento ótico de sinal são aqui investigadas, com ênfase em conversão de comprimento de onda, regeneração de fase e amplificação sensível à fase em dispositivos de niobato de lítio com inversão periódica dos domínios ferroelétricos e fibras fortemente não-lineares.

Um novo método para o desenho do perfil de inversão dos domínios ferroelétricos nos dispositivos de niobato de lítio de acordo com um espetro de conversão alvo é investigado nesta tese. O método proposto é validado numericamente e através da produção de um dispositivo real com largura de banda de conversão de 400 GHz. O dispositivo produzido é utilizado para conversão de onda multicanal de oito sinais modulados em fase, com a possibilidade adicional de sintonizar o comprimento de onda dos sinais convertidos. Observa-se a existência de um compromisso entre elevada largura de banda de conversão e eficiência do dispositivo.

São também investigadas nesta tese conversão e permuta de comprimento de onda tolerantes ao ruído de fase adicionado por fontes de bombeamento. Demonstra-se neste trabalho que a utilização de fontes de bombeamento coerentes permite evitar a adição de ruído de fase aos sinais convertidos.

Nesta tese é também analisada analítica e numericamente amplificação sensível à fase baseada em dispositivos de niobato de lítio com inversão periódica dos domínios ferroelétricos para configurações de amplificadores de um, dois ou quatro modos. É ainda avaliada a possibilidade de gerar ondas correlacionadas e de realizar amplificação sensível à fase num único dispositivo com propagação bidirecional. Com base neste esquema, demonstra-se regeneração de fase de sinais modulados em fase, porém com ganho limitado devido à baixa eficiência de conversão dos dispositivos e com desempenho afetado por instabilidades térmicas e fotorrefrativas. Motivado por estas limitações, demonstra-se amplificação de elevado ganho num amplificador sensível à fase de quatro modos, construído com uma fibra fortemente não-linear em vez de um dispositivo de niobato de lítio.

Por fim, é efetuada uma análise numérica do impacto de utilizar amplificadores sensíveis à fase em vez de amplificadores de fibra dopada com érbio no alcance em transmissão ponto a ponto de sinais e na amplificação e regeneração em redes óticas. Demonstra-se que amplificadores sensíveis à fase são mais vantajosos para formatos de modulação avançados e sistemas compostos por ligações óticas longas. As simulações assumem modelos simplificados para o ganho e ruído dos amplificadores, bem como uma versão modificada do modelo de ruído Gaussiano para estimar a potência das distorções não-lineares em sistemas com compensação total da dispersão cromática no final de cada segmento de fibra entre amplificadores.

Keywords

Optical communications, all-optical signal processing, nonlinear optics, periodically poled lithium niobate waveguides, highly nonlinear fibers, wavelength conversion, phase-sensitive amplification, phase regeneration.

Abstract

All-optical signal processing techniques are a possible way to improve the performance and efficiency of optical communication systems, but the current stage of development of such techniques is still unsatisfactory for real-world implementation. In order to invert this situation, new strategies and possibilities for all-optical signal processing are investigated here, with a particular focus on wavelength conversion, phase regeneration and phase-sensitive amplification in periodically poled lithium niobate waveguides and highly nonlinear fibers.

A new and flexible method to design the poling pattern of periodically poled lithium niobate devices according to a target conversion spectrum is investigated in this work. The proposed method is validated through numerical simulations and by producing a real device with broad conversion bandwidth of 400 GHz. The device is then used for multichannel wavelength conversion of eight phase-modulated signals, with the additional possibility to tune the wavelength of the converted signals. A trade-off between high conversion bandwidth and conversion efficiency is observed.

Advanced wavelength conversion and wavelength exchange tolerant to the phase noise added by the pump lasers are also investigated. It is shown that the additional phase noise transferred to the converted signals is eliminated by using coherent pumps, generated from the same light source.

Phase-sensitive amplification based on periodically poled lithium niobate devices is also investigated in this thesis by numerically comparing the gain properties for one-, two- and four-mode configurations. The possibility to simultaneously generate correlated waves and observe phase-sensitive amplification in a single device with bidirectional propagation is also demonstrated. Using such scheme, "black-box" phase regeneration of phase-encoded signals is experimentally demonstrated, albeit with limited net gain due to the low conversion efficiency of the device, and the limited reliability due to thermal and photorefractive instabilities. Motivated by such limitations, high-gain amplification in a four-mode phase-sensitive amplifier built with a highly nonlinear fiber instead of a periodically poled lithium niobate is demonstrated.

Finally, the impact of using phase-sensitive amplifiers instead of common erbium-doped fiber amplifiers on the reach in point-to-point transmission and on the amplification and regeneration requirements in optical transport networks is numerically investigated. The calculations show that phase-sensitive amplifiers are particularly advantageous when considering high-order modulation formats and for transport networks comprised by long links. The numerical simulations are performed using simplified models for the gain and noise properties of the amplifiers, and a modified enhanced Gaussian noise model to estimate the power of the nonlinear distortions in systems with full dispersion compensation at the end of each span of fiber.

"*If you think in terms of a year, plant a seed.*
If in terms of ten years, plant trees.
If in terms of 100 years, teach the people."
Guan Zhong

Contents

List of Figures

List of Acronyms

ADC	analog-to-digital converter
APE	annealed proton-exchanged
ASE	amplified spontaneous emission
AWG	arbitrary waveform generator
B2B	back-to-back
BER	bit error ratio
BPF	bandpass filter
BPSK	binary phase-shift keying (PSK)
BREN	Bulgarian Research and Education Network
BS	Bragg scattering
CE	conversion efficiency
cSFG/DFG	cascaded sum- and difference-frequency generation
cSHG/DFG	cascaded second-harmonic and difference-frequency generation
CW	continuous wave
DC	direct current
DCU	dispersion compensation unit
DFB	distributed feedback laser
DFG	difference-frequency generation
DRM	deleted-reversal method
DSP	digital signal processing
ECL	external cavity laser
EDFA	erbium-doped fiber amplifier
EGN	enhanced Gaussian noise
FDM	finite-differences method

FFT fast Fourier transform

FL fiber laser

FWM four-wave mixing

GN Gaussian noise

GRIIRA green-induced infrared absorption

GVD group velocity dispersion

HNLF highly nonlinear fiber

IQM in-phase/quadrature modulator

LPA layer peeling algorithm

MEGN modified enhanced Gaussian noise

MI modulation instability

MZI Mach-Zehnder interferometer

MZM Mach-Zehnder modulator

NF noise figure

NICT National Institute of Information and Communications Technology

NLI nonlinear interference

NLRN National LambdaRail Network

ODL optical delay line

OOK on-off keying

OP optical processor

OSA optical spectrum analyzer

OSNR optical signal-to-noise ratio

OSP optical signal processing

OWC optical wavelength conversion

PC phase conjugation

PCF photonic crystal fiber

PD photodetector

PI phase-insensitive

PIA phase-insensitive amplifier

PLL phase-locked loop

PM phase modulator

PMD polarization mode dispersion

PoIC polarization controller

PPG pulse pattern generator

PPLN periodically poled lithium niobate

PPLT periodically poled lithium tantalate

PRBS pseudo-random bit sequence

PS phase-sensitive

PSA phase-sensitive amplifier

PSD power spectral density

PSDR phase-sensitive dynamic range

PSK phase-shift keying

PZT lead zirconate titanate

QAM quadrature-amplitude modulation

QPM quasi-phase matching

QPSK quadrature phase-shift keying

RF radio frequency

ROADM reconfigurable optical add-drop multiplexer

RWA routing and wavelength assignment

SBS stimulated Brillouin scattering

SD signal depletion

SFG sum-frequency generation

SHG second-harmonic generation

SNR signal-to-noise ratio

SOA semiconductor optical amplifier

SPM self-phase modulation

SRS stimulated Raman scattering

SSFT split-step Fourier transform

TEC thermo-electric cooler

THG third-harmonic generation

TOD third-order dispersion

TTG two-tone generator

TWM three-wave mixing

VOA variable optical attenuator

WDE wavelength data exchange

WDM wavelength-division multiplexing

WSS wavelength-selective switch

XGM cross-gain modulation

XPM cross-phase modulation

List of Symbols

α	absorption coefficient
β	wavenumber
$\boldsymbol{\beta}$	wave vector
Γ	normalization factor
γ	nonlinear coefficient
$\Delta\beta$	phase mismatch parameter
$\Delta\beta_{eff}$	effective phase mismatch parameter
$\Delta\nu$	laser linewidth
$\Delta\phi$	phase-shift
$\Delta\phi_n$	random phase-shift
ΔK	total phase mismatch
Δt	time step
Δz	spatial step
δ	detuning parameter
ϵ_0	vacuum electric permittivity
ζ	duty-cycle
η	normalized conversion efficiency
κ	nonlinear coupling coefficient
Λ	poling period
λ	wavelength
λ_{QPM}	QPM wavelength
λ_{ZDW}	zero-dispersion wavelength
μ_0	vacuum magnetic permeability
ν	frequency
ν_{QPM}	QPM frequency
ρ	cross coupled power coefficient
ς	chirp parameter
σ	standard deviation
τ	normalized time
Φ	phase modulation function
ϕ	phase
χ	electric susceptibility
$\chi^{(1)}$	linear susceptibility
$\chi^{(2)}$	second-order susceptibility
$\chi^{(3)}$	third-order susceptibility
ψ	relative phase
Ω	centered angular frequency
Ω_p	phonon angular frequency
ω	angular frequency
ω_0	carrier angular frequency
A	normalized electric field envelope
a	magnitude of the normalized electric field envelope
A_{eff}	effective overlap area
B	synchronous normalized electric field envelope
B_{ch}	channel bandwidth
B_{el}	electrical bandwidth

B_{opt} optical bandwidth

c speed of light in vacuum

$\hat{D}$ dispersion operator

$\mathbf{D}$ electric displacement field vector

d second-order nonlinear coefficient

D_λ dispersion parameter

d_{apod} apodization function

d_{eff} effective nonlinear coefficient

$\mathbf{E}$ electric field vector

E complex electric field envelope

e elementary charge

F fast mode

f noise figure degradation factor

f_r idler to signal power ratio

G gain

g effective coupling coefficient

G_i idler gain

G_{PI} phase-insensitive gain

G_s signal gain

h Planck's constant

I electrical current

K_g grating wavenumber

k_0 vacuum wavenumber

L length

L_c coherence length

L_{eff} effective length

M transverse field distribution

N number of nodes

n refractive index

$\mathbf{n}$ noise vector

N_{ch} number of channels

n_L linear refractive index

n_{NL} nonlinear index coefficient

N_s number of spans

n_{sp} spontaneous emission factor

$\mathbf{P}$ electric polarization vector

P optical power

p number of orthogonal states of polarization

$\mathbf{P}^{(1)}$ linear electric polarization vector

$\mathbf{P}^{(2)}$ second-order nonlinear electric polarization vector

$\mathbf{P}^{(3)}$ third-order nonlinear electric polarization vector

P_{ASE} ASE power

P_{ch} channel power

P_{NLI} NLI power

q coupling coefficient

Q_n quantum noise variable

R photo-detector responsivity

$\mathbf{r}$ position vector

S slow mode

$\hat{\mathbf{s}}$ state of polarization unit vector

S_λ dispersion slope

S_{NLI} power spectral density of the nonlinear interference

S_{WDM} power spectral density of the WDM signals

$\mathbf{T}$ transfer matrix

T power transmission coefficient

t time

v_g group velocity

z direction of propagation of the wave

Chapter 1

Introduction

1.1 All-optical signal processing for optical communication systems

The way how human beings communicate with each other has drastically changed over the last two centuries, mostly due to the invention and development of new telecommunication technologies, such as the telegraph, telephone, radio and television [1]. However, none of these technologies has revolutionized the telecommunications as the Internet. With the invention and development of the Internet in 1960s and its spreading to the general public with the creation of the World Wide Web in the beginning of the 1990s [2], accessing and sharing information has never been so easy. The Internet has completely changed the way how human beings contact with each other, promoting the interaction between different cultures and traditions, as well as stimulating the spread of scientific knowledge and technological inventions. Without the Internet, human society would certainly be very different from what we currently know.

The relevance of the Internet can also be measured by numbers. For instance, the number of Internet users has more than tripled in the last decade, as shown in Figure 1.1-a), with a growth rate of about 220 million new users per year, according to the International Telecommunication Union [3]. Not only the number of users is increasing at a fast pace, but also the amount of transmitted data per user. New functionalities and services such as voice and high-definition television over Internet protocol, video streaming, cloud computing and storage, and the quick expansion of social networks has led to an exponential growth of the data traffic. As an example, according to Cisco Systems, Inc., the monthly Internet protocol traffic will approximately triplicate from 60 Exabytes/month in 2014 to about 170 Exabytes/month in 2019, as shown in figure 1.1-b) [4]. It is also expected that more than 80% of the Internet traffic in 2020 will be video contents [4].

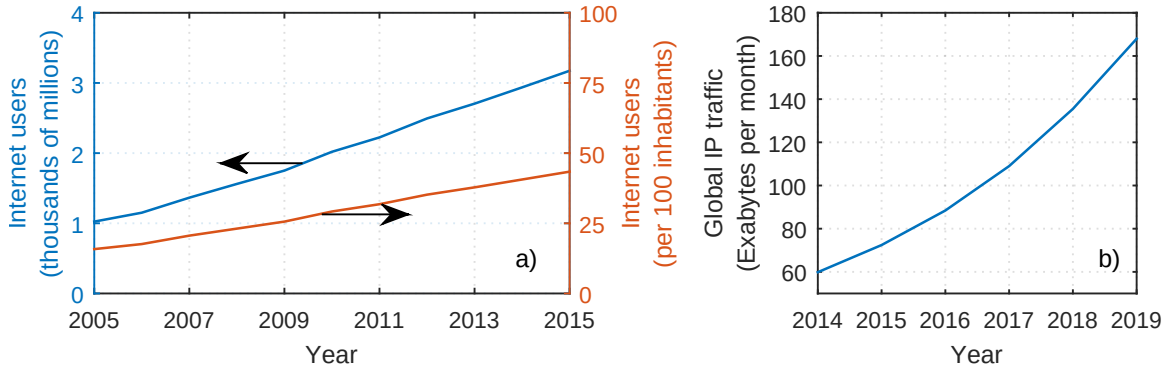

Figure 1.1: a) Evolution of the Internet users over the last decade. b) Estimated evolution of the global Internet protocol traffic. Data in a) and b) obtained from [3] and [4], respectively.

The exponential growth of transmitted data due to the expansion of the Internet has been putting serious challenges to telecommunication services providers in order to cope with the high bandwidth demands, at affordable costs. One of such challenges is how to

transmit huge amounts of data through very long distances. Fiber-optic communications systems are a viable solution for this problem as they provide a reliable, efficient and secure way to transmit data over very long distances. By using optical waves in the near-infrared region to carry information, the total available bandwidth is orders of magnitude greater than with other technologies such as, for instance, microwave systems [1]. Hence, fiber-optic systems are often the backbone structure of Internet service providers, and are the most efficient approach for long-haul transmission, core and metro networks. Furthermore, the high bandwidth demands of individual clients have led to the expansion of fiber-to-the-home architectures in which the data is transmitted through optical fibers up to the homes of the end users.

In order to cope with the seemingly endless growth of the bandwidth requirements, not only new fibers and optical transport networks must be installed, but also the efficiency of utilization and resource management of the existing fiber systems must be improved. As an example, advanced modulation formats combined with coherent detection have been proposed as a possibility to increase the spectral efficiency of transmission systems, defined as the ratio between the information rate of a transmitted channel and the bandwidth occupied by that channel [5–7]. Advanced modulation formats enhance the utilization efficiency of the fiber capacities by using different properties of light such as amplitude, phase and state of polarization to encode several bits into a single modulation symbol.

Another possibility to improve the management and utilization efficiency of the optical transport networks is to consider signal processing techniques [8]. Signal processing can be generally defined as any function or operation performed on the transmitted data signals with the ultimate purpose of increasing the efficiency and/or improve the performance of optical communication systems. Amplification, switching, routing, pulse reshaping, retiming, multicasting, wavelength conversion, add/drop, amplitude regeneration and modulation format conversion are some examples of signal processing functionalities [9, 10].

Signal processing can be implemented in the electrical or the optical domain. Signal processing in the electrical domain has several advantages over optical signal processing (OSP), in particular its technological maturity, easy access to past information stored in memory, flexibility to simultaneously perform different processing functions and massive integration [10, 11]. However, signal processing in the electrical domain implies optical-to-electrical-to-optical conversion, which in practice requires a full receiver and transmitter whenever a processing operation must be performed. This disadvantage becomes particularly relevant in wavelength-division multiplexing (WDM) systems where several data channels are transmitted at different wavelengths. In these systems, a dedicated receiver and transmitter is required per channel. As an example, the first optical communication systems required placing electrical repeaters after about 60-70 km in order to compensate the propagation losses of the fibers [1]. Since these repeaters were essentially a full receiver and transmitter, the first generations of optical systems were limited to the transmission of a single or very few data channels per fiber. With the breakthroughs of optical

amplifiers, amplification could be performed directly in the optical domain, avoiding optical-to-electrical-to-optical conversion and reducing the overall power consumption. More importantly, optical amplifiers allow simultaneous amplification of several WDM channels in a single amplifier.

Another very successful example of OSP is the development of reconfigurable optical add-drop multiplexers (ROADMs), enabled by wavelength-selective switches (WSSs). ROADMs enabled adding or dropping individual wavelength channels at a node of an optical transport network, as well as routing WDM channels to different directions, always in the optical domain [12, 13]. Before the development of ROADMs, reconfigurable add/drop of WDM channels required an optical-to-electrical-to-optical architecture and, consequently, a dedicated transponder per wavelength channel added, dropped, or passed at each node of the optical transport network [14]. In alternative, fixed optical add/drop multiplexers constructed from optical filters could be used [14]. However, the reconfigurability and flexibility of such approach is very limited, typically requiring on site intervention of a technician whenever an update or upgrade of the add/drop capabilities is needed. With the advent of WSSs and ROADMs, software-reconfigurable add/drop and routing can be performed directly in the optical domain, with the possibility of colorless, directionless and contentionless operation [15–17]. Thanks to this technology, modern optical transport networks are now evolving towards dynamic, flexible and software definable routing [17], while enabling the coexistence of data channels with different data rates and modulation formats.

In addition to avoiding optical-to-electrical-to-optical conversion, OSP offers other very attractive advantages for flexible and reconfigurable optical systems. Ultrafast operation and transparency to the bit rate are two of such advantages. In the case of signal processing in the electrical domain, the processor must evaluate and operate on each individual bit or symbol, which is typically performed at a fixed data rate [10]. In addition, electrical signal processing is limited by the speed of the electronics. Even using state-of-the-art CMOS technology, the speed of the electrical processors seems to be limited to symbol rates of about 100 Gsymbol/s, [18, 19]. In contrast, OSP allows ultrafast operation transparent to the data rate and limited only by the response time of the optical medium, usually of the order of femtoseconds [9, 10]. Unless coherent detection is used, the phase information of the transmitted data is lost during optical-to-electrical conversion as the photodetectors (PDs) are only sensitive to the intensity of the waves [20]. On the other hand, OSP techniques operate directly on the electrical field of the waves, without losing the phase information of the signals, so transparency to the modulation format is a possibility [9, 21].

The power consumption of telecommunication systems has also become a relevant issue in the recent years. It is estimated that about 3% of the global produced energy and 2% of the CO_2 emissions are related to the information and communication infrastructures [22]. It has been suggested that OSP may be a possible solution to reduce the power consumption of signal processors by removing the optical-to-electrical-to-optical conversion. However, this claim may not always be true and greatly depends on the OSP functionality. As

an example, it was shown in [23] that the energy consumed per transmitted bit in logical gates based on CMOS technology and optical-to-electrical-to-optical conversion was still lower than using photonic devices, for a single data channel.

A wide variety of techniques and physical processes can be used for OSP. Nonlinear optical phenomena have been widely investigated in the last decade for applications in OSP due to their unique properties and possibilities that can not be easily reproduced by other techniques [9, 10]. Third-order nonlinear effects such as self-phase modulation (SPM), cross-phase modulation (XPM) and FWM, and cascaded second-order nonlinear processes have already enabled the demonstration of several OSP functionalities such as add/drop in optical time-division multiplexing systems [24], multicasting [8], amplitude and phase regeneration [25–27], logical gates [28], wavelength and modulation format conversion [29,30], just to name a few examples. In addition, a wide selection of nonlinear devices for OSP is currently available. Highly nonlinear fibers (HNLFs), semiconductor optical amplifiers (SOAs), photonic crystal fibers (PCFs), tapered fibers, silicon and chalcogenide waveguides, tellurite and bismuth oxide glasses are examples of third-order nonlinear devices [9, 10, 31], whereas periodically poled lithium niobate (PPLN) and periodically poled lithium tantalate (PPLT) waveguides are the most common examples of second-order nonlinear devices [10].

From all the different nonlinear devices, PPLN waveguides offer unique advantages and properties that make them very attractive for OSP. High nonlinear coefficient, transparency over a wide spectral region (350 to 5000 nm), immunity to stimulated Brillouin scattering (SBS), SPM and XPM, negligible frequency chirp and amplified spontaneous emission (ASE) noise, compactness and the possibility of integration are some of the advantages of PPLN waveguides [20, 32, 33]. In addition, PPLN waveguides offer the unique possibility to modify its nonlinear behavior for different frequencies, herein simply referred to as nonlinear spectral response, by properly tailoring the way how the ferroelectric domains are inverted, labeled as domain engineering in this thesis. Domain engineering is a very powerful technique that allows obtaining devices with new properties and functionalities that cannot be easily reproduced with other nonlinear media.

Despite the existence of several nonlinear platforms and an extensive number of reported OSP functionalities, very few, if any, OSP units based on nonlinear phenomena have been implemented in real systems. This situation is mostly caused by high implementation complexity, strong pumping power requirements and still unsatisfactory performances of the current subsystems and devices. Even so, the highly attractive advantages of OSP have motivated a considerable effort in order to change this paradigm. Developing new strategies, improving the performance and simplifying the existing OSP techniques are critical steps to enable real-world applications. Such an approach shall take into account all the various possibilities and aspects of OSP, including the development and improvement of new and existing nonlinear devices, finding new strategies, techniques and functionalities, and reducing the footprint of OSP subsystems in optical transport networks. This is

the fundamental driving force and motivation for the work presented in this thesis.

It should be noted that the idea of completely replacing electrical signal processing by all-optical alternatives is unlikely or even undesirable because of the maturity and performance of electrical systems for certain processing functions [10]. However, there are clearly some operations that are currently performed in the electrical domain that could be greatly enhanced considering an all-optical approach. Identifying where an all-optical approach is more convenient and advantageous is also very important.

In optical transport networks with WDM technology, it may happen that different data channels with the same wavelength arrive at one node of the network and need to be routed to the same destination node. However, since both channels are allocated to the same wavelength, this situation creates a blocking problem, which is also known as wavelength contention [34,35]. Wavelength conversion is a possible solution to avoid contention problems and reduce the blocking probability [34,36]. Recently, it has been shown through numerical simulations that using wavelength converters could improve the network utilization by a factor of 2 [37]. In addition, the authors show that optical wavelength conversion (OWC) would enable 70% reduction in the number of converters compared to optical-to-electrical-to-optical alternatives by allowing simultaneous multichannel operation. These results expressly demonstrate the importance of OWC for modern optical transport networks and prove that the development of all-optical wavelength converters is very relevant. OWC becomes even more important if wavelength tunability and multichannel operation are possible to cope with reconfigurability and flexibility properties, highly desirable for modern optical transport networks [38].

If OWC units are to be deployed in real systems, any extra noise source or signal degradation in the converter should be minimized or eliminated. The most common techniques to implement OWC are based on parametric nonlinear interactions that use strong pump waves to fuel the conversion process. The finite linewidth of the light source used as pumps generates an additional phase noise contribution to the converted signals. This contribution becomes particularly relevant for high-order modulation formats such as 16-quadrature-amplitude modulation (QAM) and 64-QAM signals, or when the data channels undergo several OWC operations before reaching the final destination in an optical transport network. Hence, OWC tolerant to the additional phase noise caused by the finite linewidth of the pump waves would very attractive for such situations.

The transmission of data signals in fiber-optic communication systems is ultimately limited by the ASE noise introduced by optical amplifiers and by the fiber nonlinearities. These two mechanisms continuously degrade the transmitted signals, ultimately resulting in detection errors at the receivers. Hence, not only low-noise solutions are highly desirable, but signal regeneration may also be required at a certain point of the transmission system, whenever the number of errors reaches prohibitive values. In this regard, phase-sensitive amplifiers (PSAs) are a very interesting alternative for low-noise amplification, with noise figure (NF) values below the quantum limit of 3 dB observed for common phase-insensitive

(PI) amplifiers, such as erbium-doped fiber amplifiers (EDFAs). The low-noise properties of PSAs can potentially improve the signal-to-noise ratio (SNR) of the data channels transmitted over an optical link and extend the maximum transmission reach when compared to optical systems using EDFAs. For instance, an extension of the transmission reach of more than three times was recently reported by using a hybrid PSA + EDFA approach instead of using only EDFAs, albeit for single-channel transmission [39]. In addition, the constellation diagrams obtained therein suggest that there is a partial compensation of the nonlinear distortions due to the coherent beating between the signal and a phase-conjugated copy (idler), which must also be transmitted along with the signal in order to enable the phase-sensitive (PS) properties of the PSA. The results reported in [39] not only effectively prove that using PSAs allow extending the maximum reach for point-to-point transmission, but they also indicate that PSAs may be advantageous in terms of regeneration requirements and/or number of amplifiers in optical transport networks. In addition, the improvement of the SNR due to the low-noise properties of PSAs may enable to use higher-order modulation formats that would not be possible considering EDFAs. This possibility is particularly relevant when optical transport networks start to approach its utilization limit, as PSAs may allow increasing the capacity of the network by using more efficient modulation formats. Undoubtedly, the current stage of development of PSAs excludes any possibility of immediate implementation in optical transport networks, but the PSA technology is still being investigated and developed, so this may be a possible scenario in the future. Therefore, an analysis on the potential savings in terms of the number of amplifiers and/or regeneration requirements is very important and valuable as it would indicate whether replacing EDFAs by PSAs in optical transport networks is advantageous or not. If so, such an analysis could also foster the technological development of PSAs.

The accumulation of noise added by optical amplifiers and of signal distortions caused by the nonlinear response of the transmission fibers may degrade the transmitted data channels in such a way that signal regeneration is required at certain locations of a transmission system in order to avoid detection errors. Signal regenerators are especially important for long transmission distances where the accumulated noise is higher and/or when advanced modulation formats are considered, which require higher SNR values at the receiver for error-free operation. Currently, signal regeneration is performed in the electrical domain, requiring optical-to-electrical-to-optical conversion and a full receiver and transmitter per channel, implying significant costs and energy consumption, especially at high symbol rates [25, 40, 41]. Optical signal regeneration has been suggested as a possible alternative to overcome this limitation. Until the early 2000's, almost all optical communication systems were based on intensity modulation formats such as on-off keying (OOK) and direct detection in PDs. In this type of systems, re-amplification, retiming and pulse reshaping or amplitude regeneration are the main operations required to be performed by the regenerators [25,36]. Several all-optical strategies were proposed to perform amplitude regeneration for such systems, including the Mamyshev regenerator, amplitude regenerators

based on optical injection locking, saturable absorbers and parametric amplifier operating in saturation [11, 27, 36, 42–44]. With the advent of advanced modulation formats in which the phase of the waves is also used to encode information, not only the amplitude but also the phase of the signals needs to be regenerated or, at least, the phase noise should be minimized as much as possible. Several all-optical approaches have been investigate so far in order to achieve this purpose. One possibility is to use phase-preserving amplitude regenerators to limit the amplitude-to-phase nonlinear noise transfer, also known as the Gordon-Mollenauer effect [45, 46]. However, this strategy does not regenerate any of the phase degradations already present in the data signals. Another possibility is to consider phase-to-amplitude format conversion using delay line interferometers, followed by amplitude regeneration [47].

The phase of binary PSK (BPSK) signals can be directly regenerated using the phase-squeezing properties of PSAs, as reported in [25, 48–50], with the potential advantage of simultaneous amplitude regeneration by operating the PSA in saturation [25]. Extension to higher-order PSK formats can also be performed by combining several BPSK phase regenerators [51], or by mixing the degraded signal with a phase-conjugated harmonic of the signal in a PSA, also known as multilevel quantizer [52–55]. However, the implementation complexity of PSA-based phase regenerators is still very high and currently incompatible with real-world communication systems. Hence, further developments of this technology are of uttermost importance.

As discussed above, the advantages of OSP techniques are very promising and can potentially improve the management and utilization of the available resources of optical communication systems. However, the overall performance of such strategies still needs to be further developed, which is the main goal of this thesis. The work presented in this thesis aims to push forward the current state of the art of OSP functionalities, namely on OWC, phase regeneration and PS amplification. The possibilities investigated herein address OSP at different levels of complexity and dimensionality, including the design of advanced devices for OSP, the development of new strategies for OSP systems and subsystems, and the assessment of the impact of considering a new OSP functionality in an optical transport network.

1.2 Main contributions

The main contributions of this thesis are summarized below.

- Development and assessment of a layer peeling algorithm (LPA) combined with the deleted-reversal method (DRM) to design the ferroelectric domain inversion of PPLN devices according to a target spectral response. The LPA presented in this thesis is adapted to the design of PPLN devices with customized poling patterns. The author started investigating PPLN waveguides while working towards his Master's degree. The main motivation behind such work was to explore the parallelism between fiber

Bragg gratings and PPLN waveguides, which are both periodic structures. During the Master's degree, it was concluded that the transfer matrix method originally used to estimate the spectral response of a grating coupler is also valid for obtaining the nonlinear spectral response of a PPLN waveguide with arbitrary poling designs, as long as some approximations are taken into account [56]. Hence, the next logical step would be to explore the inverse process, in which the poling pattern should be designed according to a target nonlinear spectral response. In grating couplers, such is commonly done with the LPA by dividing the grating into several layers whose refractive index modulation is iteratively computed according to the target spectral response [57]. In this thesis, the LPA is adapted to the design of the poling pattern of PPLN waveguides, and combined with the DRM in order to produce a real device with a 400 GHz quasi-rectangular spectral response. This contribution was performed in collaboration with the National Institute of Information and Communications Technology (NICT) and resulted in publication A, shown in appendix D.

- Demonstration of tunable and multichannel OWC of 8 quadrature phase-shift keying (QPSK) channels with a 50 GHz spacing using a 400 GHz PPLN waveguide designed with the LPA and DRM. The custom-made PPLN device enabled to simultaneously convert multiple data channels with the additional possibility of tuning the wavelength of the converted channels, which would not be possible using uniform PPLN waveguides. This contribution resulted in publication B, shown in appendix D.

- Demonstration of a pump-linewidth-tolerant scheme for OWC and wavelength data exchange (WDE), used to eliminate the additional phase noise on the converted signals caused by the finite linewidth of the light sources used as pumps. The pump-linewidth-tolerant scheme was originally proposed by Dr. Guo-Wei Lu from the NICT, but all the experiments were jointly carried out by Dr. Lu and the author of this thesis. In addition, the author has also contributed on the writing process for all the publications related to this topic. This work resulted in publications C and D, shown in appendix D.

- Analysis of the influence of key parameters such as the length and conversion efficiency on the gain properties of different configurations of one-, two-, and four-mode PSAs built with PPLN devices. Even though some configurations of PPLN-based PSAs had already been experimentally demonstrated, a proper comparison between the different possibilities was still lacking. Such an analysis is performed in this thesis, where it is shown that configurations based on cascaded three-wave mixing (TWM) interactions have a gain penalty of about 6 dB with respect to those based on a single TWM process and that a four-mode PPLN-based PSA cannot be implemented in practice. This investigation resulted in publication E, shown in appendix D.

- Demonstration of PS amplification and "black-box" phase regeneration of a BPSK signal in a single PPLN device with bidirectional propagation to simultaneously gen-

erate correlated waves and perform PS amplification in opposite propagation directions. The bidirectional scheme not only enables savings in terms of PPLN devices, but also of temperature controllers and coupling optics elements. This contribution was performed in collaboration with the NICT and resulted in publication F, shown in appendix D.

- PS amplification of a 10 Gsymbol/s QPSK signal in a four-mode PSA built with a HNLF. The influence of the pump power and relative phase between the interacting waves on the gain of the amplifier is also investigated in either PS or PI operation. This work was performed in collaboration with the NICT and resulted in publication G, shown in appendix D.

- Development of simplified models for the noise properties of PSAs and lossy elements based on a semi-classical approach. The simplified models allow to discriminate the different gain properties for the correlated and uncorrelated components of the noise in optical links with several cascaded PSAs.

- Development of a simplified model for the signal distortions caused by the nonlinear behavior of the transmission fibers in optical systems with full compensation of the chromatic dispersion after each span of fiber. The simplified model, denominated in this thesis as modified enhanced Gaussian noise (MEGN), is obtained as a simplification of the Gaussian noise (GN) and enhanced Gaussian noise (EGN) models proposed by Poggiolini *et al.* [58, 59] for systems with full compensation of the chromatic dispersion after each span of fiber. The influence of parameters such as the launch power, span length and channel bandwidth on the power of the nonlinear distortions is investigated and compared with numerical simulations performed by solving the Manakov-polarization mode dispersion (PMD) equations with a split-step Fourier transform (SSFT) method. The MEGN model is able to correctly describe the influence of almost all the signal, fiber and span parameters, with the exception of the channel spacing, which leads to an overestimation of the power of the nonlinear distortions.

- Numerical comparison in terms of the number of amplifiers, regeneration requirements and the possibility of considering higher-order modulation formats for different optical transport networks using either PSAs or EDFAs. The numerical simulations are based on the simplified models for the noise properties of PSAs, lossy elements and transmission fibers. The two amplification scenarios are compared for two optical transport networks, one composed of short links and another with long links connecting the nodes of the network. The numerical analysis presented in this thesis shows that PSAs are especially advantageous in terms of signal regeneration requirements and number of amplifiers for networks comprised of long transmission links, and for high-order modulation formats in networks with short links. It is also shown in this

work that the nonlinear distortions limit the potential advantages from the low-noise properties of PSAs.

The work presented in this thesis has produced the following publications.

Publications in journals:

- G. Lu, **A. Albuquerque**, B. Puttnam, T. Sakamoto, M. Drummond, R. Nogueira, A. Kanno, S. Shinada, N. Wada, T. Kawanishi, "Pump-phase-noise-free optical wavelength data exchange between QAM signals with 50-GHz channel-spacing using coherent DFB pump," *Optics Express*, vol. 24, no. 4, pp. 3702-3713, Feb. 2016.
- **A. Albuquerque**, M. Drummond, B. Puttnam, N. Wada, R. Nogueira, "Investigation of PPLN-based PSAs for high-gain optical amplification," *Journal of Lightwave Technology*, vol. 33, no. 12, pp. 2802-2810, Jul. 2015.
- **A. Albuquerque**, B. Puttnam, J. Mendinueta, M. Drummond, S. Shinada, R. Nogueira, N. Wada, "Experimental investigation of phase-sensitive amplification of data signals in a four-mode fiber-based PSA," *Optics Letters*, vol. 40, no. 2, pp. 288-291, Jan. 2015.
- G. Lu, **A. Albuquerque**, B. Puttnam, T. Sakamoto, M. Drummond, R. Nogueira, A. Kanno, S. Shinada, N. Wada, T. Kawanishi, "Pump-linewidth-tolerant optical wavelength conversion for high-order QAM signals using coherent pumps," *Optics Express*, vol. 22, no. 5, pp. 5067-5075, Mar. 2014.
- **A. Albuquerque**, B. Puttnam, M. Drummond, S. Shinada, N. Wada, R. Nogueira, "PPLN poling design based on a discrete layer peeling algorithm combined with a deleted-reversal method," *Journal of Lightwave Technology*, vol. 31, no. 23, pp. 3892-3900, Dec. 2013.
- **A. Albuquerque**, B. Puttnam, M. Drummond, A. Szabó, D. Mazroa, S. Shinada, N. Wada, R. Nogueira, "Phase-sensitive amplification in a single bi-directional PPLN waveguide," *Optics Express*, vol. 21, no. 19, pp. 22063-22069, Sep. 2013.

An additional journal article entitled "Investigation of phase-sensitive amplification for optical transport networks" is currently under preparation for submission to IEEE/OSA Journal of Lightwave Technology, which summarizes the main achievements discussed in chapter 6.

Publications in conference proceedings:

- **A. Albuquerque**, B. Puttnam, M. Drummond, G. Lu, A. Szabo, S. Shinada, N. Wada, R. Nogueira, "PPLN-based all-optical signal processing and phase-sensitive amplification (Invited)," in *IEEE Summer Topicals Meeting Series*, Nassau, Bahamas, Jul. 2015, p. MF3.2.

- **A. Albuquerque**, B. Puttnam, J. Hirohashi, Mi. Drummond, S. Shinada, R. Nogueira, N. Wada, "Investigation of PPSLT waveguides for applications in optical communication systems," in *International Conference on Applications of Optics and Photonics (AOP)*, Aveiro, Portugal, May 2014, p. 92861K.
- G. Lu, **A. Albuquerque**, B. Puttnam, T. Sakamoto, M. Drummond, R. Nogueira, A. Kanno, S. Shinada, N. Wada, T. Kawanishi, "Coherently-pumped 20Gbaud 16QAM optical wavelength shifting free of phase noise from pumps," in *OptoElectronics and Communication Conference (OECC)*, Melbourne, Australia, Jul. 2014, p. 589-590.
- G. Lu, **A. Albuquerque**, B. Puttnam, T. Sakamoto, M. Drummond, R. Nogueira, A. Kanno, S. Shinada, N. Wada, T. Kawanishi, "Pump-linewidth-tolerant wavelength conversion with coherent pumps," in *Conference on Lasers and Electro-Optics (CLEO)*, San Jose, USA, Jun. 2014, p. SW3J.1.
- **A. Albuquerque**, B. Puttnam, M. Drummond, S. Shinada, R. Nogueira, N. Wada, "Single-pump, tunable wavelength conversion of 8$\times$12.5 Gsymbol/s QPSK channels in a quasi-rectangular PPLN," in *European Conference and Exhibition on Optical Communication (ECOC)*, London, UK, Sep. 2013, pp. P.2.10.
- **A. Albuquerque**, B. Puttnam, M. Drummond, S. Shinada, R. Nogueira, N. Wada, "Single-pump, tunable wavelength converter based on PPLN waveguides designed by the layer peeling," in *IEICE Technical Committee on Photonic Network*, Sapporo, Japan, Aug 2013, p 19-24.
- **A. Albuquerque**, B. Puttnam, M. Drummond, Á. Szabó, D. Mazroa, S. Shinada, R. Nogueira, N. Wada, "Investigation of phase-sensitive amplification in a dual pump bi-directional PPLN-based PSA," in *OptoElectronics and Communications Conference (OECC)*, Kyoto, Japan, Jul. 2013, p. ThO3-4.
- **A. Albuquerque**, B. Puttnam, M. Drummond, Á. Szabó, D. Mazroa, S. Shinada, N. Wada, R. Nogueira, "Investigation of black-box phase regeneration using single bi-directional PPLN waveguide," in *Optical Fiber Communication Conference and Exposition (OFC)*, Anaheim, USA, Mar. 2013, p. OW4C.2.

1.3 Outline

This thesis is organized as follows. Chapter 2 contains the general background on optical nonlinear phenomena used for OSP, which supports the discussion presented in the subsequent chapters. This chapter starts by briefly discussing the origin and physical processes of the linear optical phenomena of chromatic dispersion and attenuation, as well as second- and third-order nonlinear effects. Then, the effects of phase mismatching

and the so-called quasi-phase matching (QPM) technique on the efficiency of second-order nonlinear phenomena are covered. The mathematical models used to describe the evolution of the waves interacting through second- and third-order nonlinear processes are also provided in this chapter. Then, the main devices used for OSP based on nonlinear effects are briefly discussed, with a particular focus on PPLN waveguides. Chapter 2 ends with a brief overview of the most common numerical methods used to simulate the behavior of nonlinear devices.

Chapter 3 is devoted to the LPA and DRM, proposed as an effective way to design the ferroelectric domain inversions of PPLN according to a target spectral response. This chapter starts by briefly discussing common PPLN devices with customized poling patterns, followed by the description of the LPA and DRM. The effectiveness of these methods is also investigated through numerical simulations and by producing a PPLN waveguide with quasi-rectangular spectral response with a QPM bandwidth of 400 GHz.

Chapter 4 presents two different schemes for advanced OWC using PPLN waveguides. In the first part of this chapter, tunable and multichannel OWC of 8×12.5 Gsymbol/s data channels using the customized PPLN device characterized in chapter 3 is demonstrated. Then, an OWC scheme tolerant to the phase noise generated due to finite linewidth of the laser sources used as pumps is experimentally demonstrated. The pump-linewidth-tolerant scheme is also adapted to perform WDE between two data channels at the final part of this chapter.

Chapter 5 is devoted to PS amplification and phase regeneration in PSAs. In the first part of this chapter, the influence of key parameters such as the pump and signal power on the gain of six different configurations of PSAs built with PPLN waveguides are theoretically and numerically investigated. Then, a copier + PSA scheme in a single PPLN device with bidirectional propagation is proposed in order to simultaneously generate correlated waves and perform PS amplification in opposite propagation directions, using a single-pump, two-mode configuration. The same concept is employed to experimentally demonstrate "black-box" phase regeneration of a 10 Gb/s BPSK signal in a dual-pump one-mode PSA, using injection locking and an optical phase-locked loop (PLL) to respectively remove the excessive phase noise of the generated pump wave and to correct for any phase drifts in the experimental set-up. The chapter concludes with the demonstration of a four-mode PSA built with HNLFs.

Chapter 6 presents a comparison study between optical transport networks amplified by EDFAs and PSAs. This chapter starts by briefly discussing the main elements of optical transport networks and their respective functions. Then, the Dijkstra's algorithm is presented as a possible way to calculate all the shortest paths between any starting and destination node of an optical transport network, along with an algorithm to remove the redundant shortest paths. Afterwards, a numerical comparison between amplification scenarios based on EDFAs and PSAs for data transmission in a single optical link and in two different optical transport networks is presented, using simplified models to describe the

noise and gain/attenuation properties of the amplifiers, optical fibers and other passive elements of the networks, as well as the MEGN model to estimate the power of the nonlinear distortions generated in the transmission fibers.

Finally, the main conclusions are presented, along with a discussion on the envisaged directions for future work.

Chapter 2

Nonlinear optical effects and devices for all-optical signal processing

When optical waves propagate through matter, an inevitable interaction between the electromagnetic field of the waves and the charged sub-particles of the atoms in the propagating medium occurs, leading to different optical phenomena [60, 61]. At low power values, the response of the propagating medium to the electromagnetic field of the incident waves is approximately linear. The nonlinear response of the propagating medium only becomes substantial for high values of optical irradiance.

The first evidences of the nonlinear response of optical media can be traced back to the second half of the 19th century, when John Kerr discovered that a direct current (DC) electric field induces birefringence in isotropic media [62, 63] and Friedrich Pockels discovered the electro-optic effect [63,64]. In both cases, however, the nonlinear response of the propagating media was excited by a DC or low-frequency external electric field. It was not until the invention of the laser by Maiman in 1960 [65] that a sufficiently powerful and coherent optical light source with an electric field comparable to the atomic field strength was available to significantly excite the nonlinear response of the propagating medium. In fact, one year after the invention the laser, Franken *et al.* successfully demonstrated the generation of the second harmonic of light emitted by a ruby laser [66]. As a curiosity, the experimental results obtained by Franken *et al.* consisted of faint spots recorded on a photographic plate that were eliminated by the editorial staff of the journal, who considered them as undesired stains [63]. After the first demonstration of second-harmonic generation (SHG), many other nonlinear optical phenomena were demonstrated shortly after, including sum-frequency generation (SFG) [67], difference-frequency generation (DFG) [68], two-photon absorption [69], stimulated Raman scattering (SRS) [70], SBS [71] and FWM [72], just to name a few.

The nonlinear response of optical media can be described according to the electromagnetic theory of light, which addresses the interaction between optical waves and matter using the constitutive relations and Maxwell's equations for the electromagnetic field. Considering a non-magnetic medium, the overall response of the atoms and molecules of the medium can be represented by the electric displacement field vector, **D**, given by [60,61,73]

$$\mathbf{D} = \epsilon_0 \mathbf{E} + \mathbf{P}, \tag{2.1}$$

where ϵ_0 is the vacuum electric permittivity, **E** is the electric field vector of the wave, and **P** is the electric polarization vector, which accounts for the generation of electric dipole moments in the propagating medium, induced by the electric field of the incident wave [61].

Using Maxwell's equations and (2.1), the following wave equation can be obtained for a non-conducting, non-charged, dielectric medium [73]

$$\nabla^2 \mathbf{E} = \mu_0 \epsilon_0 \frac{\partial^2 \mathbf{E}}{\partial t^2} + \mu_0 \frac{\partial^2 \mathbf{P}}{\partial t^2}, \tag{2.2}$$

with μ_0 the vacuum magnetic permeability. In general, **P** is a function of **E** and can be

represented by a Taylor's expansion as

$$\begin{aligned}\mathbf{P}(t) =& \mathbf{P}^{(1)}(t) + \mathbf{P}^{(2)}(t) + \mathbf{P}^{(3)}(t) + \cdots \\ =& \epsilon_0 \chi^{(1)}(t) \otimes \mathbf{E}(t) + \epsilon_0 \chi^{(2)}(t) \otimes \mathbf{E}(t)^2 + \epsilon_0 \chi^{(3)}(t) \otimes \mathbf{E}(t)^3 + \cdots ,\end{aligned} \tag{2.3}$$

where $\otimes$ denotes the convolution operation, $\mathbf{P}^{(j)}$ is the j^{th} order term of the polarization, and $\chi^{(j)}$, the susceptibility of order j. Note that in general, the response of any optical medium to an external excitation is not instantaneous, so the electrical susceptibility terms in the previous equation are a function of t. The first term of (2.3) is responsible for the linear effects of refraction, chromatic dispersion and attenuation [61, 73], whereas the remaining ones correspond to the nonlinear response of the propagating medium. The second and third terms on the right part of (2.3) represent the second- and third-order nonlinear effects, respectively, which are further discussed in the following sections. Higher-order nonlinear terms are not considered in this work. Typically, $\chi^{(2)}$ and $\chi^{(3)}$ are smaller than $\chi^{(1)}$ by orders of magnitude, which is the reason why the nonlinear nature of $\mathbf{P}$ only becomes evident at high values of $\mathbf{E}$ and/or for a long interaction length in the nonlinear medium. In general, the linear and nonlinear susceptibility terms in (2.3) are tensorial quantities, capable of describing the different responses of anisotropic media to exciting fields in different directions [60, 61].

Nonlinear optics is a very important branch of Physics with numerous applications in real life. Medical imaging [74], generation of new light sources [66], spectroscopy [75], generation of entangled photon pairs [76] and optical signal processing in optical communication systems [10] are just a few examples of possible areas where nonlinear optics play a very important role.

In this chapter, the origin and main properties of linear optical effects are discussed in section 2.1. The physical processes and mathematical models of second- and third-order nonlinear effects are covered in sections 2.2 and 2.3, respectively, whereas section 2.4 is devoted to the numerical methods used to simulate the response of linear and nonlinear devices. In the last section of this chapter, the most important nonlinear devices for OSP are briefly discussed, particularly focusing on PPLN waveguides.

2.1 Linear Effects

As mentioned in the previous section, the linear effects originate from $\mathbf{P}^{(1)}$, which varies linearly with the electric field. In real optical materials, their response to an external excitation is not instantaneous, but rather described by a time-dependent electric susceptibility function, $\chi(t)$. The time-dependent electric susceptibility function is determined by characteristic resonance frequencies at which the electromagnetic radiation is absorbed through oscillations of the electrons of a medium [73]. The non-instantaneous response of the propagating media is also characterized by a frequency-dependent electric susceptibility.

In addition, since the refractive index, n, is related to the electric susceptibility through the relation $n = \sqrt{1+\chi}$, the non-instantaneous response of the optical media is also responsible for the so-called material chromatic dispersion [73]. In waveguided devices, the effective refractive index also depends on the profile of the mode propagating in the core and in the cladding (the evanescent field), which in turn depends on the frequency of the propagating mode [77]. Hence, optical waveguides generate an additional contribution to the chromatic dispersion, denominated as waveguide dispersion [73].

The response of any real and stable physical system must be causal, i.e., its response depends only on past and present events. Causality implies that $\chi(t<0)=0$, assuming $t=0$ as the present time instant. In the frequency domain, this condition also implies that $\chi(\omega)$ is a complex quantity, with the real and imaginary parts of the χ related through the Kramers-Kronig relations [60]. The imaginary part of $\chi(\omega)$ and, consequently, of $n(\omega)$ is the origin of propagation losses, represented by the absorption coefficient α, according to $\alpha = 2\Im\{n\}k_0$, where $\Im\{n\}$ represents the imaginary part of the refractive index and $k_0 = \omega/c$ is the vacuum wavenumber [73]. The absorption coefficient takes into account different attenuation sources of the propagating medium, including electronic and vibrational absorption, and absorption due to impurities, just to name a few [73].

Let us now assume a linearly polarized plane wave with instantaneous angular frequency ω propagating along direction z, whose electric field is represented by [77]

$$\begin{aligned}\mathbf{E}(\mathbf{r},t) &= \frac{1}{2}\left[E(\mathbf{r},t)e^{i[\omega_0 t-\beta(\omega_0)z]}+c.c.\right]\hat{\mathbf{s}}\\ &= \frac{1}{2}\left[\Gamma M(x,y)A(z,t)e^{i[\omega_0 t-\beta(\omega_0)z]}+c.c.\right]\hat{\mathbf{s}},\end{aligned} \tag{2.4}$$

where E represents the complex electric field envelope, given by $E(\mathbf{r},t)=\Gamma M(x,y)A(z,t)$ and $c.c.$ indicates the complex conjugate of the previous term. In (2.4), $\mathbf{r}$ is the position vector, ω_0 the central angular frequency of the wave, β the wavenumber, $\hat{\mathbf{s}}$ the state of polarization unit vector, Γ a normalization factor, and A a slowly space- and time-varying function, proportional to the electric field. The normalization factor is defined in such a way that $|A|^2 = P$, with P the optical power, and given by $\Gamma = \sqrt{2/(nc\epsilon_0)}$, with c the speed of light in vacuum. The transverse field distribution, M, describes the variation of the electric field along x and y and it is also normalized according to

$$\int_{-\infty}^{+\infty}\int_{-\infty}^{+\infty}|M(x,y)|^2 dxdy = 1. \tag{2.5}$$

The normalized electric field envelope can also be expressed in the frequency domain as a superposition of waves of the form [77]

$$\begin{aligned}A(z,t) &= \int_{-\infty}^{+\infty}\tilde{A}(z,\omega)e^{i[\omega-\omega_0]t-i[\beta(\omega)-\beta(\omega_0)]z}d\omega\\ &= \int_{-\infty}^{+\infty}\tilde{A}(z,\Omega)e^{i[\beta(\Omega+\omega_0)-\beta(\omega_0)]z+i\Omega t}d\Omega,\end{aligned} \tag{2.6}$$

with $\tilde{A}$ the Fourier coefficients of the normalized electric field envelope and $\Omega = \omega - \omega_0$ the angular frequency centered at ω_0. The variation of wavenumber β with the angular frequency ω can be expressed in terms of a Taylor's expansion as [77]

$$\beta(\omega) = \beta(\omega_0) + \sum_{m=1}^{+\infty} \frac{\beta^{(m)}(\omega_0)}{m!}\Omega^m, \tag{2.7}$$

with $\beta^{(m)}$ the m^{th} derivative of the wavenumber with respect to the angular frequency. By using (2.4), (2.6) and (2.7) in (2.2), and considering that the second spatial derivative of A is much smaller than the other terms (slowly-varying envelope approximation), the evolution of the normalized electric field envelope is described by [73, 77]

$$\frac{\partial \tilde{A}(z,\Omega)}{\partial z} = \left(-i \sum_{m=1}^{+\infty} \frac{\beta^{(m)}(\omega_0)}{m!}\Omega^m - \frac{\alpha(\omega)}{2} \right) \tilde{A}(z,\Omega), \tag{2.8}$$

whose solution in the frequency domain is given by

$$\tilde{A}(z+\Delta z,\Omega) = \tilde{A}(z,\Omega) \exp\left(-i \sum_{m=1}^{+\infty} \frac{\beta^{(m)}(\omega_0)}{m!}\Omega^m \Delta z - \frac{\alpha(\omega)}{2}\Delta z \right), \tag{2.9}$$

with Δz the spatial step. In the previous equations, the terms depending on $\beta^{(m)}$ represent the effects of chromatic dispersion, whereas the one depending on the absorption coefficient, α, is responsible for the propagation losses. In general, only the terms of the chromatic dispersion up to the third derivative of the wavenumber are significant in optical communication systems. The first-order term is proportional to the inverse of the group velocity, v_g, whereas the second derivative of the wavenumber is the group velocity dispersion (GVD), responsible for pulse broadening. The coefficient $\beta^{(3)}$, also known as third-order dispersion (TOD) parameter, generates a pulse distortion that becomes significant for wide-band signals or when the wavelength of the wave is close to the zero-dispersion wavelength, λ_{ZDW}, at which the GVD is null [73]. Usually, the dispersion of propagating media is not quantified in terms of the GVD or TOD parameters, but rather by the dispersion parameter, D_λ, and the dispersion slope, S_λ, defined as

$$D_\lambda = \frac{\partial \beta^{(1)}}{\partial \lambda} = -\frac{2\pi c}{\lambda^2}\beta^{(2)} \tag{2.10}$$

$$S_\lambda = \frac{\partial D_\lambda}{\partial \lambda} = \left(\frac{2\pi c}{\lambda^2}\right)^2 \beta^{(3)} + \left(\frac{4\pi c}{\lambda^3}\right)\beta^{(2)}, \tag{2.11}$$

with λ the wavelength.

As it is further discussed in the following sections, it is also useful to write (2.8) in the time domain by using the frequency/time equivalence $(i\Omega)^m \leftrightarrow \partial^m/\partial t^m$. Assuming that the absorption coefficient is approximately constant within the bandwidth of A, the following

pulse propagation equation for a linear optical medium is obtained [73, 77]

$$\frac{\partial A(z,t)}{\partial z} = \left(\sum_{m=1}^{+\infty} \frac{1}{i^{m+1}} \frac{\beta^{(m)}(\omega_0)}{m!} \frac{\partial^m}{\partial t^m} - \frac{\alpha}{2} \right) A(z,t) = \hat{D}(\omega_0, t) A(z,t), \tag{2.12}$$

where $\hat{D}$ is a dispersion operator that includes the linear effects of chromatic dispersion and propagation losses.

2.2 Second-order nonlinear effects

Second-order nonlinear effects originate from a term of **P** that depends on the square of the electric field. In order to understand the underlying optical phenomena generated from the second-order electric polarization, let us assume a linearly polarized plane wave as in the previous section, instantaneous response of the nonlinear medium and that both the electric field and $\chi^{(2)}$ are scalar quantities. Using (2.4) in (2.3), the second-order nonlinear term of the electric polarization vector becomes

$$\mathbf{P}^{(2)} = \left[\epsilon_0 d |E|^2 + \epsilon_0 \frac{d}{2} \left(E^2 e^{i(2\omega_0 t - 2\beta z)} + c.c. \right) \right] \hat{\mathbf{s}}, \tag{2.13}$$

with d the second-order nonlinear coefficient, defined as $d = \chi^{(2)}/2$ [78]. The first term on the right side of (2.13) is a quasi-DC component of the electric polarization and is responsible for a phenomenon called optical rectification, whereas the second one creates a contribution with twice the frequency of the initial wave, responsible for SHG [60].

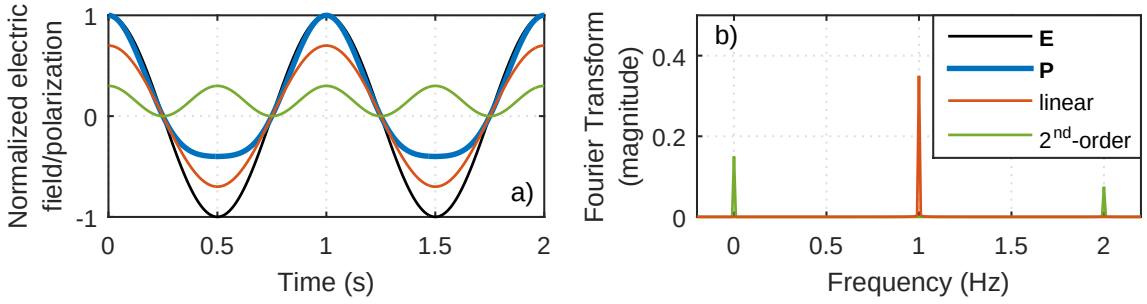

Figure 2.1: a) Normalized electric field **E** of the incident wave and respective electric polarization **P** of the propagating medium. The linear and second-order nonlinear parts of **P** are represented by the red and green curves, respectively. b) Magnitude of the Fourier transform of the linear and second-order nonlinear terms of **P**.

The response of a second-order nonlinear medium with $\chi^{(1)}$ = 0.7 and $\chi^{(2)}$ = 0.3 V/m to an incident wave with electric field amplitude of 1 V/m and frequency of 1 Hz is depicted in figure 2.1. As shown in the figure, the response of the medium is asymmetric due to the second-order nonlinear term. The second-order component not only varies with twice the frequency of the initial wave (SHG), but also has a DC offset (optical rectification). The DC

and second harmonic frequency components of $\mathbf{P}^{(2)}$ are also evident in figure 2.1-b), at 0 Hz (DC) and 2 Hz (SHG).

Second-order nonlinearities and, in general, all the even-order nonlinear terms of the electric polarization are related to the asymmetric response of the medium. At the atomic and molecular level, this means that the internal structure of the propagating medium must lack a center of inversion, otherwise even-order nonlinearities vanish [60, 61]. As an example, optical fibers are made of amorphous silica glass that shows local symmetry, so no significant second-order nonlinearities can be typically observed.

Let us now suppose that two waves with different frequencies, ν_1 and ν_2, are propagating in the nonlinear medium. The second-order nonlinear term of $\mathbf{P}$ is now given by

$$\begin{aligned}\mathbf{P}^{(2)} = \Bigg[\epsilon_0 \frac{d}{2} \Big\{ &|E_1|^2 + |E_2|^2 + E_1^2 e^{i(2\omega_1 t - 2\beta_1 z)} + E_2^2 e^{i(2\omega_2 t - 2\beta_2 z)} \\ &+ 2E_1 E_2 e^{i[(\omega_1+\omega_2)t - (\beta_1+\beta_2)z]} + 2E_2 E_1^* e^{i[(\omega_2-\omega_1)t - (\beta_2-\beta_1)z]} + c.c. \Big\}\Bigg] \hat{\mathbf{s}}.\end{aligned} \tag{2.14}$$

When two or more waves propagate in a second-order nonlinear medium, optical rectification and SHG terms from each individual wave are generated, represented by the first four terms in (2.14). In addition, the nonlinear response of the medium also promotes optical mixing between the different waves, represented in (2.14) by the fifth and sixth terms. The frequency mixing terms of $\mathbf{P}^{(2)}$ generate new waves at frequencies $\nu_{SFG} = \nu_1 + \nu_2$ and $\nu_{DFG} = \nu_2 - \nu_1$, which respectively correspond to the optical phenomena of SFG and DFG.

SHG, SFG and DFG can also be described in terms of the quantum interactions between the photons in the nonlinear media. In SHG and SFG, two incident photons are initially absorbed into an intermediate virtual state and then a single photon is emitted with frequency equal to the sum of the frequencies of the initial waves, as depicted in figure 2.2. SHG can be regarded as a particular case of SFG where the frequency of the two initial photons is the same. In DFG, a photon with frequency equal to the difference of frequen-

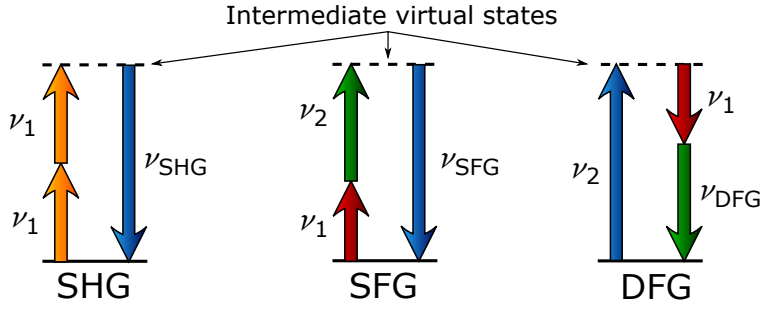

Figure 2.2: Schematic representation of photon creation/anihilation during SHG, SFG and DFG.

cies of two incident photons is created. In this case, the initial photon with higher energy is absorbed into a virtual state and decomposed into two new photons, one with the same frequency of the other initial photon, and the other with frequency equal to the difference of frequencies. As SHG, SFG and DFG involve the interaction between three photons, they are generally denominated as three-photon or TWM processes.

TWM processes have many applications in different fields of science and technology besides OSP. The possibility to generate coherent light at new frequencies has been used to produce laser sources at spectral regions where other alternatives do not exist or are not attractive in terms of output power, efficiency and stability. As an example, green and blue laser sources can be respectively obtained through SHG of radiation emitted at 1.064 μm by a Nd:YAG laser [79] and SFG of light from Nd:YAG and GaAlAs diode lasers [80]. SHG and SFG may also be used to improve the sensitivity and performance of photo-detection by converting radiation in spectral regions lacking cost-effective and high-sensitivity photo-detectors to frequency ranges where better solutions are available [81]. Further examples of applications include surface spectroscopy [82, 83], imaging microscopy [84] and frequency-resolved optical gating [85]. DFG is the underlying process of several optical phenomena, including spontaneous parametric down-conversion, parametric generation, parametric amplification and parametric oscillation. In the case of spontaneous parametric down-conversion, the decomposition of a high frequency photon via DFG is triggered by quantum vacuum fluctuations, resulting in the emission of two highly-correlated photons [86]. An optical parametric oscillator is composed by the nonlinear medium placed between two mirrors to provide optical feedback and enhance the efficiency of the parametric down-conversion process [87]. The two new photons emitted by spontaneous parametric down-conversion and from an optical parametric oscillator are entangled, so these phenomena can be used as a source of entangled photon pairs [86]. In addition, optical parametric oscillators can be used as tunable laser sources of mid-infrared radiation [88]. In the case of parametric generation and amplification, the DFG process is stimulated by an initial input photon rather than vacuum noise. During the nonlinear interaction, not only a new frequency- and phase correlated photon is generated (parametric generation), but so is a new photon with frequency equal to that of the initial one, leading to parametric amplification [87].

2.2.1 Phase-mismatch and quasi-phase matching

Efficient TWM interactions require energy and momentum conservation. Energy conservation is assured by the frequency relation of the initial and final photons: $h\nu_1 + h\nu_1 = h\nu_{SHG}$ for SHG, $h\nu_1 + h\nu_2 = h\nu_{SFG}$ for SFG, and $h\nu_2 = h\nu_1 + h\nu_{DFG}$ for DFG [87]. Conservation of momentum, on the other hand, is related to the wave vectors of the interacting waves, $\boldsymbol{\beta}$, whose magnitude is the wavenumber $\beta = nk_0$. Contrarily to energy, however, conservation of momentum in a nonlinear interaction is not intrinsically verified.

Let us consider SHG and collinear propagation as an example. The refractive index dispersion generates a non-zero wavenumber mismatch between the second harmonic and the fundamental wave, given by $\Delta\beta = \beta_{SHG} - 2\beta_1$. In turn, the wavenumber difference originates a phase mismatch between the second harmonic and the nonlinear electric polarization that linearly increases with the propagation distance z [87]. As a consequence, the radiation emitted by the individual dipoles at a certain point in the medium and the

second harmonic field that was generated in previously locations may not add constructively, and the global efficiency of the nonlinear process is low [87]. In contrast, when the phase mismatch parameter $\Delta\beta$ is zero, the waves are phase matched and the second harmonic radiation emitted by the dipoles adds constructively at any location of the optical medium. Hence, phase matching is a critical condition for efficient TWM and for FWM, as it is discussed later on.

Since any real optical medium is dispersive and in TWM interactions at least one of the waves is in a spectral region far from that of the others, achieving perfect phase matching may be challenging or even impossible. Possible solutions to increase the efficiency of the nonlinear phenomena include phase mismatching compensation by taking advantage of the phase-shift waves undergo during total internal reflection [78], or using waveguides with proper geometry, whose dispersive properties are designed to minimize the phase mismatch [73, 78]. The latter technique is particularly important to enhance the efficiency of FWM in HNLFs [73]. Another possibility is to consider a non-collinear configuration in which the waves propagate at a angle with respect to each other, properly selected to achieve wave vector matching [78]. However, if the wavelength of the interacting waves is in the normal dispersion region, which is often the case, the refractive index of the second harmonic is larger than that of the fundamental wave, so wave vector matching cannot be attained at any angle value. In addition, since the interacting waves diverge from each other, the nonlinear interaction is spatial and temporally limited to the region and time duration where the waves overlap [78]. Another common technique to achieve phase matching is to consider the birefringence properties of anisotropic media. In anisotropic materials, the refractive index not only depends on the frequency, but also on the relative orientation of the state of polarization of the waves' electric field. Hence, the phase mismatch in both collinear and non-collinear configurations can be compensated by tuning the polarization of the interacting waves to different states [78, 89]. The birefringence properties of optical media are typically affected by temperature, so this property can be used to tune the phase matching condition [87]. It should be noted, however, that $\chi^{(2)}$ is a tensorial quantity, so the effective efficiency of the nonlinear interaction depends on the state of polarization of the interacting waves [87]. As an example, the highest component of the nonlinear coefficient tensor in lithium niobate is observed when all the interacting waves are polarized according to the c-axis of the crystal. Since the birefringent phase matching requires interacting waves at different states of polarization, the highest component of the nonlinear coefficient tensor in lithium niobate cannot be used for this phase matching technique.

The efficiency of TWM processes can also be enhanced via QPM, originally proposed in [90]. In this technique, the phase mismatch between the interacting waves is compensated by periodically inverting the sign of the nonlinear coefficient. As mentioned before, the wavenumber mismatch generates a phase difference of $\Delta\phi = \Delta\beta \cdot z$ between the second harmonic and the fundamental wave. After a propagation length of $L_c = \pi/\Delta\beta$, usually denominated as the coherence length, the two waves become out of phase by π

radians, and the power of the second harmonic decreases, as it starts to flow back to the fundamental wave (see figure 2.3). After another coherence length, the phase of the waves

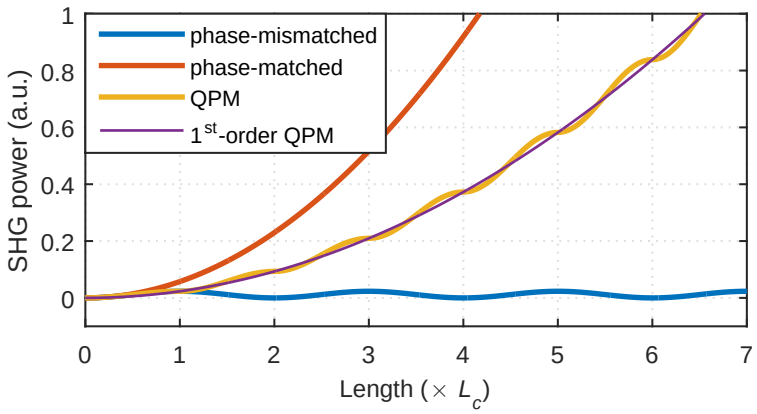

Figure 2.3: Evolution of the second harmonic power (in arbitrary units) with the propagation length in the nonlinear medium for phase mismatched, perfectly phase matched and quasi-phase matched interactions.

becomes matched again and the power of the second harmonic starts to increase. This process repeats throughout the nonlinear medium, resulting in a very low efficiency of the nonlinear interaction. The main idea of the QPM technique is to compensate the π phase-shift after each coherence length in order to keep the power flowing from the fundamental wave to the second harmonic, which is accomplished by periodically inverting the sign of $\chi^{(2)}$ [78, 87, 90]. Realistically, phase mismatch is not compensated continuously along the propagation distance, but only at discrete locations where the sign of the nonlinear coefficient is inverted. As a consequence, the efficiency is lower than when considering perfect phase matching, as shown in figure 2.3. In order to quantify how much the efficiency of the nonlinear interaction is reduced due to QPM, let us consider that the nonlinear coefficient periodically varies between $+\mathrm{d}$ and $-\mathrm{d}$ with a period $\Lambda = 2L_c$. For completeness, let us also consider that the fraction of the inversion period where the nonlinear coefficient is positive, i.e., the duty-cycle ζ, may assume any value ranging from 0 to 1. The variation of the nonlinear coefficient with z can then be described in terms of the following Fourier series [87, 91]

$$d(z) = \sum_{l=-\infty}^{+\infty} \hat{d}_l e^{-i\frac{2\pi}{\Lambda} l z}, \tag{2.15}$$

with $\hat{d}_l$ the Fourier coefficient of the l^{th} harmonic, given by [91]

$$\hat{d}_l = \begin{cases} (2\zeta - 1) \cdot \mathrm{d}, & \text{if } l = 0, \\ \frac{2}{\pi l} \sin(\pi l \zeta) \cdot \mathrm{d}, & \text{otherwise.} \end{cases} \tag{2.16}$$

According to the previous equation, the Fourier coefficients decrease with the harmonic

order by a factor of 1/*l*, thus only the lowest-order harmonics are significant for the QPM technique. Moreover, the magnitude of the Fourier coefficients is also affected by the duty-cycle, reaching a maximum value for the special case of $\zeta = 0.5$, i.e., when the sign of nonlinear coefficient is inverted at each coherence length. In this case, $\hat{d}_l$ simply becomes

$$\hat{d}_l = \frac{2}{\pi l} \cdot \mathrm{d}, \tag{2.17}$$

for *l* an odd integer.

The evolution of the second harmonic power using the QPM technique and considering only the first-order harmonic (*l*=1) is represented by the purple curve in figure 2.3. As shown in the figure, the first-order harmonic of the nonlinear coefficient is responsible for the evolution of the average power of the SHG wave, whereas the other harmonics originate the oscillating behavior of the QPM curve. Hence, it typically suffices to consider the first harmonic to characterize the evolution of the nonlinear interaction. The Fourier coefficient of the first-order harmonic also quantifies the efficiency drop. An effective nonlinear coefficient can thus be associated to QPM, given by $d_{eff} = \hat{d}_1 = 2d/\pi$ [87].

The periodic inversions of the nonlinear coefficient can also be related to a grating wavenumber, $K_g = 2\pi/\Lambda$, that also contributes to the effective phase mismatch parameter as $\Delta\beta = \beta_{SHG} - 2\beta_1 - K_g$ for SHG. Because of the dispersive properties of optical media, the QPM condition for SHG is typically achieved only at a particular wavelength, the QPM wavelength λ_{QPM}. In addition, the refractive index dispersion curve and, consequently, the QPM wavelength, depend on the temperature, so a precise control of this parameter is required in order to guarantee a stable operation. On the other hand, the temperature can also be used to tune the QPM wavelength.

2.2.2 Cascaded TWM

As mentioned in the previous subsection, the frequency/energy relation between the interacting waves in a TWM process imply that at least one of the waves is in a spectral region far from that of the other waves. For instance, the second harmonic of a fundamental wave at 1550 nm is generated at 775 nm. For applications in fiber-optic systems, simple TWM would require light sources, amplifiers and other optical devices at unconventional spectral regions, which may not be readily available, nor desirable [92].

A possible solution to overcome this problem is to consider two cascaded TWM interactions occurring simultaneously in a single nonlinear device. In a cascaded TWM process, often referred to as cascaded $\chi^{(2)}$:$\chi^{(2)}$ interaction, an intermediate SHG or SFG step converts the input waves from the conventional C-band to the second harmonic band around 775 nm [92]. The generated waves, in turn, are converted back to the C-band via DFG, as shown in figure 2.4.

The cascaded interactions shown in figure 2.4 are usually known as cascaded second-harmonic and difference-frequency generation (cSHG/DFG) and cascaded sum- and diffe-

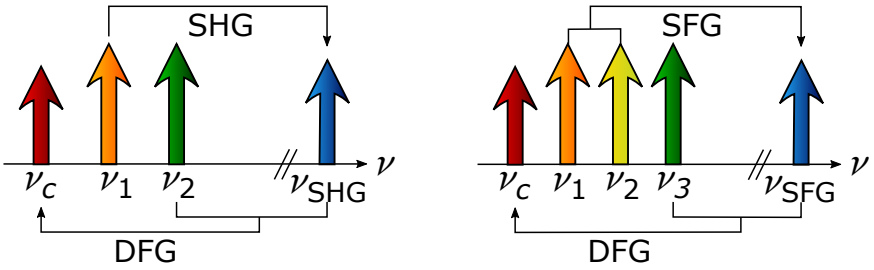

Figure 2.4: Schematic representation of cSHG/DFG (left) and cSFG/DFG (right).

rence-frequency generation (cSFG/DFG), and generate waves at frequencies $\nu_c = \nu_{SHG} - \nu_2 = 2\nu_1 - \nu_2$ and $\nu_c = \nu_{SFG} - \nu_3 = \nu_1 + \nu_2 - \nu_3$, respectively. As it is discussed in the next section, the frequency relation of the interacting waves in cSHG/DFG and cSFG/DFG is equivalent to degenerate and non-degenerate FWM [92].

In cascaded TWM processes, the poling period for the QPM technique is typically selected in order to quasi-phase match the SHG interaction in cSHG/DFG, or SFG in cSFG/DFG [92]. If the input and converted waves are not too far from each other, the phase mismatch of the DFG process is also partially compensated through QPM, even though the inversion period is selected to quasi-phase match the SHG or SFG intermediate steps.

2.2.3 Coupled-mode equations

The evolution of the electric field of the interacting waves in TWM processes can be described by considering the second-order nonlinear term of the electric polarization in Maxwell's equations. In this subsection, coupled-mode equations obtained from Maxwell's equations for SHG, SFG, DFG, cSHG/DFG and cSFG/DFG are presented, along with analytical solutions for some particular cases.

SHG

The coupled-mode equations representing the evolution of the second harmonic and fundamental wave are given by [93]

$$\frac{\partial A_1(z,t)}{\partial z} = \hat{D}_1(\omega_{0,1},t)A_1(z,t) - i\kappa_1 A_2(z,t)A_1^*(z,t)e^{-i\Delta\beta z} \tag{2.18a}$$

$$\frac{\partial A_2(z,t)}{\partial z} = \hat{D}_2(\omega_{0,2},t)A_2(z,t) - i\frac{\kappa_2}{2}A_1^2(z,t)e^{i\Delta\beta z}, \tag{2.18b}$$

whose detailed derivation is shown in appendix A. In (2.18), $\hat{D}_j$ is the dispersion operator of wave j, and κ the nonlinear coupling coefficient given by [93]

$$\kappa_j = \frac{2\pi}{\lambda_j}\sqrt{\frac{2}{n_j n_k n_l c\epsilon_0 A_{eff}}}d_{eff}. \tag{2.19}$$

In the previous equation, A_{eff} is the effective overlap area between the interacting waves, defined as [93]

$$A_{eff} = \left| \int_{-\infty}^{+\infty} \int_{-\infty}^{+\infty} M_j(x,y) M_k(x,y) M_l^*(x,y) dxdy \right|^{-2}, \tag{2.20}$$

with subscripts $j = 1$, $k = 1$ and $l = 2$ for SHG.

Equation (2.18) describes the evolution of the fundamental and second harmonic waves in a second-order nonlinear medium. If the interacting waves are continuous waves (CWs), all the time derivatives of the dispersion operator vanish. Furthermore, if propagation losses are negligible, no second harmonic wave is present at the input of the nonlinear medium and the interaction is perfectly quasi-phase matched ($\Delta\beta$ = 0), the evolution of A_1 and A_2 is given by

$$A_1(z) = \sqrt{P_1(0)}\,\mathrm{sech}\left(\kappa_1\sqrt{P_1(0)}z\right) e^{i\phi_1(0)} \tag{2.21a}$$

$$A_2(z) = -i\sqrt{P_1(0)}\tanh\left(\kappa_1\sqrt{P_1(0)}z\right) e^{i2\phi_1(0)}, \tag{2.21b}$$

where $P_1(0)$ and $\phi_1(0)$ are the initial power and phase of the fundamental wave. Even though CW waves were considered to obtain the previous equations, very important conclusions can still be drawn for modulated waves or optical pulses, provided that the dispersion effects are not dominant. For short interaction lengths, $\tanh(x) \approx x$, so $A_2 \propto A_1^2$. For longer interaction lengths, the power of the second harmonic becomes comparable to that of the fundamental wave, and $\tanh(x) \longrightarrow 1$. In this case, the amplitude of the second harmonic and fundamental waves are approximately proportional.

The phase of the second harmonic is also a very important parameter, especially for phase-modulated signals. According to (2.21), the phase of the second harmonic is proportional to twice of the fundamental wave one. Considering a modulated BPSK signal as the fundamental wave, whose amplitude is constant and its phase is 0 or π radians, the phase of the second harmonic becomes 0 and 2π, which means that the phase-modulation is removed in the second harmonic. This property is explored in section 5.2, where a frequency- and phase-correlated pump wave is obtained by removing the phase-modulation through SHG.

In order to include the effects of phase mismatch ($\Delta\beta \neq 0$), let us assume that the interaction length is short so that the power of the fundamental wave is approximately constant. In this case, the evolution of the second harmonic power becomes

$$P_2(z) \approx \eta P_1^2(0) z^2 \cdot \mathrm{sinc}^2\left(\frac{\Delta\beta}{2}z\right), \tag{2.22}$$

with $\eta = \kappa_1^2$ the normalized conversion efficiency. The normalized conversion efficiency is a common parameter to characterize the efficiency of a second-order nonlinear device, experimentally obtained by dividing the output power of the second harmonic by the square

of the device length and the square of the fundamental wave power. Another usual parameter is the so-called SHG conversion efficiency that is defined by the ratio between the power of the second harmonic and by the square of the fundamental power. Therefore, the SHG conversion efficiency is equivalent to the normalized conversion efficiency multiplied by the square of the length of the device, expressed in units of W^{-1}.

The variation of the second harmonic power with $\Delta\beta$ and z is depicted in figure 2.5, obtained by solving the differential equations using a 4th-order Runge-Kutta algorithm and the theoretical expressions (2.21) and (2.22), for $P_1(0) = 100$ mW and $\eta = 0.1$ $W^{-1}cm^{-2}$. As expected, the power of the second harmonic reaches its maximum at the QPM resonance, decreasing with $\Delta\beta$ according to a squared sinc function. Moreover, the second harmonic power grows quadratically with the propagation length, showing a very good agreement with the approximated solution (2.22). The limited conversion bandwidth of the SHG process is also an important factor for OSP of high-speed signals, as the high-frequency components of the signal become significantly attenuated, leading to signal distortion.

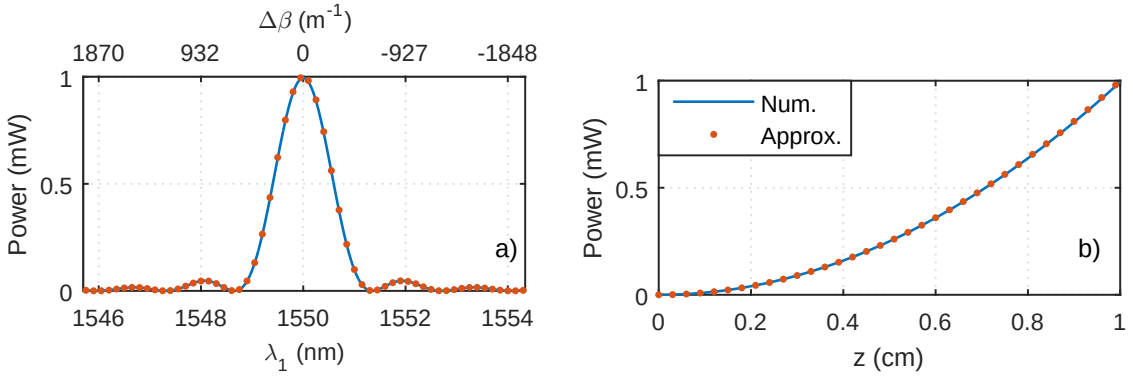

Figure 2.5: Variation of the second harmonic power with: a) λ_1, for $z = 1$ cm, and b) z, for $\Delta\beta = 0$. The solid curve was calculated through numerical simulations using a 4th-order Runge-Kutta algorithm, whereas the dots represent approximation (2.22).

SFG and DFG

The coupled-mode equations describing the SFG and DFG processes can be obtained by using the same procedure used for SHG, shown in appendix A, but considering three input waves with frequencies ν_1, ν_2 and $\nu_{\{SFG,DFG\}} = \nu_3 = \nu_2 \pm \nu_1$, where sign "$+$" corresponds to SFG and "$-$" to DFG. The following set of equations is obtained for SFG

$$\frac{\partial A_1(z,t)}{\partial z} = \hat{D}_1(\omega_{0,1},t)A_1(z,t) - i\kappa_1 A_3(z,t)A_2^*(z,t)e^{-i\Delta\beta z} \tag{2.23a}$$

$$\frac{\partial A_2(z,t)}{\partial z} = \hat{D}_2(\omega_{0,2},t)A_2(z,t) - i\kappa_2 A_3(z,t)A_1^*(z,t)e^{-i\Delta\beta z} \tag{2.23b}$$

$$\frac{\partial A_3(z,t)}{\partial z} = \hat{D}_3(\omega_{0,3},t)A_3(z,t) - i\kappa_3 A_2(z,t)A_1(z,t)e^{i\Delta\beta z}, \tag{2.23c}$$

with $\Delta\beta$ now given by $\Delta\beta = \beta_3 - \beta_2 - \beta_1 - 2\pi/\Lambda$ and κ given by (2.19), with the subscripts $j = 1$, $k = 2$ and $l = 3$. Equations (2.23) can also describe the DFG interaction by simply interchanging the subscripts 2 and 3. In this case, the phase mismatch parameter becomes $\Delta\beta = \beta_2 - \beta_3 - \beta_1 - 2\pi/\Lambda$.

Typically, one of the interacting waves in SFG and DFG processes is used to pump the nonlinear interaction and is much stronger than the other input wave (input signal), so it remains almost undepleted. In this case, the power of the pump wave may be regarded as a constant in (2.23). For simplicity, let us now consider the synchronous normalized electric field envelopes, defined as $B_3 = A_3 \exp(-i\Delta\beta z/2)$ and $B_2 = A_2 \exp(i\Delta\beta z/2)$ for the waves with frequencies ν_3 and ν_2, respectively. Assuming SFG between CW waves pumped by a wave at frequency ν_1 and with negligible propagation losses, the following solution is obtained

$$B_2(z) = \left[\cos(gz) + i\frac{\Delta\beta}{2g}\sin(gz)\right] B_2(0) - i\frac{\kappa_2^* A_1^*}{g}\sin(gz)\, B_3(0) \tag{2.24a}$$

$$B_3(z) = \left[\cos(gz) - i\frac{\Delta\beta}{2g}\sin(gz)\right] B_3(0) - i\frac{\kappa_3 A_1}{g}\sin(gz)\, B_2(0), \tag{2.24b}$$

where $g = \sqrt{\kappa_2\kappa_3 P_1 + (\Delta\beta/2)^2}$ is the effective coupling coefficient. If $B_3(0) = 0$ and assuming $\kappa_1 \approx \kappa_2 \approx \kappa_3/2 \approx \sqrt{\eta}$, the power of the SFG wave is approximately given by

$$P_3(z) \approx 4\eta P_1(0) P_2(0) z^2 \cdot \mathrm{sinc}^2(gz). \tag{2.25}$$

Similarly to SHG, the power of the sum-frequency wave grows quadratically with the interaction length and decreases according to a squared sinc function due to the phase mismatching effects, as shown by the curves depicted in figure 2.6, obtained for $\eta = 0.1$ $\mathrm{W^{-1}cm^{-2}}$, $P_1(0) = 100$ mW, $\lambda_1 = 1540$ nm, and $P_2(0) = 1$ mW. Moreover, if $B_3(0) = 0$, the normalized optical field of the sum-frequency wave is proportional to those of the input waves, which is essential for transparent OWC. However, the narrow conversion bandwidth of SFG is also a limiting factor for OSP of high-speed signals as in SHG. When $B_3(0) = 0$ and one of the waves is a strong pump wave, it is also usual to consider the SFG conversion efficiency, defined as the power ratio between the converted SFG wave and input signal (weaker input wave).

Equations (2.23) also describes a DFG interaction by simply interchanging subscripts 2 and 3. In addition, if the DFG process is fueled by a high-power pump located at ν_1, the solution of the coupled-mode equations for CW waves is also given by (2.24), with the appropriate interchange of subscripts. In this case, the DFG interaction resembles SFG, with the exception of the frequency relation of the waves. In addition, the optical field of the converted wave at ν_3 is proportional to that of the input signal and the phase information of the input signal is preserved in the converted one. Hence, this interaction will be hereinafter referred to as phase-preserving DFG.

On the other hand, if the pump wave is located at ν_2 and the input signal at ν_1, and

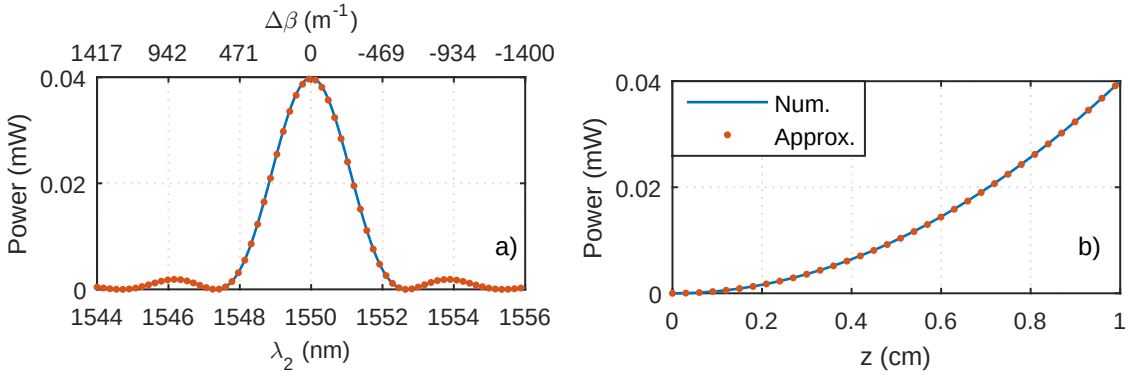

Figure 2.6: Variation of the sum-frequency wave power with: a) λ_2, for $z = 1$ cm, and b) z, for $\Delta\beta = 0$. The solid curve was calculated through numerical simulations using a 4th-order Runge-Kutta algorithm, whereas the dots represent approximation (2.25).

considering the synchronous normalized electric field envelopes $B_3 = A_3 \exp(i\Delta\beta z/2)$ and $B_1 = A_1^* \exp(-i\Delta\beta z/2)$, the evolution of the interacting waves for the undepleted pump approximation becomes

$$B_1(z) = \left[\cosh(gz) - i\frac{\Delta\beta}{2g}\sinh(gz)\right] B_1(0) + i\frac{\kappa_1 A_2^*}{g}\sinh(gz)B_3(0) \quad (2.26a)$$

$$B_3(z) = \left[\cosh(gz) + i\frac{\Delta\beta}{2g}\sinh(gz)\right] B_3(0) - i\frac{\kappa_3 A_2}{g}\sinh(gz)B_1(0), \quad (2.26b)$$

with $g = \sqrt{\kappa_1\kappa_3 P_2 - (\Delta\beta/2)^2}$. Contrarily to the previous case where g is always a real number, now it becomes imaginary when $(\Delta\beta/2)^2 > \kappa_1\kappa_3 P_1$, and the hyperbolic sines and co-sines in (2.26) become sine and co-sine functions, according to the equivalent relations $\cosh(ix) = \cos(x)$ and $\sinh(ix) = i\sin(x)$. If only the input signal and pump are injected into the nonlinear medium at ν_2 and ν_1, respectively, with $\nu_1 > \nu_2$, the optical field of the converted wave is proportional to the complex conjugate of the input signal. This interaction differs substantially from the phase-preserving DFG process described above, and is hereinafter referred to as phase-conjugating DFG. The evolution of P_3 in phase-conjugating DFG with no input converted wave becomes

$$P_3(z) = \eta P_1(0)P_2(0)\frac{\sinh^2(gz)}{g^2} \approx \eta P_1(0)P_2(0)z^2, \quad (2.27)$$

with the latter approximation valid for $g \approx 0$.

The variation of P_3 with λ_1 and z for a DFG interaction between CW waves with the pump at ν_2, $P_2(0) = 100$ mW, $\lambda_2 = 775$ nm, $P_1(0) = 1$ mW and $\eta = 0.1$ W^{-1}cm^{-2} is depicted in figure 2.7. The poling period was selected in order to obtain perfect QPM at $\lambda_1 = 1550$ nm. As shown in the figure, the conversion bandwidth of the DFG process spans over more than 100 nm for $z = 1$ cm, in contrast with the other examples given above for SHG and SFG, whose conversion bandwidth was less than 1 nm. The main reason for such a different behavior is related to the dispersive properties of the refractive index. Let

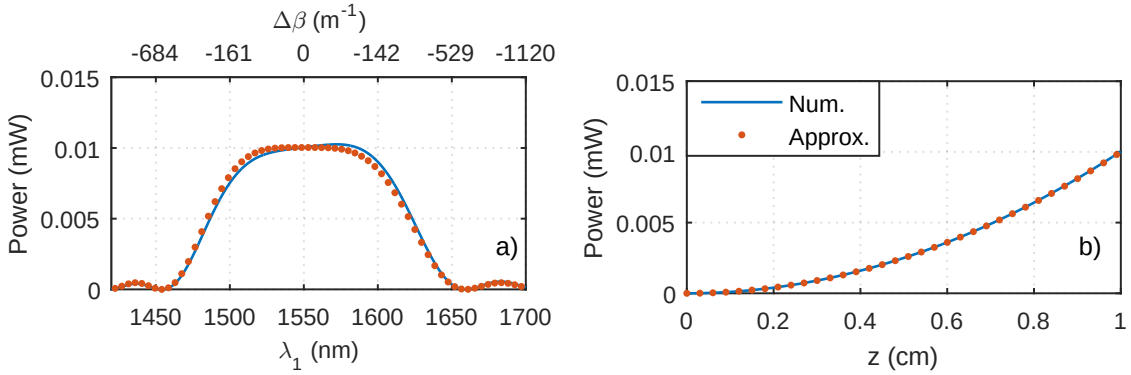

Figure 2.7: Variation of the difference-frequency wave power with: a) λ_1, for $z = 1$ cm, and b) z, for $\lambda_1 = 1550$ nm. The solid curve was calculated through numerical simulations using a 4th-order Runge-Kutta algorithm, whereas the dots represent approximation (2.27).

us first consider an SHG interaction where the frequency of the signal and of the second harmonic are detuned from the QPM frequency by $\Delta\nu$ and $2\Delta\nu$, respectively, as depicted in figure 2.8-a). Due to the dispersive effects, the frequency shift changes the refractive index of each wave by Δn_1 and Δn_2. Since the two waves are spectrally far from each other, Δn_1 and Δn_2 are usually very different. Consequently, even a small detuning from the QPM wavelength produces a considerable wavenumber mismatch, leading to a narrow conversion bandwidth. A similar effect is responsible for the narrow conversion bandwidth of SFG and phase-preserving DFG. Let us now consider an almost degenerate phase-conjugating DFG interaction where the frequency of the pump is fixed at $\nu_2 = 2\nu_1$, and the frequency of the converted signal is $\nu_3 \approx \nu_2 - \nu_1 \approx \nu_1$, in order to obtain perfect QPM. As shown in figure 2.8-b), if ν_1 is detuned from the QPM resonance by $\Delta\nu$, the converted signal is symmetrically shifted by the same amount. Moreover, if $\Delta\nu \ll \nu_1$, $\Delta n_3 \approx -\Delta n_1$ and the additional phase mismatch due to frequency detuning cancels out, which explains the wider conversion bandwidth.

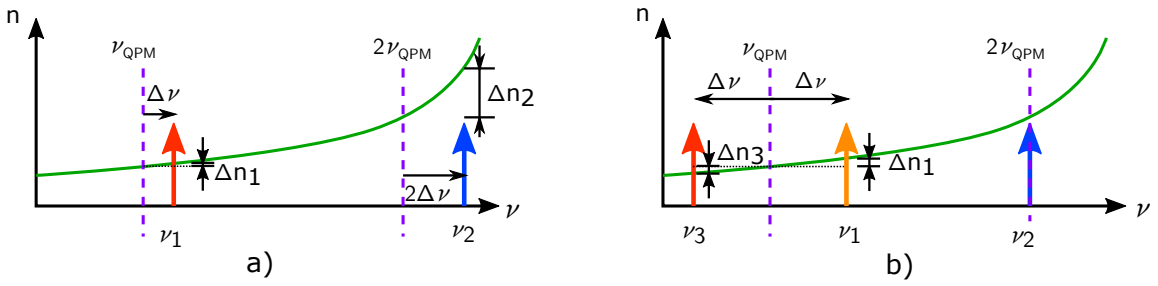

Figure 2.8: Variation of the refractive index due to frequency detuning from the QPM resonance for: a) SHG; b) phase-conjugating DFG.

Cascaded TWM

The evolution of the waves electric field in cascaded TWM processes is also described by a set of coupled-mode differential equations, obtained as for SHG, SFG and DFG. In the case of cSHG/DFG, the coupled-mode equations are given by

$$\frac{\partial A_1(z,t)}{\partial z} = \hat{D}_1(\omega_{0,1},t)A_1(z,t) - i\kappa_1 A_3(z,t)A_1^*(z,t)e^{-i\Delta\beta_1 z} \tag{2.28a}$$

$$\frac{\partial A_2(z,t)}{\partial z} = \hat{D}_2(\omega_{0,2},t)A_2(z,t) - i\kappa_2 A_3(z,t)A_4^*(z,t)e^{-i\Delta\beta_2 z} \tag{2.28b}$$

$$\begin{aligned}\frac{\partial A_3(z,t)}{\partial z} &= \hat{D}_3(\omega_{0,3},t)A_3(z,t) - i\frac{\kappa_{3,1}}{2}A_1^2(z,t)e^{i\Delta\beta_1 z} \\ &\quad - i\kappa_{3,2}A_2(z,t)A_4(z,t)e^{i\Delta\beta_2 z}\end{aligned} \tag{2.28c}$$

$$\frac{\partial A_4(z,t)}{\partial z} = \hat{D}_4(\omega_{0,4},t)A_4(z,t) - i\kappa_4 A_3(z,t)A_2^*(z,t)e^{-i\Delta\beta_2 z}, \tag{2.28d}$$

with $\nu_3 = \nu_{SHG} = 2\nu_1$, $\nu_4 = \nu_c = \nu_3 - \nu_2$, $\Delta\beta_1 = \beta_3 - 2\beta_1 - 2\pi/\Lambda$ the phase mismatch parameter for the SHG intermediate step, and $\Delta\beta_2 = \beta_3 - \beta_2 - \beta_4 - 2\pi/\Lambda$ for the DFG process. In typical OWC applications for OSP, the second harmonic of a strong CW pump wave is used to convert the input signal via DFG. Using such a configuration, the amplitude of the converted signal is not distorted due to SHG, nor its phase is doubled, but a phase conjugated copy of the input signal is created via phase-conjugating DFG.

In general, the previous set of equations cannot be solved analytically, even considering CW waves and negligible depletion of the fundamental wave in the SHG process. However, a rough approximation to $A_4(z)$ may be obtained by considering $\Delta\beta_1 = 0$ and neglecting the depletion of A_2 and of A_3. The following expression is then obtained

$$A_4(z) \approx -\kappa_1\kappa_4 A_1^2(0)A_2^*(0)\cdot\begin{cases}\frac{z^2}{2}, & \text{if } \Delta\beta_2 = 0,\\ \frac{e^{-i\Delta\beta_2 z}(1+i\Delta\beta_2\cdot z)-1}{\Delta\beta_2^2}, & \text{otherwise.}\end{cases} \tag{2.29}$$

The influence of λ_2 and the interaction length on the power of the converted wave, is shown in figure 2.9, with the SHG pump at $\lambda_1 = 1550$ nm, $P_1(0) = 100$ mW, $P_2(0) = 1$ mW and $\eta = 0.1$ W^{-1}cm^{-2}. Despite the several approximations considered to obtain (2.29), a good agreement between the numerical simulations and the theoretical expression is observed up to more than 3 cm.

The cSFG/DFG process can be described by the set of coupled-mode equations pre-

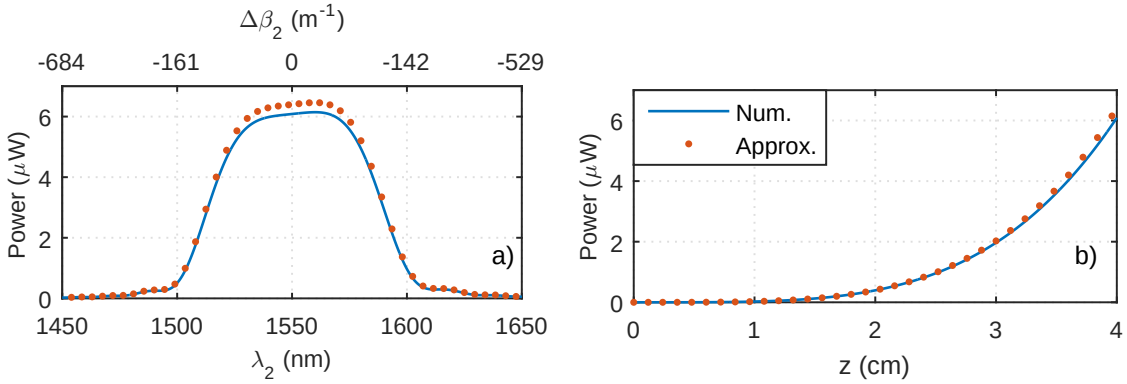

Figure 2.9: Variation of the power of the converted wave in a cSHG/DFG process with: a) λ_2, for $z = 4$ cm, and b) z, for $\lambda_2 = 1550$ nm. The solid curve was calculated through numerical simulations using a 4$^{\text{th}}$-order Runge-Kutta algorithm, whereas the dots represent approximation (2.29).

sented in (2.30), obtained using the same procedure as in appendix A for SHG.

$$\frac{\partial A_1(z,t)}{\partial z} = \hat{D}_1(\omega_{0,1},t)A_1(z,t) - i\kappa_1 A_3(z,t)A_2^*(z,t)e^{-i\Delta\beta_1 z} \tag{2.30a}$$

$$\frac{\partial A_2(z,t)}{\partial z} = \hat{D}_2(\omega_{0,2},t)A_2(z,t) - i\kappa_2 A_3(z,t)A_1^*(z,t)e^{-i\Delta\beta_2 z} \tag{2.30b}$$

$$\frac{\partial A_3(z,t)}{\partial z} = \hat{D}_3(\omega_{0,3},t)A_3(z,t) - i\kappa_{3,1}A_1(z,t)A_2(z,t)e^{i\Delta\beta_1 z} - i\kappa_{3,2}A_4(z,t)A_5(z,t)e^{i\Delta\beta_2 z} \tag{2.30c}$$

$$\frac{\partial A_4(z,t)}{\partial z} = \hat{D}_4(\omega_{0,4},t)A_4(z,t) - i\kappa_4 A_3(z,t)A_5^*(z,t)e^{-i\Delta\beta_2 z} \tag{2.30d}$$

$$\frac{\partial A_5(z,t)}{\partial z} = \hat{D}_5(\omega_{0,5},t)A_5 z,t) - i\kappa_4 A_3(z,t)A_4^*(z,t)e^{-i\Delta\beta_2 z}, \tag{2.30e}$$

with $\nu_3 = \nu_{SFG} = \nu_1 + \nu_2$, $\nu_5 = \nu_c = \nu_3 - \nu_4$, $\Delta\beta_1 = \beta_3 - \beta_2 - \beta_1 - 2\pi/\Lambda$ the phase mismatch parameter for SFG, and $\Delta\beta_2 = \beta_3 - \beta_4 - \beta_5 - 2\pi/\Lambda$ for DFG. In OWC based on cSFG/DFG, a first pump wave at ν_1 is used to convert the input signal at ν_2 through SFG, and the resulting wave is converted again via phase-preserving DFG, promoted by an additional pump wave, at ν_4. In this case, an approximated solution to the evolution of the converted wave at ν_5 for CW waves can be obtained by neglecting the depletion of the pump waves, given by

$$A_5(z) \approx \frac{\kappa_{3,1}\kappa_5 A_1(0)A_2(0)A_4^*(0)}{\Delta K^2 - g^2}\left[e^{i\Delta K z}\left(\cos(gz) - i\frac{\Delta K}{g}\sin(gz)\right) - 1\right], \tag{2.31}$$

where $\Delta K = \Delta\beta_1/2 - \Delta\beta_2$ is the total phase mismatch and $g = \sqrt{\kappa_2\kappa_3 P_1 + (\Delta\beta_1/2)^2}$. The variation of P_5 with λ_2 and the interaction length is depicted in figure 2.10, for $P_1(0) = P_4(0) = 50$ mW, $P_2(0) = 1$ mW, $\lambda_1 = 1547$ nm, $\lambda_4 = 1553$ nm, and $\eta = 0.1$ W^{-1}cm^{-2}, showing a good agreement between the numerical simulations and (2.31).

Compared to cSHG/DFG-based OWC, the conversion bandwidth of this process is much narrower, as not only the conversion bandwidth is limited by the SFG step, but also

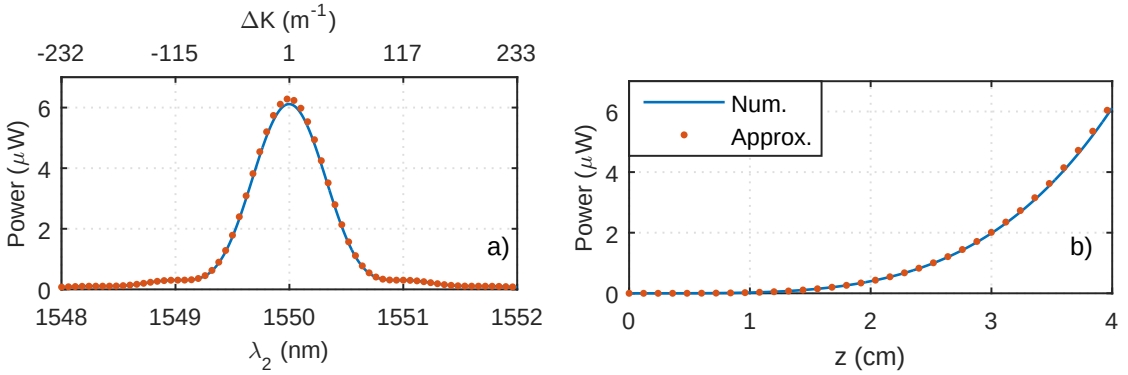

Figure 2.10: Variation of the power of the converted wave in a cSFG/DFG process with: a) λ_2, for $z = 4$ cm, and b) z, for $\lambda_2 = 1550$ nm. The solid curve was calculated through numerical simulations using a 4th-order Runge-Kutta algorithm, whereas the dots represent approximation (2.31).

by the phase-preserving DFG process, whose bandwidth is also narrow, as previously discussed.

2.3 Third-order nonlinear effects

The origin of third-order nonlinear effects can be traced to the term of **P** depending on the cubic power of the electric field. Considering a planar wave propagating in a third-order nonlinear medium, with an electric field vector described by (2.4), the third-order nonlinear electric polarization vector is given by

$$\mathbf{P}^{(3)} = \epsilon_0 \frac{\chi^{(3)}}{8} \left[E^3 e^{i(3\omega_0 t - 3\beta z)} + 3|E|^2 E e^{i(\omega_0 t - \beta z)} + c.c. \right] \hat{\mathbf{s}}, \tag{2.32}$$

where the first term corresponds to third-harmonic generation (THG) and the second one to SPM. The THG process is similar to SHG but three photons are initially absorbed instead of two, and a photon with three times the frequency of the initial photons is emitted. As in SHG, efficient THG requires phase matching of the interacting waves, which is often even more difficult to obtain due to the larger frequency difference between the fundamental wave and third harmonic. Therefore, THG is typically neglected for applications in optical communications systems, and is not further discussed in this thesis. The SPM term generates a nonlinear contribution at the frequency of the incident wave and is responsible for an intensity-dependent refractive index given by $n = (1 + \chi^{(1)} + \chi^{(3)}|E|^2/4)^{1/2}$. By considering the approximation $\sqrt{1+x} \approx 1 + x/2$ for $x \ll 1$, the intensity-dependent refractive index may be re-written as $n \approx n_L + n_{NL}|E|^2$, with $n_L = (1+\chi^{(1)})^{1/2}$ the linear refractive index and $n_{NL} = \chi^{(3)}/(8n_L)$ the nonlinear index coefficient [73].

For illustration purposes, the instantaneous response of a third-order nonlinear medium to an incident wave whose electric field is described by a harmonic wave with frequency of 1 Hz and amplitude 1 V/m, is depicted in figure 2.11, considering $\chi^{(1)}$ = 0.7 and $\chi^{(3)}$ = 0.3 V^2/m^2. As shown in the figure, the third-order term of the electric polarization vec-

tor is composed by a component at 3 Hz (THG), with an additional contribution at 1 Hz (SPM). The symmetric response of $\mathbf{P}^{(3)}$ does not mean, however, that $\chi^{(3)}$ vanishes for materials without an inversion symmetry. However, the second-order nonlinear effects are typically much stronger in non-centrosymmetric materials, so third-order nonlinearities can be neglected.

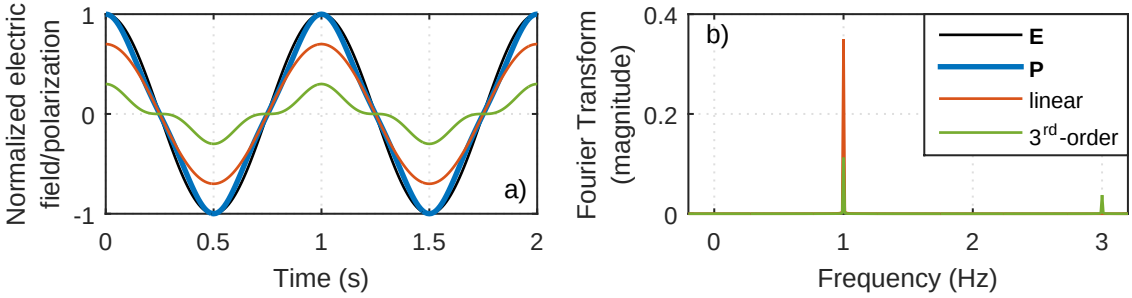

Figure 2.11: a) Normalized electric field **E** of the incident wave and respective electric polarization **P** of the propagating medium. The linear and third-order nonlinear parts of **P** are represented by the red and green curves, respectively. b) Magnitude of the Fourier transform of the linear and third-order nonlinear terms of **P**.

Let us consider three waves with frequencies ν_1, ν_2 and ν_3 propagating in a third-order nonlinear medium. In addition, let us assume that positive and negative frequencies are distinct. In this case, the third-order nonlinear electric polarization vector contains a total of 44 components summarized in (2.33), whose frequency ν_j correspond to different permutations of $\pm\nu_k \pm \nu_l \pm \nu_m$, with k, l, and m equal to 1, 2, or 3 [87].

$$\mathbf{P}^{(3)}(3\nu_k) = \frac{\epsilon_0\chi^{(3)}}{8}E_k^3 e^{i(2\omega_k t - 2\beta_k z)}, \tag{2.33a}$$

$$\mathbf{P}^{(3)}(\nu_k) = 3\frac{\epsilon_0\chi^{(3)}}{8}\left(|E_k|^2 + 2|E_l|^2 + 2|E_m|^2\right)E_k e^{i(\omega_k t - \beta_k z)}, \quad \text{for } k \neq l \neq m, \tag{2.33b}$$

$$\mathbf{P}^{(3)}(2\nu_k - \nu_l) = 3\frac{\epsilon_0\chi^{(3)}}{8}E_k^2 E_l^* e^{i[(2\omega_k - \omega_l)t - (2\beta_k - \beta_l)z]}, \quad \text{for } k \neq l, \tag{2.33c}$$

$$\mathbf{P}^{(3)}(2\nu_k + \nu_l) = 3\frac{\epsilon_0\chi^{(3)}}{8}E_k^2 E_l e^{i[(2\omega_k + \omega_l)t - (2\beta_k + \beta_l)z]}, \quad \text{for } k \neq l, \tag{2.33d}$$

$$\mathbf{P}^{(3)}(\nu_k + \nu_l - \nu_m) = 6\frac{\epsilon_0\chi^{(3)}}{8}E_k E_l E_m^* e^{i[(\omega_k + \omega_l - \omega_m)t - (\beta_k + \beta_l - \beta_m)z]}, \quad \text{for } k \neq l \neq m, \tag{2.33e}$$

$$\mathbf{P}^{(3)}(\nu_k + \nu_l + \nu_m) = 6\frac{\epsilon_0\chi^{(3)}}{8}E_k E_l E_m e^{i[(\omega_k + \omega_l + \omega_m)t - (\beta_k + \beta_l + \beta_m)z]}, \quad \text{for } k \neq l \neq m. \tag{2.33f}$$

In (2.33), the first expression is the THG term that generates the third harmonic of each wave, whereas the second one corresponds to the optical Kerr effect, that not only includes the SPM term, but also the intensity-dependent modulation of the refractive index caused by the other incident waves, i.e., XPM. The remaining terms of (2.33) correspond to the frequency mixing between different waves, a process similar to TWM in second-order nonlinear materials, but involving four waves rather than three. Therefore, this phenomenon is denominated as FWM. The frequency of waves generated through FWM, as well as the

photon creation/annihilation relations, shown in figure 2.12, are similar to two cascaded TWM. In this sense, the forth and sixth expressions of (2.33) respectively mimic cascaded SHG-SFG, and cascaded SFG-SFG interactions, so they are often denominated as third-order SFG. As shown in figure 2.12-b), three photons are absorbed and a photon with frequency equal to the sum of frequencies is emitted in third-order SFG. Likewise, the terms of the third and fifth expressions of (2.33) can be compared to cSHG/DFG and cSFG/DFG, and are usually referred to as degenerate and non-degenerate FWM, respectively. In this case, two photons are absorbed and two other are emitted, as shown in figure 2.12-c) for degenerate FWM and figure 2.12-d) for non-degenerate FWM.

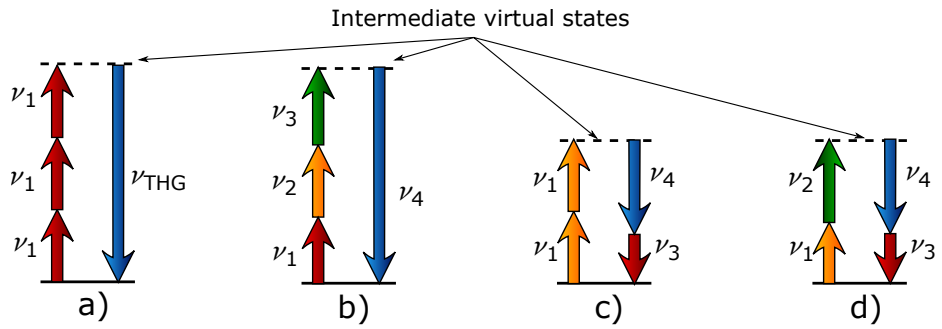

Figure 2.12: Schematic representation of photon creation/anihilation during: a) THG, b) third-order SFG, c) degenerate FWM, and d) non-degenerate FWM.

If the frequencies of the incident waves are similar, the third-order SFG generates new waves at frequencies close to the third harmonic, so the phase mismatch between the interacting waves is usually high and the efficiency of the nonlinear process is very low. Hence, third-order SFG is not further discussed in this thesis. On the other hand, the frequency of the waves generated via degenerate and non-degenerate FWM is approximately equal to that of the incident waves, and the phase mismatch can be very small, particularly if the waves are in spectral regions with low dispersion parameters. In this case, the efficiency of the nonlinear effects is high, even without any phase mismatch compensation techniques.

2.3.1 Coupled-mode equations

The evolution of the optical fields of the interacting waves in third-order nonlinear media can also be described by a set of coupled-mode equations, obtained as in the previous sections of this chapter. In this section, only the coupled-mode equations for degenerate and non-degenerate FWM are presented, as THG and third-order SFG are typically negligible for OSP.

Starting from the Maxwell's equations and considering the slowly-varying envelope approximation, the following set of equations is obtained for FWM between waves with frequencies ν_1, ν_2, ν_3 and $\nu_4 = \nu_1 + \nu_2 - \nu_3$ [73]

$$\frac{\partial A_1(z,t)}{\partial z} = \hat{D}_1(\omega_{0,1},t)A_1(z,t) + i\left(\gamma_{1111}|A_1(z,t)|^2 + 2\sum_{k\neq 1}^{4}\gamma_{1k1k}|A_k(z,t)|^2\right)A_1(z,t) + 2i\gamma_{1234}A_2^*(z,t)A_3(z,t)A_4(z,t)e^{i\Delta\beta z} \tag{2.34a}$$

$$\frac{\partial A_2(z,t)}{\partial z} = \hat{D}_2(\omega_{0,2},t)A_2(z,t) + i\left(\gamma_{2222}|A_2(z,t)|^2 + 2\sum_{k\neq 2}^{4}\gamma_{2k2k}|A_k(z,t)|^2\right)A_2(z,t) + 2i\gamma_{2134}A_1^*(z,t)A_3(z,t)A_4(z,t)e^{i\Delta\beta z} \tag{2.34b}$$

$$\frac{\partial A_3(z,t)}{\partial z} = \hat{D}_3(\omega_{0,3},t)A_3(z,t) + i\left(\gamma_{3333}|A_3(z,t)|^2 + 2\sum_{k\neq 3}^{4}\gamma_{3k3k}|A_k(z,t)|^2\right)A_3(z,t) + ib\gamma_{3412}A_4^*(z,t)A_1(z,t)A_2(z,t)e^{-i\Delta\beta z} \tag{2.34c}$$

$$\frac{\partial A_4(z,t)}{\partial z} = \hat{D}_4(\omega_{0,4},t)A_4(z,t) + i\left(\gamma_{4444}|A_4(z,t)|^2 + 2\sum_{k\neq 4}^{4}\gamma_{4k4k}|A_k(z,t)|^2\right)A_4(z,t) + ib\gamma_{4312}A_4^*(z,t)A_1(z,t)A_2(z,t)e^{-i\Delta\beta z}, \tag{2.34d}$$

where $\Delta\beta = \beta_3 + \beta_4 - \beta_1 - \beta_2$ is the phase mismatch parameter, $b = 2$, and γ_{ijkl} is the nonlinear coefficient, given by

$$\begin{aligned}\gamma_{jklm} &= \frac{3\chi^{(3)}\omega_j}{8cn_j}\frac{<M_j^*(x,y)M_k^*(x,y)M_l(x,y)M_m(x,y)>}{\sqrt{<|M_j(x,y)|^2><|M_k(x,y)|^2><|M_l(x,y)|^2><|M_m(x,y)|^2>}} \\ &= \frac{2\pi n_{NL}}{\lambda_j}\frac{<M_j^*(x,y)M_k^*(x,y)M_l(x,y)M_m(x,y)>}{\sqrt{<|M_j(x,y)|^2><|M_k(x,y)|^2><|M_l(x,y)|^2><|M_m(x,y)|^2>}} \\ &= \frac{2\pi n_{NL}}{\lambda_j A_{eff}},\end{aligned} \tag{2.35}$$

with $<M>$ an average value obtained by integrating M over the transverse directions x and y, and A_{eff} the effective overlap area. If $\nu_1 \approx \nu_2 \approx \nu_3 \approx \nu_4$, the transverse field distribution of the interacting waves is approximately the same, so γ_{jklm} can be regarded as a constant, equal to γ. Equations (2.34) can also describe the evolution of the interacting waves in degenerate FWM by disregarding (2.34b), setting b equal to 1, $\nu_2 = \nu_1$, and neglecting the XPM contribution due to A_2.

An approximated solution for (2.34) can be obtained for CW waves propagating in a lossless medium, considering two strong pump waves at ν_1 and ν_2 for non-degenerate FWM or a single pump at ν_1 for the degenerate case, with negligible power depletion. Assuming that the XPM contribution is mainly due to the power of the pump waves, the

evolution of the pumps' normalized electric field for non-degenerate FWM is given by [73]

$$A_j(z) = \begin{cases} A_j(0) \cdot e^{i\gamma[P_j(0)+2P_{3-j}(0)]z}, & \text{for non-degenerate FWM} \\ A_j(0) \cdot e^{i\gamma P_j(0)z}, & \text{for degenerate FWM,} \end{cases} \tag{2.36}$$

where index j is 1 for degenerate FWM, and 1 or 2 for the non-degenerate case. Using (2.36) in (2.34), the solution for waves with frequency ν_3 and ν_4 becomes

$$\begin{aligned} A_k(z) = e^{i\frac{\Theta}{2}z} \Bigg\{ & A_k(0) \left[\cosh(gz) + i\frac{\Delta\beta_{eff}}{2g} \sinh(gz) \right] \\ & + ib\frac{\gamma}{g} A_l(0) A_m(0) A^*_{7-k}(0) \sinh(gz) \Bigg\}, \end{aligned} \tag{2.37}$$

with k equal to 3 or 4 for the waves with frequency ν_3 or ν_4, respectively. In the case of non-degenerate FWM, $l = 1$, $m = 2$, $\Theta = 3\gamma[P_1(0) + P_2(0)] - \Delta\beta$ and the effective coupling coefficient is given by $g = \sqrt{4\gamma^2 P_1(0)P_2(0) - (\Delta\beta_{eff}/2)^2}$, with $\Delta\beta_{eff} = \Delta\beta + \gamma[P_1(0) + P_2(0)]$ an effective phase mismatch parameter, that includes the contribution of the refractive index modulation due to the Kerr effect. For a degenerate FWM interaction, $l = m = 1$, $\Theta = 2\gamma P_1(0) - \Delta\beta$, $g = \sqrt{\gamma^2 P_1^2(0) - (\Delta\beta_{eff}/2)^2}$, and $\Delta\beta_{eff} = \Delta\beta + 2\gamma P_1(0)$.

Let us now consider that an input signal at ν_3 is injected in the nonlinear medium, with no input idler, i.e, $P_4(0) = 0$. A phase-conjugated copy of the signal is generated at ν_4 through FWM (parametric generation), along with parametric amplification of the input signal by a factor of $1 + (1 + [\Delta\beta_{eff}/(2g)]^2)\sinh^2(gz)$, similarly to the phase-conjugating DFG process, discussed in the previous section.

Phase-preserving parametric generation based on FWM is also possible in third-order nonlinear media if one of the pump waves is located at ν_3, and the input signal at ν_2, as depicted in figure 2.13. The evolution of A_2 and A_4 is then given by

$$\begin{aligned} A_2(z) = e^{i(2\gamma[P_1(0)]+P_3(0)]+\Delta\beta_{eff}/2)z} \cdot \Bigg\{ & A_2(0) \left[\cos(gz) - i\frac{\Delta\beta_{eff}}{2g} \sin(gz) \right] \\ & + 2i\frac{\gamma}{g} A_1^*(0) A_3(0) A_4(0) \sin(gz) \Bigg\} \end{aligned} \tag{2.38a}$$

$$\begin{aligned} A_4(z) = e^{i(2\gamma[P_1(0)]+P_3(0)]-\Delta\beta_{eff}/2)z} \cdot \Bigg\{ & A_4(0) \left[\cos(gz) + i\frac{\Delta\beta_{eff}}{2g} \sin(gz) \right] \\ & + 2i\frac{\gamma}{g} A_1(0) A_3^*(0) A_2(0) \sin(gz) \Bigg\}, \end{aligned} \tag{2.38b}$$

with $g = \sqrt{4\gamma P_1(0)P_3(0) + (\Delta\beta_{eff}/2)^2}$ and $\Delta\beta_{eff} = \Delta\beta + \gamma[P_1(0) - P_3(0)]$.

The variation of the idler power with λ_4 for the three FWM possibilities discussed above is shown in figure 2.13, assuming no input idler wave and with length L, γ, dispersion parameter and dispersion slope at 1550 nm of 1 km, 10 $W^{-1}km^{-1}$, 0 $ps.nm^{-1}km^{-1}$ and 0.065 $ps.nm^{-2}km^{-1}$, respectively. The input power of the signal and pump waves in non-degenerate configurations is 0.1 mW and 50 mW, whereas in degenerate FWM the power

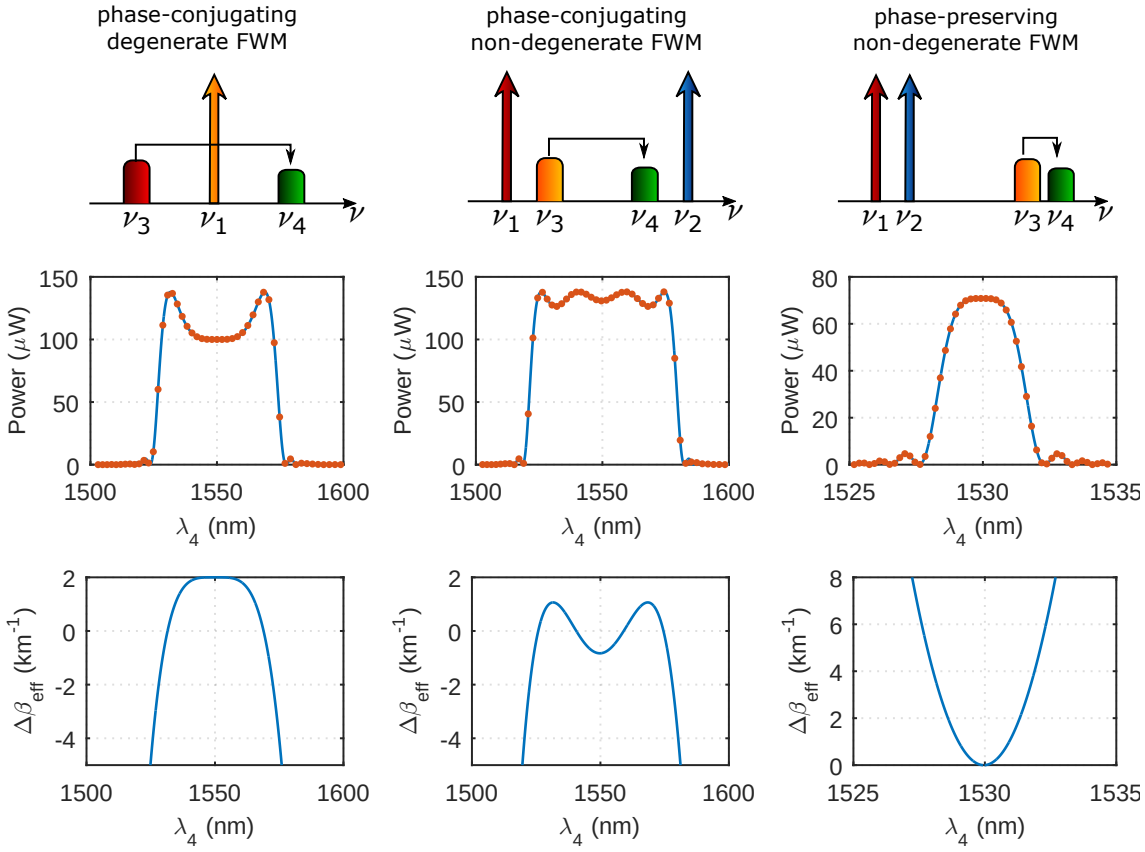

Figure 2.13: At the top of the figure, schematic representation of phase-conjugating degenerate and non-degenerate FWM, and phase-preserving non-degenerate FWM, with the respective variation of P_4 with λ_4, shown in the middle, and of $\Delta\beta_{eff}$, at the bottom. The blue solid lines of the graphics shown in the middle and bottom row are numerical results calculated by a 4th-order Runge-Kutta algorithm, whereas the orange dots are the approximated solutions.

of the pump is set to 100 mW. According to the simulated curves, the phase-conjugating FWM configurations show wide conversion bandwidths of more than 50 nm, which is a consequence of lower effective phase mismatch parameter for a wider spectral range. Since the signal is also amplified along with the generation of the idler waves, such configurations are particularly interesting for broadband amplification and/or multichannel operation. In degenerate, phase-conjugating FWM, however, the conversion efficiency and, consequently, the signal gain are not uniform along the conversion bandwidth, but reach a maximum value at approximately 20 nm apart from the pump location, where $\Delta\beta_{eff}$ is approximately 0. A wider and flatter conversion efficiency is obtained for the dual-pump non-degenerate configuration, as the absolute value of $\Delta\beta_{eff}$ is kept closer to 0 for a wider wavelength range. In both cases, the spectral efficiency is determined by the power and location of the pump waves, as well as the dispersive properties of the nonlinear gain [73].

The conversion bandwidth of phase-preserving FWM is much narrower compared to the phase-conjugating processes, of less than 5 nm. The narrower conversion bandwidth of phase-preserving FWM is a consequence of higher effective phase mismatch parameter,

even for a wavelength detuning from the maximum efficiency condition of about 3 nm. In addition, the input signal wave is partially consumed during the nonlinear process in order to generate the new idler wave, instead of being amplified as in phase-conjugating FWM interactions. In this sense, phase-preserving FWM can be compared to phase-preserving DFG, discussed in the previous section.

2.3.2 Stimulated Brillouin and Stimulated Raman scattering

Hitherto, all the described nonlinear phenomena are parametric, i.e., the total energy of the incident photons is equal to that of the emitted ones. Other nonlinear phenomena may occur in which the total energy of the photons is not conserved, but partially transferred to the nonlinear medium [73]. SBS and SRS are two examples of such non-parametric nonlinear effects that involve the participation of phonons, which are quantized lattice vibrations of the medium [94]. The difference between SBS and SRS is that the former process involves the participation of acoustic phonons, whereas optical phonons are in the origin of SRS [31, 73, 87].

In a quantum-mechanical description of SBS, one incident photon with frequency ω_p is annihilated, generating an acoustic phonon with frequency Ω_p and a Stokes photon with frequency $\omega_p - \Omega_p$, that travels in the backward direction [31]. The acoustic phonon is generated through a process called electrostriction, in which the materials become more dense in regions where the optical intensity is high [87, 95]. The beating between the incident and the Stokes waves generates a pressure wave through electrostriction acting as a positive feedback mechanism, and reinforcing the scattering process [31, 87]. Even if no input Stokes wave is injected into the nonlinear medium, the SBS process may start from the photons generated by spontaneous Brillouin scattering [73].

In SRS, however, either a photon with lower or higher energy than that of the initial photon may be emitted. In the former case, the material is excited to a more energetic vibrational state, with the creation of an optical phonon and emission of a Stokes photon with frequency $\omega_p - \Omega_p$, as in SBS. If the material is already in an excited vibrational state, an anti-Stokes photon with frequency $\omega_p + \Omega_p$ is emitted along with the relaxation of the material to a lower energy state [31, 73]. In general, the anti-Stokes scattering is much weaker than Stokes scattering due to the difference of population between the ground and excited vibrational states [95]. In SRS, the normal vibrational modes of the propagating medium beat with the incident wave and generate the Stokes wave. In turn, the Stokes wave reinforces the vibrational modes, resulting in a positive feedback mechanism, as in SBS [31, 95].

The effects of SBS and SRS can be described in terms of additional contributions to the third-order nonlinear susceptibility [87, 95]. In both processes, the generation of the Stokes wave becomes significant only when the power of the incident wave exceeds a certain threshold level, after which its power grows exponentially [73].

Even though SBS and SRS can be used for several applications in optics [73], with

the exception of Raman amplification, these nonlinear phenomena are typically impairing mechanisms for OSP in fiber-based systems. As an example, the SBS threshold in silica fibers is of only a few milliwatts [31, 73]. Hence, if strong pumps are required to implement an OSP function based on HNLFs, part of the pump power is converted to the Stokes wave, therefore reducing the efficiency of the OSP functionality, even at relatively low power. In this case, mitigation of SBS is required, which can be performed by interrupting or avoiding the exponential growth of the Stokes wave. A possible solution to mitigate SBS is by placing optical isolators between shorter spans of fiber in order to block the counter-propagating Stokes wave, but the insertion and splicing losses of the isolators may be an impeding problem. Other possibilities include modifying the fiber in order to obtain non-uniform Brillouin shift or broadening the spectral width of the pump wave. The gain spectrum of the Stokes wave in silica fibers is very narrow, of the order of a few tens of MHz [31, 73], and down-shifted by about 10 GHz with respect to the incident wave. Since the SBS gain spectrum depends on several physical and geometrical parameters, non-uniformity can be created through different dopant concentrations [96] or core geometries [97], as well as temperature [98] or strain gradients [99] along the fiber. Non-uniformity broadens the SBS gain spectrum, reducing its average value and increasing the SBS threshold [73]. The SBS can also be mitigated by increasing the spectral width of the waves, so it becomes broader than the Brillouin gain spectrum. Spectral broadening of the waves is usually accomplished via external phase-modulation with several radio frequency (RF) tones [100], as shown in chapter 5.

SRS in optical fibers can occur in both propagation directions, with a broad gain spectrum that extends over a spectral range of about 40 THz due to the amorphous nature of silica, reaching a maximum value at a frequency detuning of about 13 THz [60, 73]. The SRS threshold in optical fibers is much higher than the SBS one, of the order of about 1 W. Nevertheless, SRS may be a limiting factor for multichannel systems due to a Raman-induced power transfer among the different channels [73] or excessive Raman-induced noise [101].

2.4 Numerical methods

In the previous sections of this chapter, coupled-mode differential equations describing second- and third-order nonlinear effects were presented, including analytical approximations for some particular cases. In general, however, the solution of the coupled-mode equations must be solved numerically.

When the interacting waves are all CW, the time derivatives of the dispersion operator $\hat{D}$ vanish and the problem can simplified to solving a system of nonlinear ordinary differential equations. In this case, a common 4^{th} Runge-Kutta algorithm with constant integration step [102] can be used to integrate the differential equations, chosen as a trade-off between accuracy, step size and computational effort.

The situation becomes more complicated when computing the solution of non-CW signals, which requires solving a system of initial-value nonlinear partial differential equations. Two different approaches can be used in this case, namely the SSFT method and the finite-differences method.

In the SSFT method, the solution of the partial differential equations at each integration point is obtained in two steps, one considering only the dispersive effects, an the other accounting only for the nonlinear part of the equation [73]. In this approach, the problem is simplified to solving two simpler ordinary differential equations, one for the dispersive step and another for the nonlinear one. Moreover, an analytical closed-form solution of the dispersive step exists for the Fourier transform of the optical field of the waves (i.e., in the frequency domain), given by (2.9). Hence, the use of efficient fast Fourier transform (FFT) algorithms is critical and of uttermost importance in the SSFT method as a Fourier transform and its inverse operation need to be calculated at each integration step.

The finite-differences method is a possible alternative to the SSFT method for very long signals and/or when the computation of the FFT is very time-consuming [73]. In this method, the time- and space-derivatives are replaced by finite-differences approximations and, depending on the type of approximation, different schemes of the finite-differences method are possible, each with different implementation complexity, accuracy, convergence and stability properties [103]. A simple possibility is to consider a forward-space, centered-time method that considers a forward finite-difference for the spatial derivative and centered finite-differences for the temporal derivatives [103]. However, such scheme may require small integration steps in order to provide accurate solutions and it is conditionally stable, so a special care must be taken when choosing the spatial and temporal integration steps [103].

Another practical aspect to account when computing the solution of the differential equations is the temporal evolution of the waves. For instance, after a propagation distance of Δz, the optical waves experience a time shift of $\beta^{(1)}\Delta z$, and may go outside of the temporal integration window. A possible way to overcome this drawback is to consider a longer temporal integration window, but the computational efforts to solve the differential equation increase as well. A better alternative is to consider a time frame moving at the average group velocity of the interacting waves, allowing to keep the temporal integration window of the order of the signal duration. Mathematically, the moving time frame can be implemented by considering the transformations $t' \rightarrow t - z/v_g$ and $z' \rightarrow z$, where t' and z' are the time and space coordinates in the moving frame [73]. As a consequence, $\partial/\partial z$ becomes $\partial/\partial z' - {v_g}^{-1}\partial/\partial t'$, whereas the time-derivatives remain unchanged.

2.4.1 Total field formulation

When only a few waves propagate in a nonlinear medium, the evolution of such waves can usually be described by a small set of differential equations, with one equation for each wave. In WDM systems, however, the number of interacting waves and, consequently, the

number of differential equations to compute is large, so solving the individual coupled-mode equations becomes unpractical. In addition, if the nonlinear efficiency is sufficiently high, new cascaded interactions may occur that are not accounted in the coupled-mode equations and may significantly alter the power dynamics of the nonlinear interaction. As an example, let us consider the generation of a wave at frequency $\nu_3 = 2\nu_1 - \nu_2$ through degenerate FWM interaction. The generated wave may interact again with the existing waves through different FWM interactions, creating new contributions at, for instance, $2\nu_2 - \nu_3$, $\nu_1 + \nu_2 - \nu_3$, or $\nu_3 + \nu_1 - \nu_2$. Furthermore, it may happen that the spectra of modulated signals overlap, which causes inter-channel crosstalk, a feature that cannot be accounted for in the coupled-mode equations formalism.

A possible way to overcome the limitations described above is to consider a total field formulation [104], in which the electric fields of all the waves are included in a single optical field, as follows

$$A(z,t) = \sum_j A_j(z,t) e^{i(\omega_j - \omega_0)t}, \tag{2.39}$$

where j denotes each individual wave, and ω_0 is the central frequency of the total-field wave.

Using the total field formulation, the third-order nonlinear effects of SPM, XPM and FWM can be described by a single nonlinear Schrödinger equation, given by

$$\frac{\partial A(z,t)}{\partial z} = \hat{D}(\omega_0, t) A(z,t) + i\gamma |A(z,t)|^2 A(z,t). \tag{2.40}$$

The total field formulation greatly simplifies the problem for multiple waves by condensing all the coupled-mode equations into a single nonlinear Schrödinger equation, but it also requires small time integration step sizes or, equivalently, a large simulation spectral range. Since the total normalized electric field envelope is composed by several components at angular frequencies $\omega_j - \omega_0$, a discretization of A with a small time step size is necessary in order to avoid the aliasing phenomenon and generation of false FWM contributions. As a rule of thumb, a sampling frequency of more than three times the total bandwidth occupied by the waves is sufficient to mitigate these phenomena [105]. In addition, higher-order dispersion terms may have to be included in the total field formulation due to broader spectral bandwidth.

The total field formulation can also be applied for the simulation of second-order nonlinear interactions of multiple waves, but an extremely small time step size would be required due to the frequency difference between the waves in the fundamental and second harmonic bands. A possible solution is to consider two total optical fields, one including the waves in fundamental band (A_1), and the other the waves in the second harmonic band (A_2). The evolution of the total normalized fields A_1 and A_2 can then be described by (2.18).

The nonlinear Schrödinger equation is a good approximation to evaluate the evolution of waves propagating in a nonlinear medium with negligible birefringence [106]. However, in real fibers, imperfections of the fiber geometry induce randomly varying birefringence

effects and lead to PMD. This effect is particularly relevant for dual-polarization systems in which the information is encoded in two orthogonal states of polarization. The randomly varying birefringence effects for dual-polarization nonlinear propagation can be described by the Manakov-PMD equation, given by [106, 107]

$$\frac{\partial A_x(z,t)}{\partial z} = \hat{D}(\omega_0,t)A_x(z,t) + i\frac{8}{9}\gamma\left(|A_x(z,t)|^2 + |A_y(z,t)|^2\right)A_x(z,t) \tag{2.41a}$$

$$\frac{\partial A_y(z,t)}{\partial z} = \hat{D}(\omega_0,t)A_y(z,t) + i\frac{8}{9}\gamma\left(|A_x(z,t)|^2 + |A_y(z,t)|^2\right)A_y(z,t), \tag{2.41b}$$

where A_x and A_y are the normalized electric fields of the waves in the orthogonal states of polarization x and y. The Manakov-PMD equations are obtained by averaging the states of polarization over the random birefringence fluctuations and represent the overall effect of random birefringence after a sufficiently long propagation distance [106].

2.5 Nonlinear devices for all-optical signal processing

A wide range of nonlinear optical materials and devices can be used for OSP. In fact, any optical material behaves in a nonlinear manner at a sufficiently strong excitation, but several fundamental and technical limitations restrict the available platforms for nonlinear OSP. Even common nonlinear optical materials widely used for other applications may not be attractive for OSP in lightwave systems. High nonlinearity, resistance to strong optical pumping, ultrafast response, low losses, compactness, possibility of integration, low signal distortion and degradation, low cost and mature fabrication technology are some of the most desirable properties of nonlinear devices for OSP applications [10, 20].

Many nonlinear materials and devices with remarkable performances are already available for nonlinear OSP. HNLFs, SOAs, PCFs, tapered fibers, silicon and chalcogenide waveguides, tellurite and bismuth oxide glasses are some examples of third-order nonlinear devices [9, 10, 31], whereas PPLN and PPLT waveguides are the most common representatives of second-order nonlinear devices [10].

Despite its modest nonlinear coefficient ($<$30 $W^{-1}.km^{-1}$) compared to other third-order nonlinear media, silica HNLFs are the most common devices for OSP, due to their compatibility with fiber-based systems, the possibility of deployment in transmission links with low insertion and propagation losses [21], mature fabrication technology and the existence of commercial solutions. Furthermore, the modest nonlinear coefficient of silica HNLFs is compensated by the possibility of drawing long fibers with total length of up to a few kilometers, reducing the required pumping power to acceptable values for lightwave systems.

A silica HNLF is a silica fiber whose nonlinear coefficient is enhanced by increasing n_{NL} and by decreasing the effective overlap area. Heavy Ge doping is a possible solution to increase n_{NL} [31, 73], whereas A_{eff} can be reduced by decreasing the core dimensions, or by tighter mode confinement, achieved through higher core-cladding index contrast and/or

by producing depressed cladding structures [73].

The nonlinear coefficient of optical fibers can also be enhanced by replacing silica with another glass material with higher n_{NL}. Oxide bismuth and chalcogenide glasses such as As_2Se_3 are some examples, whose nonlinear index coefficient is larger by one or two orders of magnitude. Nonlinear coefficient values of more than 1000 $W^{-1}km^{-1}$ can be obtained for such devices [108, 109]. In the case of tapered fibers and solid-core PCFs, high nonlinear coefficients are achieved by simultaneously reducing the core size down to values that can be below 1 μm, and by increasing the index contrast, improving the mode confinement [73]. In the case of tapered fibers, higher index contrast is obtained by using air as the cladding material, whereas higher index contrast in PCFs is achieved by a cladding with embedded air holes [73, 110]. Despite the remarkably high nonlinear coefficients, high propagation losses [111–113] and photosensitive instability of chalcogenide glasses at high power levels [112,114] are some of the limiting factors for OSP applications.

Compact third-order nonlinear devices have also been intensively researched in the last years, motivated by the need of integrated solutions for photonic integrated circuits. Silicon- and chalcogenide-based waveguides or nanowires and SOAs are some possibilities, where the short interaction length is compensated by very large nonlinear coefficient values, such as 104000 $W^{-1}km^{-1}$ for a silicon-organic hybrid slot waveguide [115], or even 136000 $W^{-1}km^{-1}$ for a chalcogenide glass nanowire [111]. Silicon is a low-cost, CMOS-compatible platform with mature fabrication technology, which makes it ideal for integrated solutions, but strong two-photon and free-carrier absorption limit their performance [9, 21]. Hybrid silicon-organic solutions have been proposed to overcome this limitation [21, 115].

SOAs are devices similar to laser diodes, providing gain via stimulated emission, but with anti-reflecting coatings to avoid lasing [116]. SOAs combine large nonlinear effects, compactness, and optical gain, making them suitable choices for OSP [11, 117]. The nonlinear response of SOAs originate from several physical processes, namely spectral hole burning, carrier heating and carrier recombination that generate transient gain saturation, and phase variations due to changes of the carrier density and, consequently, of the refractive index [116, 118]. Usually, gain and phase transient dynamics of SOAs create undesirable patterning effects that degrade the optical signal itself, as well as other signals at different wavelengths. However, gain and phase modulation induced by strong signals injected into the SOA (cross-gain modulation (XGM) and XPM, respectively) can also be used to implement OSP functionalities, including OWC and optical logic gates [119]. Moreover, OSP based on FWM is also possible in SOAs [119].

Although all the nonlinear devices described above are very promising for OSP, the discussion in this thesis is limited to HNLFs and especially to PPLN waveguides, which are discussed in the following subsection. For a more comprehensive review on these third-order nonlinear devices, the reader may refer to [112, 114–116, 119–121] and the references therein.

2.5.1 PPLN

PPLN waveguides are the most common second-order nonlinear devices for OSP applications due to their intrinsic physical and technological properties. As discussed in section 2.2, efficient second-order nonlinear processes require phase matching between the interacting waves, which can be obtained through QPM. In the case of PPLN devices, QPM is achieved by periodically inverting the ferroelectric domains (periodic poling) and, consequently, inverting the sign of the nonlinear coefficient in lithium niobate crystals [20], as depicted in figure 2.14.

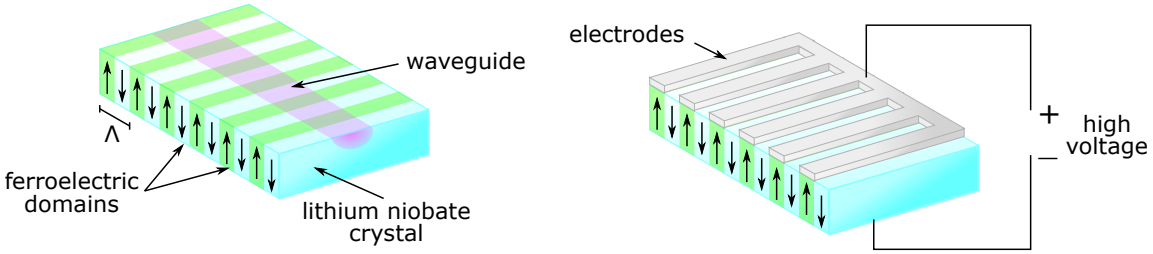

Figure 2.14: Schematic representations of a PPLN waveguide (left) and the electric poling process (right).

The most common technique to produce PPLN devices is through electric-field poling, in which high-voltage pulses are applied to electrodes on the surface of the lithium niobate crystal [20], as depicted in 2.14, on the right. Periodic poling is also possible using other ferroelectric second-order nonlinear crystals such as lithium tantalate (PPLT), potassium titanyl phosphate or potassium titanyl arsenate, but lithium niobate is the most common choice for OSP.

Lithium niobate is transparent for a wide spectral region, ranging from 350 to 5000 nm and exhibits negative uniaxial birefringence, as well as high piezoelectric, photoelastic, piroelectric, electro-optic and nonlinear coefficients [32, 122, 123]. Lithium niobate crystals can be grown by the Czochralski method [122], and high quality wafers with diameters of several centimeters are commercially available. Since lithium niobate is also the most common material to build electro-optical modulators their fabrication technology is already mature and well-developed. The nonlinear coefficient of lithium niobate is a tensorial quantity with the highest value achieved when all interacting waves are polarized along the optical axis of the crystalline structure (c direction of the hexagonal unit cell), i.e, the d_{33} component of the nonlinear coefficient tensor [33,87]. High d_{33} values of 25 pm/V for SHG pumped at 1064 nm and of 20 pm/V when pumped at 1318 nm have been reported, about two times higher than those of lithium tantalate or potassium titanyl phosphate [33].

The inclusion of waveguides in PPLN devices allows tight confinement and transversal overlap of the interacting waves over longer distances, which enhances the efficiency of the nonlinear processes and reduces the required pumping power [20]. Waveguides in PPLN devices have been produced through in-diffusion of titanium ions at high temperatures, the proton-exchange method, or by creating ridge structures via mechanical dicing or plasma

etching (dry etching) [32,124,125]. The diffusion of titanium ions into lithium niobate raises the extraordinary and ordinary refractive indexes, allowing the formation of waveguides that support both transverse magnetic and transverse electric modes [32].

In the proton-exchange method, the PPLN devices are immersed into a heated benzoic acid bath, producing a superficial exchange of protons (H^+) and lithium ions. The proton-exchange process raises the extraordinary refractive index, but lowers the ordinary one, so only transverse-magnetic modes are supported [32]. Fortunately, this corresponds to the case when all the waves are polarized along the optical axis of lithium niobate, and the highest component of the nonlinear coefficient tensor (d_{33}) can be used. The proton-exchange process may cause superficial structural phase changes due to high proton concentration, which lowers the nonlinear coefficient and increases propagation losses. A thermal annealing treatment is typically performed after the proton-exchange process to promote the diffusion of exchanged protons deeper into the lithium niobate substrate, relaxing the layer stress and avoiding a nonlinear coefficient drop [32]. Waveguides produced by this method are denominated as annealed proton-exchanged (APE) waveguides. Buried waveguides may also be produced through a reverse proton-exchange technique where an additional diffusion process of lithium ions lowers the refractive index close to the surface of the device. In this case, the mode overlap between the waves at the fundamental and second harmonic band is enhanced and the propagation losses are reduced, improving the efficiency of the PPLN devices [20,32].

Very high conversion efficiency can also be achieved in ridge waveguides, where tight confinement and mode overlap between the interacting waves is obtained due to high refractive index contrast between the lithium niobate ridge and air. Moreover, direct-bonding of the lithium niobate substrate on a lithium tantalate wafer, whose refractive index is lower, enhances the confinement of the propagating modes in the ridge waveguide, increasing the efficiency of the PPLN devices even further [125].

One of the main drawbacks and impairing mechanisms of PPLN devices is photorefractive damage, which is an induced variation of the refractive index due to the presence of visible or infrared light. This refractive index variation persists for some time even after the illumination ceases, and causes a shift of the QPM wavelength [20,32,124]. This effect is believed to be caused by several physical mechanisms including the generation of electrical charges through optical ionization of donor impurities that drift to acceptor centers, creating an internal electric field and a change of the refractive index due to the electro-optic effect [32]. Another important mechanism that affect the operation of PPLN devices is a phenomenon called green-induced infrared absorption (GRIIRA), that also contributes for photorefraction [123,126]. The GRIIRA effect is responsible for the creation of an absorption band in the infrared region induced by the presence of strong green light and, consequently, local heating that affects the QPM resonance condition [123]. The photorefractive damage and GRIIRA can be reduced by setting the PPLN temperature values of the order of 100 °C [20]. However, high temperature operation may degrade proton-exchange

waveguides due to proton diffusion into the lithium niobate substrate [124]. The photorefraction and GRIIRA in PPLN devices can also be reduced through magnesium or zinc doping of the lithium niobate substrate up to molar concentrations of the order of 5 mol% [32]. Another drawback of PPLN devices is polarization sensitivity due to the anisotropic properties of lithium niobate, which limits these devices to single-polarization operation [20]. Nevertheless, this drawback can be overcome by using polarization-diversity schemes for polarization insensitive operation [127, 128].

Compared to HNLFs, PPLN devices are compact (few centimeters long) and do not suffer from deleterious SBS. In addition, frequency chirp and spontaneous noise emission are negligible in PPLN devices. Furthermore, since the principle of operation is based on second-order nonlinear effects, PPLN devices are not affected by SPM nor XPM, which can be advantageous for certain OSP applications [20].

Periodically poled devices offer a unique possibility of designing the spectral response by engineering the inversion of the ferroelectric domains, a feature that is not easily available in other nonlinear devices. This unique advantage is further explored in chapter 3, where a method to design devices with target spectral responses is presented.

In this chapter, the main underlying physical processes, mathematical models and simulation tools of second- and third-order nonlinear effects were discussed. A brief survey on the available devices for OSP based on nonlinear processes has also been presented, with a particular focus on PPLN devices. The topics presented in this chapter provide the fundamental tools required to understand the following chapters of this thesis.

Chapter 3

Design of nonlinear devices with customized spectral response

OSP based on parametric nonlinear effects is strongly affected by the dispersive properties of the propagating medium. Not only optical pulses of waves at distinct wavelengths may propagate at different speeds, leading to walk-off effects, but dispersion is also responsible for phase mismatching in TWM or FWM interactions. Ultimately, the phase mismatching determines the spectral efficiency of these nonlinear phenomena, hereby defined simply as nonlinear spectral response.

As discussed in the previous chapter, the dispersive properties of a nonlinear medium are determined by the intrinsic frequency response of the propagating media and the waveguide geometry [73]. Even though the material dispersion may be altered via doping, the most common way to design the dispersive properties of nonlinear material is through waveguide engineering [129]. However, waveguide engineering is very challenging, requiring accurate simulations of the propagating modes, and a very good agreement between the numerical simulations and manufactured waveguides. Moreover, the dispersion properties may be severely affected by any fluctuation of the waveguide geometry. As an example, it has been suggested that to keep the fluctuations of the λ_{ZDW} of a HNLF below 1 nm it would be required to control the core size with a precision of the order of the silica bonds [130].

Periodically poled devices such as PPLN or PPLT waveguides offer an additional way to control the spectral conversion efficiency through domain inversion engineering. In these devices, the way how the ferroelectric domains are inverted determines the QPM resonance, as well as the nonlinear spectral response. This property makes periodically poled waveguides unique in comparison with other nonlinear devices. Domain engineering in periodically poled devices enables combining optical nonlinear mixing and filtering in the same device, providing new features and possibilities for OSP.

Several domain-engineered PPLN devices have already been experimentally reported, with unique properties provided by their specific poling profiles. Apodized [131], aperiodic [132] and superlattice [133] PPLN devices are some examples that have enabled reducing crosstalk between different WDM channels and/or increasing the nonlinear conversion bandwidth. The design of domain-engineered periodically poled devices has been typically based on the optimization of an initial poling pattern with known spectral response [133, 134]. However, this non-deterministic approach can be very complex and troublesome, depending on the optimization procedure. In addition, finding a good initial guess for the poling pattern may be difficult, in particular for unusual target spectral responses.

Domain engineering in PPLN devices can be compared to periodic patterning of the refractive index in co-directional couplers, such as long-period Bragg gratings. In long-period gratings, the periodic modulation of the refractive index enables efficient coupling between core and cladding propagating modes whenever the Bragg resonance condition is satisfied [135], comparable to the QPM technique in TWM. Several methods have already been proposed to design the refractive index grating of co-directional couplers in order

to obtain a target spectral response. Optimization techniques with initial guess given by the Fourier transform of the target response, and inverse scattering methods such as the Gel'fand-Levitan-Marchenko approximation and the LPA are some of the possibilities [57]. The LPA is particularly attractive for grating design due to its simplicity and accuracy, and can be implemented in either continuous or discrete versions [57].

In this chapter, a modified discrete version of the LPA is presented for poling pattern design of periodically poled devices with a target spectral response. The modified LPA is combined with a DRM, which is used in this chapter as a possible way to modify the power coupling between the interacting waves along the device. Before describing the LPA and DRM, a brief discussion on typical periodically poled devices with customized poling patterns is presented in section 3.1, which also provides the basic design concepts used in the following sections. Then, the LPA and DRM are described in sections 3.2 and 3.3, respectively. After analyzing the principle of operation and fundamentals of the LPA and DRM, numerical simulations of devices with quasi-rectangular nonlinear spectral response and with multiple QPM resonances are presented in section 3.4, to demonstrate the flexibility of the proposed methods. For simplicity, the devices with quasi-rectangular nonlinear spectral response and with multiple QPM resonances are hereby denoted as quasi-rectangular and multiple QPM devices, respectively. In the last section of this chapter, a quasi-rectangular PPLN device with a 400 GHz-wide nonlinear spectral response designed using the proposed methods is experimentally demonstrated and characterized.

3.1 Periodically poled devices

The periodic inversion of the ferroelectric domains in second-order nonlinear materials is a viable way to compensate for the phase mismatching via QPM. In ferroelectric materials such as lithium niobate or lithium tantalate, a permanent polarization of the ferroelectric domains (poling) can be induced by a strong external electric field. In such materials, periodic poling is achieved by applying a high voltage to electrodes deposited on the surface of the nonlinear crystal, as shown in figure 2.14. The electrodes on top of the crystal surface are typically produced through lithographic techniques, which means that the final poling pattern is determined by the periodicity of the mask used in the lithographic process [32]. Hence, devices with complex poling patterns can be produced by locally or globally varying the periodicity the mask used for the deposition of the electrodes.

In general, the variation of the effective nonlinear coefficient of customized periodically polled devices is modeled by the following equation

$$d_{eff}(z) = \frac{2}{\pi} d \cdot d_{apod}(z) \cdot e^{-i\left[\frac{2\pi}{\Lambda(z)} z + \Phi(z)\right]}, \tag{3.1}$$

where $d_{apod}(z)$ and $\Phi(z)$ are apodization and phase modulation functions, respectively. The apodization function describes the strength of the nonlinear interaction along the device,

varying from 0 (negligible interaction) to 1 (maximum efficiency) [131]. Several strategies can be used in order to vary the strength of the nonlinear interaction along a periodically poled device, such as varying the effective overlap area of the interacting waves, modifying the duty-cycle of the periodic inversion or skipping certain domain inversions, as is further discussed in section 3.3. The phase modulation function is responsible for local variations on the phase of the periodic inversions. In practice, the phase of the periodic inversions determines the position within a poling period where the ferroelectric domains are inverted. As an example, a single phase-shift of $\pi/2$ is performed by shifting the location of the domain inversions by $\Lambda/4$.

A few examples of common periodically poled devices with complex poling patterns are depicted in figure 3.1, including a schematic representation of the domain inversions and respective conversion efficiency spectra for SFG. The conversion efficiency spectra were obtained through numerical integration of the coupled mode differential equations for SFG using a 4th order Runge-Kutta algorithm. The SFG conversion efficiency is defined as the converted to input signal power ratio. A pump wave at 1545 nm with input power of 100 mW is considered for all cases, as well as an input signal power of 1 mW. The length, normalized efficiency, and poling period of the periodically poled device are 4 cm, 0.1 $W^{-1}cm^{-2}$ and 19.388 μm, respectively.

The most common periodically poled devices are those with uniform poling pattern, depicted in figure 3.1-a). In a uniform periodically poled device, the poling period, apodization and phase modulation functions are constant. The conversion efficiency spectra of uniform devices is approximately described by a sinc function, with a peak value at the QPM resonance, and side lobes symmetrically distributed around the main resonant peak.

Another common type of devices with customized poling profile are apodized gratings[1]. In an apodized grating, the strength of the nonlinear interaction gradually increases/decreases at the beginning/ending parts of the grating. By doing so, the side lobes observed for uniform gratings can be greatly reduced, as shown in figure 3.1-b). In figure 3.1-b), the numerical simulations were obtained for a tapered raised cosine function (Tukey function) with a roll-off factor of 1 as the apodization function, given by $d_{apod}(z) = [1 + \cos(2\pi z/L - \pi)]/2$ [136]. Despite the significant reduction of the side lobes, the conversion efficiency bandwidth of apodized devices is slightly broader and with lower peak power when compared to uniform poling patterns. This last drawback is a consequence of a lower effective nonlinear coefficient compared to a uniform grating due to the smooth transitions at the edges.

Other typical examples of devices with custom poling patterns include chirped devices, exemplified in figure 3.1-c). In a chirped grating, the poling period varies along the device in order to extend the conversion bandwidth. Within the class of chirped gratings, linearly chirped devices are the most common examples, where the poling period linearly increases (positive chirp) or decreases (negative chirp) throughout the device. Linearly chirped

[1] In this chapter, the terms grating and poling pattern are used interchangeably when referring to periodically poled devices.

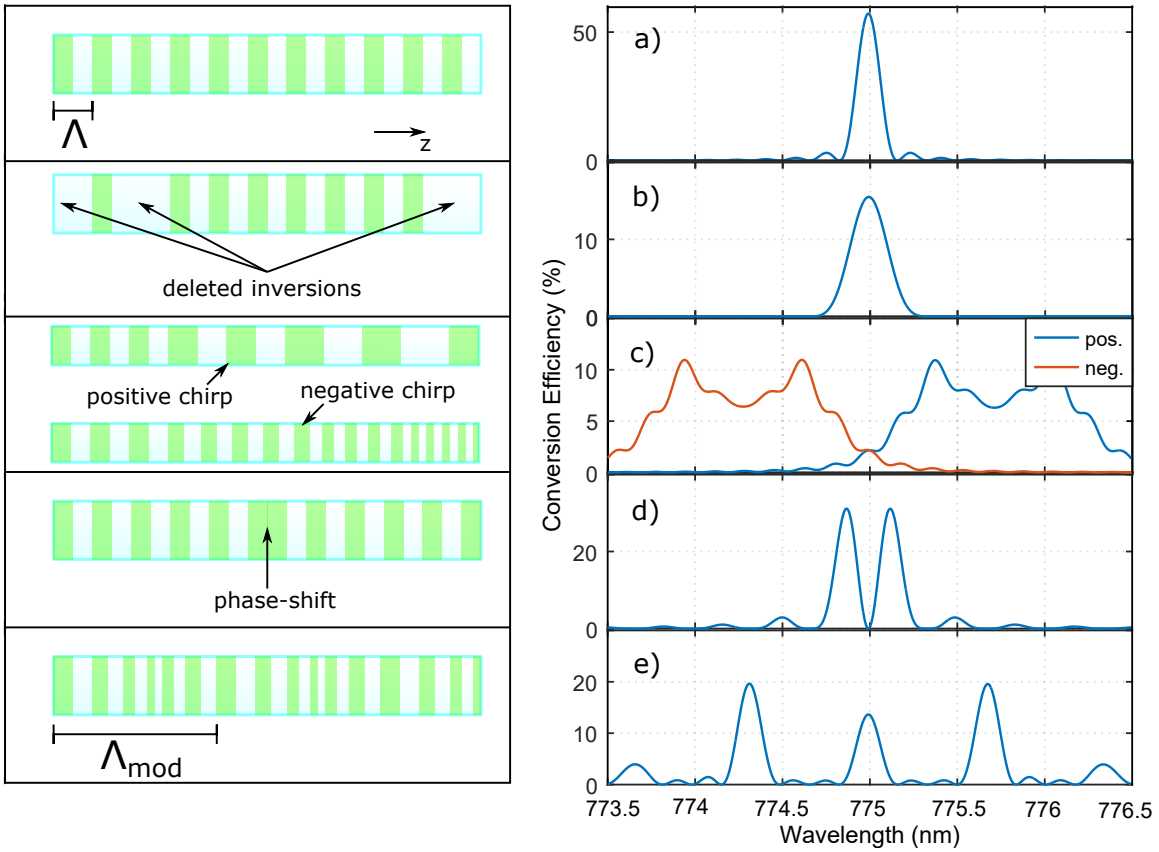

Figure 3.1: On the left, schematic representation of the poling patterns for a) uniform, b) apodized, c) chirped, d) phase-shifted, and e) superlattice periodically poled devices. On the right, SFG conversion efficiency of the corresponding poling patterns.

gratings can be modeled by $\Lambda(z) = \Lambda(0) + \varsigma z$, with ς the chirp parameter. As shown in figure 3.1, the conversion bandwidth of linearly chirped gratings with chirp parameters of 10 nm/mm and -10 nm/mm is significantly broader than in a uniform device, as a consequence of varying the QPM wavelength resonance along the device. On the other hand, the conversion efficiency is significantly reduced with respect to a uniform device as the QPM condition for a certain wavelength is achieved only for a small portion of the device.

Compared to fiber Bragg or long-period gratings, apodization is much more difficult to produce in periodically poled devices. In the former cases, apodization is obtained by varying the amplitude of the refractive index modulation along the grating. As an example, apodized fibre Bragg gratings can be produced using phase-masks with a locally varying diffraction efficiency [137]. In the case of periodically poled devices, such an approach cannot be implemented as the nonlinear coefficient can only assume two possible values, $+d$ and $-d$, depending on the polarization of the ferroelectric domains. A few strategies have been proposed to emulate the effects of apodization in periodically poled devices, which is further discussed in section 3.3.

Phase-shifted gratings are also common examples of customized poling patterns where a set of discrete phase-shifts of the periodic poling are performed at different locations

of the grating. The conversion efficiency spectrum of a phase-shifted device, with a π phase-shift at the center of the poling pattern is depicted in figure 3.1-d). According to the simulations, the phase-shift is responsible for a depression at the middle of the QPM resonant peak, similar to what is observed in high-rejection notch filters.

A superlattice periodically poled device is obtained by periodically varying the phase of the periodic poling. The poling patterns of these devices can be represented by a periodic phase modulation function, with period Λ_{mod}. An example of a superlattice is depicted in figure 3.1-e), with a phase modulation function given by $\Phi(z) = \pi/2 \cdot \cos(2\pi z/\Lambda_{mod})$ and $\Lambda_{mod} = 1$ cm. Typically, the spectral response of superlattice periodically poled devices exhibits several QPM resonances, whose peak bandwidth comparable to that of a uniform grating.

3.2 Layer-peeling algorithm

The LPA was originally proposed as a simple, flexible and easy-to-implement tool to design grating-assisted couplers with target spectral response [57, 138]. The main goal of the LPA is to determine the variation of the coupling strength between the interacting modes along the device according to a target spectral response. Despite being originally proposed for grating couplers, the LPA was also suggested as a possible way to retrieve the poling pattern of uniform and aperiodic PPLN devices from their measured conversion spectra, showing good accuracy between the calculated and real poling pattern [139]. However, the applicability of the LPA can be further expanded by actually designing the poling pattern of periodically poled waveguides with a target spectral response rather than simply retrieving the QPM structure of existing devices.

The LPA can be formulated in either a discrete or a continuous domain version. A discrete version of the LPA [57] is considered in this thesis, which assumes that a complex poling pattern can be divided into several small uniform segments (layers), with constant phase, period and coupling strength. In addition, the discrete domain version of the LPA considers that the coupling between the interacting waves occurs only at discrete scattering points and that the waves experience only pure dispersive propagation in between each pair of consecutive scattering points [57].

In order to understand how the LPA can be applied to the design of periodically poled devices let us first consider an SFG interaction between input and converted signal waves at frequencies ν_2 and ν_3, respectively. In addition, let us assume that the nonlinear interaction is pumped by a strong wave at frequency $\nu_1 = \nu_3 - \nu_2$ that remains almost undepleted during the nonlinear interaction (no pump depletion approximation). In this case, the nonlinear interaction can be simply interpreted as the coupling between two propagating modes at different wavelengths, the input and converted signal waves, as in co-directional grating-assisted couplers. However, in the case of periodically poled devices, the power coupling between the interacting waves is promoted by the nonlinear response of the devices and

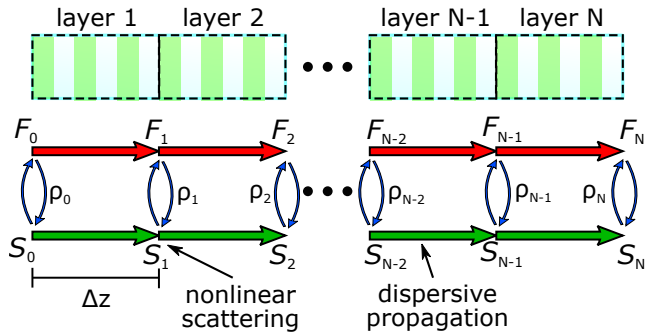

Figure 3.2: Schematic representation of the discrete model for the nonlinear interaction assumed for the LPA.

optical pumping rather than the modulation of the refractive index, as in grating-assisted couplers.

The discrete model for the nonlinear coupling between the interacting waves is schematically represented in figure 3.2. In figure 3.2, F and S are the so-called fast and slow modes, respectively proportional to the synchronous normalized electric field envelopes of the input and converted signal waves, B_2 and B_3 (see chapter 2). The discrete model for the nonlinear interactions assumes that the power coupling between the interacting waves occurs only at discrete scattering points, each characterized by a cross coupled power coefficient ρ. In between such scattering points, the waves experience pure dispersive propagation, with no nonlinear effects. This approach can be compared to the SSFT method, discussed in section 2.4.

The discrete model for the nonlinear coupling can be mathematically obtained from the evolution of the synchronous normalized electric field envelopes of the input and converted signal waves. Assuming negligible propagation losses and the no pump depletion approximation, the SFG process between the input and converted signal waves in a uniform layer j spanning from z_j to $z_j + \Delta z$ is described by the following expression

$$\begin{bmatrix} B_2(z_j+\Delta z) \\ B_3(z_j+\Delta z) \end{bmatrix} = \begin{bmatrix} \cos(g_j\Delta z) + i\frac{\Delta\beta}{2g_j}\sin(g_j\Delta z) & -i\frac{\kappa_{2j}^* A_1^*}{g_j}\sin(g_j\Delta z) \\ -i\frac{\kappa_{3j}A_1}{g_j}\sin(g_j\Delta z) & \cos(g_j\Delta z) - i\frac{\Delta\beta}{2g_j}\sin(g_j\Delta z) \end{bmatrix} \begin{bmatrix} B_2(z_j) \\ B_3(z_j) \end{bmatrix}, \tag{3.2}$$

obtained by solving (2.23).

Let us now define the slow and fast mode as $S(z) = B_3(z)$ and $F(z) = \sqrt{\lambda_2/\lambda_3}B_2(z)$, respectively, as well as the coupling coefficient $q = -i\kappa_2^*\sqrt{\lambda_2/\lambda_3}A_1^*$ and the wavenumber detuning $\delta = -\Delta\beta/2$. The effective coupling coefficient g can also be re-written as a function of δ and q as $g^2 = \delta^2 + |q|^2$. Considering the new variables, (3.2) becomes

$$\begin{bmatrix} F_j(\delta) \\ S_j(\delta) \end{bmatrix} = \mathbf{T}_j \cdot \begin{bmatrix} F_{j-1}(\delta) \\ S_{j-1}(\delta) \end{bmatrix}, \tag{3.3}$$

where F_j and S_j are optical fields of the fast and slow modes at the end of layer j and $\mathbf{T}_j$ is

a transfer matrix, given by

$$\mathbf{T}_j = \begin{bmatrix} \cos(g_j\Delta z) - i\frac{\delta}{g_j}\sin(g_j\Delta z) & \frac{q_j}{g_j}\sin(g_j\Delta z) \\ -\frac{q_j^*}{g_j}\sin(g_j\Delta z) & \cos(g_j\Delta z) + i\frac{\delta}{g_j}\sin(g_j\Delta z) \end{bmatrix}. \tag{3.4}$$

The obtained transfer matrix is now identical to that describing co-directional grating-assisted couplers presented in reference [57], which justifies why the SFG interaction can be compared to mode coupling in grating-assisted couplers.

The discrete model for the coupling between the slow and fast modes assumes that $\mathbf{T}$ can be decomposed as the product of two new matrices, $\mathbf{T}^{\mathrm{d}}$ describing pure dispersive propagation, and $\mathbf{T}_j^{\mathrm{s}}$ representing the discrete nonlinear coupling at the j^{th} scattering point. The dispersive matrix $\mathbf{T}^{\mathrm{d}}$ can be obtained by assuming no nonlinear interaction between the propagating modes by letting $q \to 0$. The following matrix is obtained [57]

$$\mathbf{T}^{\mathrm{d}} = \begin{bmatrix} e^{-i\delta\Delta z} & 0 \\ 0 & e^{i\delta\Delta z} \end{bmatrix}. \tag{3.5}$$

After propagation through a dispersive layer of length Δz, each frequency component of the fast and slow modes acquires a phase-shift of $-\delta(\Delta\omega)\Delta z$ and $\delta(\Delta\omega)\Delta z$, respectively, with $\Delta\omega$ the angular frequency detuning from the QPM resonance. In the time domain, this effect is equivalent to delaying the slow mode by a time interval of $\Delta z\delta(\Delta\omega)/\Delta\omega$ with respect to dispersionless propagation, and hastening the fast mode by the same time interval. This is the reason why F and S are denominated as fast and slow modes. The scattering matrix $\mathbf{T}^{\mathrm{s}}$ is obtained by assuming strong nonlinear coupling such that $|q| \to +\infty$, but the product $|q|\Delta z$ is finite [57]. In this case, $g \approx |q|$ and $\delta/g \approx 0$. The following scattering matrix is obtained

$$\mathbf{T}_j^{\mathrm{s}} = \frac{1}{\sqrt{1+|\rho_j|^2}} \begin{bmatrix} 1 & -\rho_j^* \\ \rho_j & 1 \end{bmatrix}, \tag{3.6}$$

with $\rho_j = -q_j^* \tan(|q_j|\Delta z)/|q_j|$ a cross coupled power coefficient.

The discrete model for the nonlinear coupling assumes that each layer is characterized by a cross coupled power coefficient, so the goal of the LPA is to determine the coefficient ρ_j of each layer, for a given target spectral response. Then, the coupling coefficient q_j can be obtained through the relation $q_j = -\rho_j^* \arctan(|\rho_j|)/(|\rho_j|\Delta z)$. In turn, the effective nonlinear coefficient d_{eff} is proportional to q, so the outputs of the LPA can be converted into a physical property of periodically poled devices.

The discrete model discussed above assumes that mode coupling occurs only at discrete scattering points. In a real device, however, the interacting modes are continuously coupled along the grating, so the discrete version of the LPA is affected by a discretization error. According to references [57, 140], the error involved in the discrete approximation is of the order of $O(\Delta z^3)$, so it can be made negligible by considering sufficiently small layers.

Now that the fundamental concepts of the discretized nonlinear coupling model have been formulated, let us consider that *S* and *F* are normalized to one, and that a unit impulse is launched into the nonlinear device in the fast mode, with no light in the slow mode. In the first scattering point at layer 0, part of the initial impulse at the fast mode is converted into the slow mode because of the nonlinear interaction. Then, the two modes undergo purely dispersive propagation through the first layer, so the fast mode is hastened by $\tau/2$ and the slow mode is delayed by the same amount, with τ a normalized time variable. Equivalently, if a moving time frame coincident with the propagation of the fast mode is considered instead, the fast mode propagates without any time delay in the moving frame referential, whereas the slow mode is delayed by one τ unit. In the following scattering point, part of the power in the fast mode is converted back to the slow mode and vice-versa. However, the new fraction of the slow mode added to the fast mode is delayed by one τ unit due to the dispersive effects. This process then repeats through all the layers of the device, as represented in figure 3.3. At the end of the periodically poled device, the

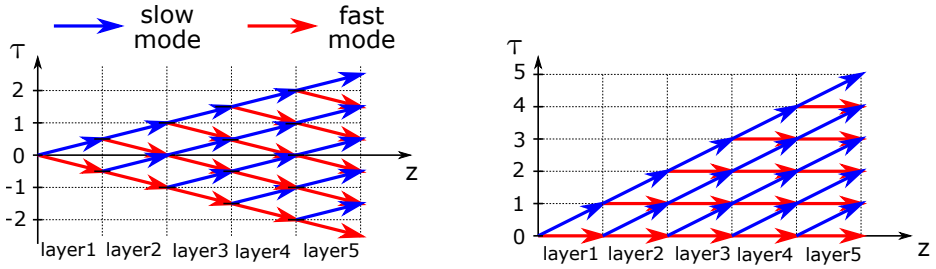

Figure 3.3: On the left, possible propagation paths in the fast and slow mode and corresponding time delays for a device composed of five uniform layers. On the right, same as the graphic on the left, but considering a moving frame coincident with the propagation of the fast mode. The power coupling between the fast and slow modes occurs at each scattering point, at the interfaces of each layer.

fast and slow modes contain several fractions of the initial impulse. These contributions arrive at different times, depending on how many layers they traveled in the slow mode, as depicted in figure 3.3. For instance, the first contributions arriving at the end of the device are the ones traveling always on the fast mode, whereas the second ones propagates once in the slow mode. This situation can be compared to a tapped delay line filter, in which the output response is the sum of several delayed fractions of the initial impulse, weighted by the filter taps [141]. In the case of the LPA, the filter taps are determined by the cross coupled power coefficient of each scattering point.

In order to determine the coefficients ρ_j let us formulate the problem in the time domain by considering the discrete Fourier transform of the propagating modes at layer j, given by [57]

$$F_j(\delta) = \sum_{\tau=0}^{N} F_j(\tau) e^{i2\delta\Delta z\tau} \tag{3.7a}$$

$$S_j(\delta) = \sum_{\tau=0}^{N} S_j(\tau) e^{i2\delta\Delta z\tau}, \tag{3.7b}$$

with $\tau = 0, 1, \ldots, N$ and N the total number of layers. The effects of the dispersive matrix on the transmitted waves can be obtained by using the time-shifting properties of the Fourier transform. Hence, after dispersive propagation through layer j, the fast and slow modes in the time domain become $F_j(\tau) = F_{j-1}(\tau + 1/2)$ and $S_j(\tau) = S_{j-1}(\tau - 1/2)$. The effects of the dispersive matrix can be further simplified by considering the moving frame coincident with the propagation of the fast mode. In this case, the fast mode propagates without any delay throughout the nonlinear device, so $F_j(\tau) = F_{j-1}(\tau)$, whereas the slow mode is delayed by one τ unit, i.e., $S_j(\tau) = S_{j-1}(\tau - 1)$. Note that the absolute and normalized time delays for each frequency component of the input signal can be related through the expression $\Delta t = 2\Delta z\delta(\Delta\omega)/\Delta\omega \cdot \tau$ [140].

Let us now consider that the length of all uniform layers is the same and a moving frame coincident with the propagation of the fast mode. The evolution of the fast and slow modes in each uniform layer described by (3.3) can thus be reformulated in the time domain, obtaining the following expression [57]

$$\begin{bmatrix} F_j(\tau) \\ S_j(\tau) \end{bmatrix} = \mathbf{T}_j^{\mathrm{s}} \cdot \begin{bmatrix} F_{j-1}(\tau) \\ S_{j-1}(\tau - 1) \end{bmatrix}, \tag{3.8}$$

where the dispersive effects are represented by delaying the slow mode by one τ unit, except for layer 0, which is just a scattering point.

Let us recall the example discussed above of a unit impulse launched in the fast mode, with no light in the slow mode, i.e., $F_0(\tau)$ is 1 for τ = 0, and 0 otherwise, and $S_0(\tau) = 0$ for any value of τ. If the moving frame coincident with the propagation of the fast mode is considered, $S_j(\tau)$ and $F_j(\tau)$ are causal, i.e, $S_j(\tau < 0) = 0$ and $F_j(\tau < 0) = 0$. By noting that the slow mode is not delayed in layer 0, the optical field of the fast and slow modes at the end of the device for τ = 0 can be obtained by consecutively applying (3.8) with the initial conditions $S_0(0) = 0$ and $F_0(0) = 1$. The following expressions are obtained at the end of the N^{th} layer [57]

$$F_N(\tau = 0) = \prod_{j=0}^{N} \frac{1}{\sqrt{1 + |\rho_j|^2}} \tag{3.9a}$$

$$S_N(\tau = 0) = \rho_N \cdot \prod_{j=0}^{N} \frac{1}{\sqrt{1 + |\rho_j|^2}}. \tag{3.9b}$$

The cross coupled power coefficient at the last layer can now be calculated as

$$\rho_N = \frac{S_N(\tau = 0)}{F_N(\tau = 0)}. \tag{3.10}$$

Since $S_N(\tau)$ and $F_N(\tau)$ are the inverse discrete Fourier transforms of the target spectral

responses at the end of the device, the previous equation can be directly used to calculate the power coupling coefficient for the last layer.

The coupling power coefficients for the other layers can now be iteratively calculated by inverting (3.8) in order to obtain the impulse responses at the end of the previous layers. The following inverting formulas are obtained [57]

$$F_{j-1}(\tau) = \frac{F_j(\tau) + \rho_j^* S_j(\tau)}{\sqrt{1+|\rho_j|^2}} \tag{3.11a}$$

$$S_{j-1}(\tau-1) = \frac{S_j(\tau) - \rho_j F_j(\tau)}{\sqrt{1+|\rho_j|^2}}. \tag{3.11b}$$

This procedure can be regarded as if the last layer of the grating was "peeled off" from the computation, and the cross coupled power coefficient for layer j-1 can now be calculated using (3.10), with $S_{j-1}(\tau)$ obtained from a forward shift operation on $S_{j-1}(\tau-1)$.

Even though the derivation of the LPA is extensive and somehow complicated, its implementation is very straightforward and simple. The LPA is summarized in algorithm 1.

Algorithm: Layer peeling algorithm
Initialization:
Obtain $S_N(\tau)$ and $F_N(\tau)$ through an inverse Fourier transform of $S_N(\delta)$ and $F_N(\delta)$;
Calculate $\rho_N = \frac{S_N(\tau=0)}{F_N(\tau=0)}$;
Algorithm:
for $j = N$ **to** *1* **do**
    Obtain $S_{j-1}(\tau-1)$ and $F_{j-1}(\tau)$ using (3.11);
    Obtain $S_{j-1}(\tau)$ through a forward shift operation;
    Calculate $\rho_{j-1} = \frac{S_{j-1}(\tau=0)}{F_{j-1}(\tau=0)}$;
end

Algorithm 1: Layer peeling algorithm.

The remaining part of this section is devoted to the required conditions and procedures to design the nonlinear spectral responses for the fast and slow mode in order to obtain realizable poling patterns. The discrete model for the nonlinear coupling can be compared to the design of digital filters, so standard discrete signal processing techniques can be used design of the nonlinear spectral responses of the slow and fast modes [57, 140]. As an example, the discretized model implies that Fourier transform of the propagating modes is periodic [141], with period $\delta_P = \pi/\Delta z$ [57]. This can be readily verified by considering the Fourier transform definitions in (3.7) and showing that $S(\delta+\delta_P) = S(\delta)$. Hence, it suffices to analyze the problem for detuning values in the range $0 \leq \delta < \delta_P$, or equivalently, $-\delta_P/2 \leq \delta < \delta_P/2$. Moreover, within this interval, the detuning parameter assumes $N+1$ distinct values, spaced by $\pi/[(N+1)\Delta z]$. This latter value is very important as it sets the best resolution achievable on the design of fine details in the target spectral response. At first sight, it may seem that the spectral resolution can be improved by increasing the number of

layers, but that is not the case. In fact, the length of each layer depends on the total number of layers according to $\Delta z = L/N$, so the detuning resolution becomes $\pi N/[L \cdot (N+1)] \approx \pi/L$, with the latter approximation valid for high N. Hence, the only way to improve the resolution on the design of the target spectral responses is to increase the length of the device. This property can be compared to the design of finite impulse response filters in which fine details on the spectral response require long impulse responses [142]. A similar result for the maximum achievable design resolution can be obtained by considering the spectral response of a uniform periodically poled device, whose conversion bandwidth is the narrowest possible for a given length value. Hence, it is also the best resolution achievable on the design of the spectral responses of customized patterns. Assuming weak nonlinear coupling, i.e, $|q|^2 \ll \delta^2$, the spectral response of a uniform periodically poled device is determined by $\text{sinc}^2(\delta L)$. The conversion bandwidth of a uniform device, defined as half the width of the main peak of the cardinal sine function, is π/L, which is agreement with the result from the discrete signal analysis.

As mentioned above, the design of fine details in the spectral response of the periodically poled devices is limited by their length. In addition, several artifacts such as undesirable ripples and overshoots on the final response due to the Gibbs phenomenon [142] may occur for target spectral responses with steep magnitude transitions. In these cases, long impulse responses in the space domain are required in order to represent the steep transitions. As a consequence, unless the device is sufficiently long to represent the ideal impulse response, a non-ideal response is observed, containing undesired ripples and overshoots. Besides increasing the length of the device, another possibility for mitigating such phenomena is by smoothing the sharp magnitude transitions using standard finite impulse response filter design techniques such as windowing [57, 142], as exemplified in figure 3.4. The impulse responses and respective power spectra of the ideal and windowed rectangular spectral responses are shown in figure 3.4, for N = 100 and considering a Blackman window [142] of order 71. The spectral response without using the windowing technique is also shown in figure 3.4-b). The windowing technique forces the impulse response to approach zero faster by multiplying it with an appropriate window function [142].

Let us now focus on the conditions for realizable pairs of spectral responses. If pump depletion is negligible, the nonlinear coupling between the input and converted waves in a periodically poled device can be regarded as a causal and stable linear system. The stability and causality properties of linear systems imply that the impulse response of the converted wave, i.e, the slow mode is absolutely summable (stability) and null for negative τ (causality) [142]. If the causality condition is not met for a given target spectral response, a possible way to design a realizable grating is to shift the initial impulse response by an interval τ_0 until it becomes causal. In the frequency domain, the shifting operation can performed by multiplying the initial non-causal response by $\exp(i2\delta\Delta z\tau_0)$.

The design of realizable spectral responses also requires defining the phase and magnitude responses of both the slow and fast mode. Let us first discuss the magnitude of

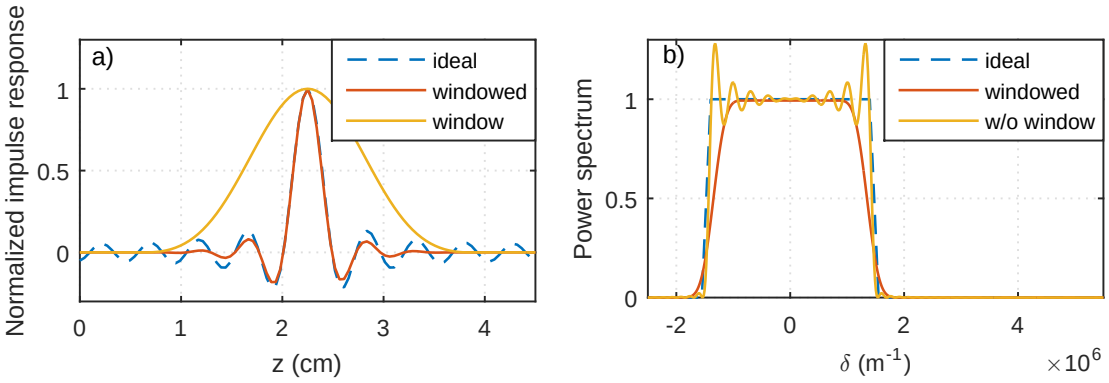

Figure 3.4: a) Normalized impulse responses of the ideal and windowed square passband filters, and the Blackman window function. b) Ideal and simulated power spectra, with and without windowing.

the fast and slow modes. The energy conservation principle for lossless devices bounds the magnitudes of the two modes and requires that the relationship $|S(\delta)|^2 + |F(\delta)|^2 = 1$ is strictly verified[2]. Therefore, if the magnitude of the spectral response for one of the modes is provided, the magnitude of the other mode is automatically defined through the previous relationship. Usually, the aforementioned windowing techniques are considered on the design of the target magnitude responses.

The phase response in the frequency domain for both modes can be chosen with a certain degree of freedom, originating different coupling coefficients q for different choices of the phase function [57, 140]. A linear phase for the converted signal (slow mode) is assumed for all the examples investigated in this chapter, but any other function can be selected, provided that the causality condition is verified. There are two main reasons for this particular choice. First, the linear phase function is one of the simplest possibilities and, in the time domain, it is equivalent to a simple time delay of the impulse response. In fact, a zero-phase function is initially assumed, but the impulse response of zero-phase systems is non-causal. Hence, a time shift operation has to be performed in order to obtain a causal response, which in the frequency domain is equivalent to adding a linear phase term. Second, if the magnitude of the spectral response for the slow mode is symmetric, it is possible to obtain only real coupling coefficients by choosing a linear phase function, as shown by the numerical simulations presented in section 3.4. When all the coupling coefficients are real, the phase modulation function consists of discrete phase-shifts of π whenever the sign of q is inverted. In practice, the discrete phase-shifts of π are much easier to produce in a real device than other complex phase modulation functions.

Let us now discuss the phase of the input signal, i.e., the fast mode. In reference [57], the slow and fast modes are described in terms of N^{th}-order polynomials, obtained by the z-transform of the respective impulse responses. It was shown in that work that for a given target spectral response $S(\delta)$, a total of 2^N different possibilities can be chosen

[2]Note that it was assumed the slow and fast modes are normalized to one.

for the phase of the fast mode. Each of such possibilities produces different coupling coefficients and poling patterns, but the same magnitude response for both modes. The different possibilities correspond to a specific selection of the N roots of the polynomial describing the fast mode or their mirror pairs around the unit circle, i.e, the inverse of their complex conjugated, also known as the reciprocal pairs [57]. Let us assume N=3 and that a, b and c are the roots of the polynomial for the fast mode. If, for instance, roots a and c are replaced by their reciprocal pairs $1/a^*$ and $1/b^*$, a different polynomial is obtained, but it still obeys the energy conservation principle $|S(\delta)|^2 + |F(\delta)|^2 = 1$. The new polynomial corresponds to a different possible choice for the phase of the fast mode.

The z-transform formalism enables choosing different valid possibilities for the phase of $F(\delta)$, but requires root-finding methods to reconstruct the fast mode polynomial [57]. When N is large, the factorization of polynomials is difficult and even small numerical errors may prevent the correct reconstruction of the polynomials. A possible solution to overcome this limitation is to consider the so-called minimum-phase response in transmission, which corresponds to the particular case of all the zeros of the fast mode polynomial being located inside the unit circle [57]. The minimum-phase response allows defining the phase of the fast mode uniquely by its magnitude, obtained by the discrete Hilbert transform of $\ln(|F(\delta)|)$, with $\ln$ the natural logarithm [57, 140, 142]. It also provides the least average coupling function and the minimum phase change and group delay [57,140]. Moreover, the minimum-phase response avoids the z-transform formalism and root-finding techniques to compute the phase of the fast mode. In fact, by choosing the minimum-phase response, the fast mode is completely determined by the amplitude of the slow mode: the energy conservation principle sets the magnitude of the fast mode to $|F(\delta)| = \sqrt{1 - |S(\delta)|^2}$; the phase is defined by the discrete Hilbert transform of $\ln(\sqrt{1 - |S(\delta)|^2})$. The minimum-phase response is also causal and stable [142], so the problem of finding a pair of realizable spectral responses is simplified to the design of a realizable response for the slow mode, which was already discussed above. Since the spectral response of the fast mode is completely determined by the slow mode, the expression “target spectral response” is used henceforth to refer to the target spectral response for the slow mode (converted signal).

The minimum-phase response is the simplest way to find the target phase of the fast-mode. However, it does not guarantee that the final cross coupled power coefficients are optimal in terms of conversion efficiency. In fact, depending on the problem at hand, there may be a better choice from the $2^N - 1$ possible solutions obtained with the z-transform formalism. However, finding the best solution amongst the possible alternatives from the z-transform formalism is also not trivial.

3.3 Deleted-reversal method

As discussed in the previous section, the outputs of the LPA are the complex cross coupled power coefficients that must be converted into a physical property of the grating-

assisted couplers or periodically poled devices. In the former case, the cross coupled power coefficients are translated into variations of the periodic refractive index modulation [57], whereas in the latter the coefficients ρ must be converted into a physical modification of the poling pattern properties and/or waveguide geometry.

The phase of the cross coupled power coefficients is directly translated into discrete or continuous phase-shifts of the refractive index modulation or the ferroelectric domain inversions. Such phase-shifts are implemented in practice by changing the position within a period where the maximum refractive index or ferroelectric domain inversions are observed.

The magnitude of the cross coupled power coefficients in grating-assisted couplers is proportional to the amplitude of the refractive index modulation, which can be freely varied from 0 to the maximum achievable value. Hence, changing the coupling strength in grating-assisted couplers is straightforward. Changing the nonlinear coupling strength in periodically poled devices is not as simple as in grating-assisted couplers, however. One possibility is to modify the effective overlap area of the interacting waves by changing the waveguide geometry and/or the refractive index profile. In general, varying the effective overlap area is complex, not practical, and very difficult to implement, as it requires changing the waveguide dimensions with very tight precision tolerances. Moreover, modifying the waveguide geometry also changes the dispersion properties of the device and, consequently, the QPM resonance. Hence, the only remaining possibility is to change the effective nonlinear coefficient d_{eff}. From the definitions of q, ρ and equation (2.19), the following relation between the effective nonlinear coefficient and the cross coupled power coefficient is obtained

$$\begin{aligned} d_{eff,j} &= -\frac{i}{2\pi A_1}\sqrt{\frac{n_1 n_2 n_3 c\epsilon_0 A_{eff}\lambda_2\lambda_3}{2}}\cdot q_j^* \\ &= i\frac{\arctan(|\rho_j|)}{2\pi A_1|\rho_j|\Delta z}\sqrt{\frac{n_1 n_2 n_3 c\epsilon_0 A_{eff}\lambda_2\lambda_3}{2}}\cdot \rho_j. \end{aligned} \tag{3.12}$$

Assuming $\lambda_2 \approx 2\lambda_3$ and that the normalized conversion efficiency for a uniform periodically poled device would be given by η, the previous equation can be further simplified into the following expression

$$\begin{aligned} d_{eff,j} &= -i\frac{\sqrt{2}d}{\pi\sqrt{\eta}A_1}\cdot q_j^* \\ &= i\frac{\sqrt{2}d\arctan(|\rho_j|)}{\pi\sqrt{\eta}A_1|\rho_j|\Delta z}\cdot \rho_j. \end{aligned} \tag{3.13}$$

According to the previous equations, the effective nonlinear coefficient is proportional to the coupling coefficient q, which may continuously vary from 0 to a maximum finite value. However, the nonlinear coefficient in a periodically poled device can only assume two distinct possibilities, $+d$ or $-d$. Two different strategies can be considered to overcome this problem, one by varying the duty cycle of the ferroelectric domain inversions, and another

is using the DRM [131].

As discussed in chapter 2, the effective nonlinear coefficient depends on the duty-cycle ζ of the ferroelectric domain inversion, defined as the fraction of the poling period where the nonlinear coefficient is positive. Considering the Fourier coefficient of the first harmonic in (2.16), the variation of the effective nonlinear coefficient with the duty-cycle is given by [131]

$$d_{eff}(\zeta) = \frac{2}{\pi}\sin(\pi\zeta)\cdot d. \tag{3.14}$$

According to the previous equation, it is possible to change the effective nonlinear coefficient by manipulating the duty-cycle of the ferroelectric domain inversions. However, not only the relation between d_{eff} and ζ is not linear, but precise control of the ferroelectric domain inversions is also required, with fabrication tolerances smaller than the poling period. In addition, the width of the ferroelectric domains and the electrodes deposited prior to the poling process does not necessarily match, which makes it even more difficult to control the duty-cycle of the poling inversions.

The DRM is another strategy to change the effective nonlinear coefficient whose principle of operation is based on eliminating some of the ferroelectric domain reversals in order to reduce d_{eff}. Thus, a maximum effective nonlinear coefficient is achieved by enabling all the possible domain inversions, whereas lower effective values are obtained by deleting some of the inversions. If no domain inversion is performed, the nonlinear conversion efficiency is very low and the effective nonlinear coefficient is approximately zero.

As previously discussed, the normalized amplitude of the effective nonlinear coefficient can be represented by the apodization function d_{apod}. Let us now assume a binary apodization variable d_b, equal to 0 if the domain inversion is deleted, or 1 in the opposite case. The goal of the DRM is to relate the discrete binary variable d_b and the apodization function. In this thesis, the choice of deleting or not the domain reversal at each poling period is performed iteratively, taking into account the entire structure that has been calculated in the previous iterations to minimize the global difference between d_{apod} and d_b. The adopted methodology is described in algorithm 2 and schematically represented in figure 3.5.

The algorithm used to implement the DRM starts by finding the position z_j where d_{apod} reaches its maximum value (global maximum), setting the corresponding value of d_b to 1, as shown at the top of figure 3.5. Then, the algorithm moves the next scattering point (middle row of figure 3.5) and evaluates the residues R_1^+ and R_0^+ by respectively considering $d_b(j+k+1)$ equal to 1 or 0. The residues R are calculated through a numerical integration of $d_b - d_{apod}$ using a trapezoidal rule. If $R_1^+ < R_0^+$, the algorithm assumes d_b equal to one, otherwise it sets d_b to zero. Next, the algorithm moves to the previous scattering point (bottom row in figure 3.5) and repeats the process by evaluating R_1^- and R_0^-, and choosing d_b equal to one or zero accordingly. After the first iteration, the proposed algorithm provides the values of d_b for the scattering points $j-1$, j and $j+1$. In the following iterations the algorithm symmetrically evaluates d_b at the adjacent points $j-k-1$ and $j+k+1$, stopping

Algorithm: Deleted-reversal algorithm

Definitions:

V: set with all the discrete scattering points of the grating;

Initialization:

Set $d_b(z_j) = 0, \forall j \in V$;

Find $j \in V$ where maximum $d_{apod}(z_j)$ is observed;

$d_b(z_j) = 1$;

$V \leftarrow V \setminus \{j\}$;

$k = 0$;

Algorithm:

while $V \neq \varnothing$ **do**

  $d_b(j+k+1) = 1$;

  $R_1^+ = \left| \sum_{l=j-k}^{j+k} \left[\frac{d_b(z_l)+d_b(z_{l+1})}{2} - \frac{d_{apod}(z_l)+d_{apod}(z_{l+1})}{2} \right] \cdot \Delta z \right|$;

  $d_b(j+k+1) = 0$;

  $R_0^+ = \left| \sum_{l=j-k}^{j+k} \left[\frac{d_b(z_l)+d_b(z_{l+1})}{2} - \frac{d_{apod}(z_l)+d_{apod}(z_{l+1})}{2} \right] \cdot \Delta z \right|$;

  if $R_1^+ < R_0^+$ **then**

    $d_b(j+k+1) = 1$;

  else

    $d_b(j+k+1) = 0$;

  end

  $d_b(j-k-1) = 1$;

  $R_1^- = \left| \sum_{l=j-k-1}^{j+k} \left[\frac{d_b(z_l)+d_b(z_{l+1})}{2} - \frac{d_{apod}(z_l)+d_{apod}(z_{l+1})}{2} \right] \cdot \Delta z \right|$;

  $d_b(j-k-1) = 0$;

  $R_0^- = \left| \sum_{l=j-k-1}^{j+k} \left[\frac{d_b(z_l)+d_b(z_{l+1})}{2} - \frac{d_{apod}(z_l)+d_{apod}(z_{l+1})}{2} \right] \cdot \Delta z \right|$;

  if $R_1^- < R_0^-$ **then**

    $d_b(j-k-1) = 1$;

  else

    $d_b(j-k-1) = 0$;

  end

  $V \leftarrow V \setminus \{j+k+1, j-k-1\}$;

  $k = k+1$;

end

Algorithm 2: Deleted-reversal algorithm.

after evaluating d_b for all scattering points.

In order to compare the performance of the deleted-reversal and duty-cycle methods on the design of the apodization function, the SFG conversion efficiency of an apodized PPLN waveguide designed using the both methods was evaluated through numerical simulations, and compared to an ideal device, with a continuous apodization function. The numerical simulations were performed using a 4^{th} order Runge-Kutta algorithm in order to solve the coupled differential equations for SFG between CW waves. A raised cosine apodization function with a roll-off factor of 0.5 is considered (see section 3.1). The poling period, length, effective overlap area and d_{33} coefficient of the simulated PPLN devices

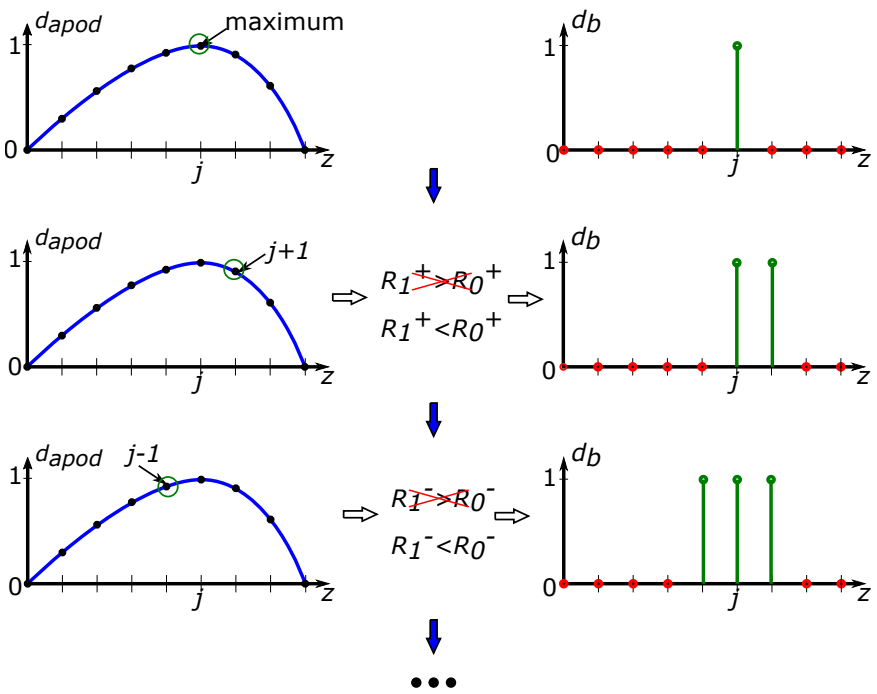

Figure 3.5: Schematic representation of the initialization and first iteration of the deleted reversal algorithm.

were 19.39 μm, 1 cm, 100 μm^2 and 23.6 pm/V, respectively. The refractive index dispersion curve is described by the Sellmeier equation for the extraordinary index of a lithium niobate substrate doped with a 5% content of MgO [143]. The wavelength and power of the pump wave were respectively set to 1545 nm and 300 mW, whereas the power of the signal was assumed to be 1 mW. The duty-cycle of the poling inversion in the DC curve was controlled with a precision of Λ/100. The simulated results are shown in figure 3.6-a).

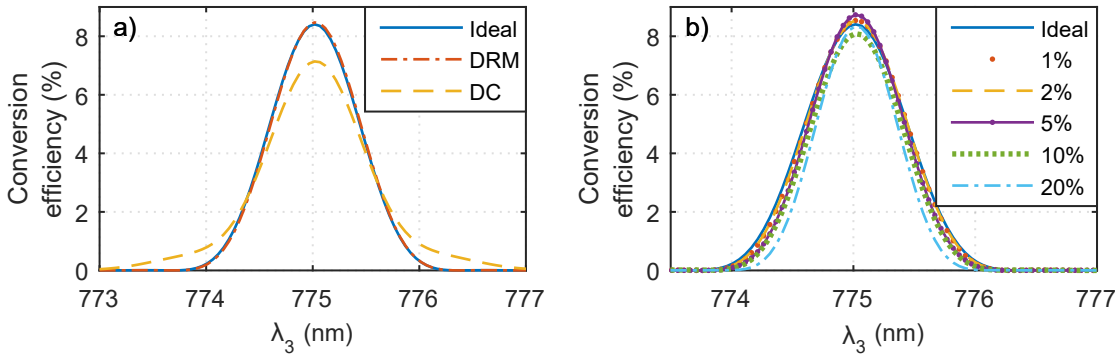

Figure 3.6: a) Simulated SFG conversion efficiency spectrum for an apodized PPLN using the DRM and by varying the duty-cycle (DC curve). b) Simulated SFG conversion efficiency for an apodized PPLN designed by the DRM, with different fractions of wrong domain reversals, located at random places of the poling pattern.

According to the simulated results, the conversion efficiency of the apodized device designed with the duty-cycle method significantly deviates from the ideal pattern, even con-

sidering a duty-cycle precision of Λ/100. On the other hand, the DRM allows to accurately reproduce the target apodization of the ideal pattern.

The tolerance of the DRM to wrong ferroelectric domain reversals at random locations of the poling pattern was also evaluated through numerical simulations, shown in figure 3.6-b). The same simulation parameters of the results in figure 3.6-a) were considered. According to the numerical simulations, the DRM was able to reproduce the apodization function without significant deviation from the ideal pattern, even with a fraction of incorrectly deleted reversals as high as 5%. The obtained results demonstrate that the DRM is a viable and robust technique to reproduce the apodization function in periodically poled devices.

The effectiveness of the proposed deleted-reversal algorithm is further evaluated in the following section for different examples of poling patterns.

3.4 Quasi-rectangular and multiple QPM devices

In order to evaluate the effectiveness of the adapted layer-peeling algorithm combined with the DRM on the design of periodically poled waveguides with customized poling patterns, two different types of devices are discussed in this section: quasi-rectangular and multiple resonance devices.

Quasi-rectangular periodically poled devices can be regarded as passband filters with an approximately rectangular spectral response. These devices have a constant efficiency within the conversion bandwidth and ideally null response elsewhere, with smooth transitions at the passband edges to reduce the Gibbs phenomenon. Compared to uniform devices, quasi-rectangular waveguides have broader conversion efficiency, which makes them attractive for broadband or multichannel applications, as it is discussed in chapter 4.

As the name suggests, multiple resonance or multiple QPM waveguides are devices whose spectral response shows several QPM resonances. Such devices have been used to demonstrate advanced all-optical signal processing functionalities such as tunable wavelength conversion and multicasting of multiple data channels [133], or phase-regeneration of QPSK channels [55].

In this section, quasi-rectangular PPLN waveguides with 400 and 1000 GHz conversion bandwidth and multiple QPM devices with different number of resonances are designed with the LPA and DRM. The spectral response of the designed devices is assessed through numerical simulations using a 4^{th} order Runge-Kutta algorithm to solve the SFG coupled differential equations for CW waves. All the simulations presented in this section assume a 5% MgO-doped PPLN with a refractive index described by the Sellmeier equation for the extraordinary index at 25°C in [143]. Unless otherwise specified, it is assumed that the length, poling period, effective overlap area and nonlinear coefficient d_{33} of the PPLN devices are 4.5 cm, 19.39 μm, 100 μm^2 and 23.6 pm/V, respectively. The wavelength of the pump wave and the power of the input signal were set at λ_1 = 1545 nm and 10 mW,

and a spatial integration step of the order of Λ/100 was considered.

3.4.1 Quasi-rectangular devices

The target and simulated spectral responses for quasi-rectangular PPLN devices with a passband bandwidth of 400 and 1000 GHz, as well as the respective coupling coefficients and poling patterns obtained with the LPA and the DRM are shown in figure 3.7. In order to reduce the Gibbs phenomenon for quasi-rectangular PPLN devices, the windowing technique was employed by using a raised cosine function (or Tukey window [136]) as the window, with a taper to constant section ratio of 0.7. A very good agreement between the target and simulated responses is verified for both examples. In the case of the 400 GHz quasi-rectangular device, a flat response within the passband is observed, with very smooth transitions at the edges of passband. In the case of the 1000 GHz device, non-negligible ripples on the converted signal power spectrum can still be observed due to the Gibbs phenomenon, which can be further mitigated by using a windowing function with narrower impulse response. The frequency resolution for the design of the target spectral response was of about 67.9 GHz, or equivalently of 69.7 m^{-1} in terms of the detuning parameter parameter. This last value is in agreement with the theoretical prediction of $\pi N/[L(N-1)]$, as discussed in section 3.2.

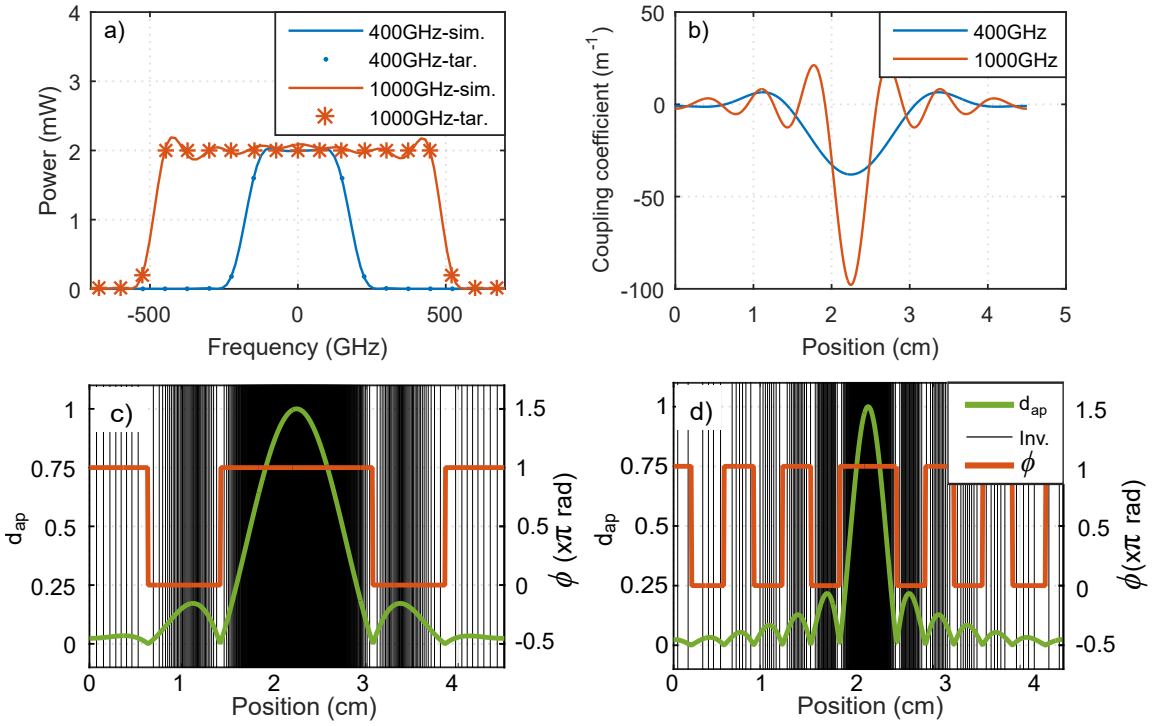

Figure 3.7: a) Simulated (sim.) and target (tar.) power spectrum of the SFG wave for 400 GHz and 1000 GHz quasi-rectangular PPLN devices, with the respective coupling coefficient functions shown in b). Apodization and phase modulation functions for c) the 400 GHz, and d) the 1000 GHz quasi-rectangular PPLN waveguides. The black vertical lines in c) and d) represent the poling inversions, obtained with the DRM.

The coupled coefficient of the quasi-rectangular devices is shown in figure 3.7-b). In both cases, the shape of the coupling coefficient resembles a sinc function, with shorter period for the 1000 GHz device. This is an expected result as the coupling coefficient is approximately given by the inverse Fourier transform of the target spectral response in the limit of weak coupling and when a minimum-phase function is selected for the fast mode [57]. In addition, the coupling coefficient of the designed devices is a real function, which can also be understood form the properties of the Fourier transform. In fact, the inverse Fourier transform of a spectral response with symmetric magnitude and antisymmetric phase (e.g., linear phase) is a real function [141].

The apodization and phase modulation of the 400 and 1000 GHz quasi-rectangular devices are respectively shown in figure 3.7-c) and 3.7-d), as well as the location of the poling inversions given by the DRM. A higher density of poling inversions is observed when the apodization function reaches higher values, proving the correctness of the DRM on the design of the apodization function in periodically poled devices. As shown in both figures, the phase modulation function corresponds to discrete phase-shifts of π, performed whenever the sign of the coupling coefficient is inverted. Again, this result is a consequence of the symmetry properties of the target response and, consequently, of q being real-valued. This is also one of the main reasons why a linear phase function is selected for the target spectral response of the slow mode. When it comes to manufacturing a real device, simple phase-shifts of π are relatively easy to produce and do not require fabrication tolerances as tight as more complex phase modulation functions.

According to (3.12), an exact relation between q and d_{eff} is obtained only for a certain amplitude value of the pump wave. In the case of the 400 GHz device, the ideal pump power is 256 mW, whereas an ideal pump power value of 1.7 W is required in order to achieve 20% SFG conversion efficiency for the 1000 GHz device. The higher pump power required in the case of the 1000 GHz device is a consequence of lower overall apodization strength and, consequently, lower effective nonlinear efficiency. This result raises a very important question on the applicability of LPA on the design of periodically poled devices: does the spectral response of devices with customized poling pattern vary for different pump power values? In addition, do propagation losses significantly affect the spectral response? In order to answer these questions, the power spectrum of the converted wave for the 400 GHz quasi-rectangular device was numerically evaluated for different pump power and absorption coefficient values. The obtained results are presented in figure 3.8, where the parameter f represents the ratio between the pump power used in the simulation compared to the ideal value provided by the LPA.

As shown in figure 3.8-a), the main consequence of increasing or decreasing the pump power, or equivalently, the parameter f, is to change the power of the converted wave, without significantly distorting the spectral response shape, as also shown in 3.8-b). Equivalent results were verified for the numerical simulations where the absorption coefficient was set to 0.1 and 1 dB/cm. This property is essential for the design of practical devices, since

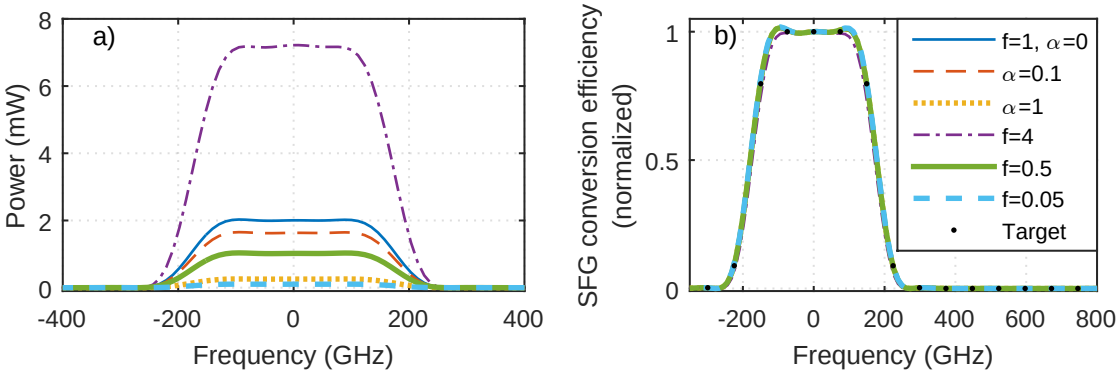

Figure 3.8: a) Converted signal power spectra and b) normalized SFG conversion efficiency at different pump power and absorption coefficient values. The parameter f represents the pump power ratio with respect to the ideal value. When not specified, f is 1 and α is 0 dB/cm.

without it, the pump power would have to be kept within tight constraints.

The LPA described in this chapter is based on simple SFG or DFG interactions in second-order nonlinear devices. However, many applications of these devices are based on SHG or cascaded TWM interactions such as cSFG/DFG. In order to evaluate the spectral response of the designed devices for SHG and cSFG/DFG interactions, the respective coupled ordinary differential equations for CW waves presented in chapter 2 were solved using a 4^{th} order Runge-Kutta algorithm and considering the customized poling pattern of the 400 and 1000 GHz quasi-rectangular PPLN waveguides. An additional DFG pump wave at 1543 nm was considered for the cSFG/DFG case, with a power value of 500 mW. The power of the input signal was set to 10 mW for both cases. The obtained results are plotted in figure 3.9.

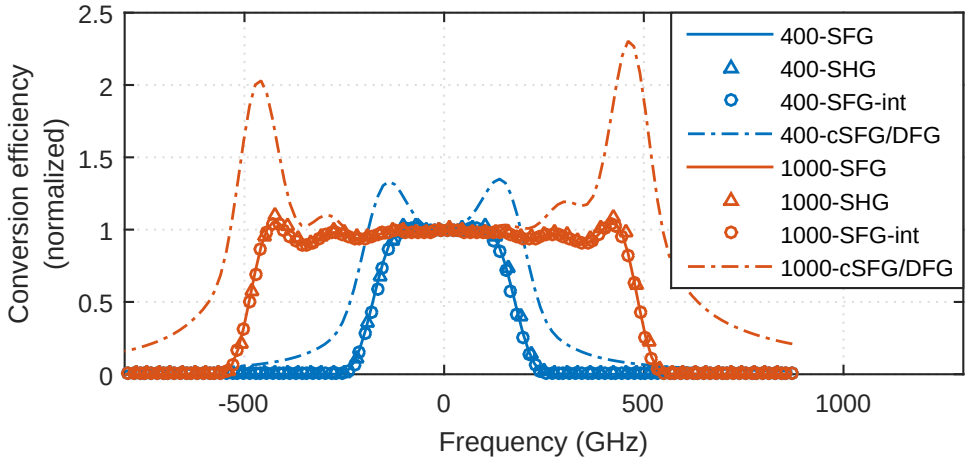

Figure 3.9: SHG, SFG and cSFG/DFG conversion efficiency spectra for the 400 GHz and 1000 GHz quasi-rectangular PPLN devices. The conversion efficiency of the intermediate SFG step in cSFG/DFG is also shown in curves “400-SFG-int” and “1000-SFG-int”.

According to the numerical simulations, the spectral response of quasi-rectangular devices remains identical for SHG, but differs substantially for cSFG/DFG. In the former case,

the obtained results are explained by very similar phase mismatching parameters for the SFG and SHG interactions within the frequency range considered in the simulations, and for the selected wavelength of the input signal and pump waves for SFG. In the latter case, broader conversion bandwidth is observed in both cases for the wave converted through cSFG/DFG compared to the target response. In addition, the edges of the spectral response are not as steep as designed, and the efficiency slowly decreases for frequencies higher than the cut-off frequency of the designed passband filter. In these transition edges, undesirable conversion peaks are also observed. Remarkably, however, the spectral response of the intermediate SFG step in a cSFG/DFG interaction is in agreement with the target design, as shown by curves “400-SFG-int” and “1000-SFG-int” in figure 3.9. The root cause for this behavior is the cascaded nature of the interaction, which leads to a more complex evolution of the interacting waves and low depletion of the intermediate SFG wave. As mentioned above, the LPA is formulated for simple SFG or DFG processes. In a cSFG/DFG interaction, if the intermediate SFG wave is not significantly depleted by the DFG step, as it was the case of the simulations presented in figure 3.9, it is expectable that the conversion spectrum for the SFG wave matches the target response. However, this is not the case for the signal generated by the secondary DFG step, which strongly depends on how the SFG wave is first generated along the device. For instance, the numerical simulations showed that the conversion bandwidth for the SFG step at the beginning of the device is initially broader than the target one, but narrows along the device due to the phase mismatching effects. At the beginning of the device, waves generated through SFG at frequencies outside the target spectral bandwidth begin to be immediately converted through DFG to the converted signal wave. Due to different phase mismatching properties of the DFG and SFG steps, broader conversion efficiency spectrum and lateral decaying tails are observed for the wave converted through cSFG/DFG with respect to the target nonlinear spectral response.

With the exception of the aforementioned main differences, the spectral response for cSFG/DFG still resembles the target one. Depending on the specific application, the lateral decaying tails and increased efficiency at the transition regions may introduce deleterious wavelength crosstalk and affect the overall performance of an optical system. A possible solution to overcome these limitations is to avoid cascaded interactions in a single PPLN waveguide, by using two separate devices with the target nonlinear spectral response in a tandem configuration, one for SFG interactions and another for DFG.

As briefly discussed in section 2.5, periodically poled waveguides with broader spectral responses can also be produced by changing the poling period along the device, as is the case of a linearly chirped waveguide, represented in figure 3.1-b). However, such type of devices typically exhibit a passband response with slowly decaying transition edges and conversion efficiency ripples within the passband [144]. In order to reduce the deleterious efficiency ripples, apodized linearly chirped devices have been suggested in [144]. The SFG and cSFG/DFG conversion efficiency spectra of an apodized linearly chirped device

and the 400 GHz quasi-rectangular PPLN waveguide discussed above are compared in figures 3.10-a) and 3.10-b), respectively. The initial poling period and chirp parameter of the apodized linearly chirped PPLN were 19.35 μm and 8.6 nm/cm, respectively, selected in order to achieve an equivalent central frequency and conversion bandwidth. A Tukey window [136] with a taper to constant section ratio of 0.53 was considered as the apodization function. In both cases, the wavelength of the SFG pump was set to 1545 nm. In figure 3.10-b), the wavelength of the DFG pump was set to 1542 nm. The power of the SFG and DFG pumps was set to 500 mW.

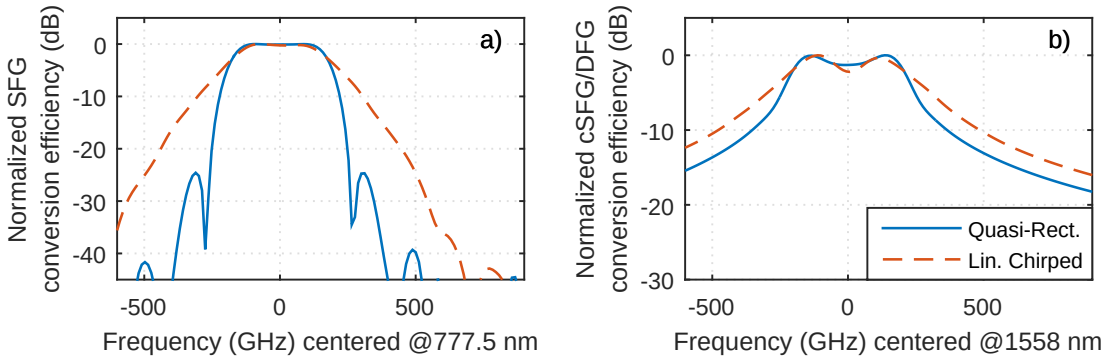

Figure 3.10: a) Normalized SFG conversion efficiency of a 400 GHz quasi-rectangular and a linearly chirped PPLN device. b) Respective conversion efficiency spectra for cSFG/DFG.

The results of the numerical simulations show that the SFG conversion spectrum for the quasi-rectangular PPLN waveguide has much steeper transition edges than the apodized linearly chirped device, making it more appropriate for applications in WDM systems where inter-channel crosstalk is an important issue. However, the absolute SFG efficiency of the apodized linearly chirped device is about 3.2 times higher than that of the quasi-rectangular PPLN, which is a consequence of deleting a higher number of poling reversals in the latter case in order to produce the target spectral response. Apodized linearly chirped gratings introduce a quadratic phase shift on the converted signals, or equivalently, a linear group delay, which means that different frequency components of the optical signals are subject to different delays (chromatic dispersion) [135]. Even though this property can be used for chromatic dispersion compensation purposes, it generally leads to pulse distortion and may be undesirable for OWC applications, for instance. In such cases, a target spectral response with linear phase (constant group delay) may be preferable as the different frequency components of the signal are simply delayed by a constant term, without pulse distortion. The designed quasi-rectangular devices may thus be a better alternative for those situations.

Similarly to what was previously discussed for the quasi-rectangular devices, lateral decaying tails can also be observed on the cSFG/DFG conversion efficiency spectrum of the linearly chirped, as depicted in figure 3.10-b). Once again, the observed result is caused by the broader conversion efficiency of the intermediate SFG step at the beginning

of the device. This result proves that the differences between the target nonlinear spectral response and the conversion efficiency spectrum for cascaded TWM interactions is not caused by the LPA itself, but is rather a consequence of the cascaded nature of the interactions. Moreover, the observed results also indicate that the conversion efficiency spectra for the intermediate SFG step and for the overall cascaded interaction are not exactly the same, regardless of the design strategy and/or poling pattern choice.

3.4.2 Multiple QPM devices

The possibility to design the poling pattern of multiple QPM devices using the LPA and DRM is evaluated in this subsection. The multiple QPM PPLN devices studied in this section were designed by choosing a target spectral response with multiple narrow bands, with different frequency separation. Numerical simulations of PPLN waveguides with 1, 2, 3 and 5 QPM resonances were performed, considering pump power values of 9.4, 36, 76 and 205 mW, respectively, in order to obtain a peak SFG conversion efficiency of about 20%. The results of the numerical simulations are shown in figure 3.11.

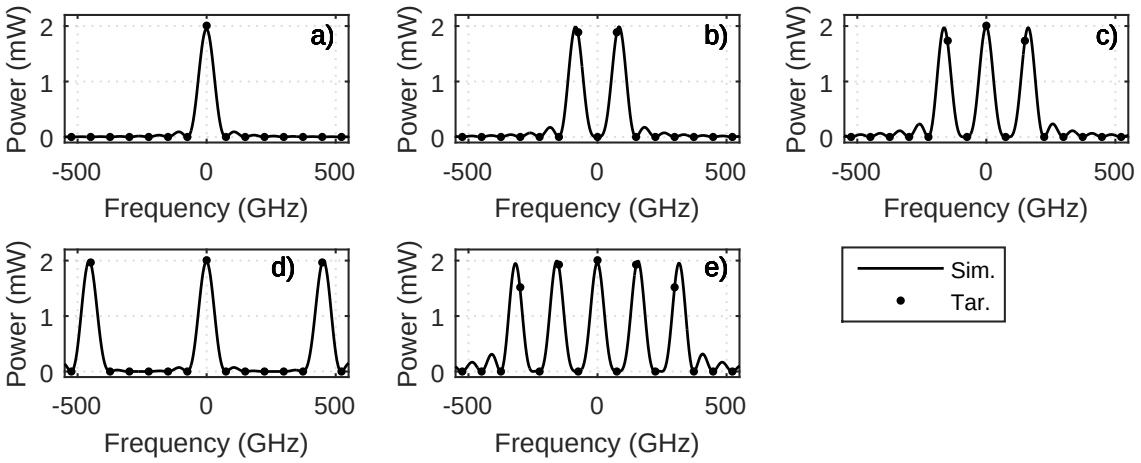

Figure 3.11: Simulated (sim.) and target (tar.) converted signal power for a) a single QPM resonance, b) two QPM resonances sperated by 150 GHz, c) three QPM resonances separated by 150 GHz, d) three QPM resonances separated by 450 GHz, and e) five QPM resonances separated by 150 GHz.

The numerical results shown in figure 3.11 prove the flexibility and accuracy of the LPA on the design of multiple QPM periodically poled devices. As discussed in the previous section, the design of multiple QPM devices is only limited by the maximum detuning parameter resolution, approximately given by $\pi/L \approx 69.7$ m^{-1}, or an equivalent frequency resolution of 67.9 GHz. The latter value exactly corresponds to the frequency separation between the dots of the target response in figure 3.11. Moreover, such a value is approximately equal to the conversion bandwidth of the device with a single QPM resonance, shown in figure 3.11-a), which in fact is a uniform PPLN waveguide. These results are in agreement with what was discussed in section 3.2 regarding the detuning resolution on the

design of target spectral responses.

The multiple resonances of the devices designed with the LPA are obtained by choosing a specific apodization profile, combined with simple phase-shifts of π, as shown in figure 3.12. In contrast, the method presented in [133] is based on a complicated variation of the phase modulation function, which may not be easy to reproduce in a real device. However, the peak efficiency of the multiple QPM devices studied in this section decreases by a factor of N^2 compared to uniform periodically poled waveguides, whereas in the method presented in [133] the efficiency drops only by a factor of N, where N is the number of QPM resonances. The reduced efficiency of the multiple QPM studied in this section is a direct consequence of decreasing the effective nonlinear coefficient, caused by deleting some of the poling reversals at some locations in the device. It should be noted, however, that the reduced efficiency is not a limitation of the LPA itself, but rather of the initial choice for the target spectral response of the slow mode. As mentioned before, a linear variation of the phase with respect to the detuning parameter was chosen for the spectral response of the slow mode and, from the properties of the Fourier transform and the symmetry of the magnitude response, a real coupling coefficient q is expected for such realizations. As exemplified in figures 3.7-c), 3.7-d) and 3.12, any real coupling coefficient is represented by a general position-dependent apodization function, whereas the phase modulation function corresponds to simple phase-shifts of π. It should be noted that the LPA would provide a different poling pattern if any other alternative for the phase of the slow mode was chosen as the initial target spectral response. In fact, if the spectral response of the devices designed with the method proposed in [133] was used as the target response for the LPA, the same poling pattern would be obtained using the LPA, with the advantages of not requiring any initial guess for the poling profile, nor any optimization technique.

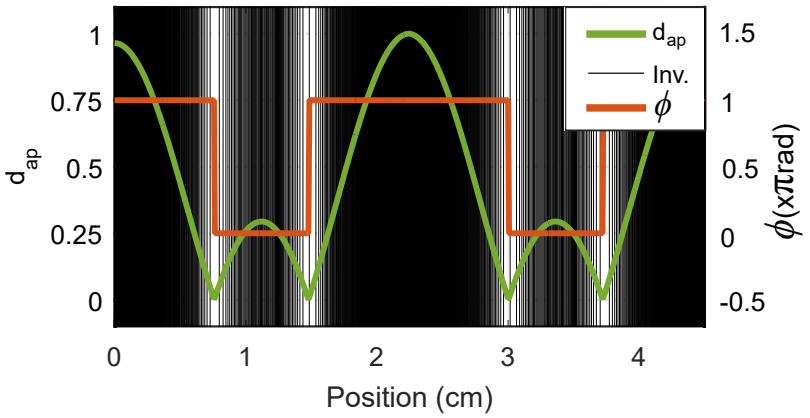

Figure 3.12: Apodization and phase modulation functions of the multiple QPM device with three QPM resonances separated by 350 GHz shown in figure 3.11-c). The black vertical lines represent the poling inversions, obtained with the DRM.

The development of a strategy to calculate the phase of the slow mode for a given magnitude response that would simultaneously maximize the conversion efficiency of the device would be highly valuable for the design of devices with customized poling pattern,

particularly when combined with the LPA. Such approach is left for future work.

3.5 Experimental validation of the layer-peeling algorithm and deleted-reversal method

In this section, the spectral response of a 400 GHz quasi-rectangular PPLN device designed with the LPA and DRM is experimentally investigated. The poling pattern of the manufactured device was designed according to the 400 GHz quasi-rectangular PPLN simulated in the previous section, but with a slightly different poling period in order to account for the waveguide dispersion effects. From the examples studied in the previous section, the 400 GHz quasi-rectangular device was chosen to prove the effectiveness of the LPA and DRM due to its relatively simple poling pattern and acceptable efficiency.

The PPLN device was manufactured by Oxide Corporation [145] using a lithium niobate substrate with a 5% MgO content in order to reduce photorefractive damage at high pumping power. The length of the lithium niobate chip was 4.5 cm. In addition, the lithium niobate chip included 50 APE waveguides, divided into five groups of ten waveguides with the same poling period, ranging from 19 to 19.4 μm, but with different waveguide width values. The width of the produced waveguides, measured before the annealing process, varied from 8.75 to 13.25 μm for each group of ten waveguides. Unfortunately, no additional details on the production process of the waveguides were provided due to the confidentiality policy of Oxide Corporation.

The experimental set-up used to characterize the spectral response of the PPLN devices is shown on top of figure 3.13. The light emitted by two external cavity lasers (ECLs) was combined in a 50:50 (3 dB) coupler after passing through a polarization controller (PolC), an EDFA, a 1 nm bandpass filter (BPF) and a variable optical attenuator (VOA). The PolCs, EDFAs, BPFs and VOAs were respectively used to align the state of polarization of the waves to the optimum axis of the PPLN, amplify the signals, remove the excess ASE noise, and control the power at the input of the device. Then, the generated waves were injected into the PPLN device through free-space coupling optics, using aspherical lenses to couple the light beams to the APE waveguides. The PPLN chip and lenses were mounted on translational stages, shown at the bottom of figure 3.13, in order to enable selecting different waveguides for characterization. The lenses were also integrated with WDM couplers which allowed separating the waves at the fundamental and second harmonic bands. A total insertion loss of about 4 dB was measured, including the losses of the WDM couplers and of the lenses. The temperature of operation of the PPLN device was set to 25°C using a thermo-electric cooler (TEC) element. The power of the signal and the pump waves at the input of the PPLN was set to 17.3 and 26.5 dBm, respectively. After wavelength conversion in the PPLN device, the waves at the fundamental and second harmonic bands were fed to optical spectrum analyzers (OSAs) for monitoring.

In order to evaluate the effectiveness of the LPA and DRM, the SFG conversion effi-

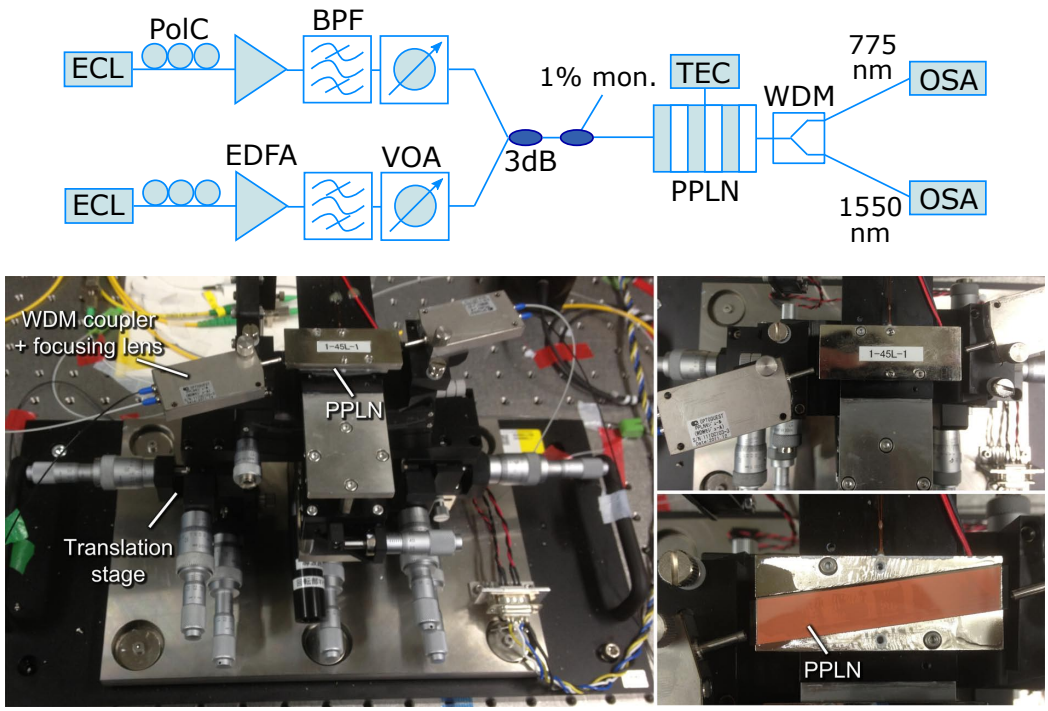

Figure 3.13: On top, experimental setup used to evaluate the spectral response of the quasi-rectangular PPLN devices designed with the LPA. At the bottom, photographs of the free-space optics system used to couple the optical waves into and out of the PPLN device.

ciency was measured for four different waveguides. The poling poling of the characterized waveguides was 19.1 μm for waveguides 1 and 2, and 19.2 μm for waveguides 3 and 4. The width of waveguides 1 and 3 was 9.25 μm, and 13.25 μm for waveguides 2 and 4. The SFG conversion efficiency curves for waveguides 1 and 2 were obtained with the pump wave at 1553 nm, and at 1556 nm for waveguides 3 and 4. The wavelength of the input signal wave was varied from 1542 to 1552 nm for waveguides 1 and 2, and from 1545 to 1555 nm for waveguides 3 and 4. The obtained results are shown in figure 3.14.

A good agreement between the measured SFG conversion curves, normalized to the efficiency at the central frequency, and the target spectral response is observed. A full width at half maximum conversion bandwidth of about 380 GHz was experimentally observed for all waveguides, which agrees well with the target spectral response. As expected, the measured conversion bandwidth of the quasi-rectangular devices is larger ($>$ 6 times) than that of a uniform PPLN with the same parameters (L = 4.5 cm, A_{eff} = 100 μm^2, P_1 = 26.5 dBm), whose normalized SFG conversion spectrum is also shown in figure 3.14 for comparison. However, as discussed in the previous section, the absolute efficiency of the quasi-rectangular devices is lower than that of a uniform PPLN, as a consequence of deleting some ferroelectric domain inversions and, consequently, of decreasing the effective nonlinear coefficient. Absolute SFG efficiencies of about 21, 15.0, 30.0 and 19% where measured for waveguides 1 to 4 at a pump power of 26.5 dBm.

Despite the good agreement between the measured and target spectral responses of

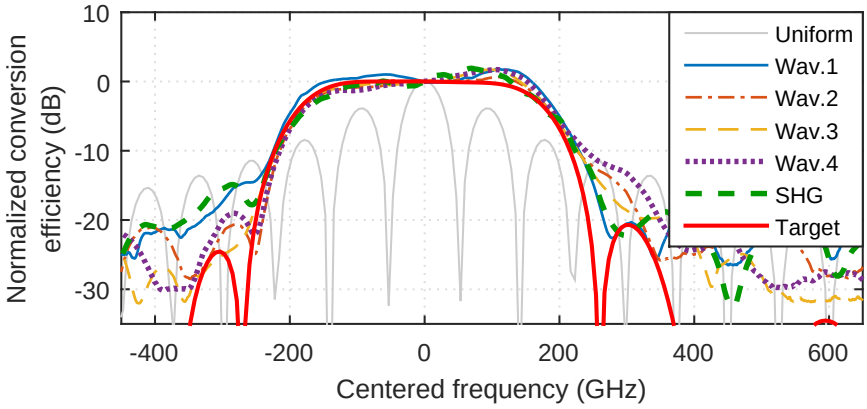

Figure 3.14: Target and experimental normalized SFG conversion efficiency spectra of four 400 GHz quasi-rectangular PPLN waveguides. The frequency is centered at 774.8, 774.6, 776.6, 776.4 nm for waveguides 1, 2, 3 and 4, respectively. The SHG conversion efficiency curve corresponds to waveguide 1, centered at 775 nm. The simulated SFG conversion spectrum of a uniform PPLN (gray curve) is also shown for comparison.

the 400 GHz quasi-rectangular devices, non-negligible differences can be found, including lower peak to side lobe ratios and asymmetric, non-flat conversion efficiency within the main peak. For waveguides 2 and 4, the peak to side lobes ratio was less than 15 dB, instead of more than 20 dB predicted by numerical simulations. As regards the flatness of the spectral response within the main peak, waveguides 3 and 4 have the worst performance, with a total variation of 3 dB. In both cases, the SFG efficiency tends to increase for higher frequencies. For waveguides 1 and 2, the total variation of the efficiency in the main peak is lower, below 1.5 dB. These results were also observed at lower pump power and with the temperature controller turned off, which excludes the possibility of local heating or temperature gradients to be the cause of such differences. As different deviations from the target spectral response are observed for different waveguides with the same poling pattern, the most plausible explanation for the observed differences are fabrication errors such as imperfections of the poling pattern, and longitudinal variation of the effective refractive index and effective area through the waveguide.

The normalized SHG efficiency for waveguide 1 is also shown in figure 3.14 for comparison. The SHG curve was obtained by turning one of the ECLs off, and setting the input power to 22.5 dBm. In this case, the input signal wavelength was varied from 1545 to 1555 nm. According to the experimental results, the normalized conversion efficiency spectra obtained for SHG and SFG are similar, which means that even though the PPLN was designed for SFG, a similar spectral response can be expected for SHG. This was also observed in the numerical simulations presented in the previous section.

The 400 GHz quasi-rectangular PPLN device was designed considering a refractive index dispersion curve for bulk MgO-doped lithium niobate, without accounting for the contribution of waveguide dispersion, as such information was not available. Nonetheless, the spectral response of the manufactured devices agrees well with the target design. In fact,

the main difference between the simulated and manufactured device due to waveguide dispersion was changing the poling period from 19.5 to 19.1μm, and from 19.6 to 19.2 μm in the case of waveguides 3 and 4.

The numerical and experimental results shown in this chapter prove the effectiveness of the LPA and the DRM on the design of customized PPLN devices with target spectral responses. The LPA and DRM proved to be good alternatives to other complex techniques, showing very good accuracy, flexibility and reliability on the design of the spectral response for SFG and SHG in periodically poled waveguides. However, it was observed that the spectral response for cSFG/DFG shows some differences compared to the target one, designed for the SFG intermediate step. Nonetheless, the final response for cascaded TWM interactions still resembles the target design, making the LPA a very useful tool to produce periodically poled devices with customized poling patterns and therefore enable new features for advanced OSP, as it is shown in the next chapter.

Chapter 4

Advanced all-optical wavelength conversion

Wavelength conversion, also known as wavelength shifting, is one of the most important signal processing functionalities for WDM systems. Wavelength conversion can potentially increase the flexibility, versatility and performance of future dynamic optical transport networks as it allows the optimization of the wavelength usage at a specific point of the network, and routing the data signals to different WDM channels [146, 147]. Moreover, wavelength conversion is a possible solution to reduce the blocking probability due to wavelength contention in wavelength-routed networks, when multiple channels at the same wavelength are routed to the same output port of a ROADM [36, 148].

Wavelength conversion can be implemented in either the electrical domain using conventional electronic repeaters with tunable output wavelength [36] or in the optical domain. OWC potentially offers several advantages over wavelength shifting in the electrical domain, including multichannel operation and the possibility to simultaneously convert a group of several data channels at different wavelengths (parallel operation) [149], no optical-to-electrical-to-optical conversion [150], high bandwidth of operation, not limited by the speed of electronics [36, 150] and wide wavelength tunability [36]. Optical wavelength converters based on parametric nonlinear interactions can also be designed for transparent conversion in terms of both data rate and modulation format [150, 151], which is a very desirable feature for modern optical transport networks, and facilitates upgrading and reconfiguring the networks [149–151]. Such a feature becomes even more important with the use of spectrally efficient advanced modulation formats. OWC is also the original build block of several other OSP functionalities including multicasting [8], all-optical logic gates [152], chromatic dispersion compensation [153], or tunable optical delays [10], just to name a few examples.

Despite the advantages of OWC, its application to real systems is still very limited, if not inexistent, mostly due to the lack of technological maturity and reliability, as well as several practical drawbacks such as modest conversion efficiency, high pump power, large footprint and stability issues [154]. Moreover, a clear proof that OWC can provide better performance, energy efficiency and lower cost compared to electrical wavelength conversion is still elusive [36]. Therefore, higher conversion efficiency, low noise operation, low signal distortion, polarization insensitivity and broad wavelength tuning range are key requisites for OWC [36, 155].

Several schemes have been proposed in order to perform OWC using either XGM, XPM, FWM or cascaded TWM effects in SOAs, HNLFs, PPLN waveguides, PCFs, silicon and chalcogenide waveguides, with the first three nonlinear media being the most representative ones [36, 109, 146, 147, 150, 154–158]. OWC can be achieved through XGM in SOAs where a strong intensity-modulated input signal modulates the gain and, consequently, the amplitude of a probe wave at the target wavelength. However, such a scheme can only be used for intensity-modulated signals. Moreover, the operation is limited by the gain recovery time, which depends on the carriers' lifetime of the SOA [36]. OWC can also be implemented using XPM combined with interferometric structures such as Mach-

Zehnder interferometers (MZIs), with SOAs placed at the arms of the interferometers, also known as MZI-SOAs, or Sagnac interferometers with an incorporated nonlinear Kerr media such as a HNLF, commonly known as nonlinear loop mirrors [36]. In both cases, a CW probe wave at the target wavelength is sent to the interferometric structure, and its phase is modulated by the intensity of an input data signal via XPM. In turn, the XPM-induced phase shift modifies the interference condition of the interferometer and, consequently, the amplitude of the output probe wave [36]. As in XGM-based OWC, this scheme can only be used for intensity modulation formats.

Transparency to the modulation format can be accomplished through OWC based on parametric nonlinear interactions such as FWM or cascaded TWM. As described in chapter 2, the complex amplitude of the converted waves via FWM, cSHG/DFG or cSFG/DFG can be proportional to either the electric field envelope of the input signal wave or its complex conjugate, allowing transparent conversion of phase and/or amplitude modulated signals. Moreover, conversion efficiencies of more than 100% may be obtained in phase-conjugating configurations by combining wavelength conversion with parametric amplification [159]. One of the main drawbacks of parametric OWC is polarization sensitivity [36], which not only limits the operation to single-polarization signals, but also requires active tracking and control of the state of polarization of the interacting waves. Nonetheless, polarization-insensitive operation has already been demonstrated using polarization-diversity configurations [150, 159, 160], or FWM in a HNLF with two pumps in orthogonal states of polarization [161]. Another possible impairing mechanism is the additional noise due to ASE in SOA-based converters, and the noise transferred from the pump waves to the converted signal during the nonlinear interactions, which requires using pumps with high optical signal-to-noise ratio (OSNR) and narrow-linewidth to avoid significant degradation.

OWC based on PPLN devices offer several advantages over SOAs and HNLFs, including negligible ASE, immunity to SBS, and no deleterious SPM-induced nonlinear phase noise (Gordon-Mollenauer effect) [45] that degrade the converted signals. Moreover, the possibility of ferroelectric domain engineering, discussed in the previous chapter, enable new properties and possibilities for advanced OWC applications.

In this chapter, two different schemes for advanced OWC using PPLN devices are proposed. In section 4.1, tunable and multichannel OWC using the 400 GHz quasi-rectangular PPLN characterized in the previous chapter is discussed. A pump-linewidth tolerant scheme for OWC with negligible pump-to-signal phase noise conversion is presented in section 4.2. Using the scheme proposed in section 4.2, WDE between two data channels is also studied in section 4.3.

4.1 Tunable and multichannel wavelength conversion

The possibility to deploy OWC units in future optical transport networks can only be-

come viable if such subsystems are able to cope with a set of fundamental requirements, namely reconfigurability, flexibility and transparency to the modulation format and data rates [36]. In this sense, parametric wavelength converters are the most suitable candidates for transparent operation and wavelength tunability, achieved by tuning the wavelength of the the pump waves, and limited only by the dispersion properties of the nonlinear medium. In addition to tunability, broadband and ultrafast operation are also very attractive features for future wavelength routed optical transport networks in order to enable OWC of WDM or orthogonal frequency-division multiplexing superchannels [162], or simultaneous conversion of several grouped WDM channels [163] in ROADMs [162, 163].

As mentioned above, the unique advantages of PPLN waveguides compared to other nonlinear devices make them an attractive choice to enable advanced OWC in future optical transport networks. OWC in PPLN devices is usually based on cSHG/DFG and cSFG/DFG interactions rather than simple TWM processes. Otherwise, one of the input or output waves would have to be in a completely different spectral region [92, 164].

Let us first discuss OWC based on cSHG/DFG. The most common scheme for OWC based on cSHG/DFG is schematically represented on the upper left side of figure 4.1. In this case, the second harmonic of a strong pump wave (P) is used to promote the conversion of an input signal (s) through phase-conjugating DFG [93]. A wide conversion bandwidth exceeding the conventional C-band can be typically obtained using such a configuration (see figure 2.7), achieved due to the dispersion properties of phase-conjugating DFG, discussed in subsection 2.2.3 and figure 2.8. The wide conversion bandwidth observed for this configuration enables broadband and/or multichannel operation, but tunability is prevented as the wavelength of the pump wave must be precisely set to λ_{QPM} to efficiently generate the second harmonic wave. On the other hand, tunable OWC through cSHG/DFG can be obtained by generating the second harmonic of the input signal, and using a pump wave to promote phase-preserving DFG, as depicted on the lower left side of figure 4.1. In this case, wavelength tunability of the converted wave (c) is achieved by varying the wavelength of the pump [165]. However, the bandwidth of both the SHG and phase-preserving DFG processes is much shorter ($\lesssim$1 nm), so broadband multichannel operation is precluded. In addition, since the electrical field of the second harmonic is proportional to the square of the input signal one, the OWC process would not be transparent to the modulation format. Hence, this OWC scheme is not very common for OWC purposes, and it is not further discussed.

Wavelength tunability can also be obtained through cSFG/DFG, using a pump wave ($P1$) to convert the input signal to the second harmonic band through SFG, and a second pump ($P2$) to convert the new wave back to the fundamental band via phase-preserving DFG. This scheme is represented on the upper right side of figure 4.1. In this configuration, wavelength tunability is achieved by tuning the wavelength of the DFG pump ($P2$) [166]. However, the conversion bandwidth is also very limited, typically shorter than 1 nm (see subsection 2.2.3), due to the same reasons discussed above for the second OWC scheme

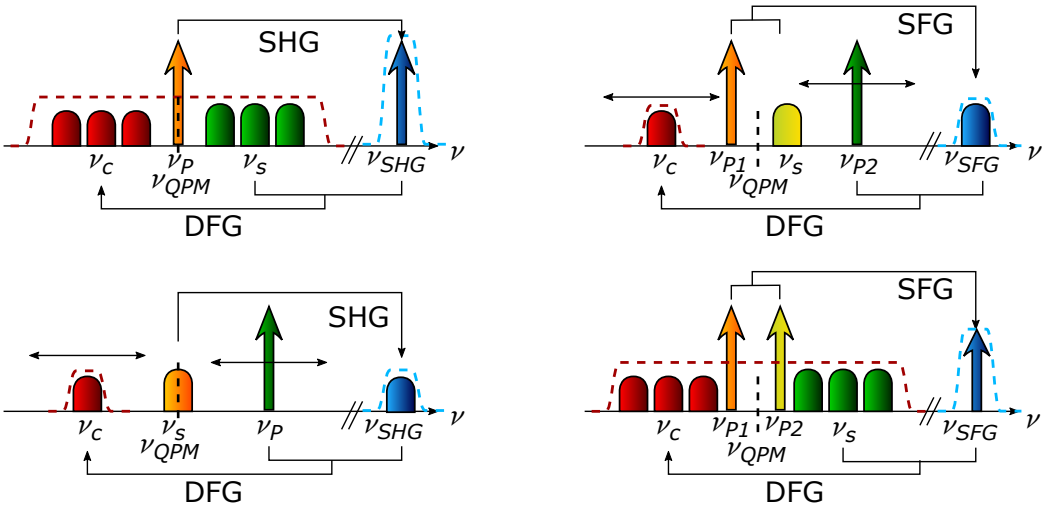

Figure 4.1: Different OWC configurations based on cSHG/DFG, on the left, and cSFG/DFG, on the right. The configurations shown on top represent the most usual schemes used for OWC. The red dashed line represents the bandwidth of the DFG process, whereas the blue one represents the conversion badwidth of the SHG or SFG interaction. The horizontal black arrows represent wavelength tunability.

based on cSHG/DFG. On the other hand, broadband and multichannel operation can also be implemented through cSFG/DFG, using the conversion scheme depicted on the lower right side of figure 4.1. This latter scheme is similar to the usual cSHG/DFG configuration shown on the upper left side of figure 4.1, but requiring two pump waves instead of a single one to generate the intermediate wave at the second harmonic band via SFG. Again, despite enabling broadband conversion, wavelength tunability is prevented in this scheme as the two pump waves must be symmetrically displaced around the QPM wavelength, and the SFG wave must be locked at $\lambda_{QPM}/2$. In addition, since an additional pump wave is required, this configuration is usually ruled out in favor of the cSHG/DFG one and is not further discussed as well.

In summary, each of the previous configurations enables either tunable or broadband/ multichannel OWC, but not both properties simultaneously. In addition, only the OWC schemes shown at the top of figure 4.1 are usually adopted due to their advantages compared to the ones depicted at the bottom of the figure.

Different advanced OWC schemes have been proposed in order to obtain tunable and broadband OWC in PPLN devices. One of the possible solutions is to consider the OWC scheme based on cSHG/DFG shown on the upper left side fo figure 4.1 in PPLN device with multiple QPM resonances [133, 167]. In this case, broadband operation is enabled by the intrinsic dispersive properties of the phase conjugating DFG step in cSHG/DFG, as discussed above for the configuration shown on the upper left side of figure 4.1. Wavelength tunability is then achieved by switching the wavelength of the pump to a different QPM resonance, which also shifts the wavelength of the converted waves according to the frequency relation $\nu_c = 2\nu_P - \nu_s$. However, the wavelength of the pump wave must be pre-

cisely tuned to one of the QPM resonances, otherwise the generation of the intermediate SHG wave is very weak and the overall conversion efficiency becomes very low. Hence, the tunability of this scheme is limited by the location of the QPM resonances.

Another possibility for tunable and multichannel OWC is to consider the scheme based on cSFG/DFG shown on the upper right side of figure 4.1 to enable wavelength tunability, and using multiple SFG pumps, one for each input channel. However, several high-power pump waves are required, which not only greatly increase energy consumption but may also lead to large inter-pump and inter-channel crosstalk. Hence, this approach is not viable for a high number of input channels. A better alternative is to consider the same cSFG/DFG configuration, but now using periodically poled devices with extended QPM bandwidth for broadband operation, and using a single pump wave $P1$ to promote SFG for all input channels simultaneously [132, 168]. Linearly chirped PPLN waveguides [132] or uniform devices with a temperature gradient applied along the device [168] are some possibilities to extend the QPM bandwidth. In both cases, the extended QPM bandwidth is obtained by varying the QPM condition along the PPLN device. In the first case, the QPM resonance is varied by locally changing the poling period, whereas the second one takes advantage of the temperature dependent nature of the refractive index and, consequently, of the QPM resonance. Another possibility is to use the quasi-rectangular PPLN waveguides discussed in the previous chapter. Compared to linearly chirped devices or uniform PPLN waveguides with temperature gradients, quasi-rectangular devices have a flatter spectral response and steeper magnitude transitions at the edges of the passband. Such properties are particularly relevant to reduce inter-channel crosstalk for OWC of multiple WDM channels.

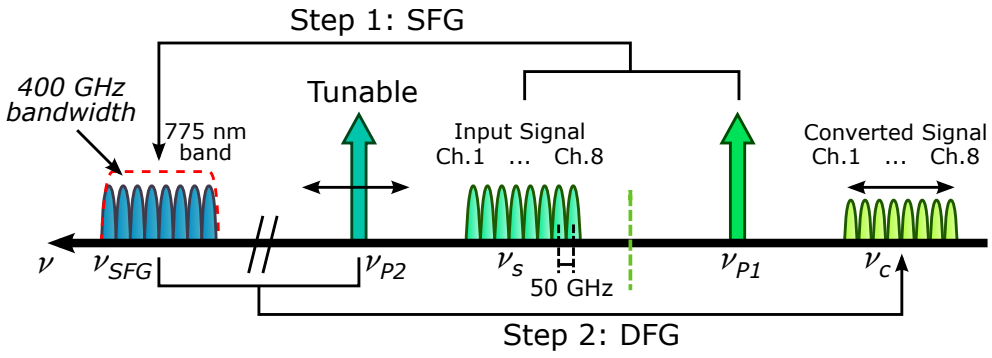

Figure 4.2: Schematic representation of the proposed scheme for tunable and multichannel OWC using a 400 GHz quasi-rectangular PPLN waveguide.

In this section, tunable and multichannel OWC is demonstrated, based on cSFG/DFG of eight QPSK data channels, using the quasi-rectangular PPLN device with QPM bandwidth of 400 GHz investigated in the previous chapter. The proposed advanced OWC scheme is depicted in figure 4.2. As depicted in the figure, eight input channels spaced by 50 GHz are converted to the second harmonic band at about 775 nm via SFG and then converted back the C-band through DFG with an additional tunable pump wave. It should be emphasized

that the proposed scheme uses a single SFG pump for multichannel operation in contrast to the first possibility discussed in the previous paragraph, which requires multiple SFG pumps. This is why the proposed scheme is referred to as single pump, tunable OWC in publication B of in appendix D, despite using an additional pump for DFG.

4.1.1 Experimental set-up

The experimental set-up used to characterize the proposed scheme is depicted in figure 4.3. The two pump waves were generated by ECLs with a laser linewidth of 500 kHz and combined in a 50:50 coupler, after passing through a PolC, an EDFA, a 1 nm BPF and a VOA, respectively used for state of polarization alignment, amplification, excessive out-of-band noise filtering and power tuning. The two pumps were then combined with the data channels using another 50:50 coupler. In this experiment, the wavelength of the SFG pump was set to 1556.73 nm, whereas the DFG pump was tuned to either 1542.6, 1543.6, 1544.6 or 1545.6 nm to demonstrate wavelength tunability.

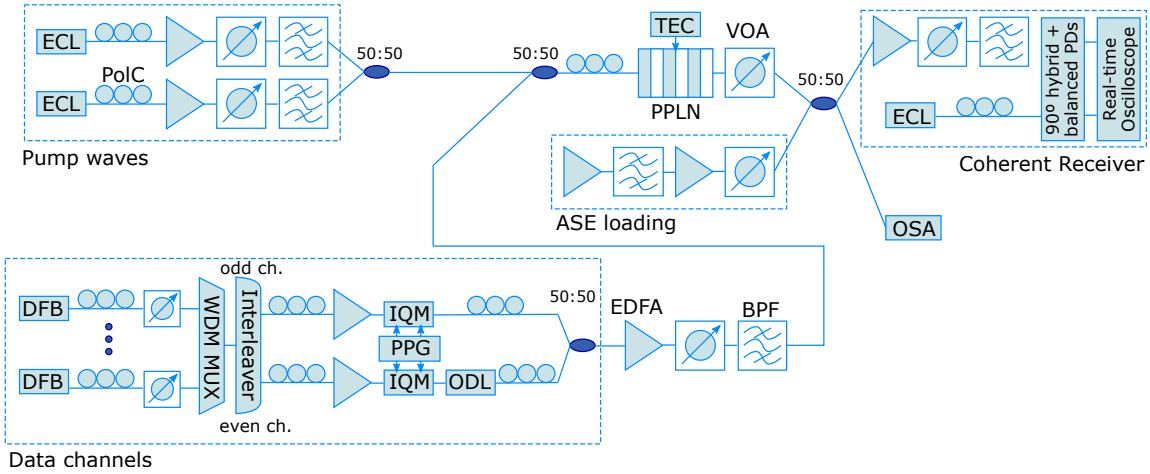

Figure 4.3: Experimental set-up used to characterize the performance of the proposed scheme.

The 12.5 Gsymbol/s QPSK data channels were generated by eight independent distributed feedback laser (DFB) lasers with an emission linewidth of about 3.5 MHz and combined in a wavelength multiplexer, after state of polarization alignment and power equalization in PolCs and VOAs. The odd and even channels were then separated using an interleaver and led to two in-phase/quadrature modulators (IQMs), each driven by two de-correlated pseudo-random bit sequences (PRBSs) of length 2^{15}-1, obtained from a pulse pattern generator (PPG), after polarization alignment and amplification to compensate for the insertion losses of the WDM multiplexer and the interleaver. An additional optical delay line (ODL) was inserted in the even channels path in order to de-correlate the even and odd channels. The even and odd channels were then combined in a 50:50 coupler after polarization alignment. The frequency separation between the data channels was set to 50 GHz, with channel 1 located at 1548.92 nm, and channel 8 at 1551.75 nm. An additional

EDFA, VOA and a 5 nm BPF were introduced in order to control the power of the input channels and remove out-of-band ASE noise.

The pump and signal waves were then injected into the 400 GHz quasi-rectangular PPLN waveguide for wavelength conversion through free space coupling optics, as shown at the bottom of figure 3.13. As mentioned in the previous chapter, the PPLN device was produced on a lithium niobate substrate doped with 5% of MgO to prevent photorefractive damage at high pumping power, and included fifty APE waveguides with different poling periods and waveguide widths. A PPLN waveguide with poling period and waveguide width of 19.2 μm and 9.25 μm was selected, chosen as a trade-off between the wavelength of the available DFB lasers, conversion efficiency and possibility of room temperature operation. The SFG conversion efficiency of the selected waveguides is represented by the curve labeled as waveguide 3 in figure 3.14. The total insertion losses of the free-space coupling system were of less than 4 dB. The length and temperature of operation of the PPLN waveguide were 4.5 cm and 25 $^{\circ}$C, respectively, with the latter being controlled using a TEC element. The input power of each modulated channel, SFG and DFG pumps was about 12.5, 24 and 18 dBm, respectively.

The performance of the wavelength converter was evaluated through bit error ratio (BER) measurements as a function of the OSNR. In order to do so, the ASE noise produced by two cascaded EDFAs interleaved by a 5 nm tunable filter was combined with the light coming out of the PPLN in a 50:50 coupler. Additional VOAs were introduced before the coupler to precisely control the OSNR of the measured signal. An OSA was placed at one of the output ports of the coupler for monitoring, whereas the light coming out from the other output port was led into a coherent receiver.

The coherent receiver included an additional EDFA, VOA and a variable bandwidth filter to remove all the waves except the channel under test. The input power to the receiver was set to -10 dBm. The receiver comprised a 90° optical hybrid connected to DC-coupled PDs. The PDs were located at the input to a 40 Gsample/s real-time sampling oscilloscope with 13 GHz analog bandwidth. A 100 KHz linewidth ECL was used as the local oscillator, and the BER measurements were performed with the DFG pump at 1545.6 nm. The DFB laser of the channel under test was replaced by another ECL with emission linewidth of 500 kHz for the BER measurements. A total of 8×10^5 symbols were considered, allowing to measure BER values up to about 10^{-6}.

4.1.2 Experimental results and discussion

The optical spectra measured with the OSA after OWC in the 400 GHz quasi-rectangular PPLN waveguide is depicted in figure 4.4-a), and detailed for the converted channels in figures 4.4-b) to 4.4-e). As expected, the wavelength of the DFG pump determined the spectral position of the converted channels, providing the tunability properties to the wavelength converter.

As discussed in the previous chapter, the spectral response of the PPLN devices de-

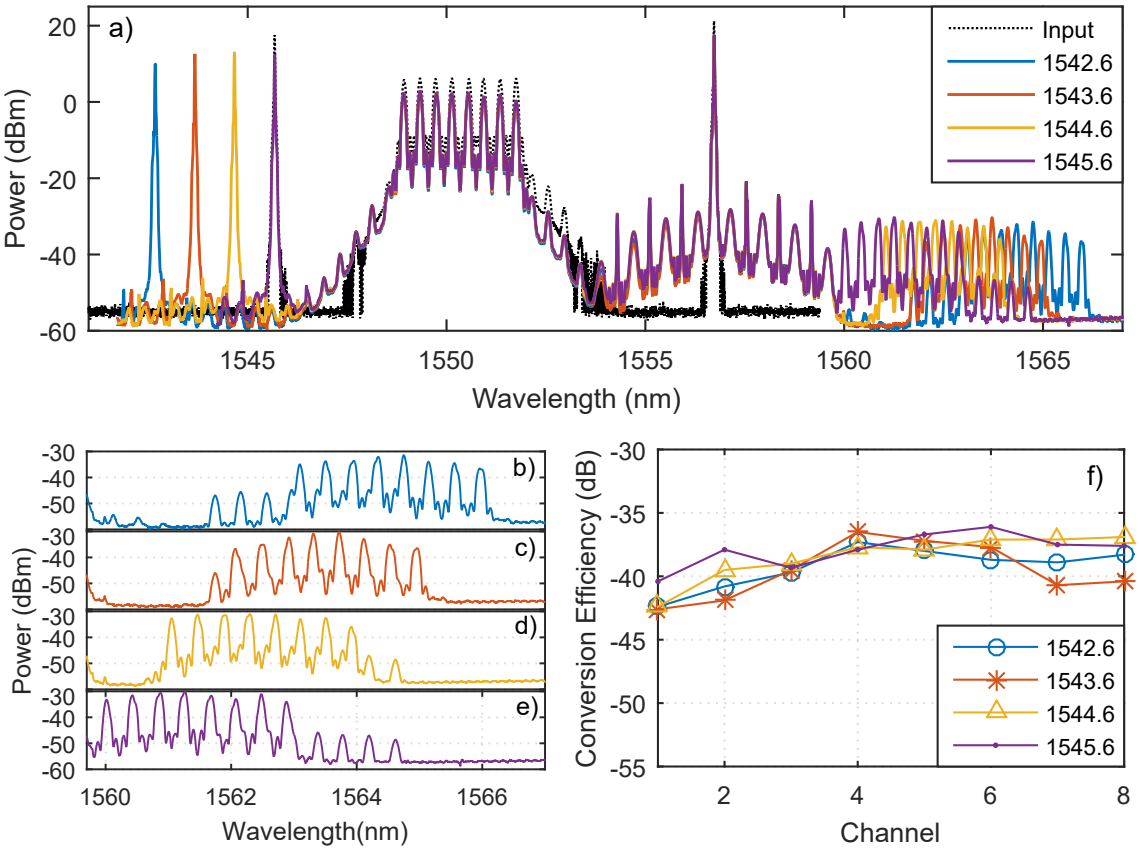

Figure 4.4: a) Optical spectra measured at the input of the PPLN device with the SFG pump at 1545.6 nm and after OWC with the DFG pump set to 1542.6, 1543.6, 1544.6 and 1545.6 nm. Detailed spectra of the converted channels with the DFG pump set to b) 1542.6, c) 1543.6, d) 1544.6, and e) 1545.6 nm. f) Conversion efficiency of each converted channel, measured with the DFG pump at 1542.6, 1543.6, 1544.6 and 1545.6 nm.

signed with the LPA for cSFG/DFG is not exactly the same as the target spectral response, as the LPA is originally formulated for SFG. Nonetheless, broadband OWC through cSFG/DFG was still possible using the manufactured quasi-rectangular PPLN device. Yet, non-negligible spurious contributions were observed at different regions of the obtained spectra, namely close to the SFG pump, to the converted and to the input signals. The spurious waves around the input data channels were already present at the input of the PPLN device and were generated through FWM between the different channels in the EDFAs and patch cords. The available patch cords used to connect the different components of the set-up, with an estimated total length of about 150 m, were made of dispersion-shifted fibers with a zero-dispersion wavelength in the C-band. Hence, the propagation of high-power waves in low dispersion patch cords led to significant generation of FWM byproducts around the input data channels.

Another group of spurious contributions was observed around the SFG pump, whose wavelength remained unchanged, even for different values of the DFG pump wavelength. Hence, these waves must have been generated from undesired cascaded TWM interac-

tions between the input channels and the SFG pump, whose wavelength was kept unchanged in all the experiments. A deeper analysis of the frequency of the spurious contributions reveals that they were generated from SFG between one of the input channels and the SFG pump, followed by DFG with another input channel. Another particular detail regarding the spectral shape of these contributions also supports this claim. In fact, it is possible to observe narrow-bandwidth spurious waves alternating with broader ones around the SFG pump. All the narrow-bandwidth contributions originate from cSFG/DFG between two odd or two even channels, with the same phase information and encoded in the same IQM. Since the optical field of the converted waves is proportional to that of one of the input channels and to the complex conjugated of the other one, their phase subtracts at the converted wave, and the data modulation is stripped, generating a narrow carrier. The other spurious contributions are a mix of de-correlated odd and even channels, so the phase modulation is not eliminated, leading to a broad spectrum bandwidth.

The most important group of spurious contributions is observed close to the converted signals, generated through SHG of the SFG pump wave, followed by DFG with the input channels. Since they partially overlap with the converted channels, the performance of the wavelength converter is particularly affected by these spurious waves. In principle, no significant SHG of the SFG pump should be expected, as the wavelength of this wave was tuned to be outside of the SHG conversion bandwidth of the quasi-rectangular device. However, the conversion bandwidth of 400 GHz is observed only at the end of the PPLN device. In fact, at the beginning of the waveguide, the accumulated phase mismatch is relatively small and the conversion bandwidth is broader than just 400 GHz. Hence, a non-negligible second harmonic of the SFG pump is generated at the beginning of the waveguide, which simultaneously interacts with the input signals through DFG, creating the spurious contributions around the converted channels. As the waves propagate throughout the device, the accumulated phase mismatch increases and the power of the waves in the second harmonic band at frequencies farther apart from the QPM resonance (e.g., the second harmonic of the SFG pump) starts to flow back to the fundamental wave. This is why the conversion bandwidth for SFG and/or SHG becomes narrower at the end of the PPLN waveguide, as discussed in the previous chapter. On the other hand, since the phase mismatch for phase-conjugating DFG is typically much lower than for SFG or SHG, the power of the spurious contributions does not start to flow back to the original waves. On the contrary, the power of the spurious waves continues to grow along the device until the second harmonic of the SFG wave is completely converted back to the SFG pump.

The spurious contributions around the converted channels can be significantly reduced by decreasing the power of the SFG pump. However, this strategy also reduces the conversion efficiency, i.e., the power ratio between the converted and input channels, which is already low, as depicted in figure 4.4-f). The measured low conversion efficiency values, of about -40 dB (including the insertion losses of the device and coupling optics), are a consequence of the lower average effective nonlinear coefficient, caused by deleting

some of the ferroelectric domain inversions. Low conversion efficiency values of about -35 and -30 dB have respectively been reported in previous OWC schemes based on linearly chirped PPLN waveguides and temperature gradients to increase the conversion bandwidth of the SFG step to values comparable to those of the 400 GHz quasi-rectangular device [132, 168]. In such schemes, the QPM resonance condition for a certain input signal wavelength is verified only at a small portion of the device, which explains the reported low conversion efficiency. Hence, a trade-off between conversion bandwidth and efficiency is verified [168], as broader conversion bandwidth implies that the portion of the device contributing to a specific QPM wavelength is smaller. The same trade-off is also verified for the quasi-rectangular devices, but in this case, broader conversion bandwidth requires deleting more ferroelectric domain inversions, as shown in figures 3.7-c) and 3.7-d), which in turn lowers the overall effective nonlinear coefficient.

A higher conversion efficiency could have been achieved by increasing the power of the pump waves, but it had to be limited in order to reduce the generation of the spurious waves. Nonetheless, further optimization of the wavelength and power of the pump waves can potentially increase the conversion efficiency to values comparable to or even higher than those reported in [132] and [168].

The performance of the proposed OWC scheme in terms of BER is depicted in figure 4.5. According to the experimental results, a maximum OSNR penalty of about 2 dB was observed at a BER of 10^{-3} for the converted channels 1 to 7, with respect to the back-to-back measurements of the input channels. A higher penalty of about 3 dB was observed for channel 8. In this case, however, the conversion efficiency was lower and the wavelength of this channel was beyond the gain bandwidth of the last EDFA. Thus, the maximum input power to the receiver was of only -17 dBm instead of -10 dBm, which led to an excessive OSNR penalty.

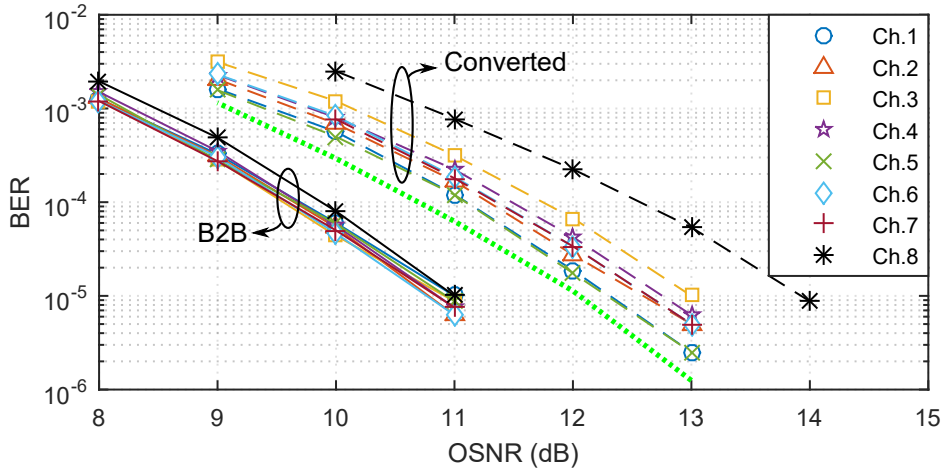

Figure 4.5: BER as a function of the OSNR, measured back-to-back, B2B, (solid lines) and after OWC (dashed lines). The green dotted line represents the variation of the BER for channel 4, measured before the PPLN device. The measurements were obtained with the DFG pump at 1545.6 nm.

The BER measurements for channel 4 obtained before the PPLN device are also represented by the green dotted line in figure 4.5. According to the obtained results, an OSNR penalty of about 1 dB is already observed before OWC, most likely caused by the spurious FWM interactions between the input channels in the EDFAs and patch cords, as discussed above.

Despite being affected by several degrading mechanisms such as pump-to-signal transferred noise and spurious cSHG/DFG interactions between the SFG pump and the input channels, the proposed scheme enabled advanced OWC of a group of several WDM channels with wavelength tunability. Better conversion efficiencies and performances can be expected by carefully selecting the wavelength and power of the interacting waves. For instance, increasing the power of the SFG pump could improve the conversion efficiency, but the spurious contributions around the converted channels would also increase. In this regard, increasing the power of the DFG pump would be a better approach as it would allow higher conversion efficiency without stronger spurious contributions affecting the converted waves. Decreasing the power of the input signal channels would also reduce all the spurious contributions, but the power of the converted channels would be reduced as well.

In summary, tunable and multichannel OWC can be achieved by using PPLN waveguides with extended QPM bandwidth. However, there is a trade-off between broad QPM bandwidth and the efficiency of the nonlinear device. Typically, higher pump power is required in order to compensate for the lower conversion efficiency. In the specific case investigated in this section, increasing the power of the DFG pump would have been the most sensible way to increase the efficiency without generating strong spurious contributions near the converted channels. However, this may not be true for different cases. In fact, depending on the wavelength of the signal and pump waves, it may happen that the most reasonable approach becomes increasing the power of the SFG pump. In addition, it is possible that increasing the power of either the SFG or DFG pump ends up generating stronger spurious waves around the converted signals and, therefore, not being desirable at all. Another possibility seems to be reducing the QPM bandwidth, which would allow higher conversion efficiency and less spurious contributions.

4.2 Pump-linewidth-tolerant wavelength conversion

In optical systems where the phase of the waves is used to encode information, phase noise becomes a very important parameter, in particular for high-order QAM formats that require higher OSNR values for error-free operation. In such systems, any additional source of noise should be eliminated or mitigated as much as possible.

Light emitted by any CW laser is not perfectly monochromatic, but its spectrum is composed by emission peaks with finite linewidth caused by fluctuations of the emission frequency. The frequency of a wave can be defined as the rate of change of its phase, so the width of the laser line can be ultimately be related to random fluctuations in the phase

of the optical field, i.e., to phase noise. Phase noise due to finite linewidth of the laser sources originates from several factors, including both technological and fundamental limitations. As an example of technical limitations, mechanical vibrations and temperature variations cause fluctuations of the resonance condition of the laser cavity, which in turn change the instantaneous emission frequency. Even without such technical limitations, spontaneous emission adds photons with random phase and frequency [1]. Moreover, any gain fluctuation in semiconductor lasers changes the carrier population and consequently, the refractive index and phase of the emitted radiation [1].

Typically, the emission spectrum of a laser can be described by a Lorentzian function, and the phase evolution in time can be modeled a random walk process, with a variance of the random phase-shifts given by [7]

$$<\Delta\phi_n{}^2> = 2\pi\Delta\nu|\Delta t|, \tag{4.1}$$

where $\Delta\phi_n$ is the random phase-shift (phase noise) due to the finite linewidth $\Delta\nu$ within a time duration Δt.

In practice, the phase drift due to finite linewidth of the laser sources produces random rotations of the constellation diagrams in arbitrary directions that must be corrected at the receiver in order to avoid detection errors. Carrier-phase estimation in coherent receivers is a common strategy to track the phase drift due to finite laser linewidth, which can be accomplished by, for instance, averaging the phase of the signal carrier using an M^{th}-power block scheme [7]. Nonetheless, even with carrier-phase estimation techniques, a penalty on the receiver sensitivity can still be observed [7], so narrow-linewidth lasers must be used as light sources when using advanced modulation formats such as 8-PSK, 16-QAM, 64-QAM or even higher-order formats.

In parametric OWC, the linewidth of the pump waves also plays a very important role on the phase noise properties of the converted signals. As the optical field of the converted signal is proportional to that of the pump waves in non-degenerate FWM and cSFG/DFG (or its square in degenerate FWM or cSHG/DFG), any noise of the pump waves is also transferred to the converted waves, including the phase noise due to finite linewidth. This issue becomes particularly relevant for optical transport networks where the signal channels may experience several OWCs before reaching the final destination node. Therefore, not only costly narrow-linewidth lasers must be used as the light sources for the signal channels, but also for the pump waves in order to prevent reaching prohibitive phase noise levels.

A possible solution to avoid the additional phase noise due to the finite linewidth of the pump laser sources is to consider a dual-pump OWC configuration, using coherent pump waves [169]. The principle of operation of the proposed scheme is depicted in figure 4.6. After OWC via either cSFG/DFG in $\chi^{(2)}$ nonlinear media or phase-preserving non-degenerate FWM in third-order nonlinear devices, the input signal at ν_s is shifted to frequency $\nu_c = \nu_{P2} + \nu_s - \nu_{P1}$, with the pump waves at frequencies ν_{P1} and ν_{P2}. As dis-

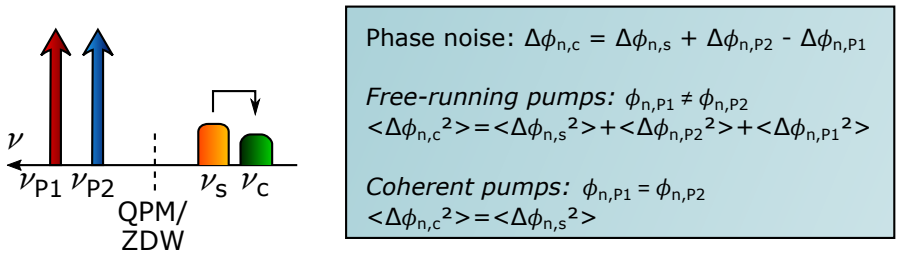

Figure 4.6: Schematic representation of pump-linewidth-tolerant OWC.

cussed in chapter 2, the normalized electric field envelope of the interacting waves when no converted signal wave is injected at the input of the nonlinear device is is proportional to $A_c \propto A_s A_{P2} A_{P1}^*$. Consequently, the phase relationship between the waves becomes

$$\phi_c + \Delta\phi_{n,c} = (\phi_s + \Delta\phi_{n,s}) + (\phi_{P2} + \Delta\phi_{n,P2}) - (\phi_{P1} + \Delta\phi_{n,P1}) + const, \tag{4.2}$$

where *const* is a constant, and $\Delta\phi_{n,j}$ the phase noise of wave j. The variance of the converted signal phase noise $\Delta\phi_{nc} = \Delta\phi_{n,s} + \Delta\phi_{n,P2} - \Delta\phi_{nP1}$, is then described by [169]

$$\begin{aligned} <\Delta\phi_{n,c}{}^2> = <\Delta\phi_{n,s}{}^2> + <\Delta\phi_{n,P1}{}^2> + <\Delta\phi_{n,P2}{}^2> + 2\mathrm{Cov}(\Delta\phi_{n,s}, \Delta\phi_{n,P2}) \\ - 2\mathrm{Cov}(\Delta\phi_{n,s}, \Delta\phi_{n,P1}) - 2\mathrm{Cov}(\Delta\phi_{n,P1}, \Delta\phi_{n,P2}), \end{aligned} \tag{4.3}$$

where $\mathrm{Cov}(x, y)$ is the covariance of the two random variables x and y.

If the interacting waves are generated from different light sources (free-running pumps), the phase noise of the waves is independent and uncorrelated, so the covariances in (4.3) vanish. In this case, the phase noise variance of the converted signal becomes $<\Delta\phi_{n,c}{}^2> = <\Delta\phi_{n,s}{}^2> + <\Delta\phi_{n,P1}{}^2> + <\Delta\phi_{n,P2}{}^2>$. Equivalently, the linewidth of the converted signal for CW operation is given by the sum of the linewidth of the other waves, similarly to the beating of a signal and local oscillator in a coherent receiver [7]. On the other hand, if the same light source is used to generate the two pump waves (coherent pumps), the phase noise is the same, so $\mathrm{Cov}(\Delta\phi_{n,P1}, \Delta\phi_{n,P2}) = <\Delta\phi_{n,P1}{}^2> = <\Delta\phi_{n,P2}{}^2>$. In this case, the phase noise from the pump waves cancels out at the converted signal, and the phase noise variance becomes equal to the input signal one. Therefore, no additional phase noise originated from the finite linewidth of the pump waves is introduced using the proposed scheme, and cheaper sources with broader linewidth such as DFBs can be deployed as pumps.

The coherent pumps can be generated in a two-tone generator (TTG) built from a Mach-Zehnder modulator (MZM) driven by an RF clock [170], or an optical frequency comb followed by a spectrum shaper to filter out the unwanted tones of the comb. The first approach is particularly suitable when the frequency separation of the input and converted signals does not exceed 100 GHz, as larger separations cannot be achieved due to the limited bandwidth of the MZMs.

In this section, a pump-linewidth-tolerant OWC in a PPLN waveguide is presented,

using a TTG to produce correlated pump waves with a frequency separation of 50 GHz.

4.2.1 Experimental set-up

The experimental set-up used for the demonstration of pump-linewidth-tolerant OWC is shown in figure 4.7. In order to minimize the phase noise of the input signal, a fiber laser (FL) with an emission linewidth of 10 KHz was used as the light source, modulated by an IQM. The IQM was driven by electric signals based on decorrelated 10 Gbaud PRBSs with length of $2^{15}-1$, generated in an arbitrary waveform generator (AWG). Next, the input signal was amplified in an EDFA and the excessive out-of-band ASE noise was removed by a 1 nm BPF. After passing through a PolC, the input signal was combined with the pump waves through the 10% port of a 10:90 coupler. For comparison, two different pump configurations were studied, one with coherent pumps and the other using two free-running lasers. In both cases, either DFBs or ECLs were used as light sources. In the coherent pumps configuration, a single DFB or ECL was used to generate the two correlated pump waves in a TTG built with a high extinction ratio MZM driven by a 25 GHz RF clock. In the free-running pumps configuration, two independent ECLs or DFBs were used as pump waves. The linewidth of the ECLs and DFBs used to generate the pump waves was of about 500 kHz and 3.5 MHz, respectively. After amplification in a high-power EDFA, noise filtering in a 2 nm BPF and state of polarization tuning, the pump waves were combined with the input signal and injected into the PPLN waveguide for OWC.

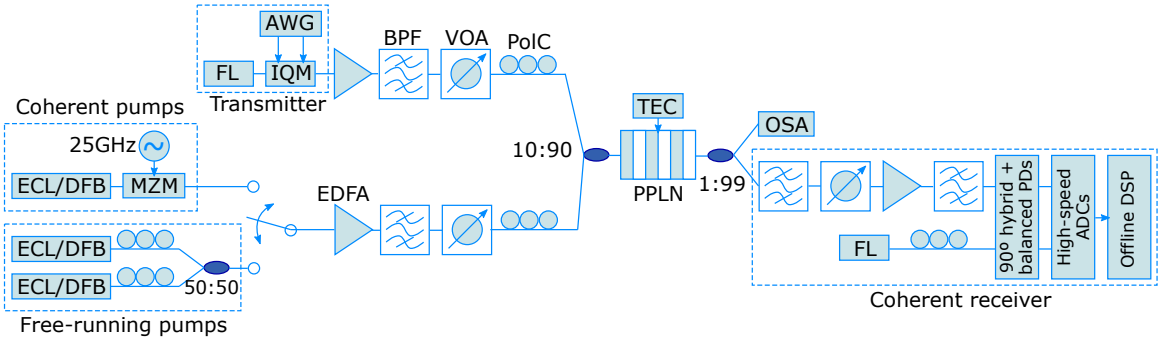

Figure 4.7: Experimental set-up used for pump-linewidth-tolerant OWC.

A uniform APE PPLN waveguide doped with 5% magnesium oxide was used in this experiment in order to prevent photo-refractive damage at high pumping power. The length, poling period, temperature of operation, λ_{QPM} and insertion losses of the PPLN device were 6 cm, 19.1 μm, 30.1 °C, 1550.4 nm and 3.25 dB, respectively. The nonlinear device was mounted on top of a TEC element to guarantee a stable temperature of operation and to tune the QPM wavelength. The experimental and simulated SHG conversion efficiency spectra of the PPLN waveguide are depicted in figure 4.8. A maximum normalized conversion efficiency of about 12 $W^{-1}cm^{-2}$ was measured at the QPM wavelength, with a full width at half maximum bandwidth of about 25 GHz.

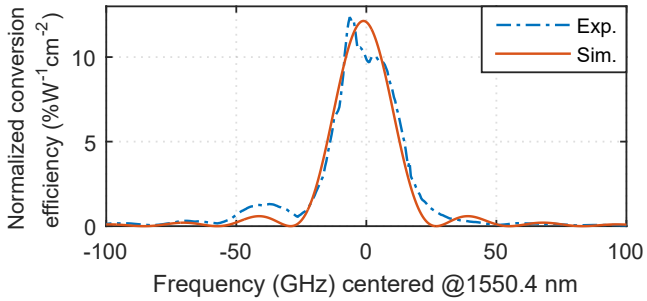

Figure 4.8: Experimental and simulated normalized SHG conversion efficiency of the PPLN waveguide used in the pump-linewidth-tolerant OWC experiment. The simulations were performed using a 4th-order Runge-Kutta algorithm.

After OWC, 1% of the light coming out of the PPLN waveguide was injected into an OSA for monitoring and the remaining signal was led into the coherent receiver block. The coherent receiver comprised a tunable BPF to remove the pump waves, a VOA, an EDFA and another BPF, before an optical 90° hybrid with balanced PDs at its output ports, that allowed varying the OSNR of the received signal. A FL with emission linewidth of 10 kHz was used as a local oscillator. The detected signals were digitized at 50 GSample/s by high-speed analog-to-digital converters (ADCs) with an analog bandwidth of 12.5 GHz. The captured data was then processed offline through digital signal processing (DSP) techniques, including compensation of skew and power imbalance, resampling, linear equalization, carrier phase-estimation, and final hard-decision circuits [171]. For a fair comparison, the same digital equalizer was used in both coherent and free-running pumps.

4.2.2 Wavelength converter characterization

Before evaluating the performance of the proposed scheme, the properties of the wavelength converter were characterized by turning the modulation off, and using ECLs as light sources for the interacting waves. The influence of the total power of the pump waves, P_T, the frequency separation between the DFG (*P1*) and SFG (*P2*) pumps, Δf_p, and between the SFG pump and the input signal, Δf_s, was evaluated by measuring the conversion efficiency (CE), signal depletion (SD) and optical spectra after the PPLN device. In this section, the CE is defined as the power ratio between the converted and input signal waves, whereas the SD is the power ratio of the input signal before and after the PPLN waveguide. The experimental results are summarized in figure 4.9. In this work, the same power for the SFG and DFG pumps was considered in order to achieve optimal performance in terms of both CE and SD.

As expected, both the CE and SD tend to increase with the total power of the pump waves as a consequence of a stronger nonlinear conversion. However, in figure 4.9-a), the CE and SD for Δf_p = 25 GHz increase up to P_T values of 27 dBm and then start to decrease. This behavior can be explained by the generation of spurious cascaded TWM

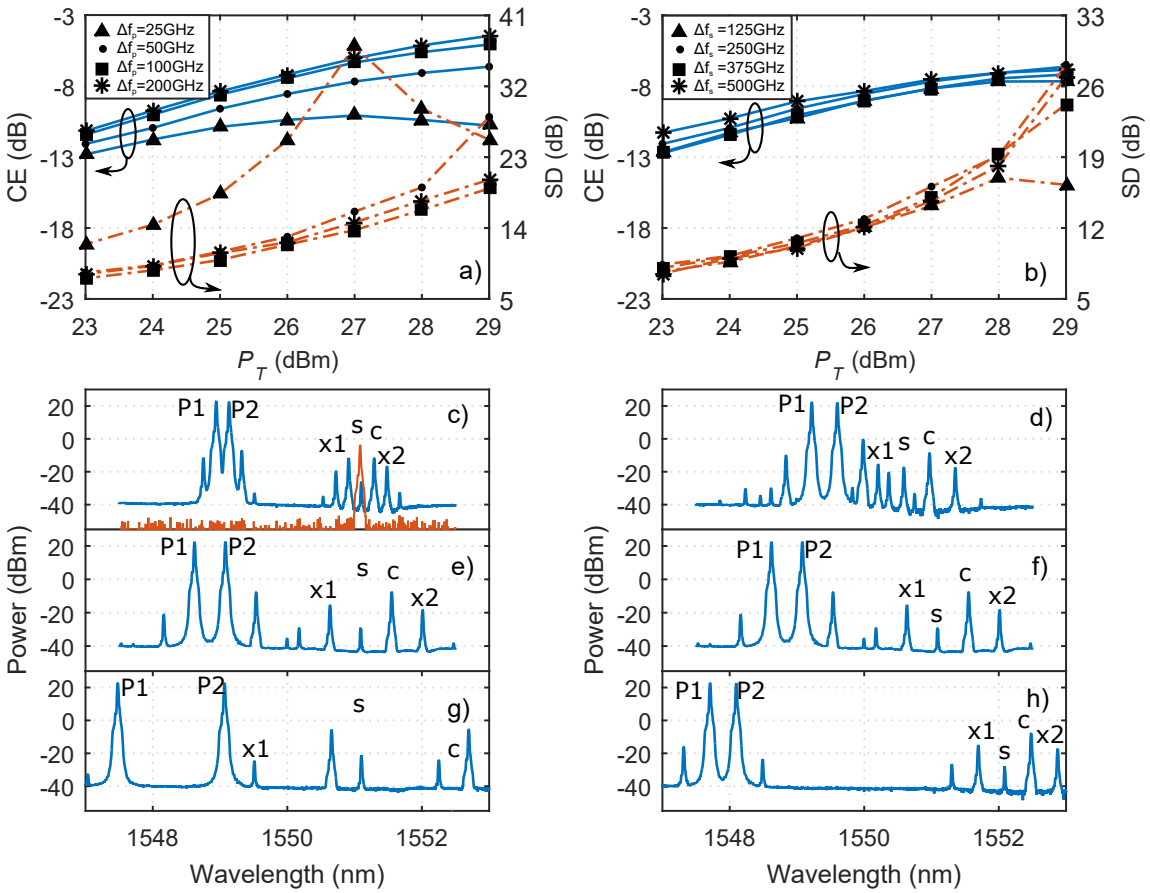

Figure 4.9: Variation of the CE (solid blue line) and SD (dashed-dotted orange line) with P_T for different a) Δf_p, for Δf_s of 250 GHz, and b) Δf_s, for Δf_p of 50 GHz. Optical spectra measured after OWC for Δf_s of 250 GHz and Δf_p of c) 25 GHz, e) 50 GHz, and g) 200 GHz. Optical spectra measured after OWC for Δf_p of 50 GHz and Δf_s of d) 125 GHz, f) 250 GHz, and h) 500 GHz. In c), the orange line represents the spectrum measured at the PPLN output with the pumps turned off. The input power of the signal was set to -1dBm for all the measurements, and the optical spectra of c)-h) were obtained for P_T = 29 dBm.

interactions that originate new waves close to the input (*s*) and converted (*c*) signals, such as waves *x1* and *x2*, shown in the optical spectra of figure 4.9. The spurious contributions at frequencies $\nu_{x1} = \nu_{P1} + \nu_s - \nu_{P2}$ and $\nu_{x2} = \nu_{P2} + \nu_c - \nu_{P1}$ partially deplete the converted and input signals, decreasing the CE and increasing the SD. The spurious waves become particularly strong when Δf_p is small as the phase mismatching condition for the SFG interactions between waves *P1* and *c*, and *P2* and *s* is close to the QPM resonance. For the particular case of Δf_p = 25GHz, the generation of the spurious waves is so strong that the input signal is fully depleted at a P_T value of 27 dBm. At higher pump power values, the power of the converted wave starts to flow back to the input signal, and both the CE and SD decrease.

The influence of P_T for different values of Δf_s is also depicted in figure 4.9-b). According to the experimental results, both the CE and SD do not significantly change with Δf_s, with the exception of the SD curve for Δf_s = 125 GHz, at P_T = 29 dBm. In this case, the

observed result can be explained by the presence of several spurious contributions close to the QPM wavelength that also interact with each other, and affect the SD of the input signal, particularly at high P_T values.

The optical spectra depicted in figures 4.9-c) to 4.9-h) also show additional spurious contributions around the pump waves that were already observed before the PPLN waveguide and were generated through FWM between the pumps in the EDFA and patch cords. Therefore, a special care must be taken when choosing Δf_p and Δf_s in order to avoid spectral overlap between the spurious FWM waves and the input and converted signals.

The influence of the input signal power, P_s, on the CE and SD was also investigated, showing that both remained almost unchanged, at least up to P_s values of 7 dBm, as shown in figure 4.10. A higher SD of about 27 dB was observed in figure 4.10 compared to the results presented in figure 4.9-b), where a SD of about 22 dB was observed for the same total pump power and frequency separation values. In fact, when the power of the input signal is almost fully depleted, the SD becomes very sensitive even to small variations of the total pump power, misalignment of the coupling optics or detuning from the QPM condition, which explains the observed differences. For instance, a variation of the SD from 19 to 27 dB was observed in figure 4.9-b) by varying P_T from 28 dBm to 29 dBm, which illustrates the sensitivity of the SD to the total pump power when the input signal is almost fully depleted.

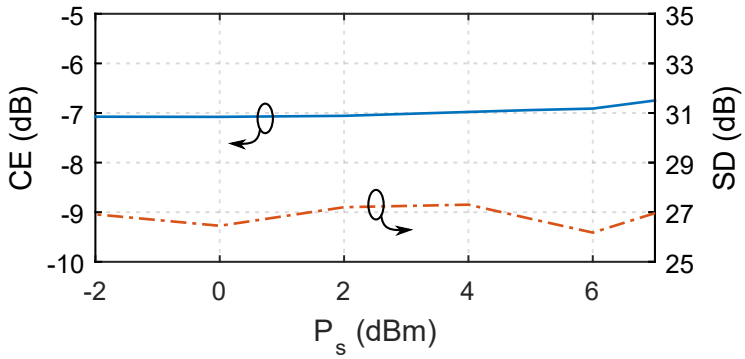

Figure 4.10: Variation of the CE (solid blue line) and SD (dashed-dotted orange line) with P_s for P_T = 28.3 dBm, Δf_p = 50 GHz and Δf_s = 500 GHz.

4.2.3 Pump-linewidth-tolerant OWC of QAM signals

After characterizing the performance of the wavelength converter in terms of CE and SD, the modulator was turned on and a FL was used as the input signal light source, emitting at 1552.52 nm. The wavelength of the pump wave in the coherent pumps configuration was set to 1548.08 nm, whereas two light sources emitting at 1547.88 nm and 1548.28 nm were considered in the free-running pumps configuration. The wavelength of the two pump waves in the free-running pumps configuration was selected in order to match that of the coherent pumps after the TTG. A frequency separation between the SFG pump and the

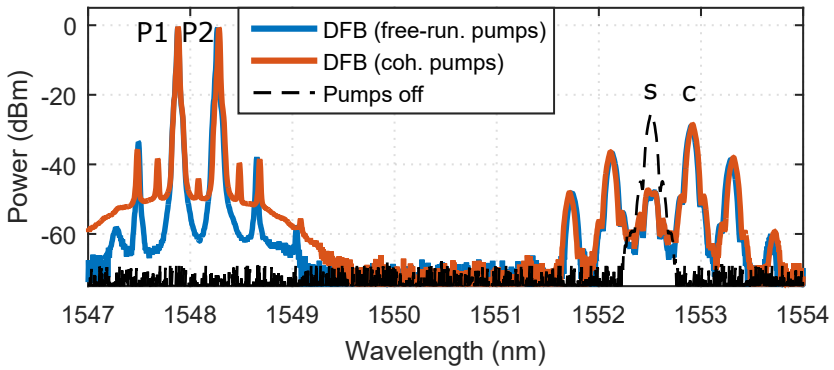

Figure 4.11: Optical spectra measured after the PPLN device for OWC of 10 Gsymbol/s 64-QAM signals, considering free-running (solid blue line) and coherent (solid orange line) DFB pumps, and when the pump waves are turned off (dashed black line).

input signal of more than 500 GHz was also considered in order to avoid spectral overlap and crosstalk between the spurious contributions, and the input and converted waves. The total pump power launched into the PPLN for OWC of QAM signals was set to 28.8 dBm, obtaining a CE of -6.5 and SD of about 25 dB for both pump configurations and using either ECLs or DFBs. The total pump power launched into the PPLN was tuned in order to maximize the SD. Usually, the remaining input signal must also be filtered out in the OWC units of optical transport networks in order to make the wavelength channel available for other data signals. If the SD of the OWC process is sufficiently high, this requirement is automatically met, without requiring additional optical filters. This is the main reason for tuning the total pump power to the maximum possible SD. The frequency separation between the two pumps was limited to 50 GHz due to the bandwidth of the TTG, so non-negligible spurious waves close to the input and converted signals are present at the output of the PPLN, as shown in figure 4.11. As discussed in the previous subsection, the spurious contributions are responsible for lower CE and SD values. The input signal power was set to 6 dBm.

In order to compare the sensitivity to the phase noise due to the finite linewidth of the pump waves, the constellation diagrams of the converted signals for both free-running and coherent pumps configurations are plotted in figure 4.12. As shown in figure 4.12, clear constellations can be observed for the converted signals using coherent pumps. In this case, the amplitude and phase noise properties of the converted signal symbols are similar using either an ECL or a DFB as the pump source. In the free-running configuration using ECLs as pumps, clear constellations are also obtained, but a small distortion of the received symbols due to the phase noise of the pumps starts to become evident, in particular for 64-QAM, at higher amplitude levels. When DFBs are used as pumps, the added phase noise is even greater, leading to strong random rotation and phase spreading of the symbols.

These results were also confirmed through BER measurements and recovered carrier phase after coherent reception, shown in figure 4.13. Considering the coherent pumps

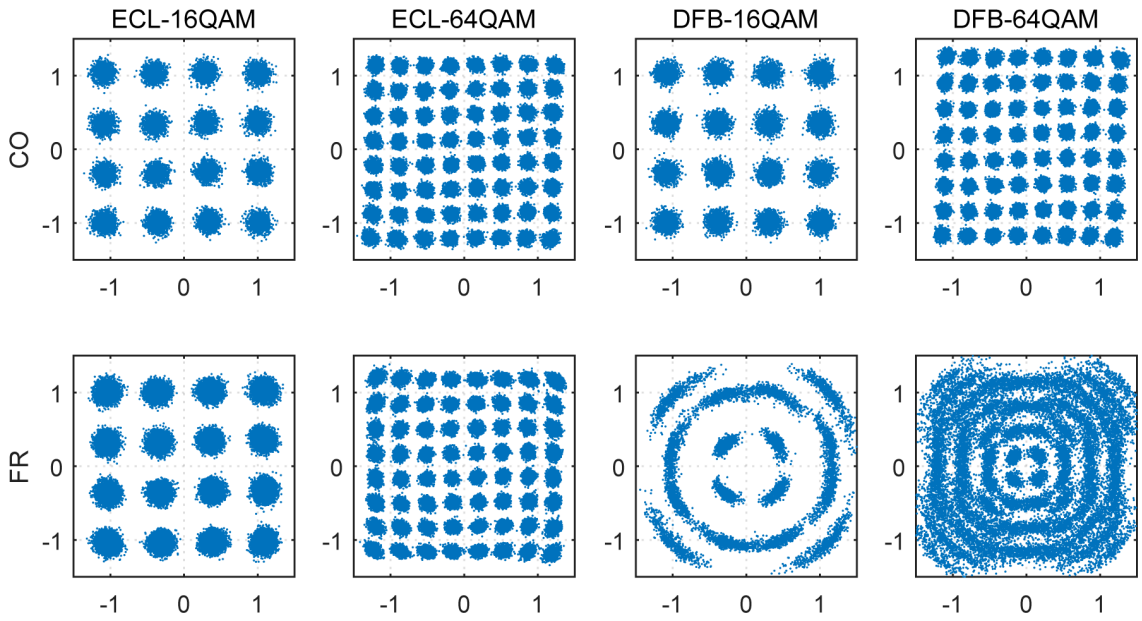

Figure 4.12: Measured constellation diagrams of the converted signals using either ECLs or DFBs as pumps, and considering both coherent (CO) and free-running (FR) pump waves. The constellation diagrams were obtained at OSNR values of 18 and 34 dB for the 10 Gsymbol/s 16-QAM and 64-QAM signals, respectively.

configuration, the BER values of the converted signals are approximately the same of the input signal ones, using either an ECL or a DFB as the pump source. Negligible OSNR penalties of less than 0.1 dB for 16-QAM and 0.3 for 64-QAM at a BER of 10^{-3} were measured for this configuration. In the case of the free-running pumps experiment, even though a small OSNR penalty of less than 0.3 dB at a BER of 10^{-3} is observed for the 16-QAM signal using ECLs, an error floor due to the additional phase noise at BER values of about 10^{-5} is observed for 64-QAM. When using free-running DFB lasers as pumps, the coherent receiver could not track the carrier phase at any OSNR value due to the strong phase noise from the pumps. BER values of the order of 10^{-1} are observed in this case.

The effectiveness of the proposed scheme is also proven by the recovered carrier phase, shown in figure 4.13-b). As depicted in the figure, the recovered carrier phase of the received signals drifts in time due to the finite linewidth of the laser sources. In the case of the input signal, the phase drift is small due to the narrow linewidth FLs used as light sources for the input signal itself and the local oscillator. This is not the case, however, for the converted signal using free-running DFB pumps, whose phase drift is stronger due to the added phase noise from the pumps. Using coherent pumps, a much weaker carrier phase drift of the converted signal is observed, similar to that of the input signal.

The constellation diagrams, BER measurements and recovered carrier phase prove that the additional phase noise from the pumps is canceled out at the converted signal and show that the proposed scheme is an effective way to eliminate the additional phase noise at OWC units.

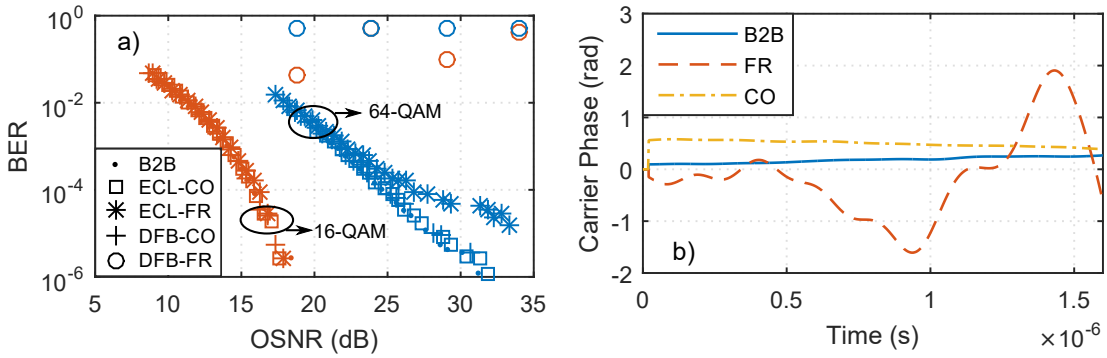

Figure 4.13: a) BER as function of the OSNR, measured with an optical resolution of 0.1 nm for the input signals measured back-to-back (B2B) and converted signals using coherent ECLs pumps (ECL-CO), free-running ECLs (ECL-FR), coherent DFBs (DFB-CO) and free-running DFBs (DFB-FR). The orange and blue curves represent the BER measurements for 16-QAM and 64-QAM signals, respectively. b) Recovered carrier phase of the input signal measured back-to-back (B2B) and of the converted 16-QAM signals, using free-running (FR) and coherent (CO) pumps.

The pump-linewidth-tolerant scheme has also been recently implemented using FWM in HNLFs, showing similar results and conclusions [172]. However, a special care regarding the launched signal and pump power had to be taken in order to mitigate distortions due to SPM, XPM and SBS, which is a disadvantage compared to OWC based on PPLN devices.

4.3 Pump-linewidth-tolerant wavelength data exchange

Data exchange is an important OSP functionality to improve the performance and efficiently manage the resources of optical transport networks, used when the information carried in two different data channels needs to be swapped in either the wavelength, time or polarization domain [173–177]. In the case of WDE, the information between two channels at different wavelengths is interchanged. Hence, WDE can be regarded as two OWC processes occurring at the same time.

WDE can be implemented using two different schemes, depicted in figure 4.14. The most straightforward method is to separate the channels into two different paths, use two independent wavelength shifters to convert the channels and combine them again, after OWC. This approach, however, requires two independent OWC blocks and additional WDM multiplexers/demultiplexers. In addition, dynamic WDE of only a few symbols or data packets requires precise alignment of the two path lengths in order to avoid symbol overlapping in the time domain after recombining the converted signals.

The second method to perform WDE is based on parametric depletion, combining simultaneous OWC through nonlinear parametric interactions and power depletion of the initial channels in a single wavelength converter. In this configuration, each channel is completely depleted and its power is transferred to the wavelength of the other channel.

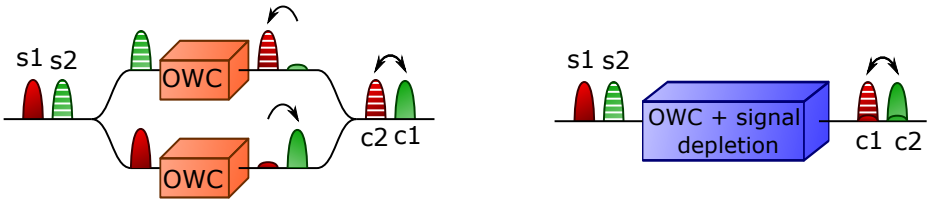

Figure 4.14: Schematic representation of WDE using two independent wavelength converters, shown on the left, and using a single wavelength converter combined with signal depletion, shown on the right.

Besides the advantage of requiring only a single device to perform WDE, this scheme can also be easily modified to allow polarization insensitive operation using a polarization diversity loop [150]. However, the optimum conditions for the OWC block in this configuration have to be precisely controlled, as any remaining undepleted signal at the original wavelength acts as a crosstalk source, hereinafter referred to as WDE crosstalk, and deteriorates the converted signal.

As discussed in the previous section, parametric OWC can be implemented using either second- or third-order nonlinear devices, but due to the advantages of immunity to SPM, XPM and SBS, the discussion in this section is limited to PPLN-based WDE. WDE in PPLN devices is based on a cSFG/DFG interaction, with two input signals at frequencies ν_{s1} and ν_{s2}, and two pump waves at ν_{P1} and ν_{P2}. Let us consider that the frequency relations $\nu_{s2} + \nu_{P1} = \nu_{s1} + \nu_{P2} = \nu_{SF} = 2\nu_{QPM}$ hold exactly. In this case, a new wave at frequency ν_{QPM} is generated through two different SFG processes, one between waves $s1$ and $P2$ (SFG1) and another between $s2$ and $P1$ (SFG2), as depicted in figure 4.15. The SFG wave then participates in two different DFG processes, one promoted by pump $P1$ that generates a converted signal at $\nu_{c1} = \nu_{s2}$ (DFG1), and another fueled by pump $P2$, at $\nu_{c2} = \nu_{s1}$ (DFG2).

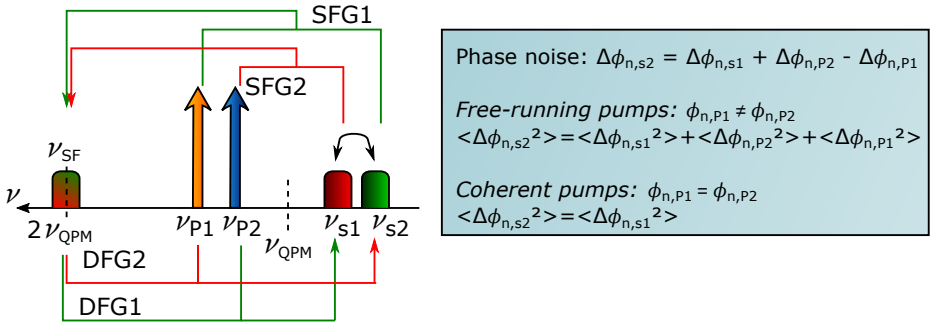

Figure 4.15: Schematic representation of pump-linewidth-tolerant WDE based on cSFG/DFG in a PPLN device.

In order to better understand the process and the optimum conditions for WDE let us consider the coupled equations describing cSFG/DFG presented in (2.30), assuming all the interacting waves are CWs, no pump depletion, perfect QPM and negligible propagation losses. Let us also assume that the waves labeled as 1, 2, 3, 4, and 5 in (2.30) are,

respectively, waves $P1$, $s2$, SF, $P2$ and $s1$ in figure 4.15. The evolution of the normalized electric field envelope of the waves is then given by

$$A_{SF}(z) = -i\kappa_{SF}\frac{A_{P1}A_{s2}(0) + A_{P2}A_{s1}(0)}{g}\sin(gz) \tag{4.4a}$$

$$A_{s1}(z) = A_{s1}(0) + \kappa_{SF}\kappa_{s1}\frac{\cos(gz)-1}{g^2}\left[P_{P2}A_{s1}(0) + A_{P1}(0)A^*_{P2}(0)A_{s2}(0)\right] \tag{4.4b}$$

$$A_{s2}(z) = A_{s2}(0) + \kappa_{SF}\kappa_{s2}\frac{\cos(gz)-1}{g^2}\left[P_{P1}A_{s2}(0) + A_{P2}(0)A^*_{P1}(0)A_{s1}(0)\right], \tag{4.4c}$$

where $g = [\kappa_{SF}(\kappa_{s2}P_{P1} + \kappa_{s1}P_{P2})]^{1/2}$. The previous equation can be further simplified when $P_{P1} = P_{P2}$, and assuming $\kappa_{s1} \approx \kappa_{s2} \approx \kappa_{P1} \approx \kappa_{P2} \approx \kappa$ and $\kappa_{SF} \approx 2\kappa$, given by

$$A_{SF}(z) = -i\left[A_{s2}(0)e^{i\phi_{P1}} + e^{i\phi_{P2}}A_{s1}(0)\right]\sin(gz) \tag{4.5a}$$

$$A_{s1}(z) = \frac{\cos(gz)+1}{2}A_{s1}(0) + e^{i(\phi_{P1}-\phi_{P2})}\frac{\cos(gz)-1}{2}A_{s2}(0) \tag{4.5b}$$

$$A_{s2}(z) = \frac{\cos(gz)+1}{2}A_{s2}(0) + e^{i(\phi_{P2}-\phi_{P1})}\frac{\cos(gz)-1}{2}A_{s1}(0). \tag{4.5c}$$

According to the previous equations, the wave at frequency $2\nu_{QPM}$ is generated by a coherent sum of the two SFG processes and contains two independent contributions, one from each input signal. Each of such independent contributions is then converted to the other channel through DFG, but not to the original input signal, at least until the latter becomes fully depleted. This situation can be better understood by considering a simpler example, such as an SHG interaction. In an SHG process, as long as the relative phase of the two waves is matched and the fundamental wave is not fully depleted, the power of the fundamental wave keeps flowing to the second harmonic. The inverse process, i.e., the power flowing back to the fundamental wave, can only occur if the phase of the two waves is mismatched. In the case of the WDE process, each of the contributions from the different input signals are converted to the SFG wave and then to the converted channel with a specific phase relation with respect to the original signals. If such phase relation is kept along the PPLN device, each of the two contributions in the SFG wave cannot return to its original wave and must be converted to the other channel through DFG. Each of the converted waves is thus composed by a fraction of the initial wave which is progressively depleted along the PPLN device, and another portion due to OWC of the other input wave.

Effective WDE with negligible crosstalk can only be implemented when the initial wave is fully depleted, which occurs when $\cos(gL) = -1$, i.e., when gL is an odd multiple of π. In this case, $A_{s1}(L) = -e^{i(\phi_{P1}-\phi_{P2})}A_{s2}(0)$ and $A_{s2}(L) = -e^{i(\phi_{P2}-\phi_{P1})}A_{s1}(0)$, so the optical field of the converted waves becomes equal to the input signals one, multiplied by an imaginary exponential term including the phase of the pump waves. Remarkably, the optimum condition for WDE is exactly the same as for complete signal depletion and total power transfer to the converted waves in a simple OWC, obtained by setting the normalized electric field envelope of one of the input signals to zero in (4.5). In addition, the optimum condition for

WDE does not depend on the power of the input signals. Therefore, a simple and easy way to find the optimum pumping conditions is to block one of the input channels, transforming WDE into a simple OWC process, and maximize the CE and SD.

As discussed in the previous section, any phase noise due to finite linewidth of the pump waves is also transparently transferred to the exchanged signals during the WDE process. The additional phase noise becomes a particularly relevant impairing mechanism for advanced modulation formats and optical transport networks with several WDE units between the initial and destination nodes. Rather than using costly narrow linewidth laser sources as pump waves, the pump-linewidth-tolerant scheme discussed in the previous section is a viable solution to mitigate the deleterious additional phase noise from the pumps during the WDE process. The effectiveness and performance of pump-linewidth-tolerant WDE is discussed in the following subsections.

4.3.1 Experimental set-up

In order to evaluate the performance of the pump-linewidth-tolerant WDE scheme, an additional input data channel was included in the experimental set-up shown in figure 4.7. With the exception of the transmitter arms (Tx), all the remaining experimental set-up was kept unchanged and is not fully described again in this subsection. The upgraded set-up is depicted in figure 4.16.

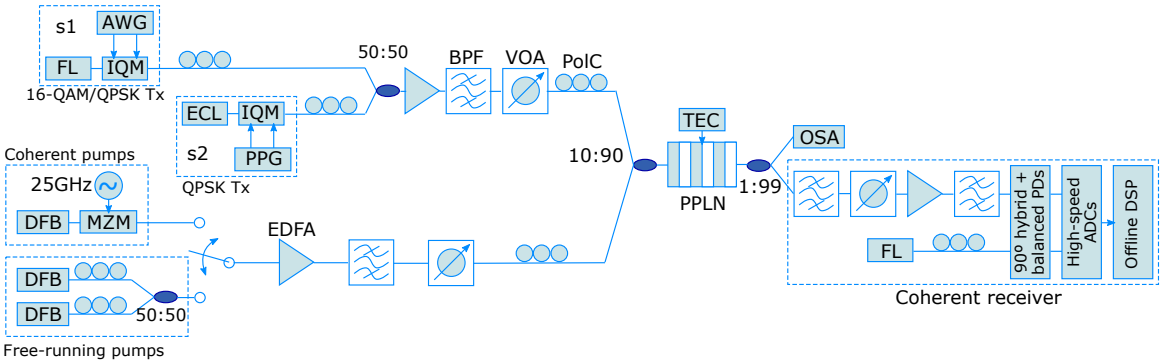

Figure 4.16: Experimental set-up for pump-linewidth-tolerant WDE.

The data channel $s1$ was generated from light emitted by a FL with linewidth of 10 kHz at 1552.48 nm, modulated by an IQM driven by two electrical signals based on decorrelated 12.5 Gsymbol/s PRBS streams of length $2^{15} - 1$, produced in a AWG. Both 16-QAM and QPSK formats were considered for channel $s1$. The other QPSK input signal ($s2$) was generated from an ECL emitting at 1552.9 nm with an emission linewidth of 100 kHz, and modulated by another IQM driven by two electric signals of decorrelated 10 Gsymbol/s PRBS streams of length $2^{15} - 1$, produced in a PPG.

The two data channels were then combined in a 50:50 coupler after passing through PolCs for state of polarization alignment, amplified in an EDFA and filtered in a 2 nm BPF. The two input signals were then combined with the pump waves before entering the PPLN

waveguide for WDE. In this experiment, the wavelength of the two pump waves was set to 1547.92 and 1548.32 nm in the free-running configuration and to 1548.11 nm when using coherent pumps.

Further details on the experimental set-up can be found in subsection 4.2.1.

4.3.2 Pump power optimization

In a simple OWC process, the CE is typically the most important property to consider, whereas the remaining power of the input signal may be secondary, or even not important at all. This is not the case for WDE, however, where any remaining initial signals degrade the exchanged ones, and the performance of the process is much more sensitive to the operation conditions. Therefore, the SD should be the main figure of merit to take into account for WDE. The main conclusions obtained in the previous section for OWC regarding the influence of parameters such as the frequency separation between the two pumps, and between the pumps and the input signals are also valid for WDE, so they are not discussed here again.

Obtaining the best pump power values for maximum SD and, consequently, the best performance conditions is not easy as the wavelength of the initial and exchanged channels is the same. A possible and accurate solution is to measure the BER of the exchanged signals at different values of the total pump power P_T. However, this approach may be quite complex and take a significant amount of time to perform, especially if no initial estimate for the optimum pump power is known. A simpler and effective alternative is to convert the WDE process into simple OWC by blocking one of the input signals, and measure the total pump power at which the maximum SD is observed. In principle, such a power value also provides the best optimum condition for WDE. In this subsection, the optimum pump power for WDE is optimized using the two methods.

In order to obtain the optimum pump power for WDE, the data modulation was turned off, and the CE and SD were measured for each OWC process by alternatively blocking one of the input signals. The obtained results are plotted in figure 4.17. Similarly to the pump-linewidth-tolerant OWC experiment discussed in the previous section, the SD increases with P_T due to stronger wavelength conversion, until it reaches a maximum value of more than 30 dB for a total pump power of about 28.5 dBm. At higher P_T values, the power of the converted signal starts to flow back to the original wave, and the SD and CE decrease. Both the CE and SD remain practically constant with P_s, with fluctuations of the SD of about 1 dB. As mentioned in the previous section, the SD is severely affected by any variation of the total pump power, detuning from the QPM condition, misalignment of the coupling optics or even changes on the state of polarization of the waves, which justify the observed fluctuations of the SD. Contrarily to what was expected, however, the maximum SD for each OWC process is not achieved at the same pump power value, but at 28.3 dBm when the input signal is at 1552.48 nm, and at 29 dBm for the other case. Until this point it was assumed that the frequency relation between the interacting waves is exactly given

by $\nu_{s2} = \nu_{s1} + \nu_{P2} - \nu_{P1}$, so the frequencies of the converted signals become $\nu_{c2} = \nu_{s1}$ and $\nu_{c1} = \nu_{s2}$. Yet, this is seldom the case in real systems as the frequency of the laser sources of each signal channel is not correlated and may drift in time. As a consequence, the overall WDE process is in fact composed of two independent OWC steps based on different cSFG/DFG interactions, with input signal $s1$ being converted to a frequency that is close, but not necessarily equal to ν_{s2}, and vice-versa. In theory and assuming perfect QPM, the optimum pump power conditions to achieve maximum SD of each individual OWC process and to minimize the WDE crosstalk of each cSFG/DFG interaction should be the same. However, any small frequency deviation from the QPM resonance due to finite precision and accuracy when tuning the wavelength of the laser sources leads to slightly different CEs and pump power values where the maximum SD is achieved. This is the reason why maximum SD is not achieved at the same pump power.

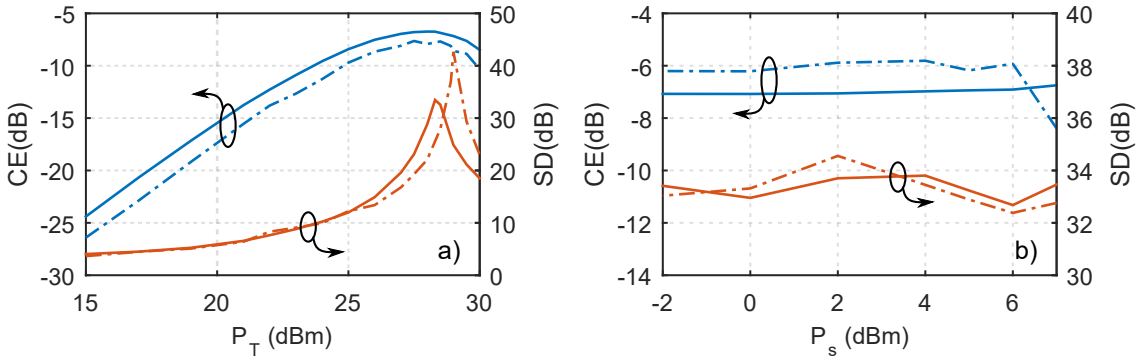

Figure 4.17: Variation of the CE and SD of each OWC process for a) P_T with P_s = 7 dBm, and b) P_s with P_T = 28.3 dBm. The solid and dashed-dotted lines represent OWC with input signal at 1552.48 nm ($s1$) and 1552.9 nm ($s2$), respectively.

The optimum pump power was also determined through BER measurements of the exchanged channels in a WDE process, with two input QPSK signals at symbol rates of 12.5 Gsymbol/s ($s1$) and 10 Gsymbol/s ($s2$). The experimental results are shown in figure 4.18, obtained at an OSNR of about 9 dB, measured with a frequency resolution of 0.1 nm. According to the experimental results, the minimum BER for signals $s1$ and $s2$ are respectively observed at P_T of 28.5 dBm and 29 dBm. These results are consistent with those obtained by measuring the SD of the individual OWC processes, proving the effectiveness of such method to determine of the best pump power conditions for WDE. In general, measuring the SD for each individual OWC process is a better strategy for an initial coarse tuning of the pump power, whereas the BER measurements are a better metric for fine tuning and direct assessment of the WDE performance.

The BER measurements also show that the tolerance range for non-optimal pump power is smaller for signal $s1$, as a consequence of stronger susceptibility to WDE crosstalk for higher baud-rate signals. The optimization of the pump power is thus crucial for WDE, as even a small deviation of less than 1 dB is enough to deteriorate the SD by more than 10 dB and the BER by one order of magnitude due to WDE crosstalk. Therefore, stable

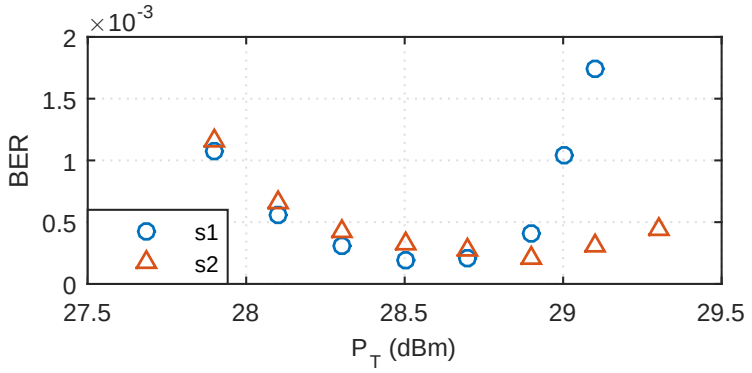

Figure 4.18: BER of the exchanged signals after WDE for different pump power values.

and precise tuning of the pump power, as well as of the PPLN temperature to guarantee a constant QPM wavelength are critical. In the following subsection, the performance of the pump-linewidth-tolerant WDE process is evaluated at an optimal pump power of 28.5 dBm.

4.3.3 Pump-linewidth-tolerant WDE of QAM and QPSK signals

The performance of the WDE process using coherent or free-running pump waves is evaluated in this subsection by inspecting the constellation diagrams and through BER measurements as function of the OSNR. Data exchange between either two 10 Gbaud and 12.5 Gbaud QPSK channels is assessed in this subsection, as well as between one 10 Gbaud QPSK and a 12.5 Gbaud 16-QAM signal.

The optical spectra of the exchanged data is depicted in figure 4.19. A CE of about -6 dB and -7 dB was observed for signals $s1$ and $s2$, respectively, in either the coherent or free-running pumps configurations. The measured CE values are consistent with those obtained for simple OWC processes, described in the previous subsection. Spurious waves around the exchanged signal can also be observed. In addition to the insertion losses, the

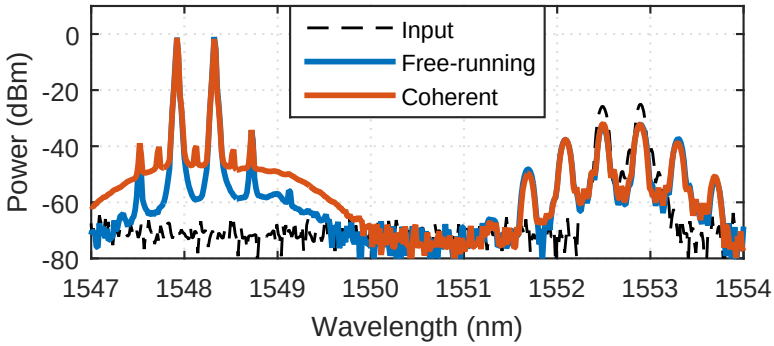

Figure 4.19: Optical spectra measured after the PPLN device for WDE between two QPSK signals, considering free-running (solid blue line) and coherent (solid orange line) DFB pumps. The spectrum of the signals at the input to the PPLN is represented by the dashed black line.

spurious waves are also responsible for reducing the CE.

The constellation diagrams of the received channels are plotted in figure 4.20 for WDE between two QPSK signals, on the left, and between a QPSK and a 16-QAM signal, on the right, using either coherent or free-running pump waves. In both cases, the phase and amplitude noise properties of the exchanged channels are deteriorated with respect to the constellations measured back-to-back (B2B). In the case of the coherent pumps configurations, a similar and symmetrical degradation of the real and imaginary parts of the received symbols is observed, caused by the WDE crosstalk. In the free-running configuration, however, the received symbols are not only affected by the WDE crosstalk, which is responsible for the amplitude noise deterioration, but also by the phase noise due to finite linewidth of the pump waves. The additional phase noise causes a greater symbol spreading around the phase angle. In order to support this claim, let us consider the standard deviations of the amplitude and phase noise for WDE between two QPSK signals as an example. As regards the amplitude noise, standard deviation values of 0.037, 0.102 and 0.113 were measured for the B2B, CO and FR constellations of signal $s1$ and of 0.037, 0.113, 0.0913 for signal $s2$, respectively. For both data channels, the degradation of the amplitude noise with respect to the back-to-back measurements was comparable, which means that the amplitude noise is degraded mostly because of the WDE crosstalk. On the other hand, standard variation values for the phase noise of 0.047, 0.102 and 0.191 were respectively obtained in constellations B2B, CO and FR for channel $s1$, and of 0.033, 0.108 and 0.230 for channel $s2$. The obtained values prove that the phase noise degradation in constellations FR is greater than in the CO ones, which can only be explained by the additional phase noise due to finite linewidth of the pumps. The symbol spreading along the phase angle is also observed in the constellation diagrams labeled OWC in figure 4.20, where the WDE scheme with free-running pumps was turned into simple OWC by blocking one of the input signals. The obtained results show negligible amplitude deterioration compared to the B2B constellations as a consequence of eliminating the WDE crosstalk. However, the symbol spreading along the phase angle is still evident, which is a consequence of the phase noise due to the finite linewidth of the pumps.

The BER measurements of the WDE process between two QPSK signals are presented in figure 4.21. OSNR penalties of about 0.8 dB and 0.3 dB at a BER of 10^{-3} were respectively measured for the 10 Gbaud and 12.5 Gbaud channels in the coherent pump configuration, whereas 4.8 dB and 4 dB penalties were observed using free-running pumps. Moreover, a BER floor at approximately 3×10^{-4} is observed for the free-running pumps configuration. Similar results were obtained for WDE between 10 Gbaud QPSK and 12.5 Gbaud 16-QAM channels, with measured penalties of 0.6 dB and 3 dB using coherent pumps. In the free-running pumps configuration, a penalty of about 3.4 dB was obtained for the QPSK signal, with an error floor at a BER of 5×10^{-4}. Due to higher susceptibility of the 16-QAM format to both phase and crosstalk noise, the DSP unit was not able to recover the signal, so incongruent and inconsistent BER measurements were obtained for

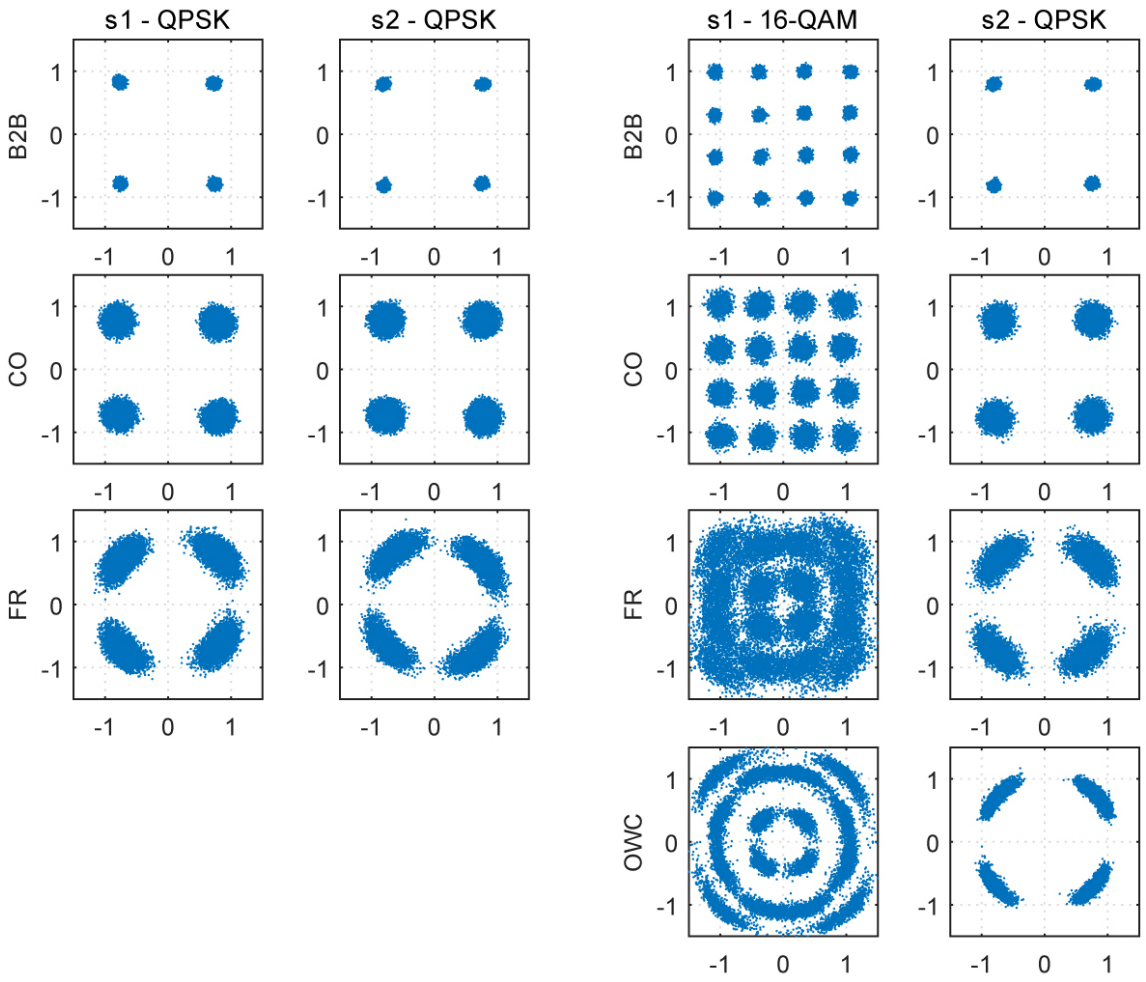

Figure 4.20: On the left, constellation diagrams for the 12.5 Gbaud QPSK (s1-QPSK) and 10 Gbaud QPSK (s2-QPSK) signals, measured back-to-back (B2B) before WDE, and after WDE using coherent (CO) and free-running (FR) pumps. On the right, constellation diagrams for the 12.5 Gbaud 16-QAM (s1-16QAM) and 10 Gbaud QPSK (s2-QPSK) signals, measured back-to-back (B2B) before WDE, and after WDE using coherent (CO) and free-running (FR) pumps. At the bottom, on the right, constellation diagrams of the 12.5 Gbaud 16-QAM and 10 Gbaud QPSK signals considering a simple OWC process and using free-running pumps. The constellation diagrams were obtained at OSNR values of about 24 dB, measured with an optical resolution of 0.1 nm.

the swapped 16QAM signal at every achievable noise level.

The effectiveness of the pump-linewidth-tolerant scheme for WDE is also proven by the recovered carrier phase of the exchanged 12.5 Gbaud QPSK signal in the DSP unit, shown in figure 4.22. A small and comparable phase drift of less than 0.6 radians for the input signal and exchanged channel in the coherent pumps configuration is observed within a time range of 1.6 μs. On the other hand, a phase drift of about 12 radians was measured using free-running pumps. Therefore, the recovered carrier-phase results prove that the phase noise from coherent pump waves is also canceled out in WDE, as previously discussed for simple OWC.

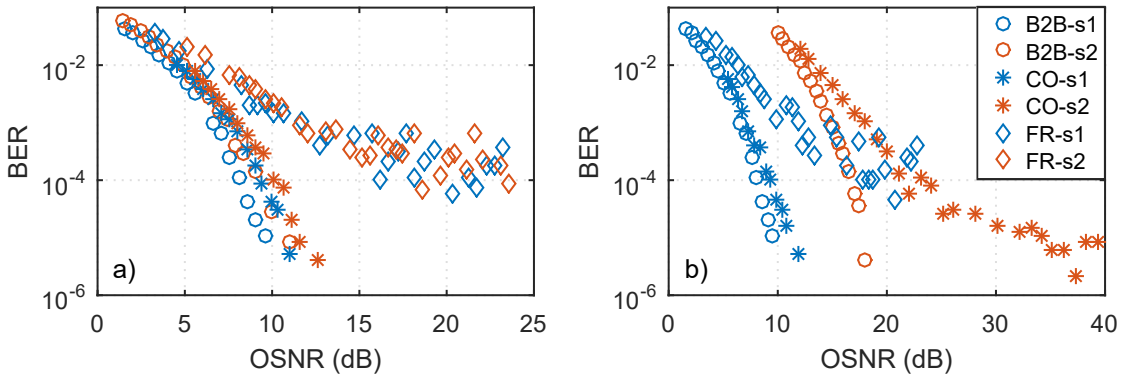

Figure 4.21: BER as function of the OSNR for WDE between a) a 12.5 Gsymbol/s QPSK channel ($s1$) and another QPSK signal at 10 Gsymbol/s ($s2$), and b) a 12.5 Gsymbol/s 16-QAM channel ($s1$) and a 10 Gsymbol/s QPSK ($s2$) signal. The obtained curves were measured back-to-back (B2B-s1 and B2B-s2), after WDE using coherent pumps (CO-s1 and CO-s2), and after WDE using free-running pumps (FR-s1 and FR-s2).

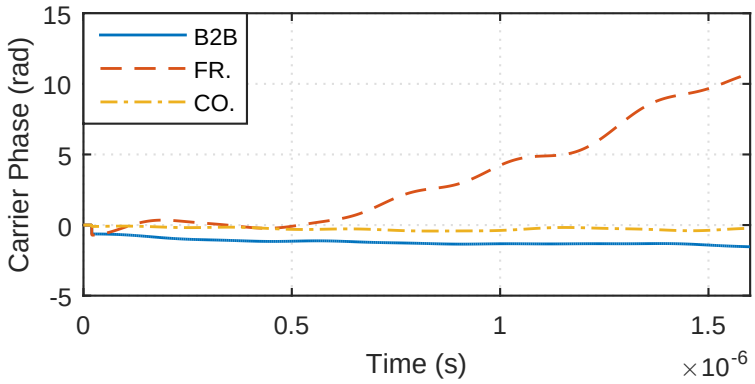

Figure 4.22: Recovered carrier phase in the DSP unit for the input and exchanged 12.5 Gbaud QPSK channel ($s1$).

In this chapter, two different schemes for OWC with advanced properties and functionalities were discussed. By using a PPLN device with a customized poling pattern, simultaneous OWC of 8 WDM channels with tunable output wavelength was demonstrated. Even though tunable operation was experimentally proved, the low conversion efficiency and non-negligible spurious waves degraded the overall performance of the wavelength converter. A trade-off between broadband operation, high conversion efficiency and generation of spurious waves was observed in the proposed strategy. A pump-linewidth-tolerant scheme was also investigated in order to mitigate the additional phase noise caused by the finite linewidth of the pump waves. The proposed scheme proved to be effective for both simple OWC of a single data signal and for WDE between two channels. Even though the pump-linewidth-tolerant scheme enables deploying cheaper laser sources as pumps (e.g., DFB lasers), the generation of the coherent pump waves required an additional lithium niobate MZM and a RF clock generator to drive the modulator. Cheaper possibilities can be investigated in order to obtain an even more attractive solution for low-noise OWC.

Chapter 5

Phase-sensitive amplification and signal regeneration

PSAs are a particular class of optical amplifiers whose gain depends on the relative phase of the input waves. The PS gain of PSAs enable unique properties and features that cannot be found in any other type of amplifier, such as possibility of direct phase regeneration [178], and low-noise amplification with noise figures below the 3 dB quantum limit of phase-insensitive amplifiers (PIAs) [179].

Historically, the first studies on optical PS detection and amplification date back to the decade of 1960 [180–182]. However, it was not until about 2005 that PSAs became relevant for applications in fiber-optics communication systems [25, 178, 183–186], driven by an increased interest in OSP solutions for high-capacity lightwave systems and several notable technological advances during the 1990s. The development of high-quality HNLFs [187], the demonstration of amplification with NF values below 3 dB [188] and the development of solutions for frequency and phase synchronization [189, 190] are some examples of such groundbreaking advances.

Two main alternatives have been used to build a PSA for OSP. One of the possibilities, originally proposed by Marhic *et al.* [191], relies on the interference of an input signal wave, also known as probe, and a strong pump at exactly the same frequency (degenerate frequency) in a nonlinear optical loop mirror, i.e., a Sagnac interferometer built with a Kerr media [26, 184]. In such kind of interferometric PSAs, the power of the pump wave at the output of each port of the interferometer is determined by the nonlinear phase shifts caused by the Kerr effect and by the relative phase between the signal and pump waves. In practice, PS amplification in interferometric PSAs originates from different reflectivity/transmissivity of the pump induced by the input probe. [26]. The other possibility to implement a PSA is based on parametric nonlinear interactions such as TWM and FWM, so they are commonly known as parametric or non-interferometric PSAs. The principle of operation of parametric PSAs is based on the coherent mixing between the new contributions generated from the parametric nonlinear interaction and the light already propagating in the nonlinear medium, at the same frequency. Depending on their relative phase, the two contributions can beat constructively or destructively, leading to signal amplification or de-amplification (attenuation), which provides the PS properties to the amplifier. Even though remarkable phase regeneration results have been reported using interferometric PSAs [26], these amplifiers are considerably impaired by SBS, which introduces uncorrelated phase fluctuations and degrades the phase correlation between the signal and pump waves [183, 192]. Consequently, interferometric PSAs have been deprecated in favor of parametric PSAs for applications in OSP. The discussion in this thesis is thus limited to parametric PSAs.

Parametric PSAs can be implemented using a wide variety of either second- or third-order nonlinear media [25, 49, 186, 193–198] and in different configurations, classified according to the number of pumps and the number of modes, i.e., the number of correlated signal and idler waves. So far, the most common choice for phase regeneration and low-noise amplification in optical systems has been based on PSAs built with HNLFs in a dual-

pump, one mode configuration, also known as degenerate idler or simply as degenerate PSA, or in a single-pump, two-mode topology, also referred to as degenerate pump or just non-degenerate PSA [25, 49, 53, 185, 198–202]. PPLN waveguides have been considered a very attractive alternative for the nonlinear media of a PSA due to their compactness, possibility of integration, negligible frequency chirp, ASE noise, SPM and XPM, and immunity to SBS [20, 203]. However, the gain of PPLN-based PSAs is typically very modest, of about 5 dB even at pump power levels above 20 dBm [203, 204]. Recently, high SHG conversion efficiencies of about 2400%/W have been reported in adhered ridge PPLN waveguides [125], which enabled achieving internal PS gain values of about 17.7 dB, but with a lower net gain of only 12 dB due to high insertion losses of 5.7 dB [50]. The reported results are very encouraging and suggest that PPLN devices are a possible alternative to build PSAs for OSP in optical communication systems. In addition, not only the common aforementioned dual-pump, one-mode and single-pump, two-mode configurations can be implemented in PPLN-based PSAs through cSHG/DFG, but different possibilities based on simple DFG can also be explored [205]. However, a proper comparison in terms of gain and conversion bandwidth for the different possibilities using PPLN-based PSAs has not yet been performed. Such a comparison should provide important and valuable conclusions on the most suitable configurations for different applications in optical systems. Hence, approximated expressions for the gain of different configurations of PPLN-based PSAs are provided in the first section of this chapter. The conversion bandwidth and the influence of the length and normalized conversion efficiency on the gain properties of the different configurations are also numerically evaluated in section 5.1.

Parametric PSAs require two fundamental conditions for stable operation. First, PSAs require frequency- and phase-correlated waves at the input of the amplifier, otherwise they become simple PIAs. Second, the relative phase of the correlated waves must be locked to the optimum gain condition in order to avoid fluctuations of the gain of the amplifier. The first condition can be fulfilled by generating several correlated emission lines from a single light source using an optical comb [53], or by the so-called copier + PSA scheme, originally proposed by Tang *et al.* [185]. The copier + PSA scheme is a viable alternative in which the correlated waves are generated first in a PI parametric amplifier, i.e., the copier amplifier, and then led to a PSA for PS operation. Not only the copier + PSA scheme is compatible with multichannel operation [193, 203, 206], but it can also be extended to dual-polarization operation [193]. However, the copier + PSA strategy requires two parametric amplifiers.

The second condition is typically more difficult to attain as it implies compensation of the chromatic dispersion effects [39, 50, 207], and possibly active control of the relative phase of the waves. For instance, in many applications of PSAs it is necessary to separate the pumps from the other waves to another optical path for re-amplification and/or excessive noise filtering [25, 202, 208], as it is discussed in subsection 5.2.2. In order to keep the phase of the waves locked at the input of the amplifier, the length of the different optical paths must be matched using ODLs, and any phase-drift caused by acoustic vibrations

and/or thermal fluctuations of the independent paths must also be compensated [25, 186]. A PLL based on a lead zirconate titanate (PZT) fiber stretcher is the most common approach to dynamically compensate the phase-fluctuations [186], which is further discussed in section 5.2. Usually, the optical PLLs are the most complex parts in a PSA, especially for multichannel operation, where an independent PLL is required for each data channel [206].

This chapter is organized as follows. In section 5.1, the influence of key parameters on the gain properties of different configurations of PPLN-based PSAs is investigated by solving the coupled mode equations describing TWM interactions. Then, in section 5.2, PS operation and phase regeneration of a BPSK data channel is experimentally demonstrated using the copier + PSA scheme to generate the correlated waves in a single PPLN waveguide with bidirectional propagation. Since PPLN devices support bidirectional operation, the copier and the PSA can be implemented in opposite directions of propagation a single device, with savings of nonlinear devices, temperature controllers and coupling optics. PS operation in a single-pump, two-mode configuration is demonstrated first in subsection 5.2.1, followed by "black-box" phase regeneration in a dual-pump, one-mode PPLN-based PSA. Four-mode PS amplification of a 10 Gsymbol/s QPSK is also investigated in section 5.3. As discussed in section 5.1, PPLN-based four-mode PSAs cannot be implemented in practice due to the narrow QPM bandwidth of the PPLN waveguides, so a HNLF is used as the nonlinear medium instead.

Further discussion on the low-noise properties of PSAs and a more complete survey on the latest achievements on PSA technology are provided in chapter 6, which is devoted to low-noise PS amplification in optical transmission systems and networks.

5.1 Phase-sensitive amplification in PPLN devices

In this section, six different configurations of either one-, two- or four-mode PPLN-based PSAs are investigated and compared, schematically represented in figure 5.1. In figure 5.1, PSA1 and PSA2 are one-mode PSA configurations, whereas PSA3, PSA4 and PSA5 are two-mode PSAs. Configuration PSA6 is a four-mode PSA.

In PSA1, a signal wave (s) at frequency ν_s is amplified by a pump (P) located at ν_P via a fully degenerate DFG process in which an initial photon is decomposed into two identical photons with half the frequency. PSA2 is another example of a one-mode configuration, which is very similar to PSA1 in the sense that the signal is also amplified by the wave at ν_{SF} through degenerate DFG. In PSA2, however, the wave at ν_{SF} is first generated through an intermediate SFG interaction between the two pumps, located at ν_{P1} and ν_{P2}. In PSA2, the wave at the second harmonic band is generated in the nonlinear device, so all the waves at the input of the amplifier can be in the typical erbium-band, around 1550 nm. Thus, compared to PSA1, PSA2 is typically more attractive for applications in optical communication systems. Nonetheless, PSA1 has already been demonstrated in optical communication systems, using an additional PPLN waveguide to generate the correlated

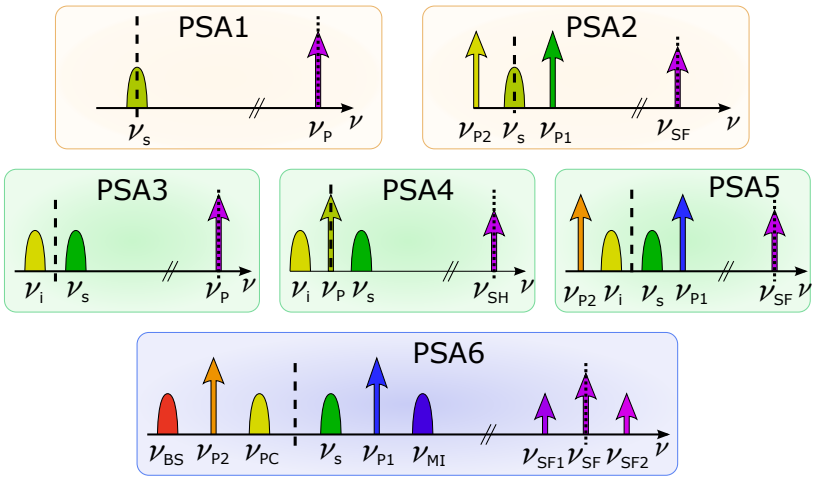

Figure 5.1: Configurations of PPLN-based PSAs studied in this section. The topologies shown in the top, middle and bottom rows respectively correspond to one-, two-, and four-mode PSAs. The dashed line indicates the QPM frequency, whereas the dotted line corresponds to the second harmonic of the QPM frequency. Subscripts: BS - Bragg scattering, i - idler, MI - modulation instability, P - pump, P1 - pump 1, P2 - pump 2, PC - phase conjugation, s - signal, SF - sum-frequency, S1 - sum-frequency 1, S2 - sum-frequency 2, SH - second harmonic.

pump at ν_P [205].

PSA3, PSA4 and PSA5 are two-mode configurations of PSAs in which a pump wave respectively located at ν_P, ν_{SH} and ν_{SF} is used to amplify both the signal and idler waves through phase-conjugating DFG. In PSA4 and PSA5, however, the waves at ν_{SH} and ν_{SF} are generated first through intermediate SHG of the pump at ν_P or SFG between pumps P1 and P2, respectively. Similarly to configuration PSA2, PSA4 and PSA5 are based on cascaded TWM processes, so all the waves at the input of the amplifier can be in the typical erbium-band.

PSA6 represents a four-mode PSA in which the signal and three idler waves located at $\nu_{PC} = \nu_{P1} + \nu_{P2} - \nu_s$, $\nu_{MI} = 2\nu_{P1} - \nu_s$ and $\nu_{BS} = \nu_{P2} + \nu_s - \nu_{P1}$ are amplified by two pumps waves, P1 and P2, through seven simultaneous TWM processes, whose frequency relations and respective phase mismatching parameters are summarized in table 5.1. The three idlers generated in four-mode PSAs are usually denominated as phase conjugation (PC), modulation instability (MI) and Bragg scattering (BS) waves [130].

Several other configurations of PPLN-based PSAs are possible, but the discussion in this thesis is restricted to the most representative ones, and using no more than two pump waves. In addition, the generation of the correlated waves required for PS operation is not discussed in detail in this section, as we are only interested on the properties of the PPLN-based PSAs. However, it should be noted that the generation of the correlated waves is a very important topic to consider in the design of a PSA. For instance, in configurations PSA1 and PSA3, the generation of the correlated pumps at the second harmonic (ν_P) typically requires using the copier + PSA strategy. Otherwise, an optical comb with an emission spectrum spanning a full octave to include the fundamental and second harmonic

Table 5.1: Frequency relations and phase matching parameters configuration PSA6.

	Frequency relation	Phase-mismatching parameter $\Delta\beta$
1)	$\nu_{SF} = \nu_{P1} + \nu_{P2}$	$\Delta\beta_1 = 2\pi\left(\frac{n_{SF}}{\lambda_{SF}} - \frac{n_{P2}}{\lambda_{P2}} - \frac{n_{P1}}{\lambda_{P1}} - \frac{1}{\Lambda}\right)$
2)	$\nu_{SF} = \nu_s + \nu_{PC}$	$\Delta\beta_2 = 2\pi\left(\frac{n_{SF}}{\lambda_{SF}} - \frac{n_s}{\lambda_s} - \frac{n_{PC}}{\lambda_{PC}} - \frac{1}{\Lambda}\right)$
3)	$\nu_{SF} = \nu_{MI} + \nu_{BS}$	$\Delta\beta_3 = 2\pi\left(\frac{n_{SF}}{\lambda_{SF}} - \frac{n_{MI}}{\lambda_{MI}} - \frac{n_{BS}}{\lambda_{BS}} - \frac{1}{\Lambda}\right)$
4)	$\nu_{SF1} = \nu_{P2} + \nu_s$	$\Delta\beta_4 = 2\pi\left(\frac{n_{SF1}}{\lambda_{SF1}} - \frac{n_{P2}}{\lambda_{P2}} - \frac{n_s}{\lambda_s} - \frac{1}{\Lambda}\right)$
5)	$\nu_{SF1} = \nu_{P1} + \nu_{BS}$	$\Delta\beta_5 = 2\pi\left(\frac{n_{SF1}}{\lambda_{SF1}} - \frac{n_{P1}}{\lambda_{P1}} - \frac{n_{BS}}{\lambda_{BS}} - \frac{1}{\Lambda}\right)$
6)	$\nu_{SF2} = \nu_{P1} + \nu_{PC}$	$\Delta\beta_6 = 2\pi\left(\frac{n_{SF2}}{\lambda_{SF2}} - \frac{n_{P1}}{\lambda_{P1}} - \frac{n_{PC}}{\lambda_{PC}} - \frac{1}{\Lambda}\right)$
7)	$\nu_{SF2} = \nu_{P2} + \nu_{MI}$	$\Delta\beta_7 = 2\pi\left(\frac{n_{SF2}}{\lambda_{SF2}} - \frac{n_{P2}}{\lambda_{P2}} - \frac{n_{MI}}{\lambda_{MI}} - \frac{1}{\Lambda}\right)$

band would be necessary, which is very difficult to produce in practice. Moreover, the way how the correlated waves are generated determines the operation of the subsequent PSA. As an example, two-mode PSAs can be used for either PS amplification transparent to the modulation format or as a phase regenerator. In the former case, transparent PS amplification is achieved by generating a phase-conjugated copy of the modulated signal in a copier amplifier [193]. In the latter case, the phase-conjugated idler must be generated from a CW signal wave, before the modulator [48]. These two possibilities are further discussed in section 5.2.

5.1.1 Coupled-mode equations and analytical solutions

In this subsection, approximated analytical solutions for the evolution of the normalized electric field of the interacting waves and signal gain along a PSA are obtained for each of the configurations depicted in figure 5.1. All the configurations discussed above can be represented by a simple or several cascaded TWM processes, modeled by the coupled-mode differential equations shown in chapter 2. In general, these equations cannot be solved analytically, unless for some specific cases and assuming certain approximations, as addressed in this subsection. For simplicity, the analytical solutions are obtained considering CW waves and negligible propagation losses. In addition, it is assumed that the nonlinear coupling coefficient for waves in the fundamental band, around 1550 nm, is almost constant and equal to κ, whereas for the waves in the second harmonic band, the nonlinear coupling coefficient is 2κ.

PSA1

As mentioned above, the principle of operation of PSA1 is based on degenerate DFG between a pump wave at ν_P and an input signal at ν_s, whose frequency relation is given by $\nu_s = \nu_P - \nu_s$. The degenerate DFG process can also be understood as an SHG interaction, but with the power flowing from the second harmonic (pump) to the fundamental wave

(signal). Hence, the evolution of the interacting waves in PSA1 can be modeled by the couple-mode equations for SHG, given by (2.18). In order to obtain an analytical solution for the evolution of the interacting waves let us assume that the normalized electric field envelope for wave j is given by $A_j = a_j \exp(i\phi_j)$, where a_j and ϕ_j are the magnitude and phase of A_j. By replacing A_j with its magnitude and phase functions, and separating the real and imaginary parts of the coupled-mode equations, the following set of equations is obtained

$$\frac{da_s}{dz} = \kappa a_s a_P \sin(\theta) \tag{5.1a}$$

$$\frac{da_P}{dz} = -\kappa a_s^2 \sin(\theta) \tag{5.1b}$$

$$\frac{d\theta}{dz} = \kappa \left(2a_P - \frac{a_s^2}{a_P}\right) \cos(\theta) - \Delta\beta, \tag{5.1c}$$

with $\theta = \phi_P - 2\phi_s - \Delta\beta z$. The evolution of a_s and a_P is determined by the sine terms of the differential equations, which in turn depend on the relative phase between the fundamental and second harmonic waves, and are responsible for the PS properties of the amplifier.

The analytical solution of (5.1) for any initial conditions can be obtained in terms of Jacobi elliptic functions, as detailed in [90]. The solution of (5.1) greatly simplifies if the signal is located at λ_{QPM}, at which $\Delta\beta = 0$, and for $\theta(z = 0) = \pm\pi/2$. In those specific cases, θ remains constant along the entire PPLN waveguide and $\sin(\theta)$ is either 1 or -1. When $\theta = \pi/2$, the power of the pump is transferred to the signal wave with maximum efficiency and, consequently, the gain of the amplifier is maximized. On the other hand, when $\theta = -\pi/2$, an opposite power transfer occurs, and the signal is depleted (de-amplification). The following solutions are obtained for the maximum and minimum gain conditions

$$a_s(z) = a_s(0) \cdot \frac{a_0}{a_0 \cosh(gz) \pm a_P(0) \sinh(gz)} \tag{5.2a}$$

$$a_P(z) = a_0 \cdot \frac{a_P(0) \pm a_0 \tanh(gz)}{a_0 \pm a_P(0) \tanh(gz)}, \tag{5.2b}$$

with g the effective coupling coefficient given by $g = \kappa a_0$ and $a_0 = \sqrt{P_s(0) + P_P(0)}$. In (5.2), the signs "$-$" and "$+$" correspond to the maximum ($\theta = \pi/2$) and minimum ($\theta = -\pi/2$) gain conditions, respectively. For any other value of θ, the gain of the amplifier is expressed in terms of the Jacobi elliptic functions, and varies between the two extreme possibilities given by (5.2). This is also true for the other PSA configurations studied in this chapter, so a similar procedure is considered for the remaining configurations in order to determine the evolution of the optical field of the waves at the maximum and minimum gain condition of the PSAs.

One-mode configurations are only suitable for phase regeneration applications because of their phase squeezing properties. For instance, let us consider a CW pump at ν_P with constant phase of $\phi_P = \pi/2$ and an input wave with a generic phase ϕ_s varying from 0 to 2π. When ϕ_s is either 0 or π, the gain of the PSA is maximized, whereas a maximum

de-amplification is observed for ϕ_s equal to $\pi/2$ or -$\pi/2$. This behavior is responsible for the so-called phase squeezing properties of the PSA, which generates a preferential gain axis on the constellation diagram of the amplified signals. The phase squeezing properties of the PSA enable phase regeneration of noisy BPSK signals by "squeezing" the phase of the data symbols towards the real axis, as further discussed in section 5.2.2.

PSA2

Configuration PSA2 is similar to PSA1 but with a principle of operation based on two cascaded TWM processes, one to generate the pump at ν_{SF} via SFG between two pump waves at frequencies ν_{P1} and ν_{P2}, followed by a degenerate DFG process for PS operation. In the case of PSA2, the wave at the second harmonic band is generated along the PSA, so the correlated waves required at the input of the PSA for PS operation are only the signal wave and pumps P1 and P2. As discussed for PSA1, the degenerate DFG interaction between the SF and signal waves can be seen as a SHG process with frequency relation given by $\nu_{SF} = 2\nu_s$. Likewise, the frequency relation of the SFG interaction through which wave SF is generated, given by $\nu_{SF} = \nu_{P1} + \nu_{P2}$, is mathematically equivalent to $\nu_{P2} = \nu_{SF} - \nu_{P1}$, which corresponds to a DFG process. Hence, the evolution of the interacting waves in PSA2 can be interpreted as a cSHG/DFG process, modeled by (2.28). Let us assume that the power of the two pumps is the same, i.e., $P_{P1} = P_{P2} = P_P/2$, where P_P is the combined power of the two pump waves, and that no SF wave is injected into the PSA. In addition, let us consider that the power of the pump waves is much higher than the signal one, so that the term depending on the square of A_1 in (2.28c) can be neglected. Following a similar procedure as for configuration PSA1, the solutions for the condition of maximum and minimum power transfer form the SF wave to signal are given by

$$a_s(z) = a_s(0) \cdot [\cosh(gz)]^{\pm 1} \tag{5.3a}$$

$$a_{P1}(z) = a_{P2}(z) = a_{P1}(0)/\cosh(gz) \tag{5.3b}$$

$$a_{SF}(z) = a_0 \cdot \tanh(gz), \tag{5.3c}$$

with $g = \kappa a_0$, and $a_0 = \sqrt{P_P(0) \mp P_s(0)}$. In (5.3), the signs "$+$" and "$-$" respectively represent the maximum and minimum gain conditions, achieved when $\phi_{SF} - 2\phi_s$ is $\pi/2$ or $-\pi/2$, or equivalently, when $\phi_{P1} + \phi_{P2} - 2\phi_s$ is π or 0.

Similarly to PSA1, PSA2 is mostly suitable for phase regeneration applications due to its intrinsic phase squeezing properties. For instance, if two CW pumps with phase $\phi_{P1} = 0$ and $\phi_{P2} = \pi$, the maximum gain condition is achieved whenever ϕ_s is equal to 0 or π, whereas the maximum de-amplification is observed at $\phi_s = \pm\pi/2$. Furthermore, no correlated wave at the second harmonic band is required at the input of the PSA in PSA2, so either an optical comb or a copier + PSA strategy can be used to generate the correlated signal wave and pumps P1 and P2. As an example, let us consider the generation of pump P2 in a copier amplifier based on a cSHG/DFG interaction from a CW pump at ν_{P1} and

a BPSK signal. According to (2.29) and assuming perfect QPM, the electric field of the generated pump P2 is approximately described by $A_{P2} \approx -\kappa^2 A_s^2 A_{P1}^* z^2/2$, so the phase of wave P2 is given by $\phi_{P2} = 2\phi_s - \phi_{P1} + \pi$. Since the phase of pump P2 is proportional to twice the phase of the input signal, the BPSK data modulation of the input signal is stripped from the generated pump, as the logical phase levels of 0 and π become 0 and 2 π in pump P2. This property is used in subsection 5.2.2 to generate a correlated CW pump.

PSA3

The principle of operation of PSA3 is based on simple DFG, which can be modeled by the coupled-mode differential equations for phase-conjugating DFG, described by (2.23). A complete analytical solution for this configuration is given by (2.26), assuming negligible pump depletion. In this section, however, only the analytical solutions for the specific cases of $\Delta\beta = 0$ and the maximum and minimum gain conditions are considered, respectively achieved when the relative phase of the interacting waves, defined as $\theta = \phi_P - \phi_s - \phi_i$, is equal to $\pi/2$ or $-\pi/2$. The evolution of the magnitude of the normalized electric field envelope for such cases is given by the following equations

$$a_s(z) = a_s(0)\cosh(gz) \pm a_i(0)\sinh(gz) \tag{5.4a}$$

$$a_i(z) = a_i(0)\cosh(gz) \pm a_s(0)\sinh(gz) \tag{5.4b}$$

$$a_P(z) \approx a_P(0). \tag{5.4c}$$

In the previous equations, $g = \kappa a_P(0)$ and the signs "$+$" and "$-$" correspond to the maximum and minimum gain conditions.

Two-mode PSAs can be used for either signal amplification transparent to the modulation format or for phase regeneration applications, depending on the phase properties of the correlated signal and idler. In order to understand how the two possibilities can be implemented in a two-mode PSA, let us consider that the correlated idler is generated from the signal and pump P waves in a copier amplifier through phase-conjugating DFG (copier + PSA scheme). In this case, the phase of the generated idler is given by $\phi_i = \phi_P - \phi_s - \pi/2$. Let us now consider that a phase-modulated signal is injected into the copier amplifier, with phase $\phi_s = \phi_{data}$, where ϕ_{data} is the phase of the data symbols. The phase of the generated idler is then given by $\phi_i = \phi_P - \phi_{data} - \pi/2$ and the relative phase of the correlated waves becomes $\theta = \phi_P - \phi_{data} - \phi_P + \phi_{data} + \pi/2 = \pi/2$. Regardless of the phase modulation of the initial signal wave, the relative phase of the interacting waves before the PSA is constant and equal to $\pi/2$, which is also the maximum gain condition for PSA3. Therefore, this strategy is a possible solution for amplification transparent to the modulation format. Let us now consider that a correlated idler is generated in the copier amplifier from a CW signal wave with constant phase ϕ_0. Then, if both the signal and correlated idler are modulated by the same phase modulator, the relative phase of the waves at the input of the PSA becomes $\theta = \phi_P - \phi_0 - \phi_{data} - \phi_P + \phi_0 + \pi/2 - \phi_{data} = -2\phi_{data} + \pi/2$. In this case, when

ϕ_{data} is either 0 or π, θ is equal to $\pi/2$ and the gain of the PSA is maximized. On the other hand, when ϕ_{data} is equal to $\pm\pi/2$, the gain of the amplifier is minimized. As discussed for one-mode configurations PSA1 and PSA2, this behavior leads to a preferential gain axis on the constellation diagram of the amplified signals (phase squeezing), which can be used for phase regeneration of noisy BPSK signals [48, 49]. The discussion provided here for PSA3 regarding the possibility of signal amplification transparent to the modulation format or phase regeneration is also valid for the other two-mode configurations, PSA4 and PSA5.

Two- and also four-mode PSAs require that both signal and idler waves are injected into the amplifier, otherwise they become PIAs. If no idler wave is injected into the PPLN, the evolution of the optical fields for configuration PSA3 is still given by (5.4), but with $a_i(0) = 0$. In this case, $a_s(z) = a_s(0)\cosh(gz)$ and the magnitude of the generated idler is given by $a_i(z) = a_s(0)\sinh(gz)$ for any phase value of the input signal and pump waves.

PSA4

Configuration PSA4 can modeled as a cSHG/DFG interaction but with wave SH generated through SHG of the input pump P. In order to obtain an analytical approximation for the maximum and minimum gain conditions of PSA4, let us assume perfect QPM for both the SHG and DFG steps and that the variation of A_{SH} is mainly due to SHG of the pump wave. This latter assumption is valid as long as the power of the signal and idler waves is much weaker than of the pump, and allows neglecting the last term of (2.28c). If the magnitude of the signal and idler waves is also the same, the solutions for the maximum and minimum gain conditions, respectively achieved for $2\phi_P - \phi_s - \phi_i$ equal to $\pi/2$ or 0, are given by (5.5).

$$a_P(z) = a_P(0)/\cosh(gz) \tag{5.5a}$$

$$a_{SH}(z) = a_0\tanh(gz) \tag{5.5b}$$

$$a_s(z) = a_i(z) = a_s(0)\cdot[\cosh(gz)]^{\pm 1}\,. \tag{5.5c}$$

In the previous equation, $g = \kappa a_0$, $a_0 = \sqrt{P_P(0) \mp 2P_s(0)}$ and the signs "+" and "−" respectively correspond to the maximum and minimum gain conditions. Let us now compare the evolution of a_s for configurations PSA3 and PSA4, assuming that the power of the signal and idler waves is the same and that the product gz is large, such that $\cosh(gz) \approx \sinh(gz)$. In the case of PSA3, the evolution of the signal power for the maximum gain condition is approximately given by $P_s(z) \approx 4P_s(0)\cosh^2(gz)$, whereas the power of the signal for configuration PSA4 is described by $P_s(z) \approx P_s(0)\cosh^2(gz)$. Hence, the gain of configuration PSA4 is approximately four times lower than for PSA3.

Let us now determine the gain of configuration PSA4 in PI operation, i.e., when no correlated idler is present at the input of the amplifier. In order to do so, let us assume that the variation of the second harmonic is mainly due to SHG of the pump wave, as assumed for (5.5). In this case, the evolution of a_P and a_{SH} is also described by equations (5.5a)

and (5.5b), but now with $a_0 = a_P(0)$. A further simplification can be performed by replacing $a_{SH}(z)$ in the differential equation of a_s and a_i, with an equivalent effective value, $\overline{a_{SH}}$, obtained by averaging $a_{SH}(z)$ along the PPLN waveguide through the following integration

$$\overline{a_{SH}} = \frac{1}{L}\int_0^L a_{SH}(z)dz = a_P(0)\frac{\ln\left[\cosh(gL)\right]}{gL}, \tag{5.6}$$

with L the length of the device. By using $\overline{a_{SH}}$ in the differential equations for the signal and idler waves, the following solution is obtained for PI operation

$$a_s(z) = a_s(0)\cosh(\overline{g}z) \tag{5.7a}$$

$$a_i(z) = a_s(0)\sinh(\overline{g}z), \tag{5.7b}$$

with $\overline{g} = \kappa\overline{a_{SH}}$. Remarkably, the expressions for the evolution of the magnitude of the signal and idler in PI operation for configurations PSA3 and PSA4 are identical. However, in the case of PSA3, the effective coupling coefficient is proportional to $a_P(0)$, whereas in PSA4 the effective coupling coefficient is proportional to $\overline{a_{SH}}$. If the product gL is large enough such that $\cosh(gL) \approx \exp(gL)/2$, the effective magnitude of wave SH is approximately given by $\overline{a_{SH}} \approx a_P[1 - \ln(2)/(gL)]$. Hence, a lower effective coupling coefficient and, consequently, lower gain is obtained for configuration PSA4 with respect to PSA3. As discussed later in this section, this difference is responsible for about four times lower gain of configuration PSA4 with respect to PSA3 in PI operation.

PSA5

Configuration PSA5 can be modeled as a cSFG/DFG process, mathematically described by (2.30). In order to obtain the analytical solutions for the maximum and minimum gain conditions of PSA5, let us assume perfect QPM for both the SFG and DFG steps, $a_s \approx a_i$ and that the power of the two pumps is the same. If the power of the pump waves at the input of the PSA is much higher than that of the signal and idler waves, the evolution of the SF wave is mainly due to SFG between the two pump waves. This latter approximation allows neglecting the last term of (2.30c). The following solution is then obtained

$$a_{P1}(z) = a_{P2}(z) = a_{P1}(0)/\cosh(gz) \tag{5.8a}$$

$$a_{SF}(z) = a_0\tanh(gz) \tag{5.8b}$$

$$a_s(z) = a_i(z) = a_s(0)\cdot[\cosh(gz)]^{\pm 1}. \tag{5.8c}$$

In the previous equation, the signs "$+$" and "$-$" correspond to the maximum and minimum gain conditions, respectively achieved when $\phi_{P1} + \phi_{P2} - \phi_s - \phi_i$ is π or 0. The effective coupling coefficient is given by $g = \kappa a_0$, with $a_0 = \sqrt{2P_{P1}(0) \mp 2P_s(0)}$. Remarkably, if the combined power of the two pumps in PSA5, $P_{P1}(0) + P_{P2}(0)$, is equal to the power of the

pump in PSA4, $P_P(0)$, the expressions for the evolution of a_s and a_i presented above are identical to (5.5). The similarity between the gain properties of PSA4 and PSA5 is further discussed later on this section.

The gain of the amplifier in PI operation can be calculated using the same procedure as for configuration PSA4. Assuming that the variation of the SF wave is mainly due to SFG of the pump waves, the evolution of a_{P1} and a_{P2} given by (5.8a), whereas a_{SF} is described by (5.8b), but now with $a_0 = \sqrt{2P_{P1}(0)}$. An equivalent effective magnitude of wave SF, $\overline{a_{SF}}$, can be devised by repeating the procedure used to obtain (5.6). By doing so, $\overline{a_{SF}}$ can also be described by (5.6), but considering the effective coupling coefficient of (5.8) and replacing $a_P(0)$ with a_0. By using $\overline{a_{SF}}$ in the differential equations of the signal and idler waves, a_s and a_i can be approximated by

$$a_s(z) = a_s(0)\cosh(\overline{g}z) \tag{5.9a}$$

$$a_i(z) = a_s(0)\sinh(\overline{g}z), \tag{5.9b}$$

with $\overline{g} = \kappa\overline{a_{SF}}$. Once again, if the combined power of the two pumps in PSA5 is equal to that of pump P in PSA4, the evolution of a_s and a_i in PI operation is exactly the same.

PSA6

Several TWM processes occur simultaneously in PSA6, whose frequency and phase-mismatching parameters are summarized in table 5.1. The evolution of the normalized electrical field envelope of the interacting waves can be expressed by the following set of differential equations, obtained for CW waves propagating in a lossless PPLN waveguide

$$\frac{dA_{P1}}{dz} = -i\kappa\left(A_{SF}A_{P2}^{*}e^{-i\Delta\beta_1 z} + A_{SF1}A_{BS}^{*}e^{-i\Delta\beta_5 z} + A_{SF2}A_{PC}^{*}e^{-i\Delta\beta_6 z}\right) \tag{5.10a}$$

$$\frac{dA_{P2}}{dz} = -i\kappa\left(A_{SF}A_{P1}^{*}e^{-i\Delta\beta_1 z} + A_{SF1}A_{s}^{*}e^{-i\Delta\beta_4 z} + A_{SF2}A_{MI}^{*}e^{-i\Delta\beta_7 z}\right) \tag{5.10b}$$

$$\frac{dA_{SF}}{dz} = -2i\kappa\left(A_{P1}A_{P2}e^{i\Delta\beta_1 z} + A_{s}A_{PC}e^{i\Delta\beta_2 z} + A_{MI}A_{BS}e^{i\Delta\beta_3 z}\right) \tag{5.10c}$$

$$\frac{dA_{s}}{dz} = -i\kappa\left(A_{SF}A_{PC}^{*}e^{-i\Delta\beta_2 z} + A_{SF1}A_{P2}^{*}e^{-i\Delta\beta_4 z}\right) \tag{5.10d}$$

$$\frac{dA_{PC}}{dz} = -i\kappa\left(A_{SF}A_{s}^{*}e^{-i\Delta\beta_2 z} + A_{SF2}A_{P1}^{*}e^{-i\Delta\beta_6 z}\right) \tag{5.10e}$$

$$\frac{dA_{MI}}{dz} = -i\kappa\left(A_{SF}A_{BS}^{*}e^{-i\Delta\beta_3 z} + A_{SF2}A_{P2}^{*}e^{-i\Delta\beta_7 z}\right) \tag{5.10f}$$

$$\frac{dA_{BS}}{dz} = -i\kappa\left(A_{SF}A_{MI}^{*}e^{-i\Delta\beta_3 z} + A_{SF1}A_{P1}^{*}e^{-i\Delta\beta_5 z}\right) \tag{5.10g}$$

$$\frac{dA_{SF1}}{dz} = -2i\kappa\left(A_{P2}A_{s}e^{i\Delta\beta_4 z} + A_{P1}A_{BS}e^{i\Delta\beta_5 z}\right) \tag{5.10h}$$

$$\frac{dA_{SF2}}{dz} = -2i\kappa\left(A_{P1}A_{PC}e^{i\Delta\beta_6 z} + A_{P2}A_{MI}e^{i\Delta\beta_7 z}\right). \tag{5.10i}$$

At this point it is important to discuss the role of the phase mismatching parameters

and how they affect the behavior of PSA6. In order to maximize the gain of the amplifier, the poling period of the PPLN device is typically chosen to quasi-phase match the SFG interaction between the two pumps, at which $\Delta\beta_1 = 0$. Fortunately, the symmetric location of the interacting waves around λ_{QPM} also imply that $\Delta\beta_2$ and $\Delta\beta_3$ are also very small for a wide spectral range. However, this is not true for the other phase mismatching parameters, which can easily scale up to very high values, even for wavelength separations between the signal and pump P1 of the order of 1 nm. As a consequence, the efficiency of such nonlinear interactions is greatly reduced, so waves SF1 and SF2 cannot be efficiently generated and no interaction between the signal or the PC waves with the BS and MI idlers occurs. In this case, PSA6 does not behave as a four-mode PSA, but rather as two independent two-mode PSAs, one for the signal and PC wave, and the other for the MI and BS idlers. In fact, only if $\nu_s \approx \nu_{P1}$ all the phase mismatching parameters become small enough to enable efficient generation of waves SF1 and SF2 and, consequently, four-mode operation.

Nonetheless, let us consider the unlikely scenario of $\nu_s \approx \nu_{P1}$ and that PSA6 effectively behaves as a four-mode PSA. In addition, let us assume $a_{P1} \approx a_{P2}$, signal and idler waves with the same power and the relative phase parameters θ_k, where k represents each TWM process of PSA6. For each of the seven TWM processes with frequency relation $\nu_l = \nu_m + \nu_n$, the respective relative phase parameters are given by $\theta_k = \phi_l - \phi_m - \phi_n$.

The maximum gain of the amplifier is obtained when the power of the pumps is transferred to the SF wave with maximum efficiency, and from the SF wave to the signal and idlers, which is verified when $\theta_1 = -\pi/2$, and $\theta_2 = \theta_3 = \pi/2$. In addition, the four-mode properties of the PSA can only be enabled if there is some power flowing from and to the SF1 and SF2 waves. However, waves SF1 and SF2 are only used to intermediate the power transfer between the signal, pump and idler waves. In order to maximize the gain of the signal, the power of the SF1 and SF2 should be as low as possible, which corresponds to the case when the power flowing from the pump waves to SF1 and SF2 and from these waves to the signal and idlers is exactly the same. In order verify this situation, the two terms on the right side of (5.10h) and (5.10i) must cancel each other, which occurs when $\theta_4 = \theta_7 = -\pi/2$ and $\theta_5 = \theta_6 = \pi/2$. In such conditions, the evolution of the pump, SF, SF1, SF2, signal and idler waves is approximately given by

$$a_{P1}(z) = a_{P2}(z) = a_{P1}(0)\tanh(gz) \tag{5.11a}$$

$$a_{SF}(z) = a_0/\cosh(gz) \tag{5.11b}$$

$$a_s(z) = a_{MI}(z) = a_{PC}(z) = a_{BS}(z) = a_s(0)\cosh(gz) \tag{5.11c}$$

$$a_{SF1}(z) = a_{SF2}(z) \approx 0, \tag{5.11d}$$

with $g = \kappa a_0$ and $a_0 = \sqrt{2P_{P1}(0) - 2P_s(0)}$. Let us now compare the evolution of the magnitude of the signal and idler waves for configurations PSA5 and PSA6. Despite the two additional idler waves in PSA6, the evolution of a_s for the maximum gain condition is

exactly the same in both configurations, so no gain advantage is obtained by considering a four-mode configuration over two-mode PPLN-based PSAs. This result differs from what is observed for fiber-based PSAs, in which four-mode configurations do offer an additional gain advantage of 6 dB compared to two-mode PSAs [209].

Small signal gain

The gain of the amplifiers for maximum and minimum gain conditions can be calculated from the analytical expressions obtained above through $G(L) = [a_s(L)/a_s(0)]^2$. For high-gain amplification purposes, strong pump waves with power levels much higher than that of the input signals are typically used. In this case, the hyperbolic sines and co-sines can be approximated by $\cosh(x) \approx \sinh(x) \approx \exp(x)/2$, and the gain of the PSAs, also known as the small signal gain, is given by (5.12a) for PSA1 and PSA3, and by (5.12b) for the remaining configurations.

$$G(L) \approx e^{2\kappa\sqrt{P_P}L} \tag{5.12a}$$

$$G(L) \approx \frac{e^{2\kappa\sqrt{P_P}L}}{4}. \tag{5.12b}$$

The previous equations were obtained assuming that $P_P = P_{P1}(0) + P_{P2}(0) = 2P_{P1}(0)$ for dual-pump configurations. Compared to PSA1 and PSA3, the small signal gain of the other configurations is four times (6 dB) lower. The main reason for the lower gain is the additional TWM step to generate an intermediate pump wave at the second harmonic band. In these cases, the power of the pump(s) is first transferred to the wave at the second harmonic band, and then to the signals. This process is not as efficient as in configurations PSA1 and PSA3, in which the power directly flows from the pump to signal wave. Hence, PSAs relying on cascaded second-order nonlinear interactions have a gain disadvantage of 6 dB compared to those based on simple DFG.

The gain of the amplifiers at the minimum gain condition can also be obtained from the analytical solutions presented above. Remarkably, the gain at the minimum gain condition is simply the inverse of $G(L)$. A common parameter to characterize the performance of phase regenerators is the so called phase-sensitive dynamic range (PSDR), defined as the ratio between the maximum and minimum gain of the amplifier. Hence, a theoretical PSDR of G^2 is expected for all configurations.

The small signal gain in PI operation, G_{PI}, for two-mode configurations PSA3, PSA4 and PSA5 can be respectively calculated from (5.4) assuming $a_i(0) = 0$, (5.7) and (5.9). In the case of PSA3, the small signal gain in PI operation is given by (5.13a), whereas (5.13b) represents the small signal gain for PSA4 and PSA5.

$$G_{PI}(L) \approx \frac{e^{2\kappa\sqrt{P_P}L}}{4} \tag{5.13a}$$

$$G_{PI}(L) \approx \frac{e^{2\kappa\sqrt{P_P}L}}{16}. \tag{5.13b}$$

Comparing (5.12) to (5.13), an additional gain factor of four (6 dB) is obtained in PS operation with respect to the respective PI configurations. The additional gain factor originates from the coherent summation of the amplified signal and idler waves and is commonly known as the 6 dB advantage of two-mode PSAs over PIAs [186]. As observed in (5.12), the small signal gain for PSA4 and PSA5 in PI operation is four times lower than for PSA3, which is again a consequence of the intermediate TWM steps.

5.1.2 Numerical simulations

In this section, the influence of the total pump power, P_P, the input signal power, P_s, and the length and normalized conversion efficiency of the PPLN device on the maximum gain of the different PSA configurations is numerically evaluated and compared to the analytical solutions obtained in the previous subsection. The simulations were performed using a 4$^{\text{th}}$-order Runge-Kutta algorithm to solve the couple-mode differential equations presented in chapter 2. The effects of the relative phase between the interacting waves and the gain spectrum of the PSAs are also numerically evaluated. Unless otherwise stated, a PPLN device with length, poling period, λ_{QPM}, temperature of operation and SHG efficiency of respectively 6 cm, 19.39 μm, 1550 nm, 25 °C and 500%/W is considered for all configurations. In addition, the wavelength of the pump wave in single-pump configurations is selected at either λ_{QPM} or λ_{QPM}/2. For dual-pump configurations, the wavelength of pump P1 is set at 1545 nm, whereas the wavelength of P2 is set to $\lambda_{P2} = 1/(2\lambda_{QPM}^{-1} - \lambda_{P1}^{-1})$.

The influence of P_P on the gain of the amplifier is depicted in figure 5.2, with the signal wavelength set to λ_{QPM} for PSA1 and PSA2, 1547 nm for PSA3, PSA4 and PSA5, and 1545.01 nm for PSA6. An input signal power of -20 dBm was considered. As expected, the maximum/minimum gain of the amplifier increases/decreases exponentially with the pump power for all configurations, with a very good agreement between the theoretical and numerical solutions up to more than P_P= 30 dBm. The numerical simulations also show that the maximum gain of PSA1 and PSA3 in PS operation for P_P of 30 dBm is about 19.4 dB, whereas 13.5 dB is measured for the other configurations. These results are in agreement with the theoretical predictions of four times (6 dB) higher gain for PSA1 and PSA3, discussed in the previous subsection.

The gain of the amplifier for two- and four-mode configurations operating in PI mode is also shown in figure 5.2. According to the numerical simulations, the gain of the amplifiers in PI operation becomes about four times (6 dB) lower than in PS operation for two-mode PSAs. This result was also observed in two-mode fiber-based PSAs [186], and is a consequence of constructive addition of the amplified signal and idler. The gain of the idler measured with respect to the input signal power or equivalently, the conversion efficiency, also increases with P_P, as expected. Furthermore, while the power of the idler is much lower than the signal one, the gain of the signal wave is relatively low. However, when the power of both waves becomes comparable, the signal and idler gain starts to grow very quickly with P_P. Smaller conversion efficiencies are also measured at lower pump power

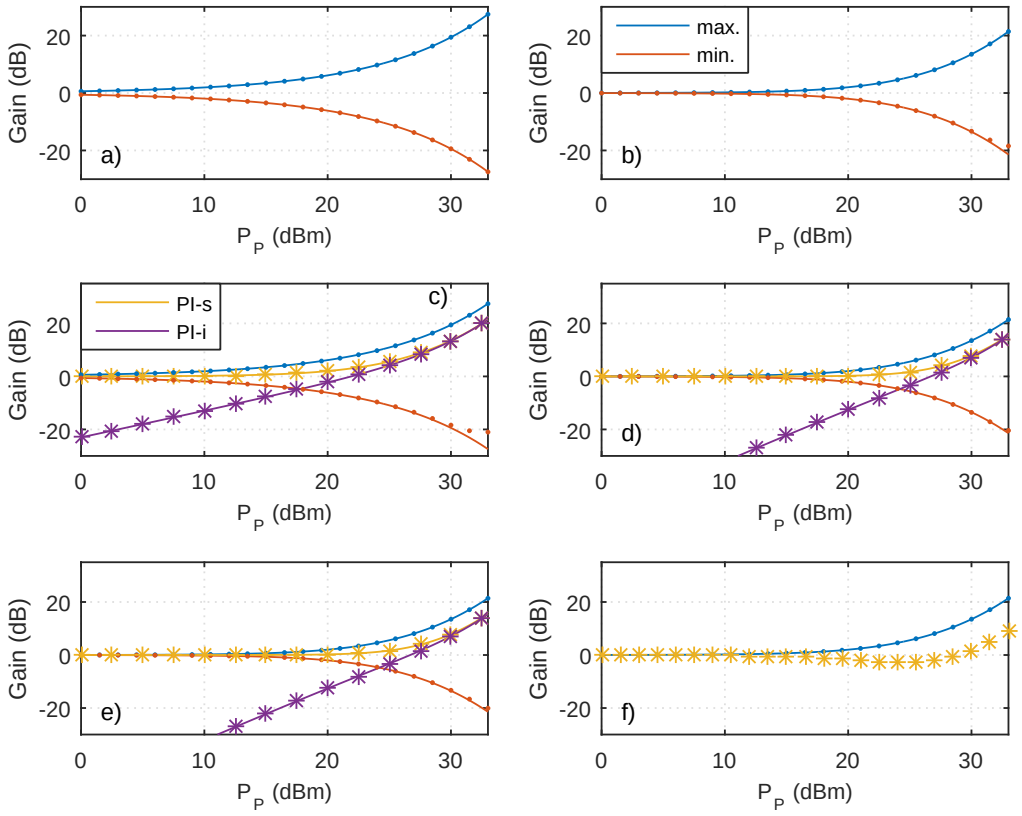

Figure 5.2: Maximum (max.) and minimum (min.) gain of the PSAs as a function of P_P for configurations: a) PSA1, b) PSA2, c) PSA3, d) PSA4, e) PSA5, and f) PSA6. The solid curves represent the theoretical solutions, whereas the dot markers correspond to the numerical results. In c), d), e) and f), the theoretical gain of the amplifiers in PI operation for the signal and idler waves is also represented by the solid curves PI-s and PI-i, with the respective numerical results shown by the asterisk markers.

for PSA4 and PSA5 than in PSA3, which is also a consequence of the intermediate TWM process required in cascaded nonlinear interactions. The gain of PSA6 in PS operation is about 16 times (12 dB) higher than in PI mode, as a result of the constructive beating of not only two, but four correlated waves. This result has also been experimentally observed in fiber-based PSAs [209]. However, the maximum PS gain of PSA6 is approximately the same of PSA4 and PSA5, which is explained by the generation of additional intermediate waves SF1 and SF2. As discussed above, the generation of intermediate waves at the second harmonic band reduce the efficiency of the power transfer from the pumps to the signal and idler waves. In the case of PSA6, the generation of the additional intermediate waves SF1 and SF2 cancels out the gain advantage of beating four correlated waves instead of only two, which results in a final gain equivalent to that of PSA4 and PSA5. This behavior is even more evident in PI operation. As shown in the figure, the gain of PSA6 in PI mode at P_P of 30 dBm is 1.4 dB, whereas a gain value of 7.8 dB is measured for PSA4 and PSA5, at the same pump power. In addition, for P_P values between 20 dBm and 25 dBm, the gain of PSA6 in PI mode decreases with the pump power. These results are also

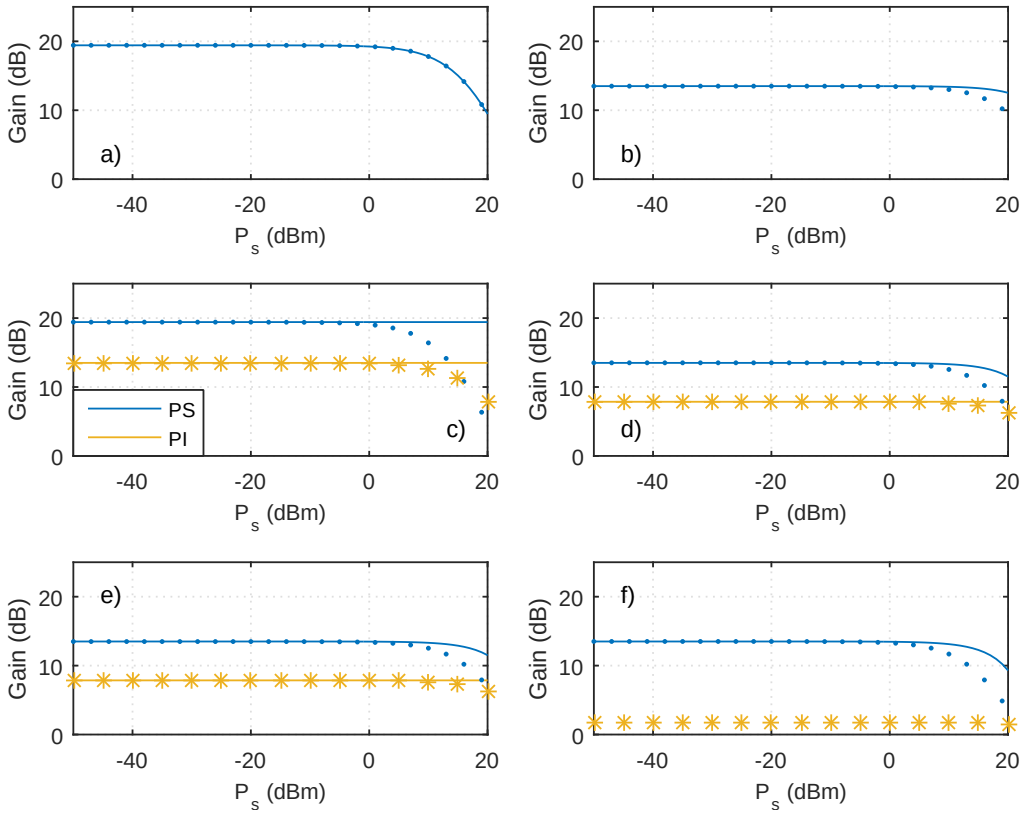

Figure 5.3: Maximum gain of the amplifiers as a function of P_s for configurations: a) PSA1, b) PSA2, c) PSA3, d) PSA4, e) PSA5, and f) PSA6. The solid curves represent the theoretical solutions, whereas the dot markers correspond to the numerical results. In c), d), e) and f), the theoretical gain of the amplifiers in PI operation for the signal and idler waves is also represented by the solid curves PI-s and PI-i, with the respective numerical results shown by the asterisk markers.

caused by power depletion of the signal, which is partially consumed to generate waves SF1 and SF2, as well as the additional idlers.

The influence of P_s on the gain of the amplifiers is depicted in figure 5.3 for P_P = 30 dBm. For all the simulated configurations, the gain of the amplifier remains almost unchanged with P_s until reaching saturation, at input signal power values around 5 dBm in PS operation, and even higher values when behaving as a PIA. A good agreement between the numerical simulations and theoretical solutions is observed far from saturation. When the amplifiers become saturated, however, the undepleted pumps approximation is no longer valid, and significant differences between the numerical simulations and the analytical expression are observed. The additional gain of 6 dB of configurations based on a single TWM process is also observed, as well as the gain advantage of 6 and 12 dB when switching from PI to PS operation in two- and four-mode configurations, respectively.

The PS properties of the amplifiers are evidenced in figure 5.4, where the gain the amplifiers is depicted as a function of ϕ_s for P_P = 30 dBm and P_s = -20 dBm. A sinusoidal variation of the gain with the signal phase is observed in all the simulated curves, with a periodicity of π for one-mode PSAs and of 2π for the other configurations. In the case of

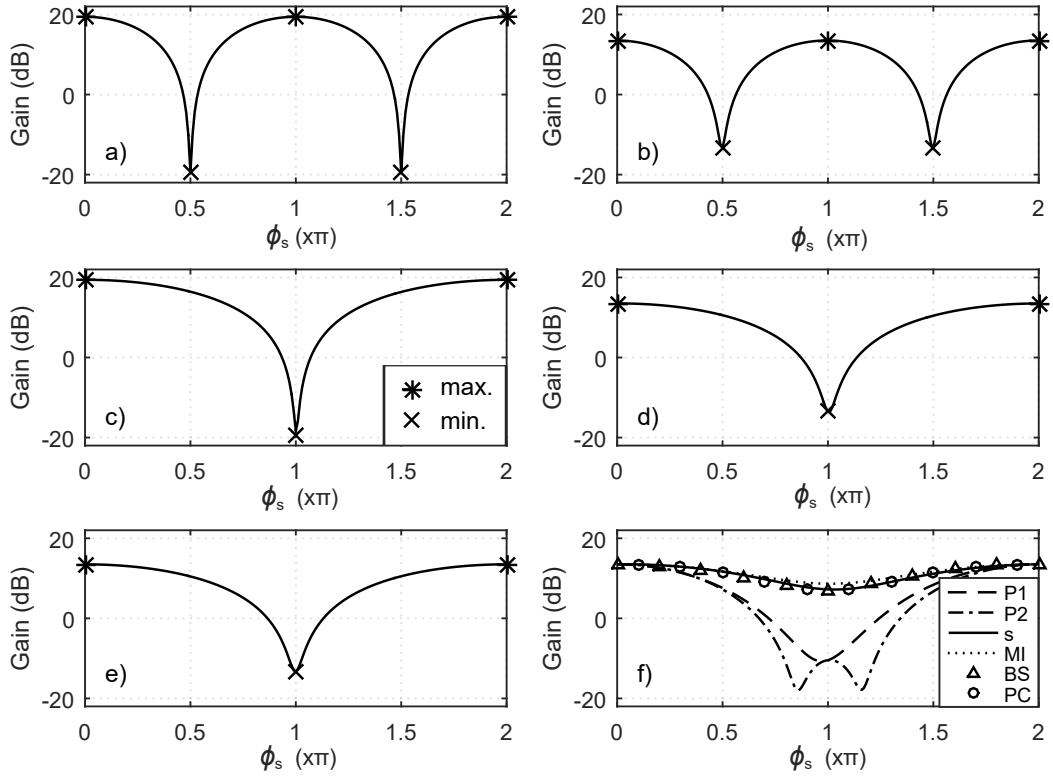

Figure 5.4: Gain of the PSA as a function of ϕ_s for configurations: a) PSA1, b) PSA2, c) PSA3, d) PSA4, e) PSA5, and f) PSA6. The asterisk and cross markers represent the theoretical gain for the maximum and minimum gain conditions.

one-mode PSAs, the optical field of the second harmonic is proportional to the square of the input signal one and, consequently, the relative phase between the interacting waves is affected by twice the phase of the signal wave. This relation explains the observed periodicity of π.

The variation of the gain of PSA6 with the phase of the signal, pumps and idler waves is plotted in figure 5.4-f). As shown in the figure, the gain of the PSA is strongly affected by the phase of P1 and P2, with a difference of more than 20 dB between the maximum and minimum gain values, whereas less than 7 dB gain variation is verified when changing the phase of the signal and idlers. Each pump wave participates in more TWM processes than the signal and the idler waves and, therefore, the pump waves have a stronger impact on the PS gain of the amplifier.

The gain spectra of the PSAs are depicted in figure 5.5 for P_P = 30 dBm and P_s = -20 dBm. In PSA1, the wavelength of the pump is also shifted to $\lambda_2/2$ in order to keep the frequency-correlation of the waves, otherwise PS operation could not be achieved. For the same reason, the wavelength of pump P2 in PSA2 is set to $\lambda_{P2} = (2/\lambda_s - 1/\lambda_{P1})^{-1}$. The gain spectra presented in figures 5.5-a) and 5.5-b), show that the maximum gain is achieved at the QPM wavelength, as expected, and that the gain quickly drops to very low values for wavelength detuning from λ_{QPM} higher than 0.25 nm, due to phase mismatching. The narrow gain bandwidth of the one-mode PSAs requires that the signal wavelength

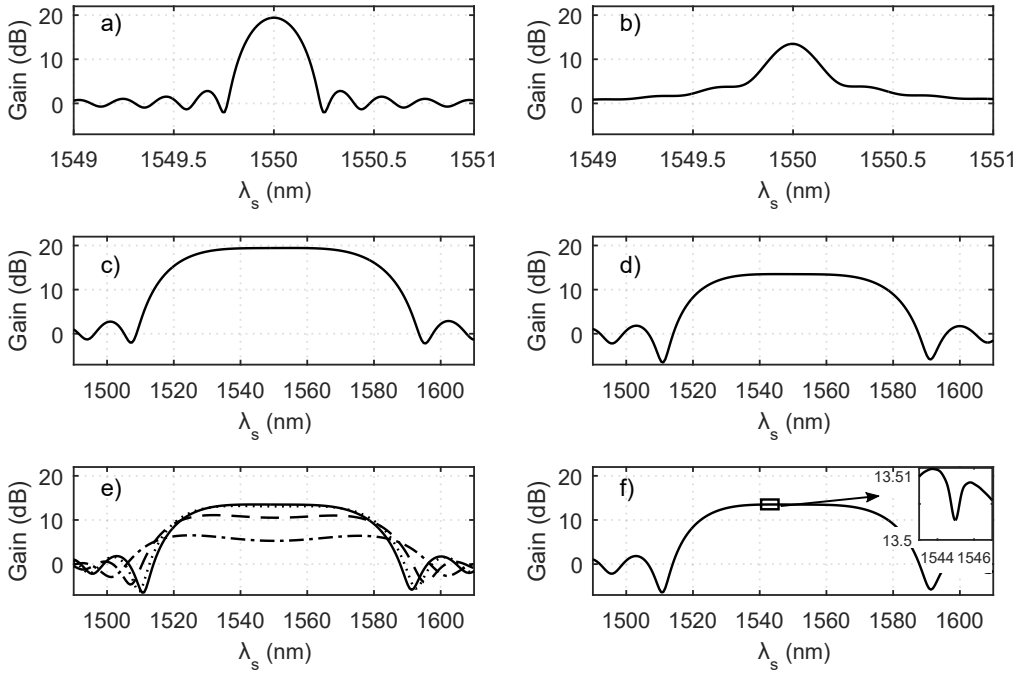

Figure 5.5: Signal gain spectrum for configurations: a) PSA1, b) PSA2, c) PSA3, d) PSA4, e) PSA5, and f) PSA6. In (e), the solid, dotted, dashed and dot-dashed lines correspond to a wavelength spacing between the two pumps of 10, 30, 50 and 70 nm, respectively.

must be properly tuned to match λ_{QPM} and that the temperature of operation is properly stabilized, otherwise the gain of the PSA becomes very low. The narrow gain bandwidth of one-mode PSAs also precludes the possibility of multichannel amplification for optical communication systems. This is not the case of two-mode PSAs, where amplification bandwidths of more than 40 nm can be obtained, as depicted in figures 5.5-c) to 5.5-e). However, the wavelength of the pump must still be precisely set to $\lambda_{QPM}/2$ in PSA3 and λ_{QPM} in PSA4 or, in the case of dual-pump configurations, the two pumps must be symmetrically placed around ν_{QPM}, such that $\nu_{P1} + \nu_{P2} = 2\nu_{QPM}$. One disadvantage of two-mode PSAs for data transmission in optical communication systems is the fact that not only the signal but also the idler channels must be transmitted throughout the optical links, so half of the transmission bandwidth is lost.

In single-pump, two-mode PSAs built with HNLFs, the flatness and bandwidth of the gain spectrum are limited not only by the dispersive properties of the fiber, but also by SPM and XPM effects, which generate an additional contribution to the effective phase mismatch parameter [73] (see also figure 2.13). A dual-pump configuration can be used as an alternative to provide flatter and wider gain bandwidth in fiber-based PSAs [73]. On the other hand, since PPLN waveguides are not significantly affected by SPM and XPM, flat and broadband gain spectra are observed for both single- and dual-pump configurations, as depicted in figures 5.5-c) to 5.5-e). Since dual-pump configurations are typically more difficult to implement in practice and with no additional benefits over the respective

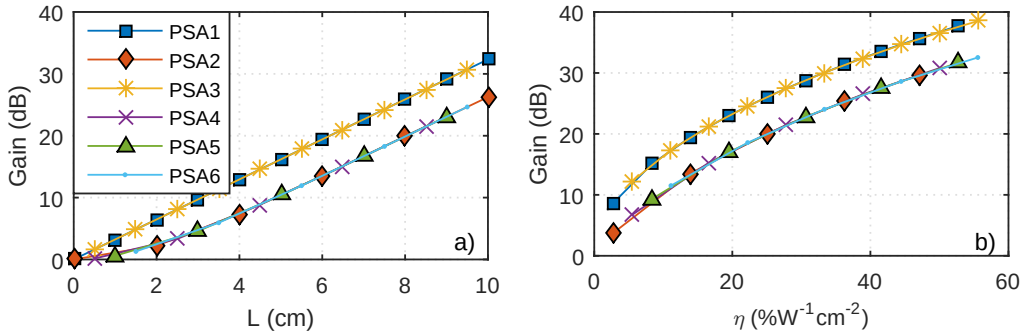

Figure 5.6: Gain of the PSA as a function of the a) length (L) for η = 13.8 %W^{-1}cm^{-2}, and b) the normalized SHG efficiency (η) for L = 6 cm.

single-pump configuration, PSA4 is more attractive for multichannel operation in optical communication systems. The gain spectra of configuration PSA5 for a wavelength spacing between the two pumps of 30, 50 and 70 nm is also depicted in figure 5.5, showing that increasing the pump spacing allows to slightly broaden the gain bandwidth, but at the expense of decreasing the gain of the amplifier.

Let us now compare the gain spectrum for configurations PSA6 and PSA5 with a pump spacing of 10 nm. According to the numerical simulations, the gain spectrum of both configurations is practically identical, with the exception of a very narrow region around λ_{P1}, at 1545 nm, detailed in the inset of figure 5.5-f). In fact, PSA6 only behaves as a four-mode PSA in that narrow spectral region, where $\Delta\beta_4$, $\Delta\beta_5$, $\Delta\beta_6$ and $\Delta\beta_7$ are small. Hence, four-mode PPLN-based PSAs do not provide any gain advantage over two-mode PSAs, in addition to the very strict frequency location of the waves in order to enable four-mode operation.

The influence of the length and normalized SHG efficiency η of the PPLN waveguides on the gain of the PSAs is plotted in figure 5.6 for P_s = -20 dBm and P_P = 30 dBm. The simulated curves show that the gain of the amplifiers increases with both L and η. According to the theoretical predictions, the gain of the amplifiers grows exponentially with L, as well as with the square root of the normalized conversion efficiency, as $\kappa = \sqrt{\eta}$. Hence, it would be preferable to increase the length of the device rather than its efficiency, but the current fabrication technology limits the usable size of the lithium niobate wafers to less than 10 cm. In addition, it is more difficult to guarantee the uniformity of the waveguide geometry for longer devices and, consequently, to keep λ_{QPM} constant along the entire device.

In summary, the influence of key parameters on the gain of different PPLN-based PSAs was discussed. Due to their limited gain bandwidth, applications of one-mode PSAs on multichannel amplification are precluded, unless one device is used for each channel or PPLN waveguides with multiple QPM resonances are considered. Still, these amplifiers can be used for phase-regeneration applications, as discussed in the following section. The high bandwidth and flat gain profiles of two-mode PSAs make them very attractive

for multichannel amplification, with the benefits of immunity to SPM, XPM and SBS when comparing to their fiber-based counterparts. Moreover, it was shown in this section that the gain flatness and amplification bandwidth is similar considering either single- or dual-pump two-mode PSAs, so single-pump configurations are preferable due to simpler implementation. However, since the correlated idlers must also be transmitted along with signal channels, half of the transmission bandwidth is lost. Nonetheless, this disadvantage can be partially compensated by placing these waves in unused bands, out of the conventional gain bandwidth of EDFAs. Four-mode PPLN-based PSAs can only be implemented if the signal is very close to one of the pump waves, and show no gain advantage compared to two-mode amplifiers, so this configuration is not attractive for amplification purposes in optical communication systems. In addition, twice the transmission bandwidth is required for the additional idler waves.

Another important conclusion from the analysis performed in this section is the additional gain of 6 dB obtained for configurations based on single TWM processes. However, in fiber optics systems, manipulation of signals in the second harmonic band is challenging. In [205], a phase regenerator for BPSK signals based on configuration PSA1 was experimentally demonstrated, using an additional PPLN device to generate the pump at the second harmonic. However, not only an extra nonlinear device is required in this approach, but the combined total insertion losses of the two devices is also higher. Thus, the additional gain advantage of 6 dB may not be enough to compensate the extra insertion losses, and the equivalent configuration based on cascaded TWM processes may actually be more advantageous.

5.2 Phase-sensitive amplification and phase regeneration in a single bidirectional PPLN device

In this section, PS amplification and phase regeneration respectively based on configurations PSA4 and PSA2, are demonstrated using the copier + PSA scheme in a single PPLN waveguide with bidirectional propagation. The proposed scheme allows generating the correlated waves in one propagation direction and PS operation in the opposite direction.

5.2.1 Phase-sensitive amplification in a single bidirectional PPLN device

The principle of operation of the proposed scheme is represented in figure 5.7. The correlated waves are generated in the copier direction through cSHG/DFG between a strong pump wave (green arrow), and a signal wave (blue arrow). After the generation of the correlated idler, the waves are injected again in the PPLN waveguide for PS operation. As depicted in figure 5.7, an optical processor (OP) based on liquid crystal on silicon technology [210] is used to equalize the power of the signal and idler waves, and to vary the relative

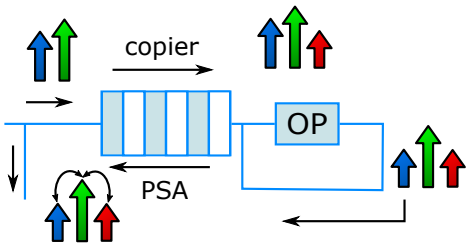

Figure 5.7: Schematic representation of the copier + PSA scheme implemented using a single PPLN waveguide with bidirectional propagation. An OP is also included to equalize the signal and idler, and to adjust the relative phase of the interacting waves.

phase of the interacting waves. In this subsection, PS amplification is investigated using configuration PSA4 discussed in section 5.1 due to its simplicity and prospects for multi-channel operation [203]. Configuration PSA3 could have also be used instead of PSA4, with a theoretical gain advantage of 6 dB (see section 5.1). However, it would require the generation of a pump wave at the second harmonic band in another PPLN device, resulting in no savings of devices and temperature controllers. In addition, the available optical components were not optimized for operation in the second harmonic band, around 780 nm, so the gain advantage of PSA3 with respect to PSA4 would be partially reduced, if not completely eliminated by the total insertion and propagation losses of the optical elements and patch cords.

The performance of the proposed bidirectional scheme is characterized by evaluating the impact of the pump-to-signal power ratio, *PSR*, and the total input power in the PSA direction, P_T, on the PS gain, obtained for PPLN waveguides with different lengths. The experimental set-up used to evaluate the performance of the bidirectional scheme is shown in figure 5.8. Two ECLs were used as light sources, tuned at 1545.5 nm (pump) and 1548 nm (signal). After state of polarization alignment using PolCs, amplification in EDFAs and out-of-band ASE noise filtering in 1 nm BPFs, the two waves were combined in a 10:90 coupler. An optical circulator (Circ.) was then inserted in the experimental apparatus to avoid light coming from the PPLN device after PS amplification returning back to the ECLs, while directing the amplified waves to an OSA for monitoring. Three different 5% MgO-doped PPLN waveguides with length of 3, 4.5 and 6 cm were used in this experiment, respec-

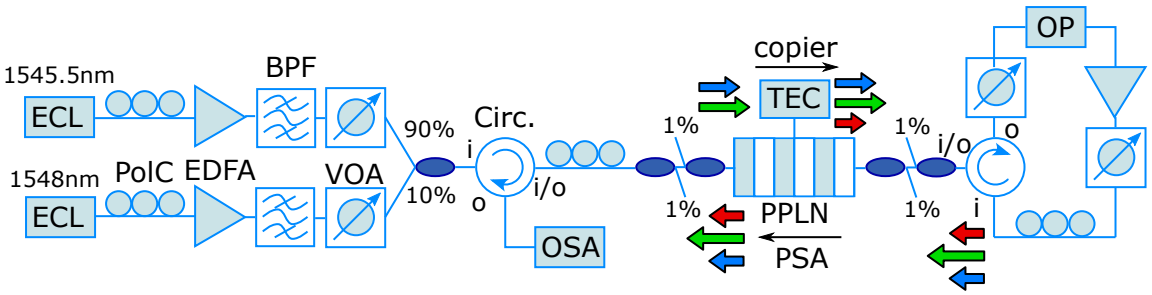

Figure 5.8: Experimental set-up used to characterize PS amplification in a bidirectional PPLN-based PSA.

tively labeled as PPLN30, PPLN45 and PPLN60. The poling period of the three PPLN devices was 19 μm. The measured normalized conversion efficiency, η, of the devices was of 21.1, 20.2 and 11.7 %W^{-1}cm^{-2} for PPLN30, PPLN45 and PPLN60, respectively. The total insertion losses were of about 3.5 to 4 dB, including the losses of the coupling optics.

After passing through the PPLN device for the first time, in the copier direction, a correlated idler *i* was generated at $\lambda_i = (2/\lambda_P - 1/\lambda_s)^{-1}$. Then, the three waves were led to the liquid crystal on silicon OP, after a VOA used to limit the maximum input power to the OP, of about 10 dBm. In addition to power equalization and variation of the relative phase between the interacting waves, the OP also enabled switching from PS to PI operation by blocking the idler wave. An additional EDFA was inserted in the loop to compensate for the attenuation of the VOA before the OP, as well as another VOA and PolC to control the power and state of polarization of the waves before entering the PPLN device for PS amplification. The power of the pump and signal waves entering the PPLN waveguide in the copier direction was of about 25.8 and 14.9 dBm, respectively. A total pump power up to 27.6 dBm was launched into the device in the PSA direction.

The experimental results and respective numerical simulations obtained by solving the coupled-mode equations for cSHG/DFG between CW waves with a 4$^{\text{th}}$-order Runge-Kutta algorithm are shown in figure 5.9. The same parameters of the experimental measurements were considered in the numerical simulations. Identical insertion losses for both sides of the PPLN device were also assumed. The optical spectrum of the signal wave obtained at the output of the PPLN in the PSA direction is shown in figures 5.9-a) to 5.9-c) for the maximum and minimum gain conditions, as well as for PI operation. According to the experimental results, an additional gain of 1.7, 3 and 0.7 were respectively obtained for PPLN30, PPLN45 and PPLN60, measured with respect to the gain in PI operation. The obtained results are far from the theoretical gain advantage of 6 dB, but such situation is only verified at high gain values, which was not the case in this experiment. As expected, a higher gain advantage is obtained with PPLN45 in comparison with the 3 cm device. However, a gain advantage of only 0.7 dB was measured for PPLN60 when an even higher advantage should be expected. The main reasons for this result are the lower normalized conversion efficiency and the higher susceptibility to λ_{QPM} detuning. In general, guaranteeing the uniformity and homogeneity of the waveguides in long devices is challenging, which typically results in lower normalized conversion efficiencies. In fact, the SHG conversion efficiency, given by $\eta \cdot L^2$, is almost the same for PPLN45 and PPLN60, of about 410 and 420 %/W, respectively. In addition, the QPM bandwidth of longer devices is narrower, so long PPLN waveguides are more sensitive to any wavelength/temperature detuning from the optimum operation condition.

The PS properties of the amplifier are evident in the results shown in figures 5.9-d) to 5.9-e). As shown in the figures, the gain of the amplifier is greatly affected by the relative phase $\Delta\phi$ applied to the pump wave in the OP. According to the experimental results, two gain maxima are observed at $\Delta\phi$ of 0.6π and 1.6π radians, whereas two minimum gain

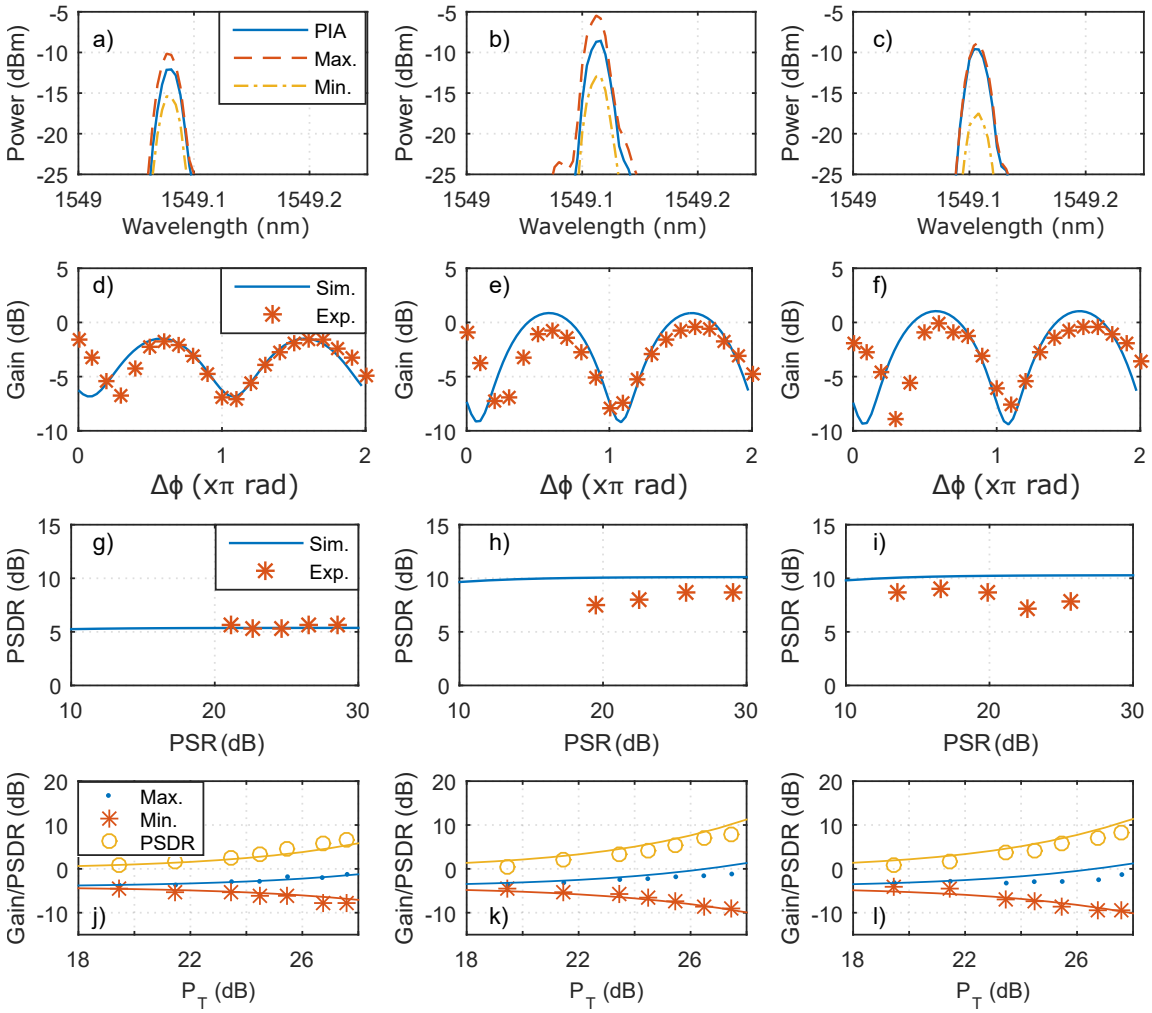

Figure 5.9: Measured optical spectra of the signal wave after PS amplification at the maximum (Max.) and minimum (Min.) gain conditions for a) PPLN30, b) PPLN45, and c) PPLN60. The output spectrum in PI operation is also shown by curve PIA, obtained by blocking the idler in the OP. Simulated and experimental variation of the gain with the relative phase-shift applied to the pump wave in the OP for d) PPLN30, e) PPLN45, and f) PPLN60. Simulated and experimental variation of the PSDR with *PSR* for g) PPLN30, h) PPLN45, and i) PPLN60, with P_T= 27.6 dBm. Variation of the PSDR and gain at the maximum (Max.) and minimum (Min.) gain conditions with P_T for j) PPLN30, k) PPLN45, and l) PPLN60, with *PSR* = 20 dB. In j), k) and l), the markers represent the experimental results, wheres the solid lines correspond to numerical simulations.

values are observed at $\Delta\phi$ of 0.3π and 1.1π radians. A good agreement is verified between the experimental results and the numerical simulations for relative phase values above 0.5π radians. For lower values of $\Delta\phi$, it was found that the real phase-shift applied to the pump wave did not match the one introduced in the OP controlling software. Nonetheless, the obtained results effectively show the PS properties of the bidirectional PPLN-based PSA.

The influence of the *PSR* on the PSDR is depicted in figures 5.9-g) to 5.9-i). According to the experimental measurements and the numerical simulations, the PSDR is practically unaffected by the *PSR*. A very good agreement between the experimental and numerical results is found for PPLN30, but PSDR values up to about 3 dB below the numerical

simulations were measured for PPLN45 and PPLN60. This discrepancy is caused by the emission of a strong green light wave, shown in figure 5.10, generated from SFG between the fundamental wave and the second harmonic. The green light emission not only partially depletes the pump wave, but it also leads to GRIIRA, which is one of the physical processes responsible for photorefractive damage in lithium niobate [123, 126], as discussed in chapter 2. Since the generation of the green light is stronger for longer devices, PPLNA45 and PPLN60 are also more susceptible to GRIIRA effects. Even though MgO-doping substantially mitigates GRIIRA effects [126], they are not completely eliminated, particularly at very high pump power and at room temperature operation. The local heating generated due to GRIIRA effects also required changing the temperature of operation in order to tune the QPM resonance condition to the pump wavelength. As an example, the temperature of operation of PPLN60 had to be tuned from 26.4 °C at P_T = 17.5 dBm to 22.6 °C at P_T = 27.6 dBm.

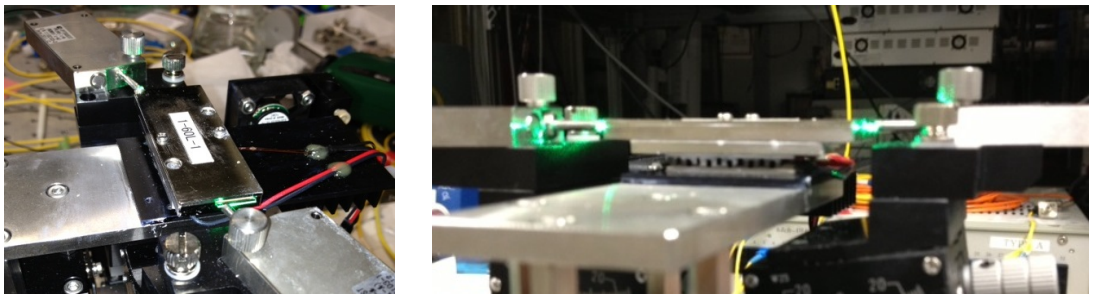

Figure 5.10: Green light emission in the PPLN device at high pump power. Courtesy of Dr. Benjamin Puttnam.

The influence of the total input power in the PSA direction, P_T, on the maximum and minimum gain and PSDR of the PSA is shown in figures 5.9-j) to 5.9-l), for a *PSR* of about 20 dB. As expected, the PSDR and maximum gain increase with P_T as a consequence of stronger pump power (note that about 99% of P_T is the pump power), with a good agreement between the experimental results and the numerical simulations. However, lower PSDR and maximum gain values were measured with respect to the numerical simulations for PPLN45 and PPLN60, in particular at high P_T values. This result is also caused by the non-negligible GRIIRA effects, as discussed above.

Despite the evident PS properties, no significant net gain could be obtained at any available pump power level due to the low conversion efficiency of the PPLN waveguides and high insertion losses. Using devices with higher conversion efficiencies such as ridge PPLN waveguides [50] is a possible way to increase the gain of the proposed scheme and use it as an amplifier in optical communication links, but such devices were not available. On the other hand, the measured PSDR values of about 10 dB suggest that, in principle, the proposed scheme can still be used for phase regeneration applications, as it is discussed in the next subsection.

5.2.2 Phase regeneration of BPSK signals in a single bidirectional PPLN device

With the advent of advanced modulation formats and coherent receivers, both amplitude and phase are used to encode several bits into a single symbol in order to increase the utilization efficiency of the available transmission bandwidth. Using such advanced modulation formats not only amplitude but also phase regeneration may be required. Several all-optical strategies have been suggested in order to achieve this purpose. Phase-preserving amplitude regenerators to limit the amplitude-to-phase nonlinear noise transfer, also known as the Gordon-Mollenauer effect [45, 46], and phase-to-amplitude format conversion using delay line interferometers, followed by amplitude regeneration [47] are some examples.

Phase regeneration of BPSK signals can be directly performed using the phase squeezing properties of PSAs, as reported in [25, 48–50], with the potential advantage of simultaneous amplitude regeneration by operating the PSA in saturation [25]. Extension to higher-order phase-encoded formats can also be performed by combining several BPSK phase regenerators [51], or by mixing the degraded signal with a phase-conjugated harmonic of the signal in a PSA [52–55].

Two main strategies have been considered to perform phase regeneration of a BPSK signal, based on either two-mode [48, 49] or one-mode [25, 50, 211] PSAs. As discussed in subsection 5.1.1 for configuration PSA3, the phase regeneration properties of two-mode PSAs can be enabled by first generating a correlated idler from a CW signal in a PI parametric amplifier (copier), and then modulate both the signal and idler waves in the same BPSK modulator [48, 49]. In a real system, this strategy is highly undesirable as it would require the generation of the correlated idler at the transmitter side. In addition, the correlated idler and pump waves must be transmitted along with the signal channel throughout the optical links until reaching the two-mode PSA for phase regeneration. Hence, this strategy is not further discussed in this thesis. The second possibility does not require any correlated idler to be transmitted along with the signal and is suitable for “black-box” (or in-line) operation, meaning that the phase regenerator can be regarded as a black-box whose inputs and outputs are only the deteriorated and regenerated signals [25].

The black-box phase regenerator is based on three main operations: phase squeezing in one-mode PSAs, generation of a low-noise correlated pump wave (also known as carrier recovery), and phase-locking of the pump phase [25]. Let us first discuss the phase squeezing properties of the PSA. The phase squeezing properties of one-mode PSAs are a direct consequence of the PS interference between the original signal photons propagating through the nonlinear medium and the new photons generated from the correlated pump waves through FWM or cSHG/DFG, as shown in figure 5.11-a). The phase of the generated photons is given by $\phi_s^{(2)} = \phi_{P1} + \phi_{P2} - \phi_s^{(1)} + const$, where $\phi_s^{(1)}$, ϕ_{P1} and ϕ_{P2} are the phases of the initial signal, pump P1 and pump P2, respectively, and *const* is a constant. The gain of the PSA is then determined by the relative phase of the generated

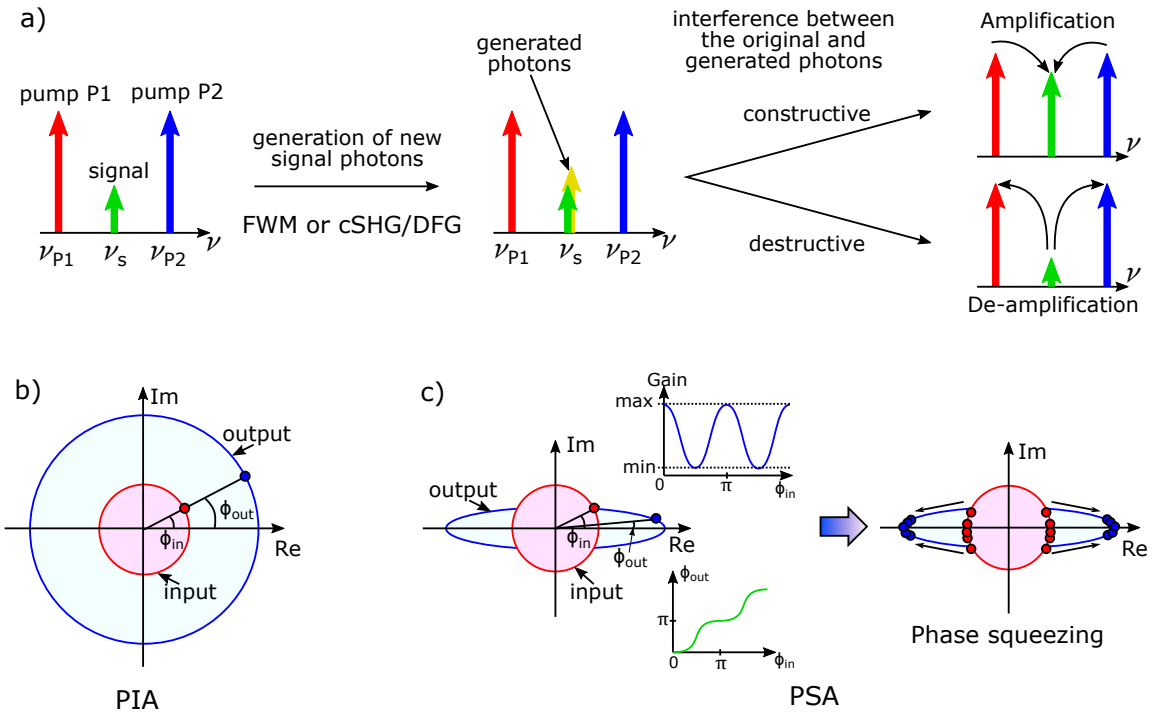

Figure 5.11: a) Schematic representation of the PS operation of PSAs based on constructive/destructive interference of original and generated photons. Illustration of the effects of a b) PIA and c) PSA on the constellation diagrams of the signal wave.

and initial signal photons, according to $\Delta\phi = \phi_s^{(2)} - \phi_s^{(1)} = \phi_{P1} + \phi_{P2} - 2\phi_s^{(1)} + const$. Hence, maximum or minimum gain values are obtained for $\Delta\phi$ equal to an even or odd multiple of π, at which constructive or destructive interference between the initial and generated signal waves is respectively observed. At any other values of $\Delta\phi$, the gain of the PSA varies between these two extreme possibilities, determined by the interference condition.

The phase squeezing properties of the PSA can be understood by the effects of the amplifier on the output constellation diagrams, illustrated in figure 5.11-b) for a PIA and 5.11-c) for a PSA. In these figures, the red lines represent the constellation diagrams of an input signal with constant amplitude and random phase, whereas the blue lines represent the respective output constellation diagrams. In the case of a PIA, both the in-phase and quadrature components of the input signal are amplified equally, so the output and input signal phases, ϕ_{out} and ϕ_{in}, are identical. Hence, no phase regeneration is observed. On the other hand, the in-phase and quadrature components experience different gain in a PSA, so the output constellation is elongated towards a preferential gain axis, leading to phase squeezing. The typical variation of the gain and output phase as function of the input signal phase is also represented in 5.11-c). As depicted in the figure, the gain of the PSA periodically varies from maximum to minimum values, depending on the input signal phase. In addition, the output phase response of the regenerator, illustrated by the green curve in figure 5.11-c), has a staircase shape with two step levels at 0 and π. The staircase shape of the signal phase transfer function is an indication of the phase regenerative properties [49].

The phase regenerative properties of the PSA can be quantified by the maximum and minimum gain of the amplifier. Let us assume that the in-phase and quadrature components of the signal wave are amplified with respective gain values of G_x (maximum gain) and G_y (minimum gain). Let us also consider that the complex amplitude of the signal symbol is generically described by $A_s = |A_s|\,[\cos(\phi_{in}) + i\sin(\phi_{in})]$. After the PSA, the complex amplitude of the signal becomes $A_s = |A_s|\,[G_x\cos(\phi_{in}) + iG_y\sin(\phi_{in})]$ and the output phase is given by [48]

$$\phi_{out} = \text{atan}\left(\frac{G_y\sin(\phi_{in})}{G_x\cos(\phi_{in})}\right) = \text{atan}\left(\frac{\tan(\phi_{in})}{PSDR}\right), \tag{5.14}$$

where $PSDR = G_x/G_y$. The PSDR determines the steepness of the staircase-shaped phase transfer function of the regenerator, with steeper phase transitions for higher PSDR values. The PSDR also defines the elongation of the output constellation diagram of the regenerator.

Let us now discuss the generation of the correlated pump waves. In order to achieve black-box operation, the correlated pumps must be generated by mixing an initial pump (P1) with the input signal through FWM or cSHG/DFG in a first PIA (copier), as depicted in figure 5.12. A new wave (P2) at frequency $\nu_{P2} = 2\nu_s - \nu_{P1}$ is generated in the copier PIA, whose phase is given by $\phi_{P2} = 2\phi_s - \phi_{P1} + const$, with $const$ a constant term. Assuming an input noisy BPSK signal with phase $\phi_{data} + \phi_{s,n}$, where ϕ_{data} represents the logic phase symbols and $\phi_{s,n}$ is the signal phase noise, the phase of P2 becomes $\phi_{P2} = 2\phi_{data} + 2\phi_{s,n} - \phi_{P1} + const$. Since ϕ_{data} is either 0 or π, the respective data modulation in P2 becomes 0 and 2π, so the modulation data is erased (modulation stripping). Consequently, a strong narrow-linewidth carrier is generated, as depicted in figure 5.12. However, an excess phase noise is also transferred to pump P2, enhanced by a factor of 2 compared to the initial phase noise in the signal.

The excess phase noise can be removed through a narrow-band filtering process such as injection locking [25, 208, 212]. Injection locking is a process in which the frequency and phase of a free-running oscillator (slave) is stabilized and locked to the emission of a master oscillator [212]. In order to guarantee stable injection locking, a narrow-bandwidth carrier needs to be fed into the slave laser, which ultimately determines the emission of the slave laser. Any frequency components other than the carrier (e.g. noise) are not locked and are attenuated with respect to the carrier. This is the main principle of operation behind narrow-band filtering through injection locking and the reason why it is necessary

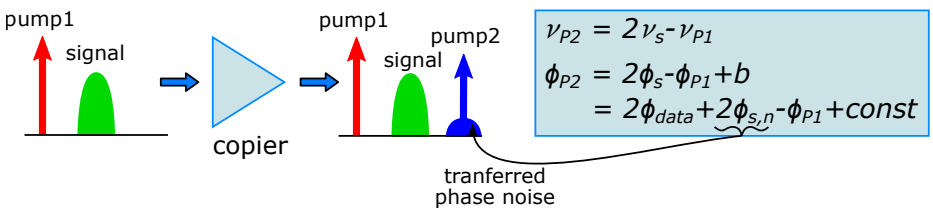

Figure 5.12: Schematic representation of the carrier recovery process using a copier PIA.

to generate a narrow-bandwidth carrier by removing the data modulation from pump P2. The bandwidth of injection locking filtering depends on the injected power level. Typically, narrower filtering properties are obtained at low input power values [212, 213]. Depending on the output power of the slave laser, injection locking can also be used to amplify the master laser emission. In [208], a pump recovery set-up based on injection locking was demonstrated, obtaining gain values of more than 40 dB.

Narrow-band filtering based on injection locking requires separating P2 from the other waves to another optical path, and combining the waves again after noise filtering. In order to keep the phase of the interacting waves locked, not only the length of the two optical paths must be aligned, but any phase drift caused by thermal and acoustic fluctuations of the optical paths must be tracked and compensated. This situation leads to the third requirement for black-box operation, i.e., the optical PLL. An optical PLL built with a PZT-based fiber stretcher is a possible solution to guarantee phase-locked waves at the input of the PSA [25, 186]. The optical PLL circuit is based on a lock-in amplifier, which produces a reference sinusoidal signal that is used to drive the fiber stretch and generates a small phase dithering on one of the interacting waves. After PS amplification, the phase dithering is converted into a small sinusoidal variation of the signal gain, which can be detected in a PD. The detected signal is then compared with the reference sinusoidal originally generated by the lock-in amplifier, providing a feedback error mechanism for the PLL circuit. Further details on the operation of the optical PLL are provided later on, when describing the experimental set-up used to demonstrate phase regeneration of BPSK signals.

In this subsection, a BPSK phase regenerator based on the copier + PSA scheme in a single bidirectional PPLN waveguide device is considered. In the proposed scheme, the correlated P2 wave is generated in the copier direction, using a discrete-mode semiconductor laser [214] for injection locking, and a PLL based on a PZT fiber stretcher to compensate for any acoustic and thermal phase drifts of the relative phase of the interacting waves.

Experimental set-up

The experimental set-up used for phase regeneration of BPSK signals in a single bidirectional PPLN device is depicted in figure 5.13. The noisy 10 Gb/s BPSK signal was generated by modulating the light emitted by an ECL in a phase modulator (PM) driven by a noise-loaded electrical signal. The drive voltage (V_π) and the 3-dB bandwidth of the PM were about 5 V and 34 GHz, respectively. A PRBS of length 2^{15}-1 was considered in this experiment. Additional white noise was provided by a noise source composed of two cascaded EDFAs interleaved by a 3 nm BPF. The contribution of each noise source was selected in order to obtain standard deviation values of the detected symbols for phase and amplitude of 0.25 and 0.1, respectively, measured before entering the PPLN for phase regeneration.

After amplification and out-of-band ASE noise filtering, part of the modulated signal

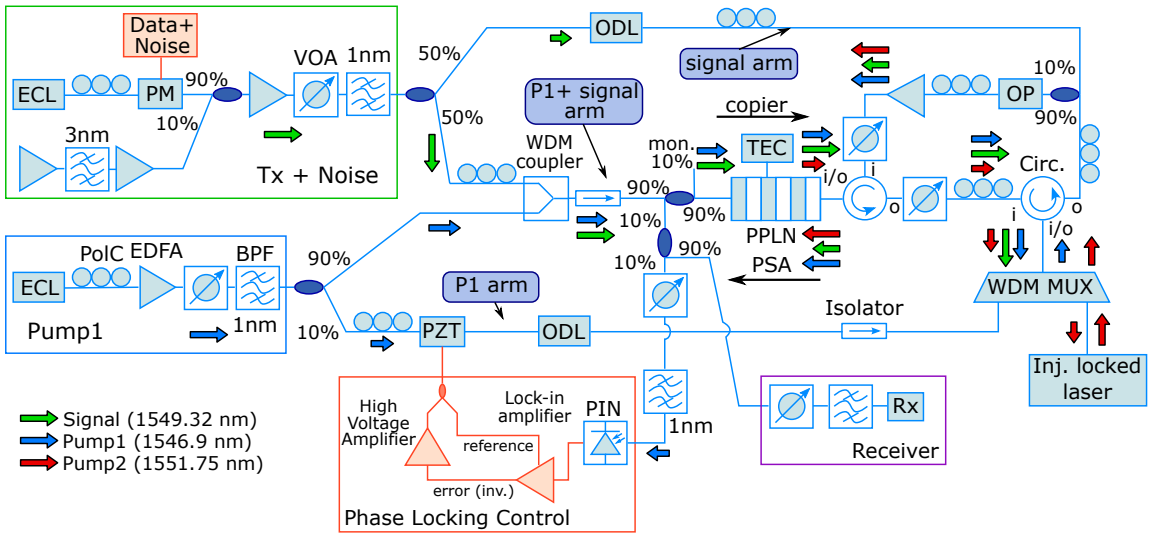

Figure 5.13: Experimental set-up used for black-box phase regeneration of BPSK signals in a single bidirectional PPLN waveguide.

was combined with the P1 wave emitted from another ECL in a WDM coupler (P1 + signal arm), and injected into the PPLN device. The length, poling period, QPM wavelength at 21 °C, content of MgO and normalized conversion efficiency of the PPLN waveguide were 6 cm, 19.1 μm, 1549.3 nm, 5% and 15.6 %W^{-1}cm^{-2}, respectively. The PPLN waveguide was chosen as a trade-off between the spectral operational range of the injection-locking laser and the passband of the WDM coupler, while enabling room temperature operation. The input power going into the PPLN waveguide in the copier direction was about 27.3 dBm.

After generation of wave P2 in the copier direction, the generated wave passed through an optical circulator (Circ.) and was led to an injection-locked laser in order to remove the excess phase-noise produced through the cSHG/DFG interaction, as proposed in [25]. A discrete-mode semiconductor laser was used as the slave laser. A VOA and a PolC were introduced before a second circulator in order to control the input power and state of polarization of the P2 wave before the injection-locked laser. In this experiment, a WDM multiplexer (WDM MUX) was used to filter all the signals except P2 at the input to the semiconductor laser, and also to combine the filtered output pump P2 with pump P1 coming from the P1 arm. The semiconductor slave laser had an emission linewidth of the order of 100 kHz, with a maximum output power of around 10 dBm. The power of the light injected into the slave laser was set to below -20 dBm for narrow filtering operation. Then, the phase-correlated pumps coming from the output (o) port of the second optical circulator were combined with the modulated signal from the signal arm in a 10:90 coupler and sent to a liquid crystal on silicon OP for power equalization and an EDFA, before entering the PPLN for phase regeneration in the PSA direction. This EDFA was introduced to compensate the attenuation required at the input of the OP due to its maximum input power constraints and the insertion losses of the other passive devices introduced in the optical path. The

power of the two pump waves was set to the same value (balanced pumps) for optimal performance. In addition to power equalization of the interacting waves, the OP allowed switching between PS and PI operation by blocking the wave P2. ODLs and PolCs were also introduced in the signal and P1 arms to guarantee path length and state of polarization alignment. The total power injected into the PPLN waveguide in the PSA direction was varied up to a maximum value of 28.9 dBm.

After phase regeneration along the PSA direction in the PPLN device, part of the regenerated signal was tapped from a 10:90 coupler, placed between the PPLN and the WDM coupler, and sent to a variable bandwidth BPF and a single polarization coherent receiver. An optical isolator was also introduced between the WDM coupler and the PPLN device in order to avoid the high-power waves coming out of the PPLN devices to return into the ECLs. The coherent receiver was composed by a 100 kHz linewidth ECL used as the local oscillator and a 90° optical hybrid received with DC-coupled PDs at the input to a 40 GSample/s real-time sampling oscilloscope, with an analog bandwidth of 13 GHz.

The acoustic and thermal drifts of the equalized path lengths were compensated by a PLL circuit based on a PZT fiber stretcher placed in the P1 arm, shown in the phase locking control box of figure 5.13. The same optical PLL described in [203, 211] was used in this work, originally based on the set-up presented in [186]. A reference sinusoidal signal with a frequency of about 20 kHz was generated in a lock-in amplifier and applied to the PZT fiber stretcher in the P1 arm. The PZT-based fiber stretcher was built by wrapping an optical fiber around a cylindrical piezoelectric element. The expansion of the PZT element caused by the applied electrical signal stretched the wrapped fiber, producing a phase shift proportional to the fiber elongation. The reference sinusoidal signal created a phase dithering tone on pump P1, which in turn was converted into a small amplitude modulation on the signal after the PSA [186]. Then, a portion of the signal wave was filtered from the remaining waves in a 1 nm BPF and detected in a PIN PD. The obtained photocurrent contained the dithering frequency component that was selected by the lock-in amplifier and compared with the original reference signal. The phase difference between the two signals provided the error control mechanism used as the feedback of the PLL circuit. The lock-in amplifier was also equipped with an internal inverting amplifier, providing an inverted copy of the error signal. The inverted error signal was amplified by a high-voltage amplifier with maximum output voltage of 200 V, combined with the reference sinusoidal signal and applied to the PZT fiber stretcher.

Experimental results and discussion

The performance of the phase regenerator was assessed by measuring the ratio between the standard deviations of the received symbols in PI and PS operation for both the amplitude and phase of the detected signals, at different pump-to-signal power ratios, PSR, and total input power in the PSA direction, P_T. In PI operation, no clear degradation or improvement of the amplitude and phase noise properties of the received signal were

verified compared to the results measured at the input of the PPLN waveguides. Thus, the standard deviation ratios for PI and PS modes can be used to infer on the performance of the phase regenerator. Effective phase or amplitude regeneration is obtained whenever σ_{PI}/σ_{PS} is greater than 1, with σ_{PI} and σ_{PS} the standard deviation in PI and PS operation, respectively.

The obtained results are shown in figure 5.14. For all the measurements, the standard deviation ratios of the phase of the received symbols are higher than 1, proving effective phase regeneration. Moreover, better phase regenerative properties tend to be observed for higher P_T values, where higher standard deviation ratios are observed. This is an expected result, as stronger pumping power leads to higher PSDR and, consequently, to better phase squeezing properties. Regarding the amplitude of the detected symbols, no clear trend with *PSR* or P_T is observed but, in general, the standard deviation ratio values for the amplitude are slightly lower than 1. This result indicates that the amplitude of the data symbols is degraded in PS operation, which is caused by phase-to-amplitude noise conversion in the PSA [49]. The phase-to-amplitude noise conversion in a PSA can be understood from the phase-sensitive gain curves shown in figures 5.4-b) and 5.11-c). Any phase drift from the optimum gain condition of the PSA caused, for instance, by phase noise, changes the gain of the amplifier and, consequently, the amplitude of the output signal.

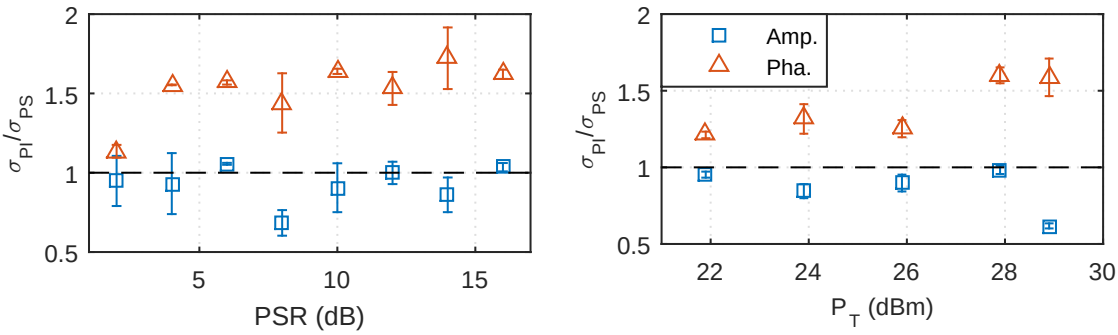

Figure 5.14: Ratio between the standard deviations of the received symbols in PI and PS operation for both the amplitude and phase of the received symbols as function of: a) *PSR* for P_T = 28.9 dBm; b) P_T for *PSR* = 10 dB.

The phase regenerative properties of the PSA are also evident in the received constellation diagrams depicted in figure 5.15. According to the constellation diagrams, not only the symbols are partially squeezed towards the real axis, but so are the transition samples, represented by the green curves. A clear degradation of the amplitude of the received symbols in PS operation can also be observed, especially for the cases where the phase squeezing is stronger. This later result is a consequence of phase-to-amplitude noise conversion, as discussed above.

The phase regenerator studied in this subsection also suffered from thermal instability and photorefractive effects that not only affected the gain of the PSA, but also the stability

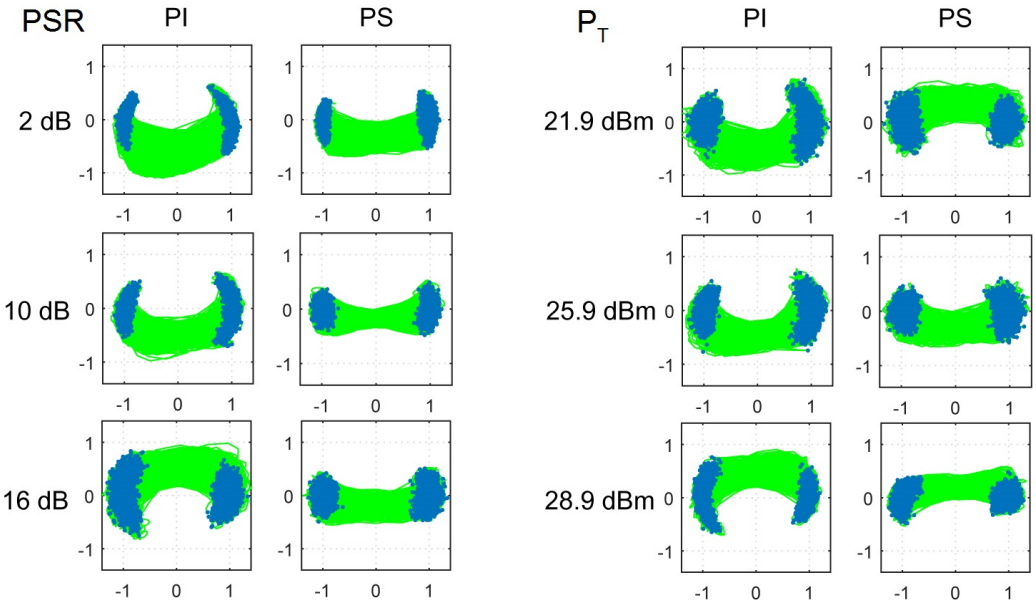

Figure 5.15: Received constellation diagrams in PI and PS operation. On the left, the constellation diagrams were obtained for different *PSR* values, with P_T = 28.9 dBm. On the right, the constellation diagrams were obtained for different values of P_T, with *PSR* = 10 dB.

of the phase-locking system. In fact, stable operation could only be observed for a few seconds, that was still enough to obtain the presented results, but prevented conducting further investigations such as receiver sensitivity measurements and/or the influence of the OSNR on the BER of the received signals. The reason for the instability of the PLL circuit is due to the combination of several impairing effects, aggravated by bidirectional propagation. One of the main problems affecting the experiment was a strong and intermittent emission of green light from the PPLN device, caused by SFG between the second harmonic and the fundamental wave. Whenever the PLL circuit tried to correct the phase drifts, the power conversion from the pumps to the second harmonic and to the signal wave was modified, thereby altering the strength of the green light emission. Because of thermal instability, photorefractive and GRIIRA effects, the variation of the green light emission changed the refractive index and the QPM condition of the PPLN device. In turn, these phenomena affected the generation of pump P2 in the copier direction and the gain of the amplifier in PS operation. According to [212], the power injected in an injection-locked laser affects the phase of the output waves, so the instability on the generation of pump P2 also created an additional phase drift contribution. The combination of all these effects made achieving stable operation of the PLL circuit very challenging, so improvements on the thermal and refractive index stability of the PPLN devices must be pursued in order to make the bidirectional PPLN-based PSA a viable technique for phase regeneration.

PPLT waveguides have been suggested as a possible alternative to PPLN devices due to their higher tolerance to photorefractive damage. However, the nonlinear coefficient of lithium tantalate is lower than of lithium niobate, and thus stronger pumping power would be

required in order to achieve comparable regenerative properties. In fact, the performance of PPLT waveguides at high pump power was investigated by the author of this thesis, showing better tolerances to GRIIRA and photorefraction [215]. However, the conversion efficiency of such devices was very low, which means that the fabrication technology and performances of the PPLT waveguides still need to be improved before they become a possible alternative.

5.3 Four-mode phase-sensitive amplification

Until recently, almost all reported applications of PSAs have been based on on either one-mode or two-mode PS parametric processes [25, 48, 49, 73]. More recently, however, PS amplification of CW signals [216] and PS broadband multicasting [209] using four-mode PSAs have been demonstrated. As discussed in section 5.1, four-mode PSAs involve the interaction between one input signal (s) and three idler waves, the MI, the PC and BS waves. It was also shown in section 5.1 that the narrow QPM bandwidth of PPLN waveguides precludes four-mode operation, as the intermediary SFG waves SF1 and SF2 could not be efficiently generated. As a consequence, no efficient mixing between the signal or PC waves with the MI or BS idlers could be observed and the supposedly four-mode PSA would actually behave as two independent two-mode PSAs. However, this is not the case for fiber-based PSAs, as no intermediary nonlinear processes are required. In this section, a HNLF is used to demonstrate four-mode PS operation and high-gain amplification of a 10 Gsymbol/s QPSK signal.

The HNLF-based four-mode PSA involves seven different degenerate and non-degenerate FWM interactions, whose frequency relations are shown in figure 5.16. As discussed in section 5.1 for configuration PSA6, four-mode PSAs provide an additional gain advantage of 16 (12 dB) compared to PIAs, which is a consequence of the coherent beating of four correlated waves. However, in the case of a four-mode PPLN-based PSAs, it was observed that the generation of the intermediate waves at the second harmonic band eliminated the expected gain advantage of 6 dB when compared to two-mode configurations. This is not the case of four-mode fiber-based PSAs, which show a gain advantage of 6 dB when compared to twp-mode PSAs as no intermediate waves at the second harmonic band need to be generated [209]. In addition, if the dominant noise source is the quantum noise, four-mode fiber-based PSAs enable an OSNR improvement of 12 dB compared to common PIAs [217].

In this section, the influence of the power of the signal and pump waves on the net gain of a four-mode PSA built with a HNLF is experimentally investigated using the copier + PSA scheme to generate the correlated idlers. The influence of the relative phase of the interacting waves on the net gain of the amplifier is also evaluated, again using an OP based on liquid crystal on silicon technology to control the phase of the interacting waves. After investigating the influence of these parameters on the gain of the amplifier, PS

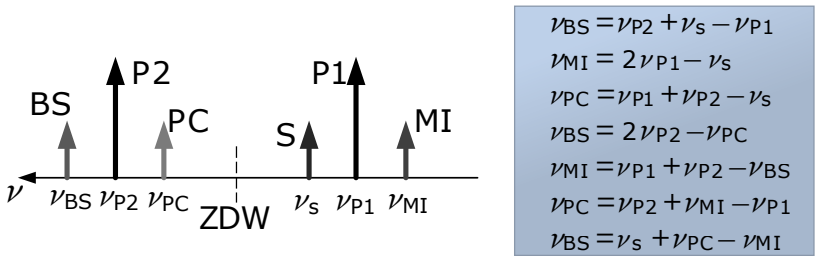

Figure 5.16: Illustration of the input waves of the four-mode PSA, with respective FWM interactions.

amplification of a 10 Gsymbol/s QPSK signal is also demonstrated and evaluated through BER measurements as a function of the OSNR. No active control of the relative phase of the interacting waves was necessary in this experiment as all the waves propagated through the same optical path between the copier and the PSA, without being affected by phase shifts due to acoustic and thermal fluctuations. Even without using an optical PLL to actively control the phase of the waves, the gain of the amplifier in PS operation remained stable for several hours, which allowed performing all the experimental measurements. This would not be the case if, for instance, the pumps had to be separated and combined again with the other waves, after re-amplification and noise filtering (pump recovery). In this case, the waves would propagate through different optical paths, creating an interferometric architecture that would require an active PLL to compensate for the phase drifts of the different paths, as in the previous section. An optical PLL might also be necessary in a real system in order to guarantee that the amplifiers always operate at the optimal phase condition, even if random events change the relative phase of the waves. Despite not requiring an active PLL to guarantee phase-locking, static optimization of the relative phase of the waves still had to be performed in an OP in order to tune the gain of the amplifier to the optimum condition.

The experimental set-up used in this experiment is depicted in figure 5.17. The two pump waves were generated in ECLs with emission linewidth of 500 kHz, at 1563.81 nm (P1) and 1543.57 nm (P2), and injected into a PM driven by three dithering tones to mitigate SBS, as reported in [49, 186]. Using this technique, the SBS threshold was

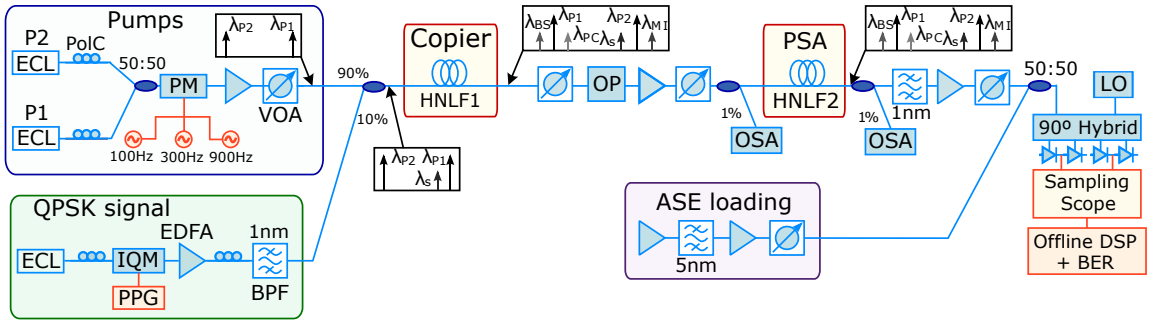

Figure 5.17: Experimental set-up used for four-mode PS amplification of a 10 Gsymbol/s QPSK signal.

increased to more than 25 dBm for each pump, as depicted in figure 5.18, measured for fiber HNLF2. Without the phase dithering tones, the SBS backscattered waves start to grow very quickly for pump power values above 14 dBm. With the dithering tones turned on, the SBS backscattered light remains below -20 dBm even for pump power values as high as 27 dBm.

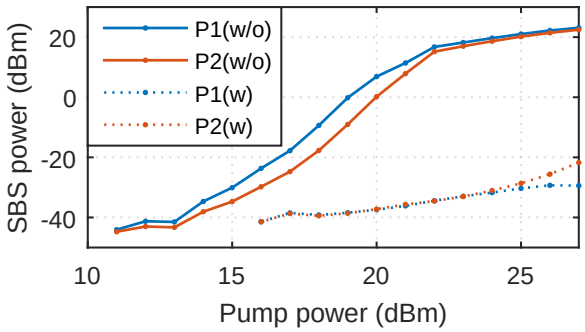

Figure 5.18: Variation of the SBS backscattered power in HNLF2 with the pump power, for pumps P1 and P2, with (w) and without (w/o) the dithering tones.

The QPSK signal was generated in an IQM from light emitted by another 500 kHz linewidth ECL, at 1561.42 nm. The IQM was driven by two PRBSs of length 2^{15}-1, generated in a PPG. After amplification in a high power EDFA, the two pumps were combined with the QPSK signal. PolCs were used to align the waves to the same state of polarization. The correlated idlers MI, PC and BS were generated in a first HNLF (HNLF1), which acted as the copier amplifier, at 1566.21, 1545.91 and 1542.24 nm, respectively. The length, λ_{ZDW}, dispersion slope at λ_{ZDW}, nonlinear coefficient and total insertion losses were 400 m, 1544 nm, 0.02 ps.nm^{-2}km^{-1}, 10 W^{-1}km^{-1} and 1 dB, respectively. After generation of the idlers, the waves were injected into the OP for power equalization and to adjust the relative phase of the interacting waves. The OP also enabled switching from PS to PI operation, by blocking the idler waves, converting the PSA into a four-mode PIA. Since all the waves propagated along the same optical path, no active control of the phase relation between the waves was required. An optical attenuator was introduced before the OP to limit the maximum input power to about 10 dBm. Because of this limitation, an additional EDFA was placed before the PSA to compensate for the attenuation and insertion losses of the OP. In reference [186], the additional VOA and EDFA were eliminated by separating the high-power pumps from the other waves before the OP. However, this strategy created an interferometric-like structure, requiring an active PLL to compensate for the temperature and acoustic phase fluctuations between the two branches of the scheme [186]. An additional VOA was inserted to control the total input power into the PSA. All the measurements were carried out with $P_{P1} = P_{P2} = P_P$, with P_{P1} and P_{P2} the power of each pump. In PS operation, the power of the signal and idlers was also equalized to the same value. Four-mode PS amplification was achieved in a second HNLF (HNLF2) whose length, λ_{ZDW}, dispersion slope at the λ_{ZDW}, nonlinear coefficient and total insertion losses were 500 m,

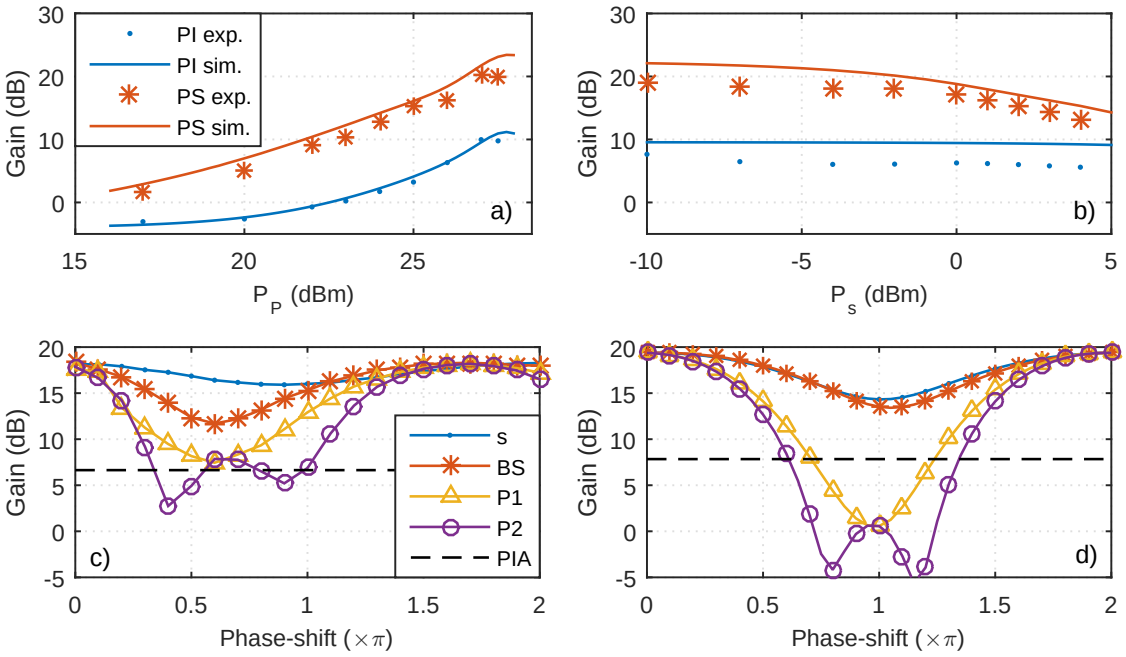

Figure 5.19: Variation of the net gain with: a) P_P, for P_s = -7 dBm, and b) P_S, for P_P = 27 dBm. The solid lines correspond to numerical simulations. c) Experimental and d) simulated variation of the net gain with the relative phase added in the OP, for P_P = 27 dBm and P_s = -3 dBm.

1549 nm, 0.02 ps.nm^{-2}km^{-1}, 17 W^{-1}km^{-1} and 3.5 dB, respectively. OSAs were introduced before and after the HNLF for monitoring and gain measurement.

After PS amplification, the output signal was filtered from the other waves and led to a coherent receiver. In order to evaluate the BER performance of the four-mode PSA, the ASE noise emitted by two EDFAs interleaved by a 5 nm BPF was combined with the signal in a 50:50 coupler. An additional EDFA and a VOA were introduced in the signal path in order to allow adjusting the OSNR at the receiver. The QPSK signal was detected in a coherent receiver comprising a 90° hybrid equipped with balanced PDs, located at the input of a 13 GHz bandwidth, 40 GSample/s real-time sampling oscilloscope. An ECL with an emission linewidth of 100 kHz was used as the local oscillator. The signal power at the input of the 90° hybrid was about 0 dBm. The received signal was then processed offline through DSP techniques, including normalization, re-timing, equalization and carrier recovery.

In order to determine the influence of P_P, the signal power, P_s, and the phase-shift applied in the OP on the net gain of the amplifier, the IQM was first turned off for CW operation, and the net gain was calculated from the optical spectra measured before and after HNLF2. The obtained results are depicted in figure 5.19. According to the obtained results, the net gain of the amplifier, defined as the signal power ratio measured after and before the PSA, strongly depends on the power of pump waves. In either PS or PI modes, the gain of the amplifier increases with the pump power, respectively achieving maximum values of 20.1 and 10 dB in PS and PI operation at P_P of 27 dBm. At P_P of about 25 dBm an addi-

tional gain of almost 12 dB was measured when switching from PI to PS operation, which is in agreement with the theoretical predictions. In figure 5.19-b), the gain of the amplifier is almost independent of the signal power P_s up to power values of -2 dBm. For higher P_P values, the amplifier starts to saturate and the gain decreases, especially in PS operation where higher gains are observed. Numerical simulations calculated by integrating the nonlinear Schrödinger equation using the SSFT method and considering the same physical parameters of the experiments are also included in figures 5.19-a) and 5.19-b). Despite being affected by several mechanisms that were not included in the numerical simulations such as residual polarization-mode dispersion, chromatic dispersion, local fluctuations of the λ_{ZDW} and the phase dithering, a good agreement between the numerical simulations and experimental results is found.

The PS properties of the PSA are shown in figure 5.19-c), where the variation of the signal gain is depicted as a function of the relative phase-shift applied in the OP. In figure 5.19-c), the phase-shift applied to the signal, BS, P1 and P2 waves is measured with respect to the phase condition at which the maximum gain is observed. According to the experimental results, a difference between the maximum and minimum values of the net gain of more than 10 dB can be observed when changing the relative phase of waves P1 and P2, whereas only about 6 and 2 dB are observed for the BS and signal waves, respectively. Despite not being shown in 5.19-c), a similar behavior was observed when changing the phase of the MI and PC waves, as also reported in [216]. An uncharacteristic gain variation of about 5 dB can be observed in curve P2 for phase values between 0.4π and 0.9π. A similar uncharacteristic behavior is present in the numerical simulations shown in figure 5.19-d). The observed experimental and numerical results can be explained by two mechanisms. Any phase-shift applied to a single wave affects more than one FWM process simultaneously, leading to an intricate power transfer between the interacting waves and, consequently, to a complex PS gain characteristic of the amplifier. The amplifier was also affected by residual chromatic dispersion, so the phase mismatching between the interacting waves in each FWM process were different, contributing to the uncharacteristic gain variation. In this experiment, the pump waves were not symmetrically displaced around the λ_{ZDW} due to two main reasons. First, a wide frequency separation between the two pumps was desired to reduce deleterious degenerate FWM between the pumps, which would create new waves at frequencies $2\nu_{P1} - \nu_{P2}$ and $2\nu_{P2} - \nu_{P1}$. Second, the wavelength of the pumps was limited by the gain bandwidth of the EDFA in the “Pumps” box of figure 5.17. The observation of the uncharacteristic gain variation in curve P2 is also very important if deploying the four-mode PSA in a real system where a PLL must be used to actively ensure operation at the optimal gain condition. If the phase of pump P2 was used as the reference phase to control the PLL it could converge and lock the phase of P2 to the local maximum observed at 0.7π radians, which clearly is not the optimum operation condition.

Even though the variation of the net gain with the relative phase-shift in the numerical

simulations resembles the experimental results, some significant differences can be found. First, a much lower minimum PS gain is observed in the numerical simulations for the signal (s), P1 and P2 curves, which is believed to be caused by effects such as PMD, fluctuations of the zero-dispersion wavelength and residual Raman amplification that were not included in the numerical simulations. Second, the minimum gain for curves BS and P1, and the local uncharacteristic gain maximum of curve P2 are observed at approximately 0.6π, whereas in the case of the numerical simulations, such conditions are observed at a relative phase-shift of π. As discussed in subsection 5.2.1, the real phase-shifts applied in the OP did not exactly coincide with the values inserted in the controlling software, particularly at low phase-shift values, which explains the observed results. This discrepancy could have been avoided by obtaining a calibration curve using a simpler interferometric set-up (e.g., an MZI), but it was also found that the calibration curves depend on the attenuation applied by the OP. Nonetheless, and despite the observed differences, the obtained results effectively prove PS operation. The net gain of the amplifier operating in PI mode is also depicted in figure 5.19-c), for comparison. A net gain value of 6.6 dB was obtained, about 11.6 dB less than the maximum gain of the amplifier in PS operation. This result is in agreement with the theoretical predictions of additional gain of 12 dB in four-mode PSA when compared to a PIA, as also verified through numerical simulations.

The optical spectra measured before and after the PSA, operating in PS and PI modes for $P_P = 27$ dBm and $P_s = 5$ dBm, are also shown in figure 5.20. According to the measured spectra, a similar noise floor at approximately -10 dBm was verified in both PS and PI operation. Since noise is uncorrelated, some noise components beat constructively in PS operation, whereas other beat destructively, resulting in an effective net gain equivalent to that of a PIA, which explains the observed result.

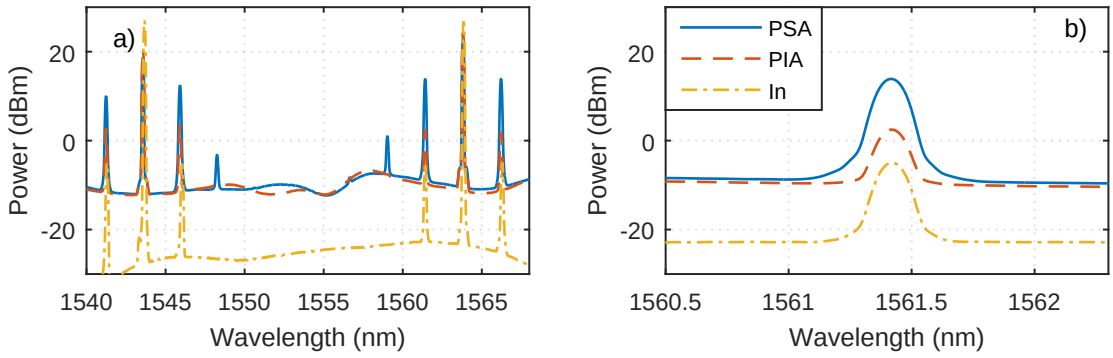

Figure 5.20: a) Optical spectra measured at the input (In) and after the PSA, in PS and PI operation. b) Measured spectra, detailed around the signal wave. The optical spectra were acquired with an optical resolution of 0.1 nm.

Given that a considerable net gain could be achieved in the four-mode PSA characterized in this subsection, the next logical step would be to determine its NF. The NF is a typical parameter used to characterize the noise performance of amplifiers, defined as the ratio between the input and output SNRs of the amplifier. However, measuring the NF

of PSAs is very challenging as the correct definition of this parameter requires accounting for the combined noise properties of the signal and idler waves [218]. This procedure becomes even more complex if the dominant noise source of the input waves is the ASE loaded by previous amplifiers and when the signal and idlers have different input OSNR, as was the case in this experiment. Hence, the NF of the amplifier is not discussed herein but, instead, we focus on the difference between the output and input OSNR of the signal wave. Output to input OSNR variations, $\Delta OSNR$, of -8.5, -8.7, and -5 dB in PS operation, and 3.4, 3.8, and 5.6 in PI mode were measured for P_P of 23, 25, and 27 dBm, respectively. In order to understand why $\Delta OSNR$ decreases in PS operation and increases in PI mode, let us analyze the gain properties of the amplifier for the signal and for the noise. According to the output optical spectra depicted in figure 5.20, a noise floor at the same power level is observed when the amplifier operates in either PS or PI mode. This result is explained by the uncorrelated nature of the incoherent noise, such that some noise components add constructively in the PSA, whereas others beat destructively. Consequently, the net gain for incoherent noise in a PSA is equivalent to that of a PIA.

The noise of the signal wave at the output of a parametric PIA or PSA includes two types of contributions. One consists of the amplified noise of the signal itself injected into the amplifier. The other is generated from the initial noise in the idler waves, which is amplified and converted to the signal. In the limit of high gain, each of such contributions is amplified and added to the signal with approximately the same gain G, so the total noise at the output of the amplifier in either PS or PI operation is approximately given by $G(P_{n,s}+P_{n,BS}+P_{n,MI}+P_{n,PC})$, with $P_{n,s}$, $P_{n,BS}$, $P_{n,MI}$, $P_{n,PC}$ the noise power at the input of the amplifier for the signal, BS, MI and PS waves, respectively. In the case of PI operation, the signal is also amplified by a factor of G, whereas a gain of about $16G$ is obtained in PS mode due to the additional correlated waves. Hence, the variation of the OSNR of the four-mode PSA can be described by the following expression

$$\begin{aligned}\Delta OSNR = \frac{OSNR_{in}}{OSNR_{out}} &\approx \frac{P_s}{P_{n,s}} \cdot \frac{G\left(P_{n,s}+P_{n,BS}+P_{n,MI}+P_{n,PC}\right)}{kGP_s} \\ &= \frac{1}{k} \cdot \frac{P_{n,s}+P_{n,BS}+P_{n,MI}+P_{n,PC}}{P_{n,s}},\end{aligned} \tag{5.15}$$

with P_s the power of the signal and k is equal to 1 in PI operation or 16 in PS mode. If the same noise power is loaded to the signal and idlers at the input of the amplifier, $\Delta OSNR$ becomes approximately equal to 4 (6 dB) for a four-mode PIA and 1/4 (-6 dB) for a PSA. However, this was not exactly the case of this experiment, as the noise power for the signal and idler waves was not the same. In fact, the dominant noise source at the input of the four-mode amplifier was the noise loaded in the previous amplifiers of the set-up, namely the EDFA after the OP. Because of non-flat ASE emission of the EDFA after the OP, the noise power level for the signal and idlers was quite different, as shown by the input optical spectrum in figure 5.20. By considering the noise power levels of the signal and idler waves at the input of the amplifier in (5.15), a theoretical $\Delta OSNR$ value of -8.73 dB is expected,

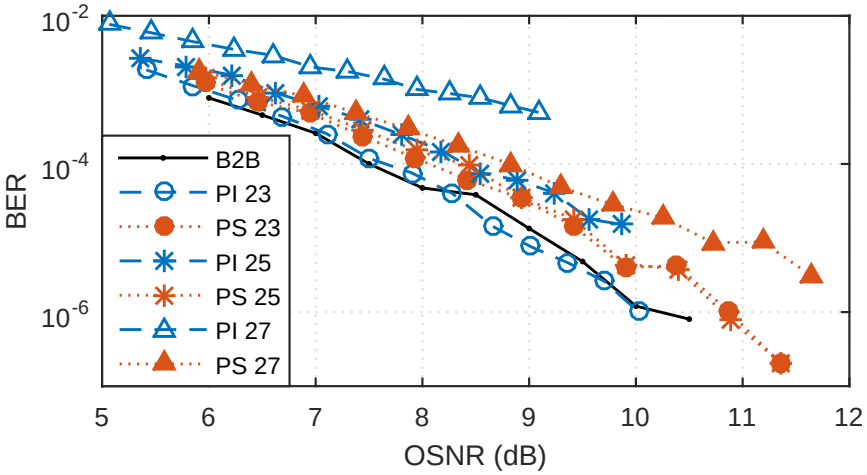

Figure 5.21: BER as a function of the OSNR, B2B, and after the PSA, operating in both PI and PS modes, with P_P values of 23, 25, and 27 dBm.

which is in a very good agreement with the measured values for P_P of 23 and 25 dBm. In PI operation, a theoretical prediction for $\Delta OSNR$ of 3.3 dB is expected, which is also in good agreement with the reported values for P_P of 23 and 25 dBm. For P_P of about 27 dBm, an OSNR improvement of only -5 dB was observed for the signal wave. This result can be explained by an additional noise mechanism, namely the pump-to-signal noise transfer that becomes stronger at high pump power levels [219]. The higher OSNR degradation verified for P_P of 27 dBm in PI operation compared to the measurements at lower P_P values also supports this explanation, but further investigations are required.

The measured BER of the received QPSK signal as a function of the OSNR is depicted in figure 5.21, for P_P of 23, 25 and 27 dBm. At such power levels, gain values of 10.8, 14.8 and 18.9 dB were respectively observed in PS operation, whereas -1.1, 2.0 and 7.5 were obtained in PI mode. For P_P = 23 dBm in PI operation the gain of the amplifier was insufficient to compensate for the insertion losses of 3.5 dB, which explains the measured value. Compared to the back-to-back (B2B) measurements, OSNR penalties of 0.3, 0.4 and 0.8 dB at a BER = 10^{-3} were measured in PS operation for P_P of 23, 25 and 27 dBm, whereas 0.2, 0.6 and 2.2 dB were measured in PI mode. A total of 5×10^6 symbols were considered in the measurements, which allowed measuring BER values of the order of 10^{-6}. For all cases, increasing the power of the pump waves produces a higher degradation of the BER, caused by stronger pump-to-signal noise transfer and stronger influence of the dithering frequencies applied to the pumps on the converted signals. For P_P of 27 dBm a large OSNR penalty is observed in PI mode compared to PS operation. The obtained result suggests that might have been an impairing mechanism that is partially mitigated in PS operation at high pump power values that does not occur in PI operation. One possible explanation could be partial cancellation of the signal distortions due to coherent mixing with the idler copies in PS operation, as suggested in [39,207], but this could not be clearly proved. A shift to higher BER values is also observed for the B2B measurements at OS-

NRs between 8.5 and 10 dB, which is believed to be caused by slight changes on the biasing of the modulator.

In this chapter, different possibilities for PS amplification based on PPLN devices were investigated. Such analysis included a theoretical and numerical investigation of the gain properties for different configurations of PSAs, and an experimental demonstration of PS amplification and phase regeneration in a PPLN device with bidirectional propagation to enable simultaneous generation of correlated waves and PS operation. As regards the numerical simulations, it was observed that configurations based on cascaded TWM interactions have a gain penalty of about 6 dB. However, since configurations based on cascaded TWM processes do not require generating waves at the second harmonic band before the PSA and dedicated optical elements to operate at such spectral regions, they may actually be a better solution for optical communication systems.

The bidirectional configuration allowed to generate correlated idler waves and PS operation in a single device, but severely suffered from GRIIRA effects, photorefraction and thermal instability, aggravated by the injection of high-power waves in both propagation directions. In addition, no net gain could be observed, nor stable operation of the PLL circuit in the phase regeneration experiment. Increasing the length and the efficiency of the PPLN devices are possible solutions to overcome these problems as it would allow increasing the gain of the PSA and/or decrease the required pump power. From the two possibilities, increasing the length of the device would be the best option because the gain of the PSA increases exponentially with the length, whereas it grows exponentially with the square root of the normalized conversion efficiency. On the other hand, increasing the length of the PPLN devices is difficult because the size of lithium niobate wafers is usually limited to just a few centimeters (< 10 cm), and it is challenging to keep the waveguide homogeneity and the QPM wavelength constant in long devices.

A four-mode PSA for high-gain amplification was also demonstrated in this chapter. However, a HNLF was used as the nonlinear medium instead of a PPLN device due to the limited performance and gain of the available PPLN waveguides, and mainly because a four-mode PPLN-based PSA cannot be implemented in practice due to the limited QPM bandwidth. Using HNLFs, PS amplification with gain values of about 20 dB was achieved.

In summary PPLN devices have several advantages and very attractive properties to build PSAs, but with limited gain and with performance instabilities when compared to HNLFs. Hence, further developments on PPLN technology should focus on increasing the efficiency and on improving the thermal and photorefractive stability. By doing so, PPLN devices can become a viable alternative for compact PSAs. In addition, the electro-optic properties of lithium niobate can be explored and combined with PS amplification for advanced applications [220].

Chapter 6

Optical transport networks based on phase-sensitive amplification

PSAs are unique amplifiers whose PS properties enable low-noise amplification with a theoretical NF of 1 (0 dB), below the quantum limit of 3 dB observed for common PIAs such as EDFAs. The remarkable low-noise properties of PSAs can potentially improve the SNR of optical links [186], and thereby extend the maximum transmission reach of optical communication systems. In optical transport networks composed of several links connecting the different nodes of the network, PSAs may potentially reduce the required number of signal regenerators, amplifiers, or even enable the transmission of higher order modulation formats that would not be possible using common PIAs.

The low-noise properties of PSAs are a direct consequence of the different correlation properties of the noise and of the signal and idler waves. In the case of incoherent and uncorrelated noise, the phase of the different noise components in the signal and idler(s) is completely random, so they beat incoherently in a PSA, with some terms adding constructively and others destructively [221]. As a consequence, the average gain for the incoherent noise in a PSA is equivalent to that of a PIA. This result can be observed in figure 5.20 where a noise floor for the signal and idlers is observed at the same power level in both PS and PI operation. On the other hand, the correlated signal and idler(s) waves beat coherently and, depending on their relative phase, they may add constructively, experiencing an additional PS gain of 6 dB in the case of a two-mode PSA, or 12 dB in four-mode PSAs [193, 221]. The additional PS gain advantage of the correlated signal and idler(s) with respect to the incoherent noise is thus responsible for the SNR improvement and the NF below the quantum limit of PIAs [217, 221].

Despite the low-noise properties of PSAs, the application of these amplifiers in real systems is still elusive and no commercial solution is available. This situation is mainly caused by high implementation complexity and insufficiently mature technology. Before PSAs become a viable solution to possibly replace at least a portion of the EDFAs in an optical transmission system, several issues must be addressed, including the generation of correlated waves, keeping the phase correlation throughout an optical link composed of several spans of fiber and PSAs, as well as multichannel and dual-polarization operation. Hitherto, none of these problems has been completely solved. Hence, the current stage of development of the PSA technology still cannot compete with EDFAs, but several groundbreaking achievements have been demonstrated in the last decade.

As regards the generation of correlated idler waves, the copier + PSA scheme [185] is an attractive solution that not only is compatible with multichannel operation [193,203,206], but it is also independent to the modulation format [199] and can be extended to dual-polarization operation [193]. However, the copier + PSAs scheme requires the transmission of both the signal and respective phase-correlated idlers, which means that at least twice the transmission bandwidth is required for two-mode PSAs or even more for higher-mode PSAs. Although this drawback can be partially compensated by the possibility to amplify outside of the C-band and with an amplification bandwidth that can exceed 150 nm [222, 223], this is still a big disadvantage of the copier + PSA scheme.

One of the most challenging problems of PSAs is to guarantee the phase correlation between the signal, idler and pump waves throughout an optical link composed of several cascaded PSAs. This issue becomes even more relevant for multichannel operation as not only full compensation of the accumulated chromatic dispersion after each span of fiber is required, but also is active control of the phase of each individual channel. The optical PLL based on a PZT fiber stretcher described in the previous chapter is a possible solution to actively control the relative phase of the interacting waves [186]. However, this strategy is not ideal for multichannel operation as a dedicated PLL circuit and fiber stretcher is required for each data channel [206]. Unfortunately, very little progress has been made to solve this problem, and the only viable solution seems to be the integration of WDM multiplexers/demultiplexers with several phase-modulators, one for each signal channel, in a single device. Recently, a PLL-free scheme has been suggested for phase regeneration applications [224], but the proposed scheme is also limited to single-channel operation.

The copier + PSA scheme also requires transmitting one or more pump waves along with the signal and idlers to keep the frequency- and phase-correlation of all the interacting waves [225]. However, the pump wave(s) must be attenuated at the output of the copier or the PSAs in order to reduce deleterious nonlinear interactions in the subsequent fiber spans. After transmission through a fiber span, the pump wave(s) must then be re-amplified/regenerated before the next amplifier of the link. In this regard, a pump regeneration/recovery stage based on injection-locking and high power amplification has been proposed to prevent significant OSNR degradation of the pump and, consequently, to avoid additional noise conversion from the pumps to the signal and idler channels [225–227].

Dual-polarization operation has been reported using either polarization diversity schemes [128, 193, 228] or dual-orthogonal polarization pumping [229–231]. Nonetheless, active control of the state of polarization of the waves may be required and the performance of the proposed schemes is severely affected by polarization mode dispersion [229].

The examples presented above summarize the main achievements and progress that have already been accomplished in order to enable PS amplification in real optical communication systems. However, it has been difficult to combine all of the aforementioned strategies and possibilities in a single device and/or platform. Moreover, the most common nonlinear devices to build PSAs, PPLN waveguides and HNLFs, usually require strong pumps and, consequently, additional amplifiers to produce such high power pumps [194]. Recently, PSAs built using different nonlinear materials with very high nonlinear coefficients have been demonstrated, which can potentially lower the pump power requirements [195, 197, 198, 201]. However, the propagation and insertion losses of such alternatives is still prohibitively high. SOA-based PSAs are a promising alternative as they allow PS amplification at significantly lower optical power levels and at a chip scale [194, 232], but with additional ASE noise. Another possibility to relax the pump power requirements is to combine distributed Raman amplification along the optical links with PSAs with lower gain [233], or to enhance the gain of a PSA via Raman amplification in the same nonlin-

ear medium [234]. PSAs can also operate in a distributed mode, yielding a theoretical NF limit of $1 + \alpha L$, with α and L the loss coefficient and length of the fiber span [183]. For comparison, the theoretical NF for ideal distributed phase-insensitive amplification (e.g., distributed Raman amplifiers) is $1 + 2\alpha L$ [183]. In this thesis, however, the discussion is limited to lumped amplification.

It is expected that further technological developments of PSAs shall greatly reduce their implementation complexity and improve the performance of these amplifiers. But even if the PSA technology can become mature enough to compete with EDFAs, it is still unclear if replacing EDFAs with PSAs in optical transport networks would be advantageous at all, or which type of networks would benefit more from changing the amplification technology. Recently, a hybrid EDFA + PSA solution has enabled extending the maximum reach on the transmission of a single channel in a re-circulating loop experiment by more than 200% with respect to a scenario based on pure EDFA amplification [39]. The reported results prove that using PSAs is in fact advantageous for single-channel long-haul transmission, but further investigations on the potential benefits of this technology in optical transport networks are required. Such kind of analysis is performed in this chapter by comparing the requirements in terms of signal regeneration and number of amplifiers for amplification scenarios based on EDFAs or PSAs. In order to do so, simplified models to represent the gain, attenuation and noise properties of the different elements in optical transport networks are considered in this chapter. Such simplified models are used to numerically evaluate the evolution of the SNR between a pair of source and destination nodes in an optical transport network, and thereby verify the signal regeneration requirements.

This chapter is organized as follows. The architecture and main components of optical transport networks are presented in the first section of the chapter, followed by the description of the Dijkstra's algorithm to obtain the shortest path between any pair of nodes of the network, as well as a strategy to limit the analysis to non-redundant shortest paths. Next, simplified models for the gain, attenuation and noise of the network elements are described in section 6.3. In this chapter, the comparison between amplification scenarios based on EDFAs and PSAs is first performed by evaluating the evolution of the SNR and maximum reach for point-to-point transmission in a single optical link, discussed in section 6.4. Then, section 6.5 is devoted to the numerical analysis of the potential savings in terms of number of regenerators and amplifiers for two different optical transport networks. The potential benefits of using PSAs in terms of path protection are also evaluated in section 6.5.

6.1 Optical transport networks architecture

An optical transport network can be defined as a set of nodes and transmission links that carry data in the optical domain, providing a way to exchange information between a group of end users [235, 236]. Usually, optical fibers are used as the physical transmission

links between the network nodes, taking advantage of the large available bandwidth, low propagation losses and compactness of optical fibers [236]. Nodes in optical transport networks are multi-functional elements that allow receiving, transmitting and processing the optical signals, if needed [236]. Nodes are multilayer elements, comprising both an electrical and an optical layer, responsible for the different functionalities and features of the node. The electrical layer of the node performs aggregation or grooming of low speed client signals into an high speed line signal in order to efficiently fill the available bandwidth. In addition, each time an optical signal degrades up to a point that avoid its correct detection, signal regeneration is required, currently performed at the electrical layer. On the other hand, add/drop, switch and amplification of optical signals is typically performed in the optical domain. Since the same nodes and transmission links may be used to exchange information between several end users, optical transport networks are capable of efficiently managing the available transmission resources, reducing costs and power consumption [235].

The structural interconnections between the nodes in a network define the network topology. Different topologies may be considered depending on the type of network, including bus, ring, star, or mesh networks [236]. Moreover, the transmission links may be unidirectional if the data is transmitted in a single direction, or bidirectional. In the later case, either a single fiber with bidirectional propagation or two optical fibers, one for each direction, may be considered.

Optical transport networks can also be classified in terms of the transport mode. In an opaque network, the optical signals undergo optical-to-electrical-to-optical conversion at every node, allowing signal regeneration, grooming and switching in the electrical domain. Thus, in this type of network the optical layer just provides point-to-point transmission between directly connected nodes. However, this transport mode suffers from scalability issues regarding cost, space, power consumption and heat dissipation [12]. In a transparent network, the signal is kept in the optical domain from the source to the destination node, without optical-to-electrical-to-optical conversion in the intermediate nodes. Thus, any regeneration or switching functionality must be implemented in the optical domain. Even though optical switching can currently be performed in ROADMs, optical signal regeneration is still a very recent technology and not mature enough for implementation in real systems [12]. A translucent transport mode is an intermediate configuration in which the signals travel in the optical domain, but may undergo optical-to-electrical-to-optical conversion at some intermediate nodes, where grooming, switching and signal regeneration can be done in the electrical domain [12]. In this chapter, we consider that the network topology is mesh (in order to guarantee survivability), using a pair of optical fibers as the interconnection links and operates in translucent mode. Moreover, all pairs of nodes may exchange data traffic. A schematic representation of a translucent mesh network with four nodes is depicted in figure 6.1.

The optical layer of the nodes in an optical transport network is composed of a cross

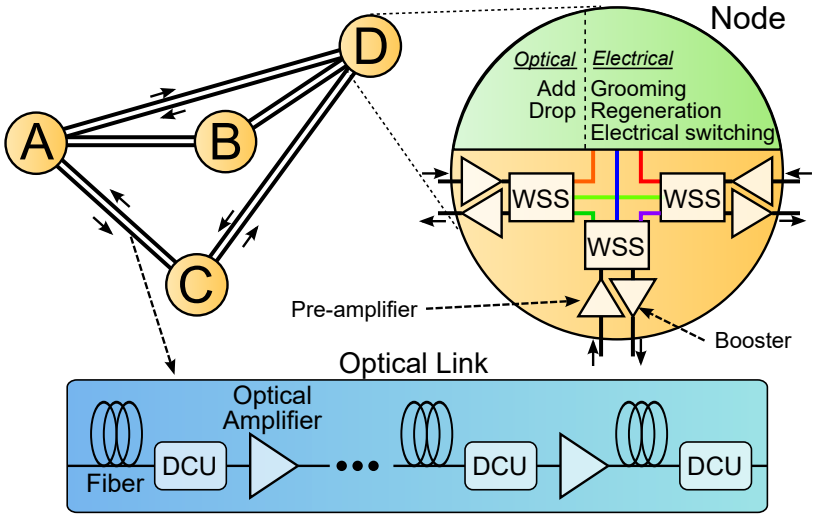

Figure 6.1: On the top left, schematic representation of the mesh network, composed of nodes, depicted in detail on the top right, and optical links (bottom).

connection structure, which includes WSSs and optical amplifiers for either boosting the power of the output signals, also known as booster amplifiers, or for pre-amplifying the input optical signals, also known as pre-amplifiers. The WSSs enable WDM multiplexing and switching the signal channels to different output ports of the node and to the add/drop structures, shown in green in figure 6.1. The optical layer of the add/drop structures is responsible for adding or dropping individual signal channels, whereas the electrical layer enables functionalities such as data grooming, electrical switching and signal regeneration. Together with the WSSs, the add/drop structure and the electrical layer defines the flexibility and reconfigurability of the node, which can be colorless, directionless and contentionless [15].

The transmission links are comprised of fiber spans interleaved with optical amplifiers in order to compensate for the propagation losses. Since PSAs require full compensation of the chromatic dispersion before each amplifier, dispersion managed links are considered, with dispersion compensation units (DCUs) placed at the end of each fiber span, as shown at the bottom of figure 6.1.

6.2 Algorithms for non-redundant shortest path calculation

In WDM systems, data sent from a source node may pass through several intermediate nodes before reaching the final destination node. The data signals are transmitted between two nodes through lightpaths, i.e., optical connections between two nodes, established by allocating the same wavelength and physical route to the connection.

For a given collection of connections between different end users, the problems of routing and assigning a wavelength to each lightpath is known as routing and wavelength assignment (RWA) [34]. RWA is an optimization problem whose goal is to establish the max-

imum number of connections while minimizing/maximizing a specific cost function (e.g., network cost, number of used wavelengths, throughput per link, etc.). The formulation and solution of RWA is a non-deterministic polynomial-time hard (NP-hard) problem [237], thus it is very demanding in terms of computational resources and very time-consuming for large instances of the problem. In general, the RWA problem requires heuristic methods [34] and data traffic patterns that were not available for any of the network scenarios investigated in this thesis. Hence, such methods are not considered here. A possible approximation is to divide the RWA problem into two subproblems, one for routing and another for wavelength assignment, which are solved separately. For the purposes of this work, wavelength assignment is secondary, so a worst-case scenario of 100% utilization of the network resources is considered, such that all the available lightpaths, i.e., the wavelength channels, are used to transmit information at every output port of each node. This clearly is not the most realistic scenario, but no data traffic heuristics are required. In addition, by doing so, the problem of RWA can be simplified to routing optimization.

Routing is the process of finding a feasible ordered sequence of transmission links and nodes between source and destination nodes, under the constraints of the network [236]. Routing is performed at the cross connection structure of the nodes, by directing an input data channel to a specific output port of the node [236]. A possible way to select the path between a source and destination node is using shortest-path algorithms, such as the Dijkstra's algorithm [34]. The Dijkstra's algorithm is a well-known method to determine the shortest path in weighted graphs with non-negative costs, originally proposed by Edsger W. Dijkstra and published in 1959 [238]. Optical networks can be regarded as undirected graphs consisting of a set of nodes, also known as vertices or points, and edges, so the Dijkstra's algorithm can be used for routing optimization. The edges of a graph, also known as arcs or lines, represent the optical transmission links between adjacent nodes and can be associated with a numeric value, usually denominated as the cost. In this context, the cost corresponds to the length of the transmission links. Graphs composed of edges with an associated cost value are known as weighted graphs.

The Dijkstra's algorithm is summarized in algorithm 3 [239,240].The Dijkstra's algorithm is initialized by considering any path of the graph with infinite cost, except for the path linking the initial node o with itself, which is set to 0. Then, the algorithm starts by looking for the nodes adjacent to o, and sets the cost of the adjacent nodes to the respective length of the links. In the following iterations, the algorithm moves to the following adjacent nodes, selecting the one with minimum cost (node u) in each iteration. Afterwards, if the total cost of going to an adjacent node v from node u ($l(u) + l_{uv}$) is lower than the cost of any other path previously computed, i.e. $l(v)$, the algorithm selects a new shortest path from o to v, whose node before v is u. By repeating this procedure, the Dijkstra's algorithm goes from node to node, updating the shortest paths at each iteration.

The outputs of the Dijkstra's algorithm are the total cost of the shortest path between nodes o and u, $l(u)$, and node $p(u)$ that represents the node before u in the shortest path

Algorithm: Dijskstra's algorithm
Definitions:
o: initial node;
$l(u)$: total length between nodes u and o;
$p(u)$: node before u in the shortest path between o and u;
l_{uv}: length of the link between nodes u and v;
V: set with all nodes of the network;
S: set with the nodes whose shortest path is already computed;
$U := V \setminus S$;
Initialization:
$S \leftarrow \varnothing$;
$U \leftarrow V$;
$p(v) \leftarrow 0, \forall v \in V$;
$l(u) = +\infty, \forall u \in U \setminus \{o\}$;
$l(o) \leftarrow 0$;
Algorithm:
while $U \neq \varnothing$ **do**
  Let $u \in U$ be the node with minimum $l(u)$;
  if $l(u) = +\infty$ **then**
    No path between u and o;
  else
    $U \leftarrow U \setminus \{u\}$;
    $S \leftarrow S \cup u$;
    foreach v *adjacent to* u **do**
      if $l(v) > l(u) + l_{uv}$ **then**
        $l(v) = l(u) + l_{uv}$;
        $p(v) \leftarrow u$;
      end
    end
  end
end

Algorithm 3: Dijskstra's algorithm.

from o to u. The nodes $p(u)$ are an efficient way to store the information about the shortest paths. As an example, let us consider the shortest path between o and u. Starting from node u, the node before u in the shortest path is $p(u)$, and the node before that one is $p(p(u))$. Hence, the shortest path can then be reconstructed by repeating this procedure until reaching node o.

The shortest path between any pair of nodes can be obtained by running the Dijkstra's algorithm for every starting node o. Assuming that the length of the links from node u to v and from v to u is the same (undirected graph), a total of $N(N-1)/2$ shortest paths can be found, with N the number of nodes. Thus, networks with a large number of nodes require computing the evolution of the SNR for a very high number of shortest paths, which grows quadratically with N. Fortunately, however, some of those shortest paths are included in

Algorithm: Eliminate redundant shortest paths
Definitions:
V: set with all nodes of the network;
m: initial node;
n: final node;
$\mathbf{L} = [L_{mn}]$: cost matrix with coefficients L_{mn} given by the $l(n)$ of the shortest path between nodes m and n;
d_{mn}: vector with all the nodes of the shortest path between nodes m and n;
U: set of the non-redundant paths;
Initialization:
$U \leftarrow \varnothing$;
$L_{mn} = 0$, for pairs of nodes m and n without a connection;
$L_{mm} = 0, \forall m \in V$;
Algorithm:
foreach $m \in V$ **do**
    Run the Dijkstra's algorithm for starting node m to obtain all the shortest paths between any pair of node m and n;
end
while $L_{mn} \neq 0$, *for any* $\{m, n\} \in V$ **do**
    Select m and n for which coefficient L_{mn} is maximum;
    foreach $u \in d_{mn}, v \in d_{mn}$ **do**
        $L_{uv} = 0$;
    end
    $U \leftarrow U \cup d_{mn}$;
end

Algorithm 4: Algorithm to eliminate redundant shortest paths.

longer ones. Let us assume a network with four nodes as an example, with the shortest path between nodes 3 and 4 given by 3→2→4, and between nodes 1 and 4 given by 1→3→2→4. Clearly, the former path is included in the latter one, so it is redundant. For the purposes of evaluating the SNR of the transmitted data, eliminating the redundant shortest paths greatly simplifies the analysis of optical transport networks. In fact, if the SNR requirements for error-free operation are guaranteed between the initial and destination nodes of a non-redundant path, they are also satisfied for any other path contained within. This is also true if any signal regenerator is required at specific nodes of the non-redundant path. Hence, it suffices to analyze the non-redundant shortest paths.

The method shown in algorithm 4 is proposed in this work to remove the redundant shortest paths. The proposed algorithm starts by obtaining the shortest paths between any pairs of initial and destination nodes, m and n, using the Dijkstra's algorithm, presented in algorithm 3. While there is at least one non-null coefficient of matrix **L**, the algorithm selects the initial and destination nodes for which the coefficient L_{mn} of matrix **L** is maximum at each new iteration. The shortest path between the selected nodes m and n is the longest shortest path that has not yet been analyzed at that point of the algorithm, and is therefore a non-redundant shortest path. Afterwards, the coefficients L_{uv} for any pairs of nodes u

and v that belong to the selected shortest path, d_{mn}, are set to 0, as they are contained within path d_{mn}, i.e, they are redundant. Path d_{mn} is then added to set U, which is the set of non-redundant paths.

6.3 Noise and gain models of optical amplifiers, fiber and attenuators

In order to compare the evolution of the SNR for amplification scenarios based on EDFAs or PSAs, simple, yet sufficiently accurate models of amplifiers, fibers, DCUs and WSSs are considered. The models adopted in this work are described in the following subsections.

6.3.1 Amplifiers

The optical amplifiers in this chapter are used to compensate the propagation losses of the transmission links and the insertion losses of any lossy element of the nodes, such as the WSSs. The discussion in this work is limited to PSAs and EDFAs, and other possibilities such as SOAs or lumped Raman amplifiers are left for future work.

EDFA

The principle of operation of EDFAs is based on stimulated emission of photons via electronic transitions from excited states of the trivalent erbium dopants. Common EDFAs allow optical amplification from 1525 to 1565 nm (C-band), with gain values that can easily exceed 20 dB [241]. The gain spectrum of an EDFA is not constant along its bandwidth, but a gain peak is typically observed at about 1530 nm [241]. Gain flattening filters built with long-period gratings are typically used in order to overcome this issue [242, 243]. For simplicity, an ideal EDFA with a constant gain of G over the entire optical bandwidth, B_{opt}, and null elsewhere is considered, as depicted in figure 6.2.

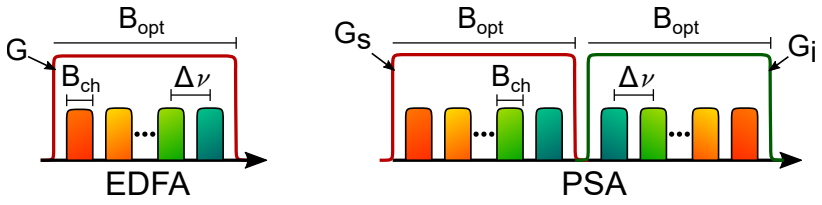

Figure 6.2: Schematic representation of the gain profile of an EDFA, on the left, and a PSA, on the right.

EDFAs have revolutionized optical communications systems as they allow to compensate the propagation losses and, consequently, to extend the transmission reach. However, an EDFA introduces additional ASE noise, which deteriorates the SNR of the signal channels. In fact, if no extra noise was added in EDFAs or any other PI linear amplifier, the

Heisenberg's uncertainty principle would be violated [179, 244]. The ASE noise is originated from spontaneous emission of uncorrelated photons that are amplified throughout the amplifier. The power of the ASE introduced by an EDFA within an optical bandwidth B_{opt} is given by [1, 241]

$$P_{ASE} = 2n_{sp}(G-1)h\nu B_{opt}, \tag{6.1}$$

where n_{sp} is the spontaneous emission factor, related to the population inversion between the excited and fundamental states [241]. In the previous equation, the factor 2 accounts for the unpolarized nature of the ASE, i.e., the ASE noise in the two orthogonal states of polarization.

The noise figure of an EDFA, defined as the input to output SNR ratio, is then given by [1]

$$NF = 2n_{sp}\left(1-\frac{1}{G}\right)+\frac{1}{G}. \tag{6.2}$$

According to the previous equation, the NF of an ideal EDFA with high gain and complete population inversion ($n_{sp} \approx 1$) is approximately 2 (3 dB). In practice, however, complete population inversion is difficult to achieve and NF values of more than 5 dB are typically observed in real amplifiers.

Parametric amplifiers

As discussed in chapter 2, the principle of operation of parametric amplifiers is based on parametric decomposition of a high energy photon or of two photons into two new photons with lower frequency through nonlinear optical mixing. A parametric amplifier can operate in either PI or PS modes. In the case of a PI parametric amplifier, no phase-conjugated idler is required at the input of the amplifier and its gain does not depend on the phase of the interacting waves. In the case of PSAs, however, both the input signal and the idler waves must be injected into the amplifier. The discussion in this chapter is limited to two-mode amplifiers due to the possibility of multichannel operation with lower bandwidth requirements compared to higher mode amplifiers such as four-mode amplifiers.

If an amplification scenario based on PSAs is considered, the signal channels and correlated idler and pump waves must all be transmitted together throughout the optical links. In reconfigurable optical transport networks, the data channels may be added, dropped, aggregated or routed to different destination locations at each node. Hence, when PSAs are considered in such systems, this means that new correlated idlers and pumps must be generated whenever a new channel is added, and transmitted along with the other waves. In addition, when a signal channel must be routed to a different destination, so must be the correlated idler and pump waves. Consequently, at least one new pump for single-pump PSAs or two in the case of dual-pump amplifiers would be required whenever a new signal channel is added or routed to a different destination node. This is clearly unfeasible and highly undesirable in practice. This problem can be overcome by considering the copier +

PSA strategy, discussed in chapter 5. In this case, the correlated idlers and pumps are first filtered out by the WSS at the input of each node. After removing the correlated idlers, the signals can be added, dropped, aggregated or routed as in a typical node, without having to care about the correlated idlers and pump waves. At the output ports of each node, the correlated idlers and pump waves are generated in a PI parametric amplifier, also known as the copier, which is also used to boost the power of the signals at the output of the node. Therefore, the PI parametric amplifier acts simultaneously as a copier and booster. Such solution is fully compatible with the already deployed nodes as only the input pre-amplifier is replaced by a PSA and the output EDFAs by PI parametric amplifiers. However, since the copier is a PIA, it introduces additional ASE noise compared to a pure PSA link. As discussed later on, the additional noise of the PIA booster does not significantly degrade the SNR of the link in the subsequent spans. For simplicity, it is also assumed that each PSA supports dual-polarization operation and is able to correct the relative phase of all the signal and idler channels for maximized gain.

The gain of the parametric amplifiers can be obtained by solving the coupled-mode differential equations describing the nonlinear interaction. Considering negligible propagation losses, no pump depletion, and respectively assuming $\Delta\beta$ = 0 or $\Delta\beta_{eff}$ = 0 for second- or third-order nonlinear interactions, the gain of the signal and idler waves is given by [226]

$$G_s = G + f_r(G-1) + 2\sqrt{f_r G(G-1)}\cos(\psi) \tag{6.3a}$$

$$G_i = f_r G + (G-1) + 2\sqrt{f_r G(G-1)}\cos(\psi). \tag{6.3b}$$

In (6.3), f_r is the idler to signal power ratio, ψ the relative phase between the interacting waves, G_s and G_i are the gain of the signal and idler waves with respect to the input signal power, and G is the signal gain in PI operation, obtained when no idler wave is injected into the amplifier, i.e, when $f_r = 0$. The signal gain in PI operation is generally given by

$$G = \cosh^2(gL), \tag{6.4}$$

where g is the effective coupling coefficient of the nonlinear interaction. The effective coupling coefficient and the relative phase depend on the type of nonlinear interaction. Approximated expressions for g and ψ for PSAs based on simple DFG, cSHG/DFG, phase-conjugating cSFG/DFG, degenerate FWM and phase-conjugating, non-degenerate FWM can be obtained from equations (2.26), (2.28), (2.30) and (2.37), summarized in table 6.1. The expressions presented in table 6.1 were obtained considering negligible effective phase mismatching, with P_P the power of the pump for single-pump PSAs, and P_{P1} and P_{P2} the power of each pump for the dual-pump cases configurations. In general, the phase mismatching effects may not be negligible over the entire amplification bandwidth, leading to a non-flat gain spectrum. The phase mismatching effects are particularly relevant for amplifiers based on degenerate FWM, where two gain peaks are typically observed around the pump wave [73, 245]. Flatter gain profiles can be achieved with parametric amplifiers

Table 6.1: Parametric gain and relative phase of the interacting waves for PSAs based on different nonlinear interactions.

Nonlinear interaction	Parametric gain g	Relative phase ψ
phase-conjugating DFG	$\sqrt{\eta P_P}$	$\phi_s + \phi_i - \phi_P + \pi/2$
cSHG/DFG	$\frac{1}{L} \cdot \ln\left[\cosh(\sqrt{\eta P_P} L)\right]$	$\phi_s + \phi_i - 2\phi_P + \pi$
phase-conjugating cSFG/DFG	$\frac{1}{L} \cdot \ln\left[\cosh(\sqrt{2\eta\sqrt{P_{P1}P_{P2}}} L)\right]$	$\phi_s + \phi_i - \phi_{P1} - \phi_{P2} + \pi$
degenerate FWM	γP_P	$\phi_s + \phi_i - 2\phi_P - \pi/2$
phase-conjugating, non-degenerate FWM	$2\gamma\sqrt{P_{P1}P_{P2}}$	$\phi_s + \phi_i - \phi_{P1} - \phi_{P2} - \pi/2$

based on second-order nonlinear effects, as discussed in section 5.1, and amplifiers based on phase-conjugating, non-degenerate FWM [73]. For simplicity, constant gains of G_s and G_i over the entire amplification bandwidth of the signal and idler bands are considered, as shown in figure 6.2. In addition, it is assumed that ψ is an even multiple of π, which corresponds to the maximum gain condition of the PSAs.

A complete and accurate analysis of the noise properties of optical parametric amplifiers, including PIAs and PSAs, should rely on the quantum theory, but such an approach is typically very complex and difficult to perform [179, 218, 246]. A semi-classical method based on the main results and principles of the quantum theory is usually sufficient to analyze the noise properties of parametric amplifiers, and easier to understand [218,219,247]. In addition, the results of the semi-classical approach are consistent with the quantum theory in the so-called large number of photons limit, i.e., when the power of the signal is much higher than the quantum vacuum noise, which is true in a typical lightwave system [247]. The semi-classical approach is based on the following results from the quantum theory:

1. Any coherent state of light is affected by quantum background fluctuations, i.e., quantum noise. Moreover, the quantum noise does not depend on the optical field of the waves and even if there are no photons (vacuum state), the quantum noise is still present. The quantum noise sets the lower limit for the noise of any optical system.

2. Quantum fluctuations are added through any mode and input port of a physical system, even if it is not used.

The statistics of the quantum noise, Q_n, are assumed to be complex Gaussian, with $<Q_n> = 0$, $<{Q_n}^2> = 0$ and power spectral density (PSD) given by $<|Q_n|^2> = h\nu/2$, where $<>$ is the expectation operator [226]. The power of the quantum noise within an optical bandwidth B_{opt} per state of polarization can be obtained by integrating the PSD with respect to the frequency, which gives $P_{Q_n} = h\nu B_{opt}/2$.

The noise properties of parametric amplifiers, including PSAs, are determined by the quantum noise at its inputs. On one hand, the quantum noise on the input signal port is

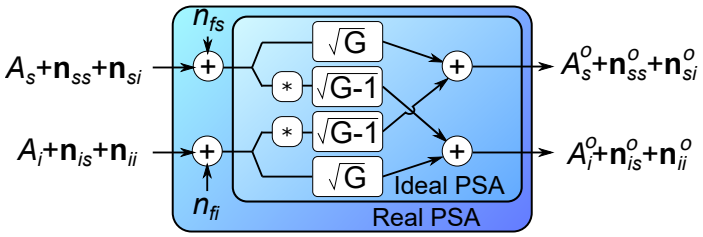

Figure 6.3: Schematic representation of the PSA model, considering an ideal PSA with NF = 1, and a real PSA with NF $>$ 1. The operator "$*$" represents optical phase conjugation.

amplified along with the signal channels. On the other hand, the quantum noise of the idler port is also amplified and coupled to the input signal, even if there is no input idler wave. In fact, if the quantum noise at the idler input port were not considered, the Heisenberg's uncertainty principle would be violated.

Let us now assume the noise vectors $\mathbf{n}_{uv}$ which contain all the different noise contributions in wave u, that were originally added to wave v at any place of the optical link, with u and v the signal (s) or idler (i) waves. The input/output relations between the optical fields and noise components of the signal and idler ports are schematically represented in figure 6.3, and mathematically described by (6.5) [218, 219]

$$\begin{bmatrix} A_s^o & \mathbf{n}_{ss}^o & \mathbf{n}_{si}^o \\ A_i^{o*} & \mathbf{n}_{is}^{o*} & \mathbf{n}_{ii}^{o*} \end{bmatrix} = \begin{bmatrix} \mu & \upsilon \\ \upsilon^* & \mu^* \end{bmatrix} \begin{bmatrix} A_s & \mathbf{n}_{ss} & \mathbf{n}_{si} \\ A_i^* & \mathbf{n}_{is}^* & \mathbf{n}_{ii}^* \end{bmatrix}. \tag{6.5}$$

In the previous equation the superscript o denotes the output signal, idler or noise components, $\mu = \sqrt{G}$ and $\upsilon = \sqrt{G-1}\exp[i(\phi_s + \phi_i - \psi)]$. Equation (6.5) not only describes the noise properties of parametric amplifiers, but can also be used to obtain (6.3). According to figure 6.3 and equation (6.5), any noise component at one of the input ports of a PSA (either signal or idler) is converted to both signal and idler output ports. These noise components are now correlated and beat coherently in the following amplifiers, experiencing PS amplification. On the other hand, any noise contribution added by other elements of the optical links is uncorrelated and experiences lower gain in the subsequent PSA, equivalent to that of a PIA. Hence, the total noise in the signal and idler waves at any point of the optical links contains both correlated and uncorrelated contributions, which justifies discriminating all the different noise terms in vector $\mathbf{n}_{uv}$.

In order to illustrate the behavior of the amplifier for correlated and uncorrelated noise terms, let us first consider a PSA with no input noise sources other than the unavoidable quantum fluctuations, i.e., $\mathbf{n}_{ss} = Q_{ns}$, $\mathbf{n}_{ii} = Q_{ni}$ and $\mathbf{n}_{si} = \mathbf{n}_{is} = 0$. Assuming $\psi = 0$, the output noise components are given by $\mathbf{n}_{ss}^o = \mu\mathbf{n}_{ss}$, $\mathbf{n}_{si}^o = \upsilon\mathbf{n}_{ii}^*$, $\mathbf{n}_{is}^o = \upsilon\mathbf{n}_{ss}^*$ and $\mathbf{n}_{ii}^o = \mu\mathbf{n}_{ii}$.

The total noise power in the signal or idler within optical band B_{opt} is then given by

$$\begin{aligned} P_{noise} &= < |\mu Q_{ns} + \upsilon Q_{ni}^*|^2 > B_{opt} = < |\mu Q_{ni} + \upsilon Q_{ns}^*|^2 > B_{opt} \\ &= (G-1)h\nu B_{opt} + \frac{h\nu B_{opt}}{2} \\ &= P_{ASE} + P_{Q_n}, \end{aligned} \tag{6.6}$$

with P_{Q_n} the power of the quantum noise and $P_{ASE} = (G-1)h\nu B_{opt}$ the noise added by the amplifier. Remarkably, the expression for the noise added by the parametric amplifier, P_{ASE}, is equal to that of an EDFA with $n_{sp} = 1$, presented in (6.1), with the exception of a factor of 2, which is related to the dual-polarization nature of the noise in erbium amplifiers. In fact, the semi-classical formalism can also be used to obtain the noise properties of an EDFA by considering an additional idler port with only quantum noise at its input, as reported in [248].

Let us now consider correlated noise components launched into the PSA, with $\mathbf{n}_{ss} = \mathbf{n}_{is}^* = Q_{ns}/\sqrt{2}$ and $\mathbf{n}_{ii} = \mathbf{n}_{si}^* = Q_{ni}/\sqrt{2}$, where the term $\sqrt{2}$ is introduced in order to have the same total input noise power as in (6.6). In this case, the total noise power in the signal or the idler would become

$$\begin{aligned} P_{noise} &= < \left| (\mu + \upsilon) \left(\frac{Q_{ns} + Q_{ni}^*}{\sqrt{2}} \right) \right|^2 > B_{opt} \\ &= \left[G - 1 + \sqrt{G(G-1)} \right] h\nu B_{opt} + \frac{h\nu B_{opt}}{2} \\ &= P_{ASE} + P_{Q_n}, \end{aligned} \tag{6.7}$$

where now $P_{ASE} = [G-1+\sqrt{G(G-1)}]h\nu B_{opt} \approx 2(G-1)h\nu B_{opt}$, with the latter approximation obtained for $G \gg 1$. Comparing (6.6) and (6.7), the noise added by the amplifier with correlated noise at its input is about twice as much as for uncorrelated noise. Therefore, a correct analysis of the noise in a link amplified by PSAs requires discriminating all the correlated and uncorrelated noise components.

The NF is an important parameter that characterizes the noise properties of optical amplifiers, defined as the input to output SNR of the amplifier when the input light is limited by shot-noise [226]. However, two different possibilities can be considered for PSAs depending on how the SNR is calculated. The simplest approach is to consider the SNR of the signal and idler waves separately. Assuming equalized signal and idler power, a theoretical NF of 0.5 (-3 dB) is expected for high gain values. This is a consequence of improving the individual SNR of the signal and idler waves, caused by the higher gain of the amplifier for the correlated signal and idlers when comparing to the gain for uncorrelated noise [226]. A more correct definition of the NF for a two-mode PSA should consider the combined SNR of the signal and idler instead [226]. In practice, measuring the combined SNR can be done by simultaneously detecting the signal and idler, filtering out the beating components between these waves [226, 249].

In order to understand how to calculate the NF of a PSA let us first consider a simpler example of an optical wave with power P, detected in a PD with two-sided electrical bandwidth B_{el} (i.e., between -B_{el} and B_{el}) and with an ideal responsivity given by $R = e/(h\nu)$, with e the elementary charge. Assuming that there is no other noise source except for the unavoidable quantum noise, an average electrical current of $<I> = R(P + 2<|Q_n|^2>B_{el})$ is measured, with the factor of 2 due to the two-sided electrical bandwidth. The SNR of the detected current is defined as the ratio $<I>^2/<\Delta I^2>$, where $<\Delta I^2> = <(I - <I>)^2>$ is the variance of the detected current, given by $<\Delta I^2> = 4R^2P<|Q_n|^2>B_{el}$. Assuming that the average current due to the quantum noise is negligible, i.e., $P \gg <|Q_n|^2>B_{el}$, the SNR becomes

$$SNR = \frac{P}{2h\nu B_{el}}. \tag{6.8}$$

The previous expression represents the SNR for PDs limited by shot noise, with no other noise source affecting the detected signals [1]. In fact, according to the quantum theory, the shot noise is no more than the beating between the incoming signal and quantum background fluctuations [248].

A similar procedure can be performed to calculate the SNR at the input and output ports of the amplifier, but taking into account both the signal and idler currents simultaneously. Assuming only the quantum fluctuations as the noise source at the input of the PSA, the SNR of the total current $I = I_s + I_i$ detected at the input of the amplifier is given by

$$SNR_{in} = \frac{P_s + P_i}{2h\nu B_{el}}. \tag{6.9}$$

On the other hand, the output SNR of the parametric amplifier for $\psi = 0$ is given by [226]

$$SNR_{out} = \frac{(P_s^o + P_i^o)^2}{2h\nu B_{el}\left[\left(\sqrt{GP_s^o} + \sqrt{(G-1)P_i^o}\right)^2 + \left(\sqrt{GP_i^o} + \sqrt{(G-1)P_s^o}\right)^2\right]}, \tag{6.10}$$

with $P_s^o = (\sqrt{GP_s} + \sqrt{(G-1)P_i})^2$ and $P_i^o = (\sqrt{GP_i} + \sqrt{(G-1)P_s})^2$ the output power of the signal and idler waves. The NF of the parametric amplifier is thus given by [226]

$$NF = \frac{P_s + P_i}{\left(P_s^o + P_i^o\right)^2}\left[\left(\sqrt{GP_s^o} + \sqrt{(G-1)P_i^o}\right)^2 + \left(\sqrt{GP_i^o} + \sqrt{(G-1)P_s^o}\right)^2\right]. \tag{6.11}$$

The previous expression is valid for a two-mode parametric amplifier in either PS or PI operation. In the former case and for equalized signal and idler power, the NF of the amplifier becomes equal to 1 (0 dB), as expected for an ideal PSA. On the other hand, when $P_i = 0$ (PIA), the NF of the amplifier becomes $NF = 2 - 1/(2G-1)^2$, which is approximately equal to 2 (3 dB) for high gain values.

In a real PSA, however, the NF may be degraded by several mechanisms such as Raman phonon seeded excess noise, transferred pump noise or residual pump noise [219].

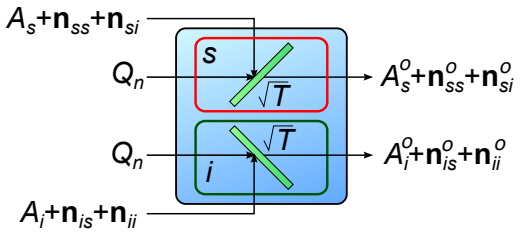

Figure 6.4: Lossy element modeled as beam-splitter with power transmission coefficient T, coupling quantum noise fluctuations to the signal and idler waves.

As an example, NF values of 1.1 dB and 1.8 dB have been respectively measured in fiber- and PPLN-based PSAs [186, 250]. Assuming that the statistics of such impairing mechanisms can also be modeled as additive white Gaussian noise, a possible way to improve the model for the noise properties of parametric amplifiers is to add new noise terms, n_{fs} and n_{fi}, at each input port of the amplifier, as depicted in the outer box of the PSA model in figure 6.3. The variance of the new noise terms is given by $<|n_{fs}|^2> = <|n_{fi}|^2> = (f-1)h\nu/2$, where f is a factor that represents the degradation of the NF. By considering the new noise sources and repeating the procedure discussed above, the NF of the PSA becomes $NF_{real} = f \cdot NF$. The NF degradation factor is always greater or equal to 1 and can be compared to the spontaneous emission factor of EDFAs. In general, f may vary with the frequency, the length of the amplifier, and/or the power of the signal and pump waves [247]. In this chapter, a constant f is assumed within the total optical bandwidth, for simplicity. The parameter f can also be used to model the additional degradation of the NF in PI parametric amplifiers.

6.3.2 DCUs and WSSs

In this chapter, ideal DCUs and WSSs with no polarization-dependent losses, negligible back-reflections and with flat response within the optical bandwidth of interest are considered. It is also assumed that the DCUs perfectly compensate all the accumulated dispersion of the span. Hence, for the purpose of evaluating the evolution of the SNR through the optical links of a network, the DCUs and WSSs can be regarded as simple loss elements, with a power transmission coefficient T, with $0 \leq T \leq 1$.

In a classical approach, the effects of a loss element are simply to decrease the power of the propagating waves. However, if an input wave with only quantum vacuum fluctuations as the noise source passes through a lossy element, the total noise power would be reduced to below the quantum limit, violating the quantum theory principles. In the semi-classical approach, this problem is overcome by modeling the lossy element as a beam combiner [226], as illustrated in figure 6.4. According to the semi-classical model, the loss elements couple uncorrelated vacuum fluctuations to the signal and idler waves in order to compensate for the attenuation of the input quantum noise, setting back the power of the quantum background fluctuations to the quantum limit. For any other noise terms at the in-

put of the loss elements, the signal and the idler waves, the semi-classical beam combiner model is equivalent to the classical approach. The effects of a lossy element on the input waves and noise terms are mathematically described by the following equations [218]

$$\begin{bmatrix} A_s^o \\ A_i^{o*} \end{bmatrix} = \sqrt{T} \begin{bmatrix} A_s \\ A_i^* \end{bmatrix} \tag{6.12a}$$

$$\mathbf{n}_{ss}^o = \begin{bmatrix} \sqrt{T}\mathbf{n}_{ss} & \sqrt{1-T}Q_n \end{bmatrix} \tag{6.12b}$$

$$\mathbf{n}_{si}^o = \begin{bmatrix} \sqrt{T}\mathbf{n}_{si} & 0 \end{bmatrix} \tag{6.12c}$$

$$\mathbf{n}_{is}^o = \begin{bmatrix} \sqrt{T}\mathbf{n}_{is} & 0 \end{bmatrix} \tag{6.12d}$$

$$\mathbf{n}_{ii}^o = \begin{bmatrix} \sqrt{T}\mathbf{n}_{ii} & \sqrt{1-T}Q_n \end{bmatrix}. \tag{6.12e}$$

6.3.3 Fiber

Optical fibers are the key components of an optical transport network. The large transmission bandwidth and very low losses of optical fibers allow exchanging a very large amount of information between several end users. In this chapter, typical standard single-mode fibers are considered with loss coefficient, nonlinear coefficient, dispersion parameter and dispersion slope at 1550 nm of 0.22 dB/km, 1.3 $W^{-1}km^{-1}$, 16.7 $ps.nm^{-1}km^{-1}$ and 0.07 $ps.nm^{-2}km^{-1}$, respectively. For simplicity, PMD and scattering effects are neglected, so the main degradation mechanisms in the transmission fibers are the propagation losses and nonlinear effects of SPM, XPM and FWM.

The propagation losses of the transmission fibers in optical links amplified with PSAs can also be modeled as a beam combiner with transmission coefficient $T = \exp(-\alpha L)$, as discussed in the previous subsection. Because of the propagation losses, new uncorrelated quantum fluctuations are added to the transmitted signals. If long spans of fibers are placed in between the PSAs, the correlated noise terms generated by the amplifiers may be attenuated to below the quantum noise limit and the uncorrelated quantum background fluctuations become the dominant noise source [199].

The nonlinear response of the transmission fibers also plays a very important role in optical communication systems. In fact, if it were not for the fiber nonlinearities and the fuse effect, extending the transmission reach could be simply performed by increasing the launch power at the transmitter [6]. The most correct and complete analysis on the impact of the nonlinear effects on the transmitted data channels would require the computation of the nonlinear Schrödinger's equation or the Manakov-PMD equations for each path of the network. However, such calculations are computationally demanding and, for a matter of simplicity, an analytical model is preferable for the problem at hand. Recently, the GN model has been proposed as an alternative possibility to model the degradation of data channels caused by the nonlinear response of the fibers in dispersion-uncompensated

links [58, 251]. The GN model is formulated assuming that the nonlinear distortions, also known as nonlinear interference (NLI), are small perturbations, manifesting themselves as additive Gaussian noise. The GN model also assumes that after propagating through a significant distance in a dispersive medium, the transmitted signals can be statistically described as stationary Gaussian noise, which is also known as the signal gaussianity approximation [58]. More recently, the same research group presented an improved version of the GN model, the so-called EGN model, which includes several terms to correct the signal gaussianity approximation [59]. The GN and EGN models allow to estimate the PSD of the NLI for a wide range of signal, span and fiber parameters, though still at the cost of demanding computations. However, with a few approximations and for certain signal and span parameters, simple, yet accurate analytical expressions can be obtained for the PSD of the NLI [58, 251, 252]. This is perhaps the most important contribution of the GN and EGN models as they provide simple tools to quickly estimate the degradation of the transmitted signals due to the fiber's nonlinear response. The GN model is also an easy way to estimate the impact of nonlinearities on the potentialities of WDM networks and thereby to simplify dimensioning and planning of optical transport networks [253].

As mentioned above, the GN and EGN models are formulated for dispersion-uncompensated systems, where the statistics of the transmitted signals and noise tend to a Gaussian distribution due to the accumulated dispersion. Even though the analytical approximations of the GN and EGN models are able to account for lumped dispersion elements (as an example, see equation (1) in [58]), the validity and accuracy of these models for dispersion-compensated systems are arguable [58, 254]. Moreover, none of the simplified expressions for the PSD of the NLI obtained with the GN and EGN model accounts for the possibility of considering lumped dispersive elements such as DCUs at the end of the fiber spans, as required for amplification scenarios based on PSAs. Thus, motivated by the lack of an alternative model with elegant analytical solutions, a MEGN model for Nyquist-WDM channels with channel bandwidth B_{ch} and frequency separation between neighboring channels of $\Delta\nu$ (see figure 6.2) is assumed to estimate the effects of the NLI. The MEGN model presented in this chapter can be regarded as a particular solution of the original GN model reference formula, given by equation (1) in [58], and the correcting terms of the EGN model, obtained for optical links with full compensation of the dispersion effects after each span of fiber, before each amplifier. The derivation of the MEGN model is detailed in appendix B.

In general, the MEGN model can be used to estimate the PSD of the NLI, $S_{NLI}(\nu)$, at any frequency component ν of the transmitted data channels. However, the full calculation of the correcting terms to remove the signal gaussianity approximation for random input signal channels still requires demanding computations. In the case of ideal Nyquist data channels with constant PSD of P_{ch}/B_{ch}, where P_{ch} is the channel power, and with constant frequency separation between the channels, the computation of $S_{NLI}(\nu)$ becomes simpler. The NLI of the transmitted signals in WDM systems is typically stronger at the center

channels [251], as these channels are more severely affected by inter-channel FWM. Remarkably, the calculation of $S_{NLI}(\nu)$ can be greatly simplified at the center channel of the transmitted data, which also corresponds to the maximum PSD of the NLI. Hence, the PSD of the NLI is only evaluated for the center frequency of the transmitted signals spectrum, at $\nu = 0$, and assumed constant for any other frequency, i.e., $S_{NLI}(\nu) \approx S_{NLI}(0)$. This approach provides a pessimistic and conservative estimate for the NLI power of the outer channels. By taking into account the previous considerations, the S_{NLI} at the center frequency of the spectrum of the transmitted signals is approximately given by

$$\begin{aligned} S_{NLI}(0) \approx & \left(\frac{4-p}{3}\right)^3 \left(\frac{P_{ch}}{B_{ch}}\right)^3 \gamma^2 {N_s}^2 \\ & \times \sum_{m=-(N_{ch}-1)/2}^{(N_{ch}-1)/2} \left(\frac{(2-\delta_m)\,{L_{eff}}^2 \alpha}{2\pi|\beta^{(2)}|} \left\{ \text{asinh}\left[\frac{\pi^2|\beta^{(2)}|}{\alpha} \left(m\Delta\nu + B_{ch}/2\right) B_{ch} \right] \right.\right. \\ & \left. -\text{asinh}\left[\frac{\pi^2|\beta^{(2)}|}{\alpha} \left(m\Delta\nu - B_{ch}/2\right) B_{ch} \right] \right\} \\ & \left. -2\frac{(1-\delta_m)(7-p)}{3B_{ch}} \Theta \int_{-B_{ch}/2}^{+B_{ch}/2} |\zeta_m(\nu_1)|^2 d\nu_1 \right), \end{aligned} \tag{6.13}$$

whose derivation is detailed in appendix B. In the previous equation, δ_m is the Kronecker delta function, equal to 1 for m = 0 and 0 otherwise, N_s is the number of spans, N_{ch} the number of channels, p is equal to 1 or 2 for single- or dual-polarization signals, respectively, and L_{eff} the effective length, given by

$$L_{eff} = \int_0^L e^{-\alpha z} dz = \frac{1 - e^{-\alpha L}}{\alpha}. \tag{6.14}$$

In (6.13), function $\zeta_m(\nu_1)$ is given by the following expression

$$\begin{aligned} \zeta_m(\nu_1) = \frac{i}{4\pi^2\beta^{(2)}\nu_1} & \left\{ \ln\left(\frac{\alpha - i4\pi^2\beta^{(2)}\nu_1\left[m\Delta\nu + B_{ch}/2\right]}{\alpha - i4\pi^2\beta^{(2)}\nu_1\left[m\Delta\nu - B_{ch}/2\right]} \right) \right. \\ & + \mathsf{E}_1\left(\left[\alpha - i4\pi^2\beta^{(2)}\nu_1\left(m\Delta\nu + B_{ch}/2\right)\right] L \right) \\ & \left. - \mathsf{E}_1\left(\left[\alpha - i4\pi^2\beta^{(2)}\nu_1\left(m\Delta\nu - B_{ch}/2\right)\right] L \right) \right\}, \end{aligned} \tag{6.15}$$

with E_1 an exponential-integral function, defined by (B.18) in appendix B. Constant Θ in (6.13) represents the influence of the modulation format, calculated by the following expression [59]

$$\Theta = 2 - \frac{<|X|^4>}{<|X|^2>^2}, \tag{6.16}$$

with X a random variable that represents the transmitted symbols. In the case of PSK modulation formats, constant Θ is equal to 1, whereas values of 17/25 and 13/21 are respectively obtained for 16- and 64-QAM signals [59]. The power of the NLI for the center

channel can be obtained by integrating S_{NLI} within the optical bandwidth of the channel. Assuming that S_{NLI} is practically constant over the entire channel bandwidth, also known as the locally white NLI approximation [251], the power of the NLI for the center channel, P_{NLI}, is approximately given by

$$P_{NLI} \approx \int_{-B_{ch}/2}^{B_{ch}/2} S_{NLI}(\nu)d\nu \approx S_{NLI}(0)B_{ch}. \tag{6.17}$$

In order to evaluate the validity and accuracy of equation (6.13), the power of the NLI for the center channel was computed using the total field formulation (see subsection 2.4.1) and the SSFT method to solve the Manakov-PMD equation (2.41) for dual-polarization nonlinear propagation with randomly varying birefringence. The simulations were performed for dual-polarization signals, assuming full compensation of the chromatic dispersion and propagation losses at the end of each span, D_λ = 16.7 ps.nm^{-1}km^{-1}, S_λ = 0.07 ps.nm^{-2}km^{-1}, $\Delta\nu$ = 50 GHz, α = 0.22 dB/km and γ = 1.3 W^{-1}km^{-1}. A total of 2^{15}-1 symbols were considered in the SSFT simulations, with space and time integration steps of Δz = 10 m and $\Delta t = 1/(3N_{ch}\Delta\nu)$. The variation of P_{NLI} with the number of fiber spans for different modulation formats is depicted in figure 6.5, obtained with the MEGN model proposed in this section, and by solving the Manakov-PMD equation with the SSFT method. For comparison, the power of the NLI is also calculated using the simplified formula for the original EGN model without dispersion compensation, given by equation (1) in [252]. The numerical results obtained with the SSFT method are used as reference to investigate the validity and accuracy of the EGN and MEGN models.

For all the modulation formats except OOK, the MEGN provides acceptable estimates of P_{NLI} with respect to the SSFT method. Moreover, the MEGN is able to reproduce the variation of the NLI power with the number of spans, but overestimating P_{NLI} with almost constant offsets of about 3.6 dB for BPSK, 4 dB for QPSK and 2.1 dB for 16-QAM. In fact, the SSFT calculations suggest that P_{NLI} is proportional to N_s^2, as it is also predicted by the MEGN model. In contrast, the EGN model indicates that the power of the NLI increases slightly superlinearly with the number of spans [58], as shown by the dashed lines in figure 6.5. Despite providing better estimates of P_{NLI} for a number of spans between 3 and 13, the EGN model does not reproduce the variation trend with the number of spans observed for the SSFT calculations. This is an expected result as the EGN model expression used to calculate the power of the NLI was devised assuming no dispersion compensation, which is clearly not the scenario considered in this work. The numerical results depicted in figure 6.5 for the EGN model clearly justify the necessity to devise the MEGN model to describe the evolution of P_{NLI} in systems with full compensation of the chromatic dispersion effects after each span of fiber.

In the case of OOK signals, the difference between the values given by the two methods decreases from more than 10 dB for less than 3 spans to a minimum difference of about 5 dB, measured at the 11th span. For a higher number of spans, the difference between the

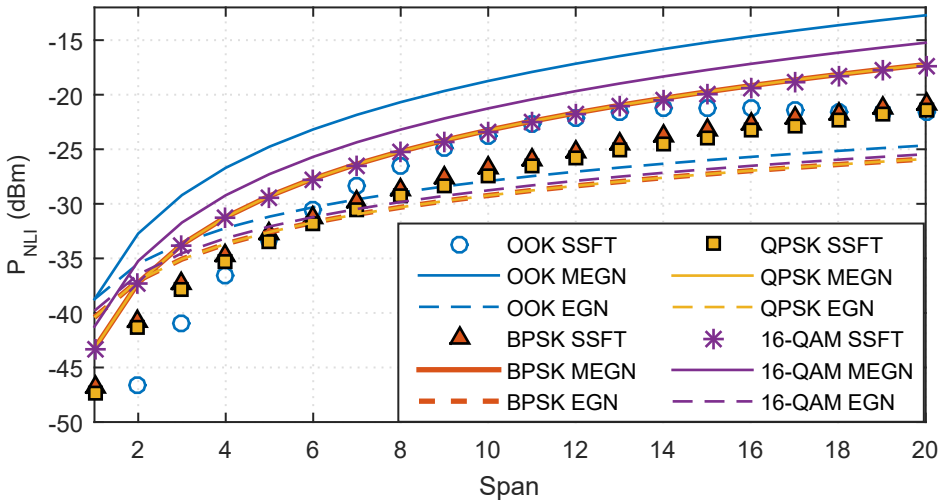

Figure 6.5: Variation of P_{NLI} with the number of spans, calculated through the SSFT method, the MEGN and the EGN models for OOK, BPSK, QPSK and 16-QAM signals. The numerical results were obtained for B_{ch} = 25 Gsymbol/s, P_{ch} = -3 dBm, L = 80 km and N_{ch} = 40.

two methods increases. Hence, the MEGN is not suitable to model the power of the NLI for OOK signals and this modulation format is not further considered in this chapter.

The influence of other parameters such as P_{ch}, B_{ch}, N_{ch} and L on P_{NLI} for the transmission of QPSK signals through 5 spans of fiber is also depicted in figure 6.6, obtained using the MEGN model and the SSFT method. As shown in the figure, the MEGN is able to reproduce the variation trend of P_{NLI} with P_{ch} and B_{ch}, but with an offset of about 3.7 dB, as it was also observed in the simulations presented in figure 6.5. A similar conclusion can be obtained for the influence of N_{ch} on the power of the NLI, except for a small number of data channels (N_{ch}<10), where the offset between the MEGN and SSFT simulations increases up to about 10 dB. This is a consequence of the approximations used to obtain (6.13), which assume a large number of channels [251, 252]. One example of such approximations is neglecting the self-channel interference correction to the GN model, which is only valid when the number of channels is large and the cross-channel interference contributions are dominant (see appendix B). In figure 6.6-d), the numerical simulations show that the MEGN model is also able to represent the influence of L on the NLI power, but only for length values above 50 km. For shorter span lengths, the MEGN simulations start to significantly deviate from the SSFT calculations. These results are explained by the approximated expression for the FWM efficiency factor (B.7), presented in appendix B.

In order to verify the influence of the channel spacing on the NLI properties, the NLI power was calculated for different $\Delta\nu$ values, using both the SSFT method to solve the Manakov-PMD equation and the MEGN model. The numerical results obtained for QPSK signals after propagation through 5 spans of fiber are shown in figure 6.7. The number of channels considered in the numerical computations was selected in order to keep B_{opt} equal to 2 THz, with $B_{opt} = N_{ch} \times \Delta\nu$. The numerical results calculated with both methods

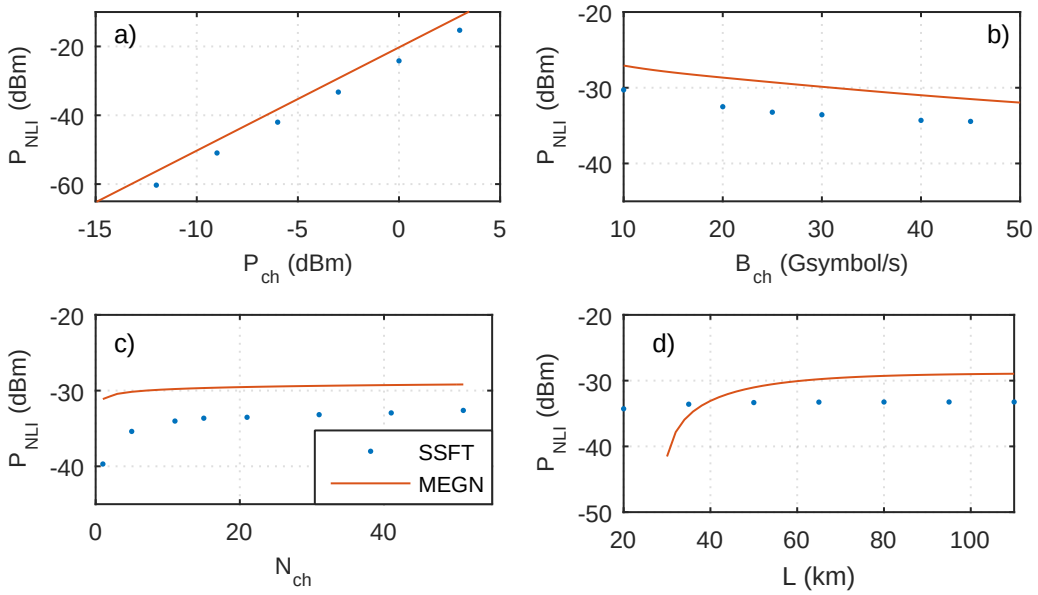

Figure 6.6: Variation of P_{NLI} with a) P_{ch}, for B_{ch} = 25 Gsymbol/s, N_{ch} = 40 and L = 80 km, b) B_{ch}, for N_{ch} = 40, L = 80 km and P_{ch} = -3 dBm, c) N_{ch}, for B_{ch} = 25 Gsymbol/s, L = 80 km and P_{ch} = -3 dBm, and d) L, for B_{ch} = 25 Gsymbol/s, N_{ch} = 40 and P_{ch} = -3 dBm. The numerical results were obtained through SSFT calculations and using the MEGN model for QPSK data channels and after propagation through 5 spans of fiber.

show that the NLI decreases with the increase of the channel spacing, which is an expected result as the inter-channel FWM contributions become weaker when the data channels are more sparsely spaced. In this case, however, the MEGN model does not correctly reproduce the variation trend of the NLI power with the channel spacing observed in the SSFT calculations. Preliminary tests suggest that the origin of this difference is most likely in the correcting term of (B.12), shown in appendix B. Unfortunately, however, the root cause for this difference could not yet be identified and further investigations are required, which are left for future work. It should be noted that eliminating the observed difference not only would provide a better approximation for the influence of the channel spacing, but it could also reduce the offset between the SSFT and MEGN curves in figures 6.5 and 6.6.

With the exception of the channel spacing, the MEGN is able to reproduce the influence of all the signal and span parameters on the NLI power. Since no better model seems to be currently available to estimate the NLI power in systems with full dispersion compensation after each span, the MEGN is still considered in this chapter. However, no further investigations on the influence of $\Delta\nu$ are considered in this chapter and a constant channel spacing of 50 GHz is assumed in all the numerical simulations presented henceforth. In this case, the MEGN is a viable alternative to estimate the power of the NLI, albeit with a non-negligible overestimation of the P_{NLI}. Since the MEGN always overestimates the NLI, it provides conservative and pessimistic scenarios for the degradation imposed by the NLI in optical links and networks with full dispersion compensation after each span of fiber.

In the following sections, the MEGN is used to estimate the impact of the NLI power on

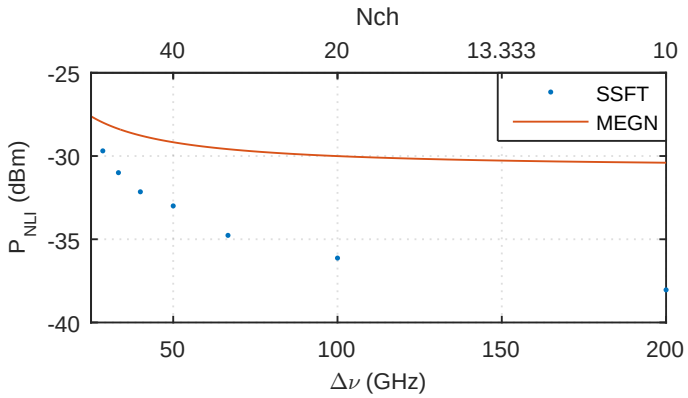

Figure 6.7: Variation of P_{NLI} with the channel spacing, obtained through SSFT calculations and using the MEGN. The numerical simulations were obtained for B_{ch} = 25 Gsymbol/s, L = 80 km and P_{ch} = -3 dBm.

the transmission through a single optical link (point-to-point transmission) and in two optical transport networks, considering amplification scenarios based on EDFAs and PSAs. In the case of the scenario based on PS amplification, since both the signal and correlated idlers have to be transmitted through the optical links, twice the number of channels are considered on the calculation of P_{NLI}. The simplified models for the gain, attenuation and ASE noise presented in the previous subsections are also considered.

6.4 Point-to-point transmission

Before comparing the two different amplification scenarios in optical transport networks, let us first investigate the evolution of the SNR, ASE and NLI power in a single optical link composed of 20 spans of fiber. The numerical results are depicted in figure 6.8, calculated using either the MEGN model or by solving the Manakov-PMD equation with the SSFT method. The numerical calculations were obtained for 40 dual-polarization QPSK channels and P_{ch} of -6 dBm. In the case of the simulations with PSAs, the number of channels considered to calculate P_{NLI} with the MEGN was 80, as both signal and correlated idlers contribute to the nonlinear distortion of the transmitted waves. The same fiber and span parameters used to obtain the numerical results shown in figure 6.5 were considered in these simulations. EDFAs and PSAs with NF values of 5 dB and 2 dB were respectively considered. The gain of the amplifiers was selected in order to keep the total power of the signal channels and noise constant after each amplifier.

The SNR was calculated taking into account both the ASE and NLI noise, according to [58]

$$SNR = \frac{2B_{ref}}{pB_{ch}} \cdot OSNR = \frac{2B_{ref}}{pB_{ch}} \cdot \frac{P_{ch}}{P_{ASE} + P_{NLI}}, \tag{6.18}$$

where B_{ref} is the optical reference bandwidth. The previous equation assumes that the NLI and ASE noise sources are uncorrelated and approximately described as additive

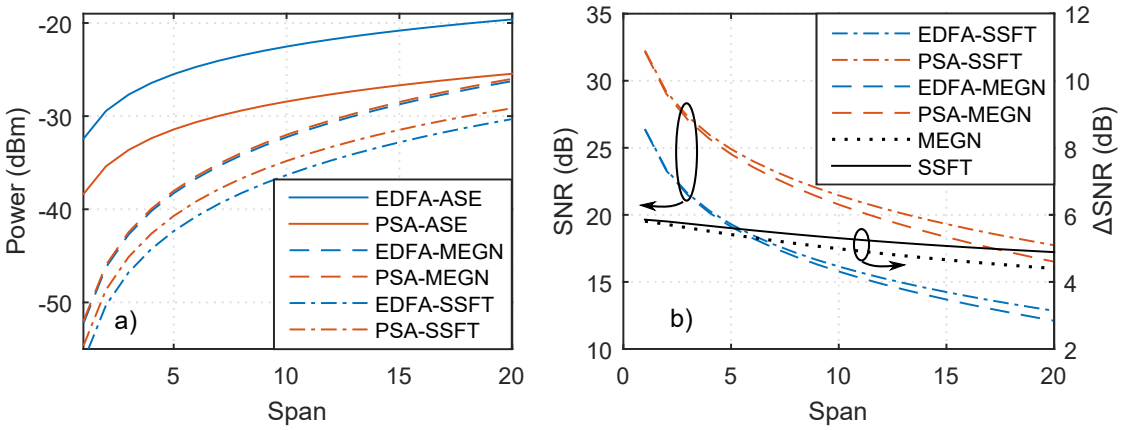

Figure 6.8: a) Variation of the ASE and NLI power within the channel bandwidth with the number of spans, obtained with the MEGN model and SSFT calculations, for an optical link amplified with either EDFAs or PSAs. b) Variation of the SNR with the number of spans assuming the NLI power calculated with the MEGN model and the SSFT method. The solid and dotted black curves represent the ratio between the SNR for an optical link amplified by PSAs and by EDFAs, obtained with the MEGN model and the SSFT method.

Gaussian noise [58].

The numerical results depicted in figure 6.8-a) show that the MEGN overestimates the NLI power with respect to the SSFT simulations in both amplification scenarios, but with a slightly lower error for the PSA scenario. In addition, even though twice the number of channels contribute to the NLI when using PSAs (signals + conjugated idlers), the numerical simulations with the SSFT method show that the NLI power increases by only 1.1 dB. In fact, the extra channels are located farther apart with respect to the center channel, so the efficiency of the nonlinear distortions generated from the additional channels is low. This effect can be observed in figure B.1, shown in appendix B, where the FWM efficiency factor decreases for larger frequency separations with respect to the center channel due to higher phase mismatch. Similar results are obtained with the MEGN model, but now the NLI power is only about 0.3 dB higher for the PSA scenario when compared to considering EDFAs. This difference is most likely caused by the approximations performed to obtain (6.13).

Let us now focus on the evolution of the ASE noise in both amplification scenarios. As shown in figure 6.8-a), the ASE power in the PSA scenario is almost 6 dB lower than in the EDFA case because of the better ASE noise properties of PSAs. In both cases, the power of the ASE grows linearly with the number of spans. When the number of spans is small, the ASE noise is the dominant noise source and an improvement of the SNR of 5.8 dB is therefore observed for PSAs, as depicted in figure 6.8-b). This result is in agreement with the theoretical predictions of SNR improvement of 6 dB [186, 218]. When the number of spans increases, however, the role of the NLI becomes more relevant and the SNR advantage of using PSAs instead of EDFAs is reduced. This result can be observed in the black curves depicted in figure 6.8-b), which represent the evolution of the

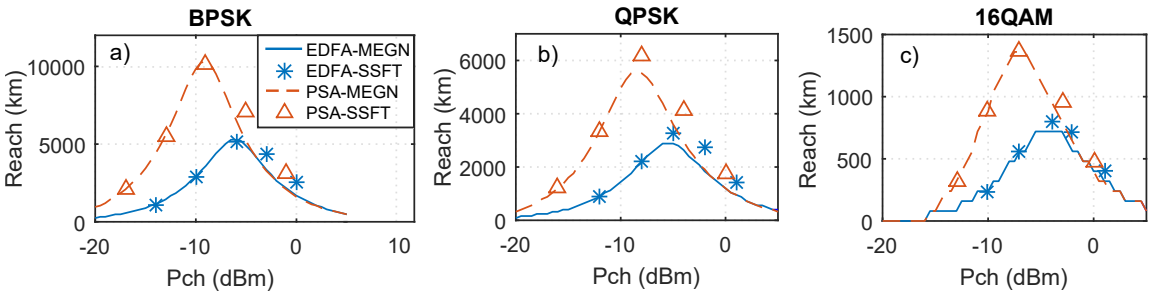

Figure 6.9: Maximum transmission reach using either EDFAs or PSAs to compensate the propagation losses, and using the MEGN model or the SSFT method to compute the power of the NLI for a) BPSK, b) QPSK, and c) 16-QAM signals.

SNR improvement obtained by considering PSAs instead of EDFA, ΔSNR, given by the ratio between the SNR obtained using PSAs and using EDFAs. According to the numerical results, ΔSNR decreases from 5.8 dB, measured after the first span of fiber, to about 4.9 dB after 20 spans of fiber. This is a direct consequence of P_{NLI} increasing quadratically with N_s, whereas P_{ASE} is approximately proportional to N_s. A slight deviation of less than 0.5 dB is also observed between the ΔSNR curves obtained with the MEGN model and the SSFT calculations, which is believed to be caused by the approximations considered to devise 6.13, as discussed above.

The influence of the launch power per signal channel, P_{ch}, on the maximum reach for transmission through a single optical link is shown in figure 6.9 for dual-polarization BPSK, QPSK and 16-QAM signals, considering either EDFAs or PSAs. Note that in this chapter it is assumed that the power per signal channel is the same when comparing the two different amplification scenarios. The power of the NLI is estimated by the MEGN model and by solving the Manakov-PMD equation with the SSFT method. The maximum reach was obtained by calculating the SNR after each span until it becomes lower than the SNR threshold required for BER below 10^{-3}. The formulas to calculate the SNR threshold for a given BER are presented in appendix C. The minimum SNR required to obtain a BER of 10^{-3} for BPSK, QPSK and 16-QAM signals is 4.77 (6.79 dB), 9.55 (9.80 dB) and 45.10 (16.54 dB), respectively. The simulations were performed considering the same fiber parameters as the calculations presented in figure 6.8, and $B_{ch} = 25$ GHz, $\Delta\nu = 50$ GHz, $L = 80$ km and $N_{ch} = 40$.

According to the numerical simulations, the maximum transmission reach increases with the launch power until reaching maximum values at about -6 and -9 dBm for BPSK, -5.5 and -8.5 dBm for QPSK, and -4.5 and -7 dBm for 16-QAM, obtained by respectively considering the amplification scenarios based on EDFAs and PSAs. For P_{ch} below such power values, the transmission reach is mainly limited by the ASE noise, so increasing the channel power improves the SNR and, consequently, the transmission reach. In addition, a very good agreement is verified for the simulations performed with the MEGN model and the SSFT method. For higher values of P_{ch}, the NLI becomes dominant and increasing the channel power reduces the maximum reach. In this case, the MEGN underestimates the

transmission reach because of the overestimation of P_{NLI}, as discussed in the previous section. Comparing the two amplification scenarios, PSAs enable longer transmission reaches at lower launch power values due to better ASE noise properties, but such reach advantage vanishes when the dominant noise source is the NLI. This situation occurs when the launch power is very high (note that P_{NLI} grows with P_{ch}^3), such that $P_{NLI} \gg P_{ASE}$ and $SNR \approx 2B_{ref}/(pB_{ch}) \cdot P_{ch}/P_{NLI}$. In this case, the SNR is determined by the power of the NLI and there is no considerable advantage of using low-noise amplifiers such as PSAs.

The optimum launch power, i.e., the launch power at which the maximum transmission reach is achieved, is obtained at lower values in the amplification scenario based on PSAs than on EDFAs. The reason for this result is explained as follows. The optimum launch power is verified when the ASE and NLI contribution are balanced, which in the case of PSAs occurs at lower values of P_{ch} due to their better ASE noise properties. At the same time, lower launch power also mean weaker NLI, which further increases the maximum transmission reaches observed in the PSA scenario. According to the numerical simulations, an extension of the maximum transmission reach of about 98% for BPSK, 94% for QPSK and 89% for 16-QAM signals is observed using PSAs instead of EDFAs.

The previous discussions reported in the literature have only considered the ASE contribution on the evolution of the noise properties and SNR in optical links amplified using PSAs [101, 218, 219, 247]. In those references, the NLI is neglected and much better performances are typically predicted with respect to EDFAs. However, it is shown here that the NLI is also important and limits the reach advantage of PSAs compared to EDFAs.

6.5 Optical transport networks

In this section, the influence of the launch power and span length on the number of amplifiers and regeneration requirements of an optical transport network amplified using either EDFAs or PSAs is investigated. The P_{NLI} is evaluated only with the MEGN model. Each optical transport network comprises several optical links, so the calculations with the SSFT method would be very time-consuming and with high computational requirements. Two real optical transport networks are considered in the numerical study, the Bulgarian Research and Education Network (BREN) [255] and the National LambdaRail Network (NLRN) [256][1], whose topologies are depicted in figure 6.10. The cost matrices of the two optical transport networks were provided through the courtesy of Dr. Rui Morais, and represent the length of the optical links as of June of 2009 for the NLRN, and as of November of 2009 for the BREN [257]. The optical transport networks considered in this chapter were selected in order to represent two opposite cases regarding the average length of the optical links. The BREN comprises 10 nodes interconnected through short links, with an average link length of 94 km. In contrast, the average link length of the NLRN is 692.4 km. The two opposite cases should provide very different results when comparing EDFA-

[1] This network has now ceased operations.

and PSA-based amplification. The main parameters of the two networks are summarized in table 6.2.

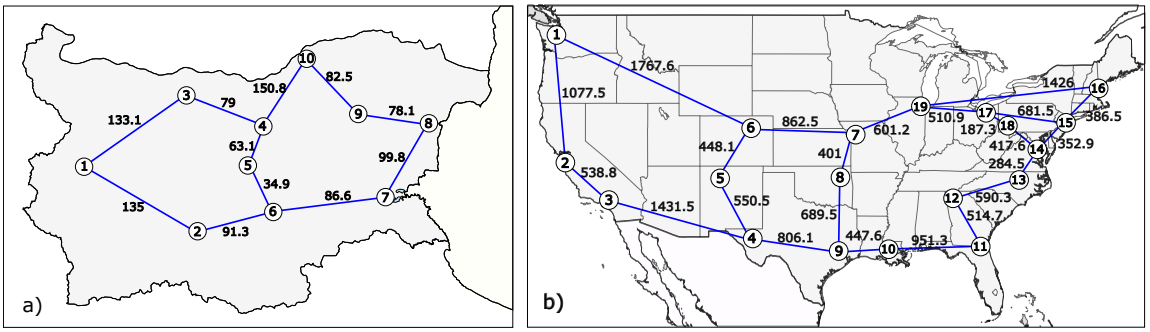

Figure 6.10: a) Bulgarian Research and Education Network. b) National LambdaRail network. The length of the optical links is expressed in kilometers.

Table 6.2: Network parameters.

Parameters	BREN	NLRN
Nodes	10	19
Links	11	23
Average link length (km)	94	692.4
Shortest link (km)	34.9	187.3
Longest link (km)	150.8	1767.6
Average connections per node	2.2	2.42

The numerical simulations assume the node and link architectures depicted in figure 6.1, and ideal WSSs and DCUs with total insertion losses of 6 dB. The optical links are divided into several spans of fibers with the same length, except for the last one, which may be shorter than the others if the total length of the link is not an integer multiple of the total link length. It is also considered that the NLI is only due to propagation along the fiber spans, and it is estimated by the MEGN model. In the case of the amplification scenario based on PSAs, twice the number of transmitted channels are considered when evaluating the power of the NLI. In addition, as discussed at the beginning of this chapter, all the idler channels are filtered out by the WSSs when entering each node, and generated again by the copier amplifiers before leaving the node. Thus, the transmission of the data signal through the links of the network is based on the copier + PSAs scheme, detailed in chapter 5. However, since the copier amplifiers are parametric PIAs, this approach introduces extra ASE noise when compared to also using a PSA as the booster amplifier (pure PSA amplification). On the other hand, any other strategy to generate a large number of correlated idler and pump waves in flexible and reconfigurable nodes seems to be very difficult to implement in practice, if not impossible (see the discussion at the beginning of this chapter). Remarkably, it was verified that the additional ASE noise introduced by the PI copier does not significantly degrade the ASE noise evolution in the subsequent optical

links. The main reason for this result is the low gain of the copier amplifiers at the output of each node, selected in order to compensate the insertion losses of 6 dB of the output WSSs. According to (6.6), the ASE power added by the amplifier grows linearly with its gain. Therefore, the noise added by the low-gain copier amplifiers is not very significant. In fact, the numerical simulations indicate that after the first span of fiber and the first PSA of the link, the ASE power within an optical bandwidth of 25 GHz is of about -36.9 dBm in the copier + PSA scheme, and -38.1 dB when using another PSA instead of the copier amplifier. This difference is quite considerable after a single span, but quickly decreases to less than 0.2 dB after propagation through ten spans of fiber.

The method used to compare the performance of optical transport networks amplified using PSAs or EDFAs was based on the procedure listed below.

1. Obtain the shortest paths of the optical transport network with the Dijkstra's algorithm and remove the redundant shortest paths using algorithm 4.

2. Evaluate the evolution of the SNR at each node of the non-redundant paths.

3. If the SNR becomes lower than the threshold SNR required to obtain a target BER of 10^{-3}, move back to the previous node of the non-redundant path and mark it as a location where signal regeneration is required. Such locations are henceforth denominated as regeneration sites. Regenerate the signals by eliminating all the ASE and NLI noise, return to the original node and evaluate the SNR at such node again.

4. If the SNR is still below the target threshold even after signal regeneration in the previous node of the non-redundant path, this means that BER values below 10^{-3} cannot be obtained. This situation may happen when two consecutive nodes in a non-redundant path are connected by very long links. In this case, stop the computation and assume that these paths cannot be used for data transmission at the given bit rate. Such paths are henceforth denominated as unfeasible paths.

The numerical simulations are also performed for both propagation directions. For instance, if nodes 1, 2, 3 and 4 form a non-redundant shortest path, the program runs for the sequences 1→2→3→4 and 4→3→2→1. This procedure is adopted in order to account for any slight differences in each propagation direction, caused by the last spans of the optical links. It should be noted that if the total length of the link is not an integer multiple of the span length, the last spans of the optical links are shorter than the others spans. Because of such differences, it may happen that signal regeneration is required at a specific node of the network in one propagation direction and at a different node in the opposite direction. More importantly, it may also happen that the number of regeneration sites in opposite directions is different.

The numerical simulations are performed for dual-polarization BPSK, QPSK, 16-QAM and 64-QAM signals, and assuming 80 signal channels, $B_{ch} = 25$ GHz and $\Delta\nu$ = 50 GHz.

Optical fibers with $D_\lambda = 16.7$ ps.nm^{-1}km^{-1}, $S_\lambda = 0.07$ ps.nm^{-2}km^{-1}, $\alpha = 0.22$ dB.km^{-1} and $\gamma = 1.3$ W^{-1}km^{-1} are considered in the computations. The NF of the copier PIAs and EDFAs is set to 5 dB, whereas a NF of 2 dB is assumed for PSAs.

6.5.1 Bulgarian Research and Education Network

The influence of the span length and launch power on the number of amplifiers, regenerators and unfeasible paths for the BREN is evaluated in this subsection, considering both the EDFA- and PSA-based amplification scenarios. It should be noted that the number of amplifiers is simply obtained from the network topology and the span length, regardless of the modulation format, launch power and amplification scenario. The variation of the number of required amplifiers with the span length is depicted in figure 6.11. As expected, the number of amplifiers decreases by using larger spans, albeit being the same for span lengths of 100 and 110 km. The BREN is composed of short links with an average length of less than 100 km, which explains why increasing the span length from 100 to 110 km does not reduce the number of amplifiers. In addition, doubling the span length for this network can only save about 30% of the required amplifiers.

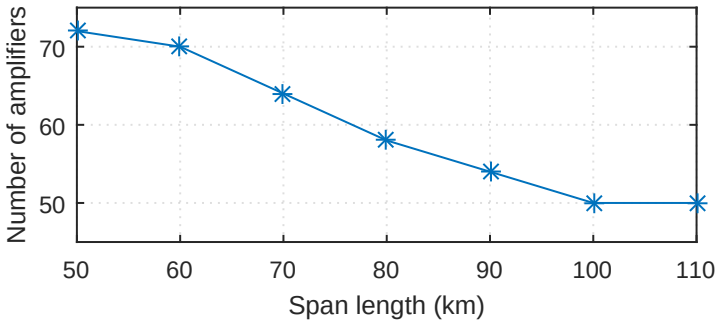

Figure 6.11: Number of required amplifiers as a function of the span length.

Let us now focus on the signal regeneration requirements for BPSK signals in both amplification scenarios. In this work, the number of regeneration sites is given by the total number of output ports of the nodes where signal regeneration is required. The numerical results are depicted in figure 6.12. According to the obtained results, the SNR of the transmitted channels remained above the required threshold for both amplification scenarios as no unfeasible paths were observed within the range of channel power and span length values considered in the simulations. In addition, no signal regeneration is required at any node of the network.

Similar results in terms of the number of unfeasible paths are obtained for QPSK signals, as depicted in figure 6.13. However, in the case of the EDFA scenario, signal regeneration is now required for long spans and at low launch power values. By considering longer spans of fiber, the gain of the amplifiers at the end of the spans must be larger in order to compensate for the higher propagation losses. In turn, the ASE noise added by

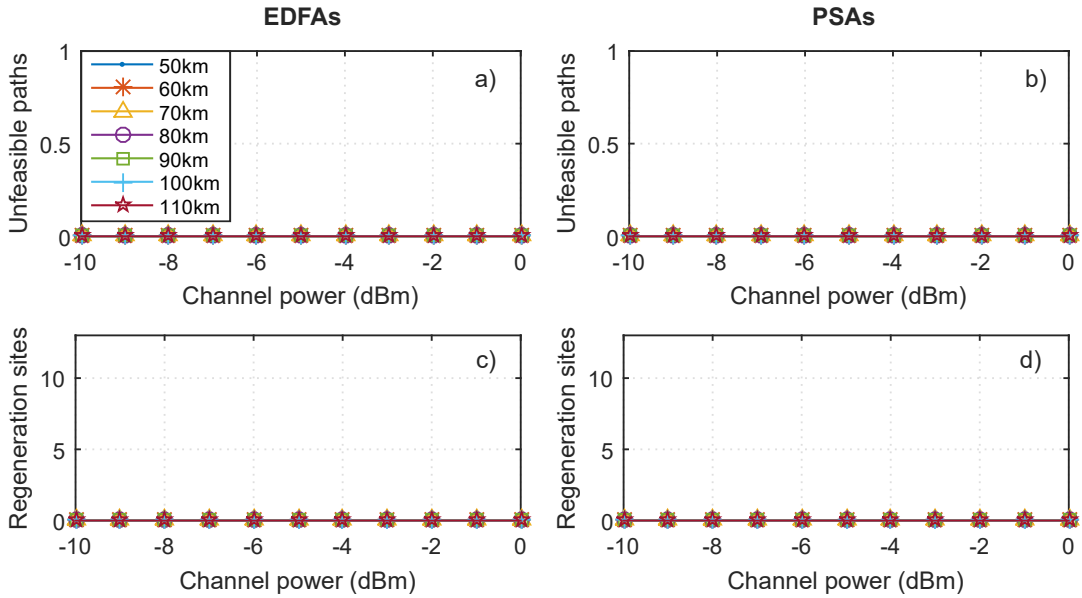

Figure 6.12: Number of unfeasible paths and regeneration sites in the BREN for different launch power per channel and span length, considering BPSK signals and amplification scenarios based on a) and c) EDFAs, b) and d) PSAs.

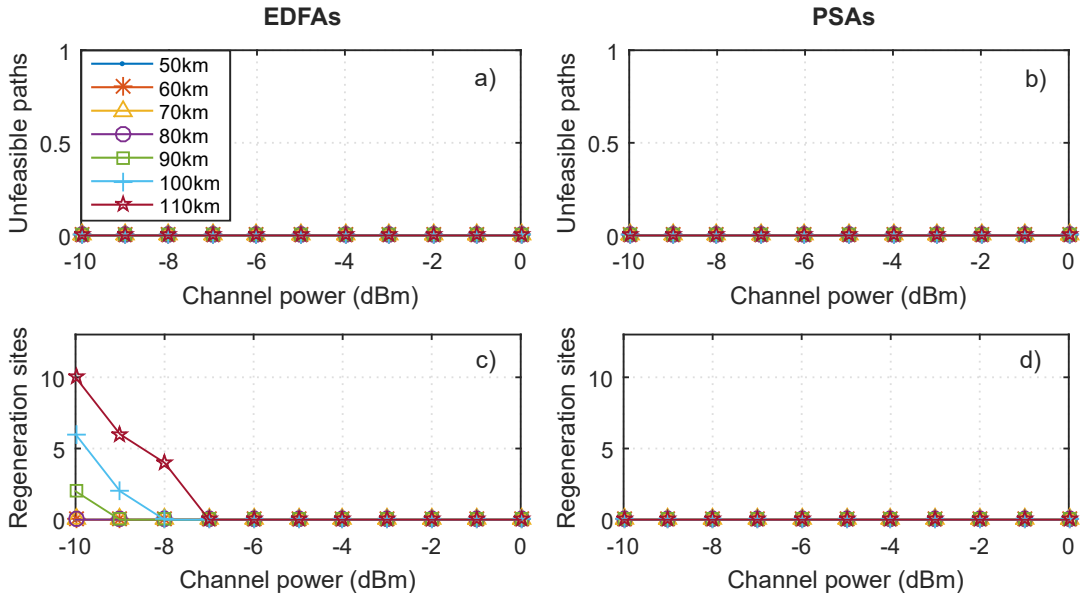

Figure 6.13: Number of unfeasible paths and regeneration sites in the BREN for different launch power per channel and span length, considering QPSK signals and amplification scenarios based on a) and c) EDFAs, b) and d) PSAs.

the amplifiers is also higher, as shown in (6.1), so stronger degradation of the SNR is observed for longer spans. In addition, at low values of P_{ch}, the dominant noise source is the ASE noise added by the amplifiers, which is determined by the gain of the amplifier and not by the power of the input waves, as shown in (6.1). In this case, the SNR is approximately proportional to P_{ch}, which justifies the higher regeneration requirements for low values of P_{ch}. On the other hand, the numerical simulations show that no signal regeneration is re-

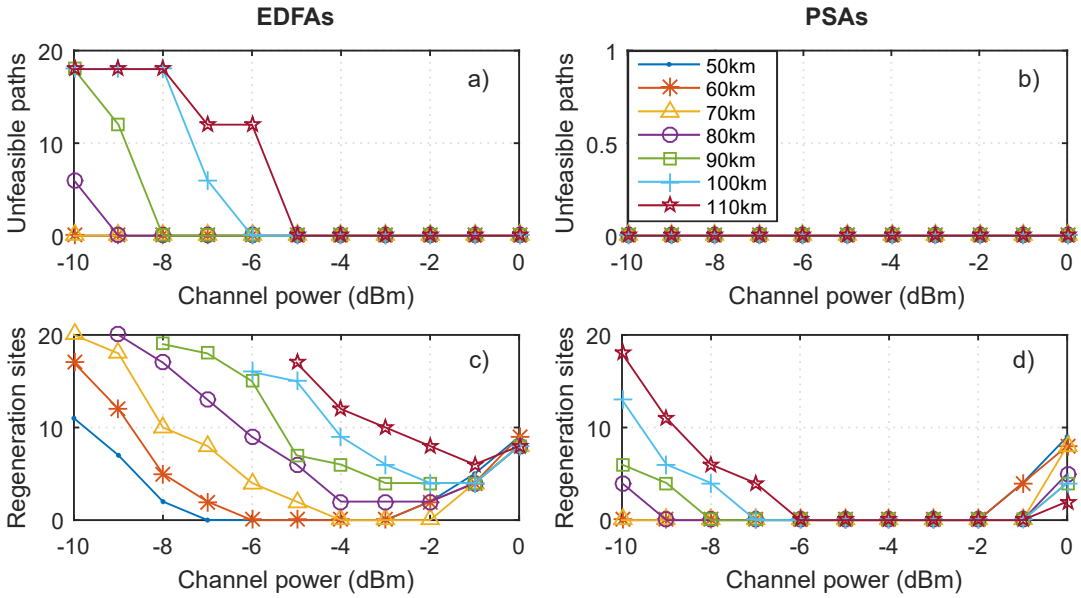

Figure 6.14: Number of unfeasible paths and regeneration sites in the BREN for different launch power per channel and span length, considering 16-QAM signals and amplification scenarios based on a) and c) EDFAs, b) and d) PSAs.

quired using PSAs at any of the investigated span length and launch power values, which is a consequence of the better noise properties of these amplifiers. Nonetheless, if the launch power is properly selected, no advantage in terms of the number of regeneration sites or amplifiers is observed for the BREN when replacing EDFAs by PSAs for BPSK and QPSK formats. The SNR requirements of such modulation formats are not very strict and the BREN is composed of very short links, so the SNR does not degrade below the minimum SNR threshold at any point of the network, even when using EDFAs.

Let us now consider the simulations for 16-QAM signals, depicted in figure 6.14. In the case of the EDFA amplification scenario, some unfeasible paths are observed for fiber spans longer than 80 km and at low P_{ch} values. Furthermore, for some specific cases (e.g., P_{ch} = -10 dBm and L = 90 km) the number of unfeasible paths is 18, considering both propagation directions. Since the total number of non-redundant shortest paths for the BREN is 9, this means that the SNR could not be kept above the required threshold for any of the paths. This is not the case of the amplification scenario based on PSAs, where no unfeasible paths were observed within the same range of parameters. In general, the number of regeneration sites is also higher in the EDFA scenario compared to using PSAs for the same channel power and span length. Even though PSAs generally provide better performances in terms of both unfeasible paths and regeneration requirements, it is still possible to transmit the signal channels without requiring any regenerator in the EDFA scenario. However, the length of the fiber spans must be shorter than 80 km and the launch power values of about -4 dBm. In the case of using PSAs, no regenerators are required for any of the simulated span lengths within a range of launch power values between -6 and -1 dBm. For 16-QAM signals, the only advantage of using PSAs instead of EDFAs would be

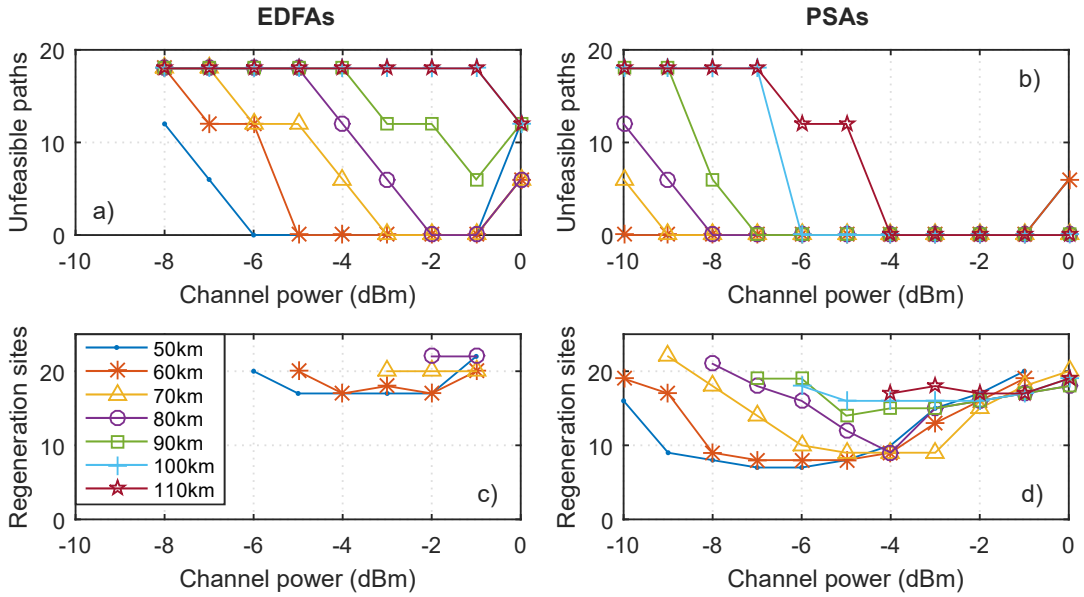

Figure 6.15: Number of unfeasible paths and regeneration sites in the BREN for different launch power per channel and span length, considering 64-QAM signals and amplification scenarios based on a), and c) EDFAs, b) and d) PSAs.

reducing the number of amplifiers from 64 to 50, achieved by increasing the span length from 70 km to 110 km.

The numerical simulations for 64-QAM signals are depicted in figure 6.15, obtained by considering an SNR threshold of 179.79 (22.55 dB), at which BER values of 10^{-3} are expected (see figure C.1). According to the numerical results, span lengths of 80 km or shorter must be considered in order to avoid any unfeasible paths, when considering the EDFA scenario. When using PSAs, it is possible to increase the span length, but a considerable number of regeneration sites is still observed. Let us consider a span length of 80 km. In the case of the EDFA scenario, a minimum of 22 regeneration sites are obtained, at P_{ch} = -2 dBm. On the other hand, only 9 regeneration sites are observed for the same span length using PSAs, at P_{ch} = -4 dBm. This corresponds to almost 60% of savings in terms of regeneration sites.

6.5.2 National LambdaRail Network

A similar analysis to that performed for the BREN is presented in this subsection for the NLRN. The variation of the number of required amplifiers with the span length is depicted in figure 6.16. In the case of the NLRN, a much larger number of amplifiers is required as the average length of the optical links is much larger than in the BREN. Moreover, by increasing the span length from 50 to 110 km, the number of required amplifiers is significantly reduced from 708 to 360, which corresponds to almost 50% of savings.

The variation of the number of unfeasible paths and regeneration sites as a function of the span length and launch power per channel for BPSK and QPSK signals are respectively

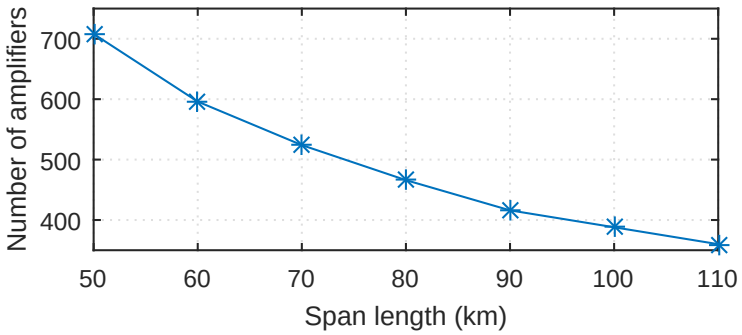

Figure 6.16: Number of required amplifiers as a function of the span length.

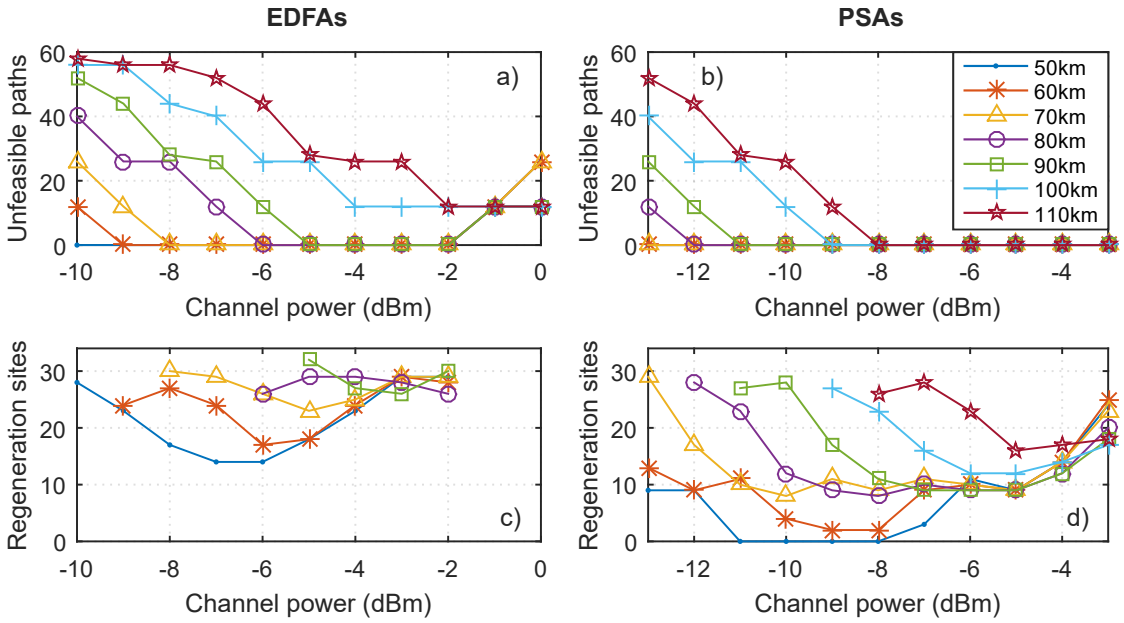

Figure 6.17: Number of unfeasible paths and regeneration sites in the NLRN for different launch power per channel and span length, considering BPSK signals and amplification scenarios based on a) and c) EDFAs, b) and d) PSAs.

depicted in figures 6.17 and 6.18. According to the numerical results, no unfeasible paths can be observed in the EDFA scenario for BPSK signals up to span length values of 90 km by properly adjusting the channel power. However, a high number of regeneration sites is observed. Even considering short span lengths of 50 km, more than 13 regeneration sites would be required for BPSK signals when using EDFAs. In the case of PSAs, no unfeasible paths can be observed even for longer span lengths of 100 and 110 km by setting the channel power to -8 dBm or above. Moreover, it is possible to avoid any signal regeneration in the PSA amplification scenario by considering short spans of 50 km, but a total of 708 amplifiers would be required.

As regards the numerical simulations for QPSK signals, depicted in figure 6.18, zero unfeasible paths can only be obtained for very short span lengths of 50 or 60 km when using EDFAs. At such span length values, not only the the number of amplifiers is very

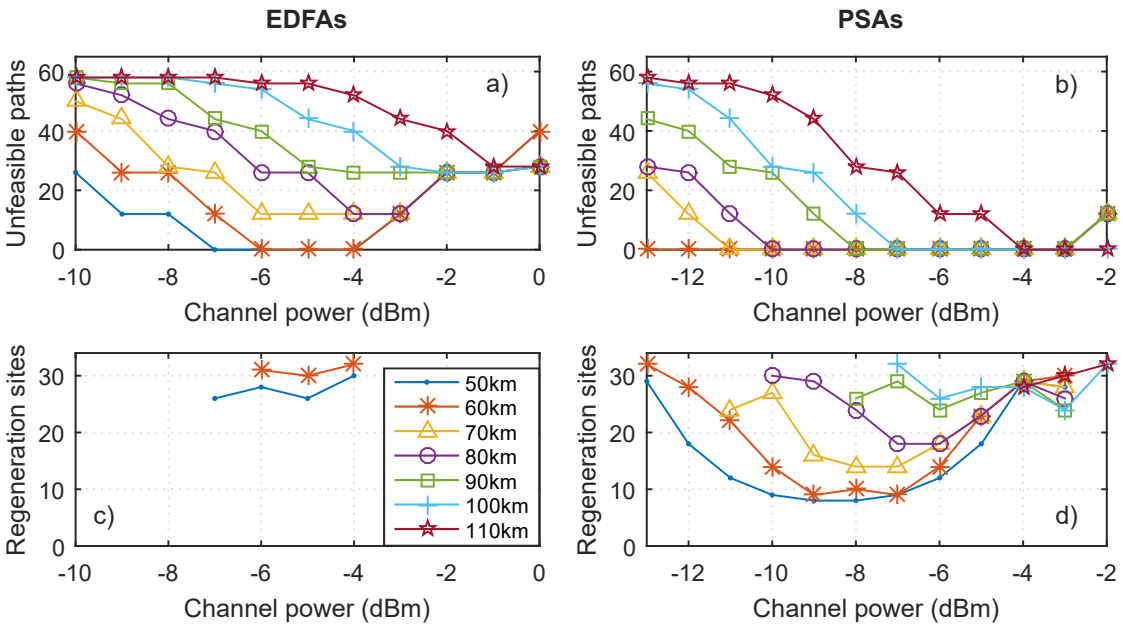

Figure 6.18: Number of unfeasible paths and regeneration sites in the NLRN for different launch power per channel and span length, considering QPSK signals and amplification scenarios based on a) and c) EDFAs, b) and d) PSAs.

high, but the required regeneration sites also exceeds 25 for any possible channel power considered in the simulations. In the case of the PSA scenario, longer span lengths can still be considered, but the number of regeneration sites can be very high as well, albeit generally lower than in the case of EDFAs. For comparison, the number of regeneration sites in the EDFA scenario for $L = 50$ km is 26, observed at P_{ch} of -5 dBm. On the other hand, only 8 regeneration sites are obtained when considering PSAs, at P_{ch} of -8 dBm. This corresponds to almost 70% less regeneration sites for the same span length. However, as mentioned above, short span lengths of 50 km requires a very high number of amplifiers. By using PSAs the span length can be increased to 70 or 80 km and still keep the number of regeneration sites below 25. For span lengths of 70 and 80 km, a total of 14 and 18 regeneration sites are respectively obtained. These results correspond to 47% and 31% less regeneration sites and savings of 26% and 34% in terms of the number of amplifiers when compared to the amplification scenario based on EDFAs, for $L = 50$ km.

Numerical simulations were also performed for 16- and 64-QAM signals, but no feasible non-redundant paths were obtained in both amplification scenarios. This is an expected result as the average link length of the NLRN is of about 700 km, so there is always at least one link where the SNR cannot be kept above the required threshold, regardless of the amplification scenario.

One of the main disadvantages of PSAs is the additional bandwidth required to transmit the correlated idler channels, which in the case of two-mode PSAs is twice as that required for EDFAs. A possible way to compensate for such disadvantage is by increasing the bandwidth of each individual signal. However, increasing B_{ch} also means that more ASE

noise is added to the transmitted signals (note that P_{ASE} within the channel bandwidth is proportional to B_{ch}). But since, PSAs have better ASE noise properties than EDFAs, it may actually be a better solution in terms of signal regeneration requirements to consider PSAs with twice the channel bandwidth. In order to verify this possibility, the influence of the signal bandwidth on the number of regeneration sites was investigated for the BREN and the NLRN, considering either EDFAs or PSAs. The numerical simulations were performed using the same fiber parameters as in the previous simulations, as well as a span length of 60 km. In both networks, 80 channels were considered for EDFAs, whereas only 40 signal channels were assumed when using PSAs. A constant channel spacing of 50 GHz was considered, so the total optical bandwidth required to transmit the signal and idler channels (PSAs) was 4 THz. In the case of the BREN, 16-QAM signals with channel power of -4 dBm and -9 dBm were respectively assumed for amplification scenarios based on EDFAs and PSAs. In the case of the NLRN, QPSK channels with P_{ch} of -5 dBm for EDFAs, and of -9 dBm for PSAs were considered in the simulations. The selected simulation parameters were chosen such that signal regeneration would be necessary for both the amplification scenarios. The obtained results are depicted in figure 6.19. According to the numerical results, the number of regeneration sites increases with the signal bandwidth for both networks and in both amplification scenarios, which is an expected result. In fact, by assuming matched filtering at the receiver, increasing the signal bandwidth also means that more ASE noise is detected by the PDs, thus explaining the observed results. In the case of the EDFAs scenario, for signal bandwidth values higher than 30 GHz for the BREN and 25 GHz for the NLRN there is at least one unfeasible path, whereas no unfeasible paths were observed using PSAs. Moreover, about 60 to 70% less regeneration sites were observed in the PSA scenario for both networks for B_{ch} values between 15 and 25 GHz.

The numerical simulations also show that fewer regeneration sites are required for the PSA scenario with twice the channel bandwidth with respect to EDFAs. For instance, 16 regeneration sites were obtained for a channel bandwidth of 15 GHz when considering EDFAs in the BREN, whereas only 9 regeneration sites were observed for PSAs and with a channel bandwidth of 30 GHz. In the case of the NLRN, the number of required regeneration sites for a channel bandwidth of 15 GHz using EDFAs was 27, whereas only 17 were required for the PSA scenario with B_{ch} of 30 GHz. The obtained results indicate that for the same transmission capacity and total optical bandwidth required to transmit both the signal and idler channels, PSAs are more advantageous than EDFAs in terms of unfeasible paths and signal regeneration. In fact, the same number of regeneration sites required for a channel bandwidth of 15 GHz in the amplification scenario based on EDFAs is verified at a B_{ch} of approximately 45 GHz when considering PSAs, for both networks. Hence, PSAs enable to triplicate the bandwidth of the transmitted channels and, consequently, to potentially compensate for the additional bandwidth lost to transmit the correlated idlers and to increase the overall transmission capacity, while keeping the same regeneration requirements of the amplification scenario based on EDFAs.

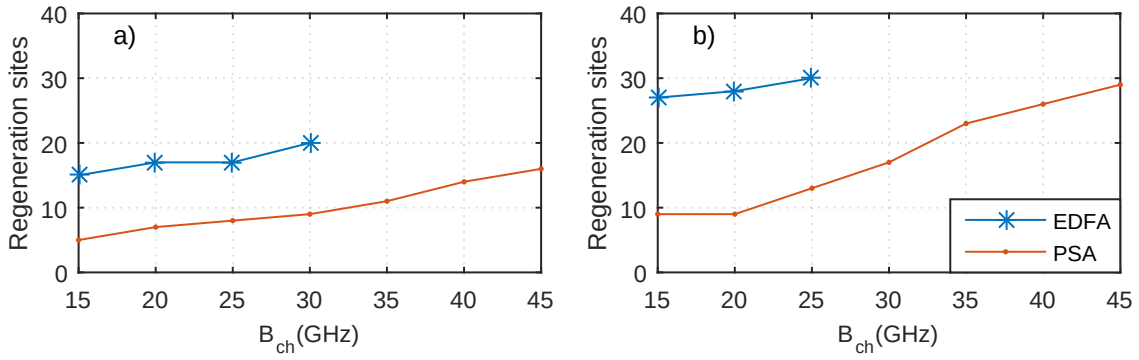

Figure 6.19: Variation of the number of regeneration sites with the channel bandwidth for a) the BREN, and b) the NLRN. Amplification scenarios based on EDFAs and PSAs are considered for both cases.

Optical transport networks are susceptible to fortuitous failures of the physical connections between the end nodes or even of some intermediate nodes. Hence, it is a common practice to define protection paths between two end nodes that correspond to possible alternatives in case of a failure. A possible strategy to define a protection path is by selecting the next shortest path that does not include any of the optical links of the working path, i.e., the original path that is selected when setting-up the connections between a pair of nodes of the network. By doing so, the working and protection paths are physically disjointed, and the protection paths can be obtained by using the Dijkstra's algorithm, after setting the elements of the cost matrix that represent the connections of the working path to infinity.

The protection paths are usually longer than the respective working paths, so additional regeneration sites may be required in order to enable network protection. In principle, the better ASE noise properties of PSAs may reduce the additional regeneration requirements when considering network protection. In order to evaluate the potential advantages of using PSAs instead of EDFAs for network protection, the additional regeneration sites required for the protection paths were numerically evaluated for both the BREN and the NLRN. The numerical simulations were carried out by following the procedure described at the beginning of this section, but without eliminating the redundant paths. In fact, the protection paths between two different pairs of nodes contained within the same non-redundant working paths may not be the same, nor even share a common link. Hence, the evolution of the SNR must be calculated for the protection paths between any pair of nodes of the network in order to verify the additional regeneration requirements.

The numerical calculations were performed for the BREN and the NLRN using the same fiber parameters as in the previous simulations and for both amplification scenarios. In the case of the BREN, eighty 16-QAM signals were considered, with launch power per channel of -3 dBm when considering EDFAs, and of -6 dBm for PSAs. The span length, channel bandwidth and channel spacing were respectively set to 70 km, 25 GHz and 50 GHz. In the case of the NLRN, two different sets of simulations were performed, each

considering a total of eighty QPSK signal channels with P_{ch} of -5 dBm for EDFAs and of -9 dBm for PSAs. The first set of simulations was carried out assuming a span length of 60 km, whereas the second one considered a span length of 50 km. The reason why two sets of simulations were performed for the NLRN is explained below. In both cases, the channel bandwidth and spacing were set to 25 GHz and 50 GHz, respectively.

According to the numerical simulations, when not considering the protection paths, no regeneration sites were required in both amplification scenarios for the BREN (see figure 6.14). However, when taking into account the protection paths, 8 regeneration sites were required for the EDFA scenario, whereas only 2 regeneration sites are required when using PSAs. In the case of the NLRN and for a span length of 60 km, a total of 52 unfeasible protection paths were observed when considering EDFAs, whereas no unfeasible protection paths were observed for PSAs. A total of 21 regenerations sites were obtained for the amplification scenario based on PSAs, with 12 of them required only for protection. Since some of the protection paths are unfeasible using EDFAs for a span length of 60 km, it was not possible to compare the potential benefits of using PSAs in terms of network protection. In order to do so, the numerical simulations were repeated for a span length of 50 km. For such a span length value, no unfeasible protection paths were observed for both amplification scenarios. When using EDFAs, a total of 33 regeneration sites were observed, with 7 of them required only for network protection. In the case of the amplification scenario based on PSAs, 6 additional regeneration sites are required for network protection, which corresponds to a total of 14 regeneration sites. The reported results show that PSAs are also advantageous for network protection as they enable a larger number of feasible alternative paths to be used for protection, and require fewer regeneration sites in the network.

A numerical comparison between amplification scenarios based on EDFAs and PSAs was presented in this chapter, using simplified models for the gain, attenuation and noise properties of the elements of an optical transport network.

A MEGN model was also presented in this chapter in order to estimate the nonlinear degradation in optical systems with full compensation of the chromatic dispersion at the end of each span. By using the MEGN model and solving the Manakov-PMD equation with a SSFT method, it was demonstrated that the NLI reduces the SNR advantage in optical links amplified by PSAs with respect to an EDFA-based amplification scenario. The numerical simulations for point-to-point transmission in a single optical link showed that almost twice the maximum transmission reach can be achieved by replacing the EDFAs with PSAs.

As regards the simulations for optical transport networks, it was shown in this chapter that no significant advantages are observed when replacing EDFAs by PSAs in optical transport networks with short links for BPSK and QPSK signals. Even for 16-QAM signals, the benefits of considering a PSA-based amplification scenario are very modest. On the other hand, about 60% less regeneration sites were observed for 64-QAM channels.

Thus, when the capacity of optical transport networks composed of short links needs to be increased by using higher-order modulation formats, PSAs may become an attractive possibility.

In the case of optical transport networks with long optical links connecting the nodes, the numerical simulations presented in this chapter showed that PSAs enable savings in terms of the number of required amplifiers and regeneration sites, with the former achieved by choosing longer spans. In optical transport networks composed of long links, an amplification scenario based on PSAs is advantageous even for lower order modulation formats such as BPSK and QPSK, but may not provide sufficient improvement of the SNR to allow using higher order formats.

PSAs are also an attractive alternative regarding network protection. The low-noise properties of PSAs not only allow a larger number of alternative routes to be used as protection paths in the case of a random failure, but they also reduce the regeneration requirements of such paths.

The numerical analysis presented in this chapter provides valuable insights into which type of optical transport networks and scenarios it would be more advantageous to consider replacing EDFAs with PSAs. In general, the numerical results show that significant savings in terms of both the number of amplifiers and regenerators can be envisaged by considering PSAs when the SNR requirements are more demanding. Hence, the benefits of considering PSAs instead of EDFAs are considerably greater when using advanced modulation formats and for optical transport networks composed of very long links.

The numerical results presented in this chapter confirm that PSAs can be a viable alternative to EDFAs when a capacity upgrade is required in an optical communication system. Nonetheless, the maturity of EDFA technology is much higher than for PSAs, and PSAs still face technological hurdles that must be overcome before they can be a serious contender.

Conclusion

Conclusions

OSP techniques have long been suggested as a possibility to increase the performance and efficiency of optical systems without requiring optical-to-electrical-to-optical conversion, and with the possibility of operation transparent to the modulation format and symbol rate. In fact, with the exception of the BPSK phase regenerator, all the OSP techniques investigated in this thesis are transparent to the modulation format and symbol rate, and can be upgraded for dual-polarization operation by using polarization-diversity loops. A few examples of successful signal processing functionalities in the optical domain have been reported and implemented in real systems, including optical amplification, and routing in WSSs built with liquid crystal on silicon technology or micro-electromechanical mirrors. However, in most cases, the low performance and high implementation complexity of the existing OSP functionalities have prevented a wider deployment of these techniques in real systems. In order to invert this situation, developing new OSP functionalities and improving the existing ones are fundamental steps. Such an approach should address OSP at different levels of complexity and dimensionality, starting from the analysis of the enabling physical processes, going up to the design and development of the devices and subsystems, and culminating in the evaluation of the benefits that the OSP functionalities bring to optical communication systems and networks. This was the main objective of the work presented in this thesis, in which different techniques for OSP enabled by the nonlinear properties of PPLN waveguides and HNLFs were investigated, focusing on the design of nonlinear devices with customized response, OWC, PS amplification and phase regeneration.

Nonlinear optics is a very important branch of Physics, with many technological applications in real life. In fiber-optic communication systems, the nonlinear response of the optical fibers is typically undesirable as it degrades the transmitted signals and limits the transmission reach. However, nonlinear phenomena are also very important and highly desirable to enable several OSP functions that would not be possible using purely linear optical processes. In this thesis, the fundamental principles of second- and third-order nonlinear phenomena were presented, including analytical expressions and numerical methods to model such processes, along with a brief description of the most common devices for nonlinear OSP. In this regard, cascaded second-order nonlinear processes in PPLN devices are a possible alternative for optical mixing and OSP functionalities. In fact, it was shown herein that cascaded TWM processes mimic FWM, but without being affected by many of the impairing mechanisms observed in other nonlinear devices such as SBS in HNLFs, or cross gain modulation and additional ASE noise in SOAs. In addition, by considering two cascaded TWM interactions in a single PPLN device instead of a simple TWM interaction, the problem of injecting waves at unusual spectral regions for optical communications systems is fully addressed.

One of the most interesting possibilities of second-order nonlinear effects in periodically poled devices is domain engineering, enabled by the QPM technique. If, on one hand, the

QPM technique is technological demanding, as it requires high-quality periodic inversions of the ferroelectric domains at the micrometer scale, on the other hand it allows to modify the nonlinear spectral response of PPLN waveguides. Domain engineering is a very powerful and versatile technique that allows to produce advanced devices, combining optical mixing and filtering capabilities in a single device. Inspired by what has long been done on the design of advanced fiber Bragg gratings and grating-assisted couplers, a modified version of the LPA was presented in this thesis for the design of PPLN devices with customized poling patterns, using the DRM to translate the coupling coefficients obtained by the LPA into variations of physical properties of the periodic poling inversions. The proposed methods proved to be flexible, effective and reliable tools on the design of the poling pattern of advanced PPLN devices, without requiring an initial guess for the poling pattern, nor complex optimization techniques. In fact, it was observed that the main challenge of the LPA was not the design of the poling pattern itself, but rather finding the best magnitude and phase functions of the target nonlinear spectral response for a specific OSP functionality. This is still an open issue that must be addressed in the future. Most likely, optimization techniques that have already been investigated for customized long-period Bragg gratings and grating-assisted couplers may still have to be considered for that purpose.

Another important open issue regarding the design of advanced PPLN devices with the LPA is the non-negligible difference between the target nonlinear spectral response for the intermediate SFG process, and the final conversion spectrum in a cSFG/DFG interaction. As demonstrated for the quasi-rectangular PPLN devices, lateral decaying tails on the conversion spectrum for cSFG/DFG were observed instead of steep magnitude transitions of the original target response. Such differences are caused by the broader conversion bandwidth of the SFG step at the beginning of the device, and are therefore very difficult to eliminate. In fact, the observed differences are not a limitation of the LPA itself, but rather of the cascaded nature of the nonlinear interactions, so they are also observed for other designing techniques. Nonetheless, the final conversion spectrum for cSFG/DFG still resembles the target one, so the devices designed by the LPA may still be used for advanced OSP, as demonstrated in chapter 4.

The LPA and the DRM are not limited to PPLN waveguides, but they can also be used for other types of periodically poled devices such as PPLT waveguides. Moreover, the proposed methods are not limited to the design of devices for applications in OSP. As an example, the LPA and the DRM can be used to develop devices for the generation of broadly tunable THz light sources [258].

After developing new methods to design PPLN devices with customized poling patterns, the next logical step would be producing a real device for advanced OSP. Amongst the wide range of possibilities, OWC is one of the most important OSP functionalities in reconfigurable optical networks, as it enables to reduce the blocking probability by solving wavelength contention problems. In such systems, it may be necessary to convert a group of WDM channels to a different spectral region, so multichannel operation and the pos-

sibility of tuning the wavelength of the converted signals are highly desirable properties. Such features were demonstrated in this work by considering a conversion scheme based on cSFG/DFG in a PPLN device with broadened QPM bandwidth. In this regard, a quasi-rectangular PPLN waveguide with an extended conversion bandwidth of 400 GHz was designed and produced using the LPA and DRM. Compared to other possibilities to produce PPLN waveguides with broader QPM bandwidth such as linearly chirped devices, the nonlinear spectral response of quasi-rectangular PPLN waveguides has steeper magnitude transitions at the cut-off frequencies. This is an important property to reduce inter-channel crosstalk, as the quasi-rectangular PPLN device can simultaneously perform OWC and select a limited number of signal channels to be converted because of its filtering capabilities. Regarding the manufactured device, a very good agreement between the measured SFG conversion efficiency spectrum and the target nonlinear spectral response was observed, which effectively proved the validity of the LPA and DRM. The observed results were quite remarkable, given the fact that the PPLN device was produced by an external company that did not provide any details on the manufacturing process nor the waveguide dispersion properties due to its confidentiality policy. Using the manufactured device, tunable wavelength conversion of eight QPSK signals was effectively demonstrated, but limited by the low conversion efficiency of the PPLN waveguide. A trade-off between broad conversion bandwidth, pump power and generation of spurious nonlinear contributions was observed. Note, however, that such a trade-off is not exclusive to the quasi-rectangular PPLN waveguides, but it is also observed for other devices with extended QPM bandwidth such as linearly chirped PPLN waveguides.

If OWC is to be deployed in a real system, not only wavelength tunability and broadband operation are highly desirable features, but the OWC units should also degrade the converted signals as little as possible. In this sense, an OWC scheme using two coherent pump waves to eliminate the additional phase noise transferred to the converted signal caused by the finite linewidth of the pumps was also investigated in this thesis. By considering coherent pumps generated from the same light source in a specific configuration of cSFG/DFG, the additional phase noise of each pump wave cancels out in the converted signal, even using inexpensive and broad-linewidth DFB lasers as light sources. Even though the phase noise added to the converted signals caused by finite linewidth of the light sources can be reduced by using costly and bulky narrow-linewidth lasers, it is not completely eliminated as in the proposed scheme. The pump-linewidth-tolerant strategy is thus an important step towards hitless OWC, which is not only transparent to the modulation format and symbol rate, but it can also be upgraded for dual-polarization operation using polarization diversity schemes.

The pump-linewidth-tolerant concept was also shown to be valid for WDE between two data channels, which can be seen as two OWC processes for each data channel occurring simultaneously in a single step. It was proven in section 4.3 that by using the proposed method the exchanged signals were degraded only by the WDE crosstalk caused by incom-

plete depletion of the input signals, without additional phase noise due to finite linewidth of the pumps. WDE in a single wavelength converter combined with signal depletion enables savings in terms of wavelength converters and optical filters when compared to a strategy based on two independent converters. However, it requires tighter control on the operation conditions such as the pump power and temperature of the PPLN chip, as the power of the remaining undepleted signal at the original wavelength greatly increases even for small deviations from the optimum operation condition. In addition, wavelength tunability is difficult as the two pumps and exchanged signals must be symmetrically placed around the QPM wavelength, and the frequency spacing between the two pumps and the two signal channels was limited by RF clock signal driving the MZM of the TTG.

The pump-linewidth-tolerant scheme investigated in this thesis is a possible way to reduce the signal degradation caused by OWC units. However, the main mechanisms limiting the performance and maximum transmission reach of optical communication systems are the ASE noise added by optical amplifiers and the signal distortions caused by the nonlinear response of the transmission fibers. PSAs are unique amplifiers that can potentially improve the performance and/or the transmission reach of optical systems in two ways. First, PSAs allow amplification with NF values below the quantum limit of 3 dB observed in PIAs, which means that PSAs introduce less ASE noise than EDFAs. Second, PSAs can be used to regenerate the phase of degraded signals. PPLN waveguides are a possible alternative to build compact PSAs, relying on either simple or cascaded TWM interactions. Depending on the type of second-order nonlinear interactions, and the number of signal, idler and pump waves, different configurations of PPLN-based PSAs are possible. If, on one hand, the configurations of PPLN-based PSAs relying on simple DFG offer an additional gain advantage of 4 (6 dB) over those based on cascaded interactions, on the other hand, they require generating waves at a completely different spectral region. Typically, such waves are produced by using an extra PPLN waveguide, and require components designed to operate at unusual spectral regions for optical communication systems. Hence, despite the lower gain, configurations based on cascaded TWM may actually be preferable.

The numerical simulations performed in this thesis showed that increasing the length of the PPLN waveguides would be the most efficient way to increase the gain of PPLN-based PSAs. However, the size of the available lithium niobate wafers limits the maximum length of PPLN waveguides to less than 10 cm. Moreover, guaranteeing the homogeneity and quality of long waveguides is very challenging. Thus, the remaining possibility to improve the gain of PPLN-based PSAs without increasing the pump power is to produce devices with better conversion efficiencies. This can be achieved by a tighter confinement and higher transversal overlap of the waves interacting throughout the waveguide.

It was also shown in this thesis that flat gain spectra with wide amplification bandwidth of over 40 nm can be obtained for two-mode PPLN-based PSAs, using either one or two pump waves. In the case of PSAs built with third-order nonlinear media, a dual-pump configuration is typically required in order to obtain flat gain spectra due to the effects

of SPM and XPM on the effective phase mismatching parameter. For broadband and multichannel amplification purposes, a single-pump configuration is easier to implement in practice and only a single pump wave needs to be regenerated in pump recovery units. A single-pump, two-mode PPLN-based PSAs can thus be a better alternative. It was also demonstrated in this thesis that it is almost impossible to implement a four-mode PSA using PPLN waveguides. Moreover, even if they could be built in practice, there would be no gain advantages compared to two-mode PSAs.

In order to enable the PS properties of PSAs, frequency- and phase-correlated waves must be generated before the amplifier, usually using the copier + PSA strategy. The copier + PSA scheme requires an additional PI parametric amplifier to generate the correlated waves, which in the case of PPLN-based parametric amplifiers also implies extra temperature controllers and coupling optics. In this work, bidirectional operation in a single PPLN device was proposed to reduce the number of devices and temperature controllers, in which the correlated waves are generated in one propagation direction and PS amplification is performed in the opposite one. Using the proposed scheme, PS amplification in a single-pump, two-mode configuration and also "black-box" phase-regeneration of a BPSK signal were experimentally demonstrated. Compared to HNLFs, PPLN waveguides are more suitable for bidirectional operation, as backscattering effects such as Brillouin and Rayleigh scattering are negligible in PPLNs devices. However, the high power launched in both propagation directions affected the thermal stability of the device, and resulted in strong GRIIRA and photorefractive damage effects. Because of such problems, the modest conversion efficiency and significant insertion losses of the available PPLN waveguides, no net gain could be observed in the two-mode PPLN-based PSA with bidirectional propagation. In addition, the photorefractive and GRIIRA effects seriously compromised the stability of the PLL set-up in the phase regeneration experiment, so the phase of the waves could only stay locked for a few seconds. The root cause of all the problems observed in the experiments using PPLN-based PSAs was the high pump power required in order to observe significant PS operation. The solution for these problems is to consider devices more resilient to photorefraction and with higher conversion efficiency. More efficient devices would allow to improve the gain of the PSA and/or to reduce the pump power.

PS amplification in a four-mode PSA was also demonstrated in this thesis using the copier + PSA scheme, and without requiring a PLL set-up to actively lock the relative phase of the interacting waves. Since four-mode PSAs are almost impossible to be implemented in practice using PPLN devices, a HNLF was used instead as the nonlinear medium. By using a HNLF, PS amplification of a QPSK signal with almost 20 dB of gain was demonstrated. A gain advantage of almost 12 dB compared to PI operation, or equivalently, an advantage of 6 dB compared to two-mode PSAs was observed, as well as an OSNR improvement of more than 8 dB for the signal channel. However, four-mode PSAs require an amplification bandwidth four times wider than conventional amplifiers because of the

additional idler bands, which is a big disadvantage for WDM systems. This disadvantage is partially compensated by broader amplification bandwidth of fiber-based parametric amplifiers, and the possibility to amplify signals in spectral regions outside the conventional band of erbium-based amplifiers. Four-mode PSAs may be especially attractive for different applications in optics, especially when the additional gain advantage is critical and the amplification bandwidth is secondary. Parametric multicasting is an example of such possibilities [209]. In addition, four-mode PSAs can be a possible solution to improve the detection sensibility for spectroscopy or sensing applications due to a higher improvement of the OSNR when compared to two-mode PSAs.

The experiments performed in this thesis clearly showed that PSAs built with HNLFs greatly outperform PPLN-based PSAs in terms of net gain and operation stability. Even using state-of-the-art devices such as ridge PPLN waveguides, the maximum net gain of PPLN-based PSAs is far below the gain values achieved in fiber-based PSAs. Hence, improving the conversion efficiency of the PPLN waveguides is a fundamental requirement in order to produce a viable alternative to fiber-based PSAs. If so, PPLN waveguides offer different possibilities that may solve some of the main technological limitations of PSAs. For instance, several waveguides can be produced in a single PPLN chip. Each of such waveguides could be used as an independent phase regenerator for multichannel operation. Moreover, the electro-optic properties of the lithium niobate substrate can be used to produce an integrated solution that combines a PM and a PSA in a single device [220]. The integrated PM could then be used as the phase actuator of the PLL circuit.

The first chapters of this thesis were devoted to the development of new methods to produce advanced devices for OSP and on the investigation of new possibilities for OWC, phase regeneration and PS amplification. However, no OSP functionality will ever be implemented in practice without a clear evidence that it actually improves the performance of the optical communication systems. Hence, an analysis on the potential benefits of considering PSAs on the amplification and regeneration requirements for point-to-point transmission in a single optical link and in optical networks comprising several links was performed in chapter 6. The main reason for choosing PS amplification over the other OSP possibilities investigated in this thesis was the non-existence of a proper analysis on the potential benefits or disadvantages of considering PSAs in optical networks.

PSAs have remarkably low-noise properties, with NF values below the quantum limit of 3 dB observed for conventional PI amplifiers. If the ASE noise added by the amplifiers is the main degradation mechanism, PSAs can potentially improve the SNR of the transmitted signals by a factor of 4 when compared to EDFAs. However, the transmission of data signals through optical fiber systems is not only limited by the ASE noise added by the optical amplifiers, but also by the nonlinear response of the fiber. The distortions introduced on the transmitted signals caused by the fiber nonlinearities are also responsible for degrading the SNR of the data signals. Since PSAs require full compensation of the chromatic dispersion effects before the amplifier, a MEGN model was devised in this thesis

in order to estimate the power of the NLI. Though the MEGN model presented in this thesis overestimates the power of the NLI, it is able to correctly model the influence of the signal, fiber and span parameters on P_{NLI}, with the exception of the channel spacing. By finding the root cause for this exception, it is expected that the overestimation of P_{NLI} observed for the MEGN can be considerably reduced.

By using the MEGN and simplified models for the noise and gain properties of the optical amplifiers, it was verified that replacing EDFAs by PSAs can potentially increase the maximum reach for long-haul transmission by a factor of two. The numerical simulations also showed that the accumulation of the NLI is very important, as it limits the maximum transmission reach and decreases the SNR advantage of considering PSAs instead of EDFAs. In fact, if not limited by the NLI, an increase of the maximum reach of about four times would be expected by replacing EDFAs by PSAs. Regarding the numerical simulations for optical networks, it was verified that replacing EDFA by PSAs do not offer significant advantages for small networks with short links connecting the different nodes, and for modulation formats such as BPSK, QPSK or even 16-QAM. However, using PSAs in networks with short links may enable the transmission of data channels with higher-order modulation formats that would not be possible considering common EDFAs, therefore increasing the transmission capacity of the optical network. In the case of large networks comprised of long optical links, PSAs allow a significant reduction on the number of amplifiers and/or the number of locations in an optical network where signal regeneration is required. As a rule of thumb, the benefits and advantages of replacing EDFAs with PSAs are considerably higher when the SNR requirements are more challenging, which is typically the case for long-haul transmission and when considering higher-order modulation formats. PSAs are also an attractive solution for network protection in two ways. First, the low-noise properties of PSAs enable a higher number of alternative paths to be used for network protection in the case of a failure in a transmission link. Second, a fewer number of additional regeneration sites are required when using PSAs in comparison to a scenario based on pure EDFA-based amplification.

As mentioned above, the NLI is a very important limitation that reduces the gain advantage of using PSAs instead of EDFAs. However, this limitation has not been properly discussed in previous works, which mainly focus on the ASE noise properties of the amplifiers. The NLI may eventually play a more important role than simply reducing the SNR advantage of PSAs over EDFAs. For a fair comparison, full compensation of the dispersion effects after each span of fiber was considered in this thesis for both amplification scenarios. In such cases, the power of the NLI grows quadratically with the number of spans. However, EDFAs are not limited by the chromatic dispersion effects and can be used for dispersion uncompensated transmission. In dispersion uncompensated systems the power of the NLI is approximately proportional to the number of spans [58]. Hence, if the number of spans is large enough, the power of the NLI in a dispersion uncompensated system amplified by EDFAs may be significantly lower than in optical links with full

dispersion compensation after each span of fiber. In turn, the lower degradation due to the NLI in dispersion uncompensated systems may partially compensate for the better ASE noise properties of PSAs, and thus reduce the advantages of considering PSAs instead of EDFAs. Such an analysis was not performed in this thesis and is left for future investigation.

In this thesis, different techniques for the design of PPLN devices with customized poling patterns, advanced OWC, PS amplification and phase regeneration were investigated, aiming to push forward the state-of-the-art in OSP and ultimately improve the performance of optical communication systems. The techniques investigated in this thesis exemplify the potential benefits of considering OSP techniques in future lightwave systems and show that further developments of devices, schemes and subsystems enable new OSP functionalities and improves the existing ones.

Future Work

Scientific research often raises more questions and creates more challenges than those it actually solves. The work presented in this thesis is not an exception and several directions for future work are envisaged, as summarized below.

- *Design of new PPLN devices with customized poling pattern using the LPA*:

  The design of PPLN waveguides with customized spectral responses enables new possibilities that are not observed in typical uniform devices by combining OWC with optical filtering. Quasi-rectangular and multiple-QPM PPLN waveguides are some examples that have enabled advanced features such as tunable and multichannel OWC and phase regeneration of QPSK signals [55]. However, many other possibilities remain unexplored. For instance, a PPLN device with conversion spectrum whose efficiency linearly increases/decreases with the wavelength detuning can be used for OWC with the possibility to track frequency drifts of the pump or input signal lasers. In this case, any wavelength detuning of the light sources is converted into a variation of the conversion efficiency, which in turn can be used as a feedback mechanism to ensure optimum operation. Moreover, the LPA can be a valuable tool to investigate and develop new devices for applications in different areas, including optical comb generation and parametric oscillators.

- *Development of optimization strategies to eliminate the difference between the target and obtained spectral response in cSFG/DFG processes*:

  As discussed in chapter 3, there are some non-negligible differences between the spectral conversion efficiency for cSFG/DFG and the initial target. One straightforward way to eliminate such differences is to use two devices with the target response in a tandem configuration, one only for SFG (or SHG) and another only for DFG. Another alternative would be developing an optimization or recursive technique to

design the spectral response of the intermediate SFG wave in a cSFG/DFG process such that the final response for cSFG/DFG matches the initial target. However, there is no guarantee that such procedure is possible. In fact, it seems to be very difficult to obtain sharp magnitude transitions on the final response for cSFG/DFG due to the cascaded nature of the interaction and the evolution of the QPM bandwidth for the intermediate SFG process along the device.

- *Development of strategies to calculate the target phase of the fast and slow modes for optimum conversion efficiency*:

  For simplicity, a linear phase for the target response of the slow mode was considered in all the examples studied in chapter 3. However, this approach was not the optimum choice in terms of the final conversion efficiency. For instance, using the optimization technique proposed in [133], the efficiency drop of each QPM resonance in multiple QPM devices is proportional to the number of resonances. On the other hand, by choosing a linear phase function for the LPA, the efficiency of each resonance inversely decreases with the square of the number of resonances. In principle, greater conversion efficiency values can be obtained by choosing different possibilities for the target phase of the slow and fast modes. Hence, developing a strategy to design the phase of the target spectral response that maximizes the conversion efficiency while keeping the desired magnitude response would be an important achievement.

- *Improve the performance of the bidirectional PSA*:

  The performance of the copier + PSA scheme in a single device using bidirectional propagation can be greatly improved by using PPLN devices with higher conversion efficiency, which in turn would require lower pump power, and also with greater resilience to thermal and photorefractive instabilities. Ridge PPLN waveguides doped with ZnO or MgO [125] are a possible solution.

- *Evaluate the impact of replacing EDFAs with PSAs in optical networks with different dispersion management mapping*:

  The use of PSAs in optical networks requires full compensation of the accumulated dispersion after each span. This is not an ideal solution for real systems as the nonlinear interference is more severe than in uncompensated systems. The best approach would be finding a way to implement a PSA without requiring dispersion compensation, but no successful solution has been proposed so far. Another possibility is to consider placing an extra DCU at the beginning of the fiber span to purposely predistort the signal, and then use another DCU at the end of the span to compensated the chromatic dispersion before the PSA. Even though this strategy requires twice the number of DCUs, it can potentially reduce the NLI [259], therefore improving the maximum transmission reach and alleviate the signal regeneration requirements in optical networks.

- *Improvement of the MEGN model*:

  The MEGN model presented in this thesis proved to be a valuable tool to estimate the power of the NLI in optical systems with full compensation of the chromatic dispersion effects after each span of fiber. Even though the MEGN model generally overestimates the power of the NLI, it correctly models the influence of all the signal, span and fiber parameters with the exception of the channel spacing. Further investigations on the main reason why the influence of the channel spacing is not correctly modeled by the MEGN model are required. It is also expected that improving the MEGN to correctly describe the influence of the channel spacing can also reduce the overestimation error on the evaluation of P_{NLI}.

- *Comparison between dispersion compensated and uncompensated scenarios*:

  PSAs require full compensation of the chromatic dispersion effects before the amplifier in order to maximize the PS gain. Hence, a dispersion-managed mapping with full compensation of the chromatic dispersion after each span of fiber was considered in the numerical simulations presented in chapter 6 for both amplification scenarios. According to the MEGN model, the power of the NLI increases quadratically with the number of spans for such systems. However, an approximately linear growth of P_{NLI} with the number of spans is expected in dispersion uncompensated links. Consequently, the advantage of better ASE noise properties of PSAs in systems with full compensation of the chromatic dispersion effects may be partially mitigated by the lower signal degradation due to NLI in dispersion uncompensated systems based on EDFAs. A proper comparison between the two scenarios is still missing and should be investigated in the future.

- *Polarization-insensitive/dual-polarization OSP*:

  One of the main challenges of OSP is polarization-insensitive operation, which has not been investigated in this thesis. In fact, the original idea for the bidirectional PSA scheme was to show phase regeneration of dual-polarization signals in a single device, using a polarization diversity loop. However, the available polarization beam splitters could not handle the required pump power values, so the copier + PSA scheme in a single device was investigated instead. With the advent of polarization-division multiplexing, polarization-insensitive operation has become one of the most desirable features for OSP and clearly deserves further research.

Bibliography

[1] G. P. Agrawal, *Fiber-optic communication systems*, 4th ed. John Wiley & Sons, 2012.

[2] A. Gokhale, *Introduction to Telecommunications*, 1st ed. Cengage Learning, 2004.

[3] International Communication Union. (2015) ICT statistics home page. [Online]. Available: http://www.itu.int/en/ITU-D/Statistics

[4] Cisco Systems, Inc. (2015) Visual networking index (VNI). [Online]. Available: http://www.cisco.com/c/en/us/solutions/service-provider/visual-networking-index-vni

[5] P. J. Winzer and R.-J. Essiambre, "Advanced modulation formats for ultra-high-speed transport networks," *Journal of Lightwave Technology*, vol. 24, no. 12, pp. 4711–4728, Dec. 2006.

[6] R.-J. Essiambre, G. Kramer, P. Winzer, G. Foschini, and B. Goebel, "Capacity limits of optical fiber networks," *Journal of Lightwave Technology*, vol. 28, no. 4, pp. 662–701, Feb. 2010.

[7] M. Seimetz, *High-Order Modulation for Optical Fiber Transmission*, 1st ed. Springer-Verlag Berlin Heidelberg, 2009.

[8] O. Yilmaz, S. Nuccio, S. Khaleghi, J.-Y. Yang, L. Christen, and A. Willner, "Optical multiplexing of two 21.5 Gb/s DPSK signals into a single 43 Gb/s DQPSK channel with simultaneous 7-fold multicasting in a single PPLN waveguide," in *Optical Fiber Communication Conference (OFC)*, San Diego, USA, Mar. 2009, p. OThM4.

[9] A. Willner, O. Yilmaz, J. Wang, X. Wu, A. Bogoni, L. Zhang, and S. Nuccio, "Optically efficient nonlinear signal processing," *Journal of Selected Topics in Quantum Electronics*, vol. 17, no. 2, pp. 320–332, Mar. 2011.

[10] A. Willner, S. Khaleghi, M. Chitgarha, and O. Yilmaz, "All-optical signal processing," *Journal of Lightwave Technology*, vol. 32, no. 4, pp. 660–680, Feb. 2014.

[11] S. Boscolo, S. K. Turitsyn, and K. J. Blow, "Nonlinear loop mirror-based all-optical signal processing in fiber-optic communications," *Optical Fiber Technology*, vol. 14, no. 4, pp. 299 – 316, Oct. 2008.

[12] S. Azodolmolky, M. Klinkowski, E. Marin, D. Careglio, J. S. Pareta, and I. Tomkos, "A survey on physical layer impairments aware routing and wavelength assignment algorithms in optical networks," *Computer Networks*, vol. 53, no. 7, pp. 926–944, May 2009.

[13] T. A. Strasser and J. L. Wagener, "Wavelength-selective switches for ROADM applications," *Journal on Selected Topics in Quantum Electronics*, vol. 16, no. 5, pp. 1150–1157, Sep. 2010.

[14] I. Kaminow, T. Li, and A. E. Willner, *Optical fiber telecommunications VB: systems and networks*. Elsevier, 2010.

[15] S. Gringeri, B. Basch, V. Shukla, R. Egorov, and T. J. Xia, "Flexible architectures for optical transport nodes and networks," *IEEE Communications Magazine*, vol. 48, no. 7, pp. 40–50, Jul. 2010.

[16] S. L. Woodward and M. D. Feuer, "Benefits and Requirements of Flexible-Grid ROADMs and Networks," *Journal of Optical Communications and Networking*, vol. 5, no. 10, pp. A19–A27, Oct. 2013.

[17] S. Gringeri, E. B. Basch, T. J. Xia, and V. Laboratories, "Technical Considerations for Supporting Data Rates Beyond 100 Gb/s," *IEEE Communications Magazine*, vol. 50, pp. 21–30, Feb. 2012.

[18] L. K. Oxenløwe, M. Galili, H. C. Hansen Mulvad, H. Hu, H. Ji, J. Xu, E. Palushani, J. L. Areal, A. T. Clausen, and P. Jeppesen, "Ultra-high-speed optical signal processing of Tbaud data signals," in *European Conference on Optical Communication (ECOC)*, Torino, Italy, Sep. 2010, p. Mo.1.A.1.

[19] K. Igarashi and K. Kikuchi, "Optical signal processing by phase modulation and subsequent spectral filtering aiming at applications to ultrafast optical communication systems," *Journal on Selected Topics in Quantum Electronics*, vol. 14, no. 3, pp. 551–565, May 2008.

[20] C. Langrock, S. Kumar, J. McGeehan, A. Willner, and M. Fejer, "All-optical signal processing using $\chi^{(2)}$ nonlinearities in guided-wave devices," *Journal of Lightwave Technology*, vol. 24, no. 7, pp. 2579–2592, Jul. 2006.

[21] L. Yan, A. Willner, X. Wu, A. Yi, A. Bogoni, Z.-Y. Chen, and H.-Y. Jiang, "All-optical signal processing for ultrahigh speed optical systems and networks," *Journal of Lightwave Technology*, vol. 30, no. 24, pp. 3760–3770, Dec. 2012.

[22] J. Wu, S. Rangan, and H. Zhang, *Green communications: theoretical fundamentals, algorithms and applications*. CRC Press, 2012.

[23] K. Hinton, G. Raskutti, P. M. Farrell, and R. S. Tucker, "Switching energy and device size limits on digital photonic signal processing technologies," *Journal on Selected Topics in Quantum Electronics*, vol. 14, no. 3, pp. 938–945, May 2008.

[24] A. Bogoni, X. Wu, S. R. Nuccio, J. Wang, Z. Bakhtiari, and A. E. Willner, "Photonic 640-Gb/s reconfigurable OTDM add-drop multiplexer based on pump depletion in a single PPLN waveguide," *Journal on Selected Topics in Quantum Electronics*, vol. 18, no. 2, pp. 709–716, Mar. 2012.

[25] R. Slavík, F. Parmigiani, J. Kakande, C. Lundström, M. Sjödin, P. A. Andrekson, R. Weerasuriya, S. Sygletos, A. D. Ellis, L. Grüner-Nielsen, D. Jakobsen, S. Herstrøm, R. Phelan, J. O'Gorman, A. Bogris, D. Syvridis, S. Dasgupta, P. Petropoulos, and D. J. Richardson, "All-optical phase and amplitude regenerator for next-generation telecommunications systems," *Nature Photonics*, vol. 4, no. Oct., pp. 690–695, 2010.

[26] K. Croussore and G. Li, "Phase and amplitude regeneration of differential phase-shift keyed signals using phase-sensitive amplification," *Journal of Selected Topics in Quantum Electronics*, vol. 14, no. 3, pp. 648–658, May 2008.

[27] P. Mamyshev, "All-optical data regeneration based on self-phase modulation effect," in *European Conference on Optical Communication (ECOC)*, Madrid, Spain, Sep. 1998, pp. 475–476.

[28] A. Bogoni, X. Wu, Z. Bakhtiari, S. Nuccio, and A. E. Willner, "640 Gbits/s photonic logic gates." *Optics Letters*, vol. 35, no. 23, pp. 3955–3957, Dec. 2010.

[29] M. Chou, K. Parameswaran, M. Fejer, and I. Brener, "Multiple-channel wavelength conversion by use of engineered quasi-phase-matching structures in $LiNbO_3$ waveguides," *Optics Letters*, vol. 24, no. 16, pp. 1157–1159, Aug. 1999.

[30] J. Wang, J. Sun, X. Zhang, D. Huang, and M. M. Fejer, "All-optical format conversions using periodically poled lithium niobate waveguides," *Journal of Quantum Electronics*, vol. 45, no. 2, pp. 195–205, 2009.

[31] M. F. Ferreira, *Nonlinear Effects in Optical Fibers*. John Wiley & Sons, 2011, vol. 2.

[32] L. Arizmendi, "Photonic applications of lithium niobate crystals," *Physica Status Solidi (A)*, vol. 201, no. 2, pp. 253–283, Jan 2004.

[33] I. Shoji, T. Kondo, A. Kitamoto, M. Shirane, and R. Ito, "Absolute scale of second-order nonlinear-optical coefficients," *Journal of the Optical Society of America B*, vol. 14, no. 9, p. 2268, Sep. 1997.

[34] H. Zang and J. P. Jue, "A review of routing and wavelength assignment approaches for wavelength-routed optical WDM networks," *Optical Networks Magazine*, vol. 1, pp. 47–60, Jan. 2000.

[35] S. J. B. Yoo, "Wavelength conversion technologies for wdm network applications," *Journal of Lightwave Technology*, vol. 14, no. 6, pp. 955–966, Jun. 1996.

[36] E. Ciaramella, "Wavelength conversion and all-optical regeneration: achievements and open issues," *Journal of Lightwave Technology*, vol. 30, no. 4, pp. 572–582, 2012.

[37] X. Wang, I. Kim, Q. Zhang, P. Palacharla, and T. Ikeuchi, "Efficient all-optical wavelength converter placement and wavelength assignment in optical networks," in *Optical Fiber Communication Conference (OFC*, Anaheim, USA, Mar. 2016, p. W2A.52.

[38] P. Petropoulos, K. R. Bottrill, S. Yoshima, Y. Sun, and D. J. Richardson, "Multi-channel all-optical signal processing based on parametric effects," in *Optical Fiber Communication Conference*, Anaheim, USA, Mar. 2016, pp. W4D–3.

[39] S. Olsson, C. Lundström, M. Karlsson, and P. A. Andrekson, "Long-haul (3465 km) transmission of a 10 GBd QPSK signal with low noise phase-sensitive in-line amplification," in *European Conference on Optical Communication (ECOC)*, Cannes, France, Sep. 2014, p. PD.2.2.

[40] J. Kakande, F. Parmigiani, R. Slavík, P. Petropoulos, and D. J. Richardson, "Phase sensitive amplifiers for regeneration of phase encoded optical signal formats," in *International Conference on Transparent Optical Networks (ICTON)*, Stockholm, Sweden, Jun. 2011, p. Tu.A.1.6.

[41] H. Taleb and K. Abedi, "Ultrafast all-optical signal processing using optically pumped QDSOA-based Mach-Zehnder interferometers," *Journal of Selected Topics in Quantum Electronics*, vol. 19, no. 5, pp. 1–8, Sep. 2013.

[42] K. Cvecek, K. Sponsel, C. Stephan, G. Onishchukov, R. Ludwig, C. Schubert, B. Schmauss, and G. Leuehs, "Phase-preserving 2R regeneration of a WDM RZ-DPSK signal using a nonlinear amplifying loop mirror," *Optics Express*, vol. 16, no. 3, pp. 1923–1928, Feb. 2008.

[43] L. M. Jones, F. Parmigiani, V. Rancano, M. Ettabib, P. Petropoulos, and D. J. Richardson, "Transmission performance of phase-preserving amplitude regenerator based on optical injection locking," in *Optical Fiber Communication Conference (OFC)*, Anaheim, USA, Mar. 2013, p. OW4C.4.

[44] M. Matsumoto, "Fiber-based all-optical signal regeneration," *Journal on Selected Topics in Quantum Electronics*, vol. 18, no. 2, pp. 738–752, Mar. 2012.

[45] J. P. Gordon and L. F. Mollenauer, "Phase noise in photonic communications systems using linear amplifiers," *Optics Letters*, vol. 15, no. 23, pp. 1351–1353, Dec. 1990.

[46] R. Slavík, A. Bogris, F. Parmigiani, J. Kakande, M. Westlund, M. Sk??ld, L. Gr??ner-Nielsen, R. Phelan, D. Syvridis, P. Petropoulos, and D. J. Richardson, "Coherent all-optical phase and amplitude regenerator of binary phase-encoded signals," *Journal on Selected Topics in Quantum Electronics*, vol. 18, no. 2, pp. 859–869, Mar. 2012.

[47] M. Matsumoto and H. Sakaguchi, "DPSK signal regeneration using a fiber-based amplitude regenerator," *Optics Express*, vol. 16, no. 15, pp. 11 169–11 175, Jul. 2008.

[48] B. J. Puttnam, D. Mazroa, S. Shinada, and N. Wada, "Phase-squeezing properties of non-degenerate PSAs using PPLN waveguides." *Optics Express*, vol. 19, no. 26, pp. B131–B139, Nov. 2011.

[49] C. Lundström, B. Corcoran, M. Karlsson, and P. A. Andrekson, "Phase and amplitude characteristics of a phase-sensitive amplifier operating in gain saturation," *Optics Express*, vol. 20, no. 19, pp. 21 400–21 412, Sep. 2012.

[50] T. Umeki, M. Asobe, H. Takara, Y. Miyamoto, and H. Takenouchi, "Multi-span transmission using phase and amplitude regeneration in PPLN-based PSA." *Optics Express*, vol. 21, no. 15, pp. 18 170–18 177, Jul. 2013.

[51] Z. Zheng, L. An, Z. Li, X. Zhao, and X. Liu, "All-optical regeneration of DQPSK/QPSK signals based on phase-sensitive amplification," *Optics Communications*, vol. 281, no. 10, pp. 2755–2759, May 2008.

[52] J. Kakande, R. Slavik, F. Parmigiani, A. Bogris, D. Syvridis, L. Grüner-Nielsen, R. Phelan, P. Petropoulos, and D. J. Richardson, "Multilevel quantization of optical phase in a novel coherent parametric mixer architecture," *Nature Photonics*, vol. 5, pp. 748–752, Oct. 2011.

[53] J. Kakande, A. Bogris, R. Slavík, and F. Parmigiani, "First demonstration of all-optical QPSK signal regeneration in a novel multi-format phase sensitive amplifier," in *European Conference and Exhibition on Optical Communication (ECOC)*, Torino, Italy, Sep. 2010, p. PDP3.3.

[54] J. Kakande, R. Slavik, F. Parmigiani, P. Petropoulos, and D. Richardson, "All-optical processing of multi-level phase shift keyed signals," in *Optical Fiber Communication Conference (OFC)*, Los Angeles, USA, Mar. 2012, p. OW1I.3.

[55] M. Asobe, T. Umeki, H. Takenouchi, and Y. Miyamoto, "In-line phase-sensitive amplification of QPSK signal using multiple quasi-phase matched $LiNbO_3$ waveguide," *Optics Express*, vol. 22, no. 22, pp. 26 642–26 650, Nov. 2014.

[56] A. A. C. Albuquerque, M. V. Drummond, and R. N. Nogueira, "Transfer matrix and fourier transform methods for simulation of second-order nonlinear interactions in a PPLN waveguide," *Journal of Lightwave Technology*, vol. 29, no. 24, pp. 3764–3771, Dec. 2011.

[57] J. K. Brenne and J. Skaar, "Design of grating-assisted codirectional couplers with discrete inverse-scattering algorithms," *Journal of Lightwave Technology*, vol. 21, no. 1, pp. 254–263, Jan. 2003.

[58] P. Poggiolini, G. Bosco, A. Carena, V. Curri, Y. Jiang, and F. Forghieri, "The GN-model of fiber non-linear propagation and its applications," *Journal of Lightwave Technology*, vol. 32, no. 4, pp. 694–721, Feb. 2014.

[59] A. Carena, G. Bosco, V. Curri, Y. Jiang, P. Poggiolini, and F. Forghieri, "EGN model of non-linear fiber propagation," *Optics Express*, vol. 22, no. 13, pp. 16 335–16 362, Jun. 2014.

[60] B. E. A. Saleh and M. C. Teich, *Fundamentals of Photonics*, 1st ed. John Wiley & Sons, 1991.

[61] E. Hecht, *Optics*, 4th ed. Pearson Education, Inc., 2002.

[62] J. Kerr, "A new relation between electricity and light: dielectrified media birefringent," *Philosophical Magazine Series 4*, vol. 50, no. 332, May 1875.

[63] N. Bloembergen, "Nonlinear optics: past, present, and future," *Journal of Selected Topics in Quantum Electronics*, vol. 6, no. 6, pp. 876–880, Jun. 2000.

[64] F. C. A. Pockels, *Lehrbuch der Kristalloptik*, 1st ed. Leipzig und Berlin, 1906.

[65] T. H. Maiman, "Stimulated optical radiation in ruby," *Nature*, vol. 187, no. 4736, pp. 493–494, Aug. 1960.

[66] P. A. Franken, A. E. Hill, C. W. Peters, and G. Weinreich, "Generation of optical harmonics," *Physical Review Letters*, vol. 7, no. 4, pp. 118–119, Aug. 1961.

[67] M. Bass, P. A. Franken, A. E. Hill, C. W. Peters, and G. Weinreich, "Optical mixing," *Physical Review Letters*, vol. 8, p. 18, Jan. 1962.

[68] K. E. Niebuhr, "Generation of laser axial mode difference frequencies in a nonlinear dielectric," *Applied Physics Letters*, vol. 2, no. 7, pp. 136–137, Apr. 1963.

[69] W. Kaiser and C. G. B. Garrett, "Two-photon excitation in CaF_2: Eu^{2+}," *Physical Review Letters*, vol. 7, pp. 229–231, Sep. 1961.

[70] E. Woodbury and W. Ng, "Ruby laser operation in the near IR," *Proceedings of the Institute of Radio Engineers*, vol. 50, no. 11, p. 2367, Nov. 1962.

[71] R. Y. Chiao, C. H. Townes, and B. P. Stoicheff, "Stimulated Brillouin scattering and coherent generation of intense hypersonic waves," *Physical Review Letters*, vol. 12, pp. 592–595, May 1964.

[72] P. D. Maker and R. W. Terhune, "Study of optical effects due to an induced polarization third order in the electric field strength," *Physycal Review*, vol. 137, pp. A801–A818, Feb. 1965.

[73] G. P. Agrawal, *Nonlinear Fiber Optics*, 4th, Ed. Academic Press, 2006.

[74] A. F. Pegoraro, A. Ridsdale, D. J. Moffatt, Y. Jia, J. P. Pezacki, and A. Stolow, "Optimally chirped multimodal CARS microscopy based on a single Ti: sapphire oscillator," *Optics Express*, vol. 17, no. 4, pp. 2984–2996, Feb. 2009.

[75] R. K. Khanna, D. D. Stranz, and B. Donn, "A spectroscopic study of intermediates in the condensation of refractory smokes: matrix isolation experiments of SiO," *Journal of Chemical Physics*, vol. 74, no. 4, pp. 2108–2115, Feb. 1981.

[76] S. Tanzilli, H. D. Riedmatten, H. Tittel, H. Zbinden, P. Baldi, M. D. Micheli, D. B. Ostrowsky, and N. Gisin, "Highly efficient photon-pair source using periodically poled lithium niobate waveguide," *Electronics Letters*, vol. 37, no. 1, pp. 26–28, Jan. 2001.

[77] D. Marcuse, *Theory of Dielectric Optical Waveguides*. Academic Press, 1991.

[78] R. D. Guenther, *Modern Optics*. John Wiley & Sons, 1990.

[79] J. E. Geusic, H. J. Levinstein, S. Singh, R. G. Smith, and L. G. Van Uitert, "Continuous 0.532-μ solid-state source using $Ba_2NaNb_5O_{15}$," *Applied Physics Letters*, vol. 12, no. 9, p. 306, Mar. 1968.

[80] L. Goldberg, M. K. Chun, I. N. Duling, and T. F. Carruthers, "Blue light generation by nonlinear mixing of Nd:YAG and GaAlAs laser emission in a $KNbO_3$ resonant cavity," *Applied Physics Letters*, vol. 56, no. 21, p. 2071, Mar. 1990.

[81] J. Warner, "Photomultiplier detection of 10.6 μm radiation using optical up-conversion in proustite," *Applied Physics Letters*, vol. 12, no. 6, p. 222, Jan. 1968.

[82] D. Bodlaki, E. Freysz, and E. Borguet, "Infrared second harmonic generation spectroscopy of Ge(111) interfaces," *The Journal of Chemical Physics*, vol. 119, no. 7, p. 3958, Jul. 2003.

[83] L. Schneider and W. Peukert, "Second harmonic generation spectroscopy as a method for in situ and online characterization of particle surface properties," *Particle & Particle Systems Characterization*, vol. 23, no. 5, pp. 351–359, Feb. 2007.

[84] X. Chen, O. Nadiarynkh, S. Plotnikov, and P. J. Campagnola, "Second harmonic generation microscopy for quantitative analysis of collagen fibrillar structure." *Nature Protocols*, vol. 7, no. 4, pp. 654–69, Mar. 2012.

[85] H. Miao, S.-D. Yang, C. Langrock, R. V. Roussev, M. M. Fejer, and A. M. Weiner, "Ultralow-power second-harmonic generation frequency-resolved optical gating using aperiodically poled lithium niobate waveguides," *Journal of the Optical Society of America B*, vol. 25, no. 6, pp. A41–A53, Jun. 2008.

[86] G. K. Kitaeva and A. N. Penin, "Spontaneous parametric down-conversion," *Journal of Experimental and Theoretical Physics Letters*, vol. 82, no. 6, pp. 350–355, Sep. 2005.

[87] R. W. Boyd, *Nonlinear Optics*, 3rd ed. Academic Press, 2008.

[88] K. C. Burr, C. L. Tang, M. A. Arbore, and M. M. Fejer, "Broadly tunable mid-infrared femtosecond optical parametric oscillator using all-solid-state-pumped periodically poled lithium niobate," *Optics Letters*, vol. 22, no. 19, p. 1458, Oct. 1997.

[89] P. D. Maker, R. W. Terhune, M. Nisenoff, and C. M. Savage, "Effects of dispersion and focusing on the production of optical harmonics," *Physical Review Letters*, vol. 8, no. 1, pp. 21–22, Jan. 1962.

[90] J. Armstrong, N. Bloembergen, J. Ducuing, and P. Pershan, "Interactions between light waves in a nonlinear dielectric," *Physical Review*, vol. 127, no. 6, pp. 1918–1939, Sep. 1962.

[91] M. Fejer, G. Magel, D. Jundt, and R. Byer, "Quasi-phase-matched second harmonic generation: tuning and tolerances," *Journal of Quantum Electronics*, vol. 28, no. 11, pp. 2631–2654, Nov. 1992.

[92] K. Gallo, G. Assanto, and G. Stegeman, "Efficient wavelength shifting over the erbium amplifier bandwidth via cascaded second order processes in lithium niobate waveguides," *Applied Physics Letters*, vol. 71, no. 8, pp. 1020–1022, Aug. 1997.

[93] M.-H. Chou, "Optical frequency mixers using three-wave mixing for optical fiber communications," Ph.D. dissertation, Stanford University, 1999.

[94] C. Kittel, *Introduction to Solid State Physics*. Wiley, 2005.

[95] P. P. Banerjee, *Nonlinear Optics: Theory, Numerical Modeling, and Applications*. CRC Press, 2003.

[96] K. Shiraki, M. Ohashi, and M. Tateda, "SBS threshold of a fiber with a Brillouin frequency shift distribution," *Journal of Lightwave Technology*, vol. 14, no. 1, Jan. 1996.

[97] K. Shiraki, M. Ohashi, and M. Tateda, "Suppression of stimulated Brillouin scattering in a fibre by changing the core radius," *Electronics Letters*, vol. 31, no. 8, pp. 668–669, Apr. 1995.

[98] J. Hansryd, F. Dross, M. Westlund, P. Andrekson, and S. Knudsen, "Increase of the SBS threshold in a short highly nonlinear fiber by applying a temperature distribution," *Journal of Lightwave Technology*, vol. 19, no. 11, pp. 1691–1697, Nov. 2001.

[99] K. Byron, M. Bedgood, A. Finey, C. McGauran, S. Savory, and I. Watson, "Shifts in zero dispersion wavelength due to pressure, temperature and strain in dispersion shifted singlemode fibres," *Electronics Letters*, vol. 28, no. 18, pp. 1712–1714, Aug. 1992.

[100] J. Hansryd and P. Andrekson, "Broadband CW pumped fiber optical parametric amplifier with 49 dB gain and wavelength conversion efficiency," in *Optical Fiber Communication Conference (OFC)*, vol. 4, Baltimore, USA, Mar. 2000, pp. 175–177.

[101] Z. Tong, A. Bogris, M. Karlsson, and P. a. Andrekson, "Raman-induced asymmetric pump noise transfer in fiber-optical parametric amplifiers," *Photonics Technology Letters*, vol. 22, no. 6, pp. 386–388, Mar. 2010.

[102] J. D. Hoffman and S. Frankel, *Numerical methods for engineers and scientists*. CRC Press, 2001.

[103] W. H. Press, S. A. Teukolsky, W. T. Vetterling, and B. P. Flannery, *Numerical Recipes in C, The Art of Scientific Computing*, 2nd ed. Cambridge University Press, 1992.

[104] P. François, "Nonlinear propagation of ultrashort pulses in optical fibers: total field formulation in the frequency domain," *Journal of the Optical Society of America B*, vol. 8, no. 2, pp. 276–293, Feb. 1991.

[105] M. Hayee and A. Willner, "NRZ versus RZ in 10-40-Gb/s dispersion-managed WDM transmission systems," *Photonics Technology Letters*, vol. 11, no. 8, pp. 991–993, Aug. 1999.

[106] D. Marcuse, C. R. Menyuk, and P. K. A. Wai, "Application of the Manakov-PMD equation to studies of signal propagation in optical fibers with randomly varying birefringence," *Journal of Lightwave Technology*, vol. 15, no. 9, pp. 1735–1745, Sep. 1997.

[107] P. Poggiolini, G. Bosco, A. Carena, V. Curri, Y. Jiang, and F. Forghieri, "A detailed analytical derivation of the GN model of non-linear interference in coherent optical transmission systems," *ArXiv:1209.0294, [physics.optics]*, Sep. 2012.

[108] N. Sugimoto, T. Nagashima, T. Hasegawa, and S. Ohara, "Bismuth-based optical fiber with nonlinear coefficient of 1360 W^{-1} km^{-1}," in *Optical Fiber Communication Conference (OFC)*, vol. 2, Los Angeles, USA, Feb. 2004, p. PDP26.

[109] M. D. Pelusi, V. G. Ta'eed, L. Fu, E. Mägi, M. R. Lamont, S. Madden, D.-Y. Choi, D. A. Bulla, B. Luther-Davies, and B. J. Eggleton, "Applications of highly-nonlinear chalcogenide glass devices tailored for high-speed all-optical signal processing," *Journal of Selected Topics in Quantum Electronics*, vol. 14, no. 3, pp. 529–539, May 2008.

[110] E. C. Mägi, L. B. Fu, H. C. Nguyen, M. R. E. Lamont, D. I. Yeom, and B. J. Eggleton, "Enhanced Kerr nonlinearity in sub-wavelength diameter As_2Se_3 chalcogenide fiber tapers," *Optics Express*, vol. 15, no. 16, pp. 10 324–10 329, Aug 2007.

[111] X. Gai, D.-Y. Choi, S. Madden, D. Bulla, and B. Luther-Davies, "$Ge_{11.5}As_{24}Se_{64.5}$ chalcogenide glass nanowires with a nonlinear parameter of 136,000W^{-1} km^{-1} at 1550nm," in *Australian Conference on Optical Fibre Technology (ACOFT)*, Melbourne, Australia, Dec. 2010, pp. 1–3.

[112] B. J. Eggleton, B. Luther-Davies, and K. Richardson, "Chalcogenide photonics," *Nature Photonics*, vol. 5, no. 3, pp. 141–148, Feb. 2011.

[113] S. Watanabe, "Optical signal processing using nonlinear fibers," *Journal of Optical and Fiber Communications Reports*, vol. 3, no. 1, pp. 1–24, Feb. 2006.

[114] A. Zakery and S. Elliott, "Optical properties and applications of chalcogenide glasses: a review," *Journal of Non-Crystalline Solids*, vol. 330, no. 1, pp. 1–12, May 2003.

[115] C. Koos, P. Vorreau, T. Vallaitis, P. Dumon, W. Bogaerts, R. Baets, B. Esembeson, I. Biaggio, T. Michinobu, F. Diederich *et al.*, "All-optical high-speed signal processing with silicon–organic hybrid slot waveguides," *Nature Photonics*, vol. 3, no. 4, pp. 216–219, Mar. 2009.

[116] J. Mørk, M. L. Nielsen, and T. W. Berg, "The dynamics of semiconductor optical amplifiers: modeling and applications," *Optics & Photonics News*, vol. 14, no. 7, pp. 42–48, Jul. 2003.

[117] M. Spyropoulou, N. Pleros, and A. Miliou, "SOA-MZI-based nonlinear optical signal processing: A frequency domain transfer function for wavelength conversion, clock recovery, and packet envelope detection," *Journal of Quantum Electronics*, vol. 47, no. 1, pp. 40–49, Jan. 2011.

[118] I. Kang, C. Dorrer, L. Zhang, M. Dinu, M. Rasras, L. Buhl, S. Cabot, A. Bhardwaj, X. Liu, M. Cappuzzo, L. Gomez, A. Wong-Foy, Y. Chen, N. Dutta, S. Patel, D. Neilson, C. Giles, A. Piccirilli, and J. Jaques, "Characterization of the dynamical processes in all-optical signal processing using semiconductor optical amplifiers," *Journal of Selected Topics in Quantum Electronics*, vol. 14, no. 3, pp. 758–769, May 2008.

[119] A. Mecozzi and J. M. Wiesenfeld, "The roles of semiconductor optical amplifiers in optical networks," *Optics and Photonics News*, vol. 12, no. 3, pp. 36–42, Mar. 2001.

[120] B. J. Eggleton, T. D. Vo, R. Pant, J. Schr, M. D. Pelusi, D. Yong Choi, S. J. Madden, and B. Luther-Davies, "Photonic chip based ultrafast optical processing based on high nonlinearity dispersion engineered chalcogenide waveguides," *Laser & Photonics Reviews*, vol. 6, no. 1, pp. 97–114, Jan. 2012.

[121] J. M. Dudley and J. R. Taylor, “Ten years of nonlinear optics in photonic crystal fibre,” *Nature Photonics*, vol. 3, no. 2, pp. 85–90, Jan. 2009.

[122] R. S. Weis and T. K. Gaylord, “Lithium niobate: summary of physical properties and crystal structure,” *Applied Physics A: Materials Science & Processing*, vol. 37, no. 4, pp. 191–203, Aug. 1985.

[123] T. Volk and M. Wöhlecke, *Lithium Niobate: Defects, Photorefraction and Ferroelectric Switching*. Springer, 2008.

[124] T. Umeki, M. Asobe, Y. Nishida, O. Tadanaga, K. Magari, T. Yanagawa, and H. Suzuki, “Highly efficient +5-dB parametric gain conversion using direct-bonded PPZnLN ridge waveguide,” *Photonics Technology Letters*, vol. 20, no. 1, pp. 15–17, Jan. 2008.

[125] T. Umeki, O. Tadanaga, and M. Asobe, “Highly efficient wavelength converter using direct-bonded PPZnLN ridge waveguide,” *Journal of Quantum Electronics*, vol. 46, no. 8, pp. 1206–1213, Aug. 2010.

[126] Y. Furukawa, K. Kitamura, A. Alexandrovski, R. K. Route, M. M. Fejer, and G. Foulon, “Green-induced infrared absorption in MgO doped LiNbO3,” *Applied Physics Letters*, vol. 78, no. 14, pp. 1970–1972, Apr. 2001.

[127] M. Asobe, H. Miyazawa, O. Tadanaga, Y. Nishida, and H. Suzuki, “A highly damage-resistant Zn:LiNbO3 ridge waveguide and its application to a polarization-independent wavelength converter,” *Journal of Quantum Electronics*, vol. 39, no. 10, pp. 1327–1333, Oct. 2003.

[128] T. Umeki, T. Kazama, O. Tadanaga, K. Enbutsu, M. Asobe, Y. Miyamoto, and H. Takenouchi, “PDM signal amplification using PPLN-based polarization-independent phase-sensitive amplifier,” *Journal of Lightwave Technology*, vol. 33, no. 7, pp. 1326–1332, Apr. 2015.

[129] B. P. P. Kuo and S. Radic, “Highly nonlinear fiber with dispersive characteristic invariant to fabrication fluctuations,” *Optics Express*, vol. 20, no. 7, pp. 7716–7725, Mar. 2012.

[130] S. Radic, “Parametric amplification and processing in optical fibers,” *Laser & Photonics Review*, vol. 2, no. 6, pp. 498–513, Dec. 2008.

[131] J. Huang, X. P. Xie, C. Langrock, R. V. Roussev, D. S. Hum, and M. M. Fejer, “Amplitude modulation and apodizatiion of quasi-phase-matched interactions,” *Optics Letters*, vol. 31, no. 5, pp. 604–606, Mar. 2006.

[132] G. Lu, S. Shinada, and H. Furukawa, “160-Gb/s all-optical phase-transparent wavelength conversion through cascaded SFG-DFG in a broadband linear-chirped PPLN waveguide,” *Optics Express*, vol. 18, no. 6, pp. 6064–6070, Mar. 2010.

[133] M. Asobe and O. Tadanaga, “Multiple quasi-phase-matched device using continuous phase modulation of $\chi^{(2)}$ grating and its application to variable wavelength conversion,” *Journal of Quantum Electronics*, vol. 41, no. 12, pp. 1540–1547, Dec. 2005.

[134] C. R. Phillips, L. Gallmann, and M. M. Fejer, “Design of quasi-phasematching gratings via convex optimization,” *Optics Express*, vol. 21, no. 8, p. 10139, Apr. 2013.

[135] T. Erdogan, “Fiber grating spectra,” *Journal of Lightwave Technology*, vol. 15, no. 8, pp. 1277–1294, Aug. 1997.

[136] F. J. Harris, “On the use of windows for harmonic analysis with the discrete Fourier transform,” *Proceedings of the IEEE*, vol. 66, no. 1, pp. 51–83, Jan. 1978.

[137] L. Erickson, D. Johnson, J. Albert, B. Malo, K. Hill, F. Bilodeau, and S. Thériault, “Apodisation of the spectral response of fibre Bragg gratings using a phase mask with variable diffraction efficiency,” *Electronics Letters*, vol. 31, no. 3, pp. 222–223, Feb. 1995.

[138] J. Skaar, L. Wang, and T. Erdogan, “On the synthesis of fiber Bragg gratings by layer peeling,” *Journal of Quantum Electronics*, vol. 37, no. 2, pp. 165–173, Feb. 2001.

[139] Q. W. Zhang, X. L. Zeng, M. Wang, T. Y. Wang, and X. F. Chen, “Retrieving quasi-phase-matching structure with discrete layer-peeling method.” *Optics Express*, vol. 20, no. 14, pp. 15 826–32, Jul. 2012.

[140] R. Feced and M. N. Zervas, “Efficient inverse scattering algorithm for the design of grating-assisted codirectional mode couplers,” *Journal of the Optical Society of America A*, vol. 17, no. 9, p. 1573, Sep. 2000.

[141] J. Proakis and D. Manolakis, *Digital Signal Processing: Principles, Algorithms and Applications*, 3rd ed. Pearson Prentice Hall, 2007.

[142] A. Oppenheim, R. Schafer, and J. Buck, *Discrete-time Signal Processing*, 2nd ed. Prentice Hall, 1999.

[143] O. Gayer, Z. Sacks, E. Galun, and A. Arie, “Temperature and wavelength dependent refractive index equations for MgO-doped congruent and stoichiometric $LiNbO_3$,” *Applied Physics B*, vol. 91, no. 2, pp. 343–348, May 2008.

[144] A. Tehranchi and R. Kashyap, “Engineered gratings for flat broadening of second-harmonic phase-matching bandwidth in MgO-doped lithium niobate waveguides.” *Optics Express*, vol. 16, no. 23, pp. 18 970–18 975, Nov. 2008.

[145] Oxide Corporation. (2016) Oxide corporation home page. [Online]. Available: http://www.opt-oxide.com/en

[146] S. Gao, E.-K. Tien, Q. Song, Y. Huang, and O. Boyraz, “Ultra-broadband one-to-two wavelength conversion using low-phase-mismatching four-wave mixing in silicon waveguides.” *Optics Express*, vol. 18, no. 11, pp. 11 898–903, May 2010.

[147] B. Filion, W. C. Ng, A. T. Nguyen, L. a. Rusch, and S. Larochelle, “Wideband wavelength conversion of 16 Gbaud 16-QAM and 5 Gbaud 64-QAM signals in a semiconductor optical amplifier.” *Optics Express*, vol. 21, no. 17, pp. 19 825–19 833, Aug. 2013.

[148] P. Runge, C.-a. Bunge, and K. Petermann, “All-optical wavelength conversion with extinction ratio improvement of 100 Gb/s RZ-signals in ultralong bulk semiconductor optical amplifiers,” *Journal of Quantum Electronics*, vol. 46, no. 6, pp. 937–944, Jun. 2010.

[149] J. Yamawaku, H. Takara, T. Ohara, A. Takada, T. Morioka, O. Tadanaga, H. Miyazawa, and M. Asobe, “Low-crosstalk 103 channel $\times$ 10 Gb/s (1.03 Tb/s) wavelength conversion with a quasi-phase-matched $LiNbO_3$ waveguide,” *Journal of Selected Topics in Quantum Electronics*, vol. 12, no. 4, pp. 521–528, Jul. 2006.

[150] H. Hu, E. Palushani, M. Galili, H. C. H. Mulvad, A. Clausen, L. K. Oxenløwe, and P. Jeppesen, “640 Gbit/s and 1.28 Tbit/s polarisation insensitive all optical wavelength conversion.” *Optics Express*, vol. 18, no. 10, pp. 9961–6, May 2010.

[151] X. Yi, R. Yu, J. Kurumida, and S. Yoo, "A theoretical and experimental study on modulation-format-independent wavelength conversion," *Journal of Lightwave Technology*, vol. 28, no. 4, pp. 587–595, Feb. 2010.

[152] J. Wang, J. Sun, X. Zhang, D. Huang, and M. Fejer, "Ultrafast all-optical three-input Boolean XOR operation for differential phase-shift keying signals using periodically poled lithium niobate," *Optics Letters*, vol. 33, no. 13, pp. 1419–1421, Jul. 2008.

[153] M. H. Chou, I. Brener, G. Lenz, R. Scotti, E. E. Chaban, J. Shmulovich, D. Philen, S. Kosinski, K. R. Parameswaran, and M. M. Fejer, "Efficient wide-band and tunable midspan spectral inverter using cascaded nonlinearities in $LiNbO_3$ waveguides," *Photonics Technology Letters*, vol. 12, no. 1, pp. 82–84, Jan. 2000.

[154] G. Contestabile, Y. Yoshida, a. Maruta, and K. Kitayama, "Ultra-broad band, low power, highly efficient coherent wavelength conversion in quantum dot SOA." *Optics express*, vol. 20, no. 25, pp. 27 902–7, Dec. 2012.

[155] J. Sun, W. Liu, J. Tian, J. R. Kurz, and M. M. Fejer, "Multichannel wavelength conversion exploiting cascaded second-order nonlinearity in $LiNbO_3$ waveguides," *Photonics Technology Letters*, vol. 15, no. 12, pp. 1743–1745, Dec. 2003.

[156] G. Contestabile and Y. Yoshida, "Coherent wavelength conversion in a quantum dot SOA," *Photonics Technology Letters*, vol. 25, no. 9, pp. 791–794, May 2013.

[157] H. Rong, Y.-H. Kuo, A. Liu, M. Paniccia, and O. Cohen, "High efficiency wavelength conversion of 10 Gb/s data in silicon waveguides," *Optics Express*, vol. 14, no. 3, pp. 1182–1188, Feb. 2006.

[158] P. Andersen, T. Tokle, Y. Geng, C. Peucheret, P. Jeppesen *et al.*, "Wavelength conversion of a 40-Gb/s RZ-DPSK signal using four-wave mixing in a dispersion-flattened highly nonlinear photonic crystal fiber," *Photonics Technology Letters*, vol. 17, no. 9, pp. 1908–1910, Sep. 2005.

[159] T. Richter, R. Elschner, A. Gandhe, K. Petermann, and C. Schubert, "Parametric amplification and wavelength conversion of single- and dual-polarization DQPSK signals," *Journal of Selected Topics in Quantum Electronics*, vol. 18, no. 2, pp. 988–995, Mar. 2012.

[160] H. Hu, R. Nouroozi, and R. Ludwig, "Simultaneous polarization-insensitive wavelength conversion of 80-Gb/s RZ-DQPSK signal and 40-Gb/s RZ-OOK signal in a Ti: PPLN waveguide," *Journal of Lightwave Technology*, vol. 29, no. 8, pp. 1092–1097, Apr. 2011.

[161] K. Inoue, "Polarization independent wavelength conversion using fiber four-wave mixing with two orthogonal pump lights of different frequencies," *Journal of Lightwave Technology*, vol. 12, no. 11, pp. 1916–1920, Nov. 1994.

[162] S. T. Naimi, S. P. . Duill, and L. P. Barry, "All optical wavelength conversion of Nyquist-WDM superchannels using FWM in SOAs," *Journal of Lightwave Technology*, vol. 33, no. 19, pp. 3959–3967, Oct. 2015.

[163] M. Matsuura, N. Calabretta, O. Raz, and H. J. S. Dorren, "Multichannel wavelength conversion of 50-Gbit/s NRZ-DQPSK signals using a quantum-dot semiconductor optical amplifier," *Optic Express*, vol. 19, no. 26, pp. B560–B566, Dec. 2011.

[164] T. Richter, R. Nouroozi, H. Suche, W. Sohler, and C. Schubert, "PPLN-waveguide based tunable wavelength conversion of QAM data within the C-band," *Photonics Technology Letters*, vol. 25, no. 21, pp. 2085–2088, 2013.

[165] H. Hu, R. Nouroozi, W. Wang, J. Yu, H. Suche, and W. Sohler, "Tunable all-optical wavelength conversion based on cascaded SHG/DFG in a Ti:PPLN waveguide using a single CW control laser," *Photonics Journal*, vol. 4, no. 5, pp. 1396–1400, Oct. 2012.

[166] H. Furukawa, A. Nirmalathas, S. Member, N. Wada, S. Shinada, H. Tsuboya, and T. Miyazaki, "Tunable all-optical wavelength conversion of 160-Gb/s RZ optical signals by cascaded SFG-DFG generation in PPLN waveguide," *Photonics Technology Letters*, vol. 19, no. 6, pp. 384–386, Mar. 2007.

[167] H. Song, O. Tadanaga, T. Umeki, I. Tomita, M. Asobe, S. Yamamoto, K. Mori, and K. Yonenaga, "Phase-transparent flexible waveband conversion of 43 Gb / s RZ-DQPSK signals using multiple-QPM-LN waveguides," *Optics Express*, vol. 18, no. 15, pp. 15 332–15 337, Jul. 2010.

[168] Y. Lee, B. Yu, C. Jung, Y. Noh, J. Lee, and D. Ko, "All-optical wavelength conversion and tuning by the cascaded sum-and difference frequency generation (cSFG/DFG) in a temperature gradient controlled Ti: PPLN," *Optics Express*, vol. 13, no. 8, pp. 2988–2993, Apr. 2005.

[169] A. Anthur, R. Watts, and K. Shi, "Dual correlated pumping scheme for phase noise preservation in all-optical wavelength conversion," *Optics Express*, vol. 21, no. 13, pp. 469–476, Jul. 2013.

[170] T. Kawanishi, T. Sakamoto, M. Tsuchiya, M. Izutsu, S. Mori, and K. Higuma, "70 dB extinction-ratio $LiNbO_3$ optical intensity modulator for two-tone lightwave generation," in *Optical Fiber Communication Conference (OFC)*, Anaheim, USA, Mar. 2006, p. OWC4.

[171] S. Savory, "Digital coherent optical receivers: algorithms and subsystems," *Journal of Selected Topics in Quantum Electronics*, vol. 16, no. 5, pp. 1164–1179, Sep. 2010.

[172] G.-W. Lu, T. Sakamoto, and T. Kawanishi, "Coherently-pumped FWM in HNLF for 16QAM wavelength conversion free of phase noise from pumps," in *European Conference on Optical Communication (ECOC)*, Cannes, France, Sep. 2014, p. P.2.18.

[173] J. Wang, Z. Bakhtiari, S. R. Nuccio, O. F. Yilmaz, X. Wu, and A. E. Willner, "Phase-transparent optical data exchange of 40 Gbit/s differential phase-shift keying signals." *Optics Letters*, vol. 35, no. 17, pp. 2979–81, Sep. 2010.

[174] J. Wang, S. R. Nuccio, H. Huang, X. Wang, J.-Y. Yang, and A. E. Willner, "Optical data exchange of 100-Gbit/s DQPSK signals." *Optics Express*, vol. 18, no. 23, pp. 23 740–5, Nov. 2010.

[175] J. Wang and A. E. Willner, "Review of robust data exchange using optical nonlinearities," *International Journal of Optics*, vol. 2012, pp. 1–25, Nov. 2012.

[176] K. K. Y. Wong, M. E. Marhic, K. Uesaka, and L. G. Kazovsky, "Wavelength exchange: a novel function for optical networks," *Information Sciences*, vol. 149, pp. 161–169, Jan. 2003.

[177] H. Hamza and J. Deogun, "Wavelength-exchanging cross connects (WEX)-a new class of photonic cross-connect architectures," *Journal of Lightwave Technology*, vol. 24, no. 3, pp. 1101–1111, Mar. 2006.

[178] K. Croussore, I. Kim, Y. Han, C. Kim, G. Li, and S. Radic, "Demonstration of phase-regeneration of DPSK signals based on phase-sensitive amplification," *Optics Express*, vol. 13, no. 11, pp. 3945–3950, May 2005.

[179] C. M. Caves, "Quantum limits on noise in linear amplifiers," *Physical Review D*, vol. 26, no. 8, Oct. 1982.

[180] B. M. Oliver, "Signal-to-noise ratio in photoelectric mixing," *Proceedings of the Institute of Radio Engineers*, vol. 49, no. 12, pp. 1960–1961, Dec. 1961.

[181] H. Haus and T. C. H., "Comments on noise in photoelectric mixing," *Proceedings of the Institute of Radio Engineers*, vol. 50, no. 6, pp. 1544–1545, Jun. 1962.

[182] H. Takahasi, *Information Theory of Quantum-Mechanical Channels*. Academic Press, 1965, vol. 1, pp. 227–310.

[183] M. Vasilyev, "Phase-sensitive amplification in optical fiber," in *IEEE/LEOS Winter Topical Meeting Series*, Sorrento, Italy, Jan. 2008, p. MB1.1.

[184] K. Croussore, C. Kim, and G. Li, "All-optical regeneration of differential phase-shift keying signals based on phase-sensitive amplification," *Optics Letters*, vol. 29, no. 20, pp. 2357–2359, Oct. 2004.

[185] R. Tang, J. Lasri, P. S. Devgan, V. Grigoryan, P. Kumar, and M. Vasilyev, "Gain characteristics of a frequency nondegenerate phase-sensitive fiber-optic parametric amplifier with phase self-stabilized input," *Optics Express*, vol. 13, no. 26, pp. 281–285, Dec. 2005.

[186] Z. Tong, C. Lundström, P. A. Andrekson, C. J. McKinstrie, M. Karlsson, D. J. Blessing, E. Tipsuwannakul, B. J. Puttnam, H. Toda, and L. Grüner-Nielsen, "Towards ultrasensitive optical links enabled by low-noise phase-sensitive amplifiers," *Nature Photonics*, vol. 5, no. Jul., pp. 430–436, 2011.

[187] T. Okuno, M. Onishi, T. Kashiwada, S. Ishikawa, and M. Nishimura, "Silica-based functional fibers with enhanced nonlinearity and their applications," *Journal of Selected Topics in Quantum Electronics*, vol. 5, no. 5, pp. 1385–1391, Sep. 1999.

[188] J. A. Levenson, P. Grangier, I. Abram, and T. Rivera, "Reduction of quantum noise in optical parametric amplification," *Journal of the Optical Society of America B*, vol. 10, no. 11, pp. 2233–2238, Nov. 1993.

[189] A. Takada and W. Imajuku, "In-line optical phase-sensitive amplifier employing pump laser injection-locked to input signal light," *Electronics Letters*, vol. 34, pp. 274–276, Feb. 1998.

[190] W. Imajuku and A. Takada, "In-line optical phase-sensitive amplifier with pump light source controlled by optical phase-lock loop," *Journal of Lightwave Technology*, vol. 17, no. 4, pp. 637–646, Apr. 1999.

[191] M. E. Marhic, C. H. Hsia, and J.-M. Jeong, "Optical amplification in a nonlinear fibre interferometer," *Electronics Letters*, vol. 27, pp. 210–211, Jan. 1991.

[192] D. Levandovsky, M. Vasilyev, and P. Kumar, "Amplitude squeezing of light by means of a phase-sensitive fiber parametric amplifier," *Optics Letters*, vol. 24, no. 14, pp. 984–986, Jul. 1999.

[193] T. Umeki, O. Tadanaga, M. Asobe, Y. Miyamoto, and H. Takenouchi, "First demonstration of high-order QAM signal amplification in PPLN-based phase sensitive amplifier." *Optics Express*, vol. 22, no. 3, pp. 2473–2482, Feb. 2014.

[194] A. D. Ellis and S. Sygletos, "Phase sensitive signal processing using semiconductor optical amplifiers," in *Optical Fiber Communication Conference (OFC)*, Anaheim, USA, Mar. 2013, p. OW4C.1.

[195] F. D. Ros, D. Vukovic, A. Gajda, K. Dalgaard, L. Zimmermann, B. Tillack, M. Galili, K. Petermann, and C. Peucheret, "Phase regeneration of DPSK signals in a silicon waveguide with reverse-biased p-i-n junction," *Optics Express*, vol. 22, no. 5, pp. 7926–7933, Mar. 2014.

[196] Y. Zhang, J. Schröder, C. Husko, S. Lefrancois, D.-Y. Choi, S. Madden, B. Luther-Davies, and B. J. Eggleton, "Pump-degenerate phase-sensitive amplification in chalcogenide waveguides," *Journal of the Optical Society of America B*, vol. 31, no. 4, pp. 780–787, Apr. 2014.

[197] M. A. Ettabib, F. Parmigiani, A. Kapsalis, A. Bogris, M. Brun, P. Labeye, S. Nicoletti, and K. Hammani, "Record phase sensitive extinction ratio in a silicon germanium waveguide," in *Conference on Lasers and Electro-Optics (CLEO)*, San Jose, USA, May 2015, p. STh1O.8.

[198] R. Neo, J. Schröder, Y. Paquot, D.-y. Choi, S. Madden, B. Luther-Davies, and B. J. Eggleton, "Phase-sensitive amplification of light in a $\chi(3)$ photonic chip using a dispersion engineered chalcogenide ridge waveguide." *Optics Express*, vol. 21, no. 7, pp. 7926–33, Apr. 2013.

[199] Z. Tong, C. Lundström, E. Tipsuwannakul, M. Karlsson, and P. A. Andrekson, "Phase-sensitive amplified DWDM DQPSK signals using free-running lasers with 6-dB link SNR improvement over EDFA-based systems," in *European Conference on Optical Communication (ECOC)*, Torino, Italy, Sep. 2010, p. PDP1.3.

[200] P. A. Andrekson, C. Lundström, and Z. Tong, "Phase-sensitive fiber-optic parametric amplifiers and their applications," in *European Conference and Exhibition on Optical Communication (ECOC)*, Torino, Italy, Sep. 2010, p. We.6.E.1.

[201] H. Sun, K. Y. Wang, and A. C. Foster, "Pump-degenerate phase-sensitive amplification in amorphous Si waveguides," in *Conference on Lasers and Electro-Optics (CLEO)*, San Jose, USA, May 2015, p. FW1D.3.

[202] C. Lundström, S. L. I. Olsson, B. Corcoran, M. Karlsson, and P. A. Andrekson, "Phase-sensitive amplifiers for optical links," in *Optical Fiber Communication Conference (OFC)*, Anaheim, USA, Mar. 2013, p. OW3C.5.

[203] B. Puttnam and Á. Szabó, "Multi-channel phase squeezing in a PPLN-PPLN PSA," in *Optical Fiber Communication Conference (OFC)*, Los Angeles, USA, Mar. 2012, p. OW3C.6.

[204] K. J. Lee, F. Parmigiani, S. Liu, J. Kakande, P. Petropoulos, K. Gallo, and D. Richardson, "Phase sensitive amplification based on quadratic cascading in a periodically poled lithium niobate waveguide." *Optics Express*, vol. 17, no. 22, pp. 20 393–20 400, Oct. 2009.

[205] T. Umeki, O. Tadanaga, A. Takada, and M. Asobe, "Phase sensitive degenerate parametric amplification using directly-bonded PPLN ridge waveguides." *Optics Express*, vol. 19, no. 7, pp. 6326–6332, Mar. 2011.

[206] S. Sygletos, M. J. Power, F. C. Garcia Gunning, R. P. Webb, R. J. Manning, and A. Ellis, "Simultaneous dual channel phase regeneration in SOAs," in *European Conference and Exhibition on Optical Communication (ECOC)*, Amsterdam, Netherlands, Sep. 2012, p. Tu.1.A.2.

[207] S. L. Olsson, T. a. Eriksson, C. Lundström, M. Karlsson, and P. A. Andrekson, "Linear and nonlinear transmission of 16-QAM over 105 km phase-sensitive amplified link," in *Optical Fiber Communication Conference (OFC)*, San Francisco, USA, Mar. 2014, p. Th1H.3.

[208] S. L. I. Olsson, B. Corcoran, C. Lundström, E. Tipsuwannakul, S. Sygletos, A. D. Ellis, Z. Tong, M. Karlsson, and P. A. Andrekson, "Optical injection-locking-based pump recovery for phase-sensitively amplified links," in *Optical Fiber Communication Conference (OFC)*, Los Angeles, USA, Mar. 2012, p. OW3C.3.

[209] Z. Tong, A. O. J. Wiberg, E. Myslivets, B. P. P. Kuo, N. Alic, and S. Radic, "Broadband parametric multicasting via four-mode phase-sensitive interaction." *Optics Express*, vol. 20, no. 17, pp. 19 363–19 373, Aug. 2012.

[210] S. Anzai, M. Mieno, Y. Komai, N. Wada, T. Yoda, T. Miyazaki, and K. Kodate, "Amplitude, phase, and bandwidth tunable high-resolution optical spectrum shaper and its application for optical communication systems," in *Conference on Optical Fiber Communication (OFC)*, San Diego, USA, Feb. 2008, p. JThA25.

[211] A. Szabo, B. Puttnam, D. Mazroa, S. Shinada, and N. Wada, "Investigation of an all-optical black-box PPLN-PPLN BPSK phase regenerator," *Photonics Technology Letters*, vol. 24, no. 22, pp. 2087–2089, Nov. 2012.

[212] F. Mogensen, H. Olesen, and G. Jacobsen, "Locking conditions and stability properties for a semiconductor laser with external light injection," *Journal of Quantum Electronics*, vol. 21, no. 7, pp. 784–793, Jul. 1985.

[213] R. Slavík, J. Kakande, and D. J. Richardson, "Practical issues and some lessons learned from realization of phase sensitive parametric regenerators," in *Optical Fiber Communication Conference (OFC)*, Los Angeles, USA, Mar. 2012, p. OW3C.4.

[214] B. Kelly, R. Phelan, D. Jones, C. Herbert, J. O'Carroll, M. Rensing, J. Wendelboe, C. Watts, A. Kaszubowska-Anandarajah, P. Perry, C. Guignard, L. Barry, and J. O'Gorman, "Discrete mode laser diodes with very narrow linewidth emission," *Electronics Letters*, vol. 43, no. 23, p. 1282, Nov. 2007.

[215] A. A. Albuquerque, B. J. Puttnam, J. Hirohashi, M. V. Drummond, S. Shinada, R. N. Nogueira, and N. Wada, "Investigation of PPSLT waveguides for applications in optical communication systems," in *Second International Conference on Applications of Optics and Photonics (AOP)*, Aveiro, Portugal, May 2014, p. 92861K.

[216] T. Richter, B. Corcoran, S. L. Olsson, C. Lundström, M. Karlsson, C. Schubert, and P. A. Andrekson, "Experimental characterization of a phase-sensitive four-mode fiber-optic parametric amplifier," in *European Conference on Optical Communication (ECOC)*, Amsterdam, Netherlands, Sep. 2012, p. Th.1.F.1.

[217] R. Malik, A. Kumpera, S. L. I. Olsson, P. A. Andrekson, and M. Karlsson, "Optical signal to noise ratio improvement through unbalanced noise beating in phase- sensitive parametric amplifiers," *Optics Express*, vol. 22, no. 9, pp. 10 477–10 486, May 2014.

[218] Z. Tong, C. J. McKinstrie, C. Lundström, M. Karlsson, and P. Andrekson, "Noise performance of optical fiber transmission links that use non-degenerate cascaded phase-sensitive amplifiers." *Optics Express*, vol. 18, no. 15, pp. 15 426–39, Jul. 2010.

[219] Z. Tong, A. Bogris, M. Karlsson, and P. Andrekson, "Full characterization of the signal and idler noise figure spectra in single-pumped fiber optical parametric amplifiers." *Optics Express*, vol. 18, no. 3, pp. 2884–93, Feb. 2010.

[220] K. Enbutsu, T. Umeki, M. Asobe, and H. Takenouchi, "Phase-sensitive amplifier using a PPLN waveguide integrated with a high-power-tolerant phase locking modulator," in *Conference on Lasers and Electro-Optics (CLEO)*, San Jose, USA, Jun. 2013, p. CM4D.6.

[221] B. Corcoran, R. Malik, S. L. I. Olsson, C. Lundström, and P. A. Andrekson, "Noise beating in hybrid phase-sensitive amplifier systems," *Optics Express*, vol. 22, no. 5, pp. 5762–5771, Mar. 2014.

[222] M. Jamshidifar, A. Vedadi, and M. E. Marhic, "Continuous-wave one-pump fiber optical parametric amplifier with 270 nm gain bandwidth," in *European Conference on Optical Communication (ECOC)*, Vienna, Austria, Sep. 2009, p. 1.1.4.

[223] R. Malik, A. Kumpera, M. Karlsson, and P. A. Andrekson, "Demonstration of ultra wideband phase-sensitive fiber optical parametric amplifier," *Photonics Technology Letters*, vol. 28, no. 2, pp. 175–177, Jan. 2016.

[224] N. K. Kjoller, F. Da Ros, K. M. Roge, P. Guan, M. Galili, and L. K. Oxenløwe, "A novel phase sensitive amplifier based QPSK regenerator without active phase-locking," in *Optical Fiber Communication Conference*, Los Angeles, USA, Mar. 2015, p. W4C.2.

[225] R. Malik, A. Kumpera, A. Lorences-Riesgo, P. A. Andrekson, and M. Karlsson, "Frequency-resolved noise figure measurements of phase (in)sensitive fiber optical parametric amplifiers," *Optics Express*, vol. 22, no. 23, pp. 27 821–27 832, Nov. 2014.

[226] Z. Tong, C. Lundström, P. A. Andrekson, M. Karlsson, and A. Bogris, "Ultralow noise, broadband phase-sensitive optical amplifiers, and their applications," *Selected Topics in Quantum Electronics*, vol. 18, no. 2, Mar. 2012.

[227] S. L. I. Olsson, B. Corcoran, C. Lundström, E. Tipsuwannakul, S. Sygletos, A. D. Ellis, Z. Tong, M. Karlsson, and P. A. Andrekson, "Injection locking-based pump recovery for phase-sensitive amplified links," *Optics Express*, vol. 21, no. 12, p. 14512, Jun. 2013.

[228] M. Ziyadi, A. Mohajerin-Ariaei, J.-y. Yang, Y. Akasaka, M. Chitgarha, S. Khaleghi, A. Almaiman, A. Abouzaid, J. Touch, and M. Sekiya, "Experimental demonstration of optical regeneration of DP-BPSK/QPSK using polarization-diversity PSA," in *Conference on Lasers and Electro-Optics*, San Jose, USA, Jun. 2014, p. STu2J.3.

[229] A. Lorences-Riesgo, F. Chiarello, C. Lundström, M. Karlsson, and P. A. Andrekson, "Experimental analysis of degenerate vector phase-sensitive amplification," *Optics Express*, vol. 22, no. 18, pp. 21 889–21 902, Sep. 2014.

[230] A. Lorences-Riesgo, C. Lundström, F. Chiarello, M. Karlsson, and P. A. Andrekson, "Phase-sensitive amplification and regeneration of dual-polarization BPSK without polarization diversity," in *European Conference on Optical Communication (ECOC)*, Cannes, France, Sep. 2014, p. Tu.1.4.3.

[231] A. Lorences-Riesgo, T. A. Eriksson, C. Lundström, M. Karlsson, and P. A. Andrekson, "Phase-sensitive amplification of 28 GBaud DP-QPSK signal," in *Optical Fiber Communication Conference (OFC)*, Los Angeles, USA, Mar. 2015, p. W4C.4.

[232] L. A. Coldren, W. Li, A. Mecozzi, M. Lu, S. Arafin, M. Vasilyev, D. Dadic, and L. Johansson, "Single-chip dual-pumped SOA-based phase-sensitive amplifier at 1550nm," in *IEEE Summer Topicals Meeting Series*, Nassau, Bahamas, Jul. 2015, pp. 88–89.

[233] H. Eliasson, S. L. I. Olsson, M. Karlsson, and P. A. Andrekson, "Mitigation of nonlinear distortion in hybrid Raman/phase-sensitive amplifier links," *Optics Express*, vol. 24, no. 2, pp. 888–900, Jan. 2016.

[234] X. Fu, X. Guo, and C. Shu, "Raman-enhanced phase-sensitive fiber optical parametric amplifier," in *Conference on Lasers and Electro-Optics (CLEO)*, San Jose, USA, May 2015, p. SW3L.5.

[235] H. J. Dutton, *Understanding optical communications*. Prentice Hall New Jersey, 1998.

[236] J. M. Senior and M. Y. Jamro, *Optical fiber communications: principles and practice*. Pearson Education, 2009.

[237] J. Leeuwen, *Handbook of theoretical computer science: algorithms and complexity*. Elsevier, 1990, vol. 1.

[238] E. W. Dijkstra, "A note on two problems in connexion with graphs," *Numerische Mathematik*, vol. 1, no. 1, pp. 269–271, Dec. 1959.

[239] T. H. Cormen, *Introduction to algorithms*. MIT Press, 2009.

[240] W. Kocay and D. L. Kreher, *Graphs, algorithms, and optimization*. CRC Press, 2004.

[241] E. Desurvire, D. Bayart, B. Desthieux, and S. Bigo, *Erbium-doped fiber amplifiers: device and system Developments*. John Wiley, 2002.

[242] J.-C. Dung, S. Chi, and S. Wen, "Gain flattening of erbium-doped fibre amplifier using fibre Bragg gratings," *Electronics Letters*, vol. 34, no. 6, pp. 555–556, Mar. 1998.

[243] C.-L. Lee and Y. Lai, "Evolutionary programming synthesis of optimal long-period fiber grating filters for EDFA gain flattening," *Photonics Technology Letters*, vol. 14, no. 11, pp. 1557–1559, Nov. 2002.

[244] H. Heffner, "The fundamental noise limit of linear amplifiers," *Proceedings of the Institute of Radio Engineers*, vol. 50, no. 7, pp. 228–232, Jul. 1962.

[245] J. Hansryd, P. A. Andrekson, M. Westlund, J. Li, and P. O. Hedekvist, "Fiber-based optical parametric amplifiers and their applications," *Journal on Selected Topics in Quantum Electronics*, vol. 8, no. 3, pp. 506–520, May 2002.

[246] C. J. McKinstrie, N. Alic, Z. Tong, and M. Karlsson, "Higher-capacity communication links based on two-mode phase-sensitive amplifiers." *Optics Express*, vol. 19, no. 13, pp. 11 977–11 991, Jun. 2011.

[247] Z. Tong, A. Bogris, C. Lundström, C. J. McKinstrie, M. Vasilyev, M. Karlsson, and P. Andrekson, "Modeling and measurement of the noise figure of a cascaded non-degenerate phase-sensitive parametric amplifier." *Optics Express*, vol. 18, no. 14, pp. 14 820–35, Jul. 2010.

[248] S. Donati and G. Giuliani, "Noise in an optical amplifier: formulation of a new semiclassical model," *Journal of Quantum Electronics*, vol. 33, no. 9, pp. 1481–1488, Sep. 1997.

[249] Z. Tong, C. Lundström, M. Karlsson, M. Vasilyev, and P. A. Andrekson, "Noise performance of a frequency nondegenerate phase-sensitive amplifier with unequalized inputs." *Optics Letters*, vol. 36, no. 5, Mar. 2011.

[250] M. Asobe, T. Umeki, and O. Tadanaga, "Phase sensitive amplification with noise figure below the 3 dB quantum limit using CW pumped PPLN waveguide." *Optics Express*, vol. 20, no. 12, pp. 13 164–72, Jun. 2012.

[251] P. Poggiolini, "The GN model of non-linear propagation in uncompensated coherent optical systems," *Journal of Lightwave Technology*, vol. 30, no. 24, pp. 3857–3879, Dec. 2012.

[252] P. Poggiolini, G. Bosco, A. Carena, V. Curri, Y. Jiang, and F. Forghieri, "A simple and effective closed-form GN-model correction formula accounting for signal non-gaussian distribution," *ArXiv:1402.3528, [physics.optics]*, pp. 1–7, 2014.

[253] M. Cantono, R. Gaudino, and V. Curri, "Potentialities and criticalities of flexible-rate transponders in DWDM networks: A statistical approach," *Journal of Optical Communications and Networking*, vol. 8, no. 7, p. A76, Jul. 2016.

[254] T. P. Almeida, M. V. Drummond, N. B. Pavlović, P. S. André, and R. N. Nogueira, "Optimal launch power prediction of a 100G PM-DQPSK dispersion-managed link with the Gaussian noise model," in *Second International Conference on Applications of Optics and Photonics (AOP)*, Aveiro, Portugal, May 2014, p. 92861X.

[255] Bulgarian Research and Education Network. (2016) Bulgarian Research and Education Network. [Online]. Available: http://www.bren.bg

[256] TelePresence Exchange International. (2014) National LambdaRail. [Online]. Available: http://www.tpex.com/learning/university-networks/national-lambdarail

[257] A. N. Pinto. (2016) Reference transport network topologies. [Online]. Available: http://www.av.it.pt/anp/on/refnet2.html

[258] P. E. Powers, K. Kramb, and J. W. Haus, "Broadly tunable terahertz source," in *Proceedings of SPIE*, vol. 7582, San Francisco, USA, Feb. 2010, pp. 758 210–758 217.

[259] S. L. I. Olsson, B. Corcoran, C. Lundström, T. a. Eriksson, M. Karlsson, and P. a. Andrekson, "Phase-sensitive amplified transmission links for improved sensitivity and nonlinearity tolerance," *Journal of Lightwave Technology*, vol. 33, no. 3, pp. 710–721, Feb. 2015.

[260] L. C. Andrews, *Special functions of mathematics for engineers*. McGraw-Hill Publishing Co., 1991.

[261] M. Abramowitz and I. A. Stegun, *Handbook of mathematical functions: with formulas, graphs, and mathematical tables*. Courier Corporation, 1964, vol. 55.

[262] J. Proakis and M. Salehi, *Digital Communications*, 5th ed. McGraw-Hill Education, 2008.

Appendices

Appendix A

Derivation of the coupled-mode equations for SHG

In order to obtain the couple-mode equations for SHG, let us revisit the example of equation (2.14), but considering $\nu_2 = \nu_{SHG} = 2\nu_1$. In addition, let us assume QPM of the second harmonic generation of the wave with frequency ν_1, such that only the terms of $\mathbf{P}^{(2)}$ with frequencies ν_{SHG} and ν_1 are relevant. Considering that the electric field of each wave is described by (2.4), the general wave equation (2.2) can be simplified and split into the following set of equations

$$\begin{aligned}\nabla^2\left(E_1 e^{i(\omega_{0,1}t-\beta_1 z)}\right) =& \frac{1}{c^2}\frac{\partial^2}{\partial t^2}\left(\left[1+\chi^{(1)}\right]\otimes E_1 e^{i(\omega_{0,1}t-\beta_1 z)}\right.\\ &\left.+\,2d\otimes E_2\otimes E_1^* e^{i[\omega_{0,1}t-(\beta_2-\beta_1)z]}\right)\end{aligned} \tag{A.1a}$$

$$\begin{aligned}\nabla^2\left(E_2 e^{i(\omega_{0,2}t-\beta_2 z)}\right) =& \frac{1}{c^2}\frac{\partial^2}{\partial t^2}\left(\left[1+\chi^{(1)}\right]\otimes E_2 e^{i(\omega_{0,2}t-\beta_2 z)}\right.\\ &\left.+\,d\otimes E_1\otimes E_1 e^{i(\omega_{0,2}t-2\beta_1 z)}\right).\end{aligned} \tag{A.1b}$$

The previous set of equations can be greatly simplified assuming that the nonlinear interaction is instantaneous and that the second-order nonlinear coefficient is constant within the optical bandwidth of interest. This approximation allows replacing the convolution operation for the nonlinear terms into simple multiplications. The previous equations can then be re-written in the frequency domain by considering (2.6), resulting in the following set of

equations

$$\nabla^2\left(M_1(x,y)\tilde{A}_1(z,\omega_1)e^{-i\beta_1 z}\right) = -\frac{\omega_1^2}{c^2}\left[n_1^2(\mathbf{r},\omega_1)M_1(x,y)\tilde{A}_1(z,\omega_1)e^{-i\beta_1 z} + 2d\Gamma_2 M_2(x,y)M_1^*(x,y)\tilde{A}_2(z,\omega_2)\otimes\tilde{A}_1^*(z,-\omega_1)e^{-i(\beta_2-\beta_1)z}\right] \tag{A.2a}$$

$$\nabla^2\left(M_2(x,y)\tilde{A}_2(z,\omega_2)e^{-i\beta_2 z}\right) = -\frac{\omega_2^2}{c^2}\left[n_2^2(\mathbf{r},\omega_2)M_2(x,y)\tilde{A}_2(z,\omega_2)e^{-i\beta_2 z} + d\frac{\Gamma_1^2}{\Gamma_2}M_1^2(x,y)\tilde{A}_1(z,\omega_1)\otimes\tilde{A}_1(z,\omega_1)e^{-2i\beta_1 z}\right]. \tag{A.2b}$$

Each of the above expressions can be split into two new equations, one describing the transverse distribution of the electric field of the wave or propagating mode in waveguided devices, and another the evolution of the normalized electric field envelope along the z direction, as detailed in references [73,77]. Considering only the second case, the evolution of normalized electric field envelope is approximately given by

$$M_1(x,y)\frac{\partial}{\partial z}\tilde{A}_1(z,\omega_1) = \left(i\sum_{m=1}^{+\infty}\frac{\beta_1^{(m)}(\omega_{0,1})}{m!}\Omega_1^m - \frac{\alpha}{2}\right)M_1(x,y)\tilde{A}_1(z,\omega_1) - id_{eff}\frac{2\pi}{\lambda_1}\sqrt{\frac{2}{n_1^2 n_2 c\epsilon_0}}M_2(x,y)M_1^*(x,y)\tilde{A}_2(z,\omega_2)\otimes\tilde{A}_1^*(z,-\omega_1)e^{-i\Delta\beta z} \tag{A.3a}$$

$$M_2(x,y)\frac{\partial}{\partial z}\tilde{A}_2(z,\omega_2) = \left(i\sum_{m=1}^{+\infty}\frac{\beta_2^{(m)}(\omega_{0,2})}{m!}\Omega_2^m - \frac{\alpha}{2}\right)M_2(x,y)\tilde{A}_2(z,\omega_2) - i\frac{d_{eff}}{2}\frac{2\pi}{\lambda_1}\sqrt{\frac{2}{n_1^2 n_2 c\epsilon_0}}M_1^2(x,y)\tilde{A}_1(z,\omega_1)\otimes\tilde{A}_1(z,\omega_1)e^{i\Delta\beta z}, \tag{A.3b}$$

where the second-order spatial derivatives of the normalized electric field envelope were neglected (slowly-varying envelope approximation). The coupled-mode equations describing the SHG process can now be obtained by re-writing (A.3) in the time domain, multiplying (A.3a) by M_1^* and (A.3b) by M_2^*, and integrating over x and y. The following equations are obtained

$$\frac{\partial A_1(z,t)}{\partial z} = \hat{D}_1(\omega_{0,1},t)A_1(z,t) - i\kappa_1 A_2(z,t)A_1^*(z,t)e^{-i\Delta\beta z} \tag{A.4a}$$

$$\frac{\partial A_2(z,t)}{\partial z} = \hat{D}_2(\omega_{0,2},t)A_2(z,t) - i\frac{\kappa_2}{2}A_1^2(z,t)e^{i\Delta\beta z}, \tag{A.4b}$$

A similar procedure can be repeated in order to determine the coupled-mode equations for SFG, DFG, cSHG/DFG, cSFG/DFG, and FWM.

Appendix B

Derivation of the MEGN model for systems with full dispersion compensation

The EGN model was originally proposed in reference [59] as a correction to the so called GN model [58], aiming to remove the signal gaussianity approximation. The derivation of the EGN model for Nyquist channels formulated assuming full dispersion compensation after each span, denominated herein as the MEGN model, is presented in this appendix. All of the equations shown here were obtained from the original work presented in references [58, 59, 107, 251, 252].

Let us first focus on the GN model. The GN model was obtained as an approximated solution to the nonlinear Schrödinger equation for single-polarization systems [73], or the Manakov-PMD equations [106] for dual-polarization signals propagating in optical fibers with randomly varying birefringence. The GN model also assumes that after propagating through a significant distance in a dispersive medium, the transmitted signals can be statistically described as stationary Gaussian noise, which is known as the signal gaussianity approximation. Moreover, the GN considers that the signal distortion due to the nonlinear effects, known as the nonlinear interference, manifests as additive Gaussian noise [58].

The main results from the GN model are summarized by the so called GN model reference formula, given by equation (1) in reference [58]. Assuming transmission in an optical medium without distributed amplification and with a perfect compensation of the propaga-

tion losses after each fiber span, the GN model reference formula is given by [58, 107]

$$\begin{aligned} S_{NLI}^{GN}(\nu) =& 2\left(\frac{4-p}{3}\right)^3 \int_{-\infty}^{+\infty}\int_{-\infty}^{+\infty} S_{WDM}(\nu_1)S_{WDM}(\nu_2)S_{WDM}(\nu_1+\nu_2-\nu)\times \\ & \left|\sum_{n=1}^{N_s}\gamma_n \cdot e^{i4\pi^2(\nu_1-\nu)(\nu_2-\nu)\sum_{k=1}^{n-1}\left[\beta_k^{(2)}L_k+\pi(\nu_1+\nu_2)\beta_k^{(3)}L_k+\beta_{DCU,k}\right]}\times \right. \\ & \left. \int_0^{L_n} e^{\left(-\alpha+i4\pi^2(\nu_1-\nu)(\nu_2-\nu)\cdot\left[\beta_n^{(2)}+\pi(\nu_1+\nu_2)\beta_n^{(3)}\right]\right)z}dz\right|^2 d\nu_1 d\nu_2, \end{aligned} \tag{B.1}$$

with S_{NLI}^{GN} and S_{WDM} the power spectral densities of the NLI and the transmitted WDM signal, respectively. In (B.1), L_k, $\beta_k^{(l)}$ and $\beta_{DCU,k}$ are the length, the l^{th} derivative of β with respect to the angular frequency and the accumulated dispersion of the DCU at the end of span k. In references [58, 59, 107, 251, 252], the absorption coefficient is defined in such a way that the power of the waves propagating in a lossy medium decrease by a factor of $\exp(-2\alpha L)$. In this thesis, however, the definition of the absorption coefficient is slightly different, such that the power of the waves decreases by a factor of $\exp(-\alpha L)$ instead. Consequently, the coefficient α in all the expressions taken from references [58, 59, 107, 251, 252] is replaced here by $\alpha/2$.

Let us now assume transmission with full dispersion compensation at the end of each span, i.e., $\beta_{DCU,k} = \beta_k^{(2)}L_k + \pi(\nu_1+\nu_2)\beta_k^{(3)}L_k$ for any span k. In this case, the GN-model reference formula becomes

$$\begin{aligned} S_{NLI}^{GN}(\nu) =& 2\left(\frac{4-p}{3}\right)^3 \int_{-\infty}^{+\infty}\int_{-\infty}^{+\infty} S_{WDM}(\nu_1)S_{WDM}(\nu_2)S_{WDM}(\nu_1+\nu_2-\nu)\times \\ & \left|\sum_{n=1}^{N_s}\gamma_n \int_0^{L_n} e^{\left(-\alpha+i4\pi^2(\nu_1-\nu)(\nu_2-\nu)\cdot\left[\beta_n^{(2)}+\pi(\nu_1+\nu_2)\beta_n^{(3)}\right]\right)z}dz\right|^2 d\nu_1 d\nu_2. \end{aligned} \tag{B.2}$$

The previous equation can be further simplified when $\beta_n^{(2)} \gg (\nu_1+\nu_2)\beta_n^{(3)}$. In addition, if the length and the nonlinear and dispersion parameters of all fibers of each span are identical, the previous equation simply becomes

$$\begin{aligned} S_{NLI}^{GN}(\nu) = & 2\left(\frac{4-p}{3}\right)^3 \gamma^2 {L_{eff}}^2 N_s^2 \int_{-\infty}^{+\infty}\int_{-\infty}^{+\infty} S_{WDM}(\nu_1)S_{WDM}(\nu_2)S_{WDM}(\nu_1+\nu_2-\nu) \\ & \times \rho_{FWM}(\nu_1,\nu_2,\nu)d\nu_1 d\nu_2, \end{aligned} \tag{B.3}$$

where ρ_{FWM} is a FWM efficiency factor [58], given by

$$\rho_{FWM}(\nu_1,\nu_2,\nu) = \left|\frac{1-e^{-\alpha L+i4\pi^2(\nu_1-\nu)(\nu_2-\nu)\beta^{(2)}L}}{\alpha - i4\pi^2(\nu_1-\nu)(\nu_2-\nu)\beta^{(2)}}\right|^2 {L_{eff}}^{-2}. \tag{B.4}$$

In the previous equations, L_{eff} is the effective length that accounts for the effects of propa-

gation losses, given by [73]

$$L_{eff} = \int_0^L e^{-\alpha z} dz = \frac{1 - e^{-\alpha L}}{\alpha}. \tag{B.5}$$

Let us now assume Nyquist-WDM channels with a constant PSD of P_{ch}/B_{ch} within the channel bandwidth B_{ch}, with P_{ch} the total channel power, and separated from each other by $\Delta\nu$, as shown in figure 6.2. Also, let us assume that the frequency is defined with respect to the center of the power density spectrum of the WDM channels. As it was shown in [251], the power spectral density of the nonlinear interference in WDM systems is usually stronger at the center channels. Thus, the discussion is limited to the evaluation of S_{NLI}^{GN} at ν=0 for simplicity, which corresponds to the worst-case scenario for the evaluation of the NLI power.

For illustration purposes, the product between the power spectral densities $S_{WDM}(\nu_1)$, $S_{WDM}(\nu_2)$ and $S_{WDM}(\nu_1 + \nu_2 - \nu)$ for seven Nyquist-WDM channels, as well as the FWM efficiency factor are depicted in figure B.1, evaluated at $\nu = 0$, and considering B_{ch} = 40 GHz, L = 80 km, $\beta^{(2)}$ = -21.3 ps^2/km, α = 0.22 dB/km and $\Delta\nu$ = 50 GHz.

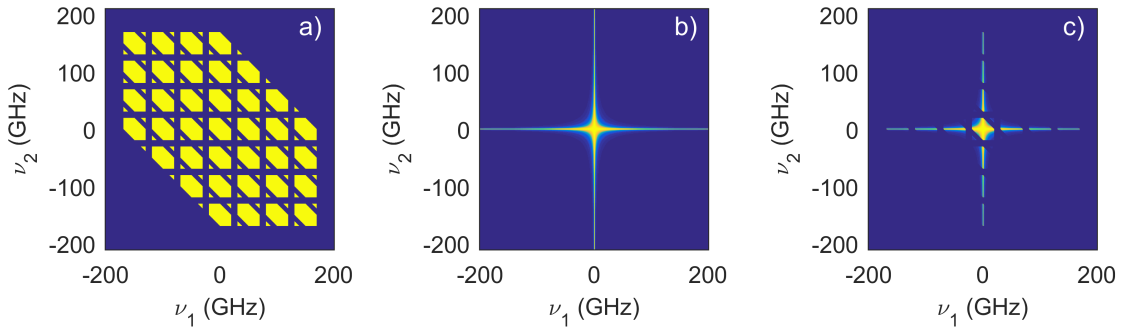

Figure B.1: a) Product $S_{WDM}(\nu_1)S_{WDM}(\nu_2)S_{WDM}(\nu_1 + \nu_2)$ for Nyquist-WDM signals. b) FWM efficiency factor. c) Product between the FWM efficiency factor and the power spectral densities of the Nyquist-WDM signals. All the figures were obtained at ν = 0.

As shown in figure B.1-a), the product between the power spectral densities of Nyquist signals is non-zero only for a discrete set of hexagonal and small triangular "islands", which define the integration domain of equation (B.1). The FWM efficiency factor is also depicted in figure B.1-b), showing that it only becomes significant when ν_1 or ν_2 are approximately 0, due to the phase mismatch effects on the FWM efficiency. The product between the FWM efficiency factor and the power spectral densities of the transmitted signals is also shown in figure B.1-c). According to the figure, the argument of the double integral in (B.1) at ν = 0 only becomes appreciable for the "islands" in figure B.1-a) centered at ν_1 = 0 and/or ν_2 = 0. The contribution at ν_1=ν_2=0 has been denoted in [58] as self-channel interference, whereas the remaining contributions as cross-channel interference. All the other "islands", known as multi-channel interference, are typically very weak and are neglected henceforth.

Another relevant conclusion obtained from figure B.1-c) is that the product between

the power spectral densities and the FWM efficiency factor is symmetrical with respect to the line $\nu_1 = \nu_2$, which can be used to simplify the evaluation of the double integral in (B.3). In addition, the hexagonal and triangular integration domains in figure B.1-a) can be approximated to square domains with edge size of B_{ch}. Bearing all these considerations in mind, (B.3) can be simplified to

$$S_{NLI}^{GN}(0) \approx 2\left(\frac{4-p}{3}\right)^3 \gamma^2 L_{eff}^2 N_s^2 \left(\frac{P_{ch}}{B_{ch}}\right)^3 \times \sum_{m=-(N_{ch}-1)/2}^{(N_{ch}-1)/2} \int_{-B_{ch}/2}^{+B_{ch}/2} \int_{m\Delta\nu-B_{ch}/2}^{m\Delta\nu+B_{ch}/2} \rho_{FWM}(\nu_1,\nu_2,0)\, d\nu_1 d\nu_2. \tag{B.6}$$

If the fiber spans are long enough such that the propagation losses are of more than 10 dB, the FWM efficiency factor at ν = 0 can also be approximated by the following expression [251]

$$\rho_{FWM}(\nu_1,\nu_2,0) \approx \frac{1}{1+\left[\frac{4\pi^2\nu_1\nu_2|\beta^{(2)}|}{\alpha}\right]^2}. \tag{B.7}$$

Using this approximation in (B.6) and evaluating the double integral, the following equation for the power spectral density of the nonlinear interference is obtained

$$\begin{aligned} S_{NLI}^{GN}(0) \approx{}& \left(\frac{4-p}{3}\cdot\frac{P_{ch}}{B_{ch}}\right)^3 \frac{\gamma^2 L_{eff}^2 N_s^2 \alpha}{2\pi^2|\beta^{(2)}|} \\ &\times \sum_{m=-(N_{ch}-1)/2}^{(N_{ch}-1)/2} (2-\delta_m)\left(i\left\{\mathrm{Li}_2\left[-i\frac{2\pi^2|\beta^{(2)}|}{\alpha}\left(m\Delta\nu+B_{ch}/2\right)B_{ch}\right]\right.\right. \\ &\left.-\mathrm{Li}_2\left[i\frac{2\pi^2|\beta^{(2)}|}{\alpha}\left(m\Delta\nu+B_{ch}/2\right)B_{ch}\right]\right\} \\ &-i\left\{\mathrm{Li}_2\left[-i\frac{2\pi^2|\beta^{(2)}|}{\alpha}\left(m\Delta\nu-B_{ch}/2\right)B_{ch}\right]\right. \\ &\left.\left.-\mathrm{Li}_2\left[i\frac{2\pi^2|\beta^{(2)}|}{\alpha}\left(m\Delta\nu-B_{ch}/2\right)B_{ch}\right]\right\}\right), \end{aligned} \tag{B.8}$$

where δ_m is the Kronecker delta function, equal to 1 for m = 0 and 0 otherwise, and Li_2 is the polylogarithm function of order 2, also known as the dilogarithm function [260], calculated through the following expression

$$\mathrm{Li}_2(x) = \int_x^0 \frac{\ln(1-y)}{y}\, dy. \tag{B.9}$$

Equation (B.8) can be simplified and expressed in terms of more conventional functions by using the approximation [251]

$$i\left[\mathrm{Li}_2\left(-ix\right) - \mathrm{Li}_2\left(ix\right)\right] \approx \pi \mathrm{asinh}(x/2). \tag{B.10}$$

The PSD of the NLI then becomes

$$S_{NLI}^{GN}(0) \approx \left(\frac{4-p}{3}\cdot\frac{P_{ch}}{B_{ch}}\right)^3 \frac{\gamma^2 L_{eff}^2 N_s^2 \alpha}{2\pi|\beta^{(2)}|} \times \sum_{m=-(N_{ch}-1)/2}^{(N_{ch}-1)/2} (2-\delta_m)\cdot\left\{\text{asinh}\left[\frac{\pi^2|\beta^{(2)}|}{\alpha}\left(m\Delta\nu + B_{ch}/2\right)B_{ch}\right] - \text{asinh}\left[\frac{\pi^2|\beta^{(2)}|}{\alpha}\left(m\Delta\nu - B_{ch}/2\right)B_{ch}\right]\right\}. \tag{B.11}$$

Equation (B.11) summarizes the GN model into a simple expression for the PSD of the NLI, evaluated at the center channel of Nyquist-WDM signals.

Let us now focus on the MEGN model. As mentioned above, the EGN and, consequently, the MEGN models include the GN model in their formulation and additional correcting terms that allow removing the signal gaussianity approximation. Hence, the PSD of the NLI for the MEGN model can be described as

$$S_{NLI}(\nu) = S_{NLI}^{GN}(\nu) - S_{corr}(\nu), \tag{B.12}$$

where S_{corr} include the correcting terms. In order to obtain a simple and manageable correction to the GN model, the same procedure followed in [252] is used to obtain S_{corr}. Such a procedure neglects the correcting terms for the self- and multi-channel interference, and accounts only for the cross-channel interference terms of the hexagonal integration domains. Assuming full compensation of the dispersion effects at the end of each span, the following correcting term is obtained [252]

$$S_{corr}(\nu) = \sum_{m\in C}(3+p)\left(\frac{4-p}{3}\right)^4 \Theta\gamma^2 {B_{ch}}^2 N_s^2 {P_{ch}}^3 \times \int_{-\infty}^{+\infty}\int_{-\infty}^{+\infty}\int_{-\infty}^{+\infty} |s_{cut}(\nu_1)|^2 s_m(\nu_2) s_m^*(\nu_3) s_m^*(\nu_1+\nu_2-\nu) s_m(\nu_1+\nu_3-\nu) \times \frac{1-e^{-\alpha L + i4\pi^2\beta^{(2)}(\nu_1-\nu)(\nu_2-\nu)L}}{\alpha - i4\pi^2\beta^{(2)}(\nu_1-\nu)(\nu_2-\nu)} \times \frac{1-e^{-\alpha L - i4\pi^2\beta^{(2)}(\nu_1-\nu)(\nu_3-\nu)L}}{\alpha + i4\pi^2\beta^{(2)}(\nu_1-\nu)(\nu_3-\nu)} d\nu_1 d\nu_2 d\nu_3, \tag{B.13}$$

where s_{cut} and s_m are normalized power spectral densities of the channel under test and of an interfering channel m, with a rectangular spectral shape and flat-top value of $1/B_{ch}$. In the previous equation, C is the set with all the indices m that represent each of the interfering channels and Θ is a constant that depends on the modulation format, calculated by [252]

$$\Theta = 2 - \frac{<|X|^4>}{<|X|^2>^2}, \tag{B.14}$$

with X a random variable that represents the constellation symbols of the transmitted data.

For simplicity, let us consider the channel centered at ν = 0 as the channel under

test and focus on evaluating $S_{corr}(0)$. In this case and by approximating the hexagonal integration islands by square domains with edge size of B_{ch}, the pulse spectra s_{cut} and s_m can be removed from the integrand of (B.13), obtaining the following expression [252]

$$\begin{aligned} S_{corr}(0) = \sum_{m\in C}(3+p)\left(\frac{4-p}{3}\right)^4 \Theta\gamma^2 N_s^2 \frac{{P_{ch}}^3}{{B_{ch}}^4} \\ \times \int_{-B_{ch}/2}^{+B_{ch}/2}\left(\int_{m\Delta\nu-B_{ch}/2}^{m\Delta\nu+B_{ch}/2}\frac{1-e^{-\alpha L+i4\pi^2\beta^{(2)}\nu_1\nu_2 L}}{\alpha - i4\pi^2\beta^{(2)}\nu_1\nu_2}d\nu_2\right. \\ \left.\times\int_{m\Delta\nu-B_{ch}/2}^{m\Delta\nu+B_{ch}/2}\frac{1-e^{-\alpha L-i4\pi^2\beta^{(2)}\nu_1\nu_3 L}}{\alpha + i4\pi^2\beta^{(2)}\nu_1\nu_3}d\nu_3\right)d\nu_1. \end{aligned} \tag{B.15}$$

In the previous equation, the two integrals with respect to frequencies ν_2 and ν_3 are independent of each other and have the same integration domain. Thus, changing the variable of integration ν_3 to ν_2 does not change the final result, and the previous equation can be simplified to

$$S_{corr}(0) = \sum_{m\in C}(3+p)\left(\frac{4-p}{3}\right)^4 \Theta\gamma^2 N_s^2 \frac{{P_{ch}}^3}{{B_{ch}}^4}\int_{-B_{ch}/2}^{+B_{ch}/2}|\zeta_m(\nu_1)|^2 d\nu_1, \tag{B.16}$$

where $\zeta_m(\nu_1)$ is given by

$$\begin{aligned} \zeta_m(\nu_1) &= \int_{m\Delta\nu-B_{ch}/2}^{m\Delta\nu+B_{ch}/2}\frac{1-e^{-\alpha L+i4\pi^2\beta^{(2)}\nu_1\nu_2 L}}{\alpha - i4\pi^2\beta^{(2)}\nu_1\nu_2}d\nu_2 \\ &= \frac{i}{4\pi^2\beta^{(2)}\nu_1}\left\{\ln\left(\frac{\alpha - i4\pi^2\beta^{(2)}\nu_1\left[m\Delta\nu+B_{ch}/2\right]}{\alpha - i4\pi^2\beta^{(2)}\nu_1\left[m\Delta\nu-B_{ch}/2\right]}\right)\right. \\ &+ \mathrm{E}_1\left(\left[\alpha - i4\pi^2\beta^{(2)}\nu_1\left(m\Delta\nu+B_{ch}/2\right)\right]L\right) \\ &\left.- \mathrm{E}_1\left(\left[\alpha - i4\pi^2\beta^{(2)}\nu_1\left(m\Delta\nu-B_{ch}/2\right)\right]L\right)\right\}, \end{aligned} \tag{B.17}$$

with E_1 an exponential-integral function, defined as [261]

$$\mathrm{E}_1(x) = \int_x^\infty \frac{e^{-y}}{y}dy. \tag{B.18}$$

The MEGN correction given by (B.16) still requires computing the integral of function $\zeta_m(\nu_1)$ with respect to frequency ν_1, which can be easily performed using standard numerical methods such as the trapezoid rule [102]. Along with the simplified expression for the nonlinear interference of the GN model shown in (B.11), equation (B.16) provides a simple way to estimate the impact of the NLI at the center channel at affordable computational effort.

Appendix C

Error probability formulas

The degradation of the transmitted signals in a communication system caused by, for instance, the noise added by amplifiers, typically results in symbol and bit errors after detection at the receivers. If the transmitted signals are affected by white Gaussian noise, the BER can be modeled by the probability to detect an error, whose variation with the SNR of the received signals is presented in this appendix. The formulas provided here assume coherent detection at the receiver and that one symbol error introduces a single bit error, which can be achieved by properly encoding the original data information (e.g., by using Gray coding) [262]. The probability of error formulas for BPSK, QPSK and M-QAM signals with rectangular constellations are given by (C.1), (C.2) and (C.3), respectively [262].

$$BER \approx Q(\sqrt{2SNR}), \tag{C.1}$$

$$BER \approx Q(\sqrt{SNR}) \left[1 - \frac{1}{2} Q(\sqrt{SNR})\right], \tag{C.2}$$

$$BER \approx \frac{4}{\log_2(M)} \left(1 - \frac{1}{\sqrt{M}}\right) \left[Q\left(\sqrt{\frac{3SNR}{M-1}}\right)\right] \left[1 - \left(1 - \frac{1}{\sqrt{M}}\right) Q\left(\sqrt{\frac{3SNR}{M-1}}\right)\right], \tag{C.3}$$

where $Q(x)$ is the so called Q-function defined as [141]

$$Q(x) = \frac{1}{2} \text{erfc}\left(\frac{x}{\sqrt{2}}\right), \tag{C.4}$$

with erfc the complementary error function given by [262]

$$\text{erfc}(x) = \frac{2}{\sqrt{\pi}} \int_x^{+\infty} e^{-t^2} dt. \tag{C.5}$$

The variation of the probability error formulas for BPSK, QPSK, 16-QAM and 64-QAM are depicted in figure C.1.

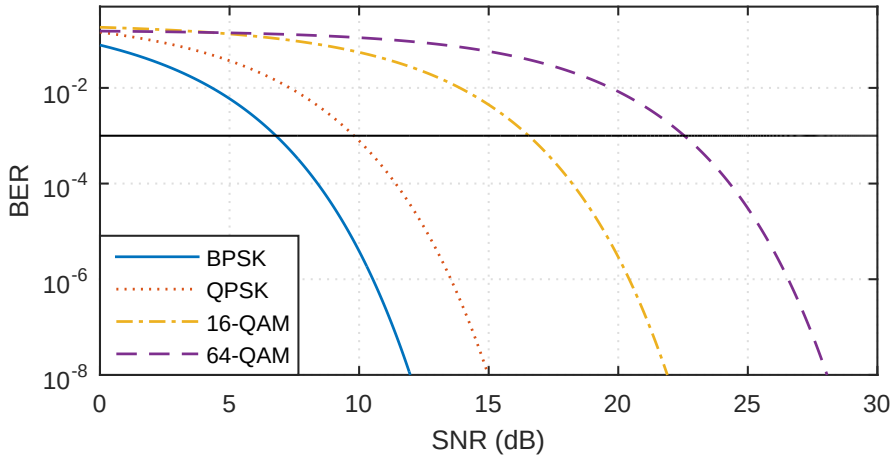

Figure C.1: Variation of the BER with the SNR for coherent detection of BPSK, QPSK, 16-QAM and 64-QAM signals. The horizontal black line represents a BER of 10^{-3}.

Appendix D

Selected publications

Publication A

PPLN poling design based on a discrete layer peeling algorithm combined with a deleted-reversal method

A. Albuquerque, B. Puttnam, M. Drummond, S. Shinada, N. Wada, R. Nogueira

originally published in *Journal of Lightwave Technology*, vol. 31, no. 23, pp. 3892-3900, December 2013.

3892 JOURNAL OF LIGHTWAVE TECHNOLOGY, VOL. 31, NO. 23, DECEMBER 1, 2013

PPLN Poling Design Based on a Discrete Layer Peeling Algorithm Combined With a Deleted-Reversal Method

A. A. C. Albuquerque, *Student Member, IEEE*, B. J. Puttnam, *Member, IEEE*, M. V. Drummond, *Member, IEEE*, S. Shinada, *Member, IEEE*, N. Wada, *Member, IEEE*, and R. N. Nogueira, *Member, IEEE*

***Abstract*—In this paper, we propose a method to design the poling pattern of periodically poled lithium niobate (PPLN) devices according to a target spectral response of the selected nonlinear interaction. This method combines a discrete layer peeling algorithm with the deleted-reversal method. The main advantages and limitations of the proposed method in terms of fabrication feasibility of the resulting poling patterns are discussed. The effectiveness of the proposed method is shown by designing PPLNs with two different types of spectral responses: quasi-rectangular bandpass filtering and multichannel filtering. We experimentally demonstrate the method by designing and producing a PPLN which allows performing wavelength conversion within a spectral response approximately given by a 400 GHz quasi-rectangular filter.**

***Index Terms*—Deleted-reversal, layer peeling, optical signal processing (OSP), periodically poled lithium niobate (PPLN), wavelength conversion.**

I. Introduction

ALL-OPTICAL signal processing (OSP) has been suggested as a viable route to enable several functionalities with the ultimate purpose of increasing the performance and efficiency of telecommunication networks [1]. Besides the possibility of ultrahigh-speed and parallel operation, it is hoped that OSP will be more cost and energy efficient compared to pure electrical signal processing, as optical-to-electrical-to-optical conversion is avoided [2], [3].

A wide variety of photonic and optoelectronic devices have been used for OSP including fiber Bragg gratings (FBGs) [4], tunable optical filters based on liquid crystals on silicon [5], silica-based highly nonlinear fibers [6], [7], photonic crystal fibers [8], silicon and chalcogenide waveguides [9], [10], semiconductor optical amplifiers [11] and periodically poled lithium niobate (PPLN) devices [12]. In the last years, PPLN devices have been widely used for OSP due to their interesting properties including ultrafast response [13], high efficiency [14], compactness [14], low spontaneous emission noise [13], possibility of room temperature operation [15] and immunity to stimulated Brillouin scattering [16]. Some examples of the possible applications of PPLN devices are tunable wavelength conversion [17], all-optical logic gates [18], demultiplexing of time-division multiplexed signals [19], add/drop [20], switching [21], spectral inversion [22], modulation format conversion [23] and signal regeneration [24], [25].

OSP in PPLN devices relies on second-order nonlinear effects such as second-harmonic generation (SHG), sum-frequency generation (SFG), difference-frequency generation (DFG) and/or cascaded interactions involving combinations of these phenomena. PPLNs are produced by periodically inverting the ferroelectric domains in a lithium niobate crystal, resulting in a periodic reversal of the sign of the nonlinear coefficient. This technique is used for enabling quasi phase matching (QPM), and compensates the phase mismatch between the interacting waves after each coherence length, increasing the efficiency of the nonlinear interaction [12]. As with FBGs, the spectral properties of a PPLN device can be designed by tailoring the periodic poling. This property demarks PPLNs from other nonlinear devices as it offers a capability to design the response of the device and enables additional functionalities. Apodized [26], aperiodic [27] and superlattice [28] PPLNs have already been reported providing attractive features such as reduced crosstalk between different WDM channels and increased spectral bandwidth of operation.

The LPA was originally proposed as a simple and flexible tool to design FBGs and grating assisted co-directional couplers with a target spectral response [29], [30]. Recently, Zhang *et al*. [31] measured the output spectra of Šolc-type linear filters based on uniform and aperiodic PPLNs. Using the LPA, they were able to retrieve the poling pattern of those devices with good accuracy.

In this paper, the LPA is used to design PPLNs with a target spectral response rather than retrieve the QPM structure of already manufactured devices combining nonlinear interactions and filtering capabilities in the same device. To the best of our knowledge, this is the first time that the LPA is used to design nonlinear devices such as PPLNs. In this paper, the LPA is adapted and combined with the DRM [26] (LPA-DRM) in order to make it compatible with known production techniques of PPLN devices.

Manuscript received May 21, 2013; revised September 10, 2013 and October 15, 2013; accepted October 15, 2013. Date of publication October 22, 2013; date of current version November 22, 2013. This work was supported by Fundação para a Ciência e Tecnologia under Grant SFRH/BD/78425/2011 and Project POFCOM (PTDC/EEA-TEL/122792/2010).

A. A. C. Albuquerque, M. V. Drummond, and R. N. Nogueira are with the Instituto de Telecomunicações, Aveiro 3810–193, Portugal (e-mail: andrealbuquerque@av.it.pt; mvd@av.it.pt; rnogueira@av.it.pt).

B. J. Puttnam, S. Shinada, and N. Wada are with the National Institute of Information and Communications Technology, Tokyo 184–8795, Japan (e-mail: ben@nict.go.jp; sshinada@nict.go.jp; wada@nict.go.jp).

Color versions of one or more of the figures in this paper are available online at http://ieeexplore.ieee.org.

Digital Object Identifier 10.1109/JLT.2013.2286614

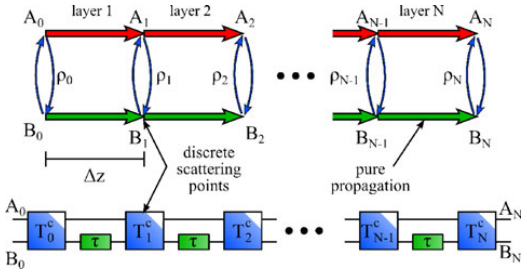

Fig. 1. On top: schematic representation of the discrete coupling model. At the bottom: block diagram of this model, using a time frame coincident with the propagation of the A mode.

This paper is organized as follows. The description of the LPA-DRM is presented in Section II, including a brief discussion on the discrete coupling model, how to adapt the LPA to PPLN devices and the limitations of this approach. In Section III, the spectral response of designed PPLNs is compared with the target response. Quasi-rectangular bandpass PPLNs with 400 GHz and 1 THz bandwidth and multichannel PPLNs (with multiple QPM peaks) are simulated in this section. Finally, Section IV is devoted to the characterization of the spectral response of the manufactured quasi-rectangular 400 GHz bandpass PPLN.

II. Layer Peeling Algorithm

The LPA was originally proposed as a simple and easy to implement method to design grating-assisted couplers. In this algorithm, the grating is consecutively reconstructed layer by layer and the coupling coefficient of each layer is computed according to the target filtering properties of the coupler. A discrete time-domain version of the LPA [30] is adopted in this paper. The discrete LPA assumes that mode coupling between two propagating modes occurs only at discrete scattering points. According to this model, in between the scattering points the modes experience only pure dispersive propagation with no coupling. A schematic representation of the discrete coupling model is illustrated in Fig. 1.

Usually, in SFG and DFG interactions the power of one of the input waves is much higher than that of the other, and it is used to pump the nonlinear interaction. If the pump is not significantly depleted, it can be assumed that it remains constant for all nonlinear interactions, and in that case, SFG and DFG may be simply interpreted as the coupling between two propagating modes, as in co-directional grating-assisted couplers. In this case, coupling between the interacting waves is promoted by the nonlinear response of the PPLN device and optical pumping rather than periodic variations of the refractive index.

As long as the no pump depletion approximation is valid, SFG and DFG between continuous wave signals propagating in a lossless medium can be modeled by a transfer matrix [32]. This transfer matrix is similar to the one describing co-directional grating-assisted couplers [30] and it becomes fully identical by adopting a proper change of variables.

Let us consider that the frequencies of the input signal and pump wave are f_2 and f_1, respectively, and that the frequency of the new wave created during the nonlinear interaction is $f_3 = f_2 \pm f_1$ ('+' for SFG and "−" for DFG). Let us also consider the variables $A = A_3 \exp(-i\delta z)$, $B = \sqrt{\lambda_2/\lambda_3} \cdot A_2 \exp(i\delta z)$ and the coupling coefficient $q = -i\kappa_3 \sqrt{\lambda_3/\lambda_2} A_1$, where δ is the wavenumber detuning, A_j, λ_j and n_j, the normalized electrical field, wavelength, and refractive index of the waves with frequency f_j, respectively, and κ_3 is the nonlinear coupling coefficient. The wavenumber detuning is related to the phase mismatching between the interacting waves by $\delta = \Delta k/2$, where $\Delta k = 2\pi\left(n_3/\lambda_3 - n_2/\lambda_2 \pm n_1/\lambda_1 \pm 1/\Lambda\right)$ is the phase mismatching parameter for SFG ('−') or DFG ('+') and Λ is the poling period. The nonlinear coefficient κ_3 is defined by [32]

$$\kappa_3 = \frac{2\pi}{\lambda_3}\sqrt{\frac{2}{n_1 n_2 n_3 c \varepsilon_0 A_{\text{eff}}}}\, d_{\text{eff}} \tag{1}$$

with c and ϵ_0 the speed of light and electrical permittivity in vacuum, A_{eff} the effective cross section of the nonlinear interaction and d_{eff} the effective nonlinear coefficient.

The evolution of A and B modes in a uniform segment (constant Λ and q) located between the positions z and $z + \Delta z$ is modeled by [30]

$$\begin{bmatrix} A(z+\Delta z, \delta) \\ B(z+\Delta z, \delta) \end{bmatrix} = T \cdot \begin{bmatrix} A(z, \delta) \\ B(z, \delta) \end{bmatrix} \tag{2}$$

where T is a transfer matrix given by

$$T = \begin{bmatrix} \cos(\gamma\Delta z) - i\dfrac{\delta}{\gamma}\sin(\gamma\Delta z) & \dfrac{q}{\gamma}\sin(\gamma\Delta z) \\ -\dfrac{q^*}{\gamma}\sin(\gamma\Delta z) & \cos(\gamma\Delta z) + i\dfrac{\delta}{\gamma}\sin(\gamma\Delta z) \end{bmatrix}. \tag{3}$$

In (3), γ is related to δ and q through $\gamma^2 = \delta^2 + |q|^2$. The transfer matrix given by (3) is now identical to the one describing co-directional grating-assisted couplers even though it was devised for SFG. In addition, if A_1 is replaced by its complex conjugate, (3) is also valid for DFG.

The discrete coupling model allows decomposition of T into the product of two transfer matrices, T^p describing pure propagation with dispersive effects, and T_k^c the discrete coupling at the k^{th} scattering point. The two transfer matrices are given by (4) and (5).

$$T^p = \begin{bmatrix} e^{-i\delta\Delta z} & 0 \\ 0 & e^{i\delta\Delta z} \end{bmatrix}. \tag{4}$$

$$T_k^c = \frac{1}{\sqrt{1+|\rho_k|^2}} \begin{bmatrix} 1 & -\rho_k^* \\ \rho_k & 1 \end{bmatrix}. \tag{5}$$

In (4), the matrix is obtained by assuming no nonlinear interaction between the modes, which can be described by letting $q \to 0$. In (5), $\rho_k = -q_k^* \tan(|q_k|\Delta z)/|q_k|$ is a cross coupled power coefficient between the interacting modes, and T_k^c is obtained assuming strong nonlinear coupling in a single scattering point ($|q| \to \infty$), so that $\gamma \approx |q|$ and $\delta/\gamma \approx 0$ [30].

The aim of the LPA is to obtain ρ_k for each layer, and then the coupling coefficients q_k through the relation $q_k =$

3894 JOURNAL OF LIGHTWAVE TECHNOLOGY, VOL. 31, NO. 23, DECEMBER 1, 2013

$-\rho_k^* \mathrm{atan}\left(|\rho_k|\right) / \left(\Delta z\,|\rho_k|\right)$. Since d_{eff} is proportional to q_k, the output coupling coefficients of the LPA can be transduced into a physical property of the PPLN. In order to determine ρ_k, a time-domain description of the discrete mode coupling is assumed. Therefore, it is convenient to define the discrete Fourier transform (DFT) of A at the k-th scattering point by

$$A_k(\delta) = \sum_{\tau=0}^{N} a_k(\tau)\, e^{i2\delta\tau\Delta z} \tag{6}$$

with $\tau = 0, 1, \ldots, N$ a time variable, N the total number of layers and $a_k(\tau)$ the Fourier coefficients at the k-th scattering point. A similar Fourier transform is defined for $B_k(\delta)$, considering now $b_k(\tau)$ as the Fourier coefficients.

Let us assume that A and B are normalized to one, a time frame coincident to the propagation of A, no sum-frequency wave at the input to the PPLN ($A_0(\delta) = 0$ and $a_0(\tau) = 0$) and a unit impulse entering the PPLN in the B mode ($B_0(\delta) = 1, b_0(0) = 1$ and $b_0(\tau \neq 0) = 0$). In the first scattering point (layer 0), part of the impulse is converted to the A mode through SFG or DFG. Then, both modes propagate along layer 1 and the B mode is delayed by a τ time unit due to the dispersive effects. As in each scattering point part of the signal is exchanged between the two modes, at the end of the PPLN A and B consist of several contributions, corresponding to different possibilities of propagation in the A or B mode in each layer. In the adopted time frame, each contribution arrives at different time instants at the end of the PPLN, depending on the number of layers travelling in the B mode. It should be noted at this point that the delay between A and B is a consequence of the specific definition of these variables relatively to A_3 and A_2. In fact, changing back to A_3 and A_2 is equivalent to compensating the dispersive effects of T^p and the time delay.

Replacing A and B by their Fourier transform, (2) may be rewritten as [30]

$$\begin{bmatrix} a_k(\tau) \\ b_k(\tau) \end{bmatrix} = T_k^c \cdot \begin{bmatrix} a_{k-1}(\tau) \\ b_{k-1}(\tau - 1) \end{bmatrix}. \tag{7}$$

In (7), the term $b_{k-1}(\tau - 1)$ is delayed by one time unit resulting from the effect of the dispersive matrix in the time frame adopted. However, as layer 0 is just a scattering point, b_0 is not delayed and $b_0(\tau - 1)$ in (7) must be replaced by $b_0(\tau)$.

The first contribution arriving at the end of the PPLN, $a_N(0)$, corresponds to the part of the input impulse that is scattered in layer 0 and propagates in the A mode until the last scattering point without exchanging power with the B mode. With this in mind, one may use (7) to obtain the Fourier coefficients of the N^{th} layer. After some algebraic manipulation, the discrete cross coupling coefficient of the N^{th} layer is given by [30]

$$\rho_N = \frac{b_N(0)}{a_N(0)} \tag{8}$$

where $a_N(0)$ and $b_N(0)$ are obtained simply by performing an inverse DFT of the target spectral response of the device.

Now that the cross coupling term is known for the N^{th} layer, the next step of the algorithm is to calculate the coefficients $a_{N-1}(\tau)$ and $b_{N-1}(\tau - 1)$ using (7). Afterwards, a similar physical interpretation can be assumed obtain ρ_{N-1} replacing $a_N(0)$ and $b_N(0)$ by $a_{N-1}(0)$ and $b_{N-1}(0)$ in (8). The remaining ρ_k coefficients are obtained by repeating this procedure.

Although the implementation of this algorithm is simple and straightforward, special care must be taken with the design of $A_N(\delta)$ and $B_N(\delta)$. For instance, steep transitions in the target spectral response may result in undesired oscillations in the final response due to the Gibbs phenomenon [30], [33]. However, standard finite impulse response (FIR) filter design techniques such as windowing can be used to reduce these oscillations [33]. Furthermore, $A_N(\delta)$ and $B_N(\delta)$ cannot be chosen independently. If $A_N(\delta)$ is already defined, the magnitude of $B_N(\delta)$ is automatically given by $|A_N(\delta)|^2 + |B_N(\delta)|^2 = 1$. However, this expression does not provide any relation for the phase of $B_N(\delta)$. A common approach to define it is to find the minimum-phase function, given by the discrete Hilbert transform of $\ln\left(|B_N(\delta)|\right)$ [30].

A. Deleted-Reversal Method

The outputs of the LPA are complex coupling coefficients, q_k, whose magnitude may take any value ranging from 0 to $+\infty$. The coupling coefficients must be transduced into a physical property to produce a real device. For FBGs, the coupling coefficient is transduced to a refractive index variation [30]. In the case of PPLN waveguides, this can be done by changing the poling pattern. However, the nonlinear coefficient in a PPLN device can only assume two distinct values, $\pm d_{33}$, where d_{33} is the highest component of the nonlinear coefficient tensor, considering all interacting waves polarized along the optical axis of the lithium niobate crystal. The DRM [26] is a possible and effective solution to overcome this problem. A maximum effective nonlinear coefficient is achieved by enabling all possible periodic inversions. However, a target lower effective nonlinear coefficient can be obtained by deleting some of the periodic inversions. This is the operation principle of the DRM. In this method, some of the periodic inversions are not performed (deleted) so the effective nonlinear coefficient is reduced.

Consider that the effective nonlinear coefficient may be expressed as $d_{\mathrm{eff}}(z) = (2/\pi)\, d_{33} d_{\mathrm{ap}}(z) \exp\left[i\phi(z)\right]$, where d_{ap} is an apodization function ($0 \leq d_{\mathrm{ap}} \leq 1$) and ϕ represents the phase modulation. The relation between q, d_{ap} and ϕ is given by

$$d_{\mathrm{ap}}(z) e^{i\phi(z)} = \frac{i}{4 d_{33}} \sqrt{\frac{c\varepsilon_0 A_{\mathrm{eff}} \lambda_2 \lambda_3 n_1 n_2 n_3}{2}} \cdot \frac{q(z)}{A_1}. \tag{9}$$

The version of the DRM presented in this article assumes that if all inversions are deleted, the efficiency is extremely low and the effective nonlinear coefficient is 0. Otherwise, the normalized effective nonlinear coefficient is 1. Thus, the goal of the DRM is to create a binary vector, d_{bin}, whose elements are 0 if the reversal is deleted, or 1 in the opposite case. The important question now is how to relate d_{bin} and d_{ap}. In this paper, the choice of deleting or not the reversal in each successive point/section takes into account the entire structure that has been previously calculated in order to minimize the difference

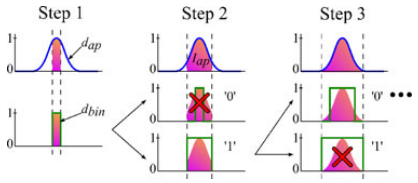

Fig. 2. Illustration of the DRM used in this paper.

between d_{ap} and d_{bin} (Fig. 2). Therefore, the following algorithm can be implemented:

1) Find the position where d_{ap} reaches its maximum value and assume 1 for the corresponding element of d_{ap};
2) Extend the domain of interest to a neighboring section and evaluate I_{ap}.

$$I_{\mathrm{ap}} = \int_{z_i}^{z_j} d_{\mathrm{ap}}(z)dz \tag{10}$$

where z_i and z_j are the starting and ending positions of the region of interest.

3) Consider that d_{bin} in the new section is 0 or 1 and evaluate I_0 and I_1

$$I_{0,1} = \sum_{k=i}^{j-1} \frac{d_{\mathrm{bin}(0,1)}(z_k) + d_{\mathrm{bin}(0,1)}(z_{k+1})}{2} \cdot \Delta z. \tag{11}$$

4) Choose 0 or 1 for the new region depending on the lowest value of $|I_{\mathrm{ap}} - I_0|$ or $|I_{\mathrm{ap}} - I_1|$;
5) Repeat 1) to 4) until the entire grating is evaluated.

In general, the phase modulation function, ϕ, is continuous and must be sampled into a set of discrete values in order to produce a real device. Afterwards, phase modulation is implemented simply by shifting the place within the period length where the domain inversion occurs.

B. Limitations

Some of the limitations of the LPA were already mentioned above, namely the Gibb's phenomenon. The capability to design a PPLN device whose spectral response includes steep transitions and/or narrow bandwidth details is comparable to the design of an FIR filter. In FIR filters, fine filtering details in the frequency domain require a long impulse response, which in turn requires a long PPLN. For instance, the narrowest bandpass filter (BPF) that can be achieved with the LPA corresponds to the case of a uniform PPLN (constant κ and Λ over the entire device). The bandwidth of a uniform PPLN is determined by the bandwidth of $\mathrm{sinc}^2(\gamma L)$, where L is the length of the device.

One should note that (9) implies that A_1 must be properly chosen to keep d_{ap} constrained between 0 and 1. If the target spectral conversion bandwidth and efficiency are too high and/or the length too short, the optical power of the pump may scale up to unreasonable values. However, as it will be shown in Section III, the variation of A_1 from the value provided by (9) within a certain range of values does not significantly distort the spectral shape of the PPLN response, but only the magnitude of the SFG or DFG conversion efficiency (defined as the ratio between the powers of the converted wave and the input signal).

Another aspect that must be considered is the limit of the no pump depletion approximation. In [32], a simple expression relating the length of the PPLN and the input power of the signal and pump waves, P_2 and P_1 respectively, was proposed. This relation is given by (11).

$$P_2 < p\frac{(\lambda_1 \pm \lambda_2)\kappa_2}{\lambda_2 k_3 \sin^2\left(\sqrt{\kappa_2\kappa_3 P_1} L\right)} P_1. \tag{12}$$

In (11), p is the ratio between the maximum acceptable pump power drop and its initial value. The signs "+" and "−" correspond to SFG and DFG, respectively. As a rule of thumb, the no pump depletion approximation yields accurate results considering maximum values of $p \approx 10\%$ [32]. As uniform PPLNs have the highest conversion efficiency, this relation may be considered a conservative estimate for other devices with more complex poling patterns.

The design of complex PPLN devices requires precise knowledge of the refractive index dispersion in order to determine the poling period and the wavenumber detuning. In PPLN waveguides, waveguide dispersion may play an important role in the final conversion response and the poling pattern. As the waveguide is typically manufactured after the poling step [12], the impact of waveguide dispersion must be properly estimated prior to poling and waveguide production.

For applications in telecommunications, cSFG/DFG plays a more important role than simple SFG or DFG interactions as all input signals are preferably in the 1.55 μm band [17], [22]. The proposed LPA is devised for non-cascaded SFG or DFG interactions. Consequently, the spectral response for cSFG/DFG is not identical to the target response. This subject is further discussed in the next section.

Finally, the LPA-DRM is limited to fabrication tolerances in the production of the target poling pattern and in the uniformity of the waveguide.

III. Numerical Design Examples

In this section, simulations of PPLN devices designed by the LPA-DRM are presented. Two different types of devices are studied: quasi-rectangular filters and multichannel PPLNs. For all the simulations presented in this section, the refractive index dispersion presented in [34] for a 5% MgO-doped lithium niobate crystal at 25 °C is assumed. It is also assumed L = 4.5 cm, Λ = 19.39 μm, A_{eff} = 100 μm^2, λ_1 = 1545 nm and d_{33} = 23.6 pm/V. The power of the input signal is 10 mW for all simulations. A common fourth-order Runge-Kutta algorithm was employed to solve the coupled mode equations for SFG and cSFG/DFG presented in [32]. The integration step used in the simulations was of the order of $\Lambda/100$.

In order to reduce the Gibb's phenomenon, a windowing technique was employed to design the target spectral response of the quasi-rectangular PPLNs. In this paper, a Tukey window [35] with a ratio of taper to constant sections of 0.7 was adopted.

3896 JOURNAL OF LIGHTWAVE TECHNOLOGY, VOL. 31, NO. 23, DECEMBER 1, 2013

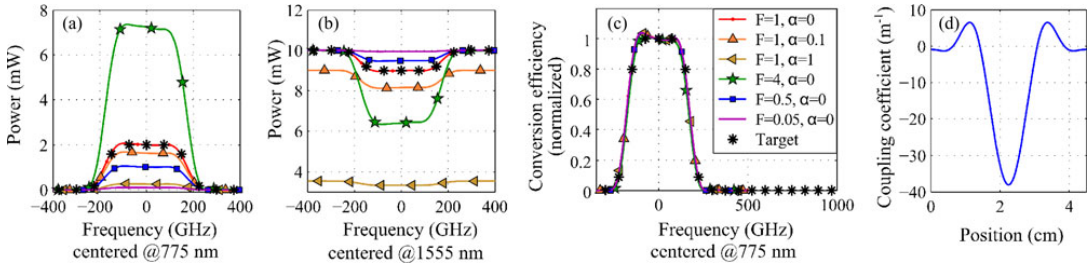

Fig. 3. (a) Output power of the SFG and (b) signal waves for the 400 GHz bandpass PPLN considering different ratios between the pump power injected into the PPLN and the ideal value provided by (9), F, and different attenuation coefficients, α (in dB/cm). (c) Normalized conversion efficiency (relatively to the central frequency). (d) Variation of the coupling coefficient along the PPLN.

A. *Quasi-Rectangular Filter*

The simulated spectral response of a 400 GHz quasi-rectangular bandpass PPLN device designed numerically by the LPA-DRM is shown in Fig. 3, for different attenuation coefficient and pump power values. The results of the simulations show that the LPA-DRM was able to effectively design a PPLN device with target filtering characteristics. In addition, these results show that propagation losses and deviations of the pump power from the value provided by (9), which is 256 mW in this case, changes the output power of the SFG interaction (Fig. 3(a)), as expected. However, the shape of the spectral response is not distorted as evident in the normalized conversion efficiency plots shown in Fig. 3(c). This property is essential for practical devices, since without it, the pump power would have to be kept within tight constraints. The output power spectrum of the signal wave is depicted in Fig. 3(b). As expected, the output power spectra shown in Fig. 3(a) and (b) are complementary, provided that the output power of the SFG wave is multiplied by a scaling factor of $\lambda_3/\lambda_2 \approx 1/2$. This scaling factor accounts for the ratio of energies carried by an identical number of SFG and pump photons.. The coupling coefficient for the quasi-rectangular bandpass PPLN is purely real and varies according to a *sinc* function (Fig. 3(d)), as reported in [30] for co-directional grating-assisted couplers.

A 1 THz quasi-rectangular bandpass PPLN with 20% SFG conversion efficiency was also designed. The results of numerical simulations on the spectral response of this device are shown in Fig. 4(a). In this case, the LPA-DRM is also able to design the desired device. However, the required pump power to have 20% conversion efficiency is now 1.70 W, about 6.6 times higher than for the 400 GHz PPLN. Hence, a tradeoff between pump power, conversion efficiency and operational bandwidth is evident. The poling patterns of the 400 GHz and 1 THz quasi-rectangular PPLNs obtained by the LPA and the DRM are shown in Fig. 4(c) and (d). For both cases, quasi-rectangular response is achieved by deleting some of the periodic inversions near the edges of the PPLN, combined with π phase shifts for the phase modulation. As the number of deleted poling inversions is higher for the 1 THz PPLN, higher pump power is required to achieve the same efficiency.

As previously stated, the LPA is not optimized for cSFG/DFG interactions. In order to evaluate the impact of this aspect, an additional DFG pump was introduced in the simulations, using the same poling pattern. Therefore, a new signal (cSFG/DFG signal) with frequency $f_5 = f_3 - f_4 = f_2 + f_1 - f_4$ is generated, where f_4 is the frequency of the DFG pump. The power and wavelength of the DFG wave was 0.5 W and 1543 nm, respectively. In Fig. 4(b) the normalized conversion efficiency for the SFG wave and the signal converted through cSFG/DFG are compared. Although the normalized conversion efficiency for the SFG signal agrees well with the designed filter, this is not the case for the wave converted through cSFG/DFG. According to the simulations, the conversion bandwidth for cSFG/DFG is higher than then the designed one. Also, the lateral limits of the spectral response are not steep transitions, and the efficiency slowly decreases for frequencies higher than the cut-off frequency of the designed filter. In these transition regions, undesirable peaks of the conversion efficiency for cSFG/DFG are observed. The root cause of these two effects is the cascaded

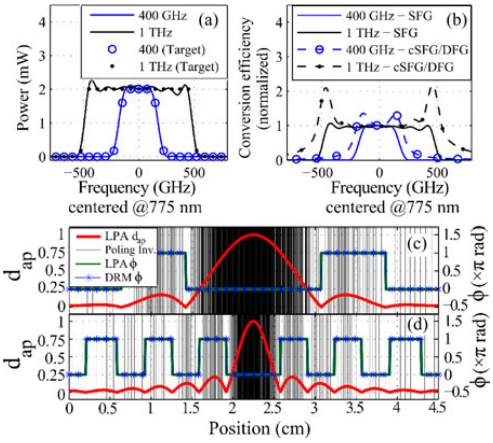

Fig. 4. (a) Output power of the SFG signal for the 400 GHz and 1 THz quasi-rectangular bandpass PPLN. (b) Normalized conversion efficiency spectra of the SFG (centered at 775 nm) and cSFG/DFG (centered at 1557.1 nm) signals in a cSFG/DFG interaction, considering the 400 GHz and 1 THz bandpass PPLNs. d_{ap} and ϕ obtained by the LPA, and position of the poling inversions and ϕ provided by the DRM for (c) 400 GHz and (d) 1 THz quasi-rectangular PPLN. In (a) and (b), it was assumed lossless propagation and pump power value satisfying (9).

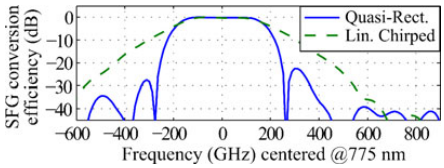

Fig. 5. Normalized SFG conversion efficiency for the 400 GHz quasi-rectangular device and an ALC- PPLN. The DRM was used to implement the apodization function of the ALC-PPLN.

nature of the interaction which leads to a more complex evolution of the signals. Due to the no pump depletion approximation, SFG and DFG can be described as simple linear systems. However, cSFG/DFG is not a linear process and the LPA cannot describe it accurately. Depending on the specific application, the lateral decaying tails and increased efficiency at the transition regions may introduce deleterious wavelength crosstalk and considerably affect the overall performance of the system. An obvious solution to overcome these limitations is to avoid the cascaded interactions along the PPLN using two different PPLN devices with target spectral responses in a tandem configuration. Thus, SFG occurs only in the first PPLN and DFG in the second device.

In Fig. 5, the normalized SFG conversion efficiency of the 400 GHz quasi-rectangular PPLN designed by the LPA-DRM is compared to an apodized linearly chirped (ALC) PPLN [36]. In ALC-PPLNs the conversion bandwidth is increased by varying the poling period along the device according to the relation $\Lambda(z) = \Lambda_0 + \beta \cdot z$, with Λ_0 the poling period at the beginning of the PPLN and β the chirp parameter. In addition, apodization techniques are also used to reduce typical conversion efficiency ripples found in common chirped PPLNs [36]. We assumed $\Lambda_0 = 19.35$ μm, $\beta = 8.6$ nm/cm and a Tukey window [35] with a ratio of taper to constant sections of 0.53 for the apodization function to obtain the same spectral half-width at full maximum and maximum ripple amplitude in the main peak. The results of the simulations show that the quasi-rectangular PPLN has much steeper transition edges than those of the ALC-PPLN, making it more appropriate for applications in WDM systems where interchannel crosstalk is an issue. However, the efficiency of the simulated ALC-PPLN would be about 5 dB higher because the number of deleted poling inversions is lower than that of the quasi-rectangular PPLN.

B. Multichannel QPM

The LPA-DRM was also used to design multichannel QPM devices. A multichannel PPLN is a device whose spectral response exhibits several QPM peaks, and can be used for multichannel wavelength conversion [28]. In [28], multichannel PPLNs were designed using a downhill simplex method to obtain an appropriate phase modulation function which controls the poling pattern of the device. In that work, a good initial guess for the phase modulation function was an essential requirement to guarantee convergence of the method and to keep the computational effort within affordable limits. The proposed LPA-DRM is also able to design multichannel PPLNs, with greater simplicity than in [28]. With the LPA, complex optimization techniques are avoided and only a simple discrete Fourier transform of the target filtering function is required. In addition, the LPA does not require any initial guess.

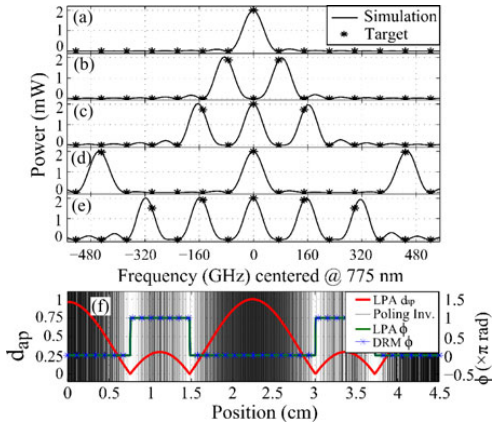

Fig. 6. Simulated spectral response for SFG of: (a) a uniform PPLN and multichannel PPLNs with (b) two channels, (c) three channels with 150 GHz spacing between the channels, (d) three channels with 450 GHz spacing between each channel, and (e) five channels. (f) d_{ap} and ϕ obtained by the LPA, and position of the poling inversions and ϕ provided by the DRM for the multichannel PPLN shown in (c).

The multichannel PPLNs presented in this section were designed by adopting a filter with multiple narrow transmission bands as the target spectral response. Simulations of PPLNs with 1, 2, 3 and 5 QPM peaks were performed considering pump power values of 9.4, 36, 76 and 206 mW, respectively, in order to obtain a maximum conversion efficiency of 20%.

The results of the simulations are shown in Fig. 6. These results show that the LPA-DRM was able to design multichannel PPLNs, with high accuracy and flexibility. As it has been discussed in Section II, the length of the PPLN determines the maximum degree of detail of its spectral response. For the 4.5 cm PPLN considered in the simulations, the spectral response can be designed with a detail resolution up to approximately 75 GHz (the distance between consecutive "$*$" design points in Fig. 6). This value is approximately equal to the spectral bandwidth of a uniform PPLN. The spectral bandwidth of each QPM peak of the PPLNs designed in this subsection is approximately the same, equal to the value for a uniform grating. Multichannel QPM PPLNs with wider QPM peaks can also be designed with the LPA-DRM, which is an additional advantage over the method proposed in [28]. However, the required pump power to achieve the same conversion efficiency may significantly increase, as reported in the previous subsection.

The multichannel PPLNs designed by the LPA-DRM do not require a complex variation of the phase modulation function as it is shown in Fig. 6(f). In this case, multiple QPM resonances are achieved by a specific apodization profile combined with simple π phase-shifts rather than complex phase modulation functions.

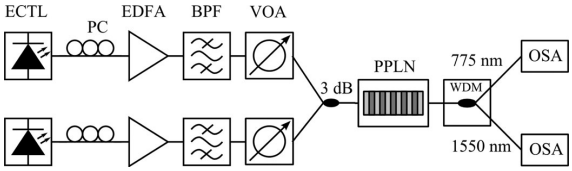

Fig. 7. Experimental setup used to evaluate the spectral response of the PPLN device.

However, the efficiency of each peak decreases by a factor of K^2 compared to uniform PPLNs, where K is the number of peaks. This is a major drawback compared to method presented in [28], where the efficiency drops only by a factor of K. The reduced efficiency is a direct consequence of decreasing the effective nonlinear coefficient in some locations of the PPLN. This drawback limits the application of LPA-DRM to the design of multichannel PPLNs with a few number of QPM resonances.

IV. Experimental 400 GHz Quasi-Rectangular PPLN

In this section, we experimentally investigate the spectral properties of four manufactured PPLN waveguides designed with the LPA-DRM. The poling pattern of the device was designed according to the 400 GHz quasi-rectangular bandpass PPLN simulated in the previous section. A lithium niobate substrate doped with 5% of MgO was used in order to prevent photorefractive damage at high pumping power. An annealed proton-exchange waveguide was included to increase the efficiency. The poling period of the different PPLN waveguides are 19.1 for waveguides 1and 2, and 19.2 μm for waveguides 3 and 4. The propagation losses of the characterized waveguides were of about 0.1 dB/cm. The length of the device was 4.5 cm.

The experimental set-up used to characterize the spectral response of the PPLN waveguides is presented in Fig. 7. Light emitted by two external cavity tunable lasers (ECTLs) was combined in a 3 dB coupler after passing through a polarization controller (PC), an erbium-doped fiber amplifier, a 1 nm BPF and a variable optical attenuator (VOA). The PCs, BPFs and VOAs were used to align the polarization of the waves to the optimal axis of the PPLN, remove the excess amplified spontaneous emission noise, and control the power at the input of the device, respectively. Then, the interacting waves were injected into the PPLN waveguide through free-space coupling with total insertion losses of about 4 dB. Reduced photorefractive damage provided by MgO doping allowed low temperature operation (25 °C) as previously reported in [15]. After nonlinear interaction in the PPLN waveguide, a WDM coupler was used to separate the signal of the spectral region of ∼775 nm from the remaining waves. Two optical spectrum analyzers were used to evaluate the spectral response of the PPLN.

Although the device was designed for SFG, the spectral response for SHG of waveguide 1 was also evaluated. In the former case, the power of the signal and pump waves were 17.33 and 26.47 dBm, respectively. The wavelength of the pump was kept at 1553 nm for waveguides 1 and 2 and 1556 nm for waveguides 3 and 4. For the signal wave it was varied from 1542 to 1552 for waveguides 1 and 2, and from 1545 to 1555 nm for waveguides 3 and 4. For SHG, one of the ECTLs was turned off and the input power was set to 22.5 dBm. In this case, the wavelength was varied from 1545 to 1555 nm. The measured SFG and SHG normalized conversion efficiencies (relatively to the central frequency) are shown in Fig. 8.

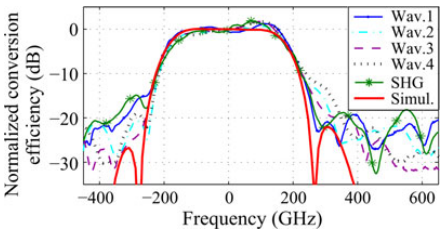

Fig. 8. Simulated and experimental normalized conversion efficiency for SFG of four 400 GHz quasi-rectangular PPLN waveguides. The SHG curve corresponds to waveguide 1. The frequency is centered at 774.8, 774.6, 776.6, 776.4 nm for waveguides 1, 2, 3 and 4, respectively.

The normalized conversion efficiency spectrum obtained for both SFG and SHG for waveguide 1 is similar meaning that even though the PPLN is designed for SFG, one can expect similar spectral responses for SHG. This was also observed in numerical simulations for both quasi-rectangular and multichannel PPLNs. The SHG conversion efficiencies, defined as the ratio between the power of the second harmonic and the square of the fundamental wave power, are 21.5, 15.7, 20.5 and 31.2%/W for waveguides 1, 2, 3 and 4, respectively.

The measured spectral response of the experimental devices is well matched to the simulated target response, especially for waveguide 1. Some discrepancies are evident in the experimental waveguides such as lower peak to side lobe ratios and asymmetric, non-flat conversion efficiency within the main peak. For waveguides 2 and 4, the peak to side lobes ratio was less than 15 dB instead of more than 20 dB predicted by numerical simulation. In terms of the total variation of the normalized conversion efficiency within the main peak, waveguides 3 and 4 have the worst performance with a total variation of 3 dB. In these cases, the efficiency increases for higher frequencies. For waveguides 1 and 2, the total variation is of about 1.5 dB. Similar results were observed at lower pump powers and with the temperature controller turned off, which excludes the possibility of local heating or temperature gradients to be the cause of such differences. Since we observed variations in the spectral response measured in waveguides that are supposed to have the same poling pattern, we believe that the differences between target and experimental responses are mainly due to fabrication errors such as imperfections of the poling pattern, and random longitudinal variation of the effective index and effective area along the waveguide.

V. Conclusion

The combination between the LPA with the DRM to design the poling pattern of a PPLN device to obtain a target spectral response is presented. The proposed method allows designing

several types of PPLN devices with simplicity and flexibility, providing feasible poling designs. Nonetheless, it should be noted that fundamental limitations of PPLNs lead to device-length-based tradeoffs between conversion efficiency, operational bandwidth, and frequency/wavelength resolution of the filter design. These limitations do not arise from the LPA-DRM itself, but from the intrinsic properties of PPLN devices, and as such may not be easily avoided. In addition, relatively tight control of the poling patterns is required, particularly to obtain truly flat spectral response, and especially to obtain the desired significant side-lobe suppression.

In order to assess the effectiveness of the proposed method, quasi-rectangular BPFs and multichannel PPLNs were numerically simulated, proving the versatility of the method. Even though only two types of devices were discussed in this paper, the proposed method should be able to design the poling pattern according to an arbitrary target spectral response, provided that such response is feasible within the constraints imposed by the physical properties of PPLNs and filter design techniques. In addition, no initial guess for the poling pattern is required, contrarily to other poling design techniques based on optimization algorithms.

Regarding the experimental PPLN waveguides produced in this paper, some differences between its spectral response and numerical simulations were found, namely lower peak to side lobe ratio, and asymmetric conversion efficiency of the main peak. These differences are due to fabrication issues which emphasize the importance development, refinement, and mastery of a good manufacturing process.

It is hoped that further investigation on new poling designs and spectral responses of PPLNs will certainly contribute for the advance of PPLN-based OSP techniques, and the LPA-DRM will be an important tool for originating those designs.

ACKNOWLEDGMENT

The authors would like to thank J. Hirohashi, Oxide Corp., Hokuto, Japan, for the fruitful discussions and for producing the PPLN device.

REFERENCES

[1] O. Yilmaz, S. Nuccio, S. Khaleghi, J.-Y. Yang, L. Christen, and A. Willner, "Optical multiplexing of Two 21.5 Gb/s DPSK signals into a single 43 Gb/s DQPSK channel with simultaneous 7-fold multicasting in a single PPLN waveguide," presented at the Opt. Fiber Commun., San Diego, CA, USA, 2009, Paper OThM4.

[2] H. Tan, Q. Nguyen-The, M. Matsuura, and N. Kishi, "Reconfigurable all-optical OTDM-to-WDM conversion using a multiwavelength ultrashort pulse source based on Raman compression," *J. Lightw. Technol*, vol. 30, no. 6, pp. 853–863, Mar. 2012.

[3] A. Willner, O. Yilmaz, J. Wang, X. Wu, A. Bogoni, L. Zhang, and S. Nuccio, "Optically efficient nonlinear signal processing," *IEEE J. Sel. Topics Quantum Electron.*, vol. 17, no. 2, pp. 320–332, Mar. 2011.

[4] R. Nogueira, M. Drummond, C. Marques, A. Albuquerque, R. Monteiro, A. Navarro, A. Teixeira, P. Andre, M. Violas, P. Monteiro, C. Sterner, and P. Fonjallaz, "All-optical signal processing techniques with fiber based devices," in *Proc. Int. Conf. Transparent Opt. Netw.*, 2009, pp. 1–2.

[5] P. Seddighian, V. Torres-Company, and L. Chen, "Simultaneous demodulation and demultiplexing of multi-rate WDM DPSK signals using a programmable wavelength-selective switch," *Opt. Exp.*, vol. 18, no. 11, p. 11657, May 2010.

[6] M. Galili, L. OxenlØwe, H. Mulvad, A. Clausen, and P. Jeppesen, "Optical wavelength conversion by cross-phase modulation of data signals up to 640 Gb/s," *IEEE J. Sel. Topics Quantum Electron.*, vol. 14, no. 3, pp. 573–579, May/Jun. 2008.

[7] J. Kakande, A. Bogris, R. Slavik, F. Parmigiani, D. Syvridis, P. Petropoulos, and D. J. Richardson, "First demonstration of all-optical QPSK signal regeneration in a novel multi-format phase sensitive amplifier," in *Proc. Eur. Conf. Opt. Commun.*, 2010, pp. 1–3.

[8] B. Zsigri, C. Peucheret, M. Nielsen, and P. Jeppesen, "Demonstration of broadcast, transmission, and wavelength conversion functionalities using photonic crystal fibers," *IEEE Photon. Technol. Lett.*, vol. 18, no. 21, pp. 2290–2292, Nov. 2006.

[9] B. Eggleton, T. Vo, R. Pant, J. Schr, M. D. Pelusi, D. Yong Choi, S. J. Madden, and B. Luther-Davies, "Photonic chip based ultrafast optical processing based on high nonlinearity dispersion engineered chalcogenide waveguides," *Laser Phot. Rev.*, vol. 6, no. 1, pp. 97–114, Jan. 2012.

[10] B. Lee, A. Biberman, A. Turner-Foster, M. Foster, M. Lipson, A. Gaeta, and K. Bergman, "Demonstration of broadband wavelength conversion at 40 Gb/s in silicon waveguides," *IEEE Photon. Technol. Lett.*, vol. 21, no. 3, pp. 182–184, Feb. 2009.

[11] C. Porzi, G. Meloni, M. Secondini, L. Poti, G. Contestabile, and A. Bogoni, "All-optical switching of QPSK signals for 100 G coherent systems," *J. Lightw. Technol.*, vol. 30, no. 18, pp. 3010–3016, Sep. 2012.

[12] C. Langrock, S. Kumar, J. McGeehan, A. Willner, and M. Fejer, "All-optical signal processing using $\chi(2)$ nonlinearities in guided-wave devices," *J. Lightw. Technol.*, vol. 24, no. 7, pp. 2579–2592, Jul. 2006.

[13] J. Shen, S. Yu, P. Liao, Z. Chen, W. Gu, and H. Guo, "All-optical full-adder based on cascaded PPLN waveguides," *IEEE J. Quantum Electron.*, vol. 47, no. 9, pp. 1195–1200, Sep. 2011.

[14] A. Bogoni, X. Wu, S. R. Nuccio, and A. E. Willner, "640 Gb/s all-optical regenerator based on a periodically poled lithium niobate waveguide," *J. Lightw. Technol.*, vol. 30, no. 12, pp. 1829–1834, Jun. 2012.

[15] M. Drummond, J. Reis, R. Nogueira, P. Monteiro, A. Teixeira, S. Shinada, N. Wada, and H. Ito, "Error-free wavelength conversion at 160 Gbit/s in PPLN waveguide at room temperature," *Electron. Lett.*, vol. 45, no. 22, p. 1135, 2009.

[16] K. Lee, F. Parmigiani, S. Liu, J. Kakande, P. Petropoulos, K. Gallo, and D. Richardson, "Phase sensitive amplification based on quadratic cascading in a periodically poled lithium niobate waveguide," *Opt. Exp.*, vol. 17, no. 22, pp. 20393–20400, Oct. 2009.

[17] H. Furukawa, A. Nirmalathas, N. Wada, S. Shinada, H. Tsuboya, and T. Miyazaki, "Tunable all-optical wavelength conversion of 160-Gb/s RZ optical signals by cascaded SFG-DFG generation in PPLN waveguide," *IEEE Photon. Technol. Lett.*, vol. 19, no. 6, pp. 384–386, Mar. 2007.

[18] J. Wang and J. Sun, "All-optical logic XOR gate for high-speed CSRZ-DPSK signals based on cSFG/DFG in PPLN waveguide," *Electron. Lett.*, vol. 46, no. 4, p. 288, Feb. 2010.

[19] F. Gomez-Agis, L. Oxenlowe, S. Kurimura, C. Ware, H. Hansen Mulvad, M. Galili, and D. Erasme, "Ultrafast phase comparator for phase-locked loop-based optoelectronic clock recovery systems," *J. Lightw. Technol.*, vol. 27, no. 13, pp. 2439–2448, Jul. 2009.

[20] A. Bogoni, X. Wu, I. Fazal, and A. Willner, "All-optical time domain 160 Gb/s ADD/DROP based on pump depletion and nonlinearities in a single PPLN waveguide," in *Proc. Opt Fiber Commun.*, San Diego, CA, USA, 2009, pp. 1–3.

[21] J. Wang, H. Fu, D. Geng, and A. Willner, "Single-PPLN-assisted wavelength-/time-selective switching/dropping/swapping for 100-GHz-spaced WDM signals," *Opt. Exp.*, vol. 21, no. 3, pp. 3756–3754, Feb. 2013.

[22] M. H. Chou, I. Brener, G. Lenz, R. Scotti, E. Chaban, J. Shmulovich, D. Philen, S. Kosinski, K. Parameswaran, and M. Fejer, "Efficient wide-band and tunable midspan spectral inverter using cascaded nonlinearities in $LiNbO_3$ waveguides," *IEEE Photon. Technol. Lett.*, vol. 12, no. 1, pp. 82–84, Jan. 2000.

[23] J. Wang, J. Sun, X. Zhang, D. Huang, and M. Fejer, "All-optical format conversions using periodically poled lithium niobate waveguides," *IEEE J. Quantum Electron.*, vol. 45, no. 2, pp. 195–205, Feb. 2009.

[24] B. Puttnam, D. Mazroa, S. Shinada, and N. Wada, "Phase-squeezing properties of non-degenerate PSAs using PPLN waveguides," *Opt. Exp.*, vol. 19, no. 26, pp. B131–B139, Nov. 2011.

[25] A. Albuquerque, B. Puttnam, M. Drummond, Á. Szabó, D. Mazroa, S. Shinada, N. Wada, and R. Nogueira, "Investigation of black-box

phase regeneration using single bi-directional PPLN waveguide," presented at the Opt. Fiber Commun. Conf., Anaheim, CA, USA, 2013, Paper OW4 C.2.

[26] J. Huang, X. Xie, C. Langrock, R. Roussev, D. Hum, and M. Fejer, "Amplitude modulation and apodization of quasi-phase-matched interactions," *Opt. Lett.*, vol. 31, no. 5, pp. 604–606, Mar. 2006.

[27] G. Lu, S. Shinada, H. Furukawa, N. Wada, T. Miyazaki, and H. Ito, "160-Gb/s all-optical phase-transparent wavelength conversion through cascaded SFG-DFG in a broadband linear-chirped PPLN waveguide," *Opt. Exp.*, vol. 18, no. 6, pp. 6064–6070, Mar. 2010.

[28] M. Asobe, O. Tadanaga, H. Miyazawa, Y. Nishida, and H. Suzuki, "Multiple quasi-phase-matched device using continuous phase modulation of $\chi^{(2)}$ grating and its application to variable wavelength conversion," *IEEE J. Quantum Electron.*, vol. 41, no. 12, pp. 1540–1547, Dec. 2005.

[29] J. Skaar and T. Erdogan, "On the synthesis of fiber Bragg gratings by layer peeling," *IEEE J. Quantum Electron.*, vol. 37, no. 2, pp. 165–173, Feb. 2001.

[30] J. Brenne and J. Skaar, "Design of grating-assisted codirectional couplers with discrete inverse-scattering algorithms," *J. Lightw. Technol.*, vol. 21, no. 1, pp. 254–263, Jan. 2003.

[31] Q. Zhang, X. Zeng, M. Wang, T. Wang, and X. Chen, "Retrieving quasi-phase-matching structure with discrete layer-peeling method," *Opt. Exp.*, vol. 20, no. 14, p. 15826, Jun. 2012.

[32] A. Albuquerque, M. Drummond, and R. Nogueira, "Transfer matrix and fourier transform methods for simulation of second-order nonlinear interactions in a PPLN waveguide," *J. Lightw. Technol.*, vol. 29, no. 24, pp. 3764–3771, Dec. 2011.

[33] A. Oppenheim, R. Schafer, and J. Buck, *Discrete Time Signal Processing*, 2nd ed. Englewood Cliffs, NJ, USA: Prentice-Hall, 1998.

[34] O. Gayer, Z. Sacks, E. Galun, and A. Arie, "Temperature and wavelength dependent refractive index equations for MgO-doped congruent and stoichiometric LiNbO3," *Appl. Phys. B*, vol. 91, no. 2, pp. 343–348, Apr. 2008.

[35] F. Harris, "On the use of windows for harmonic analysis with the discrete Fourier transform," *Proc. IEEE*, vol. 66, no. 1, pp. 51–83, Jan. 1978.

[36] A. Tehranchi and R. Kashyap, "Engineered gratings for flat broadening of second-harmonic phase-matching bandwidth in MgO-doped lithium niobate waveguides," *Opt. Exp.*, vol. 16, no. 23, pp. 18970–18975, 2008.

Authors' biographies not available at the time of publication.

Publication B

Single-pump, tunable wavelength conversion of 8×12.5 Gsymbol/s QPSK channels in a quasi-rectangular PPLN

A. Albuquerque, B. Puttnam, M. Drummond, S. Shinada, R. Nogueira, N. Wada

originally published in the proceedings of the *European Conference and Exhibition on Optical Communication (ECOC)*, London, UK, Sep. 2013, pp. P.2.10. Reprinted with the permission of IET.

Single-Pump, Tunable Wavelength Conversion of 8×12.5 Gsymbol/s QPSK Channels in a Quasi-Rectangular PPLN

André Albuquerque[(1)], Benjamin J. Puttnam[(2)], Miguel Drummond[(1)], Satoshi Shinada[(2)], Rogério Nogueira[(1)], and Naoya Wada[(2)]

[(1)] Instituto de Telecomunicações, University of Aveiro, Aveiro, Portugal, andrealbuquerque@av.it.pt
[(2)] National Institute of Information and Communications Technology, Koganei, Japan.

Abstract *We use a layer peeling algorithm to design and produce a PPLN with a 400GHz quasi-rectangular conversion response. Single-pump, tunable wavelength conversion of 8×12.5 Gsymbols/s QPSK channels in a 50GHz WDM grid is achieved with a maximum 3dB OSNR penalty.*

Introduction

The advantages of high efficiency, ultrafast response, compactness, room temperature operation, negligible spontaneous noise and frequency chirp in periodically poled lithium niobate (PPLN) waveguides make them attractive solutions for wavelength conversion and other optical signal processing functions in future fiber-optic communications systems[1–4].

Wavelength conversion in PPLN devices is usually based on cascaded second-harmonic generation (SHG) and difference-frequency generation (DFG), or cascaded sum-frequency generation (SFG) and DFG[1]. In the former case, the second harmonic of a pump wave interacts with the input signal through DFG providing broad operational bandwidth (in excess of 40 nm[1,5]), and enabling multichannel operation. However, the wavelength of the pump wave must be set to the wavelength where the quasi-phase matching (QPM) condition is satisfied (QPM wavelength) which excludes wavelength tunability of the converted signal. In wavelength converters based on cascaded SFG/DFG, the SFG signal generated by the interaction between the input signal and a pump interacts with a second pump through DFG[2]. In this case, tunability is achieved by changing the wavelength of the second pump, but broadband and/or multichannel operation is prevented as a consequence of limited operational spectral bandwidth of the SFG interaction, which is typically <0.5 nm [2].

Different strategies have been proposed to achieve both tunable, broadband/multichannel wavelength conversion. Some examples of those strategies comprise cascaded SHG/DFG in multiple QPM PPLNs[6] and increasing the operational bandwidth for SFG in cascaded SFG/DFG converters, either by applying a temperature gradient[7] or using aperiodical PPLNs[3]. In the latter cases, the QPM wavelength varies along the PPLN by changing the poling period or the temperature, which increases the conversion bandwidth. Significant oscillations of the conversion efficiency are typically observed using these approaches[3,8], thereby degrading the performance of the converter. In addition, these techniques provide very low control of the conversion response.

Here we investigate a PPLN waveguide designed with the layer peeling method to achieve quasi-rectangular spectral response with 400 GHz bandwidth. Using this device, we demonstrate multichannel, tunable wavelength conversion. The layer peeling method originally proposed to design grating-assisted couplers with target spectral responses[9], relies on dividing the PPLN into several uniform layers and computing the strength of the nonlinear interaction (which is related to the poling pattern) layer by layer, according to a target spectral response. To the best of our knowledge, this is the first time that the layer peeling method has been used to design the poling pattern of non-linear devices such as PPLNs. We show good agreement between the experimental results and predicted performance showing that this approach can be useful for the design of tunable wavelength converters and other non-linear optical signal processing applications in future optical networks.

Experimental set-up

The experimental set-up used to characterize the PPLN device is shown in Fig. 1, within the characterization set-up box. Light emitted by two external cavity tunable lasers (ECTLs) was combined in a 3 dB coupler after passing through a polarization controller (PC), an erbium-doped fiber amplifier (EDFA), a 1 nm bandpass filter (BPF) and a variable optical attenuator (VOA). Then, the interacting waves were injected into the PPLN waveguide through free-space coupling with total insertion losses of ~4 dB. The PPLN device was produced on a lithium niobate substrate doped with 5% of MgO to prevent photorefractive damage at high pumping power. The QPM period and length of the device were 19.2 μm and 4.5 cm,

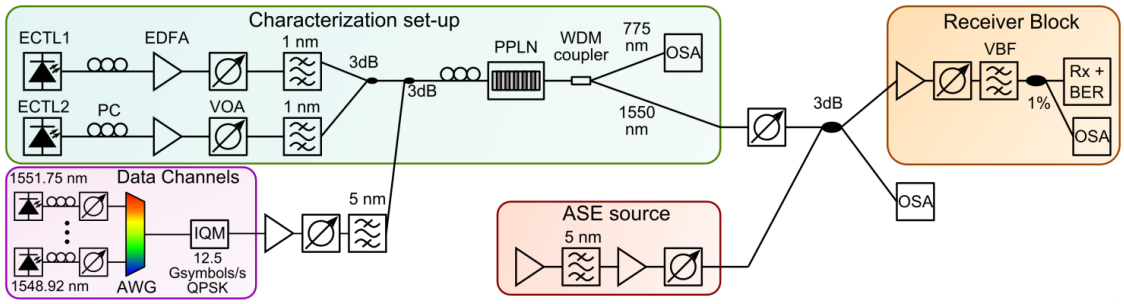

Fig. 1: Experimental set-up used to characterize the spectral response of the PPLN device and to evaluate the performance of the wavelength converter.

respectively. The temperature of operation of the PPLN was kept at 25 ºC. The powers of the ECTL1 and ECTL2 waves at the input to the PPLN were 17.33 and 26.47 dBm, respectively. The wavelength of ECTL1 was kept at 1558 nm, whereas for the ECTL2 wave it was varied from 1545 to 1555 nm. After nonlinear interaction in the PPLN waveguide, a wavelength-division multiplexing (WDM) coupler was used to separate the signal of the spectral region of ~775 nm from the remaining waves. An optical spectrum analyzer (OSA) was used to evaluate the spectral response of the PPLN for SFG.

After characterizing the spectral response of the PPLN device, the set-up was upgraded into the full apparatus depicted in Fig. 1 in order to perform wavelength conversion of 8×12.5 Gsymbol/s in a 50 GHz WDM grid. In this experiment, ECTL1 and ECTL2 are the SFG and DFG pumps, respectively. The wavelength of the SFG pump was 1556.73 nm whereas for the DFG pump it was set to 1542.6, 1543.6, 1544.6 and 1545.6 nm to demonstrate tunability. An IQ modulator (IQM) driven by a pseudo-random bit sequence was used to create the modulated channels from light emitted by 8 distributed feedback (DFB) lasers. The input power of each modulated channel, the SFG and DFG pumps was about 12.5, 24 and 18 dBm, respectively.

The performance of the wavelength converter was evaluated through bit error rate (BER) measurements as a function of the optical signal-to-noise ratio (OSNR). Therefore, ASE noise produced by two cascaded EDFAs around a 5 nm tunable filter was combined with the light coming out of the PPLN in a 3 dB coupler. The VOAs allowed precise control of the OSNR of the measured signal and the BPF enabled tuning of ASE's spectral band, enabling measurements for both through and converted channels. Afterwards, an additional EDFA, VOA and a variable bandwidth filter (VBF) were introduced before the coherent receiver (Rx), to select the channel being measured and to set the input power of the Rx to -10 dBm. The Rx comprised a 90º optical hybrid received with DC-coupled photodiodes at the input to a 40 GSample/s real-time sampling oscilloscope with a 13 GHz bandwidth. A 100 kHz linewidth ECTL was used as the local oscillator and the BER measurements were performed with the DFG pump at 1545.6 nm. The DFB laser of the measurement channel was replaced by an ECTL during BER measurements.

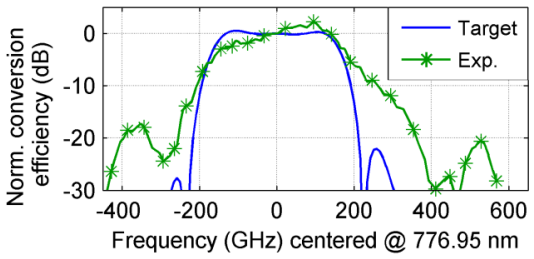

Fig. 2: Normalized experimental conversion efficiency for SFG of the 400 GHz quasi-rectangular PPLN. The solid line corresponds to the target spectral response.

Results and Discussion

The spectrum of the normalized SFG conversion efficiency (ratio between the powers of the SFG and input signal waves) for the 400 GHz quasi-rectangular bandpass PPLN is shown in Fig. 2. The conversion efficiency bandwidth for SFG of the manufactured PPLN was approximately 400 GHz as designed. However, some significant differences compared to the target response are evident from Fig. 2. The ratio between the conversion efficiency of the main peak and side lobes is approximately 10 dB instead of the 20 dB predicted by the target spectral response and the spectral response within the main peak is not as intended, but increases for longer wavelength values. A thorough analysis on the causes of these differences is currently underway, but it is believed that they originate from imperfections on the production of the waveguide and poling pattern.

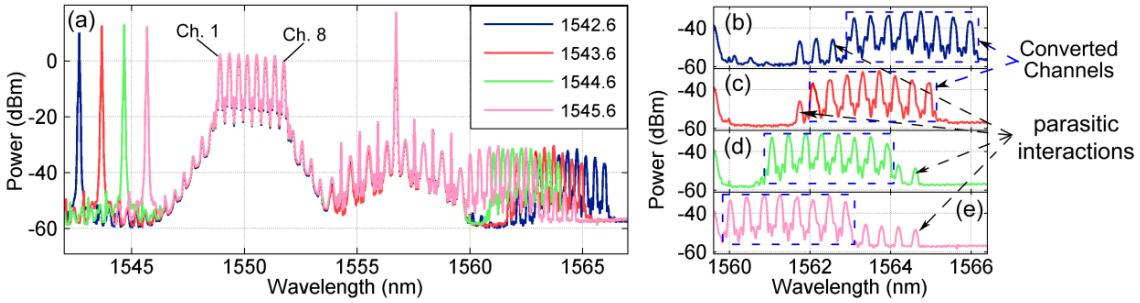

Fig. 3: (a) Measured spectrum at the output of the PPLN for different values of the DFG pump wavelength. Detail of the converted channels for DFG pump at: (b) 1542.6, (c) 1543.6, (d) 1544.6 and (e) 1545.6 nm.

Despite these imperfections, the device was still suitable for a multichannel conversion demonstration. The optical spectra obtained after wavelength conversion in the PPLN waveguide is depicted in Fig. 3, considering different wavelength values of the DFG pump. As expected, the wavelength of the DFG pump determines the spectral position of the converted channels, providing the tunability properties to the wavelength converter. The measured efficiency of the converter (ratio between the power of the input and converted signals) was -30 dB. Such low efficiency results from increasing the bandwidth of the SFG interaction as was also observed in previous works where temperature gradients or aperiodical PPLNs were used[3,7].

It was also observed that the converted channels are affected by "parasitic" contributions of different non-linear interactions. These contributions do not change even when the wavelength of the DFG pump is varied and they are caused by a cascaded SHG/DFG interaction between the second harmonic of the SFG pump and the modulated channels. The contribution of such parasitic interactions would significantly decrease if the ratio between the conversion efficiency of the main peak and side lobes of the conversion response (Fig. 2, green line with '*') was higher.

The results of the BER measurements are shown in Fig. 4. A maximum OSNR penalty of 2 dB at BER of 10^{-3} was observed for channels 1 to 7. For channel 8, a 3 dB penalty was observed. As the conversion efficiency is low and the wavelength of this channel is beyond the gain bandwidth of the last EDFA, the maximum Rx input power was of only -17 dBm, leading to an excessive OSNR penalty.

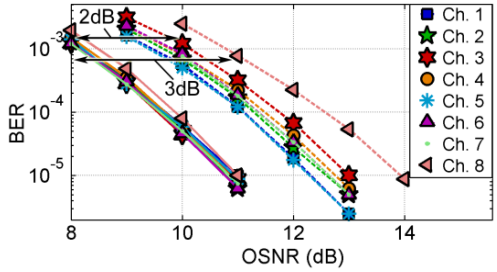

Fig. 4: BER measurements as a function of the OSNR for through (solid line) and converted channels (dashed line).

Conclusions

We demonstrated tunable and multichannel wavelength conversion using a 400 GHz quasi-rectangular PPLN designed using a layer peeling method.

The layer peeling method is proved to be effective in designing PPLN devices with a target spectral response. Flatter conversion efficiency of the main peak and higher peak to side lobe ratios are expected by improving the control of the device production. In the end, such improvement will result in reduced parasitic nonlinear interactions, and thereby in a better performing wavelength converter.

Overall these results show that adopting this design method can be advantageous for the design of PPLN waveguides for wavelength conversion and other optical signal processing applications.

Acknowledgements

The authors acknowledge J. Hirohashi, Oxide Corp. (Japan) for manufacturing the PPLN waveguide. Funding from Fundação para a Ciência e Tecnologia (FCT) through the PhD grant SFRH/BD/78425/2011 and project POFCOM (PTDC/EEA-TEL/122792/2010) are gratefully acknowledged.

References

[1] C. Langrock et al., JLT **24**, 2579 (2006).
[2] H. Furukawa et al., PTL **19**, 384 (2007).
[3] G.-W. Lu et al., Proc. OFC'10, OWP3 (2005).
[4] M. Drummond et al., Elect. Lett. **45**, 1135 (2009).
[5] M.H. Chou et al., PTL **11**, 653 (1999).
[6] M. Asobe et al., J. Q. Elect. **41**, 1540 (2005).
[7] Y.-L. Lee et al., Opt. Exp. **13**, 2988 (2005).
[8] Y.-L. Lee et al., Opt. Exp. **11**, 2813 (2003).
[9] J.K. Brenne et al., JLT **21**, 254 (2003).

Publication C

Pump-linewidth-tolerant optical wavelength conversion for high-order QAM signals using coherent pumps

G. Lu, **A. Albuquerque**, B. Puttnam, T. Sakamoto, M. Drummond, R. Nogueira, A. Kanno, S. Shinada, N. Wada, T. Kawanishi

originally published in *Optics Express*, vol. 22, no. 5, pp. 5067-5075, March 2014.

Pump-linewidth-tolerant optical wavelength conversion for high-order QAM signals using coherent pumps

Guo-Wei Lu,[1,*] André Albuquerque,[2] Benjamin J. Puttnam,[1] Takahide Sakamoto,[1] Miguel Drummond,[2] Rogério Nogueira,[2] Atsushi Kanno,[1] Satoshi Shinada,[1] Naoya Wada,[1] and Tetsuya Kawanishi [1]

[1]*National Institute of Information and Communications Technology (NICT), 4-2-1, Nukui-Kitmachi, Koganei, Tokyo 184-8795, Japan*

[2]*Instituto de Telecomunicações (IT) – pólo de Aveiro, Campus Universitário de Santiago, 3810-193, Aveiro, Portugal*

[*]*gwlu@nict.go.jp*

Abstract: Optical wavelength conversion (OWC) is expected to be a desirable function in future optical transparent networks. Since high-order quadrature amplitude modulation (QAM) is more sensitive to the phase noise, in the OWC of high-order QAM signals, it is crucial to suppress the extra noise introduced in the OWC subsystem, especially for the scenario with multiple cascaded OWCs. Here, we propose and experimentally demonstrate a pump-linewidth-tolerant OWC scheme suitable for high-order QAM signals using coherent two-tone pumps. Using 3.5-MHz-linewidth distributed feedback (DFB) lasers as pump sources, our scheme enables wavelength conversion of both 16QAM and 64QAM signals with negligible power penalty, in a periodically-poled Lithium Niobate (PPLN) waveguide based OWC. We also demonstrate the performance of pump phase noise cancellation, showing that such coherent two-tone pump schemes can eliminate the need for ultra-narrow linewidth pump lasers and enable practical implementation of low-cost OWC in future dynamic optical networks.

OCIS codes: (230.7405) Wavelength conversion devices; (060.1660) Coherent communications; (060.5060) Phase modulation; (060.1155) All-optical networks.

References and links

1. S. J. B. Yoo, "Wavelength conversion technologies for WDM network applications," J. Lightwave Technol. **14**(6), 955–966 (1996).
2. S. R. Nuccio, Z. Bakhtiari, O. F. Yilmaz, and A. Willner, "λ-Conversion of 160-Gbit/s PDM 16-QAM Using a Single Periodically-Poled Lithium Niobate Waveguide," in Optical Fiber Communication Conference/National Fiber Optic Engineers Conference 2011, OSA Technical Digest (CD) (Optical Society of America, 2011), paper OWG5.
3. A. H. Gnauck, E. Myslivets, M. Dinu, B. P. P. Kuo, P. Winzer, R. Jopson, N. Alic, A. Konczykowska, F. Jorge, J. Dupuy, and S. Radic, "All-Optical Tunable Wavelength Shifting of a 128-Gbit/S 64-Qam Signal," in European Conference and Exhibition on Optical Communication, OSA Technical Digest (online) (Optical Society of America, 2012), paper Th.2.F.2.
4. W. Peng, H. Takahashi, T. Tsuritani, and I. Morita, "DAC-free Generation and 320-km Transmission of 11.2-GBd PDM-64QAM Using a Single I/Q Modulator," in European Conference and Exhibition on Optical Communication, OSA Technical Digest (online) (Optical Society of America, 2012), paper We.1.C.3.
5. A. Sano, T. Kobayashi, A. Matsuura, S. Yamamoto, S. Yamanaka, E. Yoshida, Y. Miyamoto, M. Matsui, M. Mizoguchi, and T. Mizuno, "100x120-Gb/s PDM 64-QAM transmission over 160 km using linewidth-tolerant pilotless digital coherent detection, " European Conference in Optical Communications, paper PD2_4 (2010).
6. G.-W. Lu, T. Sakamoto, and T. Kawanishi, "Flexible high-order QAM transmitter using tandem IQ modulators for generating 16/32/36/64-QAM with balanced complexity in electronics and optics," Opt. Express **21**(5), 6213–6223 (2013).

#203826 - $15.00 USD Received 30 Dec 2013; revised 14 Feb 2014; accepted 16 Feb 2014; published 25 Feb 2014

10 March 2014 | Vol. 22, No. 5 | DOI:10.1364/OE.22.005067 | OPTICS EXPRESS 5067

7. B. Filion, W. C. Ng, A. T. Nguyen, L. A. Rusch, and S. Larochelle, "Wideband wavelength conversion of 16 Gbaud 16-QAM and 5 Gbaud 64-QAM signals in a semiconductor optical amplifier," Opt. Express **21**(17), 19825–19833 (2013).
8. G.-W. Lu, T. Sakamoto, and T. Kawanishi, "Wavelength conversion of optical 64QAM through FWM in HNLF and its performance optimization by constellation monitoring," Opt. Express **22**(1), 15–22 (2014).
9. A. P. Anthur, R. T. Watts, K. Shi, J. O. Carroll, D. Venkitesh, and L. P. Barry, "Dual correlated pumping scheme for phase noise preservation in all-optical wavelength conversion," Opt. Express **21**(13), 15568–15579 (2013).
10. S. P. O. Duill, S. T. Naimi, A. P. Anthur, T. N. Huynh, D. Venkitesh, and L. P. Barry, "Simulations of an OSNR-Limited All-Optical Wavelength Conversion Scheme," IEEE Photon. Technol. Lett. **25**(23), 2311–2314 (2013).
11. C. Langrock, S. Kumar, J. E. McGeehan, A. E. Willner, and M. M. Fejer, "All-Optical Signal Processing Using $\chi 2$ Nonlinearities in Guided-Wave Devices," J. Lightwave Technol. **24**(7), 2579–2592 (2006).
12. H. Hu, R. Nouroozi, R. Ludwig, B. Hüttl, C. Schmidt-Langhorst, H. Suche, W. Sohler, and C. Schubert, "Simultaneous Polarization-Insensitive Wavelength Conversion of 80-Gb/S Rz-DQPSK Signal and 40-Gb/s RZ-OOK Signal in a Ti:PPLN Waveguide," J. Lightwave Technol. **29**(8), 1092–1097 (2011).
13. K. Uesaka, K. K.-Y. Wong, M. E. Marhic, and L. G. Kazovsky, "Wavelength exchange in a highly nonlinear dispersion-shifted fiber: Theory and experiments," IEEE J. Sel. Top. Quantum Electron. **8**(3), 560–568 (2002).
14. T. Kawanishi, T. Sakamoto, M. Tsuchiya, and M. Izutsu, "High extinction ratio optical modulator using active intensity trimmers," in Proc. of European Conference and Exhibition on Optical Communication (ECOC 2005), Glasgow (UK), September 2005, paper Th1.6.6.

1. Introduction

Optical wavelength conversion (OWC) of high-speed optical data signals has been widely studied as a key functionality to enhance the re-configurability, non-blocking capacity, and wavelength management in future dynamic optical networks [1]. With high-order quadrature amplitude modulation (QAM) formats being more frequently proposed to increase the capacity of such networks, several OWC schemes for 16QAM and 64QAM signals have been demonstrated using nonlinear media including periodically-poled Lithium Niobate (PPLN) waveguides [2], highly-nonlinear fibers (HNLFs) [3] and semiconductor optical amplifiers (SOAs) [4]. These OWC schemes are implemented through either the cascaded 2nd-order nonlinearities or third-order nonlinearity. Both the phase and intensity information of the input signal could be preserved in the converted signal, showing the transparency in modulation format. In order to support modulation format transparency and allow multiple cascaded OWC stages in future dynamic networks, it is imperative to minimize the addition of both phase and amplitude noise, particularly for phase-noise sensitive formats, such as high-order QAM signals [4–6]. However, due to the finite linewidth of pump lasers, phase noise from the pumps is transparently transferred together with the original data to the converted signal, causing nonnegligible penalties, particularly in high-order QAM formats, which may limit the achievable performance. To minimize the added noise, costly narrow-linewidth lasers such as external-cavity lasers (ECL) or fiber lasers (FL) are usually deployed as pumps. Moreover, for 64QAM and higher orders, even ECL pumps may be not sufficient to minimize power penalty. For example, power penalties of around 4-dB at 5Gbaud [7], and 2-dB at 21Gbaud [3] have been experimentally demonstrated for converted 64QAMs at bit-error rate (BER) of 10^{-3}. It has shown that the use of costly narrow-linewidth FL as pump could help ensure the low power penalty in the OWC of 64QAM [8].

In this paper, we propose and experimentally demonstrate for the first-time, to our knowledge, a pump-linewidth-tolerant OWC for high-order QAM signals up to 64QAM, using coherent pumps in a pump-phase subtracting configuration. Since the phase of the two pumps is correlated, phase noise from each pump will be canceled out in the converted signal, which becomes independent of the pump linewidth. Hence, this scheme enables the use of low-cost distributed feedback (DFB) lasers instead of costly narrow-linewidth sources, effectively reducing the implementation cost and complexity in networks where multiple OWC units may be used to overcome contention. Previously, a similar concept has been deployed to preserve the linewidth or phase noise in OWC of un-modulated signals [9] and recently, a similar approach was used in a computer simulated OWC based on non-degenerate FWM in SOA with 16 QAM signals [10].

#203826 - $15.00 USD Received 30 Dec 2013; revised 14 Feb 2014; accepted 16 Feb 2014; published 25 Feb 2014

10 March 2014 | Vol. 22, No. 5 | DOI:10.1364/OE.22.005067 | OPTICS EXPRESS 5068

Our proposed scheme can be implemented by either cascaded sum- or difference-frequency generation (cSFG/DFG) in PPLN, or non-degenerate FWM in third-order nonlinear media. Here, we choose a PPLN due to its advantages of compactness, negligible frequency chirp and spontaneous noise, and immunity to stimulated Brillouin scattering [11]. The proposed scheme can also be implemented in a polarization diversity loop [12], enabling polarization insensitive OWC. The experimental results show that, even with 3.5-MHz-linewidth DFB pump lasers, negligible power penalties (<0.1dB for 16QAM; <0.3dB for 64QAM at BER of 10^{-3}) are achieved for both 16QAM and 64QAM signals at 10Gbaud in a coherent two-tone pump configuration. In contrast, Use of a similar set-up with free-running DFB pumps results in severe phase noise in converted 16/64QAM signals.

2. Operation principle

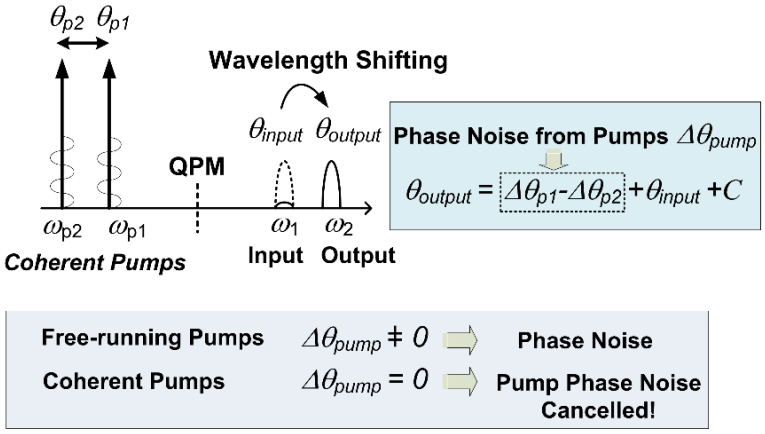

Fig. 1. Operation principle of the pump phase-noise cancellation in the pump-linewidth-tolerant wavelength converter.

Figure 1 depicts the operation principle of the pump-linewidth-tolerant OWC. After OWC, the input signal at ω_1 is shifted to the frequency ω_2, with $\omega_2 = \omega_{p1}-\omega_{p2} + \omega_1$, where ω_{p1}, ω_{p2} and ω_1 are the frequencies of pump1, pump2 and the input signal wave, respectively. This configuration is usually used to perform the data exchange between two input wavelengths [13]. To satisfy the phase matching condition and increase the conversion efficiency, ω_{p1} and ω_1 must be arranged symmetrically with respect to the PPLN's quasi-phase-matching (QPM) wavelength. Under the non-depletion approximation (pump power P_{p1}, P_{p2} » input signal power P_1), linear mapping between the input and output complex amplitudes are obtained as $A_{\omega_2} \propto A_{\omega_1} \cdot A^*_{\omega_{p2}} \cdot A_{\omega_{p1}}$, as well as the following phase relationship:

$$\theta_{\text{output}} = \theta_{\text{input}} + \Delta\theta_{p1} - \Delta\theta_{p2} + C = \theta_{\text{input}} + \Delta\theta_{\text{pump}} + C \quad (1)$$

where θ_{output}, θ_{input}, $\Delta\theta_{p1}$, $\Delta\theta_{p2}$, and C are the phase of the converted and input signals, the phase noise from pump1 and pump2, and a constant term, respectively, and $\Delta\theta_{\text{pump}} = \Delta\theta_{p1} - \Delta\theta_{p2}$. Note that the phase information in each of the two pumps is transparently transferred to the converted signal as a subtraction between them. To avoid extra phase noise introduced in the process, the phase noise from pumps, $\Delta\theta_{\text{pump}}$, should be minimized. If the pumps are synthesized in a two-tone generator (TTG) from a single laser source, the phase noise from pumps is cancelled out in the converted signal, i.e. $\Delta\theta_{\text{pump}} = 0$. Hence, wavelength conversion becomes tolerant to the linewidth of the pump signals, allowing the use of lower cost lasers and improving noise performance. The TTG may be built using either Mach-Zehnder modulators driven by a RF clock, or an optical frequency comb followed by an optical spectrum shaper. The two tone spacing could vary from a fraction of nanometer to several

#203826 - $15.00 USD Received 30 Dec 2013; revised 14 Feb 2014; accepted 16 Feb 2014; published 25 Feb 2014

10 March 2014 | Vol. 22, No. 5 | DOI:10.1364/OE.22.005067 | OPTICS EXPRESS 5069

nanometers, making it possible to cover a relative wide conversion range in the OWC. The TTG generated from a filtered optical frequency comb is more suitable and practical for the OWC based on HNLF. In this work, a TTG built with a Mach-Zehnder modulator driven by a 25 GHz clock signal was used to generate two coherent pumps with a 50 GHz frequency separation.

3. Characterization of the PPLN-based wavelength converter

In order to optimize the efficiency and minimize the crosstalk in OWC, we first used non-correlated, continuous wave (CW) signals to characterize the influence of the total pumping power and frequency separation between the interacting waves on the conversion efficiency (CE) and on the generation of spurious nonlinear contributions. The experimental set-up used for CW characterization is depicted in Fig. 2. The light emitted by two ECLs was combined in a 50/50 coupler to generate the pump waves, before optical amplification in a high power erbium-doped fiber amplifier (EDFA). Next, the two pumps were combined with the input signal generated by another ECL in a 10/90 coupler at the input to the PPLN. Optical attenuators (Attn) and polarization controllers (PCs) were used to adjust the input power to the PPLN and to align the polarization states to the optimum axis of the PPLN, respectively. The PPLN waveguide was produced on a lithium niobate substrate, doped with 5% of MgO to reduce the photorefractive damage at high pump powers. The length, poling period, temperature of operation, QPM wavelength and insertion losses of the PPLN device were 6cm, 19.1μm, 30.1°C, 1550.4nm and 3.25dB, respectively. The second harmonic generation (SHG) efficiency of the PPLN, defined as the ratio of the output SHG power to the square of the input power at the QPM wavelength, was 445%/W and the 3dB conversion bandwidth for SFG was 25 GHz. An optical spectrum analyzer (OSA) was inserted after the PPLN for monitoring.

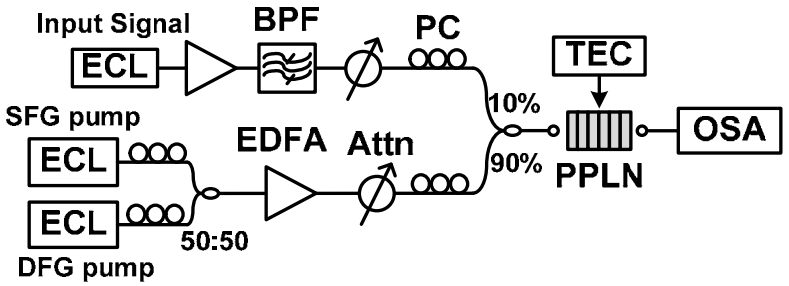

Fig. 2. Experimental set-up for CW characterization of the PPLN-based wavelength converter.

The influence of the total power of the pumps launched into the PPLN, P_T, the frequency separation between the SFG and DFG pumps, Δf_{pumps}, and the frequency separation between the input signal and the SFG pump, $\Delta f_{p\text{-}s}$, on the efficiency and generation of spurious nonlinear contributions was evaluated by measuring the CE, signal depletion (SD), and optical spectra after OWC in the PPLN device. Here, the CE is defined as the ratio of the converted signal power to that of the input signal after the PPLN with both pumps switched OFF. The SD is the power ratio of the input signal after the PPLN with both pumps switched OFF and ON, respectively.

#203826 - $15.00 USD Received 30 Dec 2013; revised 14 Feb 2014; accepted 16 Feb 2014; published 25 Feb 2014

10 March 2014 | Vol. 22, No. 5 | DOI:10.1364/OE.22.005067 | OPTICS EXPRESS 5070

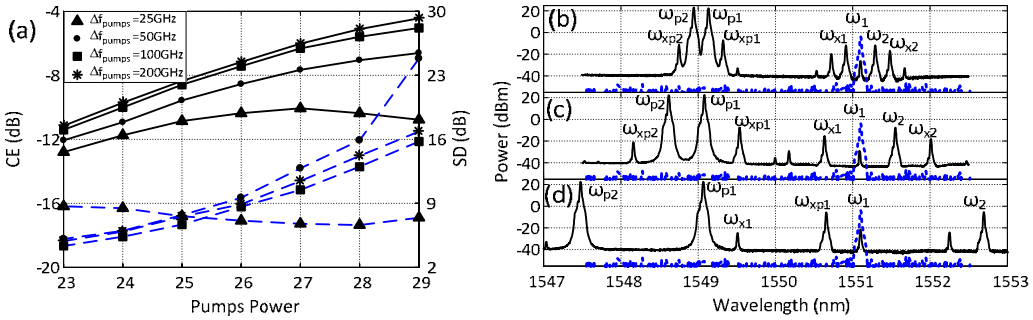

Fig. 3. (a) Variation of the CE (solid lines) and SD (dashed lines) with P_T, for Δf_{pumps} of 25 (triangles), 50 (dots), 100 (squares) and 200 (no marker) GHz. Output spectra (black solid lines) for Δf_{pumps} of (b) 25 GHz; (c) 50 GHz; and (d) 200 GHz, with P_T = 29 dBm. The blue dashed curve in (b), (c) and (d) is the spectrum of the input signal after the PPLN with the pumps turned OFF. The power of the input signal was −1 dBm and $\Delta f_{p\text{-}s}$ = 250 GHz.

The CE and SD are plotted for P_T values from 23 to 29 dBm with Δf_{pumps} values of 25, 50, 100 and 200 GHz in Fig. 3(a). As expected, both CE and SD increase with P_T, as a result of a stronger power flow from the input signal to the converted wavelength, with the exception of Δf_{pumps} = 25 GHz. In this case, the SD tends to decrease with P_T and the CE reaches a maximum value of −10 dB for P_T = 27 dBm. This behavior can be explained due to the generation of spurious contributions at frequencies close to the input and converted signals, as shown in Figs. 3(b), 3(c) and 3(d). These result from different combinations of cascaded nonlinear interactions between the pumps, input and converted signals (e.g. $\omega_{x1} = \omega_{p2} + \omega_1 - \omega_{p1}$ and $\omega_{x2} = \omega_{p1} + \omega_2 - \omega_{p2}$). For Δf_{pumps} = 25 GHz, the generation of the spurious contributions is strong, resulting in lower CE and a complex power flow between the interacting waves. By increasing Δf_{pumps}, the spurious contributions become weaker and the CE increases. In addition to the spurious contributions generated in the PPLN waveguide, two other waves (ω_{xp1} and ω_{xp2}) can be observed in the spectra of Fig. 3, symmetrically displaced around the pumps. These contributions are already observed before the PPLN and they are caused by four-wave mixing between the pumps in the EDFA and patch cords.

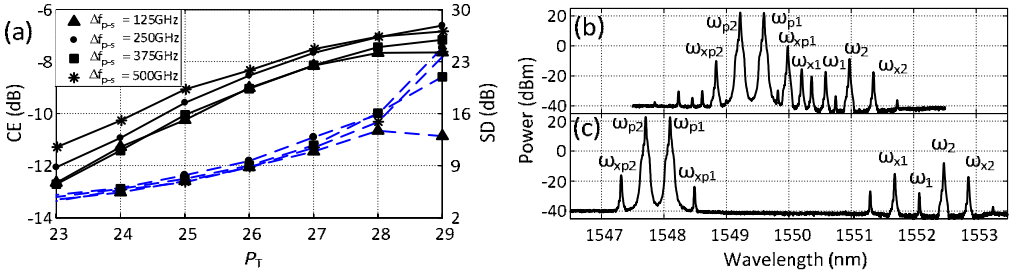

Fig. 4. (a) Variation of the CE (solid lines) and SD (dashed lines) with the P_T for $\Delta f_{p\text{-}s}$ of 125 (triangles), 250 (dots), 375 (squares) and 500 (no marker) GHz. Output spectra for $\Delta f_{p\text{-}s}$ of (b) 125 GHz and (c) 500 GHz. The power of the input signal was −1 dBm and Δf_{pumps} = 50 GHz.

The impact of $\Delta f_{p\text{-}s}$ on the CE and SD is depicted in Fig. 4, for Δf_{pumps} = 50 GHz. According to Fig. 4(a), the CE and SD values are almost independent of $\Delta f_{p\text{-}s}$. However, for $\Delta f_{p\text{-}s}$ = 125 GHz, some of the spurious contributions are very close to the QPM wavelength of the PPLN (Fig. 4(b)) and non-negligible secondary nonlinear interactions between them occur, including both cSFG/DFG and cascaded SHG and DFG interactions. Such secondary interactions are the reason why the SD values decrease for P_T higher than 28 dBm in Fig. 4(a). In addition, we also verified that the CE and SD are independent of the power of the

#203826 - $15.00 USD Received 30 Dec 2013; revised 14 Feb 2014; accepted 16 Feb 2014; published 25 Feb 2014

10 March 2014 | Vol. 22, No. 5 | DOI:10.1364/OE.22.005067 | OPTICS EXPRESS 5071

input signal, at least for signal power values up to 7 dBm, and that best performance in terms of both CE and SD is achieved for SFG and DFG pumps with equal power.

4. Pump-linewidth-tolerant OWC of 16 and 64 QAM signals

4.1 Experimental set-up

After evaluating the influence of the pump power and the frequency separation between the interacting waves on the efficiency and crosstalk in OWC, the experimental set-up depicted in Fig. 2 was upgraded to that shown in Fig. 5, in order to perform OWC of 16 and 64 QAM signals. To minimize the phase noise from the input signal, a 5kHz linewidth FL emitting at 1552.52 nm was deployed as the light source, and modulated by an in-phase/quadrature (IQ) modulator. Two de-correlated 4- or 8-level driving electronics originating from 10-Gbaud PRBS streams with length of 2^{15}-1 were generated from an arbitrary waveform generator (AWG) to drive the IQ modulator, which has a Vπ of 3.5V and an optical bandwidth of around 25GHz. For comparison, two different pump configurations were adopted. In the coherent pump configuration, the two pumps were generated from a single laser source at 1548.08 nm using a TTG, which consisted of a high-extinction-ratio optical modulator [14] driven by a 25-GHz clock. The high-ER modulator was fabricated on the x-cut $LiNbO_3$ substrate with two embedded active trimmers in each arm and has an extinction ratio of up to 60dB. The two phase-correlated coherent pumps were obtained with a 50-GHz frequency separation and a >40-dB spurious suppression ratio. In the free-running pumps configuration, two independent free-running lasers emitting at 1547.88 and 1548.28 nm were used as pumps with 50-GHz spacing. For each configuration, either 500-kHz linewidth ECLs or 3.5-MHz linewidth DFBs were deployed as laser sources for pumps. The wavelength of the pump waves was selected to achieve high $\Delta f_{p\text{-}s}$ (more than 500 GHz) in order to reduce crosstalk after OWC, as described in the previous section, and to satisfy the QPM condition of the PPLN device at low temperature of operation. In order to maximize both CE and SD, the total pump power launched into the PPLN was set to the maximum value of about 28.8 dBm (25.8 dBm for each pump), obtaining CE of −6.5 dB and SD of 25 dB, with input signal power of 6 dBm.

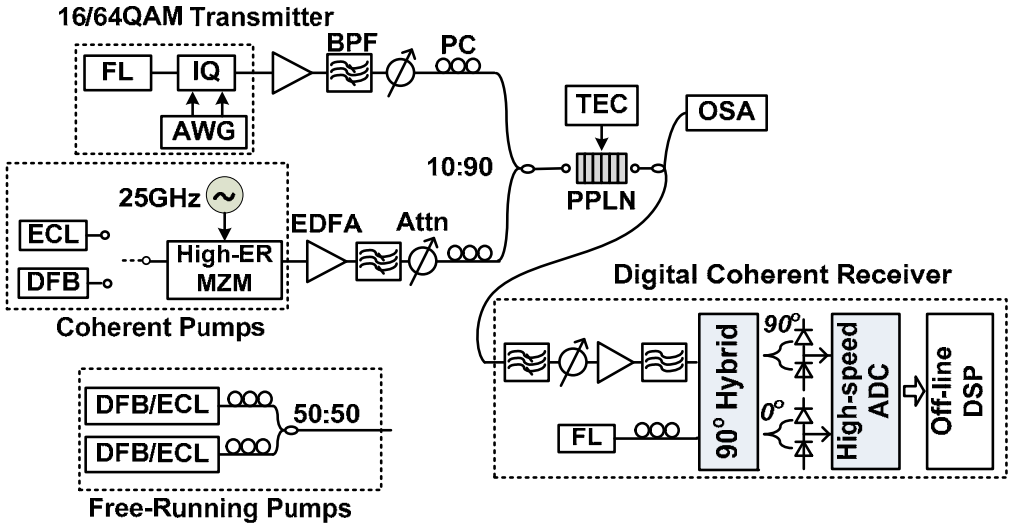

Fig. 5. Experimental set-up for OWC of 16 and 64QAM signals.

The converted signal, generated at 1552.92 nm, was detected by a digital coherent receiver after an optical filter. The receiver included another FL acting as a local oscillator (LO), an optical 90-degree hybrid and two balanced photo-detectors (PDs). After detection by the PDs,

#203826 - $15.00 USD Received 30 Dec 2013; revised 14 Feb 2014; accepted 16 Feb 2014; published 25 Feb 2014

10 March 2014 | Vol. 22, No. 5 | DOI:10.1364/OE.22.005067 | OPTICS EXPRESS 5072

the data was digitized at 50 GSamples/s using a digital storage oscilloscope with a 12.5-GHz analog bandwidth. The captured data was then processed off-line through digital signal processing (DSP), including compensation of skew, power and IQ imbalance, data resampling, linear equalization by finite impulse response filtering, carrier phase recovery and final hard-decision circuits. In order to ensure a fair comparison, the same digital equalization was deployed for the BER measurements in all configurations.

4.2 Experimental results and discussions

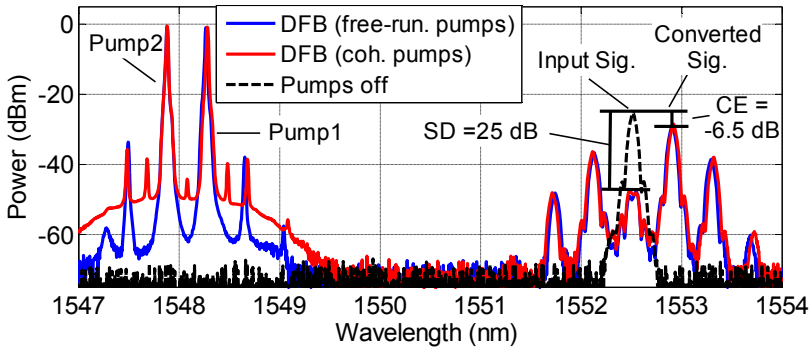

Fig. 6. Optical spectrum measured after PPLN for 64QAM conversion with DFB pump lasers in both free-running and coherent configurations.

The optical spectra after the PPLN with or without pumps for wavelength conversion of 64QAM signals are shown in Fig. 6. For both free-running pumps (ECL/DFB) and coherent two-tone pumps (ECL/DFB), similar CE and SD were obtained. To investigate the impact of the phase noise of the converted signal in the OWC process under different configurations, the corresponding carrier phase, recovered after coherent reception, is plotted in Fig. 7. To avoid additional phase noise from LO, in the coherent receiver, another FL with linewidth of around 5kHz was used as LO. Figure 7(a) shows the recovered carrier phase of the input 16QAM signal from a FL laser to serve as a reference. Figures 7(b) and 7(c) show the recovered carrier phase with free-running DFB pumps, and with coherent two-tone DFB pumps, respectively. As shown in Fig. 7(b), since the phase noise from DFB pumps were transparently transferred to the converted signal in the free-running configuration, a distinct phase variation emerged in the recovered carrier phase. For coherent two-tone pumps, shown in Fig. 7(c), even for DFB pumps, the phase noise from pumps was effectively cancelled out, resulting in stable carrier phase similar to that of a 16QAM signal with a narrow linewidth FL as a laser source. These results indirectly verify the operation of pump phase noise cancellation in the proposed OWC with coherent pumps. Further evidence was obtained by measuring the linewidth of an unmodulated signal after wavelength conversion with coherent DFB two-tone pump. It shows the similar linewidth as the input light from FL, i.e. around 5kHz. This is consistent with the theoretical analysis in [9], and also directly verifies the cancellation effect of pump phase noise in the proposed scheme.

#203826 - $15.00 USD Received 30 Dec 2013; revised 14 Feb 2014; accepted 16 Feb 2014; published 25 Feb 2014

10 March 2014 | Vol. 22, No. 5 | DOI:10.1364/OE.22.005067 | OPTICS EXPRESS 5073

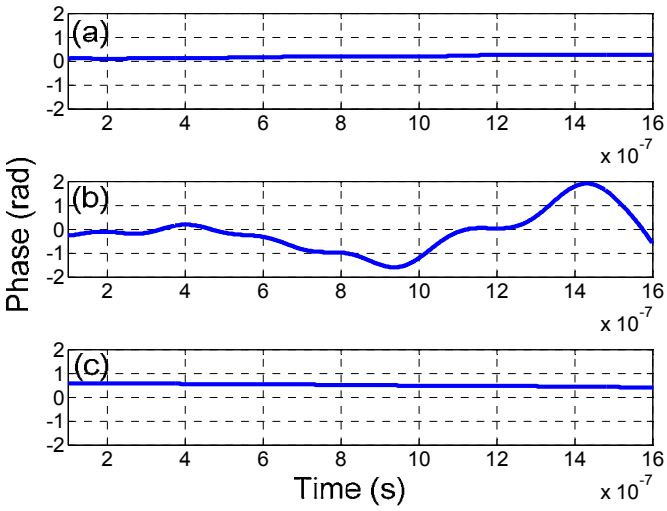

Fig. 7. Recovered carrier phase in the off-line DSP for (a) the input 16QAM signal (back-to-back configuration); (b) the converted 16QAM signal with two free-running DFB pumps; and (c) the converted 16QAM signal with coherent two-tone DFB pumps.

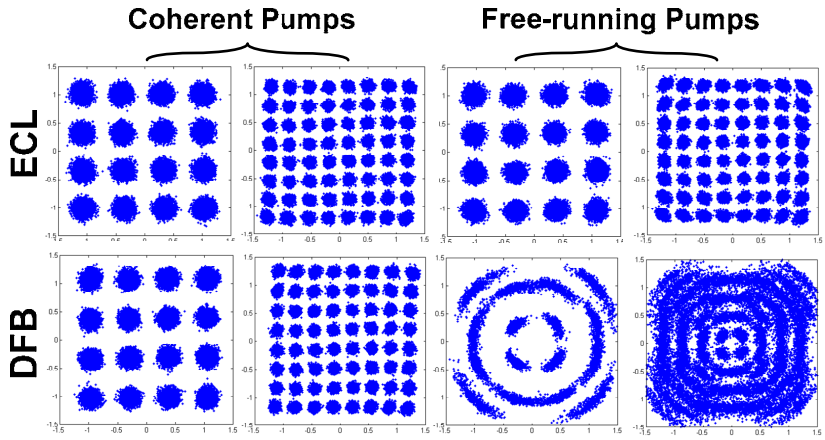

Fig. 8. Measured constellations using ECL and DFB pump lasers in coherent two-tone and free-running configurations (16QAM: OSNR = 18dB, 64QAM: OSNR = 34dB).

As shown in Fig. 8, the constellations of the converted 16/64QAMs signals were re-constructed and measured with different pump lasers and pump configurations. With coherent two-tone pumps, for either ECL or DFB pump laser, clear constellations are observed. However, with ECL pump lasers in free-running configuration, symbol rotation in phase starts to become evident in the 64QAM constellation due to additional phase noise from the free-running ECL pumps. With DFB free-running pumps, the presence of even greater pump phase noise causes clear spreading of the symbols around the unit circle for both formats, which is more severe for the higher amplitude symbols. The results can also be confirmed from the measured BER curves as a function of optical signal-to-noise ratio (OSNR) at 0.1 nm for both input and converted 16/64QAM signals, shown in Fig. 9. With coherent pump configuration, for both ECL and DFB pump lasers, negligible power penalty (<0.1dB for 16QAM; <0.3dB for 64QAM at BER of 10^{-3}) is observed compared with the input signal at 10Gbaud. However, for the case of free-running pumps, although we can get negligible power penalty

#203826 - $15.00 USD Received 30 Dec 2013; revised 14 Feb 2014; accepted 16 Feb 2014; published 25 Feb 2014

10 March 2014 | Vol. 22, No. 5 | DOI:10.1364/OE.22.005067 | OPTICS EXPRESS 5074

(<0.3 dB at BER of 10^{-3}) for 16QAM using ECL as pump laser, when increasing the modulation level to 64QAM, a 0.5-dB penalty at BER of 10^{-3} and an error floor at around $3x10^{-5}$ is observed. With free-running DFB pumps, due to the strong phase noise, even at >30-dB OSNR, a BER of around 10^{-2} was observed for 16QAM and it was not possible to demodulate the 64QAM signal for any noise level. The BER, recovered carrier phase and constellation results verify the effectiveness of the elimination of the pump phase noise in the OWC for high-order QAM with coherent two-tone pumps.

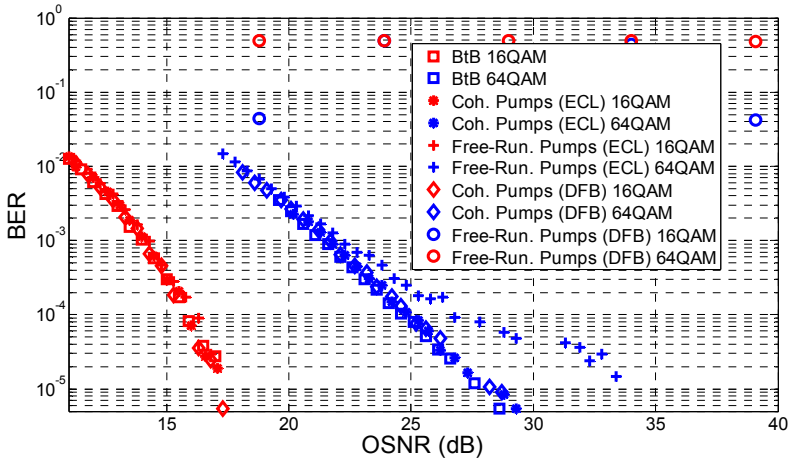

Fig. 9. Measured BER vs. OSNR curves for 16/64QAM. Squares: back-to-back (BtB), stars: coherent pumps (ECL), crosses: free-running pumps (ECL), diamonds: coherent pumps (DFB).

6. Conclusion

We propose and experimentally demonstrate a pump-linewidth-tolerant OWC scheme, suitable for high-order QAM signals. The experimental results show that, even using DFB laser as pump source, negligible power penalty is achieved for converted 16QAM and 64QAM, which can be further extended to OWC of higher-order QAM signals. The proposed scheme eases the linewidth requirement for the pump lasers, simplifies the configuration, and enables practical implementation of low-cost OWC in future dynamic optical networks.

Acknowledgments

The work was supported in part by Grant-in-Aid for Young Scientist (A) (25709031) from the Ministry of Education, Culture, Sports, Science and Technology, Japan, and Fundação para a Ciência e Tecnologia (PhD grant SFRH/BD/78425/2011).

#203826 - $15.00 USD Received 30 Dec 2013; revised 14 Feb 2014; accepted 16 Feb 2014; published 25 Feb 2014

10 March 2014 | Vol. 22, No. 5 | DOI:10.1364/OE.22.005067 | OPTICS EXPRESS 5075

Publication D

Pump-phase-noise-free optical wavelength data exchange between QAM signals with 50-GHz channel-spacing using coherent DFB pump

G. Lu, **A. Albuquerque**, B. Puttnam, T. Sakamoto, M. Drummond, R. Nogueira, A. Kanno, S. Shinada, N. Wada, T. Kawanishi

originally published in *Optics Express*, vol. 24, no. 4, pp. 3702-3713, February 2016.

Pump-phase-noise-free optical wavelength data exchange between QAM signals with 50-GHz channel-spacing using coherent DFB pump

Guo-Wei Lu,[1,3,*] André Albuquerque,[2] Benjamin J. Puttnam,[1] Takahide Sakamoto,[1] Miguel Drummond,[2] Rogério Nogueira,[2] Atsushi Kanno,[1] Satoshi Shinada,[1] Naoya Wada,[1] and Tetsuya Kawanishi[1]

[1]*National Institute of Information and Communications Technology (NICT), 4-2-1, Nukui-Kitmachi, Koganei, Tokyo 184-8795, Japan*

[2]*Instituto de Telecomunicações (IT) – pólo de Aveiro, Campus Universitário de Santiago, 3810-193, Aveiro, Portugal*

[3]*Tokai University, 4-1-1 Kitakaname, Hiratsuka, Kanagawa 259-1292, Japan*

[*]*gordon.guoweilu@gmail.com*

Abstract: An important challenge for implementing optical signal processing functions such as wavelength conversion or wavelength data exchange (WDE) is to avoid the introduction of linear and nonlinear phase noise in the subsystem. This is particularly important for phase noise sensitive, high-order quadrature-amplitude modulation (QAM) signals. In this paper, we propose and experimentally demonstrate an optical data exchange scheme through cascaded 2nd-order nonlinearities in periodically-poled lithium niobate (PPLN) waveguides using coherent pumping. The proposed coherent pumping scheme enables noise from the coherent pumps to be cancelled out in the swapped data after WDE, even with broad linewidth distributed feedback (DFB) pump lasers. Hence, this scheme allows phase noise tolerant processing functions, enabling the low-cost implementation of WDE for high-order QAM signals. We experimentally demonstrate WDEs between 10-Gbaud 4QAM (4QAM) signal and 12.5-Gbaud 4QAM (16QAM) signal with 3.5-MHz linewidth DFB pump lasers and 50-GHz channel spacing. Error-free operation is observed for the swapped QAM signals with coherent DFB pumping whilst use of free-running DFB pumps leads to visible error floors and unrecoverable phase errors. The phase noise cancellation in the coherent pump scheme is further confirmed by study of the recovered carrier phase of the converted signals. In addition to pump phase noise, the influence of crosstalk caused by the finite extinction ratio in WDE is also experimentally investigated for the swapped QAM signals.

OCIS codes: (230.7405) Wavelength conversion devices; (060.1660) Coherent communications; (060.5060) Phase modulation; (060.1155) All-optical networks.

References and links

1. M. Saruwatari, "All-optical signal processing for terabit/second optical transmission," IEEE J. Sel. Top. Quantum Electron. **6**(6), 1363–1374 (2000).
2. J. Wang and A. E. Willner, "Review of robust data exchange using optical nonlinearities," Int. J. Opt. **2012**, 575429 (2012).
3. K. Uesaka, K. K.-Y. Wong, M. E. Marhic, and L. G. Kazovsky, "Wavelength exchange in a highly nonlinear dispersion-shifted fiber: theory and experiments," IEEE J. Sel. Top. Quantum Electron. **8**(3), 560–568 (2002).
4. C. H. Kwok, B. P. P. Kuo, and K. K. Wong, "Pulsed pump wavelength exchange for high speed signal de-multiplexing," Opt. Express **16**(15), 10894–10899 (2008).
5. M. Shen, X. Xu, T. I. Yuk, and K. K.-Y. Wong, "A 160-Gb/s OTDM demultiplexer based on parametric wavelength exchange," IEEE J. Quantum Electron. **45**(11), 1309–1316 (2009).

#251508 Received 9 Oct 2015; revised 17 Jan 2016; accepted 2 Feb 2016; published 12 Feb 2016

22 Feb 2016 | Vol. 24, No. 4 | DOI:10.1364/OE.24.003702 | OPTICS EXPRESS 3702

6. X. Xu, M. Shen, T. I. Yuk, and K. K. Y. Wong, "Optical time-slot swapping based on parametric wavelength exchange," in *Asia Communications and Photonics Conference and Exhibition, Technical Digest (CD)* (Optical Society of America, 2009), paper TuC1.
7. J. Wang, Z. Bakhtiari, O. F. Yilmaz, S. Nuccio, X. Wu, and A. E. Willner, "10 Gbit/s tributary channel exchange of 160 Gbit/ssignals using periodically poled lithium niobate," Opt. Lett. **36**(5), 630–632 (2011).
8. J. Wang, Z. Bakhtiari, S. R. Nuccio, O. F. Yilmaz, X. Wu, and A. E. Willner, "Phase-transparent optical data exchange of 40 Gbit/s differential phase-shift keying signals," Opt. Lett. **35**(17), 2979–2981 (2010).
9. G.-W. Lu, A. Albuquerque, B. J. Puttnam, T. Sakamoto, M. Drummond, R. Nogueira, A. Kanno, S. Shinada, N. Wada, and T. Kawanishi, "Pump-linewidth-tolerant optical wavelength conversion for high-order QAM signals using coherent pumps," Opt. Express **22**, 5067–5075 (2014).
10. G.-W. Lu, A. Albuquerque, B. J. Puttnam, T. Sakamoto, M. V. Drummond, R. N. Nogueira, A. Kanno, S. Shinada, N. Wada, and T. Kawanishi, "Pump-linewidth-tolerant optical data exchange between 16QAM and QPSK with 50-GHz channel-spacing using coherent DFB pump, " in *European Conf. on Optical Communications* (ECOC, 2014), paper P.2.18.
11. A. P. Anthur, R. T. Watts, K. Shi, J. O. Carroll, D. Venkitesh, and L. P. Barry, "Dual correlated pumping scheme for phase noise preservation in all-optical wavelength conversion," Opt. Express **21**(13), 15568–15579 (2013).
12. R. W. L. Fung, H. K. Y. Cheung, B. P. P. Kuo, and K. K. Y. Wong, "Wavelength Exchange with Enhanced Extinction Ratio in Highly Nonlinear Dispersion-Shifted Fiber," in *Conference on Lasers and Electro-Optics/Quantum Electronics and Laser Science Conference and Photonic Applications Systems Technologies, OSA Technical Digest Series (CD)* (Optical Society of America, 2007), paper JTuA39.
13. P. Winzer, A. Gnauck, A. Konczykowska, F. Jorge, and J. Dupuy, "Penalties from in-band crosstalk for advanced optical modulation formats," in *37th European Conference and Exposition on Optical Communications, OSA Technical Digest (CD)* (Optical Society of America, 2011), paper Tu.5.B.7.
14. J. Wang and Q. Sun, "Theoretical analysis of power swapping in quadratic nonlinear medium," Appl. Phys. Lett. **96**(8), 081108 (2010).
15. T. Kawanishi, T. Sakamoto, M. Tsuchiya, and M. Izutsu, "High extinction ratio optical modulator using active intensity trimmers," in Proc. of European Conference and Exhibition on Optical Communication (ECOC, 2005), paper Th1.6.6.
16. A. Viterbi and A. Viterbi, "Nonlinear estimation of PSK-modulated carrier phase with application to burst digital transmission," IEEE Trans. Inf. Theory **29**(4), 543–551 (1983).
17. I. Fatadin and S. J. Savory, "Compensation of Frequency Offset for 16-QAM Optical Coherent Systems Using QPSK Partitioning," IEEE Photonics Technol. Lett. **23**(17), 1246–1248 (2011).

1. Introduction

In future dynamic optical networks, all optical signal processing functions are expected to be crucial building blocks to fully exploit the capacity of optical fiber beyond point-to-point communication [1]. Among these optical network functionalities, data exchange could realize the bidirectional information swapping between different wavelengths, time slots, or polarizations [2]. In the wavelength domain, this optical wavelength data exchange (WDE) is the swapping of data carried on separate wavelength channels based on parametric depletion through $\chi^{(3)}$ or cascaded $\chi^{(2)}$: $\chi^{(2)}$ nonlinearities in a single device. It consists of simultaneous signal depletion and wavelength conversion processes between two signal channels. Each input signal is power consumed and its corresponding power is shifted to the other channel, resulting in data exchange between two wavelengths in a single device. So far, several WDE implementations have been demonstrated through non-degenerate four-wave mixing (FWM) in highly-nonlinear fiber [3–6] and cascaded second-order nonlinearities in a periodically-poled lithium niobate (PPLN) waveguide [7,8].

Recently, advanced multi-level modulation formats have been widely deployed in optical communication systems to increase the capacity and spectral efficiency. With the increased number of modulation states in such multi-level modulation formats, especially in high-order phase-shift keying (PSK) and quadrature-amplitude modulation (QAM) signals, susceptibility to phase noise becomes a critical impairment. Therefore, it is crucial to avoid the introduction of phase noise when pursuing optical signal processing functionalities for high-order QAM signals. We recently proposed a coherent pumping concept to demonstrate pump-linewidth-tolerant optical wavelength conversion (OWC) [9]. Owing to the phase correlation of the pumps, the phase noise from local pumps can be cancelled out in the resultant converted signals, so it is particularly suitable for OWC of high-order QAM signals. In [10], we have applied this concept to demonstrate pump-phase-noise-tolerant WDE between 4QAM and

#251508 Received 9 Oct 2015; revised 17 Jan 2016; accepted 2 Feb 2016; published 12 Feb 2016

22 Feb 2016 | Vol. 24, No. 4 | DOI:10.1364/OE.24.003702 | OPTICS EXPRESS 3703

16QAM through cascaded sum- and difference-frequency generation (cSFG/DFG) in a single PPLN waveguide with a distributed feedback (DFB) pump laser. Similar concept has been demonstrated through FWM in highly-nonlinear fiber (HNLF) [11]. In this paper, comprehensive experimental demonstration and analysis of pump-phase-noise-free WDE between QAM signals, including WDE between 10-Gbaud and 12.5-Gbaud 4QAM signals, and the WDE between 10-Gbaud 4QAM and 12.5-Gbaud 16QAM signals, are presented with 50-GHz spacing using DFB coherent pumping. The recovered carrier phase of the input and converted QAM signals show similar behavior over time, indicating that no additional phase noise from the pumps is transferred to the converted signal after WDE and error-free operation is achieved after WDE for the swapped QAM signals. With free-running pump lasers, an error floor is observed for the swapped 4QAM signals, and it is impossible to measure the bit-error rate (BER) of the swapped 16QAM signal due to excessive phase noise. Hence, the use of coherent pumps enables the WDE between QAM signals, which is otherwise inhibited due to phase noise originating from the optical pumps. Furthermore, the narrow quasi-phase matching (QPM) band of the PPLN allows 50-GHz channel spacing WDE and provides a larger signal depletion (>30dB), compared to HNLFs with reported signal depletion of ~25dB [12], resulting in a lower inter-channel crosstalk in WDE, and making it suitable for implementation of network switching in dense WDM (DWDM) systems.

In addition to the phase noise, as discussed in [13], with the increase of modulation levels, high-order QAM signals exhibit more sensitivity to in-band crosstalk. In an ideal WDE, the input signals at the original wavelengths would be fully consumed and shifted to the counterpart wavelengths, leading to infinite extinction ratio (ER) and crosstalk-free operation. However, practically it is hard to achieve complete signal depletion in WDE and the residual power left at the original wavelengths remains as a crosstalk-like impairment on the new-generated signals. Hence, the crosstalk in WDE due to finite ER is another issue to be considered when building WDE for high-order QAM signals. In this paper, the optimal operation pump power is determined by experimentally investigating the ER of WDE and BER of converted QAM signals when tuning the pump power. The impact of crosstalk and phase noise on the swapped 4QAM and 16QAM signals is then experimentally investigated, highlighting the different behavior of these impairments in WDE.

2. Operation principle

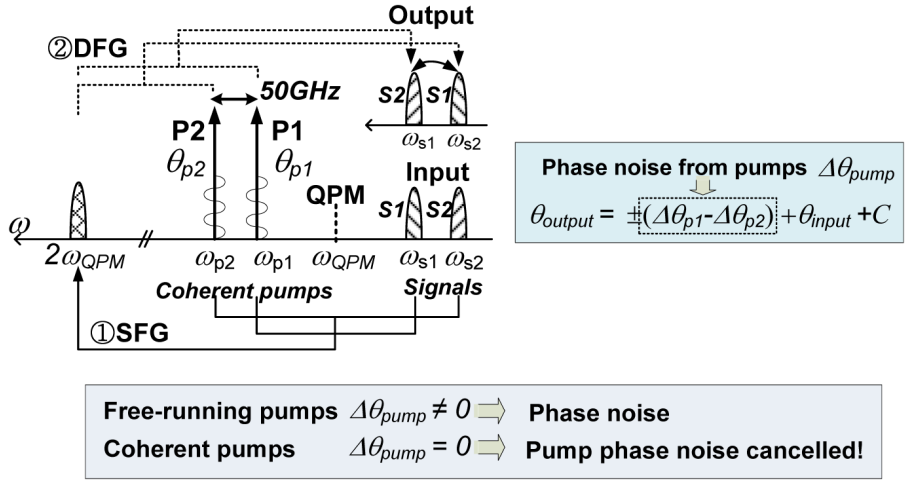

Fig. 1. Operation principle of the proposed pump-phase-noise-free WDE using coherent pumping.

#251508 Received 9 Oct 2015; revised 17 Jan 2016; accepted 2 Feb 2016; published 12 Feb 2016

22 Feb 2016 | Vol. 24, No. 4 | DOI:10.1364/OE.24.003702 | OPTICS EXPRESS 3704

The principle of operation of the pump-linewidth-tolerant WDE is shown in Fig. 1, with two pumps (P1 at ω_{p1} and P2 at ω_{p2}) and two input signals (S1 at ω_{s1} and S2 at ω_{s2}). The WDE between the two signals can be decomposed into two concurring wavelength-shifting processes, each corresponding to the combination of signal depletion and wavelength conversion, promoted by nonlinear interactions. The input data S1(S2) carried at ω_{s1} (ω_{s2}) is consumed and converted to ω_{s2} (ω_{s1}), i.e. two wavelength shifting processes, thus achieving WDE functionality in a single device. PPLNs are attractive devices for realizing WDE due to their compactness, negligible frequency chirp and spontaneous noise emission, and immunity to stimulated Brillouin scattering, although we note that the higher FWM efficiency of $\chi^{(3)}$ materials may make it attractive in some cases. To satisfy the phase matching condition and optimize the conversion efficiencies, pumps and signals must be arranged symmetrically with respect to the quasi-phase-matching (QPM) wavelength of the PPLN.

Assuming negligible pump depletion, lossless propagation, perfect phase-matching, identical pump power, and identical nonlinear coefficients for two wavelength shifting processes, the evolution of the complex amplitude of signals S1 (A_{s1}) and S2 (A_{s2}) is given by the following simplified equations [14].

$$A_{S1}(\mathrm{L}) = A_{S1}(0)\cdot\frac{\cos(\mathrm{ML})+1}{2} + A_{S2}(0)\cdot\frac{\cos(\mathrm{ML})-1}{2}e^{i(\Delta\theta_{pump}+\mathrm{C})} \tag{1}$$

$$A_{S2}(\mathrm{L}) = A_{S1}(0)\cdot\frac{\cos(\mathrm{ML})-1}{2}e^{-i(\Delta\theta_{pump}+\mathrm{C})} + A_{S2}(0)\cdot\frac{\cos(\mathrm{ML})+1}{2} \tag{2}$$

where L is the length of PPLN waveguide, C is a constant term, $\Delta\theta_{\mathrm{pump}} = \Delta\theta_{p1}$-$\Delta\theta_{p2}$, with $\Delta\theta_{p1}$ and $\Delta\theta_{p2}$ the phase of pump P1 and P2, respectively, and $M \approx \omega_{SFG}\kappa\sqrt{P(0)}$ with κ the nonlinear coupling coefficient of the 2nd-order nonlinear interaction, $P(0)$ the input pump power of P1 or P2 (assuming identical power for both pump waves), and ω_{SFG} the angular frequency of SFG wave. According to Eqs. (1) and (2), after WDE, the signals at ω_1 and ω_2 become mixture combination of swapped and remnant original signals. Here, we define the power ratio between the swapped signal and any remaining signal component at the input wavelength after WDE as extinction ratio (ER). Besides, the phase noise from pumps is transparently transferred together with the original input phase to the swapped output signal. Therefore, in order to realize superior performance of WDE for high-order QAM signals, two important components should be suppressed to preserve the original information, phase noise from pumps and crosstalk due to finite ER.

When the product of ML becomes an odd multiple of π, we can obtain the following equations from Eqs. (1) and (2).

$$A_{S1}(L) = -A_{S2}(0)e^{i(\Delta\theta_{pump}+C)} \tag{3}$$

$$A_{S2}(L) = -A_{S1}(0)e^{-i(\Delta\theta_{pump}+C)} \tag{4}$$

This corresponds to the ideal WDE without residual signals after data exchange, i.e. crosstalk-free WDE. To maximize the signal depletion, for a given PPLN waveguide, the pump power should be optimized to improve the ER, thus suppressing the crosstalk. On the other hand, according to the phase term of Eqs. (3) and (4), to reduce the phase noise from the local pumps, a straightforward approach is to deploy narrow-linewidth laser as pump sources, increasing both the implementation complexity and hardware cost. With coherent pumps deployed in WDE, $\Delta\theta_{p1} = \Delta\theta_{p2}$, allowing the phase noise from pumps to be effectively eliminated. The tolerance against the phase noise from pumps with coherent pumping allows the use of lower-cost and large-linewidth lasers as pump sources. The coherent pumps can be synthesized by using Mach-Zehnder modulator (MZM)-based two-tone generator (TTG) driven by a RF clock, or a frequency comb, followed by an optical spectrum shaper.

#251508 Received 9 Oct 2015; revised 17 Jan 2016; accepted 2 Feb 2016; published 12 Feb 2016

22 Feb 2016 | Vol. 24, No. 4 | DOI:10.1364/OE.24.003702 | OPTICS EXPRESS 3705

To demonstrate a pump-phase-noise-free WDE for high-order QAM signals, in the following sections, we first optimize the pump power by measuring the ER and BER of the swapped signals to minimize crosstalk in WDE. With the optimized ER, pump-phase-noise-free WDE between 4QAM signals, and WDE between 4QAM and 16QAM signals are experimentally demonstrated using coherent DFB pumping. The BER performance and the constellations of the swapped QAM signals are experimentally investigated with the proposed coherent pumping, and conventional free-running pumping scheme. The behavior of phase noise and finite-ER-induced crosstalk in the constellations of the swapped signals is also experimentally investigated.

3. Experimental setup

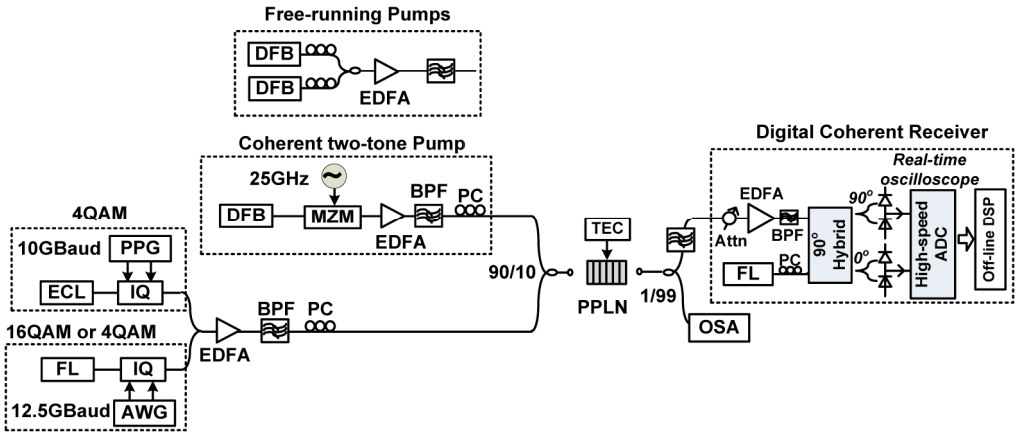

Fig. 2. Experimental setup of WDE between QAM signals with different pumping schemes (coherent pumps or free-running pumps).

The experimental setup is depicted in Fig. 2. To minimize the phase noise from the input signals, a fiber laser (FL) with linewidth of 10 kHz emitting at 1552.48 nm was deployed as one of the light sources for the input QAM signals. The light from FL was then modulated by an in-phase/quadrature (IQ) modulator, which has a 3-dB bandwidth of around 25 GHz, and a 3.5-V half-wave voltage. In order to generate 12.5-Gbaud 16QAM or 4QAM signals, two de-correlated 4- or 2-level driving electronics originating from 12.5-Gbaud PRBS streams with lengths of 2^{15}-1 were generated from a 50-GSa/s arbitrary waveform generator (AWG) to drive the IQ modulator. The other input 4QAM signal was generated from light emitted by a 100-kHz linewidth external cavity laser (ECL) at 1552.9 nm. It was modulated by another IQ modulator, which was fully driven by two de-correlated 10-GBaud binary PRBS streams with length of 2^{15}-1 from a pulse pattern generator (PPG).

For comparison, two different pump configurations were adopted. In the coherent pump configuration, the two pumps were generated from a single DFB laser with 3.5-MHz linewidth at 1548.13 nm using a TTG, which consisted of a high extinction-ratio MZM driven by a 25-GHz clock, resulting in a 50-GHz frequency separation between the two phase-correlated pumps [15]. In this work, the limited bandwidth of the MZM limited the frequency spacing between the correlated pumps, but we note that higher frequency separation may be achieved using optical combs followed by an optical spectrum shaper. In the free-running pumps configuration, two independent free-running DFB lasers emitting at 1547.92 and 1548.32 nm were used as pumps, with 50-GHz spacing. For each configuration, 3.5-MHz linewidth DFBs were deployed as laser sources for the pumps.

After optical amplification and out-of-band noise filtering, the modulated input signal and pumps were combined in a coupler with a splitting ratio of 10% and 90% respectively at the input to the PPLN. Polarization controllers (PCs) were then used to align their polarizations to

#251508 Received 9 Oct 2015; revised 17 Jan 2016; accepted 2 Feb 2016; published 12 Feb 2016

22 Feb 2016 | Vol. 24, No. 4 | DOI:10.1364/OE.24.003702 | OPTICS EXPRESS 3706

the optimum axis of the PPLN. The PPLN waveguide was produced on a lithium niobate substrate, doped with 5% of MgO to minimize photorefractive damage. The length, poling period, operation temperature, QPM wavelength and insertion losses of the PPLN device were 6 cm, 19.1 μm, 30.1°C, 1550.4 nm and 3.25 dB, respectively. The cSFG/DFG conversion bandwidth of the PPLN was of about 60 GHz, which allows OWC and WDE without significant signal distortion. After the WDE, the swapped signals were filtered out individually and detected by a digital coherent receiver. The receiver included another FL acting as a local oscillator, an optical 90-degree hybrid and two balanced photo-detectors (PDs). After detection by the PDs, the data was digitized at 50 GSa/s using a digital storage oscilloscope with a 12.5-GHz analog bandwidth, and processed off-line through digital signal processing (DSP). To provide a fair comparison, identical parameters were used in the DSP unit for detecting input QAM signals and the swapped QAM signals in both free-running and coherent pump operations. The Viterbi algorithm [16] is deployed in DSP to estimate and compensate for the frequency offset, and the tap number in smoothing filter is set as 200 for carrier phase recovery. In addition, quadrature phase-shift keying (QPSK) partitioning algorithm [17] is used for frequency offset compensation of 16QAM signals.

4. Pump-phase-noise-free WDE of QAM signals

4.1 Performance optimization of WDE in PPLN

In a typical OWC, the main figure of merit of the process is the conversion efficiency (CE), defined as the ratio of the converted signal power after the PPLN to that of the input signal before the PPLN, regardless of the power at the remaining input signal component. However, the finite ER in WDE process is also crucial since it introduces additional degradation to the output signal at the same wavelength. Fortunately, according to Eqs. (1) and (2), both maximum conversion efficiency and ER are obtained for the same pump power, corresponding to the case when the power of each input channels is totally transferred to the other channel. Another noteworthy conclusion that can be obtained from Eqs. (1) and (2) is that the optimum pump power for WDE is the same as when considering simple OWC, i.e., with $A_{S1}(0)$ or $A_{S2}(0)$ set to 0. Hence, it is possible to determine the best operation condition for WDE by measuring the pump power value at which the ER is maximized in a simple OWC.

Equations (1) and (2) were obtained assuming that $\omega_{s2} + \omega_{P2} = \omega_{s1} + \omega_{P1}$. In real systems, however, the frequency of the light sources of the channels and pump waves may not be exactly correlated and may drift in time, so the channel in ω_{s2} is converted into a frequency approximately equal, but not necessarily equal to ω_{s1}, and vice-versa. In this case, the dynamics of the system include more nonlinear interactions, but the main source for signal degradation in WDE is still the partial spectral overlap of the converted signals and the remaining power of the input channels. Nonetheless, the optimum conditions for minimized crosstalk should be the same as those devised in Section 2.

In order to experimentally obtain the optimum operation conditions for WDE, the ER and CE for each OWC were measured for different values of the pump power, with the data modulation turned off, i.e., with continuous waves (CW). The experimental results are shown in Fig. 3. As expected, the ER increases with the total pump power due to higher CE, until it reaches a maximum value of more than 20 dB for a total pump power of about 28.5 dBm. At such a pump power value, a CE of −7 dB is obtained, which includes the total insertion losses of the PPLN, of about 3.25 dB.

For higher pump power values, the power of the converted signal starts to flow back to the original wave and the ER starts to decrease. Contrarily to what was expected, the maximum ER for each OWC processes is not achieved at the same pump power value, but at 28.3 dBm when the input signal is at 1552.48 nm and at 29 dBm for the other case. These results can be explained by a slightly asymmetrical disposition of the frequency of the interacting waves

#251508 Received 9 Oct 2015; revised 17 Jan 2016; accepted 2 Feb 2016; published 12 Feb 2016

22 Feb 2016 | Vol. 24, No. 4 | DOI:10.1364/OE.24.003702 | OPTICS EXPRESS 3707

($\omega_{s2} + \omega_{P2} \neq \omega_{s1} + \omega_{P1}$), so that one of the OWC is not perfectly quasi-phase matched, requiring higher pump power values to maximize the ER. According to our numerical simulations, even a small wavelength detuning from the ideal conditions of 0.005 nm for each signal, which was the resolution of the available ECLs, is sufficient to change the optimal pump power by about 1.5 dB. Hence, the optimum operation conditions must be set as a trade-off between the ER of each OWC process, as it will also be shown in the following subsection.

The optimization of the pump power for WDE is critical since even a small deviation of less than 0.5 dB is enough to deteriorate the ER by more than 10 dB. Therefore, stable and precise tuning of the pump power and of the operation temperature of the PPLN waveguide are crucial for WDE.

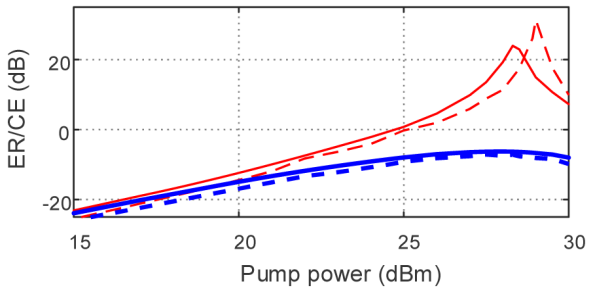

Fig. 3. Variation of the ER (thin red lines) and CE (thick blue lines) with the total pump power for each OWC process, with input signal at 1552.48 nm (solid line) and at 1552.9 nm (dashed line).

4.2 Pump power optimization by measuring BER of swapped signals

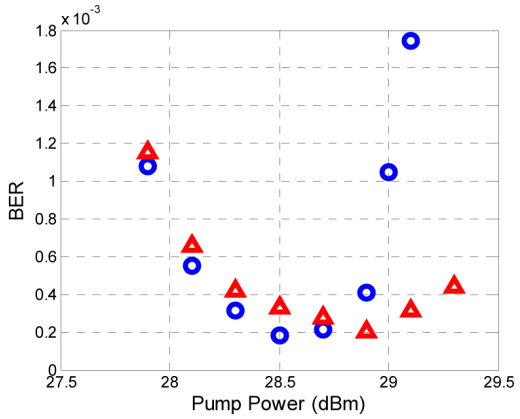

Fig. 4. Measured BERs of the converted signals after the wavelength exchange process when tuning the pump power (circles: the converted signal at 1552.9 nm; triangles: the converted signal at 1552.48 nm).

As mentioned above, due to finite ER, any un-depleted power at input wavelengths becomes deleterious crosstalk impairing the swapped signals, especially for the in-band-crosstalk-sensitive high-order QAM signals. For a given PPLN, ER is mainly dependent on the pump power. As we discussed in Section 4.1, to determine the optimal pump power, the ER has been investigated as a function of the pump power for each wavelength shifting process individually, showing the optimal pump power for wavelength shifting with input at 1552.48 nm of around 28.3 dBm, whereas the optimal one for wavelength shifting at 1552.9 nm is ~29 dBm. Here, to verify the reliability of the observed optimal pump power, we also measure the corresponding BER results of the converted signals in a WDE process, with two input 4QAM

#251508 Received 9 Oct 2015; revised 17 Jan 2016; accepted 2 Feb 2016; published 12 Feb 2016

22 Feb 2016 | Vol. 24, No. 4 | DOI:10.1364/OE.24.003702 | OPTICS EXPRESS 3708

signals launched at each signal wavelength. Figure 4 shows the measured BER of the converted 4QAM at optical signal-to-noise-ratio (OSNR) of around 9 dB when tuning the launch power. According to the BER measured as a function of pump power, the optimal pump power for the signal at 1552.48 nm is measured as around 28.5 dBm, while the optimal pump power for input signal at 1552.9 nm is around 28.9 dBm. The obtained results are consistent with those obtained based on the optimal ER. In the experiment, the total pump power was set at 28.5 dBm, in order to obtain acceptable performance for both input signals. It corresponds to ~20-dB ER, indicating that the swapped signals will suffer from around 20-dB in-band crosstalk in WDE. According to the prediction in [13], for 20-dB crosstalk, 0.5-dB and 2-dB OSNR penalties are theoretically predicted for QPSK and 16QAM at BER = 10^{-3}, respectively. This provides a benchmark for the experimental performance investigation in the following sections. With the pump power of 28.5 dBm, the measured input and output optical spectra with different pumping schemes are shown in Fig. 5. As discussed in previous session, similar ER is obtained in these two pumping schemes, which is independent on the coherence of pumps.

We note that in Fig. 4, with the same amount of BER degradation, 2×10^{-4}, two input 4QAM signals at different baud rates show different pump power tolerance range (PPTR). For the converted 12.5-Gbaud 4QAM, the measured PPTR is around 0.63 dB, while the PPTR for the converted 10-Gbaud 4QAM is around 1 dB. This should be attributed to the increased susceptibility to crosstalk for higher baud rate signals.

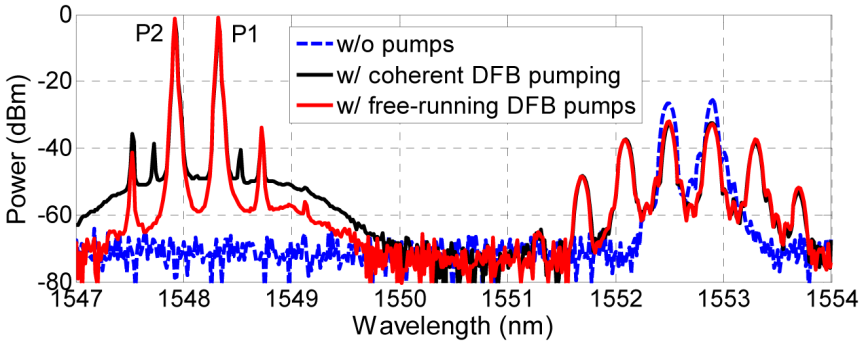

Fig. 5. Optical spectra after PPLN without pumps (dotted blue line), with coherent pumping (solid black line), and with free-running pumping (red solid line).

#251508 Received 9 Oct 2015; revised 17 Jan 2016; accepted 2 Feb 2016; published 12 Feb 2016

22 Feb 2016 | Vol. 24, No. 4 | DOI:10.1364/OE.24.003702 | OPTICS EXPRESS 3709

4.3 Pump-phase-noise-free WDE between 4QAM signals

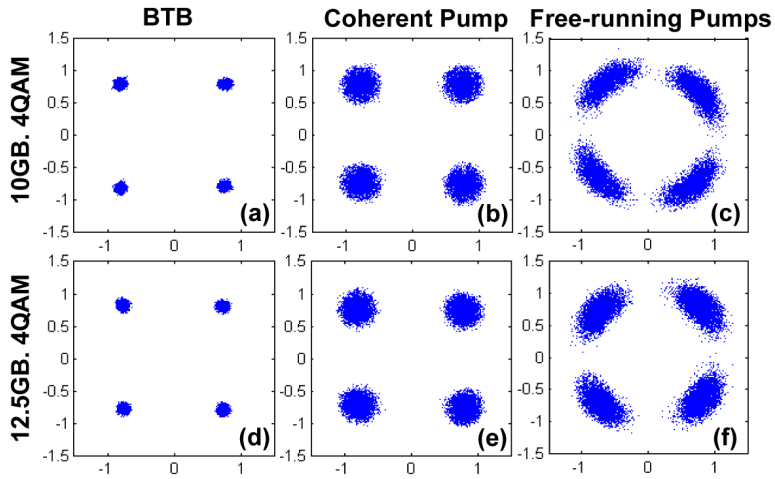

Fig. 6. Constellations of input signals: (a) 10-Gbaud (d) 12.5-Gbaud 4QAM; the swapped signals with coherent pumping: (b) 10-Gbaud and (e) 12.5-Gbaud 4QAM, and the swapped signals with free-running pumping: (c) 10-Gbaud and (f) 12.5-Gbaud 4QAM.

With two input 4QAM signals operating at different baud rates, the WDE between 12.5-Gbaud and 10-Gbaud 4QAMs is first demonstrated. Figure 6 illustrates the reconstructed constellations of the input and the swapped 4QAM signals under different pumping approaches, i.e. coherent and free-running pumping. With coherent pumping, the error-vector magnitude (EVM) of the swapped 4QAM signals is obviously increased compared to that of input signal, which is mainly due to the crosstalk introduced by finite ER in WDE. However, no additional phase noise is observed since phase noise is cancelled out with the coherent pumping. On the other hand, the free-running pumps show both high intensity noise, and high phase noise evident from symbol spreading around the phase angle. BER measurements as function of OSNR (at 0.1nm) at the receiver were also measured to verify this observation. As shown in Fig. 7, with coherent pumping, around 0.8-dB and 0.3-dB power penalty with respect to the input signal is obtained for the swapped 10-Gbaud 4QAM and 12.5-Gbaud 4QAM signals, respectively, after WDE. However, in the case with free-running DFB pumps, 4.8-dB and 4-dB power penalty is observed for the swapped 10-Gbaud and 12.5-Gbaud 4QAM signals, respectively, and a BER floor is observed for both 4QAM signals at BER of around 3×10^{-4}, due to the crosstalk and phase noise. We note that, with the same amount of phase noise, the signal at lower baud rate is more sensitive to phase noise, which explains the slightly larger penalty for 10-Gbaud 4QAM in the experiment.

#251508 Received 9 Oct 2015; revised 17 Jan 2016; accepted 2 Feb 2016; published 12 Feb 2016

22 Feb 2016 | Vol. 24, No. 4 | DOI:10.1364/OE.24.003702 | OPTICS EXPRESS 3710

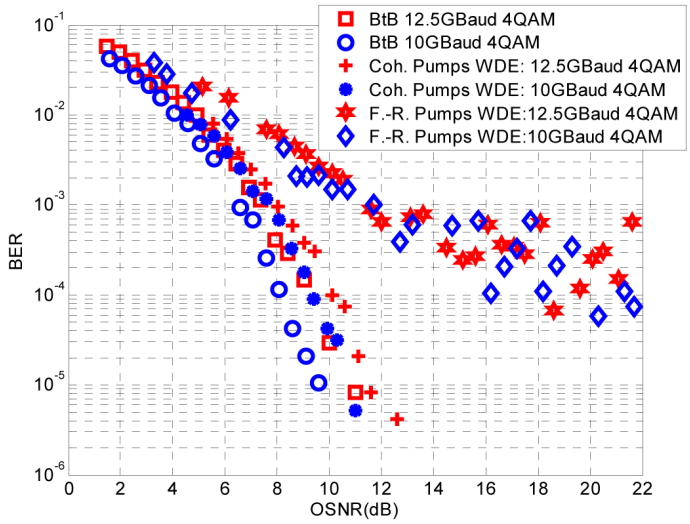

Fig. 7. BER vs. OSNR of the input signals (squares: 12.5-GBaud 4QAM, circles: 10-Gbaud 4QAM) and the swapped signals with coherent pumping (crosses: 12.5-GBaud 4QAM, stars: 10-GBaud 4QAM), and the ones with free-running pumping (hexagrams: 12.5-GBaud 4QAM, diamonds: 10-GBaud 4QAM).

4.4 Pump-phase-noise-free WDE between 4QAM and 16QAM signals

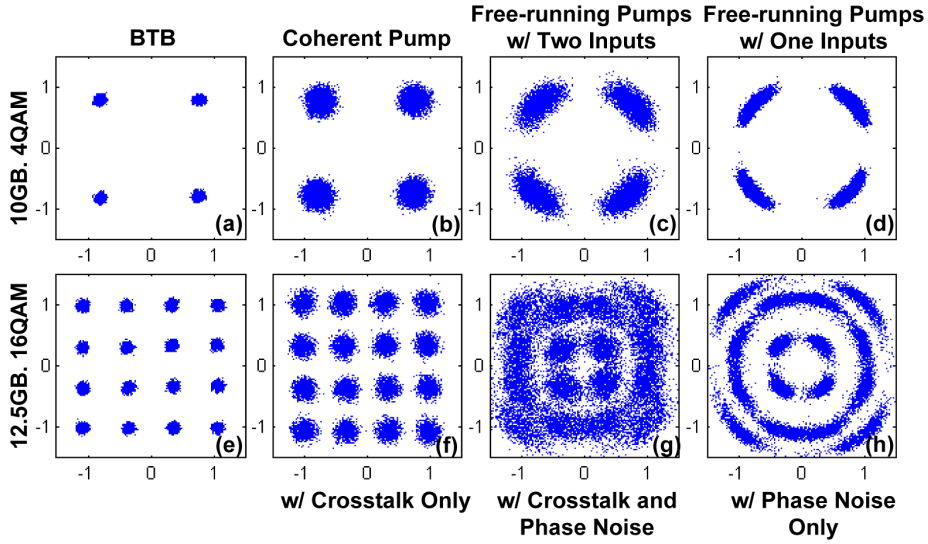

Fig. 8. Constellations of input signals: (a) 10-Gbaud 4QAM, (e) 12.5-Gbaud 16QAM; the swapped signals with coherent pumping: (b) 4QAM, (f) 16QAM, the swapped signals with free-running pumping: (c) 4QAM, (g) 16QAM, and the converted signals with only one input signals and free-running pumping: (d) 4QAM, (h) 16QAM

The WDE between 4QAM and 16QAM was also experimentally investigated. The constellations of the input signals and the swapped signals with different pump configurations are depicted in Figs. 8(a)-8(c) and 8(e)-8(g). With coherent pumps, clear constellations are observed for 4QAM and 16QAM with slightly increased EVM, which is just attributed to the crosstalk due to finite ER, whereas no visible phase noise distortion is observed owing to coherent pumping. However, with DFB free-running pumps, the obtained constellations are distorted due to both the crosstalk and the pump-originating phase noise. The presence of pump phase noise causes clear spreading of the symbols along the concentric circles

#251508 Received 9 Oct 2015; revised 17 Jan 2016; accepted 2 Feb 2016; published 12 Feb 2016

22 Feb 2016 | Vol. 24, No. 4 | DOI:10.1364/OE.24.003702 | OPTICS EXPRESS 3711

representing the signal phase, which is more severe for the higher amplitude symbols in 16QAM. This shows that with incoherent DFB pumps, the phase noise from pump severely deteriorates the swapped QAM signals. To investigate the different behavior of crosstalk and phase noise individually in the swapped signals, the performance of converted signals with only one input signal in WDE, i.e. signal wavelength shifting process, was also investigated. Figures 8(d) and 8(h) show the converted constellations for the case of free-running pumps and one input signal for 4QAM and 16QAM respectively. Here, phase noise is visible with symbol spreading along concentric circles, but no degradation caused by crosstalk can be observed, consistent with the QAM signals impaired only by phase noise. Comparing these constellations under different conditions, it is believed that the distortion due to the phase noise from free-running 3.5-MHz-linewidth DFB pumps is the dominant factor to impair the swapped signals in WDE.

The observations in constellations can also be inferred from the measured BER curves as a function of OSNR (measured at 0.1 nm) for the input and the swapped signals with coherent/incoherent pumping schemes. As shown in Fig. 9, with coherent DFB pumping, around 0.6-dB and 3-dB power penalties at BER of 10^{-3} were obtained for 4QAM and 16QAM, respectively. As discussed above, this is mainly attributed to the crosstalk introduced by finite ER (20 dB) rather than phase noise, since phase noise is eliminated in the coherent pumping. The observed power penalty for both 4QAM and 16QAM are similar to the prediction in [13] with a similar in-band crosstalk level. However, in case of free-running pumping, although it was still possible to obtain a BER curve for the swapped 4QAM signal, ~3.4-dB penalty and visible error-floor at BER of 5×10^{-4} were clearly observed. Due to the high susceptibility of 16QAM to phase noise and crosstalk, it becomes impossible to measure BER of the swapped 16QAM at any achievable noise level. This verifies the effectiveness of the elimination of the pump phase noise in the OWE for high-order QAM with coherent pumping.

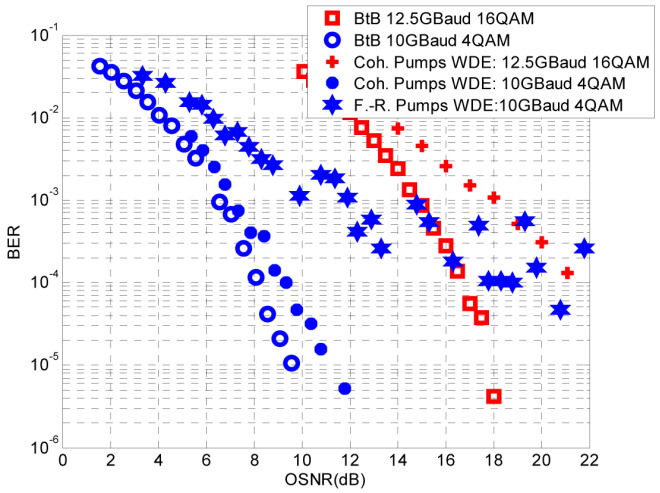

Fig. 9. BER vs. OSNR of the input signals (squares: 12.5-GBaud 16QAM, circles: 10-Gbaud 4QAM) and the swapped signals with coherent pumping (crosses: 12.5-GBaud 16QAM, stars: 10-GBaud 4QAM), and the ones with free-running pumping (hexagrams: 10-GBaud 4QAM).

4.5 Investigation of the recovered carrier phase in DSP

To detect the received QAM signals, an intradyne coherent receiver was used. The recovery of carrier phase is one of indispensable components in the offline DSP processing. It also allows insight into the impact of phase noise from the pump lasers after WDE. Figure 10 depicts the recovered carrier phase of the original input 4QAM signal where an FL was used

#251508 Received 9 Oct 2015; revised 17 Jan 2016; accepted 2 Feb 2016; published 12 Feb 2016

22 Feb 2016 | Vol. 24, No. 4 | DOI:10.1364/OE.24.003702 | OPTICS EXPRESS 3712

as the laser source (dotted red line), and those of the converted 4QAM signal with free-running DFB pumps (solid black line), and with coherent DFB pumps (dashed blue line). It is obvious that within 1.6 μs the phase variation of the converted QAM with coherent DFB pumping is comparable to that of original input QAM signal, i.e. ~0.6 rad. However, using free-running DFB pump lasers, the converted QAM signal exhibits more than 2π rad phase variation. The obtained carrier phase variation is attributed to the beating effect of input light and the LO. Here, a FL laser with 10-kHz linewidth was used as LO for detection which should add little additional phase noise. Therefore, from the observation in the recovered carrier phase further demonstrates that the coherent pump scheme is able to cancel phase noise from pump lasers, even when a DFB laser was used as pump. This also supports the observation that the increase of EVM in the converted QAM signals with coherent pumping (Figs. 8(b) and 8(f)) is not attributed to the phase noise from the pump lasers, but to the crosstalk.

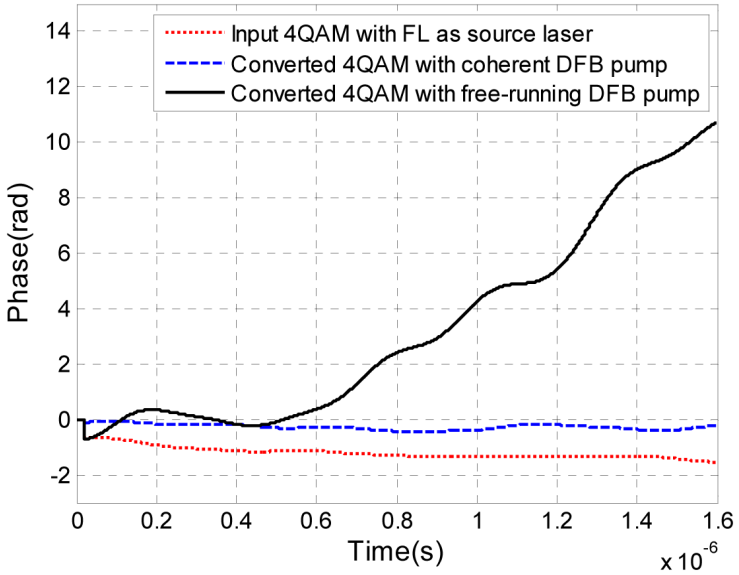

Fig. 10. Recovered carrier phase in offline DSP of the original input 4QAM signal with FL as laser source (dotted red line), the converted 4QAM signal with free-running DFB pumps (solid black line), and the converted 4QAM signal with coherent DFB pumping (dashed blue line).

5. Conclusion

We have proposed and experimentally demonstrated a WDE scheme with coherent pumps that allows cancellation of the pump laser phase noise, enabling the use of low-cost pump lasers, even for high-order QAM signals. We have experimentally demonstrated the pump-phase-noise-free WDE between 10-Gbaud 4QAM (4QAM) and 12.5-Gbaud 4QAM (16QAM) with spacing of 50 GHz, suitable for the data exchange and switching of high-order QAM signals in DWDM systems. Even using 3.5-MHz-linewidth DFB lasers as a pump sources, error-free operation was obtained for the swapped 4QAM and 16QAM signals with coherent pumping. The obtained results verify the feasibility of the proposed pump-phase-noise-free WDE scheme.

Acknowledgments

The work was supported in part by Grant-in-Aid for Scientific Research (C) (15K06033) from the Ministry of Education, Science, Sports and Culture (MEXT), Japan. A. Albuquerque also acknowledges Fundação para a Ciência e Tecnologia (FCT) for funding through the PhD grant SFRH/BD/78425/2011.

#251508 Received 9 Oct 2015; revised 17 Jan 2016; accepted 2 Feb 2016; published 12 Feb 2016

22 Feb 2016 | Vol. 24, No. 4 | DOI:10.1364/OE.24.003702 | OPTICS EXPRESS 3713

Publication E

Investigation of PPLN-based PSAs for high-gain optical amplification.

A. Albuquerque, M. Drummond, B. Puttnam, N. Wada, R. Nogueira

originally published in *Journal of Lightwave Technology*, vol. 33, no. 12, pp. 2802-2810, July 2015. Reprinted with the permission of IEEE.

2802 JOURNAL OF LIGHTWAVE TECHNOLOGY, VOL. 33, NO. 13, JULY 1, 2015

Investigation of PPLN-Based PSAs for High-Gain Optical Amplification

André A. C. Albuquerque, *Student Member, IEEE*, Miguel V. Drummond, *Member, IEEE*, Benjamin J. Puttnam, *Member, IEEE*, Naoya Wada, *Member, IEEE*, and Rogério N. Nogueira, *Member, IEEE*

***Abstract*—In this paper, different configurations of phase-sensitive amplifiers (PSAs) built with periodically poled lithium niobate (PPLN) devices are theoretically and numerically investigated, focusing on their application for amplification in optical communications systems. Single- and dual-pump configurations of one-, two-, and four-mode PSAs are discussed. For each configuration, analytical expressions for the maximum and minimum gain of the amplifiers are provided, showing the influence of the power of the pump and signal waves, as well as the length and efficiency of the PPLN waveguide. The analytical expressions are numerically validated by solving the coupled differential equations describing the nonlinear interactions in the PPLN. The obtained results show that the gain of all PSA configurations exponentially increases with the power of the pump waves, and the length and efficiency of the PPLN device, whereas it is almost independent of the power of the signal wave. In addition, it is shown in this paper that PSA configurations where an intermediate interaction is necessary to generate waves at the second-harmonic band have a gain penalty of 6 dB. It is also shown that no significant difference in terms of gain bandwidth is observed for the single- and dual-pump configurations of two-mode PSAs with an intermediate interaction. Finally, it is shown that a four-mode PSA can only be implemented under very strict conditions, with no gain advantage over two-mode PSAs.**

***Index Terms*—Nonlinear optics, periodically poled lithium niobate, phase-sensitive amplifiers.**

I. Introduction

OVER the recent years, the unique phase-sensitive (PS) properties of PSAs have been drawing considerable interest for several applications in optics and optical communications. Simultaneous phase and amplitude regeneration of phase-encoded signals [1], [2] and multilevel quantization of the optical phase [3] are examples of all-optical signal processing functionalities that have been enabled by the peculiar ability of PSAs to amplify or attenuate an input wave depending on its phase. An even more exceptional feature of PSAs is perhaps the possibility to amplify with a noise figure (NF) below 3 dB, which is the quantum limit of phase-insensitive amplifiers (PIAs), such as erbium-doped fiber amplifiers (EDFAs) [4], [5]. Due to their theoretical NF of 0 dB [5], PSAs are sometimes considered as the ultimate amplifiers, and can be potentially used to enhance the performance and extend the transmission reach of optical links originally based on amplification by EDFAs [6], [7].

However, the remarkable low-noise properties of PSAs come at the expense of implementation complexity because frequency- and phase-correlated idler waves must be generated and injected into the PSA, which may not be easily accomplished. In addition, part of the available bandwidth is lost for propagation of the idler waves. A copier + PSA scheme in which a first PIA (copier) is used to generate the correlated waves [8] and optical combs [9] are two common techniques used to produce the correlated waves.

PSAs can be built using different nonlinear media including highly nonlinear fibers (HNLFs) [5], [10], silicon waveguides [11], semiconductor optical amplifiers [12] and PPLN devices [13]. HNLFs are the most often used devices to build PSAs, but PPLN waveguides have also become very attractive due to their properties of compactness, non-existence of self-phase modulation (SPM) nor cross-phase modulation (XPM) and immunity to stimulated Brillouin scattering [13]–[15]. In addition, the recent advances on waveguide production techniques in PPLN devices have enabled achieving very high conversion efficiencies ($\sim$2000 %/W) [16], which are suitable for optical amplification purposes. In fact, high gain amplification and phase regeneration using PPLN-based PSAs have already been demonstrated [13], [15], [16]. The high insertion losses of PPLN devices can be a problem for low-noise amplification as they degrade the NF of the PSA. Nonetheless, NF values below 2 dB have already been reported in [17], even for insertion losses as high as 5 dB.

Contrarily to the other aforementioned nonlinear media whose principle of operation is based on third-order ($\chi^{(3)}$) nonlinearities, PS amplification in PPLN devices relies on second-order ($\chi^{(2)}$) three-wave mixing (TWM) processes, which include second-harmonic generation (SHG), sum-frequency generation (SFG), difference-frequency generation (DFG) and cascaded interactions of these processes. TWM are optical mixing processes in which a photon is produced from the interaction of two initial photons. In the case of SFG and SHG the frequency of the new photon is equal to the sum of that of the initial ones, whereas for DFG it is equal to the difference. SHG can be considered as a particular case of SFG in which the frequency of the initial photons is the same. Efficient TWM requires phase matching between the interacting waves, which in the case of PPLN devices is achieved by compensating the phase mismatching through periodic inversions of the ferroelectric domains (periodic poling) of a lithium niobate chip after each coherence length [14]. This technique is known as quasi phase-matching (QPM).

Manuscript received November 27, 2014; revised January 29, 2015; accepted January 29, 2015. Date of publication March 17, 2015; date of current version May 22, 2015. The work of A. Albuquerque was supported by Fundação para a Ciência e Tecnologia under the Ph.D. Grant SFRH/BD/78425/2011.

A. A. C. Albuquerque, M. V. Drummond, and R. N. Nogueira are with the Department of Pólo de Aveiro, Instituto de Telecomunicações, Campus Universitário de Santiago, 3810-193 Aveiro, Portugal (e-mail: andrealbuquerque@av.it.pt; mvd@av.it.pt; rnogueira@av.it.pt).

B. J. Puttnam and N. Wada are with the National Institute of Information and Communications Technology, Koganei, Tokyo 184-8795, Japan (e-mail: ben@nict.go.jp; wada@nict.go.jp).

Color versions of one or more of the figures in this paper are available online at http://ieeexplore.ieee.org.

Digital Object Identifier 10.1109/JLT.2015.2413932

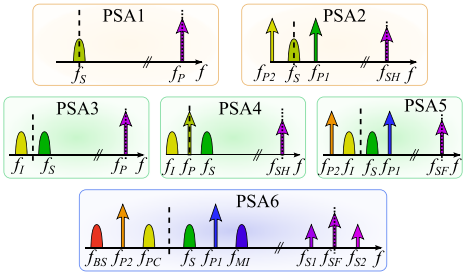

Fig. 1. Different configurations of PPLN-based PSAs studied in this work. The configurations in the top, middle and bottom rows correspond to one-, two-, and four-mode PSAs, respectively. The dashed line indicates the QPM frequency, f_{QPM}, whereas the dotted line corresponds to $2 \cdot f_{QPM}$. Subscripts: BS—Bragg scattering, I—idler, MI—modulation instability, P—pump, $P1$—pump 1, $P2$—pump 2, PC—phase conjugation, S—signal, SF—sum-frequency, $S1$—sum-frequency 1, $S2$—sum-frequency 2, SH—second harmonic.

PSAs can be implemented using different configurations, each with particular properties, which can be classified according to the number of pump waves and the number of modes, i.e., the number of signal and idler waves [18]. As cascaded TWM processes mimic four-wave mixing (FWM) [14], all the PSA configurations based on FWM in $\chi^{(3)}$ media can also be implemented using PPLN devices. In addition, PPLN devices enable the implementation of configurations that can only be built using second-order nonlinear media (configurations PSA1 and PSA3 in Fig. 1).

In this work, several configurations of one-, two- and four-mode PPLN-based PSAs are investigated and compared, with special emphasis on their application on optical amplification. Hence, the influence of the PPLN properties and the power of the pumps and signal waves on the gain of the amplifiers is analytically and numerically assessed. We note that this paper focuses only on the PSAs, without discussing how to generate the correlated waves in detail. Further information on that topic can be found in [5], [6], [13] and [16].

This article is organized as follows. The configurations of the PSAs investigated in this work are presented and briefly discussed in Section II, whereas Section III is devoted to the mathematical description of the equations governing the interaction of the waves for the different configurations, including analytical solutions of those equations for some specific cases. The numerical solutions of the equations describing the PSAs are presented and discussed in Section IV. The main conclusions of this work are summarized in Section V.

II. Configurations of PPLN-Based PSAs

The different configurations of PPLN-based PSAs studied in this work are depicted in Fig. 1, with PSA1 and PSA2 corresponding to different configurations of one-mode PSAs, PSA3, PSA4 and PSA5 to two-mode PSAs, and PSA6 to a four-mode PSA.

In PSA1, a signal (S) wave at frequency f_S is amplified by a pump (P) located at f_P via SHG, with the power flowing from the second-harmonic (pump) to the fundamental wave (signal).

TABLE I
Frequency Relations and Phase Mismatching Parameters of the Four-Mode PSA

Frequency relation	Phase mismatching parameter
1) $f_{SF} = f_{P1} + f_{P2}$	$\Delta k_1 = 2\pi\left(\frac{n_{SF}}{\lambda_{SF}} - \frac{n_{P2}}{\lambda_{P2}} - \frac{n_{P1}}{\lambda_{P1}} - \frac{1}{\Lambda}\right)$
2) $f_{SF} = f_S + f_{PC}$	$\Delta k_2 = 2\pi\left(\frac{n_{SF}}{\lambda_{SF}} - \frac{n_S}{\lambda_S} - \frac{n_{PC}}{\lambda_{PC}} - \frac{1}{\Lambda}\right)$
3) $f_{SF} = f_{MI} + f_{BS}$	$\Delta k_3 = 2\pi\left(\frac{n_{SF}}{\lambda_{SF}} - \frac{n_{MI}}{\lambda_{MI}} - \frac{n_{BS}}{\lambda_{BS}} - \frac{1}{\Lambda}\right)$
4) $f_{S1} = f_{P2} + f_S$	$\Delta k_4 = 2\pi\left(\frac{n_{S1}}{\lambda_{S1}} - \frac{n_{P2}}{\lambda_{P2}} - \frac{n_S}{\lambda_S} - \frac{1}{\Lambda}\right)$
5) $f_{S1} = f_{P1} + f_{BS}$	$\Delta k_5 = 2\pi\left(\frac{n_{S1}}{\lambda_{S1}} - \frac{n_{P1}}{\lambda_{P1}} - \frac{n_{BS}}{\lambda_{BS}} - \frac{1}{\Lambda}\right)$
6) $f_{S2} = f_{P1} + f_{PC}$	$\Delta k_6 = 2\pi\left(\frac{n_{S2}}{\lambda_{S2}} - \frac{n_{PC}}{\lambda_{PC}} - \frac{n_{P1}}{\lambda_{P1}} - \frac{1}{\Lambda}\right)$
7) $f_{S2} = f_{P2} + f_{MI}$	$\Delta k_7 = 2\pi\left(\frac{n_{S2}}{\lambda_{S2}} - \frac{n_{MI}}{\lambda_{MI}} - \frac{n_{P2}}{\lambda_{P2}} - \frac{1}{\Lambda}\right)$

Such interaction can also be understood as a fully degenerate DFG process, in which an initial photon is decomposed in two identical ones with half the frequency. PSA2 is similar to PSA1 in the sense that the signal is amplified by the second-harmonic located at $f_{SH} = 2f_S$ through SHG. In PSA2, however, the second-harmonic is first generated through an intermediate SFG interaction between the two pumps located at f_{P1} and f_{P2}. It should be noted that $f_{SH} = f_{P1} + f_{P2}$ (SFG) is mathematically equivalent to $f_{P2} = f_{SH} - f_{P1}$, which is a DFG process. Therefore, PSA2 can be modeled as a cascaded DFG and SHG (cDFG/SHG) interaction. Compared to PSA1, PSA2 is more attractive for applications in optical communications because all the input waves to the PSA can be in the typical erbium-band, around 1550 nm.

PSA3, PSA4 and PSA5 are two-mode PSAs in which a wave respectively located at f_P, f_{SH} and the SFG frequency, f_{SF}, amplifies both the signal and idler (f_I) waves via DFG. In PSA4 and PSA5, however, the waves at f_{SH} and f_{SF} are first generated through intermediate SHG of the pump at f_P and SFG between pumps at f_{P1} and f_{P2}, respectively. Thus, PSA4 and PSA5 can be considered as cSHG/DFG and cascaded SFG and DFG (cSFG/DFG) processes.

PSA6 is a four-mode configuration in which the signal and three idler waves located at $f_{PC} = f_{P1} + f_{P2} - f_S$, $f_{MI} = 2f_{P1} - f_S$ and $f_{BS} = f_S + f_{P2} - f_{P1}$ are amplified by two pumps waves (f_{P1} and f_{P2}) through seven cascaded TWM processes, whose frequency relations are shown in Table I. In fiber-based PSAs, the idler waves located at f_{PC}, f_{MI} and f_{BS} are typically denominated as phase conjugation (PC), modulation instability (MI) and Bragg scattering (BS) waves [19], respectively, which are also considered in this work.

Several other configurations of PPLN-based PSAs are possible, but the discussion in this work is restricted to the most representative ones, and using no more than two pumps waves.

III. Theoretical Model and Analytical Solutions

As mentioned in Section II, all the different configurations of PSAs presented in this work can be modeled as one or several cascaded TWM processes. Starting from the Maxwell equations, and assuming the slowly varying envelope approximation and that all the waves are continuous-waves [20], the TWM

processes in a PPLN are described by a set of coupled first-order nonlinear ordinary differential equations as reported in [20]–[22]. Each of those equations represent the evolution of the optical field of the interacting waves along the PPLN device. However, in general, the coupled differential equations cannot be solved analytically, unless for some specific cases and assuming certain approximations. The analytical solutions and the conditions for which they are valid are presented in the following sections. For simplicity, the propagation losses are neglected in this work.

A. PSA1

As mentioned in Section II, PSA1 can be modeled as a SHG interaction, described by the following set of differential equations [20], [22]

$$\frac{dA_S}{dz} = -i\kappa_S A_P A_S^* e^{-i\Delta k z} \tag{1a}$$

$$\frac{dA_P}{dz} = -i\frac{\kappa_P}{2} A_S^2 e^{i\Delta k z}, \tag{1b}$$

with A_j the optical field of the wave with frequency f_j, $\Delta k = 2\pi(n_P/\lambda_P - 2n_S/\lambda_S - 1/\Lambda)$ the phase mismatching parameter, and κ_j a nonlinear coupling coefficient, given by [20]

$$\kappa_j(\lambda_j) = d_{\text{eff}} \cdot \frac{2\pi}{\lambda_j}\sqrt{\frac{2}{n_j n_k n_l c\epsilon_0 A_{\text{eff}}}}. \tag{2}$$

In (1) and (2), λ_j and n_j are the wavelength and refractive index of the waves with frequency f_j, z is the propagation direction, c and ϵ_0 are the speed of light and electrical permittivity in vacuum, A_{eff} and d_{eff} are the effective overlap area and nonlinear coefficient, and Λ is the poling period. The optical field A_j is proportional to the electrical field of the waves and normalized in such a way that $A_j A_j^* = P_j$, with P_j the power of the wave [20].

In order to obtain an analytical solution for (1) let us assume that for neighboring waves (i.e., $|f_m - f_n| \ll f_m$), $\kappa_m(f_m) \approx \kappa_n(f_n)$, and equal to κ for waves in the frequency band of the fundamental wave, or 2κ for those in the second-harmonic band. Considering this approximation, κ can also be related to the so called SHG efficiency, η, through the expression $\kappa = \sqrt{\eta}/L^2$, where L is the length of the PPLN. It is also convenient to consider $A_j = a_j \exp(i\phi_j)$, where a_j and ϕ_j are the magnitude and the phase of the field, respectively. By separating the real and imaginary parts of (1) and by defining $\theta = \phi_P - 2\phi_S - \Delta k z$, the following set of equations is obtained

$$\frac{da_S}{dz} = -\kappa a_S a_P \sin(\theta) \tag{3a}$$

$$\frac{da_P}{dz} = \kappa a_S^2 \sin(\theta) \tag{3b}$$

$$\frac{d\theta}{dz} = \kappa\cos(\theta)\left(a_P - \frac{a_S^2}{a_P}\right) - \Delta k. \tag{3c}$$

In (3), the evolution of a_S and a_P is determined by the term $\sin(\theta)$, which depends on the phase between the fundamental and second-harmonic waves and confers the PS properties to the PSA.

The solution of (3) for any initial conditions is generally described in terms of the Jacobi elliptic functions, as detailed in [23]. However, if the signal is located at the QPM wavelength, λ_{QPM}, at which $\Delta k = 0$, and for $\theta(z=0) = \theta(0) = \pm\pi/2$, the solution of (3) is greatly simplified. In those two specific cases, θ remains constant along the PPLN and $\sin(\theta)$ is ± 1. Therefore, when $\theta = -\pi/2$ the power transfer from the pump wave to the signal and, consequently, the gain of the signal wave are maximized, whereas for $\theta = \pi/2$ an opposite power transfer occurs (minimum gain). The following closed-form solutions for $\theta = \pm\pi/2$ can then be obtained

$$a_S(z) = a_S(0) \cdot \frac{a_0}{a_0\cosh(\delta z) \pm a_P(0)\sinh(\delta z)} \tag{4a}$$

$$a_P(z) = a_0 \cdot \frac{a_P(0) \pm a_0\tanh(\delta z)}{a_0 \pm a_P(0)\tanh(\delta z)}, \tag{4b}$$

where $\delta = a_0\kappa$ and $a_0 = \sqrt{P_S(0) \mp P_P(0)}$. The signs "$-$" and "$+$" in (4) correspond to maximum ($\theta = -\pi/2$) and minimum ($\theta = \pi/2$) power transfer from the pump to the signal, respectively.

For any other value of θ, the gain of the amplifier must be described in terms of the Jacobi elliptic functions, and varies between the two extreme possibilities described in (4), as depicted in Fig. 4(a). This is also true for the other configurations studied in this work. Hence, a similar procedure to that employed in this section to determine the maximum and minimum possible values of the gain of the PSAs is used for the other configurations in the following sections.

Finally, we conclude this section by noticing that λ_{QPM} is affected by the thermal expansion of the lithium niobate substrate and especially by the variation of the refractive index with the temperature. Hence, the temperature of operation is a very important parameter that must be precisely controlled, but can also be used to tune λ_{QPM} to a desired value.

B. PSA2

The coupled differential equations describing PSA2 (modeled as a cSHG/DFG interaction) are presented in (5) [21]

$$\frac{dA_S}{dz} = -i\kappa_S A_{SH} A_S^* e^{-i\Delta k_1 z} \tag{5a}$$

$$\frac{dA_{P1}}{dz} = -i\kappa_{P1} A_{SH} A_{P2}^* e^{-i\Delta k_2 z} \tag{5b}$$

$$\frac{dA_{P2}}{dz} = -i\kappa_{P2} A_{SH} A_{P1}^* e^{-i\Delta k_2 z} \tag{5c}$$

$$\frac{dA_{SH}}{dz} = -i\frac{\kappa_{SH}^{(1)}}{2} A_S^2 e^{i\Delta k_1 z} - i\kappa_{SH}^{(2)} A_{P1} A_{P2} e^{i\Delta k_2 z}. \tag{5d}$$

In (5), $\Delta k_1 = 2\pi(n_{SH}/\lambda_{SH} - 2n_S/\lambda_S - 1/\Lambda)$ and $\Delta k_2 = 2\pi(n_{SH}/\lambda_{SH} - n_{P1}/\lambda_{P1} - n_{P2}/\lambda_{P2} - 1/\Lambda)$ are the phase mismatching parameters for the SHG and DFG processes, respectively. Two different nonlinear coupling coefficients are defined for the second-harmonic wave, $\kappa_{SH}^{(1)}$ for SHG and $\kappa_{SH}^{(2)}$ for DFG.

Let us assume that the power of the two pumps is the same, i.e., $P_{P1} = P_{P2} = P_P/2$, where P_P is the total pump power, and $P_S \ll P_P$ so that the first term of (5d) can be neglected. Following a similar procedure to that performed in Section III-A, and defining $\theta_1 = \phi_{SH} - 2\phi_S - \Delta k_1 z$ and $\theta_2 = \phi_{SH} - \phi_{P1} - \phi_{P2} - \Delta k_2 z$, the solutions for the maximum and minimum gain of the amplifier are given by

$$a_S(z) = a_S(0) \cdot [\cosh(\delta z)]^{\pm 1} \tag{6a}$$

$$a_{P1}(z) = a_{P2}(z) = a_{P1}(0)/\cosh(\delta z) \tag{6b}$$

$$a_{SH}(z) = a_0 \cdot \tanh(\delta z), \tag{6c}$$

with $\delta = \kappa a_0$, and $a_0 = \sqrt{2P_{P1}(0) \mp P_S(0)}$. The variables θ_1 and θ_2 represent the relative phase of the interacting wave of each TWM interaction. In (6a), the sign "+" corresponds to the maximum gain, achieved for $\theta_1 = +\pi/2$, whereas "−" is the solution of the minimum gain, for $\theta_1 = -\pi/2$. In both cases $\theta_2 = -\pi/2$.

C. PSA3

PSA3 is modeled as a DFG interaction whose coupled differential equations are given by [20]

$$\frac{dA_S}{dz} = -i\kappa_S A_P A_I^* e^{-i\Delta k z} \tag{7a}$$

$$\frac{dA_I}{dz} = -i\kappa_I A_P A_S^* e^{-i\Delta k z} \tag{7b}$$

$$\frac{dA_P}{dz} = -i\kappa_P A_S A_I e^{i\Delta k z}, \tag{7c}$$

with $\Delta k = 2\pi(n_P/\lambda_P - n_S/\lambda_S - n_I/\lambda_I - 1/\Lambda)$.

By defining $\theta = \phi_P - \phi_S - \phi_I - \Delta k z$, assuming perfect phase matching ($\Delta k \approx 0$) and that the power of the pump remains undepleted, the maximum and minimum gain of the PSA can be obtained as in Section III-A. The evolution of the optical fields for the maximum and minimum gain values of PSA3 is then given by

$$a_S(z) = a_S(0)\cosh(\delta z) \pm a_I(0)\sinh(\delta z) \tag{8a}$$

$$a_I(z) = a_I(0)\cosh(\delta z) \pm a_S(0)\sinh(\delta z) \tag{8b}$$

$$a_P(z) \approx a_P(0), \tag{8c}$$

where $\delta = \kappa a_P(0)$, and the signs "+" and "−" correspond to the cases for maximum and minimum gains, obtained for $\theta = \pi/2$ and $\theta = -\pi/2$, respectively.

As discussed before, a PSA requires that both signal and idler waves must be present at the input of the amplifier, otherwise it becomes a PIA. Hence, if no idler wave is injected into the PPLN, the evolution of the optical fields in the PPLN device for configuration PSA3 is also given by (8), but with $a_I(0) = 0$.

D. PSA4

Configuration PSA4 can be described as a cSHG/DFG interaction as in PSA2. Thus, (5) can also be used to describe the evolution of the optical fields of the interacting waves, provided that the subscripts $P1$, S and $P2$ are respectively replaced by S, P and I.

In order to obtain an analytical solution for the cases of maximum and minimum gain of PSA4 let us define two relative phase variables, $\theta_1 = \phi_{SH} - 2\phi_P - \Delta k_1 z$ (SHG) and $\theta_2 = \phi_{SH} - \phi_S - \phi_I - \Delta k_2 z$ (DFG). Also, let us assume that both mismatch parameters are approximately 0, $a_S(z) = a_I(z)$, and that the variation of the second harmonic is mainly due to SHG of the pump wave, so that the second term of the right side of (5d) is approximately 0. Considering these approximations the following solution for PSA4 is obtained

$$a_P(z) = a_P(0)/\cosh(\delta z) \tag{9a}$$

$$a_{SH}(z) = a_0 \cdot \tanh(\delta z) \tag{9b}$$

$$a_S(z) = a_I(z) = a_S(0) \cdot [\cosh(\delta z)]^{\pm 1}, \tag{9c}$$

where the signs "+" and "−" corresponds to the maximum and minimum gains, achieved for $\theta_2 = \pi/2$ and $\theta_2 = -\pi/2$, respectively, and with $\theta_1 = -\pi/2$ in both cases. In (9), $\delta = \kappa a_0$ and $a_0 = \sqrt{P_P(0) \mp 2P_S(0)}$.

As in Section III-C, the maximum gain of PSA4 can be compared to its phase-insensitive (PI) equivalent, i.e., with no input idler wave. In order to do so, let us also assume that the variation of the second harmonic is mainly due to SHG of the pump wave, which is valid as long as the power of the signal and the idler is much lower than that of the pump wave. In that case, the evolution of a_P and a_{SH} is also described by (9a) and (9b), but now with $a_0 = a_P(0)$. Since the evolution of the second-harmonic is known, a further simplification can be done by replacing $a_{SH}(z)$ in the differential equations of a_S and a_I by an equivalent effective value, $\langle a_{SH} \rangle$. The following solution is obtained

$$a_S(z) = a_S(0) \cdot \cosh(\bar{\delta} z) \tag{10a}$$

$$a_I(z) = a_S(0) \cdot \sinh(\bar{\delta} z), \tag{10b}$$

where $\bar{\delta} = \kappa \langle a_{SH} \rangle$. The effective magnitude of the second-harmonic can be obtained by averaging $a_{SH}(z)$ along the PPLN through

$$\langle a_{SH} \rangle = \frac{1}{L}\int_0^L a_{SH}(z)dz = a_P(0)\frac{\ln[\cosh(\delta L)]}{\delta L}. \tag{11}$$

E. PSA5

PSA5 is modeled as a cSFG/DFG process, whose coupled differential equations are given by [20]

$$\frac{dA_{P1}}{dz} = -i\kappa_{P1} A_{SF} A_{P2}^* e^{-i\Delta k_1 z} \tag{12a}$$

$$\frac{dA_{P2}}{dz} = -i\kappa_{P2} A_{SF} A_{P1}^* e^{-i\Delta k_1 z} \tag{12b}$$

$$\frac{dA_{SF}}{dz} = -i\kappa_{SF}^{(1)} A_{P1} A_{P2} e^{i\Delta k_1 z} - i\kappa_{SF}^{(2)} A_S A_I e^{i\Delta k_2 z} \tag{12c}$$

$$\frac{dA_S}{dz} = -i\kappa_S A_{SF} A_I^* e^{-i\Delta k_2 z} \tag{12d}$$

$$\frac{dA_I}{dz} = -i\kappa_I A_{SF} A_S^* e^{-i\Delta k_2 z}. \tag{12e}$$

In (12), the phase mismatching parameter for SFG is given by $\Delta k_1 = 2\pi(n_{SF}/\lambda_{SF} - n_{P1}/\lambda_{P1} - n_{P2}/\lambda_{P2}$

$-1/\Lambda$), whereas the one for DFG is $\Delta k_2 = 2\pi(n_{SF}/\lambda_{SF} - n_S/\lambda_S - n_I/\lambda_I - 1/\Lambda)$.

In order to obtain the analytical solution for maximum and minimum gain of PSA5 let us define two relative phase parameters, $\theta_1 = \phi_{SF} - \phi_{P1} - \phi_{P2} - \Delta k_1 z$ for SFG and $\theta_2 = \phi_{SF} - \phi_S - \phi_I - \Delta k_2 z$ for DFG. Also, let us assume perfect QPM (Δk_1 and Δk_2 approximately equal to 0) and that the variation of the sum-frequency wave is mainly due to SFG of the two pump waves (the second term in (12c) is approximately 0). If $a_{P1} \approx a_{P2}$ and $a_S \approx a_I$, the following solution is obtained

$$a_{P1}(z) = a_{P2}(z) = a_0/\cosh(\delta z) \tag{13a}$$

$$a_{SF}(z) = a_0 \cdot \tanh(\delta z) \tag{13b}$$

$$a_S(z) = a_I(z) = a_S(0) \cdot [\cosh(\delta z)]^{\pm 1}. \tag{13c}$$

In (13), the signs "+" and "−" correspond to the maximum and minimum gains, achieved for $\theta_2 = \pi/2$ and $\theta_2 = -\pi/2$, respectively, and $\theta_1 = -\pi/2$ in both cases. The parameter δ is given by $\delta = \kappa a_0$, with $a_0 = \sqrt{2P_{P1}(0) \mp 2P_S(0)}$.

The gain of the amplifier in PI operation can be obtained as described in Section III-D. By assuming that the variation of the sum-frequency wave is mainly due to SFG of the pump waves, a_{P1}, a_{P2} and a_{SF} are also given by (13a) and (13b), but with $a_0 = \sqrt{2P_{P1}(0)}$. By replacing $a_{SF}(z)$ in the differential equations of a_S and a_I by its equivalent effective value, $\langle a_{SF} \rangle$, the evolution of a_S and a_I in PI operation is given by

$$a_I(z) = a_S(0) \cdot \sinh(\bar{\delta} z) \tag{14a}$$

$$a_S(z) = a_S(0) \cdot \cosh(\bar{\delta} z), \tag{14b}$$

where $\bar{\delta} = \kappa \langle a_{SF} \rangle = \ln[\cosh(\delta L)]/L$, obtained by averaging the optical field of the sum-frequency wave along the PPLN as in (11).

F. PSA6

As mentioned in Section II, PSA6 involves seven different TWM processes whose frequency relations and respective phase mismatching parameters are given in Table I. The evolution of the different interacting waves in PSA6 can be described by

$$\frac{dA_{P1}}{dz} = -i\kappa_{P1}^{(1)} A_{SF} A_{P2}^* e^{-i\Delta k_1 z} - i\kappa_{P1}^{(2)} A_{S1} A_{BS}^* e^{-i\Delta k_5 z} - i\kappa_{P1}^{(3)} A_{S2} A_{PC}^* e^{-i\Delta k_6 z} \tag{15a}$$

$$\frac{dA_{P2}}{dz} = -i\kappa_{P2}^{(1)} A_{SF} A_{P1}^* e^{-i\Delta k_1 z} - i\kappa_{P2}^{(2)} A_{S1} A_S^* e^{-i\Delta k_4 z} - i\kappa_{P2}^{(3)} A_{S2} A_{MI}^* e^{-i\Delta k_7 z} \tag{15b}$$

$$\frac{dA_{SF}}{dz} = -i\kappa_{SF}^{(1)} A_{P1} A_{P2} e^{i\Delta k_1 z} - i\kappa_{SF}^{(2)} A_S A_{PC} e^{i\Delta k_2 z} - i\kappa_{SF}^{(3)} A_{MI} A_{BS} e^{i\Delta k_3 z} \tag{15c}$$

$$\frac{dA_S}{dz} = -i\kappa_S^{(1)} A_{SF} A_{PC}^* e^{-i\Delta k_2 z} - i\kappa_S^{(2)} A_{S1} A_{P2}^* e^{-i\Delta k_4 z} \tag{15d}$$

$$\frac{dA_{PC}}{dz} = -i\kappa_{PC}^{(1)} A_{SF} A_S^* e^{-i\Delta k_2 z} - i\kappa_{PC}^{(2)} A_{S2} A_{P1}^* e^{-i\Delta k_6 z} \tag{15e}$$

$$\frac{dA_{MI}}{dz} = -i\kappa_{MI}^{(1)} A_{SF} A_{BS}^* e^{-i\Delta k_3 z} - i\kappa_{MI}^{(2)} A_{S2} A_{P2}^* e^{-i\Delta k_7 z} \tag{15f}$$

$$\frac{dA_{BS}}{dz} = -i\kappa_{BS}^{(1)} A_{SF} A_{MI}^* e^{-i\Delta k_3 z} - i\kappa_{BS}^{(2)} A_{S1} A_{P1}^* e^{-i\Delta k_5 z} \tag{15g}$$

$$\frac{dA_{S1}}{dz} = -i\kappa_{S1}^{(1)} A_{P2} A_S e^{i\Delta k_4 z} - i\kappa_{S1}^{(2)} A_{P1} A_{BS} e^{i\Delta k_5 z} \tag{15h}$$

$$\frac{dA_{S2}}{dz} = -i\kappa_{S2}^{(1)} A_{P1} A_{PC} e^{i\Delta k_6 z} - i\kappa_{S2}^{(2)} A_{P2} A_{MI} e^{i\Delta k_7 z}. \tag{15i}$$

At this point it is important to briefly discuss the role of the phase mismatching parameters and how they affect the behavior of PSA6. In order to maximize the gain of PSA6, the poling period of the PPLN is typically chosen in order to quasi-phase match the SFG interaction between the two pumps, which results in $\Delta k_1 = 0$. Fortunately, Δk_2 and Δk_3 are also very small in a wide spectral range around the QPM wavelength due to the symmetric frequency distribution of the interacting waves. However, this is not true for the other phase mismatching parameters, which can easily scale up to very high values even for wavelength separations between the signal and pump 1 (P1) of ∼1 nm. As a consequence, the efficiency of such nonlinear interactions is greatly reduced and the terms in (15) representing those interactions can be neglected. In that case, the waves $S1$ and $S2$ cannot be efficiently generated and no possible interaction between the signal or the PC wave with the BS and MI idlers can occur. Hence, PSA6 cannot behave as a four-mode PSA. In fact, unless $f_S \approx f_{P1}$, PSA6 behaves as two independent two-mode PSAs, one for the signal and PC wave pair and the other for the MI and BS waves.

Let us then assume that $f_S \approx f_{P1}$ so that all the phase mismatching parameters are approximately 0. In addition, let us consider that $a_{P1}(z) \approx a_{P2}(z)$, $a_S(z) \approx a_{MI}(z) \approx a_{PC}(z) \approx a_{P1}(z)$ and, consequently, $a_{S1}(z) \approx a_{S2}(z)$. Finally, let us define seven relative phase parameters, θ_k, where k represents each TWM process of PSA6, whose frequency relation between the interacting waves can be generally expressed by $f_l = f_m + f_n$. Then, each variable θ_k is given by $\theta_k = \phi_l - \phi_m - \phi_n$. The maximum gain of the amplifier corresponds to the case when the power of the pumps is maximally transferred to the SFG wave and from the SFG wave to the signal and idlers, which is verified when $\theta_1 = -\pi/2$, and $\theta_2 = \theta_3 = \pi/2$. In addition, the four-mode properties of the PSA can only be enabled if some power is somehow transferred from and to the $S1$ and $S2$ waves, but their overall power must be very low (ideally 0) in order to maximize the gain of the signal. This means that the two terms in (15h) and (15i) must cancel each other, which occurs when $\theta_4 = \theta_7 = -\pi/2$, and $\theta_5 = \theta_6 = \pi/2$. The evolution of the magnitude of the optical fields of PSA6 is then given by

$$a_{P1}(z) = a_{P2}(z) = a_{P1}(0)\tanh(\delta z) \tag{16a}$$

$$a_{SF}(z) = a_0/\cosh(\delta z) \tag{16b}$$

$$a_S(z) = a_{MI}(z) = a_{PC}(z)$$
$$= a_{BS}(z) = a_S(0)\cosh(\delta z) \quad (16c)$$
$$a_{S1}(z) = a_{S2}(z) \approx 0, \quad (16d)$$

with $\delta = a_0\kappa$ and $a_0 = \sqrt{2P_{P1}(0) - 2P_S(0)}$.

G. Small Signal Gain

The analytical expressions provided in the previous sections for the optical field of the signal wave can be used to calculate the maximum gain of the different PSAs through $G(L) = [a_S(L)/a_S(0)]^2$. For applications in optical amplification, the input power of the signal, P_S, is typically much lower than that of the pump wave, P_P, and the gain of the PSAs, henceforth designated as the small signal gain, is given in (17a) for PSA1 and PSA3, and in (17b) for the remainder configurations

$$G(L) = \exp(2\sqrt{P_P}\kappa L) \quad (17a)$$
$$G(L) = \frac{\exp(2\sqrt{P_P}\kappa L)}{4}. \quad (17b)$$

The previous equations were obtained assuming that the gain is high enough so that $\cosh(x) \approx \sinh(x) \approx \exp(x)/2$, and that $P_P(0) = P_{P1}(0) + P_{P2}(0) = 2P_{P1}(0)$ for dual-pump configurations. Compared to PSA1 and PSA3, the small signal gain of the remainder configurations is four times (6 dB) lower.

The small signal gain for PI operation, G_{PI}, can also be calculated using (8) with $a_I(0) = 0$ for PSA3, (10) for PSA4 and (14) for PSA5. The small signal gain in PI operation is then given by (18a) for PSA3, and (18b) for PSA4 and PSA5

$$G_{\mathrm{PI}}(L) = \frac{\exp(2\sqrt{P_P}\kappa L)}{4} \quad (18a)$$
$$G_{\mathrm{PI}}(L) = \frac{\exp(2\sqrt{P_P}\kappa L)}{16}. \quad (18b)$$

Comparing (17) and (18) for two-mode PPLN-based PSAs, an additional gain of 6 dB is obtained when switching from PI to PS operation.

IV. Numerical Simulations

In this section, numerical simulations of the influence of P_P, P_S, L and η on the maximum gain of the different PSA configurations are presented and compared to the analytical solutions obtained in the previous section. The simulations are performed using a common fourth-order Runge–Kutta method to solve the coupled differential equations describing the TWM interactions. The effects of the relative phase between the interacting waves and the impact of the wavelength of the signal on the gain of the PSA are also investigated. However, since no analytical expression could be obtained for the influence of these parameter on the gain of the amplifiers, only numerical simulations are presented. Unless otherwise stated, a PPLN device with length, poling period, QPM wavelength, temperature of operation and SHG efficiency of respectively 6 cm, 19.39 μm, 1550 nm, 25°C and 500%/W is considered for all configurations. In addition, the wavelength of the pump wave in single-pump configurations is selected at either λ_{QPM} or $\lambda_{QPM}/2$. For dual-pump configurations, the wavelength of the first pump (λ_{P1}) is 1545 nm, whereas the wavelength of the other pump is $\lambda_{P2} = 1/(2\cdot\lambda_{QPM}^{-1} - \lambda_{P1}^{-1})$.

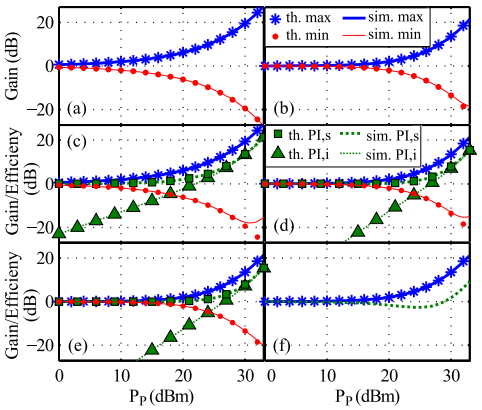

Fig. 2. Variation of the gain/conversion efficiency with P_P for configurations: (a) PSA1, (b) PSA2, (c) PSA3, (d) PSA4, (e) PSA5, and (f) PSA6. The curves labeled as "th. max/min" and "sim. max/min" correspond to theoretical and numerical solutions for maximum/minimum gain of the amplifiers, respectively. Likewise, those with labels "th. pi,s/i" and "sim. pi,s/i" correspond to the theoretical and numerical solutions in PI operation for the signal/idler wave. For all configurations, $P_S = -20$ dBm.

The influence of the total pump power, P_P, on the gain of the amplifier is depicted in Fig. 2 for the different PSA configurations. In the simulations of Fig. 2, λ_s was set to λ_{QPM} for PSA1 and PSA2, 1547 nm for PSA3, PSA4 and PSA5, and 1545.01 nm for PSA6. As expected, the maximum (minimum) gain of the amplifier increases (decreases) exponentially with P_P for all configurations. A very good agreement between the theoretical and numerical solutions is observed for all configurations up to more than $P_P = 30$ dBm. The numerical simulations also show that the maximum gain of PSA1 and PSA3 in PS operation at P_P of 30 dBm is about 19.4 dB, whereas $\sim$ 13.5 dB is measured for the other configurations. These results are in agreement with the theoretical predictions of four times (6 dB) higher gain for PSA1 and PSA3, as aforementioned in Section III-G. The main reason for such a difference is that in the case of PSA1 and PSA3 the wave at the second-harmonic band (f_{SH} or f_{SF}) is already present at the input of the PPLN, whereas in the other cases it has to be generated first through an intermediate SHG or SFG interaction, which reduces the gain of the amplifiers.

The gain of the amplifier operating in PI mode is also shown in Fig. 2, for two- and four-mode configurations. The numerical simulations show that for high values of P_P the gain of the amplifiers in PS operation becomes about four times (6 dB) higher than that in PI mode for two-mode PSAs, as mentioned in Section III-G. This result is also observed in two-mode PSAs built with HNLFs and it is a consequence of constructive interference of the correlated signal and idler waves [5]. The conversion efficiency of the idlers waves, defined as the power ratio between the output idler and input signal, for configurations PSA3, PSA4 and PSA5 in PI operation is also shown in Fig. 2.

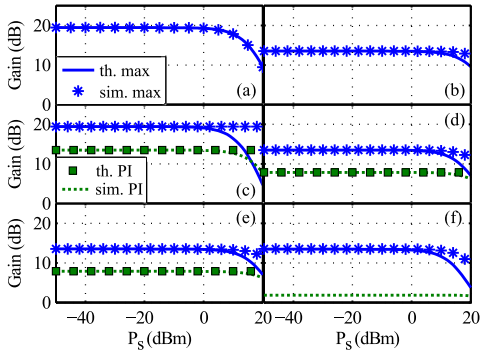

Fig. 3. Variation of the gain with P_S for configurations: (a) PSA1, (b) PSA2, (c) PSA3, (d) PSA4, (e) PSA5, and (f) PSA6. The curves labeled as "th. max" and "sim. max" correspond to theoretical and numerical solutions for maximum gain of the amplifiers, respectively. Curves "th. pi" and "sim. pi" correspond to the theoretical and numerical solutions in PI operation for the signal wave. For all cases, $P_P = 30$ dBm.

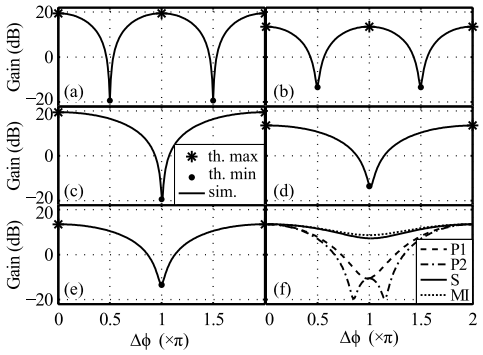

Fig. 4. Variation of the gain with the phase of the signal for configurations: (a) PSA1, (b) PSA2, (c) PSA3, (d) PSA4, (e) PSA5, and (f) PSA6. The markers "$*$" and "$\bullet$" correspond to theoretical maximum and minimum gains of the amplifiers, respectively. In (f), the dashed, dot-dashed and dotted curves correspond to the variation of the gain with the phase of P1, P2 and MI waves, respectively. For all cases, $P_P = 30$ dBm and $P_S = -20$ dBm.

As expected, the conversion efficiency of the idler increases with P_P, and the signal gain only becomes significant when the signal and the idler have similar power values. Moreover, at low P_P values, the conversion efficiency in PSA4 and PSA5 is much lower than in PSA3, which is a consequence of requiring intermediate SHG and SFG steps prior to the idler generation. For PSA6, the gain of the amplifier in PI mode for $P_P = 30$ dBm is 1.8 dBm, whereas a gain of 7.8 dB was measured for PSA4 and PSA5. In PSA6, the generation of the BS and MI idlers requires intermediate SFG steps, in which part of the power of the signal and of the PC idler is converted to the S1 and S2 waves, respectively. Thus, the lower PI gain of the four-mode configuration compared to PSA4 and PSA5 is caused by partial depletion of the signal and PC waves in the intermediate SFG steps. The PS gain of PSA6 is about 16 times (12 dB) higher than that in PI mode as a result of the constructive interference of not only two, but four correlated waves. However, as the maximum PS gain of PSA6 is approximately the same of PSA4 and PSA5, the higher additional gain of the four-mode amplifier when switching from PI to PS operation is only due to the lower PI gain.

The variation of the gain with the input signal power, P_S, is shown in Fig. 3. The results show that the gain of the amplifiers is almost independent of P_S until saturation, at power values of $\sim$5 dBm, and then decreases for higher P_S values. As the gain of the amplifier in PI operation is lower, saturation is achieved at higher P_S values ($>$10 dBm). A very good agreement between the analytical expressions and numerical simulations is observed when the amplifiers are not in the saturation regime. While in saturation, the approximation of undepleted pumps no longer remains valid, which explains the observed differences. The PS properties of the PSAs are evidenced in Fig. 4 where the gain of the amplifiers is depicted as a function of the phase of the signal wave relatively to the maximum gain condition, $\Delta\phi$. For all configurations a sinusoidal variation of the gain with $\Delta\phi$ is observed, with a periodicity of π for one-mode PSAs and 2π for the remainder configurations. In Fig. 4(f), the gain of the four-mode PSA is strongly affected by the phase of the

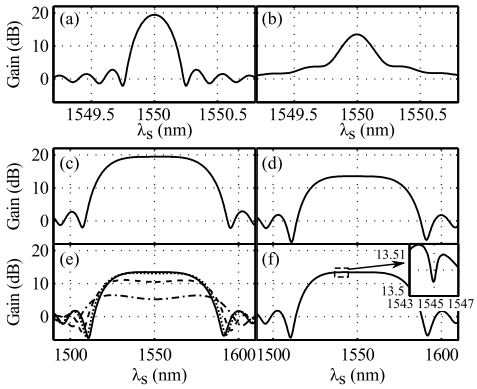

Fig. 5. Variation of the gain with λ_S for (a) PSA1, (b) PSA2, (c) PSA3, (d) PSA4, (e) PSA5, and (f) PSA6. In (e), the solid, dotted, dashed and dot-dashed lines correspond to a wavelength spacing between the two pumps of 10, 30, 50 and 70 nm, respectively. For all cases, $P_P = 30$ dBm and $P_S = -20$ dBm.

pumps, with more than 20 dB difference between the maximum and minimum gains, whereas less than 7 dB gain variation is verified when changing the phase of the signal and MI waves. Similar lower gain variations are observed when changing the phase of the BS and PC waves, which results from the fact that each pump wave participates in more FWM processes than the signal or an idler wave.

The impact of the wavelength of the signal wave on the gain of the one-mode PSAs is depicted in Fig. 5(a) and (b). As expected, a maximum gain value is achieved at λ_{QPM} (1550 nm), but quickly drops to very low values for wavelength detuning from λ_{QPM} higher than 0.25 nm due to the phase mismatching effects. Therefore, for one-mode PPLN-based PSAs not only the frequency and phase of the waves must be correlated, but also λ_S must be precisely tuned to match λ_{QPM}, or λ_{QPM} must be tuned to λ_S by changing the temperature of operation. Nonetheless, any possibility of multichannel amplification for

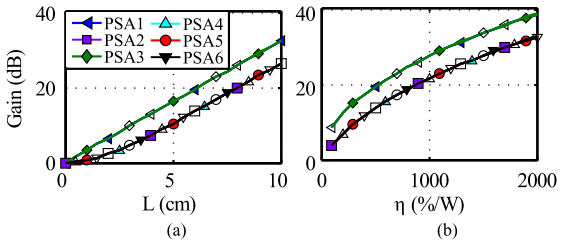

Fig. 6. Variation of the gain of the PSA with (a) L for $\eta = 500\%$/W, and (b) η for $L = 6$ cm. In both cases, $P_P = 30$ dBm and $P_S = -20$ dBm. Curves with hollow markers correspond to the analytical solutions, whereas those with filled markers are numerical simulations.

optical communication systems is precluded in both ways. On the other hand, as Fig. 5(c)–(f) suggest, the wavelength of the signal can be chosen within more than 40 nm without any significant gain variation, making two-mode PSAs suitable for multichannel amplification. However, in order to achieve high gain, the wavelength of the pump must be precisely set to $\lambda_{QPM}/2$ (PSA3) or λ_{QPM} (PSA4) in the case of single-pump configurations, or symmetrically detuned around λ_{QPM} for dual-pump configurations, so that $f_{P1} + f_{P2} = 2f_{QPM}$, with $f_{QPM} = c/\lambda_{QPM}$. In addition, since the frequency of the interacting waves must be correlated, any detuning of the signal wave from f_{QPM} must also be symmetrically applied to the idler wave.

In single-pump, two-mode PSAs built with HNLFs, the flatness and bandwidth of the gain are usually limited by SPM and XPM effects [24]. A dual-pump configuration can be used to provide flatter and wider gain bandwidth in fiber-based PSAs. However, in two-mode PPLN-based PSAs, flat and broadband gain characteristics are observed in both single- and dual-pump configurations, as depicted in Fig. 5(c)–(e). In fact, as shown in Fig. 5(e), if the frequency spacing between the two pumps becomes too large, although the gain bandwidth is slightly increased, the gain considerably drops. Since a dual-pump configuration typically implies higher implementation complexity, single-pump configurations of PPLN-based PSAs are more attractive. Comparing the results depicted in Fig. 5(e) for wavelength spacing of the pumps of 10 nm and Fig. 5(f), the curves are almost identical, with the exception of a very narrow region around λ_{P1}, at 1545 nm (inset in Fig. 5(f)). In fact, PSA6 only behaves as a four-mode PSA in that narrow spectral region, where Δk_4, Δk_5, Δk_6 and Δk_7 are small.

The influence of the length (L) and normalized efficiency (η) of the PPLN on the gain of the PSAs is depicted in Fig. 6. The curves show that the gain of the amplifiers increases with both the length and the normalized efficiency of the PPLN. The aforementioned gain advantage of 6 dB for PSA1 and PSA3 also holds for high values of the length and efficiency of the PPLN device.

V. Conclusion

In this work, different configurations of PPLN-based PSAs were theoretically and numerically investigated, showing the influence of the power of the pump and signal waves, length, and conversion efficiency of the PPLN devices on the gain of the amplifiers.

Due to their limited gain bandwidth, any application of one-mode PSAs on multichannel amplification is precluded. Still, one-mode PSAs can be used for phase regeneration applications of single channels. On the other hand, high bandwidth and flat gain profiles of two-mode PSAs make them very attractive for simultaneous amplification of multiple channels, achieved even when using only a single pump. However, half of the gain bandwidth is lost for generating the idlers. This can be partially compensated by placing the idlers in unused bands, typically out of the conventional EDFA gain bandwidth. Four-mode PSAs can only be implemented if the signal is placed very close to the pump, with higher implementation complexity and with no gain advantage compared to two-mode PSAs. Even if the wavelength of the signal could be freely selected, four-mode PSAs would require twice the amplification bandwidth of a two-mode amplifier for generating the additional idler bands. Therefore, four-mode PSAs built with PPLN devices are not attractive for applications in optical systems.

PPLN waveguides are very interesting devices to implement PSAs for amplification in optical systems, with intrinsic properties such as immunity to Brillouin scattering, SPM and XPM that make them an attractive alternative to $\chi^{(3)}$ nonlinear media. Moreover, new configurations of PSAs are enabled using PPLN devices, due to the additional option of generating and injecting correlated waves in the spectral band of the second harmonic. These configurations, labelled as PSA1 and PSA3 above, are equivalent to PSA2 and PSA4, but with a gain advantage of 6 dB. Although, manipulation of signals in the second harmonic band may be very challenging using fiber-based implementations, applications using free-space optics have proven to be straightforward.

References

[1] R. Slavík, F. Parmigiani, J. Kakande, C. Lundström, M. Sjödin, P. A. Andrekson, R. Weerasuriya, S. Sygletos, A. D. Ellis, L. Grüner-Nielsen, D. Jakobsen, S. R. Herstrø M, R. Phelan, J. O'Gorman, A. Bogris, D. Syvridis, S. Dasgupta, P. Petropoulos, and D. J. Richardson, "All-optical phase and amplitude regenerator for next-generation telecommunications systems," *Nature Photon.*, vol. 4, pp. 690–695, 2010.

[2] J. Kakande, A. Bogris, R. Slavík, F. Parmigiani, D. Syvridis, P. Petropoulos, and D. Richardson, "First demonstration of all-optical QPSK signal regeneration in a novel multi-format phase sensitive amplifier," in *Proc. IEEE Eur. Conf. Exhib. Opt. Commun.*, Torino, Italy, 2010, vol. 1, pp. 1–1.

[3] J. Kakande, R. Slavík, F. Parmigiani, A. Bogris, D. Syvridis, L. Grüner-Nielsen, R. Phelan, P. Petropoulos, and D. J. Richardson, "Multilevel quantization of optical phase in a novel coherent parametric mixer architecture," *Nature Photon.*, vol. 5, pp. 748–748, Oct., 2011.

[4] C. Caves, "Quantum limits on noise in linear amplifiers," *Phys. Rev. D*, vol. 26, no. 8, pp. 1817–1817, 1982.

[5] Z. Tong, C. Lundström, P. A. Andrekson, C. J. McKinstrie, M. Karlsson, D. J. Blessing, E. Tipsuwannakul, B. J. Puttnam, H. Toda, and L. Grüner-Nielsen, "Towards ultrasensitive optical links enabled by low-noise phase-sensitive amplifiers," *Nature Photon.*, vol. 5, pp. 430–430, Jul. 2011.

[6] P. Andrekson, "Applications of phase-sensitive parametric amplification," presented at the Optical Fiber Commun. Conf., Los Angeles, CA, USA, 2012, p. OM3B.6.

[7] S. Olsson, C. Lundström, M. Karlsson, and P. A. Andrekson, "Long-haul (3465 km) transmission of a 10 GBd QPSK signal with low noise

phase-sensitive in-line amplification," presented at the Eur. Conf. Optical Commun., Cannes, France, 2014, p. PD.2.2.
[8] R. Tang, J. Lasri, P. S. Devgan, V. Grigoryan, P. Kumar, and M. Vasilyev, "Gain characteristics of a frequency nondegenerate phase-sensitive fiber-optic parametric amplifier with phase self-stabilized input," *Opt. Exp.*, vol. 13, no. 26, pp. 281–281, 2005.
[9] J. Kakande, A. Bogris, R. Slavik, F. Parmigiani, D. Syvridis, P. Petropoulos, D. Richardson, M. Westlund, and M. Sköld, "QPSK phase and amplitude regeneration at 56 Gbaud in a novel idler-free non-degenerate phase sensitive amplifier," presented at the Optical Fiber Commun. Conf., Los Angeles, CA, USA, 2011, p. OMT4.
[10] C. Lundström, B. Corcoran, M. Karlsson, and P. A. Andrekson, "Phase and amplitude characteristics of a phase-sensitive amplifier operating in gain saturation," *Opt. Exp.*, vol. 20, no. 19, pp. 21400–21400, 2012.
[11] F. D. Ros, D. Vukovic, A. Gajda, K. Dalgaard, L. Zimmermann, B. Tillack, M. Galili, K. Petermann, and C. Peucheret, "Phase regeneration of DPSK signals in a silicon waveguide with reverse-biased p-i-n junction," *Opt. Exp.*, vol. 22, no. 5, pp. 7926–7926, 2014.
[12] A. D. Ellis and S. Sygletos, "Phase sensitive signal processing using semiconductor optical amplifiers," presented at the Optical Fiber Commun. Conf., Anaheim, CA, USA, 2013, p. OW4C.1.
[13] A. Albuquerque, B. J. Puttnam, M. Drummond, A. Szabó, S. Shinada, N. Wada, and R. Nogueira, "Phase-sensitive amplification in a single bi-directional PPLN waveguide," *Opt. Exp.*, vol. 21, no. 19, pp. 22 063–22 069, 2013.
[14] C. Langrock, S. Kumar, J. McGeehan, A. Willner, and M. M. Fejer, "All-optical signal processing using χ (2) nonlinearities in guided-wave devices," *J. Lightw. Technol.*, vol. 24, no. 7, pp. 2579–2592, Jul. 2006.
[15] B. J. Puttnam, D. Mazroa, S. Shinada, and N. Wada, "Phase-squeezing properties of non-degenerate PSAs using PPLN waveguides," *Opt. Exp.*, vol. 19, no. 26, pp. B131–B139, 2011.
[16] T. Umeki, O. Tadanaga, A. Takada, and M. Asobe, "Phase sensitive degenerate parametric amplification using directly-bonded PPLN ridge waveguides," *Opt. Exp.*, vol. 19, no. 7, pp. 6326–6326, 2011.
[17] M. Asobe, T. Umeki, and O. Tadanaga, "Phase sensitive amplification with noise figure below the 3 dB quantum limit using CW pumped PPLN waveguide," *Opt. Exp.*, vol. 20, no. 12, pp. 13 164–13 172, Jun. 2012.
[18] C. Lundström, S. L. Olsson, B. Corcoran, M. Karlsson, and P. A. Andrekson, "Phase-sensitive amplifiers for optical links," presented at the Optical Fiber Commun. Conf., Anaheim, CA, USA, 2013, p. OW3C.5.
[19] S. Radic, "Parametric amplification and processing in optical fibers," *Laser Photon. Rev.*, vol. 2, no. 6, pp. 498–498, 2008.
[20] A. A. C. Albuquerque, M. V. Drummond, and R. N. Nogueira, "Transfer matrix and Fourier transform methods for simulation of second-order nonlinear interactions in a PPLN waveguide," *J. Lightw. Technol.*, vol. 29, no. 24, pp. 3764–3771, Dec. 2011.
[21] K. J. Lee, F. Parmigiani, S. Liu, J. Kakande, P. Petropoulos, K. Gallo, and D. Richardson, "Phase sensitive amplification based on quadratic cascading in a periodically poled lithium niobate waveguide," *Opt. Exp.*, vol. 17, no. 22, pp.20 393–20 400, 2009.
[22] T. Suhara and M. Fujimura, *Waveguide Nonlinear-Optic Devices*, 1st ed. New York, NY, USA: Springer, 2003.
[23] J. Armstrong, N. Bloembergen, J. Ducuing, and P. Pershan, "Interactions between light waves in a nonlinear dielectric," *Phys. Rev.*, vol. 127, no. 6, pp. 1918–1939, Sep. 1962.
[24] G. P. Agrawal, *Nonlinear Fiber Optics*, 4th ed. New York, NY, USA: Academic, 2006.

Authors' biographies not available at the time of publication.

Publication F

Phase-sensitive amplification in a single bi-directional PPLN waveguide

A. Albuquerque, B. Puttnam, M. Drummond, A. Szabó, D. Mazroa, S. Shinada, N. Wada, R. Nogueira

originally published in *Optics Express*, vol. 21, no. 19, pp. 22063-22069, September 2013.

Phase-sensitive amplification in a single bi-directional PPLN waveguide

André Albuquerque,[1,*] Benjamin J. Puttnam,[2] Miguel Drummond,[1] Áron Szabó,[3] Dániel Mazroa,[3] Satoshi Shinada,[2] Naoya Wada,[2] and Rogério Nogueira[1]

[1]*Instituto de Telecomunicações, Campus Universitário de Santiago, Aveiro 3810-193, Portugal*
[2]*Photonic Network System Laboratory, NICT, 4-2-1 Nukui-Kitamachi, Koganei, Tokyo 184-8759, Japan*
[3]*Department of Telecommunications & Media Informatics, Budapest University of Technology & Economics, Magyar tudósok körútja 2, Budapest 1117, Hungary*
[*]*andrealbuquerque@av.it.pt*

Abstract: We investigate phase-sensitive amplification (PSA) and phase regeneration of a binary phase-shift keying (BPSK) signal using a single periodically poled lithium niobate (PPLN) waveguide. The PPLN is operated bi-directionally in order to simultaneously achieve phase correlated signals and phase-sensitive (PS) operation. We use injection-locking for carrier phase recovery and a lead zirconate titanate (PZT) fiber stretcher to correct path length deviations in the in-line phase regenerator. We observe a trade-off between high PS gain provided by high pumping power and stability of the device.

OCIS codes: (130.3730) Lithium niobate; (190.4970) Parametric oscillators and amplifiers.

References and links

1. J. Kakande, F. Parmigiani, R. Slavik, P. Petropoulos, and D. J. Richardson, "Phase sensitive amplifiers for regeneration of phase encoded optical signal formats," in *International Conference on Transparent Optical Networks* (2011), pp. 1–4.
2. K. Cvecek, K. Sponsel, C. Stephan, G. Onishchukov, R. Ludwig, C. Schubert, B. Schmauss, and G. Leuchs, "Phase-preserving amplitude regeneration for a WDM RZ-DPSK signal using a nonlinear amplifying loop mirror," Opt. Express **16**(3), 1923–1928 (2008).
3. M. Matsumoto and H. Sakaguchi, "DPSK signal regeneration using a fiber-based amplitude regenerator," Opt. Express **16**(15), 11169–11175 (2008).
4. R. Slavík, F. Parmigiani, J. Kakande, C. Lundström, M. Sjödin, P. A. Andrekson, R. Weerasuriya, S. Sygletos, A. D. Ellis, L. Grüner-Nielsen, D. Jakobsen, S. Herstrøm, R. Phelan, J. O'Gorman, A. Bogris, D. Syvridis, S. Dasgupta, P. Petropoulos, and D. J. Richardson, "All-optical phase and amplitude regenerator for next-generation telecommunications systems," Nat. Photonics **4**(10), 690–695 (2010).
5. K. Croussore and G. Li, "Phase and amplitude regeneration of differential phase-shift keyed signals using phase-sensitive amplification," J. of Sel. Top. in Quant. Elect. **14**, 648–658 (2008).
6. Z. Tong, C. Lundström, P. A. Andrekson, C. J. McKinstrie, M. Karlsson, D. J. Blessing, E. Tipsuwannakul, B. J. Puttnam, H. Toda, and L. Grüner-Nielsen, "Towards ultrasensitive optical links enabled by low-noise phase-sensitive amplifiers," Nat. Photonics **5**(7), 430–436 (2011).
7. C. Caves, "Quantum limits on noise in linear amplifiers," Phys. Rev. D Part. Fields **26**(8), 1817–1839 (1982).
8. B. J. Puttnam, D. Mazroa, S. Shinada, and N. Wada, "Phase-squeezing properties of non-degenerate PSAs using PPLN waveguides," Opt. Express **19**(26), B131–B139 (2011).
9. M. V. Drummond, J. D. Reis, R. N. Nogueira, P. P. Monteiro, A. L. Teixeira, S. Shinada, N. Wada, and H. Ito, "Error-free wavelength conversion at 160 Gbit/s in PPLN waveguide at room temperature," Electron. Lett. **45**(22), 1135 (2009).
10. K. J. Lee, F. Parmigiani, S. Liu, J. Kakande, P. Petropoulos, K. Gallo, and D. Richardson, "Phase sensitive amplification based on quadratic cascading in a periodically poled lithium niobate waveguide," Opt. Express **17**(22), 20393–20400 (2009).
11. C. Langrock, S. Kumar, J. E. McGeehan, A. E. Willner, and M. M. Fejer, "All-optical signal processing using $\chi(2)$ nonlinearities in guided-wave devices," J. Lightwave Technol. **24**(7), 2579–2592 (2006).
12. B. J. Puttnam, Á. Szabó, D. Mazroa, S. Shinada, and N. Wada, "Multi-channel phase squeezing in a PPLN-PPLN PSA," in *Optical Fiber Communication Conference* (2012), p. OW3C.
13. T. Umeki, M. Asobe, H. Takara, T. Kobayashi, H. Kubota, H. Takenouchi, and Y. Miyamoto, "First demonstration of multi-span Transmission using phase and amplitude regeneration in PPLN-based PSA," in *Optical Fiber Communication Conference* (2013), p. OW1I.7.
14. A. Szabo, B. J. Puttnam, D. Mazroa, S. Shinada, and N. Wada, "Investigation of an all-optical black-box PPLN-PPLN BPSK phase regenerator," Photon. Tech. Lett. **24**(22), 2087–2089 (2012).

#188721 - $15.00 USD Received 22 Apr 2013; revised 12 Jul 2013; accepted 21 Jul 2013; published 12 Sep 2013
(C) 2013 OSA 23 September 2013 | Vol. 21, No. 19 | DOI:10.1364/OE.21.022063 | OPTICS EXPRESS 22063

15. C. Lundström, B. Corcoran, M. Karlsson, and P. A. Andrekson, "Phase and amplitude characteristics of a phase-sensitive amplifier operating in gain saturation," Opt. Express **20**(19), 21400–21412 (2012).
16. Z. Zheng, L. An, Z. Li, X. Zhao, and X. Liu, "All-optical regeneration of DQPSK/QPSK signals based on phase-sensitive amplification," Opt. Commun. **281**(10), 2755–2759 (2008).
17. A. Albuquerque, M. Drummond, R. N. Nogueira, B. J. Puttnam, S. Shinada, N. Wada, Á. Szabó, and D. Mazroa, "Investigation of black-box phase regeneration using single bi-directional PPLN waveguide," in *Optical Fiber Communication Conference* (2013), p. OW4C.2.
18. T. Volk and M. Wöhlecke, *Lithium Niobate – Defects, Photorefraction and Ferroelectric Switching* (Springer Series in Material Science, 2008), pp. 82–95.
19. T. Umeki, O. Tadanaga, and M. Asobe, "Highly efficient wavelength converter using direct-bonded PPZnLN ridge waveguide," J. of Quant. Electron. **46**(8), 1206–1213 (2010).

1. Introduction

Amplified spontaneous emission (ASE) introduced by optical amplifiers and non-linear phase noise continuously deteriorate optical signals propagating in optical fiber links, limiting the maximum transmission distance. Thus, noiseless amplification and regeneration of distorted signals are key functionalities to extend the reach of optical networks. All-optical regeneration has recently shown many advantages in processing coherent-optical signals [1], proving that it can be a viable alternative to costly and power consuming optical-to-electrical-to-optical regenerators.

Until the early 2000s, research on all-optical regeneration was focused only on amplitude regeneration. However, with the advent of phase-shift keying (PSK) modulation formats in commercial systems, it is necessary to regenerate both amplitude and phase of the signal, requiring the development of new techniques. Phase-preserving amplitude regeneration [2] and phase-to-amplitude conversion followed by amplitude regeneration and reconversion to a phase modulated signal [3] are some of the proposed scenarios. A more straightforward option is to regenerate the phase directly by taking advantage of phase squeezing properties of PS amplifiers [4]. Amplitude regeneration is also possible when operating in saturation regime [4,5]. Furthermore, PS amplifiers allow a noise figure below the 3 dB theoretical limit of phase-insensitive amplifiers (PIAs) [6,7], enabling low noise amplification along with amplitude and phase regeneration.

The fundamental operation principle of a PSA-based phase regenerator is the property of amplifying or de-amplifying a signal according to the relation between its phase and the phase of other optical pumps [4]. This behavior leads to different gain values for orthogonal quadrature components in a constellation diagram, and naturally squeezes the phase of the signal towards the axis of maximum gain [8]. Most of the PSA-based phase regenerators reported so far have been based on highly non-linear fibers using non-linear techniques such as four-wave mixing [4,5] and self-phase modulation [5]. Recently, phase regenerators based on cascaded second harmonic and difference frequency generation (cSHG/DFG) in PPLN devices have been attracting considerable interest due to their high non-linear coefficient, compactness, low crosstalk and spontaneous emission, no intrinsic frequency chirp, immunity to stimulated Brillouin scattering and ability to operate at room temperature [8–11]. These devices are produced by periodic reversal of the ferroelectric domains in a lithium niobate chip to enhance the non-linear interaction efficiency through quasi-phase matching (QPM) [11]. Single- and multi-channel phase squeezing [8,12], as well as "black-box" phase regeneration [13,14] of BPSK signals were already demonstrated in PPLN-based PS amplifiers using one non-linear device to generate phase correlated idlers/pumps (copier stage [4,15]) followed by a second one to perform PS operation. Each PPLN device requires precise temperature tuning to ensure that the QPM condition is satisfied at the operating wavelengths [8]. In [13], a PPLN-based phase regenerator for BPSK signals was demonstrated, requiring three different PPLN waveguides. As these devices are sensitive to the polarization, the number of required PPLN waveguides doubles in polarization multiplexed systems. Furthermore, even more devices may be necessary for regeneration of higher order PSK modulation formats such as quadrature PSK [16].

In a previous work [17], we proposed using a single PPLN waveguide with bi-directional propagation to simultaneously generate a phase-correlated idler/pump in one direction

#188721 - $15.00 USD Received 22 Apr 2013; revised 12 Jul 2013; accepted 21 Jul 2013; published 12 Sep 2013

23 September 2013 | Vol. 21, No. 19 | DOI:10.1364/OE.21.022063 | OPTICS EXPRESS 22064

(designated as copier direction in section 2, and pump generation direction in section 3), and to perform PSA in the opposite one (PSA direction). As only one PPLN waveguide and a single temperature controller are required, the proposed scheme enables potential savings in terms of costs and energy consumption. In this work, we expand the investigation performed in [17] to include experimental characterization of bi-directional PPLN-based PS amplifiers for three waveguides with different lengths.

2. PSA characterization

In this section the PS properties of a PPLN-based PS amplifier with bi-directional propagation are characterized, evaluating the impact of pump-to-signal power ratio, PSR, total input power in PSA direction (including signal, pump and idler waves, measured in the PS mode), P_{PS}, and the length of the PPLN waveguide. Due to simpler implementation and prospects for multi-channel operation [12], a degenerate pump configuration for the PS amplifier is adopted. In this configuration, the second harmonic of the pump wave interacts with the signal one through difference frequency generation. The experimental apparatus is depicted in Fig. 1. The light sources used in this experiment consisted in two external cavity tunable lasers (ECTLs) tuned at 1545.5 (pump) and 1548 nm (signal). The two signals were aligned to the same state of polarization, amplified, filtered with a band-pass filter (BPF) with 1 nm bandwidth and combined in a 90% coupler. The optical circulators enabled operation in both propagation directions.

Three different PPLN waveguides with lengths of 3, 4.5 and 6 cm length and doped with 5% of MgO in order to reduce photorefractive damage were used in this experiment. The poling period of all PPLNs was 19 μm. The conversion efficiencies, defined as the SHG output power divided by the square of the coupled input power, were of about 190, 410 and 420%/W, for 3, 4.5 and 6 cm, respectively. The QPM wavelength at 27°C for the 3, 4.5 and 6 cm waveguides was 1545.3, 1545.6 and 1545.7 nm. The total insertion losses were about 3.5 dB. The P_{PS} values obtained in this work were measured before coupling light from the optical fiber to the PPLN waveguide, so they do not account insertion losses. As the two light waves propagate along the PPLN waveguide in the copier direction, a phase-correlated idler is generated with wavelength (λ) and phase (ϕ) relations given by $1/\lambda_i = 2/\lambda_p - 1/\lambda_s$ and $\phi_i = 2\phi_p - \phi_s$, where the indices *s*, *p* and *i* stand for signal, pump and idler, respectively [8]. After idler generation, the three waves entered an optical processor (OP) based on a liquid crystal on silicon used to equalize the power, change the relative phase between the interacting waves and switch between PS and phase-insensitive (PI) mode by blocking the idler. Maximum input power constraints and high losses required a variable optical attenuator (VOA) before the OP and an erbium-doped fiber amplifier (EDFA) after it. Then, the interacting waves were sent back to the PPLN for PS operation and to an optical spectrum analyzer (OSA) for analysis. The power of the pump and signal waves entering the PPLN in the copier direction was 25.8 and 14.9 dBm, respectively. A total power up to 27.6 dBm was launched into the device in the PSA direction.

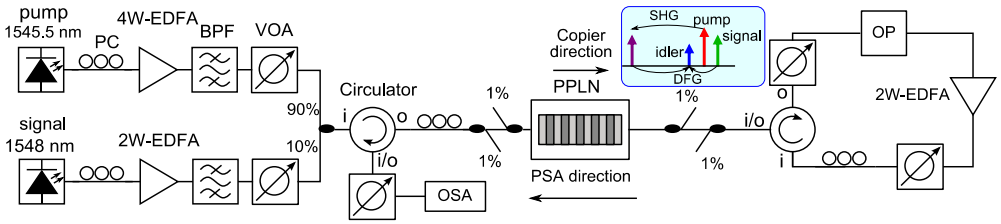

Fig. 1. Experimental set-up used to characterize PS amplification. BPF - band-pass filter; EDFA - erbium-doped fiber amplifier; OP – optical processor; OSA – optical spectrum analyzer; PC - polarization controller; VOA - variable optical attenuator.

#188721 - $15.00 USD Received 22 Apr 2013; revised 12 Jul 2013; accepted 21 Jul 2013; published 12 Sep 2013

23 September 2013 | Vol. 21, No. 19 | DOI:10.1364/OE.21.022063 | OPTICS EXPRESS 22065

2.1. Results and discussion

The comparison between experimental results and numerical simulations using the model presented in [10] describing the cSHG/DFG interaction is depicted in Fig. 2. In the numerical simulations, it was assumed identical insertion losses for both sides of the PPLN device.

Phase sensitive operation is clearly evident in results shown in Figs. 2(a)-2(c). The PS gain, defined as the ratio between the signal power in PS and in PI modes, depends on the phase added to the pump wave, exhibiting maximum gain and attenuation (minimum gain) peaks for phase values of around 1.6π and π, respectively. The phase sensitive dynamic range (PSDR), defined as the ratio between the maximum gain and maximum attenuation [8] reached values of approximately 5.3, 8.6 and 8.8 dB for the devices with 3, 4.5 and 6 cm, respectively. In Figs. 2(d)-2(f), the experimental results and numerical simulations show that the PSDR increases with the PSR, but for PSR values higher than 15 dB this variation is small. In Figs. 2(g)-2(i), the results indicate that the PSDR increases with P_{PS}. As higher P_{PS} means higher pumping power for the same PSR value, this is an expected result. For the 3 cm waveguide a good agreement between experimental data and simulations is verified. For the other devices, the experimental values are up to 3 dB lower than the simulations. This discrepancy is thought to originate from power loss resulting from sum-frequency generation between the SHG and the input signals. In these devices, intense green light emission was observed for high pumping powers as previously. This phenomenon was also observed in [8], where it was suggested that it is the result of sum-frequency generation between the SHG and the input signals. Green light emission along with green light induced infrared absorption (GRIIRA) in lithium niobate depletes the power of the second-harmonic and decreases the PSDR [8,18]. In addition, the QPM temperature changed due to residual photorefractive damage. As higher PSDR means better phase regenerative properties [8], higher PSR and P_{PS} would be desirable. However, these effects cause a trade-off where, on one hand, increasing pump power results in stronger green light emission, GRIIRA and photorefractive damage. On the other hand, reducing the signal power degrades the optical signal-to-noise ratio.

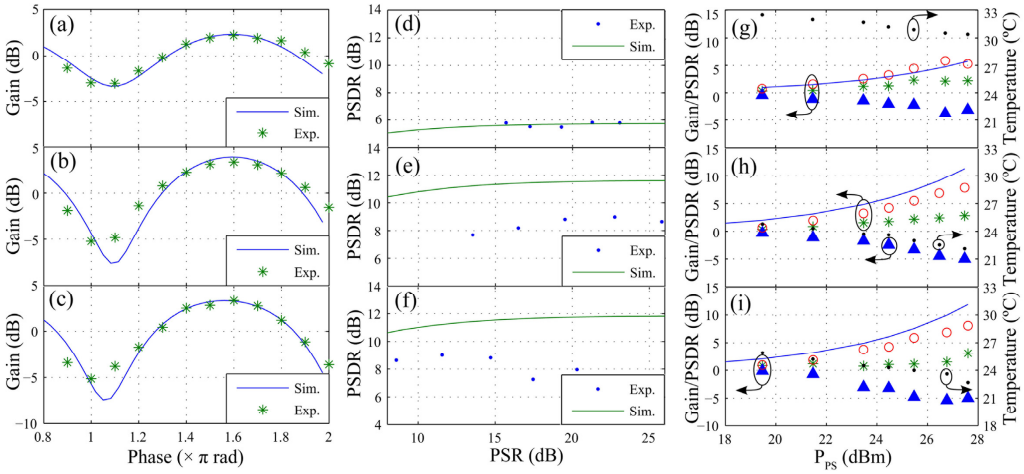

Fig. 2. Experimental results for the devices with lengths of: (a), (d) and (g) 3 cm; (b), (e) and (h) 4.5 cm; (c), (f) and (i) 6 cm. (a)-(c) Experimental and simulated PS gain as a function of the phase added to the pump wave in the OP for P_{PS} of 27.6 dBm and PSR of 10 dB. (d)-(f) Experimental and simulated PSDR curves as a function of the PSR for P_{PS} = 27.6 dBm. (g)-(i) Maximum experimental PS gain (asterisks) and attenuation (triangles), simulated (solid curve) and experimental (circles) PSDR and QPM temperature (dots) as a function of P_{PS}, for PSR = 10 dB.

#188721 - $15.00 USD Received 22 Apr 2013; revised 12 Jul 2013; accepted 21 Jul 2013; published 12 Sep 2013

23 September 2013 | Vol. 21, No. 19 | DOI:10.1364/OE.21.022063 | OPTICS EXPRESS 22066

3. Black-box regenerator for BPSK signals

In this section, a bi-directional PPLN-based "black-box" phase regenerator for BPSK signals is investigated. The set-up used in these experiments is depicted in Fig. 3. In order to enable "black-box" operation, a non-degenerate pump configuration for the PS amplifier is adopted in this section. This configuration allows the generation of a modulation-free phase-correlated idler in the pump generation stage that will later act as the second pump (Pump2) for PSA. Although this configuration differs from the one characterized in section 2, the main qualitative conclusions of the influence of parameters such as P_{PS} and PSR are still valid. In this case, it is the second harmonic of the input signal that interacts with the pump waves through DFG. It should be noted that the wavelength and phase relations of the generated wave are now given by $1/\lambda_{p2} = 2/\lambda_s - 1/\lambda_{p1}$ and $\phi_{p2} = 2\phi_s + 2\phi_{sN} - \phi_{p1}$, where the indices *s*, *p1*, *p2* and *sN* stand for signal, Pump1, Pump2 and signal noise, respectively. Therefore, the BPSK modulation is stripped, but an excess phase noise $2\phi_{sN}$ is transferred to the generated second pump [4]. In order to reduce the excess phase noise and improve carrier recovery performance, an injected-locked semiconductor laser is introduced in the set-up as well as an electrical phase-locked loop (PLL) and a PZT fiber stretcher to compensate slow path length deviations [4].

A noisy 10 Gb/s phase modulated signal was generated by modulating the light emitted by an ECTL with a phase modulator (PM) driven by a noisy electrical signal. A pseudo random bit sequence of length 2^{15}–1 was used in this experiment. Additional white noise was provided by a noise source composed by two cascaded EDFAs interleaved by a 3 nm BPF. The contribution of each noise source was selected in order to obtain standard deviation values of the detected symbols for phase and amplitude of 0.25 and 0.1, respectively, before entering the PPLN for phase regeneration. Part of the modulated signal was combined with the Pump1 wave emitted from another ECTL in a WDM coupler and injected into the PPLN device. In this experiment, a PPLN that was not characterized in the previous section was selected. The new PPLN was chosen as a trade-off between the spectral operational range of the injection-locking laser and the pass band of the WDM coupler, while enabling room temperature operation. The PPLN waveguide length, poling period, QPM wavelength at 21°C, MgO content and SHG conversion efficiency were 6 cm, 19.1 μm, 1549.3 nm, 5% and 560%/W, respectively.

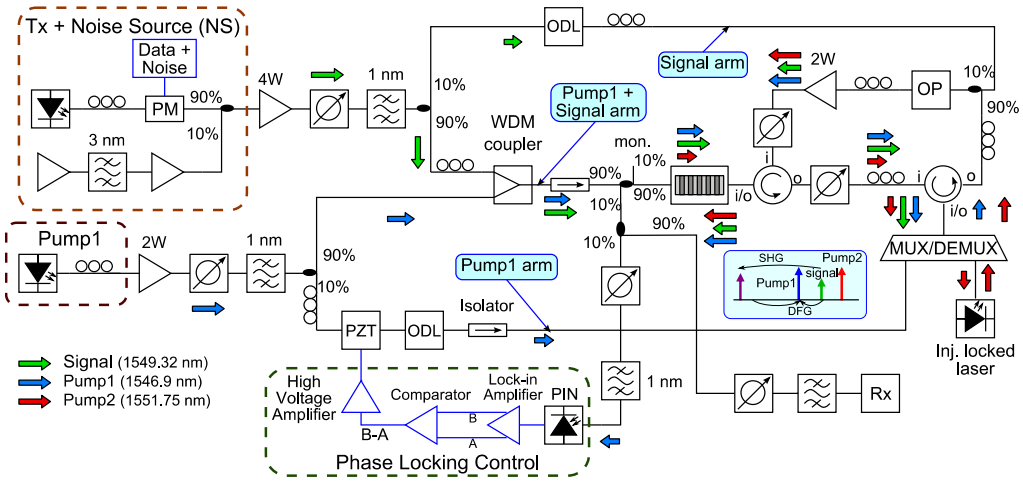

Fig. 3. Experimental set-up for the bi-directional PPLN-based black-box regenerator with injection-locking for carrier recovery. MUX/DEMUX – WDM multiplexer/demultiplexer; ODL – optical delay line; OP – optical processor; Rx – coherent receiver.

After generation of the Pump2 wave in the PPLN, the excess phase noise was reduced by the semiconductor injection-locked laser as in [4]. The WDM multiplexer/demultiplexer (MUX/DEMUX) was used to filter all the signals except Pump2 at the input to the

#188721 - $15.00 USD Received 22 Apr 2013; revised 12 Jul 2013; accepted 21 Jul 2013; published 12 Sep 2013

23 September 2013 | Vol. 21, No. 19 | DOI:10.1364/OE.21.022063 | OPTICS EXPRESS 22067

semiconductor laser and also to combine its output signal with the other pump coming from the Pump1 arm. Then, the phase-correlated pumps were combined with the modulated signal from the Signal arm and sent to an OP and an EDFA for power equalization and amplification before entering the PPLN for phase regeneration. The function of this EDFA is to compensate for the attenuation required at the input of the OP due to maximum input power constraints and for passive losses. As in the previous section, the OP allowed switching from PI to PS mode by blocking the pump2 signal. The input power going into the PPLN waveguide in the pump generation direction was about 27.3 dBm whereas in the PSA direction it was varied up to a maximum value of 28.9 dBm. Optical delay lines (ODLs) and polarization controllers (PCs) were also introduced in the Signal and Pump1 arms to guarantee path length and polarization alignment.

A part of the regenerated signal was tapped from a 10% tap located between the PPLN and the WDM coupler and sent to a variable bandwidth BPF and a single polarization coherent receiver. The coherent receiver was composed by a 100 kHz linewidth ECTL used as the local oscillator and a 90° optical hybrid received with DC-coupled photodiodes at the input to a 40 GSample/s real-time sampling oscilloscope with a 13 GHz bandwidth. The deviations of the equalized path lengths were compensated by a PLL shown in the phase locking control box in Fig. 3 and a PZT fiber stretcher in the Pump1 arm, as described in [6]. The feedback error signal for the PLL was obtained from a fraction of the regenerated signal after the PSA stage.

3.1. Results and discussion

In order to evaluate the performance of the regenerator the ratio between the standard deviations of the received symbols in PI and PS mode (σ_{PI}/σ_{PS}) for both amplitude and phase was measured, for different values of PSR and P_{PS}. The total number of received symbols used to obtain the standard deviation values was 4096. It should be noted that even though the nomenclature for the signal and pump wave is different in this section, PSR is still the pump-to-signal power ratio and P_{PS} includes the power of the signal, Pump1 and Pump2 waves. In the PSA stage, no significant changes on the standard deviation values for the phase and amplitude of the detected symbols were observed before and after the PPLN device, in PI operation mode. Therefore, the ratio σ_{PI}/σ_{PS} is a simple and accurate measurement of the regenerative properties in the PS mode. Effective phase or amplitude regeneration occurs when $\sigma_{PI}/\sigma_{PS} > 1$, with better regenerative performances for higher σ_{PI}/σ_{PS}. The obtained results are depicted in Fig. 4.

For all the measurements performed (Fig. 4(a) and Fig. 4(b)) the ratios σ_{PI}/σ_{PS} in terms of phase are higher than 1, proving effective phase regeneration when the operation mode switched from PI to PS. In addition, higher PSR and P_{PS} values resulted in better phase regenerative performances, which is in agreement with the PSDR measurements shown in the previous section. The phase squeezing characteristic of the bi-directional PPLN-based PS amplifier is evident from the constellation diagrams depicted in Fig. 4(c) and the phase histograms shown in Fig. 4(d). By switching from PI to PS mode, the phase of the received symbols is squeezed towards the real axis of the constellation diagram and the distribution of the angles of the '0' and 'π' symbols becomes narrower. Amplitude regeneration would be expected for PSR ratios close to 0 dB as the PS amplifier operates in the saturation regime [15], but it was not observed in this experiment. Even though higher pumping power results in better phase regeneration, the results shown in Fig. 4(b) suggest that additional amplitude noise is also introduced, as a result of phase-to-amplitude noise conversion [15].

#188721 - $15.00 USD Received 22 Apr 2013; revised 12 Jul 2013; accepted 21 Jul 2013; published 12 Sep 2013

23 September 2013 | Vol. 21, No. 19 | DOI:10.1364/OE.21.022063 | OPTICS EXPRESS 22068

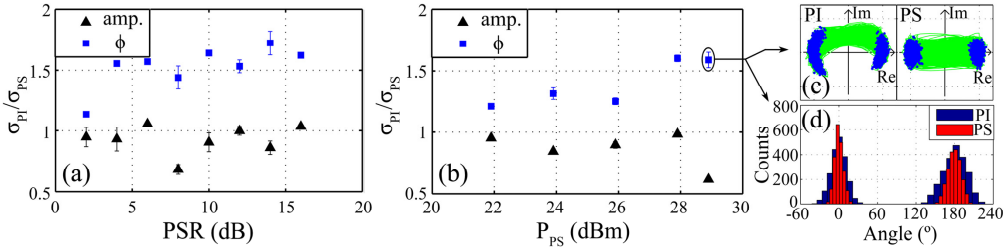

Fig. 4. Ratio between the standard deviations of the received symbols in PI and PS operation modes for amplitude and phase as function of: (a) PSR with P_{PS} = 28.9 dBm; (b) P_{PS} with PSR = 10 dB. Received constellations (c) and phase histograms (d) of the received symbols in PI and PS modes.

The regenerator studied in this section also suffered from green-light induced refractive index change and GRIIRA, affecting both PS gain and system stability. Refractive index variation modifies the optical path length of the Pump1 + Signal arm and the generation of the second pump, affecting both injection locking and the operation of the PLL. Although the time during which the system remained stable was greater than any measurement time, improvements on thermal and refractive index stability of the PPLN must be pursued in order to make bi-directional PPLN-based PSA a viable technique for phase regeneration.

4. Conclusion

An experimental investigation of a PSA set-up and in-line phase regenerator relying on a single bi-directional PPLN for both generation of phase-correlated signals and PS operation is reported. In both cases, best performance in terms of PSDR and phase regeneration occurred for higher PSR and P_{PS} values.

A trade-off between high PS gain provided by high pump power and system stability was observed due to green-light induced refractive index changes, photorefractive damage and GRIIRA. Moreover, the bi-directional nature of the proposed scheme enhances this limitation. Therefore, it is crucial finding a way to mitigate these issues as well as developing new devices with higher efficiencies to reduce high pump power requirements. One possible solution is to replace the annealed proton-exchange PPLN devices used in this work by direct-bonded ZnO-doped PPLN ridge waveguides, as in [19]. Besides their higher non-linear efficiency, direct-bonded ridge waveguides are more resistant to deleterious photo-induced effects.

The results presented in this work show that PSAs can be implemented in a single PPLN waveguide with bi-directional propagation. Further improvements in the set-up/PPLN waveguide and the possibility of photonic integration will reduce the amplification requirements and allow savings of devices, temperature controllers and complexity. These advantages become especially attractive for regeneration of multi-level phase-encoded signals as BPSK regenerators have been suggested as elementary building blocks [4,16] and in polarization multiplexed systems.

Acknowledgments

Funding from Fundação para a Ciência e Tecnologia (FCT) through the PhD grant SFRH/BD/78425/2011 and projects CONTACT (PTDC/EEA-TEL/114144/2009) and POFCOM (PTDC/EEA-TEL/122792/2010) are gratefully acknowledged.

#188721 - $15.00 USD Received 22 Apr 2013; revised 12 Jul 2013; accepted 21 Jul 2013; published 12 Sep 2013

23 September 2013 | Vol. 21, No. 19 | DOI:10.1364/OE.21.022063 | OPTICS EXPRESS 22069

Publication G

Experimental investigation of phase-sensitive amplification of data signals in a four-mode fiber-based PSA

A. Albuquerque, B. Puttnam, J. Mendinueta, M. Drummond, S. Shinada, R. Nogueira, N. Wada

originally published in *Optics Letters*, vol. 40, no. 2, pp. 288-291, January 2015.

288 OPTICS LETTERS / Vol. 40, No. 2 / January 15, 2015

Experimental investigation of phase-sensitive amplification of data signals in a four-mode fiber-based PSA

André A. C. Albuquerque,[1,*] Benjamin J. Puttnam,[2] José M. D. Mendinueta,[2] Miguel V. Drummond,[1] Satoshi Shinada,[2] Rogério N. Nogueira,[1] and Naoya Wada[2]

[1]*Instituto de Telecomunicações, Campus Universitário de Santiago, 3810-193 Aveiro, Portugal*

[2]*National Institute of Information and Communications Technology, 4-2-1, Nukui-Kitamachi, Koganei, Tokyo 184-8795, Japan*

**Corresponding author: andrealbuquerque@av.it.pt*

Received September 25, 2014; revised November 30, 2014; accepted December 1, 2014; posted December 1, 2014 (Doc. ID 223811); published January 15, 2015

In this Letter, we investigate the influence of the phase and power of pump and signal waves on the gain of a four-mode phase-sensitive amplifier (PSA) built with a highly nonlinear fiber (HNLF), using a copier + PSA scheme to generate phase- and frequency-correlated idler waves. Using such an amplifier, low-noise amplification of a 10 Gsymbol/s quadrature phase-shift keying (QPSK) signal, with net gain of ~20 dB and less than 1 dB optical signal-to-noise ratio (OSNR) penalty at a bit error ratio (BER) of 10^{-3}, was achieved. We also verified an additional net gain of 11.6 dB when switching from phase-insensitive to phase-sensitive operation, which is in good agreement with theoretical predictions of 12 dB.

OCIS codes: (060.0060) Fiber optics and optical communications; (060.2320) Fiber optics amplifiers and oscillators; (060.4370) Nonlinear optics, fibers; (190.0190) Nonlinear optics; (190.4380) Nonlinear optics, four-wave mixing; (190.4410) Nonlinear optics, parametric processes.

http://dx.doi.org/10.1364/OL.40.000288

In recent years, phase-sensitive amplifiers (PSAs) have become very attractive for applications in fiber-optic communication systems because of their unique phase-sensitive (PS) properties, which enable amplification below the quantum-limited 3 dB noise figure (NF) of phase-insensitive amplifiers (PIAs), such as erbium-doped fiber amplifiers (EDFAs) [1,2]. As PSAs have a theoretical NF of 0 dB, they can be used to improve the NF of an amplified optical link, enhancing its performance and allowing extension of the maximum transmission reach [3].

Furthermore, PSAs can be built using a wide range of nonlinear devices that can be designed to provide a broad amplification bandwidth within and/or outside the conventional EDFA gain bandwidth [4]. Periodically, poled lithium niobate waveguides [5], and especially fiber-optic parametric amplifiers (FOPAs) built with HNLFs [2–4,6], are the most common examples of such devices.

PS amplification in FOPA-based PSAs is achieved via four-wave mixing (FWM) interactions, which mediate a power transfer from the pump(s) to the signal/idler(s) (amplification) or vice-versa (de-amplification), depending on the relative phase of the interacting waves [6,7].

PSAs can be classified according to the number of modes, i.e., the number of signal and idler waves, and the number of pump waves [8]. Until now, almost all reported applications of PSAs have been based on either one-mode [7] or two-mode [6,9,10] PS processes. Recently, however, PS amplification of continuous-wave signals [8] and PS broadband multicasting [11] using four-mode PSAs have been demonstrated.

In four-mode PSAs, two pump waves (P1 and P2), one input signal (S), and three idler waves, denominated as modulation instability (MI), phase conjugation (PC), and Bragg scattering (BS) idlers interact in the nonlinear medium, as depicted in Fig. 1. As in any other PSA, all the signal, pump, and idler waves must be present at the input of the four-mode PSA, and their frequency and phase must be correlated to enable PS properties. Moreover, four-mode PSAs directly involve six different FWM processes, whose frequency relations are shown in the table of Fig. 1, in addition to several other spurious interactions. Therefore, the implementation architecture and power dynamics are more complex than in one-mode or two-mode PSAs [11]. Despite this disadvantage, four-mode PSAs provide an additional gain of 12 dB compared to FOPAs operating in phase-insensitive (PI) mode, i.e., without the idlers at the input of the amplifier. Consequently, four-mode PSAs offer an extra gain of 6 dB over two-mode PSAs, including both single and dual pump configurations [11]. In addition, only considering the signal wave, it also provides an OSNR improvement of 12 dB over a PIA, when the dominant noise source originates from quantum fluctuations (quantum noise) [12]. Although such advantages come at the expense of reducing the effective available bandwidth because of the generation of the additional idler sidebands, such a drawback is partially compensated by the broader and flatter gain bandwidths [10,13] enabled by the dual pump configuration, which makes four-mode PSAs suitable for multichannel amplification. Nonetheless, half of the available bandwidth is lost, compared to dual pump two-mode PSAs, to obtain the gain advantage of 6 dB.

The frequency- and phase-correlated idlers can be generated using optical combs [14], or the so-called

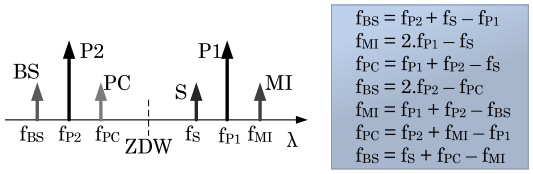

Fig. 1. Illustration of the input waves of the four-mode PSA.

0146-9592/15/020288-04$15.00/0

January 15, 2015 / Vol. 40, No. 2 / OPTICS LETTERS 289

copier + PSA scheme [2,6,9], in which a first PI-FOPA (copier) is used to generate the correlated idlers from the input signal and pump waves.

In this Letter, the influence of the pump and signal powers on the net gain of a four-mode PSA are experimentally evaluated, using the copier + PSA scheme and an optical processor (OP) based on liquid crystal on silicon (LCOS) technology to statically control the relative phase of the interacting waves. PS amplification of a 10 Gsymbol/s quaternary phase-shift keying (QPSK) signal is also evaluated through bit-error ratio (BER) measurements as a function of the optical signal-to-noise ratio (OSNR). To the best of our knowledge, this is the first report on the performance evaluation of data signals amplified by four-mode FOPA-based PSAs.

The experiments were carried out using the setup depicted in Fig. 2. The two pump waves were generated in 500 kHz linewidth external cavity tunable lasers (ECTLs) at 1563.81 nm (P1) and 1543.57 nm (P2), and injected into a phase modulator (PM) driven by three dithering tones to mitigate stimulated Brillouin scattering (SBS) [2,6]. Using this technique, the SBS threshold was increased to more than 25 dBm for each pump. The QPSK signal (S) was generated in an in-phase and quadrature modulator (IQM) from light emitted by another 500 kHz linewidth ECTL at 1561.42 nm. The IQM was driven by two pseudo-random bit sequences of length 2^{15}–1, generated by a pulse pattern generator (PPG). After amplification in a high power EDFA, the two pumps were combined with the QPSK signal. Polarization controllers (PolCs) were used to align the waves to the same state of polarization.

The frequency- and phase-correlated MI, PC, and BS waves were generated in HNLF1 (copier stage) at 1566.21, 1545.91, and 1542.24 nm, respectively. The length, zero dispersion wavelength, dispersion slope, nonlinear coefficient, and total insertion losses of the HNLF were 400 m, 1544 nm, 0.02 $ps \cdot nm^{-2} \cdot km^{-1}$, 10 $W^{-1} \cdot km^{-1}$, and 1 dB, respectively. After idler generation, the interacting waves were injected into the OP for power equalization and to adjust the relative phase of the interacting waves. The OP also enabled switching from PS to PI operation, by blocking the idler waves, converting the PSA into a four-mode PIA. As all the waves propagated along the same optical path and with negligible group delay, no active control of the phase relationship between the waves was necessary, contrary to the experiments in [7] and [2]. Because of the maximum input power limitations of 10 dBm, a variable optical attenuator (VOA) was placed before the OP and an EDFA was inserted before the PSA to compensate for the attenuation and insertion losses of the OP. An additional VOA was inserted to control the total input power into the PSA. In this Letter, all the measurements were carried out with $P_{P1} \approx P_{P2} \approx P_P$, where P_{P1} and P_{P2} are the power of the two pump waves. In PS operation, the power of the idlers was kept equal to that of the signal. The length, zero dispersion wavelength, dispersion slope, nonlinear coefficient, and total insertion losses of HNLF2 were 500 m, 1549 nm, 0.02 $ps \cdot nm^{-2} \cdot km^{-1}$, 17 $W^{-1} \cdot km^{-1}$, and 3.5 dB, respectively. The optical spectra and gain properties of the PSA were evaluated using optical spectrum analyzers (OSAs).

To evaluate the BER performance, amplified spontaneous emission (ASE) noise produced by two EDFAs interleaved by a 5 nm bandpass filter (BPF) was loaded to the QPSK signal, after filtering out the pump and idler waves, using VOAs to adjust the OSNR.

The QPSK signal was detected in a coherent receiver at the input to a 13 GHz bandwidth, 40 GSample/s real-time sampling oscilloscope. A 100 kHz linewidth ECTL was used as the local oscillator (LO). The signal power at the input of the hybrid was about 0 dBm. The received signal was then digitally processed offline, which included normalization, re-timing, equalization, frequency-recovery and carrier-recovery.

The gain of an optically pumped amplifier strongly depends on the power of the signal and pump waves. Hence, the influence of the power of each pump, P_P, and of the signal wave, P_S, on the net gain (ratio between the signal power after and before the PSA) was evaluated by attenuation control of the VOA before the PSA and of the OP. The experimental results are depicted in Figs. 3(a) and 3(b). As expected, in either PS or PI modes, the net gain increases with P_P, achieving maximum values of 20.1 and 10 dB in PS and PI operation, respectively, at P_P of 27 dBm. For P_P of about 25 dBm, even though the amplifier was affected by polarization-mode dispersion, spurious FWM interactions, residual chromatic dispersion, and phase dithering, the additional gain observed when switching from PI to PS operation was close to the theoretical 12 dB additional gain of four-mode PSAs. For P_S values below −2 dBm, the gain of the amplifier is almost independent of the signal power, and of the order 20 dB. For higher P_S values,

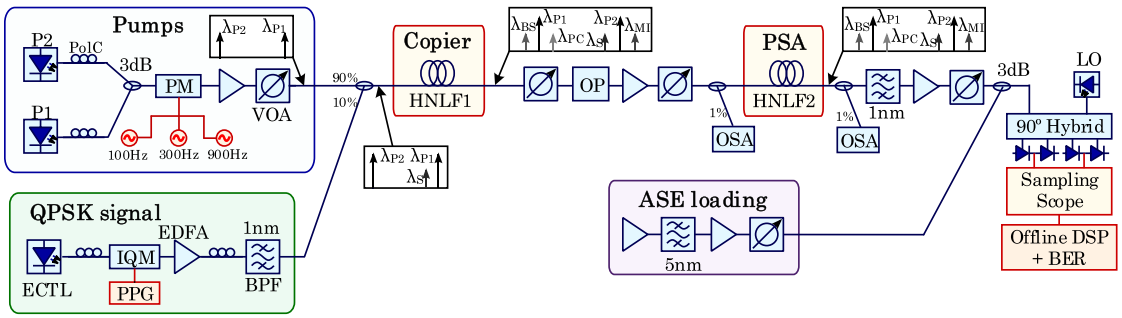

Fig. 2. Experimental setup.

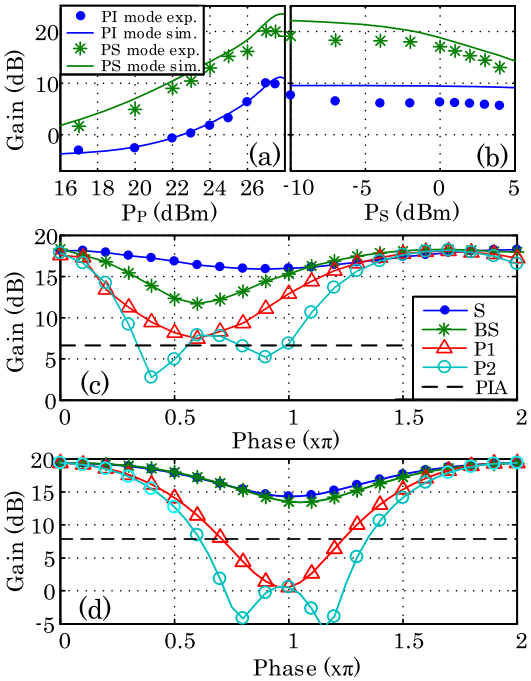

Fig. 3. Variation of the net gain with: (a) PP, for $P_S = -7$ dBm; and (b) PS, for $P_P = 27$ dBm. The solid lines correspond to numerical simulations. (c) Experimental and (d) simulated variation of the net gain with the relative phase added in the OP, and for $P_P = 27$ dBm and $P_S = -3$ dBm.

the amplifier starts to saturate and the gain decreases, especially in PS mode, when higher gain values are observed. Numerical simulations calculated by integrating the nonlinear Schrödinger equation using a split-step Fourier method [10] were also included in Figs. 3(a) and 3(b). Compared to the experimental results, a similar variation of the gain with the power of the signal and pump waves is observed, but we note that gain values calculated by the numerical simulations are typically 0.5–3 dB higher. Such gain difference is explained by polarization-mode dispersion, phase dithering combined with residual chromatic dispersion, and local fluctuations of the core size and shape, which reduce the gain in a real PSA–FOPA and were not included in the simulations [10].

The PS properties of the PSA are evidenced in Fig. 3(c), where the net gain of the signal, defined as the ratio between the power of the signal after and before the amplifier, as a function of the relative phase shift applied by the OP, is shown. In Fig. 3(c), the phase shift applied to the S, BS, P1, or P2 waves is measured relative to the phase condition for which the maximum gain is observed. A typical sinusoidal variation of the net gain with the relative phase of the waves is observed as in one- and two-mode PSAs [6]. According to the experimental results, a difference between the maximum and minimum values of the net gain of more than 10 dB can be observed when changing the relative phase of waves P1 and P2, whereas only about 6 and 2 dB are observed for the BS and S waves, respectively. A similar behavior could be observed when changing the phase of the MI and PC waves, as was also reported in [8]. An uncharacteristic gain variation of about 5 dB is observed in curve P2 of Fig. 3(c) for phase values between 0.4 and 0.9π. A similar variation is also observed in the numerical simulations shown in Fig. 3(d). This behavior may be primarily explained by two mechanisms. On one hand, in four-mode PSAs, any relative phase variation affects more than one FWM process simultaneously, which leads to an intricate power transfer among the interacting waves, and thus to a complex PS gain characteristic of the amplifier. On the other hand, a wide frequency spacing between the two pumps was desired to reduce deleterious FWM interactions between them ($2\times f_{P1} - f_{P2}$ and $2\times f_{P2} - f_{P1}$). To fulfill this requirement and because of the limited gain bandwidth of the EDFA used to amplify the pump waves (pumps box of Fig. 2), the two pumps could not be symmetrically tuned around the zero dispersion wavelength of the HNLF. Therefore, the four-mode PSA was also affected by residual chromatic dispersion effects. The numerical simulations of Fig. 3(d) also show that the two mechanisms contribute for the behavior observed in Fig. 3(c). Compared to the numerical simulations, the minimum net gain was measured at lower values of the relative phase in the experiments. This arises from an artifact of the OP processor, whose real phase shifts did not exactly coincide with the values inserted in its controlling software, which we use in Fig. 3(c). The net gain of the amplifier operating in PI mode is also depicted in Fig. 3(c), for comparison. In this case, a net gain value of 6.6 dB was obtained, which is about 11.6 dB less than the maximum gain of the amplifier while operating in PS mode.

The optical spectra measured before and after the PSA, operating in PS and PI modes for $P_P = 27$ dBm and $P_S = -5$ dBm, are shown in Fig. 4(a). According to the measured spectra, a similar noise floor at approximately −10 dBm is obtained at the output of the amplifier, in both PS and PI modes. This is an expected result because the noise components are incoherent and uncorrelated, so the amplifier behaves as a PIA for the noise in both modes.

The BER measurements of the QPSK signal as a function of the OSNR are depicted in Fig. 4(b), for P_P of 23, 25, and 27 dBm, in both PS and PI modes. At such power levels, net gain values of 10.8, 14.8, and 18.9 dB were observed in PS mode, whereas −1.1, 2.0, and 7.5 dB were obtained in PI mode. For P_P of 23 dBm in PI mode, a negative net gain was measured because the internal gain of the PSA was insufficient to compensate for the insertion losses (3.5 dB). Compared to the back-to-back (B2B) measurements, OSNR penalties at BER $= 10^{-3}$ of 0.3, 0.4, and 0.8 dB for P_P of 23, 25, and 27 dBm in PS mode, and 0.2, 0.7, and 2.2 dB in PI mode were measured. A total of 5×10^6 symbols were considered for the BER measurements. The experimental results suggest that there is at least one impairing mechanism that is partially mitigated in PS mode, but additional measurements are required to identify the exact cause. Additionally, a shift to higher BER values is observed for the B2B measurements at OSNRs between 8.5 and 10 dB, which we believe to be caused by poor biasing of the modulator.

Concerning the noise properties of the amplifier, two possible NF definitions can be considered for a PSA. The

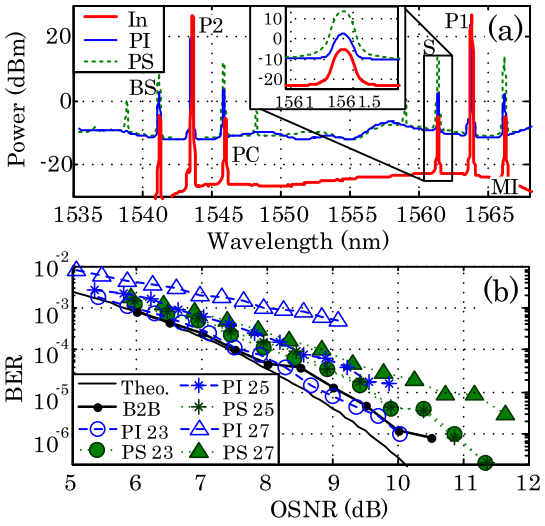

Fig. 4. (a) Optical spectra measured at the input of the PSA (In) and after the PSA, in PS and PI operation modes, with a wavelength resolution of 0.1 nm. (b) BER as a function of the OSNR, B2B, and after the PSA, operating in both PI and PS modes, with Pp values of 23, 25, and 27 dBm.

most correct one accounts for the combined noise properties of the signal and idler waves [15]. However, measuring the NF of the combined signal and idlers is difficult because the signal and idler waves have different OSNRs before the amplifier. This would require a detailed and thorough analysis, which is outside of the scope of this Letter. A more practical PSA NF definition considers only the input and output OSNR of the signal wave. Using this approach, NF values of −8.5, −8.7, and −5 dB in PS mode, and 3.4, 3.8, and 5.6 in PI mode were measured for P_P of 23, 25, and 27 dBm, respectively. Considering only the signal wave and given that the noise of the signal and of each idler wave is uncorrelated, a theoretical OSNR variation of −12 dB is expected for input waves impaired by quantum noise, or −6 dB in the case of the dominant noise source not being quantum noise [12,16]. For a reference bandwidth of 0.1 nm at a wavelength of 1550 nm, the quantum noise limit is −61 dBm [16]. However, the noise level of the input waves is much higher than this limit, as depicted in Fig. 4(a), because of the noise added by the EDFA after the OP. This noise is also uncorrelated, which enabled an improvement of the OSNR [2]. Hence, a maximum OSNR improvement of 6 dB would be expected in PS mode as long as the OSNR of the signal and idler waves was equal at the input to the PSA, which was not the case in these measurements. Recently, Malik *et al.* [12] showed that, when the quantum noise is not the dominant noise source, unbalanced signal-idler input OSNRs can enhance the OSNR of the signal [12]. In this experiment, an OSNR improvement of the signal wave of ∼9 dB was measured, at the expense of degrading the OSNR of the BS idler by ∼5 dB.

In summary, we experimentally investigated the influence of the signal and pump powers on the net gain of a four-mode FOPA-based PSA, showing that the gain is primarily determined by P_P and that P_S becomes important only when the amplifier starts to saturate.

We also demonstrated high-gain amplification (∼20 dB gain) of a 10 Gsymbol/s QPSK signal in the four-mode PSA, achieving an OSNR penalty lower than 1 dB at a BER of 10^{-3}. An additional gain of ∼12 dB was obtained when switching the amplifier from PI to PS operation modes, as well as an OSNR improvement of 5 dB, in contrast to the OSNR degradation higher than 3 dB in PI mode.

The reported gain and performance results are very encouraging and can be further improved by using HNLFs with better characteristics, and optimization of the pumps wavelength to minimize chromatic dispersion. Combined with the possibility of amplification outside of the erbium band, high gain and low noise properties make four-mode PSAs very interesting candidates to improve the performance of lightwave communication systems.

A. Albuquerque acknowledges funding from Fundação para a Ciência e Tecnologia (FCT) through the Ph.D. grant SFRH/BD/78425/2011.

References

1. C. Caves, Phys. Rev. D **26**, 1817 (1982).
2. Z. Tong, C. Lundström, P. A. Andrekson, C. J. McKinstrie, M. Karlsson, D. J. Blessing, E. Tipsuwannakul, B. J. Puttnam, H. Toda, and L. Grüner-Nielsen, Nat. Photonics **5**, 430 (2011).
3. P. Andrekson, in *Optical Fiber Communication Conference (OFC)* (Optical Society of America, 2012), paper OM3B.6.
4. S. Radic, Laser Photon. Rev. **2**, 498 (2008).
5. A. Albuquerque, B. J. Puttnam, M. Drummond, Á. Szabó, S. Shinada, N. Wada, and R. Nogueira, Opt. Express **21**, 22063 (2013).
6. C. Lundström, B. Corcoran, M. Karlsson, and P. A. Andrekson, Opt. Express **20**, 21400 (2012).
7. R. Slavík, F. Parmigiani, J. Kakande, C. Lundström, M. Sjödin, P. A. Andrekson, R. Weerasuriya, S. Sygletos, A. D. Ellis, L. Grüner-Nielsen, D. Jakobsen, S. Herstrøm, R. Phelan, J. O'Gorman, A. Bogris, D. Syvridis, S. Dasgupta, P. Petropoulos, and D. J. Richardson, Nat. Photonics **4**, 690 (2010).
8. T. Richter, B. Corcoran, S. L. Olsson, C. Lundström, M. Karlsson, C. Schubert, and P. A. Andrekson, in *European Conference and Exhibition on Optical Communication (ECOC)* (Optical Society of America, 2012), paper Th.1.F.1.
9. B. J. Puttnam, D. Mazroa, S. Shinada, and N. Wada, Opt. Express **19**, B131 (2011).
10. G. P. Agrawal, *Nonlinear Fiber Optics*, 4th ed. (Academic, 2006).
11. Z. Tong, A. O. J. Wiberg, E. Myslivets, B. P. P. Kuo, N. Alic, and S. Radic, Opt. Express **20**, 19363 (2012).
12. R. Malik, A. Kumpera, S. L. I. Olsson, P. A. Andrekson, and M. Karlsson, Opt. Express **22**, 10477 (2014).
13. C. J. McKinstrie, S. Radic, and A. R. Chraplyvy, IEEE J. Sel. Top. Quantum Electron. **8**, 538 (2002).
14. J. Kakande, A. Bogris, R. Slavik, F. Parmigiani, D. Syvridis, P. Petropoulos, D. Richardson, M. Westlund, and M. Sköld, in *Optical Fiber Communication Conference (OFC)* (Optical Society of America, 2011), paper OMT4.
15. Z. Tong, A. Bogris, C. Lundström, C. J. McKinstrie, M. Vasilyev, M. Karlsson, and P. A. Andrekson, Opt. Express **18**, 14820 (2010).
16. B. Corcoran, R. Malik, S. L. I. Olsson, C. Lundström, and P. A. Andrekson, Opt. Express **22**, 5762 (2014).